Self-Excited Aerodynamic Unsteadiness Associated with Passenger Cars

DAVID BOYD SIMS-WILLIAMS

Self-Excited Aerodynamic Unsteadiness Associated with Passenger Cars

Volume 1 of 2

David B. Sims-Williams

A Thesis submitted for the degree of Doctor of Philosophy

University of Durham

School of Engineering

2001

ABSTRACT

Passenger cars are bluff bodies and are prone to unsteady phenomena with scales comparable to the scale of the vehicle itself. This type of large-scale, self-excited unsteadiness is the subject of the present work. Aerodynamic unsteadiness can be important for two reasons. It can cause unsteady pressures and forces on the car and it can impact the time-averaged flow through the generation of Reynolds stresses.

A range of parametric two-dimensional bodies have been used in the development of novel experimental techniques and analyses and for CFD validation. Detailed investigations have been undertaken on the Ahmed model and on models of a Rover 200 passenger car in wind tunnels at Durham and at MIRA at scales of up to 40%. A method was developed which makes it possible to visualise periodic flow structures from measurements made sequentially in the wake or on the model surface.

Unsteady flows for fastback passenger cars were found to be much less periodic than for two-dimensional vortex shedding cases. Pressure fluctuations were significantly lower on the model surface than in the wake resulting in limited unsteady forces. Unsteady flow structures, Strouhal numbers and levels of unsteadiness were similar for the Rover 200 model with and without a backlight spoiler and for the Ahmed model, indicating that sharp corners do not have a dominant effect on unsteadiness.

Two principal unsteady structures were observed in the wake of the fastback shapes. A structure was observed at Strouhal numbers around 0.1 involving the alternate strengthening of the two c-pillar vortices in an antisymmetric mode. At Strouhal numbers in the range 0.3 to 0.6 an unsteady structure was observed consisting of the oscillation of the strength of the two c-pillar vortices in a symmetric mode. At the same time the location of the vortices oscillates in the vertical direction.

CONTENTS

VOLUME 1

VOLUME 2

TABLES

DECLARATION

I confirm that no part of the material offered has previously been submitted by me for a degree in this or any other University. If material has been generated through joint work, my independent contribution has been clearly indicated. In all other cases material from the work of others has been acknowledged and quotations and paraphrases suitably indicated.

Signed: ……

David Sims-Williams

Date: ……

COPYRIGHT

ACKNOWLEDGEMENTS

It is my pleasure to record my gratitude to my supervisor, Dr Robert Dominy, for the support, guidance, freedom and encouragement which he has offered me throughout this project.

I am indebted to the staff at the School of Engineering. I would like to mention in particular the efforts of Mr Brian Blackburn, Mr Ian Glassford and Mr Stuart Watson in the mechanical workshop, Mr Ian Hutchinson in the electronics workshop and Mr Trevor Nancarrow and Mr Michael Wilson for computer support.

I am grateful to the Engineering and Physical Sciences Research Council, who provided funding for this project, to MIRA, who made it possible for me to use their model wind tunnel and to Rover Group, who provided support in a number of ways. I would like to thank Dr Jeff Howell and Dr Geoff Le Good in particular.

This work has undoubtedly been furthered by discussions with Dr Jerry Ismael, Dr Alex White, Professor Li He and Dr David Gregory-Smith, for which I am grateful. I have also enjoyed discussions on a wide range of topics with Dr Anthony Ryan, Dr Sue Crossland and Paul Gordon.

Finally, I would like to thank my brother and my parents, for giving me so many opportunities.

1. INTRODUCTION

1.1 Summary

This thesis investigates large-scale aerodynamic unsteadiness typical of bluff bodies, particularly in the context of passenger vehicles which exhibit strong trailing vortices. Large-scale refers to the fact that the unsteady structures being investigated are of a similar scale to the vehicle itself, as opposed to "turbulence" which generally refers to unsteady flow structures which are small compared with the time-averaged flow structure. A key element to this work is the development of experimental techniques and methods of analysis that make it possible to investigate these unsteady flow structures, it is hoped that the techniques themselves may prove of benefit beyond the insight which they have provided in the present work.

This chapter aims to put passenger car aerodynamics in context by considering it from industrial and historical points of view before discussing vehicle flow structures. The role of computational fluid dynamics (CFD) for passenger cars is addressed. This chapter also provides a critical review of research into large scale unsteadiness around bluff bodies and concludes with detailed objectives for the present work.

Chapter 2 presents experimental details, ranging from the apparatus used to the formulation and validation of the techniques developed during this research. Chapter 3 presents the experimental results for the various two-dimensional and three-dimensional bluff bodies tested. The work on two-dimensional models was used to validate novel experimental techniques and also to facilitate the study of some geometric parameters. The three-dimensional models provide a flow more relevant to fastback passenger cars. Chapter 4 provides details of the CFD work undertaken; much of this involved cataloguing the sensitivity of the CFD results to the modelling parameters selected and assessing the ability of a commercial code and limited computational resource to analyse large scale aerodynamic unsteadiness. Chapter 5

seeks to tie together the various results obtained in this work and by others. Chapter 6 provides the main conclusions of the research and chapter 7 indicates some suggestions for future work.

1.2 Passenger Car Aerodynamics

1.2.1 Motivations

Before discussing the technical details of the aerodynamics of passenger cars, some effort will be made to put this research into context. Work in the field of passenger car aerodynamics involves the analysis and control of a number of different aerodynamic parameters (eg: drag, aerodynamic noise). This work is ultimately motivated by the consumer's requirements in terms of the production vehicle's performance, comfort etc. Table 1.1 categorises some of the different customer requirements (listed across the top of the table) and the aerodynamic parameters to which they relate (listed up the left hand side). Intersections in the matrix indicate specific requirements. Additionally, the customer will have requirements in terms of aesthetics, functionality and cost. These three requirements will generally constrain the aerodynamic development. The vehicle aerodynamicist must therefore work within the scope dictated by these additional constraints in order to achieve acceptable levels for the various aerodynamic parameters in table 1.1 (in other words, achieving a low drag by making the car 20 metres long would not be acceptable).

Fuel consumption is influenced by vehicle weight, engine efficiency, drive-train losses, rolling resistance and aerodynamic drag; the relative importance of these parameters depends on the type of driving. Because aerodynamic drag varies with velocity squared while drive-train and rolling resistance are approximately constant, fuel consumption at high speed will be primarily dictated by aerodynamic drag. For typical urban driving cycles the majority of fuel consumed goes to accelerating the

	Performance	**Handling**	**Mechanical well-being**	**Comfort**	**Visibility**
Drag	-consumption -emissions -top speed				
Lift, **Pitching Mom.**		-directional stability -braking			
Side Force, **Yaw, Roll Mom.**		-cross-wind sensitivity			
Unsteadiness		-unsteady forces		-wind noise -vibrations	-mirror vibration
Interior Flows			-cooling for: -engine -brakes etc.	-cooling -heating -ventilation	-de-misting
Surface Flows					-soiling -wiper lift

Table 1.1 – Motivations and areas of work in Passenger Car Aerodynamics

vehicle after applying the brakes, so the vehicle mass becomes the dominant parameter. Sovran (1983) analysed the influence of parameters, including aerodynamic drag, on fuel economy for the American Environmental Protection Agency (EPA) driving schedules. For a typical American car of the day he found influence coefficients (% change in fuel consumption for 1% change in drag) of 0.574, 0.341, 0.202 for EPA Highway, Composite and Urban driving cycles respectively. Data from Daimler-Benz AG, reported by Emmelmann and Hucho (1998a) for a more modern vehicle indicates influence coefficients of 0.42 for the Euromix cycle and 0.25 for the New European Driving Cycle (NEDC) which was introduced in 1996.

The relationship between aerodynamic lift and pitching moment and vehicle handling is discussed by Howell (1998) and by Howell and Le Good (1999). They

performed track tests in which the driver assessed the handling characteristics of a range of European passenger cars and of one car with a range of aerodynamic modifications. They found that vehicles with higher lift and nose down pitching moment handled less well in terms of straight line stability and high speed lane changing and they report similar observations for high speed cornering and braking. Nose down pitching moment leads toward oversteer (steering instability) at high speeds which is an obvious mechanism to explain their observations. However, the adverse effect on handling appears quite large relative to the magnitude of the lift forces involved. It has therefore been speculated that higher rear lift may be a symptom of flow structures which also involve low frequency unsteadiness or high cross-wind sensitivity and that this contributes to the adverse handling.

Steady state cross-wind sensitivity is tested as a matter of course in the development of passenger cars. The effect of transient cross-winds caused when passing road-side furniture (bridge abutments, tunnel exits etc.) can be simulated at full scale by driving a car past a line of fans. At least eight facilities of this type exist for use by the automotive industry (Klein and Jex (1980)). Unfortunately these tests can only be performed once a road-going prototype is available. Also, this approach does not lend itself to detailed aerodynamic work due to the inclusion of so many non-aerodynamic factors and due to difficulties in instrumentation, compared with conventional wind-tunnel tests. Transient cross-wind testing at model scale is a subject of academic research (eg: Ryan (2000), Dominy and Ryan (1999), Ryan and Dominy (1998), Docton (1997), Macklin et al (1996)). Peak yawing moments for this type of transient case are often higher than the steady state values measured for the same cross wind and vehicle velocities. This can be partially explained by the fact that, as the vehicle enters the cross wind, only the front of the vehicle experiences a side force. Furthermore, if the flow exhibits hysteresis which delays the onset of separation then low transient pressures are observed at the front of the leeward side of the model. For transient cross-winds it is potentially the driver's overreaction to the sudden yawing moment which constitutes the greatest danger.

Unsteady side forces have also been investigated by Nguyen et al (1997) and Pearse and Baker (1998) but for statistically stationary turbulent cross-wind conditions.

Unsteadiness inherent in the flow around passenger cars occurs over a sufficiently wide range of frequencies that it has several distinct effects. High frequency unsteadiness due to essentially "random" turbulence or potentially due to vortex shedding from appendages such as roof racks or radio aerials manifests itself as noise and this is now a major issue for automotive manufacturers. Some research (unattributable) has indicated that passengers particularly dislike aerodynamic noise, compared with engine or road noise. This suggests that, as the noise resulting from these other sources is reduced, at least equal reductions in aerodynamic noise must be achieved. Several industrial facilities have therefore been heavily modified for the purpose of aeroacoustics work (eg: Cogotti (1997), Kohl (1998)). The correlation between quiet-flow tunnel measurements and real on-road aerodynamic noise has been examined by Peric et al (1997). They found good agreement at frequencies above about 400hz but that the natural wind introduces significant additional noise at lower frequencies, particularly in the sub-audible range around 1hz where the majority of the incident wind turbulence is concentrated. Ukita et al (1997) used Computational Fluid Dynamics (CFD), model tests and road tests to examine "wind throb", a pressure pulsation inside the car near the lower limit of human hearing, due to an open sunroof. Watkins and Oswald (1999) examined the vibration of wing mirror glass which causes image blurring. They found that the glass vibration in the frequency range responsible for blurring was almost exclusively due to aerodynamic unsteadiness.

Large scale, low frequency (sub-audible) unsteadiness is the subject of this work. Frequencies below the lower threshold of human hearing (20hz) but above the suspension natural frequency (typically 1.0-1.5hz for European cars) can cause vibration, although this does not seem to be a significant problem. Frequencies resulting from unsteadiness in the vehicle wake near the vehicle suspension natural

frequency are obviously a potential danger, however. Aerodynamic effects at even lower frequencies are the suspected cause of handling instabilities observed on-road at high speed; no aerodynamic investigations have been published, however.

Although unknown to most drivers, the reduction of window soiling is actively pursued by vehicle aerodynamicists (eg: Yamane et al (1997), Uchida et al (1997), Koike et al (1999)). This is generally accomplished by using a spoiler at the top of the back window (often present to cause a separation and reduce rear lift) to direct a small stream of fluid down the back window. This provides a flow of clean air at a velocity of a few metres per second and hence avoids the adhesion of dirt from under the car which is suspended in the recirculation region behind the vehicle.

1.2.2 Historical Review

Although vehicle aerodynamics now encompasses several areas of work, historically, drag reduction was far and away the main concern of aerodynamicists. Figure 1.2.1 from Hucho (1998a) shows the gradual reduction in drag coefficient since 1900. Hucho (1998a) divides the history of road vehicle aerodynamics into four eras which he terms “Basic Shapes”, “Streamlining”, “Detail Optimisation” and “Shape Optimisation”.

In the first era, from about 1900-1925, attempts at improving the aerodynamics of road vehicles generally involved borrowing shapes from other fields (eg: marine). In some cases, the form of the entire vehicle body was made to resemble a torpedo or an airship, while in others, the shape of only part of the car was “borrowed”; this was so in the case of boat tails, where the back of the car was made to resemble the stern of a ship. Even in cases where the entire body was made to resemble an aerodynamic shape, the wheels, suspension and other ancillaries (sometimes the driver!) were unfaired, greatly increasing the total drag of the vehicle.

During the “Streamlining” era, which extended from about 1921 to 1974, the increased understanding of aerodynamics derived from the development of aircraft

was applied with some success to road vehicles. Initially, aerodynamicists produced designs which gave too little consideration to practicalities and which were too far removed from existing cars to be appealing to the public, but in time less extreme shaping on the part of the aerodynamicists meant that aerodynamics began to play a part in car design. A key step in this period, highlighted by Hucho and Sovran (1993), was the use of a blunt rear end. By tapering the rear end fairly sharply so that the flow approaches separation, and then truncating the body just ahead of the separation point, a vehicle of acceptable proportions can be achieved with reasonable drag. This is generally referred to as a "Kamm-back" although, according to Hucho (1998a) the patent literature indicates Koenig-Fachsenfeld as the inventor.

In the early 1970s the era of "Detail Optimisation" (discussed in detail by Hucho et al (1976)) began and it continues today. In this approach, the overall vehicle shape may be specified by a stylist and the aerodynamicist makes relatively minor modifications to the shape of individual details such as the shape of the A-pillar or the bonnet leading edge. Through the use of substantial wind-tunnel testing, various details of the body are optimised so that a significant overall drag reduction is achieved without changing the styling of the car.

Following the first oil crisis in the winter of 1973-1974, the motivation for reduced drag increased dramatically. This led to Hucho's era of "Shape Optimisation". The demand for large drag reductions allowed aerodynamicists to start with low-drag shapes, of the overall proportions required for the final vehicle, and modify them until they were suitable as a real vehicle. During this modification phase the progressive and inevitable drag increases from the original, low-drag shape are carefully monitored. Although Hucho (1998a) describes this era as ongoing, it appears that it is the stylists, rather than the aerodynamicists, who undertake the initial design of vehicles for most manufacturers today.

1.2.3 Flow Structures Typical of Passenger Cars

The shape of passenger cars is dictated largely by styling and ergonomics rather than by aerodynamic issues. For this reason, road vehicles are bluff bodies, exhibiting large separated wakes and multiple closed separation regions (eg: at the front of the bonnet). Unlike ships and aircraft, a road vehicle's drag is dominated by pressure drag and not skin friction; this makes understanding the flow structure a major issue. Separations are prone to unsteadiness and so the large separated regions typical of vehicle aerodynamics can be expected to lead to low frequency unsteadiness with length scales up to the scale of the vehicle itself.

For driving speeds for which aerodynamic considerations are important, passenger car Reynolds numbers (based on the square root of the frontal area) vary in the range of approximately 1.7×10^6 to 3.9×10^6; thus boundary layers are turbulent. Although maximum local Mach numbers may be much higher than the vehicle's speed, they are low enough for compressibility to be neglected.

The low aspect ratio (order 1) of a car means that the flow is fundamentally three-dimensional and the two-dimensional or quasi-three-dimensional approaches used for aircraft wings or turbomachinery blading are not appropriate. Slanted a-pillars and c-pillars produce separations at acute angles to the free-stream direction which lead to strong longitudinal trailing vortices in the vehicle wake, again producing a highly three-dimensional flow-field.

Figure 1.2.2 from Hucho (1998a) shows a schematic of the flow around a typical passenger car shape, illustrating a-pillar and c-pillar vortices. Ahmed et al (1984) provide a detailed study of the importance of the "backlight angle" (defined in fig 1.2.3) on the flow structure and hence on the drag of an idealised "fastback". Figure 1.2.4 (based on data from Ahmed et al (1984)) shows the variation of drag with backlight angle and illustrates the drag peak which occurs at the critical backlight angle; Figure 1.2.5 illustrates the flow structure at the critical backlight angle. The

high drag is almost entirely due to the low pressure on the backlight itself caused by the high turning of the flow as it reattaches before the end of this surface. At lower backlight angles the size of this recirculation zone is reduced, as is the minimum pressure within it, while at higher backlight angles the flow is no longer able to reattach within the length of the backlight and so the recirculation zone on the backlight merges with the upper recirculation bubble behind the base. This results in less flow turning in the wake and hence higher pressures on the backlight and the base. Nouzawa et al (1990), determined that notchbacks display a similar, but less extreme, sensitivity to the "apparent backlight angle", the angle between the top of the backlight and the trailing edge of the trunk deck. The flow structure for notchbacks in the high-drag (low apparent backlight angle) state contains trailing vortices similar to those for fastbacks, but also involves an "arch" vortex whose two ends terminate on the trunk deck (see figure 1.2.6 from Nouzawa et al (1990)) in place of the closed recirculation on the backlight of fastbacks.

Road vehicles operate, by definition, near the ground. The impact of the ground will be almost exclusively inviscid, with the exception of any boundary layer formed on the ground due to the acceleration of the air under the car. In the case of a real car driving in still conditions, the vehicle travels through stationary air and past a stationary road surface, hence, in the wind tunnel analogy, the ground plane should move past the model. Various methods have been used to simulate a moving ground plane including a moving belt, tangential blowing, symmetry, and distributed or discrete boundary layer suction. These techniques are compared and contrasted by Hucho (1998b), Carr(1997), Mercker and Wiedemann (1990), Carr and Eckert (1994) and numerous others. Unfortunately, ground simulation generally involves a trade-off between the correctness of the simulation and the convenience with which testing can be carried out; the convenience of the fixed ground board makes it a popular choice. Various studies have been performed to quantify the importance of the relative movement of vehicle and ground plane. Fago et al. (1991) looked at the importance of moving ground simulation for a very simple shape with a smooth

underbody in ground proximity and concluded that ground simulation becomes unimportant at ground clearances greater than 10% of the model height (typical road cars have ground clearances of more than 15% of the vehicle height). They also point out, however, that ground simulation can significantly affect the flow structure and hence have more far-reaching implications than might be expected. Howell and Goodwin (1995) tested an idealised car shape without wheels to assess the importance of ground simulation on parametric changes. They found that at realistic ground clearances the effects of backlight angle and even underbody roughness were essentially unaffected by ground simulation although the *absolute* values of lift and drag were. Howell and Hickman (1997) then undertook a similar investigation with a more realistic idealised car which included wheels and some cooling flow. They determined that fixed ground testing was sufficient to determine the effect of most geometric changes with the exception of changes which affect the flow around the wheels (eg: changes to the front bumper, undertray and engine bay airflow).

The definitive work on isolated rotating wheels is that of Fackrell (1974). The applicability of isolated wheel studies to road cars appears to be limited, however, due to Axon et al's (1999) discovery that, while rotation decreases the drag of an isolated wheel, the opposite is true of a wheel in a shroud. It is believed that this effect will be even greater when the wheels are mounted on a realistic car shape which will generally result in flow across the wheel (Axon et al's (1999) apparatus was essentially symmetric). Wickern et al (1997) also performed shrouded wheel tests and, although they found that rotation decreased wheel drag at zero yaw, when the wheel and shroud were yawed relative to the oncoming flow, rotation increased drag.

Road vehicle aerodynamics is further complicated by the various inlets and outlets for internal flows. In order to simplify external aerodynamic work, particularly with models, it is common to test without the presence of these internal flows either by

simply omitting them from the model or, in the case of a real car, by blocking them off.

1.3 CFD for Vehicle Aerodynamics

1.3.1 Flow Simulation Approaches

A brief description of types of flow solver is given here in order to provide some perspective before focusing on the approaches actually adopted for vehicle aerodynamics. A more thorough review of types of flow solver for vehicle aerodynamics may be found in Ahmed (1998).

The earliest fluid flow simulations were based on potential flow theory. Potential flow solutions can be obtained analytically and we need only solve for the areas of the flow field we are interested in (eg: the model surface). However, potential flow is inviscid and incompressible and without viscosity we cannot accurately model the flow around a car. For streamlined shapes potential flow solutions combined with numerical "boundary layer solvers" have proved useful. However, the large areas of separated flow present for a bluff body can only be handled if these regions are specified by the user explicitly, as if they were part of the body. Obviously this means that the user must have a detailed knowledge of the flow structure in advance of the simulation so the predictive ability of this approach is limited.

All other types of solver are based on a spatial discretisation of the flow domain through some sort of computational grid and the subsequent solution of equations at these discrete points. Equations of varying complexity may be chosen depending on what assumptions about the flow can be tolerated. For the Mach and Reynolds numbers of passenger car aerodynamics, the Navier-Stokes equations are appropriate and these may be simplified by the assumption of incompressibility given the low Mach numbers involved. In principle it is possible to solve these equations time-accurately and thereby achieve a very accurate prediction of the flow

around the car. This approach is called Direct Numerical Simulation (DNS). However, the computational grid must be fine enough and the time-step small enough to resolve all of the scales of the flow and with current computational power this is only possible at very low Reynolds number (eg: <5000). Sandham et al (1996) point out that the ratio of the problem geometry to the smallest turbulent eddies varies with $Re^{3/4}$ and hence the number of cells required in a three-dimensional domain will increase with $Re^{9/4}$. Extrapolating from a channel flow DNS by Sandham et al (1996) to a typical road vehicle case with Reynolds number of $7x10^7$ (based on the size of the domain) we find that we would require $2.5x10^{19}$ cells. Assuming that 50 bytes of memory are required to store variables for each cell, we would require $1.3x10^{21}$ bytes of RAM whereas current supercomputers only have $O(10^{11})$ bytes of memory (eg: Cray T3D 1996). Computers are becoming more powerful all the time so it is reasonable to assume that it is just a matter of time before such calculations are possible. We can use Moore's Law (equation 1.1) to estimate performance improvements with time:

$$P \propto B^t \tag{1.1}$$

(where P is performance, t is time in years and B is a constant)

Using Emerson's (1996) observed value of B = 1.56 (ie: performance doubles every 15 months) we find that our DNS will not be possible until circa 2048. For this reason the majority of simulations of passenger cars in Europe and the USA make use of turbulence modelling, whereby the mixing action of sub-grid eddies is modelled empirically and included through the Reynolds stress terms in the time-averaged Navier-Stokes equations. In Japan it seems to be common to use as fine a grid as possible and to simply ignore the effects of sub-grid turbulence (Ahmed (1998), eg: Tsuboi et al (1988), Nouzawa et al (1992), Yamane et al (1997)). Large Eddy Simulation (LES) provides a compromise between DNS and conventional turbulence modelling; in this case a grid is used which is able to resolve the larger

turbulent eddies so that the role of the turbulence model is reduced. Because this approach requires a fine grid and a time-accurate computation, it is computationally expensive but as computational power increases, LES should become increasingly attractive.

1.3.2 Strengths and Weaknesses of CFD for Vehicle Aerodynamics

CFD can provide distinct advantages over wind-tunnel or on-road testing. Arguably the greatest benefit of CFD is the fact that it makes a great deal of information about the flow field readily available, compared with wind tunnel tests. This is particularly true for unsteady flows where the experiments are particularly difficult. It also avoids the various complications associated with supporting stings, rolling roads and wind-tunnel blockage which compromise the experimental model of the real situation.

The main disadvantage of CFD currently is its accuracy. This is limited due to numerical errors resulting from the finite spatial and temporal resolution and due to the limited realism of turbulence models.

When CFD was first applied to vehicle aerodynamics, attempts were made to predict the overall forces on the vehicle as would be measured in a wind tunnel. The predictions were poor, however, and CFD received heavy criticism. Similar shortcomings were identified in the field of turbomachinery where CFD has been used extensively. Instead of attempting to predict absolute performance, turbomachinery designers moved to using CFD to predict the relative performance of different designs (eg: Casey (1996), Singh et al (1995)); provided that the designs are similar the predictions can be quantitatively accurate. This approach is gaining increasing recognition in the automotive sector (eg: Ahmed (1998)). Some care is required here for bluff body flows due to the possibility of critical geometries. These will generally depend on flow separations which are notoriously poorly predicted by CFD. The user therefore requires a good understanding of the flow structure in order

to assess whether the flow is close to a critical condition which might not be accurately predicted.

CFD is unlikely to rival wind tunnel testing for small geometric changes which are easily accomplished in the wind tunnel (eg: the fitting of a spoiler). Larger scale changes such as a change in the curve of a backlight are more difficult to accomplish on a physical model, however, and so may be easier to model with CFD. As mentioned earlier, CFD is an excellent tool for flow structure investigations.

1.4 Aerodynamic Unsteadiness

1.4.1 Importance of Aerodynamic Unsteadiness

Aerodynamic unsteadiness can be important both due to unsteady and time-averaged effects.

An unsteady flow will produce unsteady pressures, forces and moments on the vehicle. At high frequencies, pressure fluctuations manifest themselves as noise, and there is an ongoing effort in the motor industry to reduce aerodynamic noise. Slightly lower frequency fluctuations may produce vibrations which cause discomfort to the driver and passengers. The natural frequency of the suspension of passenger cars is typically in the 1.0-1.5hz region and if aerodynamic fluctuations occur in this zone they may have a significant effect on the handling of the vehicle. It has been speculated that even lower frequency aerodynamic fluctuations may make it difficult to maintain a straight heading at high speed. Current trends are for reduced vehicle weight and increased driving speed, both of which will increase the importance of unsteady forces and moments.

The second effect of unsteadiness is its impact on the time-averaged flow field. It is important to distinguish between the terms steady-state and time-averaged. The former implies that the flow is actually steady while the second allows for the flow

to be unsteady in a periodic or random fashion, the average being taken over an integer number of periods or over a time much larger than the time-scale associated with the unsteadiness. Non-linearity in the behaviour of fluids will produce differences between a steady-state and a seemingly identical time-averaged flow. Viscosity may appear to be an obvious source of non-linearity in that it provides a non-conservative force, but it is not a necessary ingredient; He (1996a) demonstrates non-linearity in the one-dimensional, unsteady, Euler equations for conservation of momentum and energy. The terms which quantify this difference between steady-state and time-averaged are generally referred to as the "Reynolds stress" terms in the time-averaged Navier-Stokes equations and, although these are often discussed in terms of small-scale unsteadiness associated with turbulence, large-scale unsteadiness is generally ignored.

An important example of the impact of unsteadiness on time-averaged quantities is the increase in pressure drag caused by unsteadiness in the wake of bluff bodies. Unsteadiness in the wake region will increase mixing between the wake and the surrounding, higher energy, fluid which will mean that the wake will close more rapidly. A higher rate of wake closure is synonymous with greater turning of the fluid and higher velocities near the rear of the body, both of which act to reduce the base pressure (the pressure on the rear of bluff bodies). The most straightforward illustration of this is the reduction in the base pressure of two-dimensional bluff bodies due to vortex shedding. Roshko (1954) provides base pressure measurements for a number of such bodies with and without splitter plates in the wake to inhibit vortex shedding. For a normal flat plate he found that a centreline splitter plate in the wake increased the base pressure from Cp = -0.84 to –0.54. A similar experiment was performed by Sims-Williams et al (1999) who, pragmatically, mounted the centreline splitter plate on a force balance in order to preclude any argument that the blockage of the splitter plate was increasing the base pressure on the normal plate. The force on the splitter plate was confirmed to be negligible, its maximum possible impact on the base pressure (corresponding to the accuracy of the force balance)

being less than $\Delta Cp = \pm 0.02$. It is logical to speculate that unsteadiness will also reduce the pressure at the rear of more complicated bluff geometries such as road vehicles. Unsteadiness can be expected at the upper rear of the vehicle where the flow separates and it will then lead to lower pressures on the backlight. This is particularly serious because low pressures here will not only increase drag but will also increase rear lift which, as discussed in section 1.2.1, has been linked to adverse effects on all aspects of vehicle stability at high speed (straight line stability, lane changing, cornering and braking) (Howell (1998) and Howell and Le Good (1999)).

CFD predictions have traditionally assumed steady-state flow. As discussed above, non-linear effects mean that this assumed steady flow is not equivalent to the time-average of the real (unsteady) flow. Although it is usual to account for effect of small scale unsteadiness through the use of a turbulence model, larger scale unsteadiness is generally ignored. This leads to significant but as yet unquantified errors in the prediction. CFD predictions can therefore be improved by identifying situations where a time-accurate simulation is appropriate and by determining the relevant time-scales to simulate. The need for unsteady simulations in order to obtain accurate time-averaged predictions for road vehicles is being recognised increasingly, eg: Gaylard et al (1998), Perzon et al (1999).

The importance of our own understanding of flows should also not be overlooked, since in many engineering situations we would ultimately hope to manipulate the flow to obtain some sort of performance improvement. Richardson, in a printed discussion of Carmody (1964), states that “it appears unlikely that a flow possessing distinct and large-scale periodic characteristics can be adequately described and understood in terms of a time-mean flow.”

1.4.2 Large Scale Unsteady Phenomena

1.4.2.1 Vortex Shedding from Two-Dimensional Bodies

Probably the best known unsteady phenomenon is vortex shedding. This phenomenon occurs in the wake of two-dimensional bluff bodies and has been the subject of several hundred if not thousands of academic papers, in fact McCroskey (1977) muses that "the problem of a bluff cylinder in a crossflow was invented to insure a perpetual livelihood for fluid dynamicists". The most referenced description of the mechanism of vortex shedding is that of Gerrard (1966). He describes how the shear layer separating from one side of a circular cylinder rolls up into a vortex and as this vortex grows it begins to draw fluid across from the opposite side of the wake, producing two effects. Firstly, the fluid approaching from the other side of the wake bearing opposite signed vorticity severs the vortex from the body (at which point we say that it is shed). Secondly, drawing fluid from the other side of the wake initiates the formation of a vortex on that side so that a repeating pattern of vortex shedding from opposite sides of the body is established. Vortex shedding is sometimes discussed in terms of moving separation points on the rear of the body; while this may be the case for bodies with rounded rear surfaces (eg: circular cylinders) it is by no means an essential ingredient. This is demonstrated theoretically by Abernathy and Kronauer (1962) and practically by the fact that bodies with fixed separation points (eg: normal flat plates) exhibit equally distinctive vortex shedding to those with moving separation points. Roshko's (1954) paper provides details of vortex shedding for a range of different two-dimensional bluff bodies including shedding frequencies and base pressures. He demonstrates the considerable impact of the shedding on base pressure by suppressing the shedding with a centreline splitter plate and hence increasing the base pressure on the body (as discussed in section 1.4.1). Morkovin (1964) reviewed a large number of papers on circular cylinder vortex shedding and hence mapped the effect of Reynolds number on flow structure, drag and Strouhal number S (see equation 1.2).

$$S = \frac{fd}{U} \tag{1.2}$$

where S is Strouhal number, f is frequency, d is diameter and U is free-stream velocity

Figure 1.4.1 (from Morkovin (1964)) shows the variation of drag coefficient and Strouhal period (1/S) with Reynolds number. Table 1.2 summarises the important Reynolds number regimes for circular cylinders based largely on Morkovin (1964) and Roshko (1993). The author has attempted to draw a fair consensus from the literature since considerable discrepancies exist with respect to the regime names and transition Reynolds numbers beyond $Re=1x10^5$.

Gerrard (1966) provides an explanation for the constancy of Strouhal number in the subcritical regime. He explains that the shedding frequency will decrease with the width of the wake and with the thickness of the shear layers. A wide wake means that the fluid must travel further to cross the wake and thick shear layers imply less concentrated vorticity and hence that more fluid must cross the wake to sever a vortex from the body. Increasing Reynolds number will reduce the formation length but will thicken the shear layers, thus producing no net effect on Strouhal number. The effects of Reynolds number on formation length and shear layer thickness are not independent, since the higher entrainment into thicker shear layers will erode the formation region.

Various researchers have defined specific dimensions and velocities in order to obtain universal Strouhal numbers which will be independent of the shape of the body. For instance Roshko (1954) defined a universal Strouhal number based on U_b (defined in equation 1.3) and wake dimension d' obtained from his notched-hodograph theory. This collapsed the data for a circular cylinder, normal flat plate and 90° wedge however Gerrard (1966) pointed out that this approach was unable to

Approximate Reynolds Number Range	**Regime**	**Description**
1 - 50		Laminar. Steady. Two-Dimensional.
50 - 200	Pure Karman Range	Laminar throughout. Perfectly periodic. Clear vortices. Two-Dimensional. This regime has provided a multitude of excellent flow visualisation photographs.
200 - $1x10^5$	Subcritical	Laminar boundary layers. Transition to turbulence in the separated shear layers moving forward with increasing Reynolds number. Nearly constant Strouhal number. Increasing three-dimensionality (with reducing span-wise scale).
$1x10^5 – 4x10^5$	Critical	Laminar separation bubble followed by turbulent reattachment and finally turbulent separation further around cylinder than for Subcritical regime. Loss of dominant periodicity. Rapid decrease in base suction and hence drag. Asymmetric flow possible due to formation of bubble on one side of cylinder only.
$4x10^5$-$3.5x10^6$	Supercritical	Recovery of periodicity. S~0.4 Formation of vortices is not clear. Splitter plate in wake has little effect indicating localised instabilities in each shear layer.
$3.5x10^6 – 1x10^7$+	Transcritical	Transition to turbulent boundary layers on front of cylinder without laminar separation bubble. S~0.3 Splitter plate in wake has some effect suggesting that the unsteadiness is antisymmetric again.

Table 1.2 – Circular cylinder Reynolds number regimes

collapse data obtained with different levels of free-stream turbulence. Griffin (1981) obtained improved collapse for a wide range of bodies by using a measured wake width (d') at the end of the formation region.

$$U_b = U\sqrt{1 - Cp_b} \tag{1.3}$$

where U is the free-stream velocity and Cp_b is the base pressure

The reason for the loss of periodicity in the Reynolds number range between $1x10^5$ and $4x10^5$ is not clear and has received surprisingly little attention. Bearman (1984a) puts forward the observation that separation lines which are discontinuous in the spanwise direction could remove the two-dimensionality of the flow and hence suppress two-dimensional shedding. He indicates that the "breakdown" of laminar separation bubbles at different circumferential positions along the span could remove sufficient two-dimensionality to have the same effect. He quotes a Reynolds number range of 8.5×10^5 to 3.5×10^6, within the "supercritical" range of table 1.2; this suggests that his separation bubble breakdown refers to the substitution of natural transition in place of laminar separation and turbulent reattachment. In order to explain the suppression of shedding from the start of the "critical" regime ($Re=1\times10^5$) through a similar mechanism, the reattachment after the laminar bubbles would have to occur at variable circumferential positions along the span.

1.4.2.2 Shedding from Three-Dimensional Bodies

As discussed, vortex shedding is a two-dimensional phenomenon and is significantly weakened by various forms of three-dimensionality (Bearman (1984a)). Figure 1.4.2 from Basu (1986) (but based on experiments performed by others) shows the variation in fluctuating lift coefficient for circular cylinders of different aspect ratios with one end in the free stream and clearly illustrates that the three dimensionality interferes with the shedding. Figure 1.4.3, also from Basu (1986), shows the local variation in fluctuating surface pressure coefficient along the span of circular

cylinders of different aspect ratios. This figure reveals that the impact of the flow around the free end on the shedding is not straightforward, since the fluctuating pressure is actually higher near the end although the three dimensionality decreases the overall level of fluctuating pressure. We should also note from this figure that the localised end effects extend about one diameter from the end of the cylinder. Although it would be naïve to assume conventional vortex shedding will occur from bodies of near unity aspect ratio, several researchers have found antisymmetric unsteady flow structures (which can be considered to be a form of vortex shedding) for geometries ranging from axisymmetric bodies to detailed passenger car models.

Cometta (1957) made hot-wire measurements behind a sphere and identified periodic unsteadiness up to a Reynolds number of $4x10^4$. He proposed the periodic shedding of inter-linking vortex loops, although his measurements were not actually sophisticated enough to provide any information about the structure of the unsteady flow field. Taneda (1978) performed an excellent set of flow visualisation experiments for a sphere. At Reynolds numbers between 10^4 and $3.8x10^5$ the wake forms a strong wave-like motion starting about two diameters behind the sphere; the Strouhal number for this unsteady motion is approximately 0.20. The wave motion seems to be contained in one plane (ie: antisymmetric), as illustrated by figures 1.4.4 and 1.4.5 from Taneda (1978). Above a Reynolds number of $3.8x10^5$ the wake takes on a new structure, illustrated in figure 1.4.6 from Taneda (1978), which remains unaltered up to a Reynolds number of at least 10^6. This new flow structure corresponds to a reduction in drag and to the development of a steady side force. No dominant frequencies were observed for the high Reynolds number flow regime although the structure was observed to rotate slowly around the axis of the sphere, changing direction of rotation at approximately S=0.004.

Roberts (1973) made measurements with two hot-wires in the wake of a disk as did Fuchs et al (1979) and Berger et al (1990), the latter also making some measurements in the wake of a sphere at Reynolds numbers below Taneda's (1978)

critical value of $3.8x10^5$. They all found periodic unsteadiness at a Strouhal number of 0.135 for the disk and Berger et al (1990) observed unsteadiness around Taneda's (1978) Strouhal number of 0.20 for the sphere. Smoke flow visualisation by Berger et al (1990) indicated a similar flow structure to Taneda's (1978) for both geometries and they describe it as originating from the rear of the recirculation region.

Roberts (1973), Fuchs et al (1979) and Berger et al (1990) positioned their probes several diameters downstream of the disk and made measurements with the two probes at the same radius but with various angular separations around the circumference. Cross-spectral analyses between the signals from the two probes indicated that the signals at S=0.135 were highly coherent at 180° angular spacing with coherence minima at 90° spacing. The signals from the two probes were in phase when the probes were within 90° angular spacing but abruptly shifted to be 180° out of phase at larger spacings (see figure 1.4.7). This indicates that the wake fluctuation is antisymmetric as observed by Taneda (1978). Berger et al (1990) performed similar measurements behind a sphere and report a similar flow structure although, surprisingly, they did not observe any significant cross-spectral phase distribution. Berger et al (1990) went on to vibrate the disk using a variety of modes and achieved "lock-in" with vibration in the nutation mode. They repeated their probe measurements and found near unity coherence the whole way around their traverse with a phase distribution which exactly mimicked the circumferential position of the probe (see figure 1.4.7), indicating helical "shedding" from the disk. They concluded that the unexcited structure was also helical despite the fact that their results for the unexcited disk clearly indicate that it was antisymmetric.

Hamidy (1991) made unsteady measurements behind a very idealised square backed passenger car model in ground proximity at Reynolds numbers between $8x10^4$ and $4x10^5$. He reports vortex shedding from the sides of the base at a Strouhal number of 0.23 despite the presence of a horseshoe and trailing vortex system. Figure 1.4.8

illustrates schematically the shed vortices (ignoring the time-averaged horseshoe and trailing vortices). Duell and George (1992 and 1999) also investigated unsteady wake flows behind simple square backed bluff bodies in ground proximity at similar Reynolds number ($2.3x10^5$ based on base dimension), however, they did not observe any unsteadiness near a Strouhal number of 0.20. They did observe other unsteady phenomena which will be discussed later.

As discussed in section 1.2.3, the slanted rear windscreen of most passenger cars produces a time-averaged wake dominated by a pair of counter-rotating vortices originating from the c-pillars. Unsteady flow structure investigations for axisymmetric geometries without base slant cannot therefore be expected to be applicable for the majority of passenger cars. Morel (1980) provides a valuable investigation into the effect of base slant. He tested a cylinder whose axis was aligned with the airflow with an elliptic nose and a range of base slant angles at a Reynolds number of $9.4x10^4$. When the base slant angle was less than 48° to the horizontal he obtained a flow structure with strong trailing vortices similar to that of fastback passenger cars. At higher backlight angles this structure was replaced by a simple separation with higher base pressure and consequently lower drag. For base slant angles above the critical value, he observed clear periodicity which he describes as “shedding” although, at sub-critical base slant angles, only a very indistinct spectral hump was visible, centred around S=1.25. The shedding occurred at S=0.52 at a base slant of 43° and decreased in frequency as base slant was increased to S=0.20 with a vertical base. Xia and Bearman (1983) continued on from Morel’s work, confirming and extending his results. In particular, they examined the nature of the shedding using cross-spectral analysis between two probes and smoke flow visualisation. Their cross-spectral results indicate that the shedding was antisymmetric for the vertical base although their flow visualisation indicates that vortices were sometimes shed simultaneously from both sides, possibly in the form of vortex rings. With a slanted base, the vortices appear to be shed antisymmetrically from the top and bottom of the slant with the vortex on the

trailing edge of the slant being more intense but correlated over a smaller angular distance. Unfortunately their cross spectral results are for a half circumference only so it is not strictly possible to rule out some form of pseudo-helical shedding altogether. Morel (1980) and Xia and Bearman (1983) both found that the intensity of the shedding seemed to be greatest at a slant of 70°, probably because a small inclination of the base to the vertical imposed a fixed orientation for the shedding, as concluded by Xia and Bearman (1983). Xia and Bearman's (1983) flow visualisation shows that vortices on the trailing edge of the slant are shed from very close to the body, compared with geometries without base slant where the vortices are shed from the back of a recirculation region; this probably accounts for the compactness of the vortices shed from the trailing edge.

Goh (1994) tested a scale model of a real fastback car at a Reynolds number of $6.7x10^5$ based on width. Goh (1994) reports essentially two-dimensional vortex shedding from the top and bottom of the base at a Strouhal number of 0.25 (based on the base height – this is estimated to be equivalent to $S\approx0.29$ based on the square root of the frontal area). Unlike Hamidy (1991), Goh (1994) observed pressure fluctuations on the model base at the shedding frequency. The vortex shedding from the base produced a perturbation of the trailing c-pillar vortices. In and around the trailing vortices, horizontal, cross flow velocity fluctuations were found at the shedding frequency but there were no corresponding vertical velocity fluctuations. The cross flow velocity fluctuations at the shedding frequency were coherent but out of phase at the two cores. Goh (1994) interpreted these results to indicate that the c-pillar vortices were moving in and out together in a horizontal plane due to the shedding of transverse vortices from the base. Figure 1.4.9 shows Goh's (1994) schematic of the vortex motion. This interpretation is based on the motion of the vortex core appearing as a fluctuating horizontal velocity and overlooks the impact of displacing the streamwise vorticity. A probe located at the core of a trailing vortex will see only axial velocity; if the vortex is displaced outwards, the probe will see a horizontal velocity as the vortex moves but will then see a downwards velocity

since the probe will no longer be at the vortex core. The relative importance of the second effect will be $\zeta h_b/4\pi SW$ (ζ is vorticity non-dimensionalised by model width W, S is Strouhal number based on base height h_b and we assume that vorticity is made up of equal contributions from horizontal and vertical shear). This parameter was estimated to be around 0.5 for Goh's case so the proposed side to side meandering of the vortices would have produced a vertical velocity fluctuation of half the amplitude of the observed horizontal fluctuation. Goh's observations could have been produced by the movement of the vortex cores following an inclined elliptic pattern in a symmetric manner. Bearman (1997) further confirms the presence of vortex shedding from the base of this model using particle image velocimetry (PIV).

Nouzawa et al (1992) undertook unsteady experiments and simulations on an idealised notchback at a Reynolds number of $3.1x10^5$ (based on the square root of the frontal area). They found periodic unsteadiness for the critical afterbody geometry (corresponding to maximum drag) including lift and drag fluctuations. The unsteady mechanism which they describe consists of the arch vortex on the trunk deck (see figure 1.2.6) "intensifying alternately just like a Karman vortex and separating from the rear window…". This suggests a mechanism which is symmetric between the two sides of the model although their limited wake measurements suggest that the fluctuation is antisymmetric between the two sides. The frequency observed corresponds to a Strouhal number of 0.46, based on the square root of base area (it is not clear what dimension would be most appropriate to use in the calculation of Strouhal number in this case). For lower apparent backlight angles they found evidence of periodic unsteadiness in the lift component only (at a slightly lower frequency) while at higher apparent backlight angles no periodic unsteadiness was observed.

Ishihara and Takagi (1999) made unsteady pressure measurements in the wake of a scale model of a real notchback car using a rake of 252 simple total pressure probes.

Although they found pressure fluctuations of ±0.3 dynamic heads one half car length behind the model, they did not identify any periodic frequencies or unsteady flow structures.

1.4.2.3 Recirculation Bubble Pumping

In addition to observations of a shedding phenomenon, Berger et al (1990) observed an axisymmetric unsteady mode within the recirculation region behind a disk (at S=0.05) and a sphere. Flow visualisation revealed axial oscillations of the point of wake closure which led them to term this the "pumping" mode. The results of Fuchs et al (1979) show a spectral peak at around S=0.04 for their disk and indications are that this was the axisymmetric pumping phenomena. Duell and George (1992 and 1999) also found similar pumping of the free stagnation point at S=0.07 behind their square backed bluff body. Because of the proximity of the ground plane, their pumping mode is actually antisymmetric in the vertical plane, based on the approximate anti-phase of fluctuating pressures on the top and bottom of the model base at the pumping frequency.

1.4.2.4 Shear Layer Instability

At the sides of the recirculation region, Berger et al (1990) observed an instability in the shear layer at a Strouhal number of 1.62 (based on disk diameter) which seems likely to be due to a Kelvin-Helmholtz shear layer instability as reviewed by Roshko (1993). Care should be taken in the use of Strouhal number here because Roshko (1993) reports that, based on observations with circular cylinders, the Strouhal number for this type of instability will scale with $Re^{1/2}$. Although this type of high frequency shear layer instability was not discussed by Taneda (1978) it is clearly visible in his smoke flow visualisation at sub-critical Reynolds number (see figure 1.4.10). Berger et al (1990) describe the phenomenon as the shedding of ring vortices (illustrated schematically in figure 1.4.11) but point out that the structure is not particularly coherent (coherence levels between probes were around 0.25-0.3)

and smoke flow visualisation showed rings often becoming inclined and linking up with each other.

Duell and George (1992 and 1999) also found a shear layer instability (at S=1.157). However, they report that unsteady pressures measured on the model base were essentially out of phase between the two sides at this frequency, which argues against the shedding of axisymmetric ring vortices described by Berger et al (1990). Duell and George (1999) hypothesise a pseudo-helical shedding mechanism which involves vortices being shed along the two sides of the model alternately with inclined vortices along the top and bottom edges of the model connecting the vortices from the two sides in order to satisfy Helmholtz's second vortex theorem which prevents a vortex filament from terminating within the fluid (eg: see Milne-Thompson (1948)). This unsteady structure is illustrated schematically in figure 1.4.12. It should be noted that they describe the pseudo-helical shedding occurring from the edges of the model itself whereas Berger et al (1990) describe their shedding type structure originating at the rear of the recirculation region.

Duell and George (1992, 1999) made hot-wire measurements in the shear layer enclosing the recirculation region behind their model and found that the dominant frequency seemed to decrease in steps of factor two as they moved further downstream. They concluded that this was due to repeated vortex pairing. Various researchers (eg: Brown and Roshko (1974)) have observed an initial instability in planar shear layers at low Reynolds number which produces laminar waves and then discrete two-dimensional (line) vortices. Winant and Brownland (1974) were the first to observe pairs of these vortices to roll around each other and merge to form larger vortices at twice the initial spacing. They observed repeated vortex pairings until the pairing was constrained by the dimension of the domain. It is not difficult to envisage a similar pairing mechanism for ring vortices but it is not clear how pairings could occur for the pseudo-helical structure of Duell and George (1992, 1999) since adjacent turns of the helix are unable to roll around each other. The presence of vortex pairing could therefore be considered to provide an argument

against the pseudo-helical structure that they propose. The shedding of inclined ring vortices or linked inclined rings (illustrated schematically in figures 1.4.13 and 1.4.14 respectively) would provide a structure better able to undergo vortex pairing. This structure would also be closer to Berger et al's (1990) ring vortices but would account for the out-of-phase pressures observed on the model base by Duell and George (1992, 1999).

Duell and George (1999) go on to conclude that vortex pairing in the shear layer repeats so that vortices reach the free stagnation point and are shed into the intermediate wake at the pumping frequency. The possibility of linking the pumping mode to the shear layer instability is attractive. However, the lowest frequency they actually observed in the shear layer was 2.27 times the pumping frequency and, because the shear layer vortices are antisymmetric in the horizontal plane whereas the pumping mode is axisymmetric in the horizontal plane, the shear layer frequency should be half the pumping frequency. Slightly more than two additional pairings would therefore be required in the final 13% of the shear layer (the distance between the most downstream hot-wire measurement and the free stagnation point) whereas the average axial distance per pairing up to this point is 29% of the recirculation distance and we would expect later pairings to require more rather than less space due to the larger size of the vortices involved.

1.4.2.5 The Multiple Longitudinal Vortex Theory

Wang et al (1996) used Particle Image Velocimetry (PIV) to obtain instantaneous plots of secondary flow vectors and vorticity for a typical fastback passenger car. Their plots did not show the familiar pair of c-pillar vortices found in steady-state measurements but instead showed several smaller, more concentrated vortices scattered in the wake. Averaging several PIV snapshots caused the conventional c-pillar vortices to return. Bearman (1997) concluded that the time-averaged vortices usually attributed to the c-pillars are actually the sum of many small vortices originating from various features on the car. The apparently random variation from

one PIV plot to the next must therefore imply that the individual vortices are generated in an unsteady manner or that they behave in a very unsteady fashion after being generated.

It seems more plausible that the vortices observed by Wang et al (1996) are generated from the c-pillar, as in the traditional understanding, but that the separation is unsteady, thereby accounting for the individual instantaneous vortices. The longitudinal vortices found in the wake of passenger cars are similar to those generated by delta wings at incidence, and much work has been undertaken in this field. Squire et al (1963) observed small longitudinal vortices of the same sense as the main trailing vortices in their study of delta wings at high subsonic and supersonic Mach numbers, their flow structure is depicted in fig 1.4.15. Smoke and laser sheet flow visualisation by Payne et al (1991) seems to confirm the existence of these sub-vortices for delta wings at low speed. The observations of Squire et al (1963) and of Payne et al (1991) were essentially time-averaged and they reported that the position of the sub-vortices did not change with time. Squire et al attribute the formation of the vortices to a shear instability, presumably of the type later described by Brown and Roshko (1974) for simpler plane shear layers. Gad-el-Hak and Blackwelder (1985) observed another type of discrete vortex in the formation of trailing vortices by seeping dye out of the leading edge of delta wings in a tow tank. They found that vortices were periodically shed along the entire leading edge, as illustrated in figure 1.4.16. These vortices then underwent vortex pairing, similar to that discussed by Winant and Browand (1974). Initially they were not confident that the main vortices were simply the result of several pairings because the dye became too diffuse to make clear observations after repeated pairings but they eventually came to exactly that conclusion (Gad-el-Hak and Blackwelder (1987)). It is somewhat surprising that Gad-el-Hak and Blackwelder (1985) did not observe the discrete vortices of Squire et al (1963) and Payne et al (1991) given that their sweep angle was similar to that of Squire et al (1963) and their Reynolds and Mach numbers were similar to those of Payne et al (1991). It is possible that the discrete

vortices first observed by Squire et al (1963) could actually be formed periodically (as for the full length periodic vortices of that Gad-el-Hak and Blackwelder (1985)) but always in the same position, thereby accounting for their appearance in steady observations. In the wake at any one time, therefore, some of these vortices would be present and some would be too weak to observe. This would provide PIV snapshots similar to those observed by Wang et al (1996). The constant-position discrete vortices observed by Squire et al (1963) have not been reported in steady observations of the trailing vortices behind road cars. It could be that perturbations from the flow around the front of a road car causes them to move up and down the c-pillar. This would further contribute to the apparently random distribution of instantaneous vortices observed by Wang et al (1996).

1.4.2.6 Longitudinal Vortex Breakdown

For longitudinal trailing vortices above a critical strength, a phenomenon known as "vortex breakdown" occurs. Upstream of breakdown the vortex is essentially steady and axisymmetric and its structure varies only slowly in the axial direction; at breakdown the axial component of velocity decelerates rapidly and the flow diverges around a region of reversed flow. Figure 1.4.17 from Lambourne and Bryer (1961) shows the two main forms of breakdown over a delta wing. At the top of the photograph is a spiral breakdown while at the bottom is a bubble breakdown. In the case of the bubble breakdown, the rear of the bubble is open and sheds fluid periodically. In the case of the spiral breakdown the vortex transforms into a large diameter spiral which breaks up itself after one or two turns. The sense of the spiral is opposite to the rotation of the vortex, as shown more clearly in the computational result of Tromp and Beran (1996) in figure 1.4.18. There is some evidence that the two forms of breakdown are in fact opposite extremes of the same phenomena. For instance, Payne et al (1991) observed what appeared to be vortex rings shed from the rear of a bubble breakdown and concluded that as the pitch of the spirals in a spiral breakdown becomes very small the spirals become indistinguishable from rings and periodic shedding.

In most investigations into breakdown, vortices were generated with a swirl angle distribution given by equation 1.4 using a swirl-vane apparatus, allowing the critical vortex strength for breakdown to be determined.

$$\phi = \arctan\left(\frac{\upsilon R_o}{r}\left(1 - e^{-\left(\frac{r}{R_o}\right)^2}\right)\right) \qquad (1.4)$$

where ϕ is swirl angle, r is radius, ν is a non-dimensional vortex strength and R_o is an arbitrary reference dimension.

Hall (1972) reviewed the work to date and found that the critical peak swirl angle varied with axial pressure gradient but was generally above 40º and could be as high as 50.5º, as reported by Harvey (1962) for a parallel duct. Tromp and Beran (1996) quoted a critical vortex strength of 1.53 which, making logical assumptions about their non-dimensionalisation, is equivalent to a peak swirl angle of 44º. Much of the work on vortex breakdown has been performed at low velocities in order to aid flow visualisation but Hall (1972) notes that the phenomenon is fairly independent of Reynolds number, citing the work of Lambourne and Bryer (1961) at Reynolds numbers which are similar to those appropriate for passenger cars.

Figure 1.4.19 shows the breakdown observed by Harvey (1962), the Reynolds number was approximately $4x10^4$ based on vortex length before breakdown and upstream disturbances were minimised to guarantee laminar flow. For this reason the breakdown in this case occurs in two parts: first a closed bubble forms in the core region provoking transition to turbulent flow, the classical vortex structure is then re-established for a short length before the final, bubble type, breakdown occurs (see figure 1.4.19 from Harvey (1962)).

Sedney (1979) assessed that the trailing vortices behind an idealised passenger car could reach the critical strength required to exhibit vortex breakdown, although his interest was only in steady state implications.

1.4.2.7 Longitudinal Vortex "Structured Disturbance"

Trailing vortices have been observed to exhibit an intermittent flow structure which we will term simply a "structured disturbance". This has been observed experimentally by Bandyopadhyay et al (1991) behind a vortex generating apparatus and by Goh (1994) behind a passenger vehicle model. The structured disturbance consists of the intermittent ejection of low momentum fluid from the vortex core in the radial and tangential directions. Because this phenomenon is intermittent rather than periodic it has proved difficult to examine in detail.

1.4.2.8 Wind Throb

As mentioned in section 1.2.1, "wind throb" is a pressure pulsation inside the passenger compartment near the lower limit of human hearing which is caused by openings such as windows or a sunroof. Unsteadiness in the flow around the outside of the car excites a cavity tone inside the passenger compartment. In their study of wind throb, Ukita et al (1997) observed vortices periodically breaking away from the leading edge of an open sunroof and hence exciting the natural frequency of the passenger compartment cavity. Wind throb provides an interesting challenge to model at reduced scale since the external flow excitation frequency and internal resonant frequencies will scale differently with velocity and model size.

1.4.3 Summary of our Understanding of Unsteadiness for Road Vehicles

For square backed geometries, including trucks and vans as well as estate cars, indications are that we can expect some form of vortex shedding from the sides of the base and largely axial pumping of the free stagnation point. There is some discrepancy about the expected Strouhal number for the shedding but the majority of work indicates S ≈ 0.2 based on base dimension. Pumping seems to occur between S

= 0.04 and S = 0.07. In some cases helical structures have been proposed but the evidence is not convincing. A Kelvin-Helmholtz instability in the shear layer has been observed at S > 1 for models but the Strouhal number of this phenomenon should not be expected to be independent of Reynolds number. Indications are that a critical Reynolds number could exist around $3.8x10^5$; virtually all of the work reviewed was performed below this value so these observations must be viewed with some trepidation (the Reynolds number for a car on the motorway will be greater than $1x10^6$).

The flow around cars with sloping c-pillars is very different from that around square-backs due to the presence of the c-pillar trailing vortices. All research indicates that the c-pillar vortices eliminate unsteady shedding from the sides of the car and unsteady structures generally seem to be much harder to identify. Some researchers do report periodic unsteadiness which usually involves vortices across the backlight or trunk deck. Some unsteady phenomena local to individual trailing vortices have been investigated such as vortex breakdown and the structured disturbance. Different methods of formation of the trailing vortices have been discussed, including unsteady mechanisms, but no consensus exists.

1.5 Scope and Objectives of This Investigation

1.5.1 Scope

This work will investigate the unsteady flow around several bluff bodies. These will include a set of simple two-dimensional bodies, the Ahmed idealised passenger car geometry and scale models of a real car, the Rover 200. The work will be confined to the investigation of self-excited, large-scale periodic structures. Externally imposed excitation such as fluctuating ambient wind conditions will therefore not be considered, nor will structures whose length scale is much smaller than the size of the body (turbulence). Spectral methods will be used so the analysis of unsteadiness will be from a periodic viewpoint. In many cases unsteady flow structures include

both periodic and aperiodic elements. This can be considered to consist of an amplitude and/or frequency modulation of an essentially periodic flow.

1.5.2 Objectives

Subject to the qualifications given above, the main objectives of this work are as follows:

-To develop experimental techniques for the investigation of large scale aerodynamic unsteadiness for passenger cars.

-To develop our understanding of the time dependent air flow around passenger cars, concentrating in particular on periodic structures in the wake.

-To determine the applicability of idealised and scale model testing for the investigation of large scale unsteadiness.

-To provide some insight into the impact of design parameters on self-excited large scale aerodynamic unsteadiness.

-To provide time-accurate experimental data for CFD validation and to investigate the ability of CFD to predict large scale unsteadiness.

-To investigate the impact of large-scale unsteadiness on CFD simulations.

2. EXPERIMENTAL TECHNIQUES

2.1 Apparatus

2.1.1 Wind Tunnels

2.1.1.1 Durham 0.85mx0.55m Tunnel

The Durham 0.85mx0.55m tunnel is of the open jet, open return design. The tunnel consists of an upstream centrifugal fan followed by a wide-angle diffuser, settling chamber and nozzle. Either a fixed ground board or a rolling road assembly can be positioned downstream of the nozzle, although all of the work presented here was performed with a fixed ground board. The wide angle diffuser includes a number of splitter vanes in order to prevent diffuser stall. Screens are used in the settling chamber to control flow uniformity and free-stream turbulence. Most tests were performed at the maximum tunnel speed of approximately 27m/s. Flow uniformity is within 1% on velocity and 2% of dynamic head on total pressure in the region of the model. The boundary layer was traversed at the model position using a flattened total pressure tube (dimension ~0.2mm) and the displacement and momentum thickness were found to be 4.4mm and 3.8mm respectively. These thicknesses correspond to between 12% and 18% of the ground clearance of the models used.

Some modifications to the arrangement of screens in this tunnel were carried out early in the project in order to improve flow uniformity. Originally, the most downstream screen was very close to the contraction so the upstream potential influence of the contraction produced low velocity flow through the screen near the edge of the tunnel. This reduced the loss across the screen in this region resulting in strong jet wakes at the periphery of the working section. Removing this screen eliminated the jet wakes as shown in figure 2.1.1 (note that these measurements were made with the ground board removed from the tunnel). A new screen was later added further upstream in the settling chamber in order to reduce the turbulence

intensity, this had no significant effect on the flow uniformity in the working section.

Turbulence intensity (u'_{hw}/U) in the empty working section is approximately 5%. Figure 2.1.2 shows a typical spectrum for the velocity recorded by a hot-wire in the empty working section at full speed. Quite a strong tunnel characteristic frequency is apparent centred at 15hz. This frequency is presumably due to a Kelvin-Helmholtz (K-H) instability in the tunnel jet shear layer since its Strouhal number appears to scale with $Re^{0.5}$ (as described by Roshko (1993) for K-H instabilities) and it is in the correct range based on an estimation of the shear layer momentum thickness and equation 2.1 (from Roshko (1993)). The frequency band between 13hz and 17hz contributes approximately 2.4% to the turbulent intensity in the empty tunnel (calculated as described in section 2.3.1.2) if we extend the band to 10hz to 20hz the contribution of this peak to turbulence intensity increases to 3.4%. A very sharp spectral peak is present at 31hz and this has been attributed to electrical noise due to its sharpness and because its frequency was always invariant to within less than 0.4hz. Weaker additional characteristic frequencies are observed at 116hz and 174hz. The rotational speed of the fan is 20hz and the blade passing frequency is 240hz however neither of these frequencies were observed in the working section.

$$f_o = 0.017\frac{U}{\theta} \qquad (2.1)$$

where f_o is the frequency of the most unstable K-H wave, U is the jet velocity and θ is momentum thickness.

Garry et al (1994) investigated the importance of the proximity of the downstream end of the test section to the model and recommended a distance of 4 times the base dimension (square root of base/frontal area) or more. The configuration of the Durham tunnel permits a long ground-board and there is no collector so this distance

is easily exceeded. The proximity of the start of the test section to the model is another important consideration. The distance between the end of the contraction and the front of the vehicle in a number of industrial automotive facilities was reviewed (based on data published by Kuenstner et al (1992), Mercker et al (1997) and Hucho (1998b)) and was found to vary between about 1 and 3 times the base dimension. On the other hand Ahmed et al (1984) positioned their model some 4.8 base dimensions downstream of the nozzle in their tunnel. Hucho (1998b) reports pressures measured on the tunnel floor of the BMW full size wind-tunnel with different longitudinal vehicle positions; based on this work a model position 2.2 base dimensions downstream of the contraction seems sufficient to avoid interaction between the flow in the nozzle and around the model. Although Garry et al (1994) were interested only in the proximity of the end of the test section, a careful inspection of their results suggests that the distance between the start of the test section and the front of the model begins to have an effect when this is less than about 2.5 base dimensions. The models in the Durham tunnel were positioned approximately 4.5 base dimensions downstream of the contraction.

Blockage correction was not used for a number of reasons. Firstly, the aim of this work is flow structure understanding rather than the precise quantification of absolute body forces. Also, it is not clear that the correction methods routinely used for forces are appropriate for scaling frequencies so it was felt better not to risk confusing the results by applying an unreliable correction factor. It should be noted that none of the models exceeded a blockage of 10% of the cross-sectional area of the nozzle exit.

2.1.1.2 MIRA Model Wind Tunnel

The model wind tunnel at the Motor Industry Research Association has an open jet working section of 2mx1m. The tunnel is driven by a downstream 12 blade axial fan. The return is best described as semi-open since it is not ducted but the building enclosing the tunnel is not large compared with the tunnel itself. The tunnel was

operated in fixed-ground configuration for the work described here and step suction at the start of the working section was used to minimise the boundary layer on the tunnel floor. A tunnel velocity of around 25m/s was used for the majority of the work presented in this thesis. In the absence of a model in the tunnel, the velocity in the working section is uniform to within about 2% and turbulence intensity in the region occupied by the model is approximately 1%, as reported by Brown et al (1998). Figure 2.1.3 shows the spectrum for a hot-wire in the empty working section of the tunnel which agrees with Brown et al's (1998) turbulence intensity of 1%. Spectral peaks are observed at 6.3hz, 50.0hz and between about 80 and 90hz. The spike at 50hz is assumed to be due to mains electrical noise. The reported fan rotational speed was 8.8hz and the blade passing frequency was therefore 105hz. Although the frequencies observed in the working section are similar to the fan frequencies their ratio is 13.5 not 12 so they do not appear to be due to the fan.

2.1.1.3 Durham (Plint) 0.46mx0.46m tunnel

The Durham Plint tunnel has a closed working section 1.22m long and 0.458mx0.458m in cross section. The tunnel is driven by an upstream 36 blade centrifugal fan and has an open return. Tests were performed at the maximum tunnel speed of approximately 21m/s. The turbulence intensity was measured to be less than 0.25%. The fan rotational speed is approximately 17hz and the blade passing frequency is therefore 600hz.

2.1.2 Wind Tunnel Models

2.1.2.1 Two-Dimensional Symmetric Models

A family of two-dimensional symmetric models were used to investigate vortex shedding. The models were all of the same basic shape (illustrated in figure 2.1.4) with differing dimensions given in table 2.1. End plates were used in order to encourage two-dimensional flow, although, particularly in the case of the "Docton" model, the aspect ratio was not sufficient to expect this to be achieved. The models were constructed from thin (~3mm) plastic sheet and had pressure tappings located around both sides at mid-height. The tappings were made from 17swg stainless

tubing (1.1mm bore) and were all manufactured to be of identical length (18mm) to facilitate transfer function correction (discussed in section 2.2.5).

Model	Length	Width	Height	Corner Radius	Tappings
Docton	522	194.5	146	55	74
PARAD1	522	132.3	360	37.5	70
PARAD2	557	132.3	360	55	74

Table 2.1 - Two-dimensional symmetric models

2.1.2.2 Racing Car Wing/Gurney Flap Model

Some testing was undertaken on a racing car wing fitted with a Gurney flap, as illustrated in figure 2.1.5. Although this geometry is obviously not directly related to passenger cars, some of these results have been included in this thesis because they provide a good illustration of the capacity of some of the experimental techniques developed. The wing was mounted in the Durham Plint 0.46mx0.46m tunnel from one end on the Plint 3-component balance. The balance was locked in position except during force measurements. The wing had a chord of 214mm and a span of 430mm and used endplates just off the walls of the tunnel to minimise end effects. The Gurney height was 10mm (4.6% chord) which is a typical height for racing car Gurney flaps. The wing had 34 pressure tappings at mid-span which were relayed via hypodermic tubing embedded in the wing.

2.1.2.3 Ahmed Models (three-dimensional)

The Ahmed form (first used by Ahmed et al (1984)) is the most popular idealised car geometry. Figure 2.1.6, (reproduced from Ahmed et al (1984)) illustrates the geometry at ¼ “scale” (scale being somewhat arbitrary in the case of such an idealised geometry). As discussed in section 1.2.3, this model demonstrates a critical backlight angle (generally 30°) where the drag reaches a maximum before dropping

off at higher backlight angles (note that as backlight angle is varied the length of the backlight surface is kept constant).

In the Durham tunnel, a 1/8 scale Ahmed model was used with a 30° backlight. As will be discussed later, either the high or low drag flow structure could be achieved in this tunnel in this configuration although the high drag structure was more stable. The upper half of the model was constructed from fibreglass (~4mm thick) and the lower portion was solid wood. The upper half contained 51 pressure tappings along the centreline and an additional 18 tappings on one side of the backlight.

In the MIRA tunnel, a ¼ scale Ahmed model was used. This model was constructed from plywood and, although it had static pressure tappings, these were not used. The model had interchangeable backlights in order to adjust backlight angle. Force measurements indicated that the flow structure switched from the high drag to low drag state between 27.5° and 30° backlight angle; all of the detailed investigations were therefore performed with a 27.5° backlight angle.

Some key dimensions of the two Ahmed models are included in table 2.2.

Form	Scale	Frontal Area (A) (m^2)	Base Dim. $\sqrt{A}$ (mm)	Length (mm)	Width (mm)	Total Height (mm)	Ground Clear to Sills (mm)
Ahmed	12.5%	0.028	167	522	195	169	25
Ahmed	25%	0.112	333	1044	389	338	50
Rover 200	15%	0.043	208	596	254	213	33
Rover 200	40%	0.308	555	1588	676	568	88

Table 2.2 - Three-dimensional model parameters

2.1.2.4 Two-Dimensional Ahmed Model

A two-dimensional model identical to the centreline profile of the Ahmed model was used to assess the importance of the c-pillar vortices on the flow structure bi-stability observed for three-dimensional models and to provide a test case for CFD which would be less computationally demanding than a three-dimensional simulation. This model was constructed from 3mm plastic sheet and measured 470mm long by 360mm wide (the direction of extrusion). It was fitted with identical 17swg (1.1mm bore)x18mm pressure tappings along the centreline, primarily in the region of the backlight. Like the two-dimensional symmetric models, it had end plates to encourage two-dimensional flow but unlike these models it was designed to be mounted in ground proximity. Removable backlights allowed backlight angles of 10°, 20°, 22.5°, 25°, 27.5° and 30° to be tested in order to home in on the critical setting. The model had approximately 36 tappings although the exact number depended on the backlight fitted.

2.1.2.5 Rover 200 Models

A 15% model of the Rover 200 was manufactured at Rover's technical centre at Gaydon for testing in the Durham tunnel. The model was made by CNC machining a hard foam positive based on the CAD data for the production car. This was used to create a mould which was in turn used to make the fibreglass shell for the final model. The model was fitted with identical static pressure tappings arranged as follows: 55 on the centreline, 40 over half the backlight and 15 in a line across the backlight to verify symmetry.

A 40% model of the Rover 200 was also manufactured by Rover for testing in the MIRA model tunnel. In this case the final model itself was machined from hard foam.

Both models had removable rear spoilers at the top of the backlight (all production vehicles are fitted with a rear spoiler). Some work was done to ensure that the

spoiler on the 15% model had a similar effect to that obtained for larger models and higher Reynolds number as will be discussed in section 3.6.1.1. As a result of this, much of the work done with the 15% model was done with a very slightly oversized spoiler made up from 0.3mm aluminium sheet.

Both models were fitted with flat underbodies for the testing reported here. There were minor differences in the positioning of the floor pans and the step between the floor pan and rear bumper because the floor pan on the 40% model covered a semi-detailed underfloor. The 15% model was tested with and without a set of 5 aluminium roughness strips (measuring 10mmx2.5mmx180mm); these were sized based on experience gained in the work published by Howell and Goodwin (1995). The front and rear strips were mounted in the positions of the axles, spanning the distance between the wheel arches, and the remaining strips were spaced evenly between the front and rear strips. The models had identically shaped wheels and were mounted with equivalent ground clearance to the sills (minor differences in the floor pan arrangement mentioned above meant that the relative ground clearance to the underfloor was therefore slightly less for the 40% model).

The models did not have wing mirrors or internal cooling flows. The influence of leaks to the interior of the 15% model at the junction between the upperbody and undertray was measured by testing with and without sealing tape on this seam. Sealing the underfloor changed C_D by 0.014 and C_L by 0.036 (primarily at the rear); this was considered to be a significant change and so the underfloor was sealed to the upper body for all testing.

Both models have the option to be mounted from overhead with an internal balance, separately supported wheels and a rolling road. However, for the majority of the work presented here, they were supported over a fixed ground board through their wheels. Mounting the models through their wheels obviously avoids the interference of any supporting strut. As an aside, the 15% model was tested with an overhead

strut positioned to mimic its position when in use but without actually coming into contact with the model. The interference of the strut was found to seriously affect both the absolute forces (by between 0.016 and 0.034 on C_D and by between 0.016 and 0.072 on C_L) and the effectiveness of the backlight spoiler, halving its effect on drag and quartering its effect on rear lift. The models were only mounted on a "live" balance for force measurements, other measurements were carried out either with the balance locked (MIRA) or using a rigid "dummy" balance (Durham) in order to avoid any vibration due to the flexibility of the balance.

2.1.3 Computer Data Logging and Control

Data logging and control was accomplished using an MS-DOS based computer fitted with an Amplicon PC-30PGH card. This card provides 8, 12bit differential input analogue channels which were used for data logging. An onboard pre-amplifier applied gains between 1 and 8 which were set under program control based on a test sample for each channel in order to obtain optimal resolution. The card has a clock speed of 2MHz and can achieve a total throughput of around 30khz. For the majority of work, a sampling rate of 800hz per channel was used and data were recorded in sets of 2048 points in time per channel. Block mode sampling was used to obtain near simultaneous sampling of the different channels. Second order analogue 250hz low-pass filters were used in order to provide anti-aliasing. The PC30-PGH card also provides three configurable 8 bit digital ports which were used for the control of the traversing equipment and the scanivalve. The software used for data logging, control, calibration and analysis was written in FORTRAN by the author.

2.1.4 4-Axis Traverse

A four axis (three linear, one angular) traverse was used for probe positioning under computer control. Figure 2.1.7 shows the unit installed in the MIRA model wind tunnel. The three linear axes made it possible to position the probe at a required x,y,z coordinate in the tunnel and the angular axis made it possible to align the probe with the local flow in one angular direction. This can be used to minimise errors by

reducing reliance on the incidence calibration of the probe or in order to allow the probe to be used in flows which would exceed the incidence calibration range of the probe. When probe alignment was performed this was normally based on an earlier run made without probe alignment. Positional resolution of the traverse is between 5 and 13μm on the linear axes and is within 0.5° on the angular axis however the absolute accuracy of the system is limited by the measurement of a datum probe position relative to the model (which was made to an accuracy of approximately 1mm). The traversing gear was designed and commissioned by the author.

2.2 Instrumentation

2.2.1 Pressure Transducers

Pressures were measured with Sensor Technics 103LP10D pressure transducers. These are differential units with a range of ±1000Pa and feature internal supply regulation and temperature compensation. The manufacturer quotes thermal sensitivity errors (for 50°C temperature change) of 0.5% full-scale output (FSO) on offset and span and long term drift of 0.2% FSO over 1 year. The transducers were calibrated periodically against a silicon fluid micromanometer; all transducers were calibrated simultaneously. Sensitivity was found to vary by less than 0.5% between calibrations throughout the duration of the project. Offset voltages were measured at least on a daily basis to minimise temperature and drift effects. The manufacturer's reported response time for the transducers is 200μs (5kHz).

2.2.2 Hot-Wires / Hot-Wire Anemometers

2.2.2.1 Apparatus

A range of Dantec single hot-wires and supports were used through the course of the investigation. The majority of the work was performed using Dantec 55M01 constant temperature anemometers although some work was performed with a TSI Flow-Point 1500 unit. Manufacturer recommended overheat ratios (R/Ro) of 1.8 were used.

2.2.2.2 Advantages and Limitations of Hot-Wire Probes

Hot-wires are the most common type of unsteady probe and are capable of very high frequency response (sometimes exceeding 300khz) however they do have shortcomings. Individual wires cannot differentiate between positive and negative incidence and so various methods have been applied to overcome this problem. The "flying hot-wire" technique (eg: Wark et al 1990)) propels the probe head through the flow at sufficient speed to ensure that the flow relative to the probe is always dominated by the velocity of the probe itself. Unfortunately this method introduces obvious difficulties, not least of which is the fact that the probe cannot take continuous measurements at the location of interest. Various methods have been applied where the convected wake of a heated-wire is observed by another wire in order to resolve the directional ambiguity (eg: Müller (1983)). Alternatively it is possible to overcome these problems by using at least 4 wires (eg: Döbbeling et al (1990)) or film surfaces (eg: Goh (1994)) and the numerical solution of a set of non-linear calibration equations. Hot-wires are very fragile and quite expensive, particularly when multiple wires are required in close proximity, so careful attention is required to avoid damaging them. The build up of dust on the very thin (5μm diameter typically) wires can have a significant effect on the wire sensitivity so frequent recalibration is required for accurate measurements. Hot-wires are able to measure velocity only and cannot measure static or total pressure. The latter provides an index to entropy (in steady flows) and hence is essential in the determination of loss (entropy gain). This is a significant limitation for hot-wires.

2.2.2.3 Single Hot-Wire Calibration for Velocity

An individual hot-wire or hot-film (deposited on a slender circular cylinder) responds to both the magnitude and the relative direction of the flow impinging on it.

$$E = f(|U|, \alpha, \beta) \tag{2.2}$$

where E is the voltage across the wire, |U| is the velocity magnitude and α, β indicate the relative direction of the flow and the wire.

Several methods have been proposed to independently model the effect of the velocity. King (1914) proposed the following relationship for the effect of the velocity magnitude:

$$E^2 = E_o^2 + BU^n \tag{2.3}$$

where E_o, B and n are constants.

This remains the most widely used hot-wire calibration equation. Bruun et al (1988) evaluated a number of alternative equations including polynomial and spline fits (see table 2.3 - data from Bruun (1995)) and found that King's equation could be bettered only by multi-interval spline fits. Spline fits add significant complexity and are computationally demanding for a relatively unimportant improvement in accuracy so King's equation was used in the present study. The voltage under zero flow conditions, E_o, was determined by averaging zero velocity measurements and B and n were determined using a regression technique. Calibration data for a cylindrical hot-film probe was also found to be well represented by this model.

Equation	ε_u (%)
$E^2 = E_o^2 + BU^n$ simultaneous E_o, B, n solution	0.11
$E^2 = E_o^2 + BU^n$ increment, n	0.15
$E^2 = E_o^2 + BU^n$ increment, E_o	0.15
$E^2 = E_o^2 + BU^{1/2} + CU$	0.46
$U = A + BE + CE^2$	2.5
$U = A + BE + CE^2 + DE^3$	0.24
$U = A + BE + CE^2 + DE^3 + GE^4$	0.15
$U = A + B(E^2) + C(E^2)^2$	0.80
$U = A + B(E^2) + C(E^2)^2 + D(E^2)^3$	0.15
Spline Fit - 1 interval	0.23
Spline Fit - 2 intervals	0.14
Spline Fit - 3 intervals	0.14
Spline Fit - 4 intervals	0.071
Spline Fit - 5 intervals	0.053
Spline Fit - 6 intervals	0.055

Table 2.3 - Accuracy of hot-wire calibration equations (5-50m/s) - data from Brunn (1995)

2.2.2.4 Single Hot-Wire Calibration for Incidence

It is common to model the effect of flow direction by replacing U in equation 2.3 with an effective velocity. Hinze (1959) proposed a method for a two-dimensional flow which was extended to three dimensional flow by Jørgensen (1971):

$$U_e^2 = U_n^2 + k^2 U_t^2 + h^2 U_b^2 \qquad (2.4)$$

where k and h are constants (typically k =0.2, h =1.05),

$U_n = U \cos\alpha \cos\beta$, $U_t = U \sin\alpha$ and $U_b = U \cos\alpha \sin\beta$

Substituting U_e for U in equation 2.3:

$$E^2 = E_o^2 + B\left(U_n^2 + k^2 U_t^2 + h^2 U_b^2\right)^{\frac{n}{2}} \qquad (2.5)$$

This suggests that the response of the wire to flow in the different component directions is uncoupled. Bruun and Tropea (1980, 1985) found that k and h are functions of β and α respectively and both will be weak functions of |U|. Furthermore, Bruun et al (1990) found that B and n will also be weak functions of β and α.

Hot-wire incidence calibrations are usually performed in order to use multiple wires to determine flow direction. In order to do this it is convenient to express the incidence response of each wire via equations which are then solved simultaneously for all of the wires on the probe. In the present investigation however, where only single wires were used, there is less benefit from describing the incidence behaviour of the wires via equations. Therefore a two-dimensional look up table was used instead, whereby U_e/U is stored for a range of α and β in 2.5 degree increments and linear interpolation is used between the discrete data points.

2.2.3 Surface Mounted Hot-Film Gauges

2.2.3.1 Apparatus

Dantec type 55R47 single element surface hot-film gauges were used in constant temperature mode with an overheat ratio (R/R_o) of 1.3 using DISA 55M10 anemometers. The gauges are designed to be glued to the surface of the model however it was possible to achieve greater flexibility and economy by mounting the gauges with double sided tape. This allowed the gauges to be repositioned or removed from the model altogether (so that they did not obscure pressure tappings). The gauges were mounted on pieces of adhesive tape which were larger than the gauges themselves with a non-adhesive area directly under the gauge itself. This was

necessary in order to allow the gauge to be removed without the bending which would occur as the adhesive directly underneath it was peeled off the surface.

2.2.3.2 Surface Mounted Hot-Film Gauge Theory

A surface mounted hot-film gauge essentially consists of a small, thin, heated element. The resistance of the element will increase with its temperature as for a hot-wire probe. It has been shown (Bellhouse and Schultz (1966)) that the power dissipated by the element depends on the wall shear stress as described by equation 2.6. The application of this equation assumes that the thermal boundary layer is entirely contained within laminar flow (ie: within the laminar sublayer of a turbulent boundary layer).

$$Q = C_1 \tau_w^{1/3} + Q_o \tag{2.6}$$

Where Q is the total power dissipated, C_1 is a constant, τ_w is the wall shear stress and Q_o is the power dissipated under zero flow conditions.

If the gauge is operated in constant temperature mode then $Q \propto E^2$ and we can rearrange equation 2.6 to obtain equation 2.7:

$$\tau_w = C_2 \left(E^2 - E_o^2 \right)^3 \tag{2.7}$$

In theory, the constant C_2 can be obtained by calibration but this involves considerable difficulties. In order to find C_2 we must expose the gauge to a boundary layer of known shear stress, however, the value of C_2 will depend on the individual mounting of the gauge which suggests that any calibration needs to be performed in situ. In some circumstances it is possible to mount the gauge on a plate which can then be manufactured into the surface of the model thereby circumventing the otherwise paradoxical situation outlined above. Alternatively the shear stress could be measured by some other means capable only of time-averaged

measurement (eg: a Preston tube) and the hot-film could then be used in order to obtain time-accurate measurements. It is more common to take the approach used here and to forego a calibration, accepting arbitrary units for shear stress and some variation in sensitivity for different mounting locations. This still allows the observation of the varying levels of unsteadiness at different locations on the surface as well as the varying level of time-averaged shear stress, both of which can be used to determine the state of the boundary layer.

2.2.3.3 Surface Mounted Hot-Film Gauge Inaccuracies

In practice, the heat lost to the substrate, Q_o, tends to be much larger than $C_1\tau_w^{1/3}$, the heat lost to the passing flow (see equation 2.6). This makes the gauge very sensitive to non-aerodynamic effects and can lead to errors if sufficient care is not taken. Particular sources of inaccuracy include:

2.2.3.3 a) Local transient heating of the model due to gauge re-positioning:

Figure 2.2.1 shows the transient value of the zero-flow offset voltage for a hot film gauge when it is repositioned. The gauge heats up the surface of the model immediately around it with approximate thermal equilibrium being reached within about 600s (for a fibreglass model with a wall thickness of approximately 3mm). As the model warms up, the heat transfer to the substrate and hence gauge voltage (E_o) reduces by 0.035v typically. Equation 2.8 (based on equation 2.7) allows us to quantify the error which would occur if the zero-flow voltage were measured immediately after gauge repositioning without allowing time for thermal equilibrium to occur.

$$\frac{\text{measured shear stress}}{\text{actual shear stress}} = \frac{\left[(E-E_o)^2-(E_o+E_{error})^2\right]^3}{\left[(E-E_o)^2-E_o^2\right]^3} \qquad (2.8)$$

If we assume that the steady state conduction to the model leads to a zero-flow gauge voltage E_o = 2.85v while aerodynamic convection increases this voltage by

0.35v ($E - E_o = 0.35v$) and we have an error on the zero-flow offset voltage of 0.035v due to transient heating of the model then the measured shear stress will be 26% lower than the actual shear stress.

2.2.3.3 b) Thermal resistance of local mounting:

The heat lost to the surface of the model by conduction will vary according to the individual mounting. Figure 2.2.1 also illustrates the variation in zero-flow gauge reading for three mounting locations, the gauge was repositioned at 0s, 600s and 1290s. In this case, differences in E_o of 0.05v were found to be typical. As suggested by Reichert and Azad (1977), this is likely due to small changes in the amount of contact between the gauge and the model.

2.2.3.3 c) Air-flow heating of the model:

Because the Durham tunnel is low speed and of the open circuit type, the temperature of the air in the tunnel remains very nearly atmospheric. Nevertheless, it was found that the zero-flow offset voltage E_o measured with the tunnel and model "cold" was typically 0.03v below that measured immediately after the tunnel had been running. By allowing the tunnel (and model) to warm up for 15 minutes before logging E_o, the shift in E_o from before to after a run was reduced to 0.004v which is equivalent to a maximum error of 3.2% on shear stress, assuming typical flow conditions.

2.2.3.3 d) Instrument drift:

Figure 2.2.2 shows the transient value of E_o for 2 hours immediately following activation of a hot-film gauge from cold. DISA recommend that the 55M10 constant temperature anemometer be allowed to warm-up for at least 15min (900s) prior to measurements and indicate that thermal equilibrium may not be reached for 2 hours (7200s). The initial downward slope in figure 2.2.2 subsides after 2000s suggesting that initial warm-up is complete. Upward, drift then occurs at a rate of 0.012v/hour.

2.2.4 Five-Hole Pressure Probes

The head of a typical five-hole probe is shown in figure 2.2.3. Pneumatic probes such as five-hole probes use the differential pressure between the different holes in the head of the probe to determine the direction of the airflow onto the probe as well as the total and static pressure of the airflow. They generally provide better accuracy and convenience than hot-wires for steady measurements. Five-hole probes are the most common configuration however comparable results can be achieved with only four holes (eg: Hooper and Musgrove (1991)). In order to accommodate high incidence angles (including reversed flows) more complicated probes with up to fourteen holes can be used. Multi-hole probes may be operated in the "nulled" mode so that opposing holes read the same pressure and the head is directed into the airflow. Only a simple calibration is then required to determine the local total and static pressures. When probes are used in more restricted spaces, as in turbomachinery applications, it is usual to fix the angle of the probe in advance and to use a more involved calibration to determine the relative flow angle and total and static pressures. This method also allows data to be gathered more quickly. In the present work, the probes were operated in this latter configuration. However, it was possible to null the probe in one axis and in many cases this was done based on an earlier, preliminary run. This makes it possible to take measurements in areas where the flow is at high angles of incidence relative to the axial direction and takes advantage of the fact that the probe calibration will be slightly more accurate at low incidence angles. Also, for areas where the direction of the flow is changing with time, directing the probe into the average flow direction reduces the risk that the probe's incidence range will be exceeded during part of the unsteady cycle.

Table 2.4 gives some details of the various probes used during this project, including the incidence calibration range and the probe's frequency response corresponding to a 10% attenuation of the fluctuating pressure signal. The probes were all calibrated using a computer controlled calibration rig which systematically varied the

incidence of the probe in a small calibration tunnel. During the calibration, the reference total and static pressures were initially determined using a pitot-static probe although, later in the project, a calibration of the static pressure drop across the tunnel nozzle was performed in order to avoid the need for the pitot-static probe. This made it possible to accommodate larger incidence ranges in the relatively confined jet without the risk of the pitot-static probe and the sting of the five-hole probe clashing (the head of the five-hole probe was maintained at a fixed location). Calibrations were performed using pitch and yaw increments of 2.5° and this data was stored in a look-up table. When interrogating the calibration, a linear interpolation was used between calibration points. The heads of probes 5h_03 and 5h_04 were shaped in order to maximise incidence range by repeatedly reshaping and recalibrating the probe heads until an optimum was achieved. Figures 2.2.4 to 2.2.6 show the calibration maps for incidence, total and static pressure coefficients for probe 5h_03.

Probe	Head Diameter	Tube Bore	Head Type	Pitch x Yaw Range	Freq. for 10% Attenuation
5h_01	3.5mm	0.2-0.58mm	Forward Facing Cone	35°x35°	9hz
5h_02	5.5mm	1.2mm	Forward Facing Pyramid	35°x35°	33hz
5h_03	3.3mm	0.69mm	Forward Facing Pyramid	40°x40° or 50°x30°	38hz
5h_04	2.4mm	0.51mm	Forward Facing Pyramid	40°x40° or 50°x30°	20hz

Table 2.4 - Details of five-hole probes used

Dominy and Hodson (1993) investigated the impact of probe head geometry, free-stream turbulence, Reynolds number and Mach number on the calibration of five-hole pneumatic probes. They reported two distinct Reynolds number effects: the

first caused by separation from the probe head when the probe is at incidence and the second by the size of the separation bubble from the front of the probe at small incidence angles. At low Reynolds number this separation bubble extends further down the probe, reducing the pressure at the side holes and hence increasing the dynamic pressure coefficient. The probe Reynolds numbers for the current investigation fall within the range of importance of both of these effects so the errors associated with varying Reynolds number were quantified over the full range of the calibration. For a reduction in Reynolds number of 20% from the free-stream value, errors on pitch and yaw angle were generally below 2° and errors on dynamic pressure were of the order of 2%, with the exception of data at high pitch angles where the probe exhibits relatively poor sensitivity. As the goal of this investigation is flow structure understanding rather than quantification of losses these levels of error have been considered acceptable and a probe calibration at approximately free-stream Reynolds number has been applied for all measurements.

2.2.5 Tubing Transfer Function Correction

The Sensor Technics pressure transducers have a response time of 200μs (1/5000hz) and it is usual for pressure transducers to have frequency responses well in excess of the frequencies associated with large scale aerodynamic unsteadiness around passenger vehicles. The tubing between the measurement point and the transducer, however, can exhibit a response which is highly frequency dependent and it is this which usually limits the frequency response of the system. The tubing frequency response is a function of viscous, momentum and elastic (compressibility) effects. Due to the finite volume of the transducer chamber (and any associated connector or valve assembly) and the compressibility of air, a certain quantity of air must flow down the tube in order to pressurise this volume. Viscosity in the tubing acts against this movement of air and hence dampens the response of the system. Tudeman (1975), in a theoretical study, showed that even in a situation with negligible transducer volume the pressure waves themselves require some local compression

(and hence movement) of the air, so viscous attenuation effects can never be eliminated. The tubing will also exhibit a natural frequency due to the combined presence of fluid mass and elasticity (compressibility). This results in the amplification of the signal near the natural frequency or its harmonics.

These distortion effects can obviously be eliminated by eliminating the tubing itself and mounting the transducers locally. For surface pressure tappings this is sometimes possible but precludes the use of a mechanical scanning device and requires either a very large number of individual transducers or that transducers are remounted a large number of times. For probes the situation is more difficult but not impossible; various researchers have constructed probes with miniature high-response pressure transducers built into the probe head itself (eg: Cook (1989), Cherrett et al (1992), Sims-Williams (1994), Gossweiler et al (1995)). The primary problem with this approach is that it is very difficult to obtain miniature transducers with adequate pressure sensitivity for accurate measurements at the low Mach numbers and consequently small differential pressures typical of road vehicles.

Alternatively, it is possible to measure the distortion effects associated with remote transducers and then to correct for them. Irwin et al (1979) describe such a technique for lengths of tubing connected to static tappings and a similar method has been applied here both for surface pressure measurements and also for pneumatic probe measurements. The apparatus used to measure the transfer function of the tubing/probe system is shown in figure 2.2.7. The loud speaker pressurises a closed volume which is connected to a small chamber via a short length of rubber hose (to isolate mechanical vibrations). A reference pressure transducer records the instantaneous pressure inside the chamber and a typical static pressure tapping or a pneumatic probe head may be connected to the other side of the chamber. Plastic tubing connects the static pressure tap or the 5 hole probe to the pressure transducers to be used for the eventual wind tunnel measurements. The loudspeaker is excited with a swept sine wave (typically from 6Hz to 300Hz with a sweep period of 0.75s)

and the pressures measured at all of the transducers are logged in sets of 2048 samples. Fast Fourier transforms (FFTs) of the pressure signals are calculated using a routine due to Press et al (1992) and the complex transfer function of each tube is defined as:

$$T(f) = \frac{B(f)}{A(f)} = \frac{B(f)A^*(f)}{|A(f)|^2} \tag{2.9}$$

where A is the Fourier transform of the pressure recorded by the reference signal and B is the Fourier transform of the transducer connected to the tubing under test.

In order to obtain high quality results, between 50 and 500 sets of 2048 samples were recorded and an average transfer function was computed. A Hanning windowing function was applied to reduce the effect of the finite data set length thereby significantly improving the quality of the results (windowing is discussed in section 2.3.1.1).

Figure 2.2.8 shows the measured transfer function for a typical static tapping system consisting of the tapping itself, 450mm of 1mm internal diameter Portex tubing, a scanivalve and a short length of additional tubing connecting it to the pressure transducer. The effects of resonance and of viscous attenuation as frequency increases are apparent. We can estimate the effective speed of sound in the tubing using equation 2.10. Assuming a total tube length of 470mm to allow for the scanivalve internals and connection to the transducer, the effective sound speed is 140m/s. The first two natural frequencies according to simple organ pipe theory (equation 2.11) are therefore 74hz and 222hz respectively. The actual maxima (50hz and 212hz) are pushed to lower frequencies by the fact that the amplitude generally decreases with frequency due to viscous attenuation. Figures 2.2.9 and 2.2.10 show the transfer functions for 5 hole probes 5h_01 and 5h_03 respectively (for probe details see section 2.2.4). The probes use small diameter hypodermic

tubing to minimise probe head size and this leads to greater attenuation than for the static tapping system. These probe transfer functions are therefore critically damped.

$$a_o = \frac{360Lf}{\theta} \tag{2.10}$$

where a_o is effective sound speed, L is the tubing length, and θ is the phase shift at frequency f

$$f_{resonant} = \frac{a_o}{4L}, \frac{3a_o}{4L}, \frac{5a_o}{4L} \ldots \tag{2.11}$$

The effectiveness of the transfer function correction technique can be seen for probe 5h_01 in figures 2.2.11 and 2.2.12 where saw and square wave test signals have been applied to the speaker and the correction technique has been used to infer the pressure fluctuation at the point of measurement. Note that the high frequency fluctuations at the leading edge of the square wave are present in the reference signal and are unconnected with the correction technique. These are due to resonance in the excitation chamber which is excited by the high frequencies associated by the sharp leading edge of the square wave. The choice of periodic test signals is purely for convenience, the correction technique is equally effective for periodic and non-periodic signals.

The ultimate frequency response of the corrected system will still be dependent on the attenuation in the tubing since signal to noise ratio will effectively worsen when attempts are made to recover highly attenuated signals. For a 1m long tube a frequency response of about 1 or 2khz is probably as high as can be achieved before the signal to noise ratio deteriorates beyond acceptable limits.

The application of this technique to multi-hole probes is slightly more complex than for static tappings. The pressure traces for each of the holes is corrected according to the transfer function of the appropriate tube and the five-hole probe incidence calibration is then applied using these instantaneous pressures. The use of a

calibration map obtained from a steady-state calibration for instantaneous pressures in a fluctuating flow assumes that the flow around the probe head may be considered to be quasi-steady. The parameter of importance for determining if a flow may be considered to be quasi-steady is the reduced frequency (given in equation 2.10). This parameter compares the time-scale associated with the development of the flow around the probe head and the time-scale associated with the unsteadiness. The assumption that a flow is quasi-steady is generally acceptable at reduced frequencies below 0.1 to 1. These values correspond to crudely estimated phase errors of 6° and 60° respectively. At a velocity of 25m/s, with a probe head diameter of 3.3mm, this range of reduced frequency corresponds to frequencies between 120hz and 1.2Khz which is sufficient for the work presented in this thesis. When the combination of corrected pressures was not within the range of the five-hole probe calibration map, the out-of-range data was replaced by time-interpolating between the nearest preceding and following in-range data.

$$\text{reduced frequency} = \frac{2\pi fd}{U} \tag{2.10}$$

In order to validate the use of the transfer function correction technique for pressure probes, a five-hole probe with and without transfer function correction was tested directly against a hot-wire probe. A single-element hot-wire probe (Dantec type 55 P01) was calibrated for velocity in straight ahead flow and was subsequently calibrated at constant velocity over a range of incidence angles as described in sections 2.2.2.3 and 2.2.2.4 respectively. The five-hole probe used was 5h_01 which had the worst transfer function of any of the probes used in this work. Both probes were placed in the wake of one of the two-dimensional symmetric models (as shown in figure 2.2.13) which exhibits vortex shedding at a frequency of 58hz at a free stream velocity of 25m/s. The two probes were displaced by 20mm in the direction of extrusion of the body (ie: out of the page in figure 2.2.13). The hot-wire axis was

in the across-wake direction in order to provide sensitivity in the plane of the primarily two-dimensional flow. The hot-wire voltage was calibrated to provide time traces of effective velocity. After the transfer function correction and incidence calibration were applied to the pressures from the five-hole probe, the resulting data were used with the hot-wire incidence calibration to predict the effective velocity that would be reported by the hot-wire. Figure 2.2.14 compares time traces of hot-wire effective velocity according to the hot-wire and five-hole probe with transfer function correction; to demonstrate the impact of the correction, figure 2.2.15 provides the same comparison but without the application of the transfer function correction. Table 2.5 quantifies the level of error (the standard deviation of the instantaneous difference between traces) on effective velocity between the hot-wire and five-hole probe and, for comparison, for two hot-wires at the same spacing. This suggests that the difference between the two traces in figure 2.2.14 is primarily due to differences in the local flowfields at the two probe locations.

Probes	Standard Deviation (m/s)
Hot-Wire vs Hot-Wire	3.2
Corrected five-hole Probe vs Hot-Wire	3.8
Uncorrected five-hole Probe vs Hot-Wire	5.4

Table 2.5 - Discrepancies between probes at 20mm spacing

As a further comparison between the hot-wire and five-hole probe, the distribution of effective velocity autospectral density and phase at the shedding frequency across the wake of the body is plotted in figures 2.2.16 and 2.2.17 respectively. (This type of analysis will be discussed in detail in section 2.3.1.) The agreement between the hot-wire and transfer function corrected 5 hole probe is very good. There are no

systematic errors on autospectral density. On the left hand side of figure 2.2.17, phase errors are within 2° and the large difference at x=0 is unsurprising because phase is discontinuous at this location. The roughly constant phase discrepancy on the right hand side of figure 2.2.17 is surprising given the excellent agreement on the left hand side, a discrepancy of this type could be caused by a misalignment of the probes relative to the vehicle of approximately 5mm. Even with this error, the average phase discrepancy is less that 8° which should be acceptable. It is worth noting that without transfer function correction the phase error would be of the order of 100°. This work was published in Sims-Williams and Dominy (1998a).

2.2.6 Force Balances

2.2.6.1 Six-Component Force Balance

The design of the six-component force balance used for work in the Durham 0.85m x 0.55m tunnel is described by Docton (1997). Briefly, the balance basically consists of two parallel plates, one live (ie: connected to the model) and one mounted to a rigid reference. Six load cells bridge the two plates and each load cell is connected to the live plate via a thin steel link (1.6mm diameter). The links are designed to transmit force along their length but to be pliant in bending in order to isolate the load cell from forces in other directions.

The balance was calibrated using a calibration frame designed for the purpose. First, pure forces were applied to an arbitrary calibration centre and sensitivities of each of the six load cells to the three forces were computed. Moments about the calibration centre were then applied by applying forces at known locations offset from the calibration centre. The sensitivity of the load cells to the moments could then be determined by first removing the calculated response of the cells to the force used in generating the moment. Once a matrix containing the sensitivities of the six load cells to the three forces and three moments was determined this was inverted to provide a calibration matrix used to determine forces and moments from the output of the load cells in a wind tunnel measurement. These forces and moments about the calibration centre are then transposed to a more useful location such as the midpoint

of the wheelbase on the ground plane; in fact the usual practice is to quote front and rear lifts rather than quoting a pitching moment and this convention has been adopted here. The entire process was automated by FORTRAN routines written by the author.

Because the calibration frame uses pulleys to generate horizontal forces from hanging masses, the friction in these pulleys was measured in order to asses the level of error it could introduce into the calibration. The maximum possible error due to pulley friction was calculated to be less than 0.004 (~1%) on C_D. The actual error can be expected to be much smaller because the calibration measurements were taken with both increasing and decreasing loads in order to minimise hysteresis effects. Similar levels of error can be attributed to non-linearity in the sensitivity of the balance with and without the weight of a model and underfloor support frame and to inaccuracies due to the pressure transducer measuring reference dynamic pressure. Docton (1997) performed a thorough investigation into cross loading within the balance (ie: erroneous loading reported on one component due to loading of other components). He recorded a maximum error of 6% of the applied loading however errors of 1-2% were more typical, in keeping with the present author's own observations in practice. In the wind tunnel, the testing procedure adopted for force measurements involved averaging three tares and six measurements per tare in each configuration (18 measurements in total). Each individual measurement consisted of logging for 2.5s at 800hz per cell (ie: logging for a total of 46 seconds for each configuration). Each set of 18 measurements in each configuration was inspected for spurious points. This procedure resulted in repeatability within two counts (ie: ±0.002 on C_D). This repeatability was verified from day to day, for remounting the model on the balance, and for re-taping the seam between the bodyshell and the undertray.

The balance was used primarily as an underfloor balance supporting the Rover 200 model through its wheels as described in section 2.1.2.5 but could also be used inside the same model with an overhead strut support for rolling road testing.

The possibility of recording unsteady forces was investigated. The Rover 200 model was set up with overhead support and internal balance in order to minimise the live mass and moment of momentum. The wheels were mounted separately to further minimise live mass. Despite these efforts, the mechanical system was still prone to a number of resonant frequencies (7hz, 12hz, 23hz, 44hz, 62hz and 170hz) within the band of interest which overwhelmed any unsteady aerodynamic forces. The possibility of correcting for the effect of mechanical resonances through the development of a technique similar to the tubing transfer-function correction method described in section 2.2.5 was investigated. However, this system proved to be much more difficult to model in this way because the relationships between steady applied loading and the forces recorded at the six load cells did not hold for unsteady forces. Applying excitation using one component produced mechanical resonance which appeared in a number of components. Various other complications exist, for instance the transfer functions would have to be determined for the assembled balance and model combination because the mass and moment of inertial of the model are important to the system response. Difficulties also exist in the generation of the known unsteady forces and moments in the appropriate components. Several of these challenges were overcome and it is possible to envisage a method of accounting for the interdependence of the different components through the use of a 6x6 matrix of transfer functions. Nevertheless, it was decided not to develop this option due to the considerable time it would require to implement and the risk that further difficulties would appear, further complicating the system.

2.2.6.2 Plint Three-Component Force Balance

The Plint three-component balance mounts on the side of the Plint 0.46mx0.46m tunnel and supports models in the tunnel via a cantilever rod. The balance incorporates a “shaker” and this was used immediately before each reading in order

to reduce the hysteresis caused by friction in the balance pivots. Wing incidence sweeps were performed during which the incidence was varied in two degree steps over a range of around 30 degrees. During each sweep the incidence was swept first from the minimum to maximum and then back to the minimum with measurements taken both on the way up and down in order to further combat hysteresis. Zero-flow offset voltages were recorded three times before and after each sweep. The measurements were found to be repeatable to within 1% and 3% on the measured C_L and C_D values respectively.

2.2.7 Flow Visualisation

2.2.7.1 Smoke Flow Visualisation

Smoke flow visualisation was used to provide an initial assessment of flowfields around the models and to investigate bi-stability for the two-dimensional and three-dimensional (standard) Ahmed models. Wand-type smoke generators were used which produce smoke by feeding oil to the heated tip of the wand which is positioned in the airflow. Smoke flow visualisation was generally performed at reduced tunnel velocity (<10m/s). The smoke flow was recorded either using a standard VHS video camera, a digital camera, or a single lens reflex (SLR) camera with print film.

2.2.7.2 Surface Oil Flow Visualisation

Surface oil flow visualisation was used primarily to identify separations, in particular, laminar separation bubbles which are not easily observed by other means. A mixture of paraffin and fluorescent powder was prepared and painted onto the model in the wind tunnel. The powder is produced for use in the printing industry and was supplied by H. Haeffner & Co. The tunnel was generally run at full speed causing the mixture to streak according to the local surface flow. With time (<1 hour), the paraffin evaporates and leaves almost dry powder (drying was accelerated in some cases through the use of a 500 watt floodlamp shining into the working section. The model was then removed to a darkroom and illuminated with two UV lights (UVL-56 366nm, 0.12A@220V) to cause the powder to fluoresce, providing

maximum contrast. Photographs were taken with a SLR camera fitted with an 80mm macro lens and Skylight 1A (UV) filter using standard balance print film (ISO 100-400). A tripod and cable release were used since exposures of several seconds were typical.

2.3 Analysis Techniques

2.3.1 Spectral Analysis

A variety of texts dealing with spectral analysis are available. In the course of this study; Bendat and Piersol's (1980) book on the subject was used extensively for its mathematical and physical insight. The FORTRAN code for the calculation of Fast Fourier Transforms (FFTs) was taken from Press et al (1992) which also provided a good discussion of the spectral techniques. Finally, Hamidy (1991) provides a concise summary of some spectral functions commonly applied for unsteady aerodynamic analysis.

2.3.1.1 The (Fast) Fourier Transform

The essence of spectral analysis lies in the representation of a time function in terms of a superposition of a number of sine waves at different frequencies, each having a specific amplitude and phase offset (ie: a Fourier series). The Fourier transform effectively determines these amplitudes and phase offsets.

In the general case, both the input and output of the Fourier transform can be complex functions however, for real time-history data the input data will obviously contain no imaginary component. In this case the output from the "two-sided" Fourier transform will be a complex function which is symmetric about 0hz. It is therefore usual to express the transform as a "one-sided" function of twice the magnitude contained entirely in the positive frequency domain. This is the convention which has been adopted in the present work.

The implementation of spectral analysis to physical problems is almost synonymous with the Fast Fourier Transform (FFT), in fact the proliferation of Fourier methods can probably be attributed largely to the numerical efficiency of the FFT. The principal constraint imposed by the FFT is that the number of data points must be of the form 2^n. This can be achieved by a range of methods such as zero padding at the start and end of data sets but in the present work the data was simply logged in data sets of appropriate length (generally 2048 points in time).

Aliasing is an important phenomenon whenever using discrete sampling. When data is sampled at discrete points in time at some frequency it is only possible to resolve spectral components up to half this frequency (called the Nyquist critical frequency). Any components at higher frequencies that may be present in the underlying signal will not therefore be handled correctly. The "energy" (contribution to mean square deviation from the mean) contained in these components will nevertheless appear in the discretely sampled signal and will be reflected back from the Nyquist frequency in the frequency domain as illustrated in figure 2.3.1 from Press et al (1992) for a double-sided spectrum. Although aliasing is generally discussed in conjunction with spectral analysis it actually occurs at the point that the data is sampled discretely and can be observed in the sampled time series before any spectral analysis has been applied. In order to avoid misleading results due to aliasing in the present work, a set of low pass filters were used to remove frequency components above the Nyquist frequency before the data was sampled (data was generally sampled using a set of matched 250hz second-order analogue filters and a sampling rate of 800hz).

Practical time-series will always be of finite length. This is equivalent to an infinite time-series which is multiplied by a square wave of unity magnitude extending in the time domain from zero to the duration of the finite time series. The transform of the finite data series and underlying, infinite series, will not therefore be identical and we are really interested in the Fourier transform of the infinite time-signal. The sharp edges of the "window" through which we view the time-signal result in

"leakage" of amplitude at one frequency into adjacent frequency bands (also called bins). A better approximation of the transform of the underlying time-signal can be obtained by smoothing the sharp edges of the time window through which we view the signal. Various time windowing functions exist which vary from zero amplitude at time zero to unity magnitude and back to zero at the end of the sampling duration. Figure 2.3.2 from Press et al (1992) shows the level of leakage for a selection of windowing functions including the default square window. In the present investigation, a Hanning window (labelled Hann in figure 2.3.2) was used in almost all cases. The Hanning window consists of a phase-shifted and raised sine wave so that it has zero amplitude at the start and end of the sampling period and unity amplitude in the middle.

2.3.1.2 Autospectral Density Function

The autospectral density function (also called the power spectrum or power spectral density) indicates the contribution of various frequency components to the mean square value of the time record. It is defined as:

$$G_x(f) = \frac{2|X(f)|^2}{T} \tag{2.12}$$

where $G_x(f)$ is the autospectral density at frequency f, X is the Fourier transform of the signal, and T is the total sampling time.

As can be seen from equation 2.12, the autospectral density is based on the square of the Fourier transform and so will be real, containing no phase information. An important property of the autospectral density function is that, unlike the Fourier transform, several autospectral density functions based on different time-histories can be averaged to remove spurious noise inevitably present in real data.

It is common to plot the standard deviation of the signal from a probe or set of static tappings against position to show the spatial distribution of unsteadiness. A more detailed insight can be gained by plotting the autospectral density (at a given frequency) against position; this makes it possible to differentiate between the effects of different unsteady phenomena which occur at different frequencies. It is also possible to effectively integrate the autospectral density over a frequency range in order to determine the standard deviation of the original signal due to that frequency band. For discrete, one-sided spectra the appropriate formulation is given by equation 2.13:

$$x'(f_1 to f_2) = \sqrt{\frac{\sum_{f_1}^{f_2} |G_x(f)|}{nf_{\log}}} \tag{2.13}$$

where x' is the standard deviation of time series x due to frequencies between f_1 and f_2 , G_x is the autospectral density of x, n is the number of samples in the original time series and f_{log} is the logging frequency for the original time series.

2.3.1.3 Cross-Spectral Density Function

The cross-spectral density function is defined as:

$$G_{xy}(f) = \frac{2X^*(f)Y(f)}{T} \tag{2.14}$$

where Gxy(f) is the cross-spectral density at frequency f, X is the Fourier transform of one signal and Y is the Fourier transform of a second signal

Cross-spectral density will, in general, be a complex function so the real and imaginary coefficients can be rearranged into amplitude and phase. Arguably of greatest interest in the context of the present work is the relative phase of frequency

components in the two signals. As for the autospectral density function, the cross-spectral density functions of several pairs of signals can be averaged to improve data quality. The autospectral density function is actually a specific case of the cross-spectral density function in which the cross-spectral density is calculated between a signal and itself.

Two probes can be used to provide two unsteady signals and the cross-spectral density can be calculated relating the two signals. If one probe is held at a fixed position and the other takes measurements sequentially at locations throughout the flow then plotting the phase of the cross-spectral density as a function of position can be particularly revealing. The phase distribution at a particular frequency can indicate the structure of the unsteadiness at that frequency (eg: axi-symmetric, anti-symmetric, helical). The rate of change of phase with position indicates the propagation rate of the unsteadiness. An unsteady phenomenon can be expected to leave a trail which is convected approximately with the local flow velocity, it may also send out pressure pulsations which travel at the speed of sound (relative to the local flow velocity) in all directions. Other phase change rates indicate that the local flow is actively involved in the unsteadiness.

2.3.1.4 Coherence Function

The coherence function is defined as:

$$\gamma_{xy}^2(f) = \frac{\left|G_{xy}(f)\right|^2}{G_x(f)G_y(f)} \tag{2.15}$$

The coherence function can be calculated for the same situations as the cross-spectral density function. The magnitude of the coherence calculated from average cross and autospectral densities based on multiple time series (sets) indicates the extent to which frequency components of the two signals are correlated. A value of unity indicates that the two signals are perfectly correlated and zero indicates that they are uncorrelated. For instance, two signals may contain energy at the same

frequency but from independent sources so the relative phase and amplitude between the two signals at this frequency will be unrelated and the coherence will be low. On the other hand, if the frequency component is due to a common factor then the relative phase and amplitude between the two signals will be similar for each set and the coherence will be high.

2.3.2 Unsteady Reconstruction Method

Many experimental techniques involve the measurement of the flow at a series of discrete points in turn (eg: pressure probes, hot-wires, Laser Doppler Anemometry). A time-averaged understanding of the flow can be obtained by assembling the individual measurement points to examine a line or plane through the flow. Statistically stationary unsteady parameters may also be considered to be "time-averaged", (eg: turbulence intensity) since they do not vary with time. As discussed above, the use of two probes and cross-spectral analysis can give us an insight into the unsteady flow structure however these results require interpretation and different researchers do not always draw the same conclusions from the same data. Particle Image Velocimetry (PIV) has provided a significant advantage over all previous techniques in that it provides simultaneous velocity data over an entire plane, thereby greatly aiding our understanding. Bearman et al (1997), in their description of their own state-of-the-art PIV system, highlight the measurement of time-accurate pressure fields as an important unsolved problem.

This challenge has been addressed by the development of a new analysis technique which effectively synchronises a set of non-simultaneous time histories relative to a periodic phenomenon of interest. This is done by phase-referencing the time histories to a reference signal which is measured simultaneously at a fixed location in the flow. For situations where the unsteadiness is externally imposed (eg: due to blade passing in a turbine) this is routinely accomplished by triggering the sampling from the external excitation. Perry and Watmuff (1981) attempted to use a similar approach for investigating self-excited unsteadiness by triggering from the signal output from a fixed probe in the flow. They achieved some success however the

frequency and amplitude modulations present in a real self-excited flow caused sufficient difficulties that they ultimately resorted to oscillating the body in order to impose perfect periodicity (Perry and Watmuff (1981), Watmuff et al (1983)). In order to determine phase in real, intrinsically unsteady flows which are not perfectly periodic, the approach used here determines the reference signal phase at the post-processing stage. This permits the use of Fast Fourier Transforms (FFTs) which can incorporate several periods into the calculation of an average phase.

For simplicity, we will discuss only one "signal" at the measurement point, however, if the measurements are taken with a five-hole probe several "signals" exist (eg: total pressure, three velocity components etc). Each of these quantities undergoes an identical process.

For each time history taken at a measurement point, a simultaneous time history is taken at the reference point. A Fourier transform is calculated for this reference signal and its phase at the frequency of interest is determined. A Fourier transform is also calculated for the signal at the measurement point and this is then phase shifted according to equation 2.16.

$$\theta_{new}(f) = \theta_{old}(f) - \theta_{ref}(f_{peak}) \bullet \frac{f}{f_{peak}} \tag{2.16}$$

where $\theta_{new}(f)$ and $\theta_{old}(f)$ are the new and old phase of the signal at the measurement point at frequency f and θ_{ref} is the phase of the reference signal at the frequency of interest f_{peak}

An inverse Fourier transform will later be computed for the phase adjusted spectrum of the measurement signal. This procedure effectively applies a time shift to the signal at the measurement point based on the temporal position of the reference signal relative to the periodic phenomena of interest. This synchronises the primary frequency of interest and all of its harmonics relative to a global reference signal. The harmonics are important partly as they will serve to make up non-sinusoidal waveforms but also because higher harmonics will become dominant in certain situations. For example, for a vortex shedding case, the total pressure on the wake centreline will be affected in the same way by vortices being shed on either side of the body and so will vary at twice the shedding frequency.

Spectral peaks for real experimental data will generally span a range of frequencies. In order to produce a meaningful idealised periodic flow-field each peak is concentrated at a single frequency by summing the magnitude of the Fourier transform over a frequency band. This is performed for the primary frequency of interest and for its harmonics; the magnitude of the measurement signal Fourier transform is put to zero at all other frequencies. The resulting spectrum is the ideal (infinite) spectrum corresponding to the ideal (infinite) time-history to be reconstructed. Because we are working with finite spectra and time-histories, however, this spectrum should be convolved with the spectrum of the appropriate windowing function so that each spectral peak takes the form of the appropriate leakage function as shown in figure 2.3.2 from Press et al (1992). The need for this convolution has been avoided by using a rectangular windowing function whose

leakage is zero at all integer frequency bin offsets from the central frequency. Rectangular windowing functions are generally avoided because it is usual to perform forward FFTs of data which contains frequencies which fall between the discrete frequency bins, thereby revealing the large side lobes. Our idealised spectrum, however, represents frequencies corresponding to precise frequency bins only.

The width of frequency bands attributed to each harmonic will generally affect the magnitude of the periodic unsteadiness in the reconstructed flow-field. This is because real experimental data can be expected to contain background noise and over-wide bands will transform this noise into additional energy in the periodic signal. Obviously this effect will become more severe if large amounts of noise exist in the spectral region of the frequency of interest. The band-widths used were selected manually based on the width of spectral peaks and examination of raw and reconstructed time histories. It was considered better to use bands that were too narrow rather than two wide in order to avoid adding spurious unsteadiness to the reconstructed data. Ideally the width of the frequency bands would be determined algorithmically, minimising subjectivity in the processing of the data.

Through the course of an experimental run the exact peak frequency can be expected to drift (for instance due to drift in the tunnel velocity). For this reason spectral peaks are concentrated on the same frequencies for all measurement points even if the frequency of the original peak varies from one measurement point to the next by small amounts.

For three-dimensional flows, levels of periodicity and coherence are often low. For example, Ishihara and Takagi (1999) measured simultaneous, time-resolved wake pressures using a rake of over 200 simple total pressure probes (with tubing transfer correction) in the wake of a passenger car model. Although they found significant unsteadiness, they could not identify any unsteady structure. In order to observe

even weakly periodic structures, the reconstruction technique uses several time histories recorded at each measurement point and the synchronisation procedure is performed for each one using the corresponding reference signal (as are the filtering operations). It is then possible to average the phase adjusted Fourier transforms in order to improve data quality. Note that averaging Fourier transforms which have not been phase adjusted would destroy the periodic component of interest as its phase will vary randomly between time histories. Using the root of the average square of the Fourier transform was tested as an alternative for determining a typical magnitude but was found to over-predict the level of unsteadiness.

Results from this technique applied to vortex shedding cases for validation were first published in Sims-Williams and Dominy (1999) and are also included in chapter 3 of this thesis. Further demonstrations of the technique may be found in Crossland et al. (2000).

2.3.3 Vorticity

Vector fields often fail to reveal all of the vortices present in a flow because weaker vortices are often not apparent when stronger velocity fields are superimposed on them. This can be due to other, larger vortices or due to the superposition of non-vortical flows. Vorticity was therefore routinely calculated and examined along with the corresponding vector fields. Streamwise vorticity is defined in equation (2.17) and vorticity in other planes is obtained through a straightforward realignment of the variables.

$$\zeta = \frac{\partial u_y}{\partial x} - \frac{\partial u_x}{\partial y} \tag{2.17}$$

where ζ is vorticity and u_x and u_y are velocities in the x and y directions respectively.

Simple cell-centred first-order differencing was used so that vorticity was computed for midpoints between measurement points. The use of higher order spatial differencing (eg: as applied by Davis (1982)) was not felt appropriate because discontinuities in the flow over multiple grid points were considered to be a more serious threat than truncation error. Note that the peak vorticity determined by any numerical method of this type will depend on the grid density. In this work identical grids were used where appropriate and were scaled with the geometry for tests performed at different scales.

2.3.4 Probability Density Function

A representation of probability density function was calculated for selected time histories by dividing up the range of observed values into a finite number of bins (usually 100) and calculating the probability of the data falling in each bin. This can reveal details about the nature of the unsteadiness of the flow. An example is the shear stress probability distribution for a boundary layer undergoing natural transition from laminar to turbulent as illustrated (for an ideal case) in figure 2.3.3. When the flow is laminar the shear stress is low and is confined to a relatively narrow range of values, when the flow is turbulent the shear stress jumps to a higher level and will be distributed over a broader range of values with an approximately normal distribution.

2.3.5 Effects of Non-Linearity Combined with Time-Averaging

The availability of a time-accurate five-hole probe allows the critical evaluation of more common techniques used with standard five-hole probes. It is common practice to record time-averaged voltage signals from laboratory instruments (eg: pressure transducers) and then to apply calibrations to the time-averaged voltage. This approach is valid provided that the unsteadiness can be neglected or the quantity of interest is linearly related to the voltage. Pressure transducers generally have a linear calibration characteristic so this approach is valid for measuring time-averaged surface pressures. The response of five-hole probes to total and static pressures is obviously linear (with the exception of relatively minor Reynolds and

Mach number effects). On the other hand, the probe response to incidence will not be perfectly linear, so in a fluctuating flow the application of time-averaging to the raw voltages (or hole pressures) will distort the reported total and static pressures and flow direction. For a five-hole probe without transfer function correction, the viscous effects in the tubing effectively apply an element of time averaging to the fluctuating pressure signals so some time-averaging error is inevitable.

In order to assess the effect of time-averaging, pressure and velocity fields were determined from a five-hole probe with and without transfer function correction applying the time-averaging after and before the five-hole probe calibration respectively. Figures 2.3.4 to 2.3.6 demonstrate the difference on total pressure coefficient in the wake of one of the two-dimensional symmetric models (PARAD2). The greatest errors are most closely correlated with the fluctuating cross-flow velocity (shown in figure 2.3.7) rather than with fluctuating axial velocity or pressure coefficients. This is in keeping with the above discussion of the primary non-linearity being in the incidence-sensitivity of the probe. With a maximum fluctuating cross-flow velocity of around 20% of the free-stream velocity the error on total pressure can be seen to be in the region of 10% of the free-stream dynamic head.

2.3.6 Reynolds Stresses

The Navier-Stokes equations apply to the instantaneous flow. If we want to consider the time-average of an unsteady flow we cannot simply put the time-derivative terms to zero. Instead we must time-average the equations which gives rise to additional terms generally called the “Reynolds stress” terms after Osborne Reynolds, who was the first to undertake this procedure (see for instance Hinze (1959)). There are nine Reynolds stress terms in the time-averaged (or Reynolds-averaged) equations for conservation of momentum, three “normal” stress terms which act normal to the boundaries of the element of fluid being considered and six “shear” stress terms which act along the boundaries. The usual notation for the derivation of these terms

is to express velocities in each direction in terms of the mean and fluctuating components as in equation 2.18.

$$u_x(t) = \overline{u}_x + u'_x(t) \tag{2.18}$$

where $u_x(t)$ is the velocity in the x direction at a given location as a function of time, t, $\overline{u}_x$ is the time-average of $u_x(t)$ and $u'_x(t)$ is therefore the fluctuating component of $u_x(t)$

The Reynolds stresses then scale with the average of the product of the different pairs of u' components (ie: $\overline{u'_x u'_x}$, $\overline{u'_x u'_y}$, $\overline{u'_x u'_z}$, $\overline{u'_y u'_x}$, $\overline{u'_y u'_y}$, $\overline{u'_y u'_z}$, $\overline{u'_z u'_x}$, $\overline{u'_z u'_y}$, $\overline{u'_z u'_x}$). In order to actually produce stresses we need to multiply these terms by the fluid density but, given that all of the work done here is at low speed we will work with the average fluctuating velocity products given above.

In order to determine the Reynolds stresses produced by a particular large scale unsteady flow structure a software bandpass filtering operation was performed on the individual velocity components before the instantaneous products were calculated.

3. EXPERIMENTAL RESULTS

3.1 Introduction

This chapter presents wind tunnel results for a number of bluff bodies, each of which is presented in a separate section. Simple two-dimensional shapes were used in the development of the experimental techniques and provide a degree of validation since we have a good idea of what to expect in terms of the unsteady flow structures. These models were also used to facilitate parametric changes. They are easier to modify than more complicated three-dimensional shapes, fewer measurements are required to provide a good description of the flow and they provide less computationally demanding test cases for CFD. Results are also presented for two three-dimensional models (Ahmed and Rover 200) in order to focus on flow structures specific to passenger cars. Each model has been examined first from a time-averaged point of view, and then from an unsteady point of view. In many cases reconstructions of periodic elements of the flow-field have been undertaken using the method described in section 2.3.2. In addition to figures showing sequences of images, these reconstructions are presented as animations in .avi format on the CD-ROM which accompanies this thesis.

3.1.1 Coordinate System and Conventions

The coordinate system used in this work is illustrated in figure 3.1.1, note that z is axial, y is vertical and x is cross flow. The x origin is taken to be on the centreline and the y origin is on the ground plane. For positions in the wake the z origin was taken to be at the most rearward point on the model (as shown in figure 3.1.1) while for positions on the model the z origin was taken to be at the front of the model.

Positions in the wake are generally non-dimensionalised using the “base dimension” except for the racing car wing where the chord is used. The base dimension was taken to be the width of the 2D symmetric models and the square root of the frontal area for the 3D models. For the 2D Ahmed model the base dimension was taken to be the square root of the frontal area for a 3D Ahmed model of the same scale.

Positions on the surface are non-dimensionalised by the maximum dimension of the model in that direction (eg: axial positions are non-dimensionalised by the model length).

Force measurements on vehicle models were resolved into drag, total lift, front lift and rear lift at the "contact patches" (so an axial force at mid-height on the model will produce drag, positive front lift and negative rear lift but obviously no total lift). Although all six force components were measured, the models were only tested at zero yaw angle so side force, yawing and rolling moments were always small and will not therefore be discussed. Forces on the racing car wing were resolved into drag, downforce (negative lift) and nose-up pitching moment about the ¼ chord position. Forces have been non-dimensionalised by the dynamic pressure and model frontal area for 3D models or chord × span for the racing car wing ($chord^2$ × span for pitching moment).

3.2 Two-Dimensional Symmetric Models

Details of model geometry and construction can be found in section 2.1.2.1.

3.2.1 Steady Data

3.2.1.1 Surface Oil Flow-Visualisation

Surface oil flow visualisation was performed as described in section 2.2.7.2. The flow velocity was 25m/s, corresponding to a length-based Reynolds number of $8.9x10^5$ or a width-based Reynolds number of $2.3x10^5$. Figure 3.2.1 shows the locations of the photographs presented in the following figures.

Figure 3.2.2 shows the surface oil flow near the front of the PARAD1 model and reveals a laminar separation bubble similar to the one observed by Dominy (1995a) at the end of the forward radius on the Ahmed model. The separation line is well defined at z/L=0.056 slightly before the end of the radius as indicated, at this point the local surface is at 13° to the axial. The reattachment position varies between approximately z/L=0.08 and z/L=0.11.

Figure 3.2.3 shows the surface oil flow near the front of the PARAD2 model. The pattern is similar to that of the PARAD1 model with separation at z/L=0.088 (6° from the axial) and reattachment occurring between z/L=0.11 and z/L=0.13.

Figures 3.2.4 and 3.2.5 show surface oil flow at the rear of the PARAD1 and PARAD2 models respectively. The oil/powder mixture was only painted onto the model up to a position safely upstream of the separation. The mixture then streaked downstream along the surface up until the separation point. The separation occurs a short distance downstream of the start of the trailing radius in both cases. For the PARAD1 model the separation occurs at z/L=0.95 at which point the model surface is at 16° to the axial. For the PARAD2 model the separation occurs at z/L=0.94, 21° around the radius. The width between separation points for the PARAD1 and PARAD2 models are 0.98W and 0.94W respectively.

3.2.1.2 Surface Pressures

Figure 3.2.6 shows the surface pressure distribution at mid-height on the three two-dimensional symmetric models (DOCTON, PARAD1, PARAD2). The positions of the separation lines determined from oil-flow visualisation are indicated. In all cases the separations occur just after the start of an adverse pressure gradient. The larger radius on the corners of the PARAD2 model, compared with the PARAD1 model results in a less severe suction peak at the front of the model but a lower minimum pressure at the rear since the separation is delayed until further around the radius. The DOCTON model has the same corner radius as the PARAD2 model but the same radius-to-width ratio as the PARAD1 model. At the front of the model its pressure distribution falls between those of the other two models which seems logical. At the rear, however, it appears to separate ahead of either of the other two models; this can probably be attributed to its lower aspect ratio. It was not therefore felt appropriate to make further comparisons between the DOCTON model and the PARAD models.

Boundary layer trips were fitted to the PARAD1 and PARAD2 models. The trips were made from layers of roughened aluminium tape with a width of 0.25R (where R is the corner radius of the model). The trip thickness was increased until the laminar separation bubble was suppressed down to half the usual test Reynolds number.

Figures 3.2.7 and 3.2.8 show the effect of the trips on the surface pressure distribution for the PARAD1 and PARAD2 models respectively. The trips have a significant effect in their immediate vicinity. This is probably due to the local flow over the trip rather than to the suppression of the laminar bubble since these are usually very thin compared with their length and so have negligible effect on the surface pressure distribution. With the trips, the point of minimum suction for both models corresponded to a tapping in the trip itself. The trips have no effect on the pressure distribution on the remainder of the model. Trips were fitted as part of the standard testing configuration from this point onwards.

Figures 3.2.9 and 3.2.10 indicate the effect of Reynolds number (tunnel velocity) on the surface pressure distribution. The slight delay in separation at higher Reynolds number accentuated the suction peaks ahead of the separations at the front and rear of the model.

Figure 3.2.11 quantifies the effect of model misalignment on the surface pressure distribution. The 1.5 to 2.0 degree changes in alignment used were well in excess of the maximum misalignment that could occur in error. Unsurprisingly, the pressure distributions were sensitive mainly to yaw misalignment, and this sensitivity occurred at the front of the model. A 2.0° change in yaw produced a maximum CP change of 0.15.

3.2.1.3 Steady Wake

Five-hole probe measurements were made in the wake of the PARAD models in a plane extending from 1 to 3 model widths downstream of the models and over 1.8 model widths, as indicated in figure 3.2.12. This traverse area was chosen to be as close as possible to the model without the local flow direction anywhere in the plane falling outside the incidence range of the five-hole probe.

Figures 3.2.13 and 3.2.14 show the time-averaged total pressure distributions and velocity vectors in the wakes of the PARAD1 and PARAD2 models respectively. Figures 3.2.15 and 3.2.16 show the static pressure distributions in the wakes of the models. Pressures have been non-dimensionalised by the total and static pressures recorded at the reference pitot-static probe upstream of the model and off-centre. Figures 3.2.17 and 3.2.18 show the distribution of y-axis vorticity, positive (red) corresponding to clockwise vorticity looking into the page. Vorticity has been non-dimensionalised using the free-stream velocity and the width of the models.

These plots indicate true time-averaged quantities. In other words, unsteady measurements were made with the five-hole probe using transfer-function correction (see section 2.2.5) before applying the probe incidence calibration at each point in

time. The resulting quantities (Po, Ps etc) were then time-averaged. This approach is more correct than the usual practice of simply recording time-averaged transducer voltages as discussed in section 2.3.5. In order to provide enough data for good quality spectral analyses, 15 sets of 2048 points in time were recorded at each location.

The flow-fields for the two models are generally similar. The wake of the PARAD1 model (small radius corners) is more diffuse, total and static pressure gradients are lower, the wake is wider and vorticity (velocity gradient) is lower.

3.2.1.4 Three-Dimensionality (Time-Averaged)

Although the PARAD models are nominally two dimensional, their aspect ratio is very low (span/width = 2.72, span/length = 0.69) so three-dimensionality is inevitable. Figure 3.2.19 shows the time-averaged distribution of total and static pressure along a line in the spanwise direction (the direction of extrusion) in the wake of the PARAD1 model. The positions of the two endplates and the ground plane on which the models were mounted are shown. We see only a relatively small region (less than 0.5W) near the mid-span position where the gradients are small. Maximum out-of-plane (spanwise) velocities within this region (where the two-dimensional wake surveys were performed) are between 4% and 5% of the free-stream velocity for the PARAD1 and PARAD2 models. The spanwise velocities corresponded to a down-sweep near the centreline as the wake closes asymmetrically in the spanwise direction due to the presence of the ground plane. This induces up-sweep outside the wake through the production of large-scale streamwise vortices.

3.2.2 Unsteady Data

3.2.2.1 General Unsteady Data

Figure 3.2.20 indicates the level of surface pressure fluctuation around the mid-height position on the PARAD models with trips. This data was obtained by measuring the fluctuating pressures at each tapping using a scanivalve and transfer

function correction (see section 2.2.5) and then calculating the standard deviation of the pressure fluctuation at each point. As for the wake measurements, 15 sets of 2048 samples were recorded at 800hz at each tapping for a total of 30720 samples over 38s for each tapping. The values are non-dimensionalised using the free-stream dynamic pressure recorded at the pitot-static probe.

The maximum level of surface pressure fluctuation at the rear of the models is around 7%-8% of the dynamic pressure, the PARAD1 model demonstrating slightly more unsteadiness than the PARAD2 model. The location of maximum surface pressure fluctuation at the rear of the models occurs immediately upstream of the separation point (indicated by the oil flow visualisation in section 3.2.1.1). Similar or larger levels of unsteadiness exist at the front of the model where the time-averaged pressure gradients are high.

Figures 3.2.21 and 3.2.22 show typical pressure coefficient time-traces at the positions of minimum time-averaged pressure for the PARAD1 and PARAD2 models respectively. Figures 3.2.23 and 3.2.24 show the corresponding probability density functions which are symmetric and "normally" shaped.

3.2.2.2 Wake Spectral Analysis

Figures 3.2.25 and 3.2.26 compare the levels of fluctuating total pressure (standard deviation) in the wake of the PARAD1 and PARAD2 models. This data was obtained from a five-hole probe traverse using transfer-function correction.

Figures 3.2.27 and 3.2.28 are typical time-traces of the fluctuating velocity reported by a hot-wire at the reference location indicated in figure 3.2.12. The hot-wire was aligned with the x-axis to provide maximum sensitivity to unsteadiness in the plane of the nominally two-dimensional flow. The hot-wire "effective" velocity (see section 2.2.4) has been non-dimensionalised by the free-stream velocity. Figures 3.2.29 and 3.2.30 show the corresponding probability density functions. These are somewhat asymmetric, indicating that the unsteadiness corresponds to the passing of

packets of low-velocity fluid of varying intensity between which the flow approaches a more uniform condition.

Figures 3.2.31 and 3.2.32 show the autospectral densities of the reference hot-wire effective velocity for the PARAD1 and PARAD2 models respectively. These plots are the averages of autospectral densities calculated for each of 510 sets of 2048 points in time at 800hz (ie: $1.0x10^6$ samples and a total sampling time of 22 minutes). For the PARAD1 model, a clear spectral peak is observed corresponding to a Strouhal number of 0.313 (based on free stream velocity and model width) and a weak spectral peak is visible at twice this frequency. For the PARAD2 model the main peak is at S=0.361, the second peak at twice this frequency is weak but visible. This strongly periodic fluctuation is the result of vortex shedding from the body. As discussed in section 2.1.1.1, the small spectral peak at around 15hz is present when the tunnel working section is empty. With the models in the tunnel the peak contains between 1.2 and 1.5 times as much unsteadiness as it does with the tunnel empty. This can be considered to be a small increase and can be attributed to broad band unsteadiness due to the models and to the amplification of background unsteadiness by the time-averaged gradients in flow variables produced by the models.

Figure 3.2.33 shows the variation of the vortex shedding Strouhal number with Reynolds number obtained by varying the tunnel velocity. A significant slope is apparent as is a significant level of variation from run to run (up to 0.05).

Figures 3.2.34 and 3.2.36 show the fraction of the local total pressure coefficient fluctuation due to a narrow frequency band around the shedding frequency. This is determined by calculating the autospectral density of the total pressure coefficient at each location and then effectively integrating over the required frequency band as described in section 2.3.1.2 and dividing by the standard deviation of the fluctuating total pressure coefficient. This provides a good measure of the level of periodicity of the local flow and makes it possible to discount the amplification of unsteadiness by strong time-averaged gradients. For both models this frequency is most dominant

outboard of the maximum fluctuation (ref: figures 3.2.25 and 3.2.26) and drops to a minimal contribution on the centreline. This is because the total pressure on the wake centreline will be affected identically by vortices being shed on either side of the body and so will fluctuate at twice the shedding frequency. Figures 3.2.35 and 3.2.37 show the same quantity as figures 3.2.34 and 3.2.36 except at twice the frequency. As expected this frequency is generally strongest on the centreline. It gets much stronger as we move downstream along the centreline indicating that the vortices move towards the centreline as they travel downstream.

During the unsteady wake traverses with the five-hole probe a reference hot-wire probe was positioned in the wake at x/W=0.3, z/W=2.0 as indicated in figure 3.2.12. The cross-spectral density (CSD) and coherence between the fluctuating total pressure at the five-hole probe and the fluctuating effective velocity reported by the hot-wire was calculated as described in sections 2.3.1.3 and 2.3.1.4 for each five-hole probe location. The strongest CSD peak (near the shedding frequency) at each location was identified automatically in order to allow for some drift in the shedding frequency during the course of an experimental run. The coherence and CSD phase at this frequency were then extracted. Figures 3.2.38 and 3.2.39 show the resulting coherence distribution in the wake of the PARAD1 and PARAD2 models respectively. As for the narrow band levels of fluctuation, coherence at the shedding frequency is very low on the centreline. Note the significantly higher levels of coherence for the PARAD1 model. Figures 3.2.40 and 3.2.41 show the CSD phase, as described above, for the two PARAD models. This has been presented as the phase distribution on a series of lines across the wake at different axial positions. We can see a 180° phase shift between the two sides of the wake due to alternate shedding of vortices. On the centreline the phase at the shedding frequency becomes random and so has not been plotted.

We can determine a propagation velocity for the vortices away from the model from the offset between phase curves at subsequent axial locations (see equation 3.1). For the PARAD1 model, the phase shift at the outside of the traverse region is about

250° between z/W=1.0 and z/W=3.0 at S=0.313 so the propagation velocity is approximately 90% of the free stream velocity, for the PARAD2 model the corresponding propagation velocity is approximately 84% of the free stream velocity.

$$\frac{u_{propagation}}{U_{fs}} = \frac{\Delta z}{U_{fs}\Delta t} = \frac{\Delta z}{\frac{U_{fs}\theta}{360°f}} = \frac{\Delta z}{\frac{U_{fs}\theta W}{360°SU_{fs}}} = \frac{360°S\frac{\Delta z}{W}}{\theta} \qquad (3.1)$$

where $u_{propagation}$ is the rate of downstream propagation of the vortices, U_{fs} is free stream velocity, Δz is an axial displacement and θ is the corresponding phase shift at frequency f (Strouhal number S) and W is the model width

Figures 3.2.42 and 3.2.43 show the $\overline{ux'uz'}$ distributions in the wake of the PARAD1 and PARAD2 models respectively due to frequency bands around the vortex shedding frequency (see section 2.3.6). This is the Reynolds shear stress component acting to entrain fluid from outside the wake. We see that the vortex shedding for the PARAD1 model produces significantly higher Reynolds stresses.

3.2.2.3 Three-Dimensionality (Unsteady)

Figure 3.2.44 shows the distribution of unsteadiness observed at the centre-hole of a five-hole probe (without using transfer-function correction) in the wake of the PARAD1 model. This provides a crude method of assessing the spanwise distribution of the level of unsteadiness. We see a broad region of low gradient near mid-span (almost 1W) compared with the time-averaged quantities (ref. figure 3.2.19). The shedding frequency at mid-span was confirmed to be the dominant frequency over the range of spanwise positions considered. The phase distribution between the fluctuating total pressure (according to a five-hole probe with transfer function correction) and the signal from a hot-wire at mid-span (on the opposite side of the wake) is shown in figure 3.2.45. We see that the shedding at mid-span leads

the shedding towards the ends slightly. The phase shift is limited to about 30° within two model widths of the mid-span position, until the smooth phase distribution is lost within about 0.5W of the lower endplate. Figure 3.2.46 shows the spanwise distribution of coherence between fluctuating total pressure and the signal from the hot-wire at mid-span. We see that coherence remains high (between 0.8 and 0.9) for around 1W at mid span.

Maximum levels of out-of-plane (spanwise) velocity fluctuation for the wake surveys at mid-span were around 13% of the free-stream velocity for both the PARAD1 and PARAD2 models. The maximum level of fluctuation in the spanwise velocity at mid-span due to 10hz bands near the shedding frequency was about 4% of the free-stream velocity for both models (calculated as described in section 2.3.1.2). This compares with in-plane velocity fluctuations of up to 30% of the free stream velocity for the same frequency band.

3.2.2.4 Wake Unsteady Reconstruction

The unsteady reconstruction technique described in section 2.3.2 was applied to the wake surveys behind the PARAD models. Two bands of 1.5hz each were used, one at the shedding frequency and one at twice the shedding frequency. As discussed before, this second frequency is essential in capturing the fluctuating flow on the centreline. Figure 3.2.47 is a sequence of instantaneous vector fields in the wake of the PARAD1 model. The vortices are much less pronounced than those that we are used to seeing in flow visualisation studies in the “Pure Karman Range” at Reynolds numbers of O(100). Figure 3.2.48 shows the corresponding sequence of vorticity, revealing the presence of distinct vortices which appear as a simple meandering of the velocity vectors when the axial flow is superimposed on them. Vorticity has been non-dimensionalised using free-stream velocity and the model width. The vorticity sequence illustrates the mechanism put forward by Gerrard (1966) whereby a vortex is drawn across the wake where it severs the other vortex from the body causing it to be shed. Figure 3.2.49 shows the corresponding sequence of fluctuating

total pressure coefficient. Note the regions outside the wake where the total pressure coefficient exceeds unity. This is a real phenomenon and is discussed in section 5.2.

Figures 3.2.50, 3.2.51 and 3.2.52 illustrate sequences of velocity vectors, vorticity and total pressure coefficient for the PARAD2 model. The unsteady flow structures are essentially the same as for the PARAD1 model but are slightly less pronounced.

3.2.2.5 Surface Pressure Spectral Analysis

Figures 3.2.53 and 3.2.54 illustrate the average autospectral density observed at tappings at z/L=0.94 on the PARAD1 model and z/L=0.91 on the PARAD2 model respectively. These positions correspond to the points of minimum pressure in the time-averaged flow (see figure 3.2.6) and are just forward of the separation line. Although the rest of the tappings were connected to a scanivalve, these tappings were connected directly to separate transducers so that they could be logged continuously throughout an experimental run. The large amount of data collected (approximately 510 sets of 2048 samples) makes it possible to achieve clear spectral plots. Obvious spectral peaks are observed at the shedding frequency for both models. A large amount of background unsteadiness is observed at low frequencies generally. A 4hz band around the 15hz peak corresponding to the tunnel frequency provides a Cp fluctuation of about 0.025 (calculated as discussed in section 2.3.1.2). This level of fluctuation is in keeping with the influence we would expect from the background unsteadiness at this frequency. As discussed in section 2.1.1.1, the free-stream velocity fluctuation in the empty tunnel for this frequency band was 2.4%, which equates to nominally 5% on dynamic head; note that the time-averaged pressure coefficient at this location on the model is about Cp=0.5 (see figure 3.2.11). As discussed in section 2.1.1.1, the spike at 30hz is due to electrical interference and will be ignored. There is some evidence of spectral spikes at the high frequency end of the spectrum however these are too indistinct to analyse further. For spectra based on fewer samples these high frequency “peaks” are indiscernible, furthermore, the level of pressure fluctuation due to these peaks is negligible (note that these spectra are plotted on a log scale).

Figure 3.2.55 illustrates the contribution of unsteadiness near the shedding frequency to the surface pressure fluctuations on the PARAD models. This was calculated as described in section 2.3.1.2. We see that the maximum level of unsteadiness at the rear of the models due to this band occurs at the same locations as the maximum surface pressure fluctuation, z/L=0.94 and z/L=0.93, just upstream of the separation line. The peak levels of pressure coefficient fluctuation due to this band are 0.021 and 0.011 for the PARAD1 and PARAD2 models respectively. Levels of unsteadiness due to this band are also high at the front of the model.

Figure 3.2.57 shows the quantity plotted in figure 3.2.55 divided by the local surface pressure fluctuation. This provides a measure of how periodic the local pressure fluctuations are. We do not see a significant peak in this plot near the front of the model so the high levels of unsteadiness due to the shedding band in figure 3.2.55 are simply due to the presence of broad-band unsteadiness combined with high pressure gradients on the model surface in this region. The surface pressures are most periodic some distance upstream of the separation at z/L=0.87 and z/L=0.86 for the PARAD1 and PARAD2 models respectively, at these locations the spectral band around the shedding frequency contributes 37% and 25% of the pressure fluctuation. This is a significant proportion but broad-band unsteadiness still contributes the bulk of the unsteadiness.

Figure 3.2.56 shows the contribution of unsteadiness at twice the shedding frequency to the surface pressure coefficient fluctuation and figure 3.2.58 shows this quantity as a proportion of the total local pressure coefficient fluctuation. The maximum pressure coefficient fluctuation due to this band occurs just downstream of the separation line at z/L=0.96 and z/L=0.95 for the PARAD1 and PARAD2 models respectively. The importance of this spectral band to the local pressure fluctuation reaches a peak slightly further downstream of the separation at z/L=0.98 for both models. Again both the levels of unsteadiness and levels of periodicity are higher for the PARAD1 model, with maximum band limited pressure coefficient fluctuations of 0.008 and 0.004 for the PARAD1 and PARAD2 models and

maximum fractions of local unsteadiness of 0.17 and 0.16. As for the shedding frequency band, high levels of band limited fluctuation are present for the band at twice the shedding frequency near the front of the model however we do not observe a corresponding peak in figure 3.2.58 indicating that this is simply due to the presence of broad-band unsteadiness in this region.

During the unsteady surface pressure measurements, a hot-wire was positioned at the reference location in the wake (x/W=0.3, z/W=2.0), as indicated in figure 3.2.12. Cross-spectral analyses were therefore possible between the time-accurate surface pressure measurements and the effective velocity signal from the hot-wire. Figure 3.2.59 indicates the cross-spectral phase between the hot-wire and the surface pressure fluctuations at the shedding frequency. Figure 3.2.60 shows the coherence between the hot-wire signal and the local pressure fluctuations. The data is much less coherent towards the front of the models for the –ve x side of the PARAD2 model (this is the opposite side to the hot-wire). This lack of coherence explains the large random fluctuation of phase seen in these regions. Nevertheless, we can see that the pressure fluctuations are approximately in phase on each side of the model and are approximately 180° out of phase with the pressure fluctuations on the opposite side. The latter observation is in keeping with the fluctuations being the result of vortex shedding. The loss of coherence between the two sides of the PARAD models indicates that a significant proportion of the unsteadiness near the shedding frequency is unconnected with the shedding itself. This extra unsteadiness is not coherent across the wake in the same way as the shedding is and so results in diminished coherence on the side of the model away from the hot-wire.

3.2.3 Summary

Table 3.1 summarises some key parameters relating to the flow around the PARAD1 and PARAD2 models. The relevant figures from which the data has been extracted have been indicated where appropriate.

Parameter	PARAD1	PARAD2	Figures
corner radius	0.283 W	0.416 W	
Strouhal number S	0.313	0.361	3.2.31, 3.2.32
start of laminar separation bubble	0.06 L	0.09 L	3.2.2, 3.2.3
front axial position of CP_{min} (no trips)	0.06 L	0.07 L	3.2.6
front CP_{min} (no trips)	-2.03	-1.57	3.2.6
separation at rear – axial position	0.95 L	0.94 L	3.2.4, 3.2.5
separation at rear –surface to axial	16°	21°	3.2.4, 3.2.5
separation at rear - width	0.98 W	0.94 W	3.2.4, 3.2.5
rear axial position of CP_{min}	0.94 L	0.91 L	3.2.6
rear CP_{min}	-0.67	-0.76	3.2.6
rear axial position of CP'_{max}	0.94 L	0.93 L	3.2.19
rear CP'_{max}	0.08	0.07	3.2.19
rear axial position of CP'_{max}(shed band)	0.94 L	0.93 L	3.2.55
rear CP'_{max}(shed band)	0.021	0.011	3.2.55
rear axial position of CP'_{max}(shed)/CP'	0.87 L	0.86 L	3.2.57
rear CP'_{max}(shed)/CP'	0.369	0.245	3.2.57
rear axial position of CP'_{max}(2× shed)	0.96 L	0.95 L	3.2.56
rear CP'_{max}(2× shed)	0.008	0.004	3.2.56
rear axial pos. of CP'_{max}(2× shed)/CP'	0.98 L	0.98 L	3.2.58
rear CP'_{max}(2× shed)/CP'	0.17	0.17	3.2.58
maximum vorticity at z/W=1.1	1.7 U_{fs}/W	2.4 U_{fs}/W	3.2.17 3.2.18
maximum CPo' (standard deviation)	0.31	0.31	3.2.25, 3.2.26
width between points of maximum Cpo'	0.68 W	0.61 W	3.2.25, 3.2.26
typical coherence in the wake	0.93	0.82	3.2.38, 3.2.39

Table 3.1 – Flow parameters for the PARAD models

3.3 Racing Car Wing/Gurney Flap

A Gurney flap is a thin strip of material attached at the trailing edge of the pressure surface of an aerofoil in order to increase the downforce of a wing of limited size. Gurney flaps are used extensively in motorsport where downforce is desirable in order to increase cornering speeds but where regulations severely restrict the dimensions of wings and other aerodynamic components of the car.

Although this geometry is obviously not directly related to passenger cars it has been included because it provides a good illustration of the application of many of the experimental techniques used throughout this thesis. Also, the high periodicity of the flow for the Gurney flap helps to put the results for the other geometries into context.

Non-dimensionalisation has generally been based on the aerofoil chord, the primary exception being Strouhal number, which has been based on the base dimension (the sum of the Gurney height and trailing edge thickness). The wing was mounted to produce downforce as it would be on a racing car. Therefore, in this section only, we will consider positive lift to be in the direction of positive downforce. (Note that elsewhere in this thesis lift is upwards.)

The test Reynolds number was 3.1×10^5 based on free-stream velocity and wing chord or 1.7×10^4 using the base dimension. Details of the experimental arrangement are given in section 2.1.2.2. An analysis of this and related work is given in Sims-Williams et al (1999).

3.3.1 Steady Data

3.3.1.1 Forces

Note that no blockage correction was applied, so while the general behaviour of the aerofoil will be correct, the lift and drag coefficients would both be lower in an unbounded domain, particularly at high incidence.

Figure 3.3.1 shows the lift versus incidence curve for the aerofoil with and without the Gurney flap while figure 3.3.2 shows the drag versus incidence curve. The behaviour of the aerofoil is fairly typical although it does not generate as abrupt a stall as would generally be expected, with only a small drop in lift and a fairly progressive increase in drag. The Gurney flap increases both lift and drag at a given incidence but does not have a dramatic effect on the shape of the characteristics.

When choosing an aerofoil and configuration for a high lift application it is useful to look at the trade off between lift and aerodynamic efficiency (lift/drag). This is plotted in figure 3.3.3 for the aerofoil with and without Gurney. We see that increasing incidence significantly beyond the point of maximum lift/drag is an inefficient method of increasing lift. The fitting of a Gurney is a much more efficient approach with a relatively small loss of efficiency for a twofold increase in lift. The optimum incidence of the aerofoil is essentially unaffected by the fitting of the Gurney. The remainder of results presented will be for the +1° incidence condition which is a realistic design point, being just beyond the point of maximum lift/drag.

3.3.1.2 Surface Pressures

Figure 3.3.4 shows the surface pressure distribution at mid-span for the aerofoil with and without Gurney flap. Note that the effect of the Gurney is not restricted to its immediate vicinity but extends over the entire of both the pressure and suction surfaces.

3.3.1.3 Steady Wake

The wake centreline behind the aerofoil with and without Gurney was surveyed with five-hole probe 5h_04. In the case of the plain aerofoil, time-resolved measurements were not considered necessary but in the case with Gurney, where the flow was much more unsteady, time-accurate measurements were made using transfer function correction (see section 2.2.5) and then time-averaged. Data was logged at 3000hz through 4^{th} order 1000hz low pass filters. For the steady measurements one

set of 2048 points was recorded at each location while for the time-resolved measurements this was increased to 10 sets. No probe nulling was used.

Figure 3.3.5 shows the distribution of total pressure coefficient behind the wing without the Gurney. The trailing edge of the aerofoil is drawn in for clarity and the white region surrounding it indicates the region in which no measurements were made. Note the greater total pressure loss due to the adverse pressure gradient and consequently thicker boundary layer on the suction surface compared with the pressure surface. Figure 3.3.6 shows contours of total pressure coefficient in the case with Gurney. Again the geometry has been drawn in for clarity, including the Gurney flap itself. The extended white region behind the aerofoil indicates the area in which the flow incidence exceeded the calibration range of the probe. Note that although the wake with the Gurney flap is wider, it closes more rapidly than in the case without Gurney. The greater divergence between contours of total pressure with the Gurney indicate greater mixing between the fluid in the wake and that outside.

3.3.2 Unsteady Data

3.3.2.1 General Unsteady Data

Figure 3.3.7 shows the fluctuating total pressure coefficient behind the Gurney flap. A distinct region of elevated unsteadiness exists which is significantly larger than the total pressure wake of figure 3.3.6. The level of unsteadiness within this region is surprisingly constant at around 30% of the free stream dynamic pressure.

Fluctuating pressures on the surface were also measured using transfer function correction (as described in section 2.2.5). These were found to be essentially constant everywhere and the level of the fluctuations was only about 3% of the free-stream dynamic pressure. Probability densities for surface pressure fluctuations closely resembled normal distributions.

3.3.2.2 Wake Spectral Analysis

Figure 3.3.8 shows the autospectral density for a hot-wire behind the wing with Gurney flap. This is the average of 6200 spectra each calculated for a time history of 2048 points (ie: a total logging time of 70 minutes at 3000hz). A very clear peak is visible at a Strouhal number of S=0.181 (based on free-stream velocity and the base dimension). This is consistent with vortex shedding from the rear of the Gurney flap. A much smaller spectral peak is visible at the first harmonic frequency (S=0.362). Unsteadiness increases as frequency decreases except below S=0.181. This could be due to the superposition of the strong spectral peak on a general trend for increased unsteadiness at lower frequencies so that the slope becomes exaggerated above the peak and the two trends cancel out below it.

Figure 3.3.9 shows the total pressure fluctuation resulting from a 30hz frequency band around the shedding frequency (calculated as described in section 2.3.1.2) as a fraction of the local total pressure fluctuation. This provides a good index to periodicity at a given frequency. We see that this frequency dominates over a wide region behind the Gurney flap, with the notable exception of the wake centreline. As discussed previously, we would expect the total pressure to fluctuate at twice the shedding frequency on the centreline since it will be affected identically by vortices shed on either side of the body; this result is therefore unsurprising.

Figure 3.3.10 shows the total pressure fluctuation resulting from a 30hz frequency band at twice the shedding frequency as a fraction of the local total pressure fluctuation. As expected this frequency dominates on the wake centreline but is much less significant elsewhere.

Figure 3.3.11 shows the cross-spectral phase (see section 2.3.1.3) between the reference hot-wire and total pressure fluctuation at the shedding frequency. We see an abrupt phase shift across the centreline resulting from the nominally anti-symmetric unsteady flow structure. We can see the propagation of the vortices in the

direction of the local flow manifest as a steadily increasing phase shift in the downstream direction.

Figure 3.3.12 shows the coherence (see section 2.3.1.4) between the reference hot-wire and the total pressure fluctuation at the shedding frequency. The coherence is very high (between 0.9 and 1.0) almost everywhere, including well outside the wake. The only exception is the wake centreline, again because this region will be dominated by the first higher harmonic.

3.3.2.3 Wake Unsteady Reconstruction

The reconstruction technique described in section 2.3.2 was used to visualise the periodic flow behind the wing with Gurney. The analysis used the time-accurate data recorded with the five-hole probe and employed the fixed hot-wire probe for the phase reference signal. Two bands 1.5hz wide at S=0.18 and S=0.36 were used to determine the magnitude of the unsteadiness. This band width was chosen by manually inspecting original and reconstructed time traces based on different band widths. Data has been plotted everywhere that measurements were recorded although the data should be ignored in the regions blanked out in earlier plots where the average flow was not within the probe incidence range.

Figure 3.3.13 provides a sequence of plots of velocity vectors over one shedding period. Note that the level of unsteadiness is not actually high enough to reverse the free stream flow in the vortex street well behind the geometry so the vortices appear as a meandering wake. Figure 3.3.14 shows the corresponding fluctuating vorticity field. We are now able to see the distinct vortices being convected along in the wake. Figure 3.3.15 shows the corresponding sequence for total pressure coefficient. We see packets of total pressure loss corresponding to the cores of the shed vortices. We also see regions of high total pressure which appear outside the wake as the vortices are being formed and which are then convected downstream. The production of transient total pressure above the upstream total pressure is a real effect which will be discussed in section 6.3. The sequences of figures 3.3.13

through 3.3.15 are provided as “avi” format animations on the CD-ROM which accompanies this thesis.

3.3.2.4 Surface Pressure Spectral Analysis

Time-accurate pressures were measured on the surface of the aerofoil using the transfer function correction technique described in section 2.2.5. Figure 3.3.16 illustrates the importance of unsteadiness near the shedding frequency to the surface pressure unsteadiness at mid-span (calculated as described in section 2.3.1.2). We see that the shedding does affect the surface pressure unsteadiness on both surfaces, particularly as we move closer to the trailing edge. However, recall from section 3.3.2.1 that the total surface pressure unsteadiness is only about 3% of the free-stream dynamic pressure. A similar analysis performed for the first higher harmonic indicated that this frequency contributed only about 5% of the local unsteadiness (0.15% of the dynamic pressure) with no distribution around the aerofoil. This very low level of fluctuation, with no obvious distribution, is probably due to broadband unsteadiness rather than the periodic structure in the wake.

The reference hot-wire probe was logged during the unsteady surface pressure measurements in order to allow cross-spectral analyses. Figure 3.3.17 shows the phase between the hot-wire and the local surface pressure fluctuations. We see that the two surfaces are each at approximately constant phase and that they are approximately out of phase with each other. This will result in the maximum possible fluctuating lift for a given level of surface pressure unsteadiness. The unsteady reconstruction method was used to reconstruct fluctuating pressure distributions and these were then integrated around the aerofoil in order to determine the fluctuating lift. As expected from the low levels of fluctuating pressure, the fluctuating lift was calculated to be only $C_L'=0.02$ on an average value of $C_L=1.88$.

Figure 3.3.18 indicates the coherence between the reference hot-wire and the surface pressure fluctuations at the shedding frequency. With the exception of the flow around the leading edge and one (probably spurious) point just behind mid-chord,

the coherence is very high. This indicates that the fluctuations at this frequency are the result of the vortex shedding rather than any background unsteadiness.

3.4 Two-Dimensional Ahmed Model

Details of the construction of this model are provided in section 2.1.2.4. As discussed at the start of this chapter, positions on the model surface have been non-dimensionalised by the model length while all other non-dimensionalisation has been based on the square root of the frontal area of a 3D Ahmed model of equivalent scale. This dimension is equal to 1.16 times the height of the model (excluding ground clearance).

3.4.1 Steady Data

3.4.1.1 Surface Pressures

The model was tested with a number of backlight angles, maintaining constant backlight length as for the three-dimensional Ahmed geometry. Figure 3.4.1 shows the effect of backlight angle on the pressure distribution on the upper half of the model. At low backlight angles (less than 22.5° to the horizontal) the pressure on the backlight decreases with increasing backlight angle. When the backlight angle exceeds 22.5°, however, the flow separates at the top of the backlight and does not reattach. In this case the pressure on the roof is maintained over the backlight. The separated backlight results in slightly increased pressures on the rear half of the roof but has no impact further forward.

The model demonstrates a laminar separation bubble on the forward radii as for the PARAD models (discussed in section 3.2.1.1). Boundary layer trips were fitted to the model using the same approach as for the PARAD models. The trips were made from layers of roughened aluminium tape with a width of 0.22R (where R is the corner radius of the model). The trip thickness was increased until the laminar separation bubble was suppressed down to half the usual test Reynolds number, this occurred with a trip thickness of 0.56mm (0.012R). The pressure distributions of figure 3.4.1 are for the model with boundary layer trips on the forward radius; figure 3.4.2 shows the pressure distributions with and without trips for 20° and 30° backlight angles and indicates the positions of the trip leading and trailing edges.

The trips result in a much sharper suction spike on the forward radius however, as for the PARAD models, the tappings affected are those in the immediate vicinity of the trip itself so this could be a very localised effect due to the flow over the trip rather than due to the suppression of the laminar separation bubble. The trips have no effect on pressures elsewhere on the model.

3.4.1.2 Surface Oil Flow Visualisation

Figures 3.4.3 through 3.4.5 show surface oil flow visualisation on the backlight of the 2D Ahmed model at backlight angles of 10°, 20° and 30° respectively. At 10° there is evidence of the fluid in the boundary layer slowing down at the top of the backlight but it is not clear if a small separation bubble is formed or not. At 20° there does appear to be a separation at the corner at the top of the backlight with reattachment at approximately z/L=0.82. This region closely corresponds to the location of minimum pressure on the model surface (see figure 3.4.1). With a backlight angle of 30° the flow separates just after the start of the backlight and does not reattach (figure 3.4.5). In this case the oil and paint mixture was applied upstream of the backlight only, the oil streaks to the separation line and then drips down the backlight under the influence of gravity. Some evidence of flow three-dimensionality is visible in these drips.

3.4.1.3 Steady Wake

Figures 3.4.6 and 3.4.7 show velocity vectors behind the model at mid-span for 20° and 30° backlight angles respectively. This data is not based on true "time-averages" (see section 2.3.5) and no check has been made that the incidence remains within the range of the probe. Figures 3.4.8 and 3.4.9 show total pressure coefficient in the same region and figures 3.4.10 and 3.4.11 show vorticity in the direction of the x-axis (positive vorticity is counter-clockwise looking into the page).

The wake of the separated 30° backlight starts off larger and closes more slowly, resulting in a much longer wake. The reduced downwash for the 30° backlight is in keeping with the higher backlight pressures and with reduced rear lift. Peak levels of

vorticity are slightly higher in the case of the 20° backlight although they are confined to a smaller region.

3.4.2 Unsteady Data

3.4.2.1 General Unsteady Data

Figure 3.4.12 shows the fluctuating pressure coefficient (standard deviation) on the upper surfaces of the 2D Ahmed model at selected backlight angles. These measurements were made with a single transducer and scanivalve using the transfer function correction technique described in section 2.2.5. There are high levels of unsteadiness around the front radius which are likely due to the high time-averaged pressure gradients in this area (see figure 3.4.1). As for the time-averaged quantities, the distinction between different backlight angles is visible on the rear half of the model only. The sub-critical backlight angles produce an unsteadiness peak at the location of the time-averaged suction spike at the top of the backlight (figure 3.4.1), this location also corresponds to the closed separation visible in figure 3.4.4. In the case of the fully separated 30° backlight, unsteadiness increases as we move down the backlight and reaches a peak just before the end of the backlight. The highest localised unsteadiness on the backlight occurs for the 22.5° geometry and corresponds to 10% of the free-stream dynamic pressure (recall that this is the steepest backlight angle for which the flow does not become "fully separated" and this geometry also produces the lowest time-averaged pressure).

Figures 3.4.13 through 3.4.15 show the fluctuating pressure reported at the centre-hole of the five-hole probe in the wake of the model, without applying transfer-function correction. This provides a crude method of assessing regions of unsteadiness without the need to store time-history data during the experimental run. We see that the unsteadiness is concentrated in the shear layers, particularly in the upper shear layer. The unsteadiness is slightly greater for the 22.5° backlight than for the 20° case but the most concentrated unsteadiness occurs for the fully separated, 30° backlight.

Figure 3.4.16 shows the level of total pressure coefficient fluctuation (standard deviation) along a vertical line at mid span in the wake at z/sqrt(A_{3D})=1.73. These measurements were made using transfer function correction (refer to section 2.2.5) and are based on 30720 points in time recorded at each point in space (38s logging time at 800hz). Unsurprisingly, we see low unsteadiness outside the wake for the lower backlight angles with a relatively uniform level of unsteadiness across the wake. There is some evidence of increased unsteadiness in the shear layers, however the coarseness of the grid spacing makes this difficult to observe. The fully separated, 30° backlight produces the highest level of unsteadiness (almost 40% of the free stream dynamic pressure) and this occurs in its upper shear layer, confirming the structure observed in figure 3.4.15. The high level of unsteadiness in the upper shear layer of the 30° case is somewhat surprising since the sub-critical backlight angles demonstrate higher vorticity (compare figures 3.4.10 and 3.4.11). The taller wake is better resolved by the coarse point spacing and it is possible to observe a clear reduction in unsteadiness in the middle of the wake followed by increased unsteadiness in the lower shear layer.

Figures 3.4.17 through 3.4.19 show probability density function, calculated as described in section 2.3.4, for time-accurate pressures recorded on the backlight of the 2D Ahmed model. The locations chosen approximately correspond to the positions of maximum unsteadiness in figure 3.4.12. In all cases the probability density distributions resemble normal distributions which argues against dominant periodicity or bi-stability.

Figures 3.4.20 through 3.4.22 show probability density function calculated for the effective velocity reported by a single element hot-wire (wire element aligned with y-axis) in the wake of the 2D Ahmed model at the locations indicated. These locations were chosen to correspond to the rear of the regions of high unsteadiness in the upper shear layer observed in figures 3.4.13 through 3.4.15. These probability density functions resemble slightly skewed normal distributions. This indicates that

packets of velocity significantly above the average velocity are less common than packets of velocity significantly below the average velocity.

3.4.2.2 Wake Spectral Analysis

Figures 3.4.23 through 3.4.25 show average autospectral densities for the hot-wire probe at the same reference locations as figures 3.4.20 through 3.4.22. These average autospectral densities are based on 660 sets of 2048 point time-records (1.35×10^6 points logged over 28 minutes at 800hz). We can see generally higher unsteadiness at low frequencies with a weak spectral peak at the background tunnel frequency of 15hz (visible in figure 2.1.2 and discussed in section 2.1.1.1). This peak is only slightly greater in amplitude than for the empty tunnel (which can be attributed to higher broadband unsteadiness at low frequencies with the model in the tunnel) so this peak has been ignored in the remainder of analyses. For the sub-critical backlight angles of 20° and 22.5°, we see distinct spectral peaks at S=0.50 (based on free-stream velocity and square root of frontal area for an equivalent three-dimensional Ahmed model). This corresponds to a Strouhal number of S=0.43 based on the model height (excluding ground clearance). There is evidence of a weak spectral hump at the first higher harmonic for the 20° case. In the case of the fully separated 30° backlight (figure 3.4.25) there is no distinct spectral peak visible with only a weak hump at S=0.27 (S=0.23 based on model height). The levels of broad-band unsteadiness are higher for the fully separated flow than for sub-critical backlight angles, however.

Figure 3.4.26 shows the fraction of the local total pressure fluctuation due to frequencies near those highlighted in figures 3.4.23 through 3.4.25 along a line at mid span at $z=1.73\text{sqrt}(A_{3D})$ behind the model. For the sub-critical (20° and 22.5°) cases the contribution of the specified frequency band drops off outside the wake and is marginally higher in the shear layers than in the middle of the wake (although, as noted previously, the limited spatial resolution of the measurements makes this difficult to observe). For the fully separated case, the contribution of the specified frequency band to the local unsteadiness is approximately uniform over the region

investigated. Worth noting is the fact that the 20° backlight appears significantly more periodic than the 22.5° backlight.

Figure 3.4.27 shows the cross-spectral phase between the reference hot-wire (discussed previously) and the fluctuating total pressure coefficient at the critical frequencies identified in figures 3.4.23 through 3.4.25 for the same line in the model wake at z=1.73sqrt(A_{3D}). The calculation of cross-spectral phase is described in 2.3.1.3. In all three cases, the lead appears to come from a location low in the wake (approximately y/sqrt(A_{3D})=0.20) and the rest of the wake then follows. The upper bound of the wake lags by about 180° however the continuous phase distribution, at least in the 20° and 22.5° cases, argues against a conventional vortex shedding flow structure.

Figure 3.4.28 shows the coherence between the reference hot-wire and the fluctuating total pressure coefficient at the critical frequencies for the same line in the wake (for calculation details see section 2.3.1.4). For the sub-critical backlight angles we see high coherence throughout the wake including shear layers, particularly for the 20° backlight where coherence is around 0.9. The coherence then drops off outside the wake. For the fully separated 30° backlight, the coherence is much lower and is relatively uniform over the traverse region with a slight trend for higher coherence in the upper shear layer.

3.4.2.3 Wake Unsteady Reconstruction

The reconstruction technique described in section 2.3.2 was used to visualise the periodic element of the flow in the wake of the 2D Ahmed model with 22.5° backlight. The unsteadiness contained within 1.5hz bands at the fundamental frequency (S=0.5) and first higher harmonic (S=1.0) was attributed to the periodic structure. The use of such narrow bands is somewhat conservative in this case and will tend to underestimate the strength of the periodic structure.

Figure 3.4.29 provides a sequence of plots of total pressure coefficient and velocity vectors over one cycle. We can see the release of one packet of low total pressure

from the wake core in figure 3.4.29b. Note that this is significantly different from a conventional two-dimensional vortex shedding case where two packets of low total pressure are released per cycle. We can also see the convection of a packet of total pressure coefficient greater than unity outside the upper shear layer. The presence of transient total pressure exceeding the upstream value will be discussed in section 5.2.

Figure 3.4.30 shows the reconstructed vorticity field over one cycle for the 2D Ahmed model with 22.5° backlight. The two shear layers alternately lengthen and shorten and the upper shear layer seems to shed a packet of vorticity (fig 3.4.30c). It is difficult to say whether the lower shear layer also sheds (between fig 3.4.30d and 3.4.30e). The vorticity reconstruction demonstrates a nominally anti-symmetric unsteady structure (although the time-averaged flow is actually asymmetric) whereas its effect on total pressure could be described as symmetric since only one packet of low total pressure is shed during each cycle.

3.4.2.4 Surface Pressure Spectral Analysis

Figure 3.4.31 shows the fraction of the surface pressure fluctuation due to specified frequency bands around the frequencies noted in figures 3.4.23 through 3.4.25 (calculated as described in section 2.3.1.2). The contribution of the critical frequency is not particularly high at the top of the backlight where unsteadiness is highest for the sub-critical backlight angles (see figure 3.4.12). Instead the contribution of the specified frequency increases as we move down the backlight. Of interest is the fact that the specified frequency band for the fully separated case contributes a much higher proportion of the backlight unsteadiness than in the case of the sub-critical backlight angles. This could be because the separation at the end of the backlight segregates the wake unsteadiness from the surface pressure unsteadiness for the sub-critical backlight angles but it could also be because the fully separated case simply demonstrates a very large amount of broadband unsteadiness at low frequencies generally.

Figure 3.4.32 shows the cross-spectral phase (see section 2.3.1.3) calculated between the reference hot-wire (discussed previously) and the pressure fluctuations on the model surface near the specified frequencies of interest. No particular phase distribution can be observed which suggests that the unsteadiness originates in the wake and propagates upstream at the speed of sound (relative to the local fluid velocity). Figure 3.4.33 shows the corresponding coherence, calculated as described in section 2.3.1.4. In all cases we see low coherence near the front of the model with coherence gradually increasing towards the rear. Coherence is highest for the 20° case and is lowest for the fully separated, 30° case.

3.5 Ahmed Model (Three-Dimensional)

This chapter presents results for the Ahmed geometry (first used by Ahmed et al (1984)). A "1/8 scale" model was tested in the Durham wind tunnel and a "1/4 scale" model was tested in the MIRA model tunnel (scale being somewhat arbitrary for such an idealised geometry). Details of the models are provided in section 2.1.2.3.

3.5.1 Steady Data

3.5.1.1 Smoke Flow Visualisation (1/8 scale)

The centrepiece of Ahmed et al's (1984) original work was the sensitivity of the flow around the model to the angle of the backlight (backlight angle is defined in figure 1.2.3). Ahmed et al (1984) found that drag increased to a maximum at a backlight angle of 30° and as backlight angle was increased beyond 30°, the flow underwent a step change and the drag was reduced dramatically (see figure 1.2.4). The two flow structures have been aptly termed the high drag and low drag flow structures. Ahmed et al (1984) found that, although the high drag structure was the natural state at 30°, they could produce the low drag structure with the 30° backlight by introducing a vertical splitter plate on the centreline in the wake.

Figures 3.5.1 and 3.5.2 show smoke flow over the backlight of the Ahmed model with 30° backlight in the Durham tunnel with the high drag and low drag flow structures respectively. In the Durham tunnel it was found that both structures could be produced with the 30° backlight at the same operating conditions with or without a splitter plate in the wake. It was found that when the tunnel was started up from rest the flow would be in the low drag state but would then switch to the high drag structure after a few minutes. The flow could be manually switched between flow structures by using a flat plate to guide the flow onto the slant surface or to force it to separate. Once initiated, the low drag flow structure would persist for several minutes while the high drag structure would persist indefinitely. Reducing the Reynolds number from $Re(sqrt(A))=1.9\times10^5$ to $Re(sqrt(A))=1.5\times10^5$ made it

possible to maintain the low drag structure for longer periods (ie: up to 30min). Figures 3.5.3 and 3.5.4 show smoke flow around the c-pillar viewed from behind the model and illustrate the difference in the flow in this region for the two structures. We see the that high drag flow structure (figure 3.5.3) draws the flow from the side of the model onto the backlight more strongly, producing a more intense trailing vortex.

3.5.1.2 Surface Oil Flow Visualisation (1/8 scale)

The following surface oil flow visualisation photos are the work of Dominy (1995b) using the methods described in section 2.2.7.2. They were performed before the start of the research presented here but have not been published previously and so are included for reference (black and white images similar to figure 3.5.5 were published in Dominy (1995a) and Sims-Williams and Dominy (1998b)).

Figure 3.5.5 shows oil flow over the upper half of the model front (the hatched area in the wire-frame image). We can see a laminar separation bubble at the end of the front radius of the model, similar to those discussed for the PARAD and 2D Ahmed models.

Figure 3.5.6 shows oil flow over the rear upper half of the Ahmed model with 30° backlight in the high drag flow regime. We can see the flow on the side of the model curving upwards to round the c-pillar and the separation pattern on the backlight. Figure 3.5.7 shows this separation pattern more clearly. We see a "D" shaped separated region at the top of the backlight which has a slightly surprising central tail which extends to the trailing edge of the backlight. This feature is not included in Ahmed et al's (1984) flow schematic (reproduced as figure 1.2.5). The flow from the side of the model separates at the sharp c-pillar and forms the c-pillar trailing vortex. Well inboard of the c-pillar it is possible to observe a faint "reattachment" line where the flow wrapped up in the c-pillar vortex impinges on the backlight. From here fluid on the surface flows both inboard towards the main recirculation region and outwards toward the distinct, straight, separation line at approximately 7°

to the c-pillar. Between this separation line and the c-pillar will be a small trailing vortex of opposite rotation to the main c-pillar vortex as is observed for delta wings (eg: Gad-el-Hak and Blackwelder (1985)) and suggested for fastback passenger cars by Goh (1994). Note that this vortex was not included in Ahmed et al's (1984) flow schematic.

3.5.1.3 Surface Pressures (1/8 scale)

Figure 3.5.8 shows the pressure distribution on the centreline of the upper surface of the model for both flow structures with a backlight angle of 30°. The pressures were measured using a bank of 5 pressure transducers which were connected to sets of 5 tappings in turn. In order to maintain the low drag flow structure long enough for these measurements to be made, the tunnel velocity was reduced to provide a Reynolds number of $Re(sqrt(A))=1.5\times10^5$ (the high drag pressures were measured at $Re(sqrt(A))=1.9\times10^5$). An additional pressure transducer was used to monitor the pressure on the middle of the backlight at all times in order to verify the flow structure during the measurements. Backlight pressures extracted from Ahmed et al (1984) have been included and show excellent agreement.

In figure 3.5.8, we see a large suction spike around the front radius of the model. Just downstream of the point of minimum pressure there is a distinct change in the gradient in the pressure rise, this could be due to the laminar separation bubble in this area (the approximate extents of the bubble have been indicated in the figure for clarity). There is very little difference in the pressures on the front half of the model between the high and low drag flow structures but the difference on the backlight is considerable. The pressure begins to drop before the end of the roof (the backlight starts at z/L=0.816) in both cases but is then almost constant downstream of the separation for the low drag case. However, for the high drag case the pressure continues to drop and reaches a minimum around the middle of the backlight before increasing so that the pressure at the trailing edge of the backlight is almost identical in both cases.

3.5.1.4 Surface Mounted Hot-Film Gauges (1/8 scale)

Surface mounted hot-film gauges were used to investigate the time-averaged and fluctuating shear stress near the centreline around the front radius of the model. The techniques and procedures discussed in section 2.2.3 for minimising errors were employed (ie: allowing sufficient warm-up time etc) and multiple sets of measurements were made with two different gauges in order to assess repeatability. For some of this work, the data logging frequency was increased from 800hz to 5khz and 2.5khz filters were used for anti-aliasing in place of the usual 250hz filters. As discussed in section 2.2.3, no absolute calibration of the gauges was performed but their output was calibrated to be linear with shear stress. Figure 3.5.9 shows the time-averaged shear stress around the front radius of the model (the radius ends at z/L=0.096), the error bars indicate repeatability. We see a maximum shear stress just ahead of the separation (at z/L=0.06) and shear stress then drops off almost to zero within the bubble before increasing again downstream of the bubble. For a simpler case we would expect the shear stress after the bubble to be higher than that in front due to transition to turbulence in the separated shear layer and the associated steeper velocity gradient. However, the velocity outside the boundary layer varies rapidly with position in this region. Based on the static pressure distribution of figure 3.5.8 we would expect the velocity outside the boundary layer to be a maximum at the start of the bubble (where the static pressure is a minimum) and by the end of the bubble the static pressure has increased dramatically, implying a large reduction in velocity and hence shear stress (for the same boundary layer shape).

Examining time-traces of the instantaneous shear stress at different locations provides excellent insight into the condition of the boundary layer. Figure 3.5.10 shows a trace of shear stress ahead of the bubble, figure 3.5.11 shows a trace at the point of minimum shear within the bubble and figure 3.5.12 shows a trace of the shear stress downstream of the bubble. Figure 3.5.11 illustrates a laminar, low shear baseline with intermittent packets of higher shear, presumably associated with turbulent spots in the separated shear layer. Figure 3.5.12 then illustrates the high unsteadiness of the reattached turbulent boundary layer. Although the level of time-

averaged shear is no higher than that ahead of the bubble, as discussed above, the dramatic increase in unsteadiness, compared with figure 3.5.10, confirms the transition to turbulence.

3.5.1.5 Steady Wake (1/8 scale)

A five-hole probe (5h_03) was traversed on the centreline above the rear of model and in the wake for the high drag flow condition (it was not possible to maintain the low drag flow reliably for long enough periods of time to perform wake traverses). Conventional "steady" measurements were made, in other words, no transfer function correction was applied and the probe incidence calibration was applied to pressures based on averaged transducer voltages (see section 2.3.5). This traverse was made at $Re(sqrt(A))=3.1\times10^5$. Figure 3.5.13 shows the resulting velocity vector field (the side profile of the model has been drawn for clarity). The probe was aligned with the axial direction and where the observed incidence of the flow was not within the calibration range of the probe no vectors are plotted. This does not imply actual recirculation throughout the entire region without vectors. Also indicated in figure 3.5.13 are the locations of the various traverse planes across the wake which will be presented later.

Figure 3.5.14 shows the total pressure coefficient determined by the five-hole probe for the same traverse of the wake centreline. The white region where no contours are plotted indicates the region where the incidence of the flow onto the probe exceeded the probe calibration range. Interestingly, the wake closes quite quickly up to z/sqrt(A)=1.0 and then the total pressure contours extend downstream roughly parallel to the ground plane. Figure 3.5.15 shows the corresponding static pressure field. We see the low pressure region over the backlight extending onto the roof and we see a region of high pressure centred around y/sqrt(A)=0.9, z/sqrt(A)=0.75 downstream of the rapidly closing wake. The highest static pressures occur near the ground plane some distance behind the model where the closing wake effectively impinges on the ground.

Wake traverses were performed with five-hole probes (5h_01 and 5h_03) in the wake of the 1/8 scale Ahmed model with 30° backlight and high drag flow at a number of planes indicated in figure 3.5.13. The traverses at z/sqrt(A)=0.78, 1.56 and 3.13 were performed without probe nulling and are based on conventional "steady" measurements without the use of transfer-function correction before time-averaging (see section 2.3.5). Data out of the range of the probe incidence calibration has been extrapolated from the calibration range for these planes (the only region where the flow incidence actually exceeded the probe calibration range was on the centreline at z/L=0.78). For the traverse at z/sqrt(A)=1.0, transfer-function correction was used to record accurate unsteady pressures and velocities and these were then time-averaged. At each location 20 sets of 2048 points in time were logged at 800hz per channel (ie: 51.2 seconds logging time at each location). In this case the probe was aligned with the local flow to ensure that the probe remained within its incidence range at all times. The traverses at z/sqrt(A)=0.78, 1.56 and 3.13 were performed at $Re(sqrt(A))=1.9\times10^5$ while the traverse at z/sqrt(A)=1.0 was performed at $Re(sqrt(A))=3.0\times10^5$. Full width wake traverses were performed in all cases.

Figure 3.5.16 shows the in-plane velocity vectors for the various wake traverse planes, a rear view of the model has been drawn in this and subsequent figures for clarity. Figure 3.5.17 shows corresponding plots of streamwise vorticity (defined in section 2.3.3) and figure 3.5.18 shows plots of total pressure coefficient.

We see that the flow is dominated by the two c-pillar trailing vortices. These are obvious in the vector plots, the plots of vorticity and the plots of total pressure coefficient, the vortex centres corresponding to the highest total pressure loss. As the vortices move downstream they become less intense both in terms of vorticity and total pressure loss. At the most upstream location the vortices are centred around x/sqrt(A)=±0.3 and y/sqrt(A)=0.45 and as they move downstream, they are drawn towards the ground plane and outwards. This has been described as being due to the

action of the reflection of the vortices in the ground plane (Bearman (1984b)). At the same time, their shape transforms from being elongated in the vertical direction to being elongated in the horizontal direction. Of interest in the vorticity plots at the upstream planes are two smaller vortices, outboard of the c-pillar vortices, which rotate in the opposite direction. These are believed to be the vortices formed immediately inboard of the c-pillars, between the flow wrapped up in the main c-pillar vortices and the backlight.

3.5.1.6 Steady Wake (1/4 scale)

A cross-wake five-hole probe traverse was performed behind a ¼ scale Ahmed model in the MIRA model tunnel (using 5h_02). In this tunnel, force measurements indicated that the flow structure switched from the high drag to the low drag regime between a backlight angle of 27.5° and 30°. Therefore the wake measurements were made at a backlight angle of 27.5°. Transfer-function correction was used to make time-accurate measurements which were then time-averaged (see section 2.3.5) (15 sets of 2048 points in time were recorded at 800hz at each location); no probe nulling was used. The Reynolds number was $Re(sqrt(A))=6.4\times10^5$. Because time in the MIRA tunnel was quite limited, it was necessary to perform only a very coarse traverse.

Figure 3.5.19 shows velocity vectors at z/sqrt(A)=0.78, figure 3.5.20 shows the corresponding streamwise vorticity and figure 3.5.21 shows total pressure coefficient. The vortices are less intense than for the 1/8 scale measurements both in terms of vorticity and total pressure loss. Note that the non-dimensionalisation of vorticity using the free stream velocity and a dimension of the model provides a fair comparison between different scales and velocities however, different grid spacing (relative to the model size) can affect the vorticity calculated simply because high localised velocity gradients cannot be resolved by coarser grids.

3.5.2 Unsteady Data – 1/8 Scale

3.5.2.1 General Unsteady Data (1/8 scale)

Figure 3.5.22 shows the fluctuating pressure reported at the centre hole of the five-hole probe, without using transfer function correction, for the centreline wake traverse presented in figures 3.5.13 through 3.5.15. As discussed previously, this provides a crude index to flow unsteadiness without the need for true time-resolved measurements. We see the highest levels of unsteadiness above the backlight and indications are that the flow is considerably more unsteady closer to the backlight (where reliable measurements could not be made). Unsteadiness is slightly higher in the wake than outside.

Figure 3.5.23 shows the level of fluctuating total pressure coefficient from true time-accurate measurements made one base dimension behind the 1/8 scale Ahmed model with 30° backlight in the high drag regime. We see higher unsteadiness in the wake than outside, as expected, with the highest unsteadiness around the periphery of the c-pillar vortices, particularly at the upper inboard side of them. The total pressure fluctuation at this location corresponds to approximately 25% of the free stream dynamic pressure.

Figure 3.5.24 shows a time trace of the effective velocity returned by a single element hot-wire (element aligned with the y-axis) located at x/sqrt(A)=0.36, y/sqrt(A)=0.84 and z/sqrt(A)=0.78 in the wake of the model. This location approximately corresponds to the region around the periphery of the trailing vortex demonstrating the highest unsteadiness at this axial location. The hot-wire velocity demonstrates intermittent drops in velocity but no obvious periodicity is visible. Figure 3.5.25 shows the corresponding probability density function, this is quite close to a normal distribution suggesting that most of the velocity fluctuation is effectively random. The intermittent packets of low velocity observed in figure 3.5.24 result in a slightly skewed distribution with a “foot” on the left hand side of the peak.

3.5.2.2 Wake Spectral Analysis (1/8 scale)

Figure 3.5.26 shows the autospectral density for the hot-wire discussed above. The spectrum is the average of approximately 6000 spectra, each calculated from a set of 2048 points in time (a total logging time of 250 minutes at 800hz) in order to make it possible to observe even weak spectral humps. We see a peak at 13hz (S=0.083) which is near the background tunnel frequency and a weak spectral hump at S=0.35 (55hz). The sharp peak at 30hz is due to electrical noise, as discussed previously, and should be ignored. As is typical, we see generally higher unsteadiness at lower frequencies.

Figure 3.5.27 shows the level of total pressure unsteadiness (standard deviation), due to a 5hz band around S=0.08, as a fraction of the local total pressure unsteadiness (calculated as described in section 2.3.1.2). We see that the unsteadiness at this frequency dominates outside of the wake but is of much lower importance inside the wake. This is in keeping with the assumption that unsteadiness at this frequency is simply a result of the tunnel unsteadiness. Figure 3.5.28 shows the same quantity but for a 10hz band around S=0.34. By contrast this frequency has the greatest importance inside the wake. It is strongest around the periphery of the c-pillar vortices although not at the location of maximum total pressure unsteadiness in figure 3.5.23. Nevertheless, indications are that this is the frequency of interest.

During the time accurate wake survey with the five-hole probe the reference hot-wire discussed above was logged simultaneously. Figure 3.5.29 shows the distribution of cross-spectral phase (calculated as described in section 2.3.1.3) at S=0.08 between the reference hot-wire and the total pressure recorded by the time-accurate five-hole probe one base dimension behind the model. (Note that the strongest peak near this frequency is chosen for each time-history, allowing for a small amount of drift of the dominant frequency through the course of an experimental run). The phase inside the wake is almost constant and lags the phase outside the wake, again in keeping with the excitation at this frequency coming from the tunnel. Figure 3.5.30 shows the phase distribution at S=0.34. The plot is

somewhat difficult to interpret because of regions where the phase shifts between -180° and +180° however the basic structure is clear enough. The two sides of the wake are in phase indicating that the unsteady structure is symmetric rather than anti-symmetric and there is a phase gradient between the area around the top and bottom of the c-pillar vortices and between an area on the centreline at the top of the wake and the rest of the flow. This suggests that the vortices are moving in a roughly vertical direction with a connection to the flow coming off the centre of the backlight.

Figures 3.5.31 and 3.5.32 show the coherence (calculated as described in section 2.3.1.4) between the reference hot-wire and the total pressure fluctuations at S=0.08 and S=0.34 respectively. In both cases we see high coherence near the hot-wire location, as would be expected. At S=0.08 the coherence is high outside the wake but, with the exception of the immediate vicinity of the hot-wire, is relatively low in the wake. Again this indicates that this frequency is simply due to the tunnel excitation. At S=0.34 the coherence is generally low everywhere, again with the exception of the immediate vicinity of the reference hot-wire. This suggests that much of the unsteadiness at this frequency is due to broadband unsteadiness rather than a dominant periodic structure. This is in keeping with the shallow spectral hump on top of a high baseline in the autospectral density plot of figure 3.5.26.

3.5.2.3 Wake Unsteady Reconstruction (1/8 scale)

The reconstruction technique described in section 2.3.2 was applied at S=0.34 for the 1/8 scale Ahmed model with 30° backlight and high drag flow. This analysis used the same data from the time-accurate five-hole probe and reference hot-wire as for the unsteady measurements presented above. One 5hz band was used to determine the amplitude of the unsteadiness. Reconstructions were also performed including higher harmonics but these simply introduced spurious noise into the resulting animations.

Figure 3.5.33 shows a sequence of plots of total pressure coefficient and velocity vectors over one cycle. This figure is also provided as an avi animation on the CD-ROM which accompanies this thesis. We see that the two vortices elongate simultaneously in the vertical direction and then split off total pressure loss (and vorticity) from the bottom of the vortices which moves down towards the ground plane and outwards. The plots are surprisingly clear given the low coherence in figure 3.5.32. The level of symmetry of the unsteady flow is particularly remarkable.

3.5.3 Unsteady Data – ¼ Scale

3.5.3.1 General Unsteady Data (1/4 scale)

Figure 3.5.34 shows the level of fluctuating total pressure coefficient at z/sqrt(A)=0.78 in the wake of the ¼ scale Ahmed model with 27.5º backlight in the MIRA model tunnel. As expected, we see generally higher levels of unsteadiness inside the wake than outside. The base level of unsteadiness outside the wake is lower than for the 1/8 scale measurements (compare with figure 3.5.23) in keeping with the lower turbulence intensity of the MIRA tunnel. We do not see the distinct regions of elevated unsteadiness around the periphery of the vortices seen for the 1/8 scale model however this may be due simply to the inability of the coarse grid to resolve these details. We see a region of elevated unsteadiness on the centreline near the ground plane.

Figure 3.5.35 shows a typical time trace from the reference hot-wire in the model wake and figure 3.5.36 shows the probability density distribution for this hot-wire. In this case we do not see such obvious low velocity spikes in the time trace or the corresponding “foot” in the probability density distribution which we observed for the 1/8 scale case (figures 3.5.24 and 3.5.25).

3.5.3.2 Wake Spectral Analysis (1/4 scale)

Figure 3.5.26 shows the autospectral density calculated for the reference hot-wire from 100 sets of 2048 points in time. As is typical, we see generally higher unsteadiness at low frequency, although this is less pronounced than in the Durham tunnel. We see some evidence of a spectral peak at S=0.078 and an obvious peak at

S=0.58. The tunnel signature without a model in the working section (figure 2.1.3) contains a lot of energy between 80hz and 90hz so the small peak in this region has been attributed to the tunnel. The empty tunnel also exhibits a small peak between 5hz and 10hz suggesting that the peak at S=0.078 may also be due to the tunnel rather than the model.

Examining the level of total pressure unsteadiness due to a narrow frequency band around S=0.08 as a proportion of the local total pressure fluctuation, as plotted in figure 3.5.38, tends to confirm that this frequency is due to the wind tunnel rather than the model. We can see that the proportion of unsteadiness due to this frequency is much higher outside the wake than inside. Furthermore, no pattern is discernible in the phase distribution between the reference hot-wire and total pressure fluctuation at this frequency (figure 3.5.40) and the coherence at this frequency between the hot-wire and fluctuating total pressure is particularly low throughout the wake (see figure 3.5.42).

Figure 3.5.39 shows the total pressure fluctuation due to a narrow band around S=0.58 as a proportion of the local total pressure fluctuation (calculated as described in section 2.3.12). We see that this frequency is responsible for the unsteadiness from under the car on the centreline, however, it does not appear to dominate the c-pillar vortices in the same way as the S=0.34 peak did for the 1/8 scale model (compare with figure 3.5.28). The cross-spectral phase distribution at this frequency in figure 3.5.41 consists of largely horizontal contour lines indicating a symmetric unsteady structure which involves oscillations primarily in the vertical direction (as for the S=0.34 peak at 1/8 scale). The corresponding cross-spectral coherence distribution of figure 3.5.43 indicates relatively high coherence over a significant area on the side of the reference hot-wire with elevated coherence on the groundplane and around the c-pillar vortex on the opposite side of the wake. This suggests coupling between the unsteadiness on the two sides of the model at this frequency.

3.5.3.3 Wake Unsteady Reconstruction (1/4 scale)

The unsteady reconstruction technique described in section 2.3.2 was used to investigate the unsteady flow structure associated with the spectral peak at S=0.58 seen in figure 3.5.37. Figure 3.5.44 provides a sequence of plots of total pressure coefficient and velocity vectors over one period. Although the flow is different to that observed for the 1/8 scale model and although the measurement grid is very coarse, we can identify a very similar flow structure. We see that the two c-pillar vortices periodically strengthen together and this is visible both in terms of the centreline downwash and total pressure loss at the vortex cores. As the vortices strengthen they move towards the ground plane where we see a band of low total pressure across the width of the model near the bottom of the model. This band of loss seems to be deposited by the vortices which then weaken and move upwards together.

3.6 Rover 200

Details of the two Rover 200 models used (15% and 40% scale) are given in section 2.1.2.5. Both models were manufactured from the CAD data for the real car. However, some modifications were made to the construction of the spoiler on the 15% model as will be discussed in section 3.6.1.1. The aluminium "shell" type spoiler in figure 3.6.1 was ultimately adopted and used as standard for all of the subsequent testing. Also shown in figure 3.6.1 is the solid spoiler moulding based on the CAD data. The aluminium shell spoiler was shaped over the solid spoiler and so is of almost identical dimensions.

3.6.1 Steady Data

3.6.1.1 Forces (15% and 40% scale)

Forces on the Rover 200 models were measured using six-component underfloor balances (eg: as discussed in section 2.2.6.1). As discussed in section 2.1.2.5, both models had a smooth underfloor however the position of this relative to the body shell differed slightly for the two models. Also, the 15% model had the option of roughness strips and these were fitted as the standard condition whereas the 40% model was tested only without roughness strips. The effect of the roughness strips at 15% was to increase the drag coefficient (CD) by approximately 0.008, to increase front lift coefficient (CLF) by 0.032 and to decrease rear lift coefficient (CLR) by 0.032. Both models were set up with their sills level at a ground clearance of 33mm at 15% scale (88mm at 40% scale, equivalent to 220mm full scale).

Figures 3.6.2, 3.6.3, 3.6.4 and 3.6.5 show the measured force coefficients for a range of spoilers at 15% and 40% scales in the Durham and MIRA tunnels respectively. The lines drawn between points have been included for clarity and do not imply that the effects of other spoiler sizes can be interpolated between the conditions tested. Greater concern was given to producing a similar effect with the spoiler at both scales than to reproducing the same absolute forces. The solid fibreglass spoiler originally manufactured for the 15% model based on the CAD data did not produce

the same effect on drag and rear lift as achieved for the 40% model. The spoiler on the full size car is largely open at the rear whereas, at 15%, the fibreglass spoiler was made with this surface closed. A number of card spoilers were tested which made it possible to leave this rear surface open and to examine the effect of spoiler geometry on the forces. Simply fitting a piece of card to the upper surface of the original solid spoiler using double sided tape produced a significant reduction in drag (10 counts) and rear lift (5 counts) as shown in figures 3.6.2 and 3.6.5 respectively. Apart from a very minor increase in spoiler height due to the thickness of the card (<0.5mm) the only difference in geometry was that the trailing edge of the spoiler was now sharp compared with the small radius present on the fibreglass spoiler. "Oversized" shell spoilers, consisting of the basic spoiler extended in the downstream direction, were tested to verify that the test condition was not "just short" of producing a sudden change in flow structure. These oversized spoilers progressively reduced rear lift and drag but did not produce any discontinuity in forces or sudden change in flow structure. The aluminium shell spoiler (shown in figure 3.6.1) adopted for all further testing was formed over the original solid spoiler but had an open rear face and, most importantly, a sharp trailing edge. Its outside dimensions were within less than 0.5mm of the original geometry. As can be seen, it produced a similar effect to that of the spoiler on the 40% model for all of the forces, namely, a reduction in drag of 14 counts (cmp. with 25 counts at 40%) and a reduction in rear lift of 92 counts (cmp. with 98 counts at 40%).

3.6.1.2 Surface Oil Flow Visualisation (15% scale)

Surface oil flow visualisation was performed on the 15% Rover 200 model with and without the rear spoiler as described in section 2.2.7.2. Photographs of the surface oil flow are provided in figures 3.6.6 to 3.6.11.

The flow patterns are essentially the same with and without the spoiler except for the rear of the model. In both cases we can see that the front of the bonnet and the front of the roof are free from separation. There is evidence of near stagnant flow on the bottom of the windscreen but there is no recirculation. The a-pillar vortex is visible

along the front side-glass. Moving up the side-glass, we see first an impingement onto the surface, then an area of upsweep followed by a distinct separation line. The vortex is drawn up towards the roof and "loses contact" with the surface (ie: no longer produces a separation line) after it passes the b-pillar and moves over the top of the model.

Without the spoiler the flow remains attached at the transition from roof to backlight whereas the spoiler obviously produces a separation across its full width. The c-pillar vortex separation seems to occur in both cases approximately at the trim-line at the c-pillar. There is very little evidence of the effect of this vortex on the backlight flow without the spoiler although we can see that the flow is drawn towards the c-pillar in the outboard region of the backlight whereas it is drawn towards the centreline further inboard. With the spoiler, there is evidence of a swirling flow on the backlight a significant distance inboard of the c-pillar. The direction of the swirl appears to be opposite to the rotation of the c-pillar vortex. This indicates that the swirling is the result of upsweep at the centreline on the model surface due to the recirculation behind the model rather than the impingement of the c-pillar vortex onto the backlight.

3.6.1.3 Surface Pressures (15% scale)

Figure 3.6.12 shows the location of surface pressure tappings on the centreline of the model. Figure 3.6.13 shows the pressure distribution around the centreline of the model with and without the spoiler; the pressure distribution holds few surprises. The pressures forward of the roof and on the underside are unaffected by the spoiler. Some increase in pressure along the roof is visible with the spoiler in place which is somewhat surprising since the spoiler essentially extends the line of the roof. This increase in pressure must be due to the slight step at the front of the spoiler. As expected, the separation due to the spoiler relieves the suction spike at the top of the backlight but the pressures towards the bottom of the backlight and on the base of the model below the backlight are very similar with and without the spoiler.

Figures 3.6.14 and 3.6.15 compare the pressure distributions on the backlight with and without the spoiler. The greatest effect of the spoiler is to reduce the suction around the c-pillar. The region of swirling flow observed in the oil flow of figure 3.6.1.1 corresponds to a region of low pressure on the backlight, as shown in figure 3.6.15.

Figure 3.6.16 shows the pressure distribution for a line of tappings across the full width of the backlight. The pressure distribution is essentially symmetric although some discrepancy exists around the c-pillar without the spoiler. Again note that the greatest increase in pressure due to the spoiler is towards the outboard edges of the backlight.

3.6.1.4 Smoke Flow Visualisation (15% scale)

Figure 3.6.17 through to figure 3.6.20 show smoke flow on the centreline of the 15% Rover 200 model. These tests were run at a reduced tunnel velocity resulting in a Reynolds number (based on square-root of frontal area) of 1.1×10^5 whereas the majority of testing with this model was at a Reynolds number of 3.8×10^5. For figures 3.6.17 and 3.6.18 the smoke was injected in front of the model just above the stagnation streamline. The separation produced by the spoiler is visible over the backlight. For figures 3.6.19 and 3.6.20 the smoke was injected under the model in order to reveal the extent of the rear recirculation region. Without the spoiler the recirculation is limited to the region below the backlight however with the spoiler we see some smoke makes it all the way up the backlight to the rear face of the spoiler.

3.6.1.5 Steady Wake (15% scale)

A five-hole probe was traversed on the centreline above the rear of model and in the wake. Conventional “steady” measurements were made, in other words, no transfer function correction was applied and the probe incidence calibration was applied to pressures based on averaged transducer voltages (see section 2.3.5). Figures 3.6.21 and 3.6.22 show the resulting velocity vector field. The probe was aligned with the

axial direction and where the observed incidence of the flow is not within the calibration range of the probe no vectors are plotted. This does not imply actual recirculation throughout the entire region without vectors. As expected from the oil and smoke flow visualisation, in the case without spoiler, the flow follows the length of the backlight before separating. A larger separation region is visible with the spoiler although the length of the region in which the probe is out of range is approximately one base dimension ($A^{1/2}$) both with and without the spoiler. Also indicated in figures 3.6.21 and 3.6.22 are the locations of the various traverse planes across the wake which will be presented later.

Figures 3.6.23 and 3.6.24 show total pressure coefficient on the wake centreline. The white region indicates the area in which the flow was not within the incidence range of the probe. We can see that with the spoiler total pressure losses are greater and the wake is larger.

Figures 3.6.25 and 3.6.26 show static pressure coefficient on the wake centreline. Note the low pressure region over the roof of the model without the spoiler which is further forward than might be expected. The pressure in this region is higher with the spoiler but we do not see the static pressure increasing in the axial direction which indicates that the increasing surface pressure in this region (see figure 3.6.13) is a localised effect near the model surface.

Figures 3.6.27 and 3.6.28 show the time-averaged effective velocity recorded by a single element hot-wire traversed in the same region as the five-hole probe. The axis of the hot-wire element was aligned with the y (vertical) axis. In this case the results correspond to a true time-average of time-accurate measurements. The hot-wire cannot distinguish between forward and reversed flow which makes it impossible to directly observe recirculation behind the model. However, we would expect to see a minimum in the velocity magnitude in the wake corresponding to a region where the flow changes direction. Ideally the minimum would actually be at zero velocity but in practice the point will not be stationary so positioning the probe at the average

location of zero velocity will not result in a recording of zero average velocity. Surprisingly, we do not see this characteristic pattern, instead velocity simply continues to decrease as we get closer to the model. This suggests that the recirculation velocities are too low for subtleties to be observed. It should be noted that the recirculation region is probably very sensitive to probe interference and this may be producing spurious results in this area.

A five-hole probe was traversed in a number of planes at different axial positions indicated in figures 3.6.21 and 3.6.22. The probe was directed in the axial direction with no local nulling (see section 2.2.4) and only "steady" measurements were made (see section 2.3.5).

Figures 3.6.29 and 3.6.30 show velocity vectors without and with the spoiler and figures 3.6.31 and 3.6.32 show corresponding plots of streamwise vorticity (see section 2.3.3) non dimensionalised by the free-stream velocity and the base dimension ($A^{1/2}$). Figures 3.6.33 and 3.6.34 show contours of total pressure coefficient and figures 3.6.35 and 3.6.36 show static pressure coefficient. No data is plotted in areas where the incident flow angle was out of range of the probe calibration. The data has been plotted using the same contouring intervals at all axial positions in order to see the effect of the spoiler and the development of the wake as we move downstream. The only exception to this is that the vorticity plots upstream of the rear of the car (figure 3.6.31a,b and figure 3.6.32a,b) have been plotted using twice the contouring range in order to accommodate the concentrated vorticity of the a-pillar vortices in this area.

The most obvious feature of the wake are the familiar c-pillar trailing vortices. These do not actually take the form of vortices until z/sqrt(A)=0.75 or arguably later for the case with spoiler. Immediately behind the car at z/sqrt(A)=0.05 we see a band of vorticity (figures 3.6.31c and 3.6.32c) which corresponds to the region of high total pressure gradient in figures 3.6.33c and 3.6.34c around the edge of the wake. The c-pillar vortices are obvious in the vector fields and vorticity fields and

correspond to regions of low total and static pressure. They are markedly stronger without the spoiler in all respects (ie: stronger vorticity, higher loss) as would be expected. As we move downstream, as well as becoming more diffuse, the c-pillar vortices move downwards and outwards. This behaviour is typical and has been described as being due to the influence of the image of the c-pillar vortices in the ground plane by Bearman (1984b).

The a-pillar vortices are visible in the velocity vector plots upstream of the rear of the car (figures 3.6.29a,b and 3.6.30a,b) but are overwhelmed by the strong vector fields as the wake closes behind the car. The vortices are still apparent in the vorticity fields up to z/sqrt(A)=1.5 using the current scales. In fact, the vortices would still apparent at z/sqrt(A)=3.0 if we were to refine the contour scale according to the local vorticity levels. The total pressure loss associated with the a-pillar vortices is more distinct than the vortices themselves and is visible as an appendage to the top of the wake. This is more apparent in the case with spoiler because the strong c-pillar vortices without the spoiler tend to draw the a-pillar vortices down and towards the centre of the wake where they are surrounded by high loss.

Based on the probe measurements on the wake centreline and the cross-wake traverses described above, the plane one base dimension behind the model was selected as the best location to concentrate further analysis.

Figures 3.6.37 and 3.6.38 show velocity vectors one base dimension behind the model without and with spoiler respectively. Figures 3.6.39 and 3.6.40 show the corresponding vorticity fields and figures 3.6.41 and 3.6.42 show contours of total pressure coefficient. These plots represent the true time-averaged quantities based on time-accurate measurements (see section 2.3.5). At each point in space 20 sets of 2048 points in time were logged. During these traverses the probe was approximately nulled to the local flow according to previous traverses without probe nulling.

The symmetry of the wake serves to confirm the reliability of the experimental set-up. Some asymmetry is apparent for the a-pillar vortices and for the total pressure field below the left c-pillar vortex for the case with spoiler. The differing positions of the a-pillar vortices could have been caused by a minor misalignment of the model in the tunnel. If the model were yawed slightly to the left in the tunnel then this would move the a-pillar vortices to the left and would cause the right hand a-pillar vortex to be stronger in keeping with what we observe. The difference in the total pressure loss below the left hand c-pillar vortex could also be tied to a similar small yaw angle so that the right hand c-pillar vortex becomes slightly stronger.

3.6.1.6 Steady Wake (40% scale)

Figures 3.6.43 and 3.6.44 show velocity vectors one base dimension behind the 40% scale model in the MIRA tunnel without and with spoiler respectively. Figures 3.6.45 and 3.6.46 show the corresponding vorticity fields and figures 3.6.47 and 3.6.48 show contours of total pressure coefficient. These plots represent true time-averaged quantities based on time-accurate measurements (see section 2.3.5). Because testing time at MIRA was much more limited than in the Durham tunnel, testing was concentrated on the case with spoiler, since this is the real car geometry. The plots without spoiler are therefore based on a half wake traverse which has been mirrored in these figures. Also, only one set of 2048 points in time was logged at each location for the case without spoiler where 10 sets were recorded with the spoiler. No probe nulling was used in either case. Unfortunately, a leak developed in the pneumatic tubing system on the reference side of the transducers during testing (the transducers are located within the sub-atmospheric plenum chamber in the MIRA tunnel and are piped up to an exterior reference pressure). This affected the traverse of the left hand side of the wake in the case with spoiler and, although the problem was recognised at the time, it was not possible to repeat the run due to time constraints. A simple pressure offset has been applied to the recorded pressures during the affected run and this has made it possible to recover the data with surprisingly little additional error.

The wake of the 40% model exhibits more rapid closure than that of the 15% model, demonstrated most obviously by the fact that the wake features are all closer to the ground plane. The faster wake closure is linked to the c-pillar vortices and these are stronger for the 40% case. The levels of streamwise vorticity are higher (compare figures 3.6.45 and 3.6.46 with figures 3.6.39 and 3.6.40) as are the levels of total pressure loss at the vortex cores (compare figures 3.6.47 and 3.6.48 with figures 3.6.41 and 3.6.42). As discussed above, the drawing of c-pillar vortices downwards and outwards is often attributed to the reflection of these vortices in the ground plane. At 40% scale the vortices are closer to the ground but are not further from the centreline than they were at 15% scale so the stronger vortices should be considered to be the result of faster wake closer and not vice-versa. The a-pillar vortices are as visible in the wake of the 40% model as they were in the wake of the 15% model, both in the vorticity plots and the total pressure plots. They seem to contain slightly more vorticity at 40% and their total pressure loss is more localised. This seems to be in keeping with higher levels of non-dimensional shear stress due to increased turbulence at higher Reynolds number. The influence of the stronger c-pillar vortices on the a-pillar vortices is considerable and they appear much closer to the wake centreline at 40% scale.

3.6.2 Unsteady Data – 15% Scale

3.6.2.1 General Unsteady Data

Figure 3.6.49 shows the level of fluctuating pressure coefficient on the surface of the Rover 200 model with and without spoiler at 15% scale. Peak levels of fluctuating pressure coefficient reach CP'=0.1 but levels below 0.05 are more typical. Comparing with the time-averaged pressure distributions (figure 3.6.13) we generally see peaks in unsteadiness corresponding to pressure spikes or troughs in the time-averaged pressure distribution. For example at the suction around the front of the bonnet (z/L=0.03), at the partial stagnation at the bottom of the windscreen (z/L=0.30) and at the suction around the top of the windscreen (z/L=0.45). Levels of unsteadiness on the underfloor are generally low, with slight increases at the front and rear. We see that the spoiler decreases the level of unsteadiness on the centreline

of the rear of vehicle including the rear roof, base and rear underfloor although unsteadiness at mid-height on the backlight is increased slightly.

Figures 3.6.50 and 3.6.51 show the levels of fluctuating pressure coefficient on the backlight without and with the spoiler respectively. As for the time-averaged pressure distribution, the spoiler results in a more uniform distribution across the backlight with a decrease in the unsteadiness at the c-pillar and an increase in unsteadiness on the centreline. With the spoiler a distinct region of high unsteadiness is visible in the approximate location of the swirling surface flow seen in figure 3.6.11.

Figures 3.6.52 and 3.6.53 show example time-traces of the fluctuating pressure coefficient at z/L =0.86 on the centreline of the backlight of the 15% scale Rover 200 model without and with spoiler respectively. As indicated by the distributions of time-averaged and unsteady pressure given by figures 3.6.13 and 3.6.49, the level of both average and fluctuating pressure with and without spoiler are similar at this location. Although the plots do not show anything near pure, sinusoidal unsteadiness, we can identify a dominant time-scale of around 0.05s (1/20hz) in the case without spoiler, with less periodicity and longer time-scales in the case with the spoiler. Figures 3.6.54 and 3.6.55 show pressure coefficient time-traces near the c-pillar again without and with the spoiler. With no spoiler we see a much lower time-averaged pressure (as expected from figure 3.6.14) and slightly more unsteadiness. In both cases we see evidence of higher frequencies in the unsteadiness compared with the centreline.

Figures 3.6.56 and 3.6.57 indicate the level of fluctuating effective velocity recorded by a hot-wire aligned with the y-axis on the centre-plane behind the model. The levels of peak unsteadiness reach approximately 20% of the free-stream velocity both with and without the backlight spoiler. The regions of peak unsteadiness generally correspond to regions of high spatial velocity gradient (high shear) indicated in figure 3.6.27 and 3.6.28. The separation at the spoiler produces a region

of high shear and hence an additional region of high unsteadiness, compared with the case without spoiler. Surprisingly, the region of moderate shear at the backlight separation in the case without spoiler does not produce a region of high unsteadiness.

Figures 3.6.58 and 3.6.59 again show the level of fluctuating hot-wire effective velocity but in this case for the development of the wake through a number of cross-stream planes. We generally see unsteadiness associated with the a-pillar vortices and regions of high gradient around the edge of the recirculation region (at z/L=0.05) and with the c-pillar vortices. For the c-pillar vortices we observe distinct pockets of higher unsteadiness at the top outboard and lower inboard sides of the vortices at z/L=0.75 and z/L=1.0. Peak levels of velocity unsteadiness in this region are between 15% and 20% of the free-stream velocity.

Figures 3.6.61 and 3.6.62 show the levels of fluctuating total pressure coefficient (standard deviation of total pressure coefficient recorded with time-accurate five-hole probe) at z/L = 1.0 behind the Rover 200 model without and with spoiler. As for the fluctuating hot-wire velocity, we see pockets of high unsteadiness at the top outboard and lower inboard sides of the c-pillar vortices. Peak levels of total pressure unsteadiness are around 25% of the dynamic head.

Figures 3.6.62 and 3.6.63 show time-traces of hot-wire effective velocity at reference locations in the wake (x/sqrt(A)=-0.24, y/sqrt(A)=0.24, z/sqrt(A)=0.75 without spoiler and x/sqrt(A)=-0.14, y/sqrt(A)=0.24, z/sqrt(A)=0.75 with spoiler). These locations are near the outboard side of the lower packet of high unsteadiness at z/L = 0.75 (see figures 3.6.58d and 3.6.59d). In general we see a much greater proportion of the fluctuation at higher frequencies than observed in the surface pressure traces (figures 3.6.52-3.6.55) with typical time scales of 0.02s (1/50hz). Figures 3.6.64 and 3.6.65 show probability density distributions for hot-wire effective velocity at the reference hot-wire locations. In the case with spoiler there is

some obvious asymmetry, indicating occasional packets of high-velocity fluid (of variable intensity) passing the probe.

Figures 3.6.66 and 3.6.67 show probability density functions for the fluctuating surface pressure coefficient on the centreline of the backlight without and with the spoiler. Figures 3.6.68 and 3.6.69 show the corresponding probability density distributions for the surface pressure coefficients near the c-pillar. All of these figures show fairly standard distributions for normally distributed unsteadiness, providing no indication of pure periodicity or switching between distinct flow structures.

3.6.2.2 Wake Spectral Analysis

3.6.2.2a Contributions of frequency bands to unsteadiness:

During the time-accurate five-hole probe surveys of the model wake, simultaneous measurements were taken with a single hot-wire probe at a fixed reference location. For the Rover 200 model without spoiler this location was x/sqrt(A)=-0.24, y/sqrt(A)=0.24, z/sqrt(A)=0.75 while with the spoiler the location was slightly further inboard at x/sqrt(A)=-0.14, y/sqrt(A)=0.24, z/sqrt(A)=0.75. These locations were chosen based on a number of criteria. Firstly, they are near maxima in the fluctuating velocity field (see figures 3.6.58d and 3.6.59d). They are a short distance off-centre in order to make it possible to capture both axi-symmetric and anti-symmetric structures with the hot-wire probe. Also, they are relatively close to the ground plane, which facilitates probe mounting and minimises the length of the probe support intruding into the flow.

Figures 3.6.70 and 3.6.71 show autospectral densities calculated for the effective velocity recorded at the reference hot-wire behind the 15% Rover 200 model without and with spoiler respectively. It should be noted that these spectra are the average of spectra calculated for each of 8640 sets of 2048 points in time recorded during a half wake traverse. As observed for other geometries, we see more general unsteadiness at low frequencies. Both with and without the spoiler we see a spectral

peak at 15.2hz (Strouhal number = 0.119 based on free stream velocity and base dimension). A spectral peak exists at this frequency in the tunnel even in the absence of a model (as discussed in section 2.1.1.1) so it would not generally be appropriate to attribute this peak to the model. As for the PARAD models, the peak is slightly higher with the models in the tunnel than without (between 1.2 and 1.5 times more contribution to velocity standard deviation) which could be attributed to broadband unsteadiness and the amplification of tunnel unsteadiness due to time-averaged gradients. However, a spectral peak is apparent for the 40% Rover 200 model in the MIRA tunnel at a similar Strouhal number (as will be discussed in section 3.6.4.2). Some cautious analysis has therefore been performed for this peak under the supposition that it corresponds to the "lock-in" of the model unsteady flow structure with that of the tunnel. We also see spectral peaks near 40hz without and with the spoiler (Strouhal numbers of 0.301 and 0.319). A 10hz band around this frequency produces between 6 and 7 times more velocity fluctuation than is observed in the empty tunnel for the same frequency band. Although this peak is relatively distinct with the spoiler, in the case without the spoiler it blends into a broad hump. Analysis has been performed for a Strouhal number near the high frequency end of this hump (ie: S=0.471) in order to assess any associated flow structure.

Steep spatial gradients of time-averaged flow variables can be expected to correspond to higher levels of fluctuation across a wide range of frequencies. In order to distinguish regions of the flow-field dominated by a given periodic structure from regions which demonstrate high unsteadiness simply due to high time-averaged gradients the fraction of the local unsteadiness due to a specific frequency has been calculated. The formulation for the calculation of the contribution of a given frequency band to the local standard deviation is given in section 2.3.1.2 and the resulting value is then divided by the local standard deviation.

Figures 3.6.72 and 3.6.73 show the fraction of the standard deviation of hot-wire effective velocity due to frequencies near S=0.12 on the wake centreline behind the Rover 200 model without and with spoiler respectively. We see that this frequency

dominates outside of the wake but its influence is much reduced inside. The same behaviour is confirmed by figures 3.6.74 and 3.6.75 which show the fraction unsteadiness due to this frequency for hot-wire effective velocity through the wake development. This is in keeping with the frequency being due to a tunnel influence rather than due to the model. However, it should be noted that although this frequency provides less of the total unsteadiness inside the wake than outside it is still providing around a quarter of the unsteadiness within the wake.

Figures 3.6.76 and 3.6.77 show the fraction of the standard deviation of hot-wire effective velocity due to frequencies near S=0.31 on the wake centreline behind the Rover 200 model without and with spoiler respectively. Figures 3.6.78 and 3.6.79 show the fraction of hot-wire effective velocity unsteadiness though the wake development. This frequency has reduced influence outside the wake confirming that it is due to the flow around the model. It demonstrates a high level of dominance on the wake centreline close behind the model, particularly for the case with spoiler. The cross planes indicate that it is also important at the upper outboard side of the c-pillar vortices. The regions where this peak is most dominant largely correspond to regions of high unsteadiness observed in figures 3.6.56 through 3.6.59 suggesting that it dominates the unsteady wake.

Figures 3.6.80 and 3.6.81 show the fraction of the standard deviation of hot-wire effective velocity due to frequencies near the upper bound of the spectral hump in figure 3.6.70 (around S=0.47) for the wake of the Rover 200 model without spoiler. These figures are similar in appearance to figures 3.6.76 and 3.6.78, suggesting that a single structure may vary in frequency between S=0.30 the upper bound of the spectral hump near S=0.5.

Figures 3.6.82 and 3.6.83 show the fraction of the standard deviation of total pressure unsteadiness (measured using a time-accurate five-hole probe) due to frequencies around S=0.12 one base dimension behind the Rover 200 model. As for the hot-wire results of figures 3.6.72 through 3.6.75, we see that this frequency is

stronger outside the wake than within indicating that this frequency is at least primarily due to the tunnel.

Figures 3.6.84 and 3.6.85 show the fraction of the standard deviation of total pressure unsteadiness due to frequencies around S=0.31 one base dimension behind the Rover 200 model without and with spoiler respectively. The structures in both cases are largely similar, demonstrating the familiar regions of high unsteadiness and periodicity at the upper outboard and lower inboard sides of the c-pillar vortices. These plots are very similar to the corresponding plots for hot-wire effective velocity (figures 3.6.78e and 3.6.79e), showing the lower inboard region of high unsteadiness extending to the centreline in the case with spoiler. Figure 3.6.86 shows the total pressure standard deviation fraction for Strouhal numbers near 0.47 for the case without spoiler. As for the hot-wire results, the contribution of this frequency band is similar to that of the band near S=0.31.
A five-hole probe traverse was also performed just behind the model at z/L = 0.05. The contributions of frequency bands to total pressure coefficient unsteadiness were similar to those for hot-wire velocity as discussed above for results at z/L=1.0.

3.6.2.2b Cross spectral phase:
As discussed in section 2.3.1.3, cross-spectral phase calculated between measurements at two locations can reveal a great deal about the unsteady flow structure.

Figure 3.6.87 shows the distribution of cross-spectral phase at S=0.12 between the reference hot-wire and the total pressure recorded by the time-accurate five-hole probe through the wake one base dimension behind the Rover 200 model without spoiler. (Note that the strongest peak near this frequency is chosen for each time-history, allowing for a small amount of drift of the dominant frequency through the course of an experimental run). With the exception of some localised phase gradient near the reference hot-wire location and a small phase shift between the inside and outside of the wake, we see an approximately constant phase throughout the traverse

plane. Figure 3.6.88 shows the corresponding distribution in the case with spoiler. Although the phase distribution is not particularly clear we can see some evidence of a phase shift of approximately 180° between the two sides of the wake. This indicates the presence of an anti-symmetric flow structure. Note that part of the reason for the apparently "noisy" phase distribution is that the phase is shifting between ±180° on the right hand side of the wake.

Figures 3.6.89 and 3.6.90 show the phase distributions for total pressure at S=0.31. We see a well defined phase distribution which is similar for both cases and for figure 3.6.91 (the phase distribution for S=0.47 in the case without spoiler). Of primary interest is the fact that the phase distributions are symmetric, indicating a symmetric unsteady flow structure rather than an anti-symmetric one. The presence of steep phase gradients around the core of the time-averaged c-pillar vortices suggests that the dominant aspect of the unsteady structure lies on the oscillation of the location of the vortex cores.

3.6.2.2c Coherence:

Figures 3.6.92 and 3.6.93 show levels of coherence at Strouhal numbers near 0.12 between the reference hot-wire effective velocity and total pressure coefficient recorded throughout the wake (calculated as discussed in section 2.3.1.4). The coherence is significantly lower in the case with spoiler (generally less than 0.2) indicating that the flow in this case shields the wake interior from the tunnel unsteadiness. We see some increase in coherence near the reference probe location as could be expected since all frequencies can be expected to be coherent as separation approaches zero. For the case without spoiler we generally see higher coherence outside the wake (around 0.7), in keeping with this frequency being due, at least primarily, to background tunnel noise.

Figures 3.6.94 and 3.6.95 show levels of coherence at $S \approx 0.31$ between the reference hot-wire effective velocity and total pressure coefficient. Levels of coherence are similarly low (<0.4) for both cases. Again we see an increase in

coherence where the probes are close together but apart from that there is little structure to observe. The same is true of figure 3.6.96 which shows the coherence near S = 0.47 in the case without spoiler.

Similar analyses were performed at z/L = 0.05. The distributions of band-limited total-pressure fluctuation at various frequencies are very similar in structure to the equivalent hot-wire measurements presented in figures 3.6.74c and 3.6.75c. The coherence was generally lower than at z/L = 1.0 and no clear phase distributions were observed.

3.6.2.2d Band-limited Reynolds shear stress:

Figures 3.6.97 and 3.6.98 show the Reynolds shear stresses acting in the axial direction due to velocity fluctuations near S = 0.31 one base dimension behind the Rover 200 model without spoiler (see section 2.3.6). Figures 3.6.99 and 3.6.100 show the corresponding plots for the case with spoiler. Somewhat surprisingly we see stronger band-limited Reynolds stresses acting to close the wake in the case with spoiler than without. This is probably best attributed to the stronger periodicity at this frequency in the case without spoiler.

3.6.2.3 Wake Unsteady Reconstruction

The unsteady reconstruction technique, described in section 2.3.2 was applied to the time-accurate five-hole probe wake surveys behind the Rover 200 model. The fixed hot-wire probe (at x/sqrt(A)=-0.24, y/sqrt(A)=0.24, z/sqrt(A)=0.75 without spoiler, and at x/sqrt(A)=-0.14, y/sqrt(A)=0.24, z/sqrt(A)=0.75 with spoiler) was used to provide the phase reference signal. Separate reconstructions were performed for each of the frequencies of interest. The synchronised time-histories have been rearranged to provide sequences showing the fluctuating flow-field. These sequences are presented both as selected plots in paper figures and as animated ".avi" files on the CD-ROM which accompanies this thesis.

Figure 3.6.101 shows total pressure and velocity vectors one base dimension behind the 15% Rover 200 model without spoiler reconstructed from one 4hz wide band around 15hz (S=0.12). The secondary flow velocity vectors exhibit some weak anti-symmetric unsteady behaviour while the unsteady flow is dominated by a fairly strong symmetric structure. Figure 3.6.102 shows the corresponding sequence in the case with spoiler. The vectors in this case demonstrate a strong non-symmetric behaviour to one side only while the total pressure fluctuation seems to consist of a superposition of symmetric and anti-symmetric flow structures. The combination of unsteadiness at this frequency due to the tunnel and due to the model may account for this rather surprising flow structure.

Figure 3.6.103 illustrates the reconstructed flow without spoiler at S=0.31 (one 4hz band at 40hz). The unsteady structure in this case is well defined and consists of the c-pillar vortices varying in strength in a symmetric manner and moving towards the ground plane as they strengthen. The variation in the strength of the vorticity field is accompanied by a strong variation in the total pressure loss at the vortex cores. Figure 3.6.104 illustrates the corresponding flow structure for the case with spoiler. The structure is very similar to the case without spoiler at S=0.31 but the oscillations are stronger. A reconstruction was also performed at S=0.47 for the upper end of the spectral hump in figure 3.6.70. Again the same symmetric structure is observed whereby the c-pillar vortices vary in strength and vertical location. The structure is weaker and the plots slightly noisier than at S=0.31, in keeping with the less well defined spectral peak.

Reconstructions were performed including higher harmonics (of the S=0.31 cases) however these simply resulted in spurious noise in the time-histories and flow plots, indicating that no coherent data was present at the harmonic frequencies. This is in keeping with spectra observed in the wake which did not indicate the presence of any spectral peaks at higher frequencies (eg : figures 3.6.70, 3.6.71).

Reconstructions were also performed for the unsteady five-hole probe traverse at z/L=0.05. Both cases demonstrated some general oscillation of the boundaries of the

total pressure loss region but the unsteady structures were considerably weaker than at z/L=1.0. The only marked unsteady structure was a variation in the level of downwash on the centreline in the case without spoiler (at S~0.31), as the downwash velocity increases an indent is formed in the top of the total pressure loss region. Note that a large proportion of the flow at this plane is beyond the incidence range of the probe so the area available for observation is effectively limited to the periphery of the wake.

3.6.2.4 Surface Pressure Spectral Analysis (15% scale model)

Time-accurate measurements were made of the pressure on the surface of the Rover 200 model in the Durham tunnel with and without backlight spoiler using the transfer-function correction method described in section 2.2.5. The majority of the tappings were connected to a scanivalve which logged 20 sets of 2048 points in time at 800hz at each tapping. Selected tappings were connected to separate transducers and were logged simultaneously to the scanivalve measurements. This made it possible to compute higher quality averaged spectra at these tappings (from just under 1000 sets of 2048 points instead of 20 sets) and provided phase reference signals for cross-spectral and unsteady reconstruction analyses. A reference hot-wire probe was again used in the wake and logged simultaneously with each tapping as for the time-accurate five-hole probe traverses.

Figures 3.6.106 and 3.6.107 show average autospectral densities (20 sets) for surface pressure fluctuations at the base of the windscreen on the centreline of the Rover 200 model without and with spoiler respectively. As for the time-averaged pressure distribution on the forward half of the car, there is no significant difference between the case with and without spoiler. We can see the familiar spectral peak at S=0.12 (again based on free-stream velocity and square root of frontal area) but there is no evidence of the peak observed in the wake near S=0.31. There are also some spectral humps at S=1.14 and above.

Figures 3.6.108 and 3.6.109 show average autospectral densities (~1000 sets) for surface pressure fluctuations at the suction point at the top of the windscreen. Again there is no difference between the case with and without spoiler. The spectral hump around S=1.14 is more obvious as are humps at slightly higher frequencies compared with the base of the windscreen. Analyses performed for the humps at frequencies above S=1.14 produced very similar results to those for the hump at S=1.14. We will therefore discuss only the hump at S=1.14 and the additional, higher frequencies can be assumed to be part of the same structure. The reason for the repeatable and distinct spectral humps is not obvious. Note that these humps are visible in part because they are at relatively high frequency where broadband unsteadiness is limited, these peaks have very little impact on the fluctuating pressure on the model surface. The total unsteadiness above S=1.0 (130hz) amounts to a surface pressure fluctuation of less than 1% of the dynamic head.

Figures 3.6.110 and 3.6.111 show average autospectral densities (~1000 sets) for pressure fluctuations on the centreline of the backlight at z/L=0.86. We now see differences between the spectra with and without the spoiler. The spectral peak at S=0.12 is more distinct in the case without spoiler while the spectrum with spoiler contains more energy at lower frequencies generally. A peak has appeared at S=0.57 which is most distinct in the case with spoiler. The peaks at S=1.14 and above are again visible and are more distinct than further forward on the model. The peak observed in the wake near S=0.31 (~40hz) is still not visible. The peak at 60hz is an exact harmonic of the spurious peak at 30hz attributed to electrical noise and so has also been assumed due to this source.

Figures 3.6.112 and 3.6.113 show average autospectral densities (~1000 sets) for pressure fluctuations on the backlight near the right hand c-pillar. There is generally more unsteadiness at all frequencies at this position compared with the centreline, in keeping with the steeper pressure gradients in the region of the c-pillar (see figures 3.6.14 and 3.6.15). As for the backlight centreline, the S=0.12 peak is more distinct in the case without spoiler while the case with spoiler contains more energy below

this frequency. The peaks near S=0.57 and at S=1.14 and above are visible but are much less distinct than at the backlight centreline.

Figure 3.6.114 shows the level of fluctuating pressure coefficient (standard deviation) on the model centreline due to a 4hz frequency band around S=0.12 (calculated as discussed in section 2.3.1.2). This figure closely resembles the distribution of total unsteadiness on the model surface (figure 3.6.49). The principal exceptions being at the bonnet suction point (z/L=0.034), the bottom of the windscreen (z/L=0.296) and in the base region where the S=0.12 band unsteadiness distribution (fig 3.6.114) demonstrates less distinct peaks than the total unsteadiness distribution (fig 3.6.49). These observations are demonstrated more clearly in figure 3.6.115, which shows the unsteadiness due to this frequency band as a proportion of the local unsteadiness. Note again that we only see differences between the cases with and without spoiler from the middle of the roof back. Also, note from figure 3.6.114 that the maximum level of unsteadiness due to this frequency band is approximately 5% of the dynamic head. This is comparable to the level of fluctuation in the dynamic head due to this frequency band in the empty working section.

Figure 3.6.116 shows the cross-spectral phase for the spectral peak near S=0.12 between pressure fluctuations on the model centreline and the velocity at the reference hot-wire in the wake. Over much of the model we see a distinct slope in the phase distribution. Using a similar analysis to that of equation 3.1 we can determine an axial propagation velocity for the unsteadiness of approximately 0.15 times the free stream velocity on the upper surface of the model and 0.25 times the free-stream velocity on the underside of the model. This is surprising, as is the apparent phase minima near the bottom of the windscreen (z/L=0.296). In a simple case, a phase minima would be expected at the source of an unsteady phenomenon from which its influence propagates outward in all directions. This would not appear to be the case here given that figures 3.6.114 and 3.6.115 showed that this frequency was very weak at the base of the windscreen.

Figure 3.6.117 shows the coherence for the spectral peak near S=0.12 between pressure fluctuations on the model centreline and the velocity at the reference hot-wire in the wake. We see coherence values between 0.15 and 0.55 over the entire model, with slightly higher values in the case without spoiler than with.
Figure 3.6.118 shows the level of static pressure coefficient unsteadiness due to the same 4hz band at S=0.12 for a row of tappings across the backlight from one c-pillar to the other. We see much increased levels of unsteadiness due to this band near the c-pillars, particularly in the case without spoiler. Maximum levels of unsteadiness due to this 4hz band are around 4% of the free-stream dynamic pressure. Figure 3.6.119 shows the phase distribution between surface pressure fluctuations across the backlight and the reference hot-wire. We see an approximately constant phase both with and without spoiler. This is consistent with a symmetric unsteady flow structure. Figure 3.6.120 shows the coherence between the backlight surface pressure fluctuations and the hot-wire velocity fluctuations in the wake. Again we see no clear pattern in the coherence distribution with slightly higher levels of coherence for the case without spoiler.

Figure 3.6.121 shows the level of fluctuating pressure coefficient (standard deviation) due to a 15hz frequency band around S=0.57 on the model centreline (again calculated as discussed in section 2.3.1.2). Figure 3.6.122 shows the proportion of the local unsteadiness due to this frequency band. We see that this band, unlike the S=0.12 band, provides a relatively high degree of the unsteadiness at the suction point at the front of the bonnet (z/L=0.034), at the semi-stagnation at the bottom of the windscreen (z/L=0.296) and in the base region. We see relatively high levels of unsteadiness due to this band on the underbody, particularly at the rear in the case without spoiler.

Figure 3.6.123 shows the cross-spectral phase between the unsteady pressure logged by one of the permanently connected tappings at z/L=0.57 and elsewhere on the centreline of the model. We see an approximately constant phase distribution which

suggests a high propagation velocity (ie: at the speed of sound). The principal exceptions being in the base region and at the rear of the underbody in the case without spoiler where the phase distribution suggests that the unsteadiness is propagating forwards from the rear of the model. Figure 3.6.124 shows the coherence between the same fixed pressure tapping and elsewhere on the model centreline. The coherence approaches unity near the tapping as would be expected but apart from that no real patterns are evident.

Figure 3.6.125 shows the level of fluctuating pressure coefficient due to the 15hz band at S=0.57 across the backlight. We see a gentle increase in band-limited unsteadiness towards the c-pillars, particularly in the case without spoiler. Levels of unsteadiness due to this band are less than 1% of the dynamic pressure. Figure 3.6.126 illustrates the cross-spectral phase between the pressure at the left-hand c-pillar and across the backlight near S=0.57. The phase is approximately constant indicating that any unsteadiness is primarily symmetric rather than anti-symmetric at this frequency. Figure 3.6.127 shows the coherence between the tapping at the left hand c-pillar and tappings across the backlight. As expected we see a rise in coherence to unity as we approach the reference tapping and with coherence dropping to around 0.3 on the opposite side of the backlight.

The analyses presented above were also performed for the spectral peaks at S=1.14 and above (S=1.44) and the results were very similar to those for S=0.57, although with reduced absolute levels of unsteadiness. The results for S=1.14 and S=1.44 in particular were indistinguishable. This suggests that many of the differences between the analysis at S=0.12 and S=0.57 might be due to differences in broadband unsteadiness at high and low frequencies rather than to the behaviour of distinct periodic phenomena.

Figures 3.6.128 and 3.6.129 show the proportion of local surface pressure unsteadiness due to a 4hz frequency band centred at S=0.12. We see that this band contributes as much as 50% of the unsteadiness near the c-pillar and centreline. As

for time-averaged quantities, the distribution over the backlight is much more uniform in the case with spoiler. Figures 3.6.130 and 3.6.131 show the proportion of unsteadiness due to a 15hz band centred at S=0.57. In this case the highest unsteadiness is towards the bottom of the backlight. Figures 3.6.132 and 3.6.133 show the distribution of unsteadiness due to a 20hz band at S=1.14. This frequency provides the most interesting distribution with distinct maxima, particularly in the case with spoiler (fig 3.6.133). In the case with spoiler this point of maximum periodicity roughly corresponds to the centre of the swirl on the surface (visible in the flow visualisation of figure 3.6.11). Unusually, the case without spoiler provides lower gradients with a weak peak further inboard.

3.6.2.5 Surface Pressure Unsteady Reconstruction

Figure 3.6.134 shows the fluctuating surface pressure on the left side of the backlight reconstructed (as discussed in section 2.3.2) from two 4hz bands centred near S=0.57 and S=1.14 for the case without spoiler. The phase reference for the reconstruction in this case was a static pressure tapping at z/L=0.86 on the model centreline. Figure 3.6.135 shows the corresponding reconstruction for the case with spoiler. In this case, particularly in the avi animation, we seem to see the formation of a region of low pressure corresponding to the area of swirling flow on the backlight due to the formation of the c-pillar vortex. This area of low pressure breaks away from the c-pillar and moves down the backlight and out of the region of measurements.

Reconstructions were performed for the other spectral peaks observed for this model (S=0.12, S=0.31, S=1.44). These were generally similar to the reconstruction above for the case without spoiler in that they demonstrated pressure oscillations in phase across the backlight so that the contour lines oscillate in the direction of their local normal.

3.6.2.6 Surface Mounted Hot-Film Results

Measurements were made with surface mounted hot-film gauges on the backlight of the 15% scale Rover 200 model (see section 2.2.3 for a description of surface hot-film gauge technique).

Figure 3.6.136 shows the time-averaged shear stress on the centreline of the roof, spoiler (optionally) and backlight of the Rover 200 model. Without the spoiler we see much higher shear stress at the top of the backlight; with the spoiler the shear stress is highest on the spoiler itself but drops on the separated backlight as would be expected. Figure 3.6.137 shows the corresponding level of fluctuating shear stress (standard deviation) which mimics the time-averaged shear stress distribution. We see a drop in unsteadiness as we move down the backlight and, in the case with spoiler, we see a distinct drop in unsteadiness between the spoiler ($z/L<0.83$) and the separated backlight ($z/L>0.83$).

Figure 3.6.138 shows the time-averaged shear stress around the c-pillar while figure 3.6.139 shows the corresponding fluctuating shear stress. Unsurprisingly, both time-averaged and fluctuating shear stress are much higher for the case without spoiler, with a decrease as we move away from the c-pillar onto the backlight.

Figure 3.6.140 shows a typical autospectral density of the fluctuating shear stress, in this case on the centreline at $z/L=0.86$ without spoiler. We see the familiar spectral peak at $S=0.12$ (15hz) and the spike due to electrical noise at 30hz but no other peaks. As for the various pressure and velocity spectra discussed already, we see a generally higher concentration of unsteadiness as we move to lower frequencies. Spectra at locations around the c-pillar and on the centreline with and without spoiler were inspected and proved to be similar to the spectrum provided in figure 3.6.140.

Figure 3.6.141 shows the coherence spectrum between the shear stress at $z/L=0.86$ on the model centreline and the effective velocity at the reference hot-wire in the wake in the case without spoiler. We see a distinct coherence peak at 15hz ($S=0.12$),

the frequency associated with background tunnel unsteadiness and at 30hz due to electrical noise as usual. Otherwise the coherence is generally very low.

3.6.3 Unsteady Data – 40% Scale

3.6.3.1 General Unsteady Data

Figures 3.6.142 and 3.6.143 show the fluctuating total pressure coefficient in the wake of the 40% scale Rover 200 model in the MIRA tunnel without and with spoiler respectively. Note that, as discussed in section 3.6.1.6, the data for the case without spoiler is based on a half wake traverse with only one set of 2048 points in time recorded at each location while the survey in the case with spoiler is based on a full traverse and 10 sets of 2048 points in time at each location. (For the equivalent wake surveys in the Durham tunnel 20 sets of 2048 points in time were recorded at each location.) The distribution of total pressure unsteadiness for the 40% model is generally similar to that of the 15% model (compare with figures 3.6.60 and 3.6.61). The principal differences are that all elements of the wake are closer to the ground plane at 40%, as they were for the time-averaged wake features (compare figures 3.6.41 and 3.6.42 with 3.6.47 and 3.6.48) and the level of background unsteadiness outside the wake is much lower at 40% due to the lower level of free-stream turbulence in the MIRA tunnel.

Figure 3.6.144 shows a time-trace of the fluctuating velocity reported by a hot-wire in the wake of the 40% Rover 200 model with spoiler. As for the 15% case, there are no dominant periodicities visible in the raw time-trace. Figure 3.6.145 shows the probability density distribution corresponding to hot-wire measurements in the same location. This is very similar to that for the 15% model (figure 3.6.65) with a somewhat asymmetric distribution, indicating the passing of packets of high velocity of variable intensity between which the flow approaches a more steady condition.

3.6.3.2 Wake Spectral Analysis

Figure 3.6.146 shows the average hot-wire velocity autospectral density for the 40% Rover 200 model with spoiler (based on 8400 sets of 2048 points). The unsteadiness

is slightly more concentrated towards low frequencies, as it was for the 15% model (see figure 3.6.71). In this case we see two distinct spectral peaks at S=0.10 and S=0.50 (compared with S=0.12, S=0.32 at 15%). The majority of the work done on the 40% Rover 200 model in the MIRA tunnel was at a Reynolds number of 9.3×10^5 but a limited amount of data was collected at reduced velocity in order to isolate Reynolds number effects. Figure 3.6.147 shows the hot-wire velocity autospectral density for the 40% Rover 200 model with spoiler at a Reynolds number of 3.8×10^5, this corresponds to the standard Reynolds number for the 15% model in the Durham tunnel. Because the amount of data is limited and because the frequencies are low compared with the logging frequency it is difficult to observe the spectral peaks reliably but there does appear to be a peak at S=0.57. This suggests that the increase in the Strouhal number for the second peak from 0.32 to 0.50 between the 15% and 40% models is not simply due to the increase in Reynolds number.

Figure 3.6.148 shows the fraction of total pressure unsteadiness due to a 5hz band at S=0.10 one base dimension behind the 40% Rover 200 model with spoiler. This frequency seems to have the greatest importance outside of the wake although it is strong on the centreline low in the wake. Figure 3.6.149 shows the fraction of total pressure unsteadiness due to a 10hz band at S=0.50. In this case we see a more familiar distribution, with maximum values around the periphery of the c-pillar vortex, in particular at positions above and inboard of the cores. The proportion of unsteadiness due to this band drops off outside the wake but it still remains significant.

Figure 3.6.150 shows the cross-spectral phase near S=0.10 between the reference hot-wire signal and the fluctuating total pressure one base dimension behind the 40% Rover 200 with spoiler. We see that the two sides of the wake are out of phase, indicating the presence of an anti-symmetric unsteady flow structure. The phase distribution becomes more random outside the wake. Figure 3.6.151 shows the corresponding phase distribution near S=0.50. In this case the phase distribution is symmetric, indicating a symmetric unsteady structure. The distribution is similar to

that at S=0.31 for the 15% model (see figure 3.6.90), the main differences reflecting the lower and wider time-averaged wake for the 40% model.

Figure 3.6.152 shows coherence between the reference hot-wire velocity and five-hole probe total pressure near S=0.10 in the case with spoiler. No real distribution is visible and the phase is generally low (<0.5) although not as low as for the 15% model (see figure 3.6.93). At S=0.50 the coherence is somewhat higher although still below 0.5 in most places with no real distribution (see figure 3.6.153).

3.6.3.3 Wake Unsteady Reconstruction

The unsteady reconstruction technique (see section 2.3.2) was applied to the unsteady five-hole probe survey of the wake of the 40% Rover 200 model with spoiler.

Figure 3.6.154 shows total pressure coefficient and velocity vectors reconstructed from a 3hz band at S=0.10. We see a clear anti-symmetric flow structure whereby the two c-pillar vortices alternate in strength both in terms of the vector and total pressure fields.

Figure 3.6.155 shows total pressure coefficient and velocity vectors reconstructed from a 6hz band at S=0.50. The structure in this case is symmetric, with the two c-pillar vortices increasing in strength together and then breaking up. The vortices seem to move to the ground plane and then outboard as they break up. The reconstruction seems to be of lower quality than at S=0.10 particularly for the vectors on the centreline. This is somewhat surprising given the generally higher coherence at S=0.50 than at S=0.10 (compare figs 3.6.152 and 3.6.153).

4. CFD SIMULATIONS

4.1 Introduction

Computational Fluid Dynamic (CFD) simulations were performed using the commercial package Star-CD. The Star-CD solver is typical of multi-purpose commercial CFD codes in that it uses a pressure correction method and is able to use a wide range of structured and unstructured grids. Also typically, it allows the user to select from a range of turbulence models, differencing schemes and solution algorithms (eg: steady and unsteady).

This chapter will first catalogue the observed sensitivity of the solution to a number of modelling parameters based on two-dimensional simulations. Results obtained using CFD are invariably dependent on the modelling decisions taken by the user so it is important to understand which parameters are of importance so that attention can be focussed on them. Unfortunately, the sensitivity of the solution to modelling parameters sometimes means that an experienced user can effectively manipulate the solution until a desired result is obtained. Results in this section are deliberately not compared with the experimental results since it is often possible to obtain a nearly correct solution for the wrong reasons.

Comparisons will then be made between the predicted and measured results for several of the geometries tested during the course of the project.

4.2 Sensitivity to Modelling Parameters

4.2.1 Computational Grid and Domain Size

A number of hexahedral based grid topologies were evaluated for use with the two-dimensional symmetric models. Figure 4.2.1 shows the evolution of grid designs. Initially, an o-grid was used near the model (with grid lines projecting normal to the model surface crossed approximately orthogonally) surrounded by a Cartesian grid.

Grid embedding was used at the transition between the two structures and elsewhere in order to facilitate the expansion of cells in the far field while maintaining acceptable cell aspect ratio. However, errors associated with the grid embedding boundaries were observed; figure 4.2.2 illustrates spuriously high total pressures in the region of an embedding boundary. For this reason grid embedding was ultimately eliminated from the topologies and a pure o-grid was used. This structure provides a natural cell expansion moving away from the model. The use of a nominally square domain served to reduce cell skewness in the corners of the domain. The chief weakness of the grid structure ultimately adopted is that cells projected from the parallel sides of the model maintain the same axial dimension at large distances from the model surface and this results in both poor aspect ratios and very large step changes in cell size in the far field. This was considered acceptable since flow gradients in the region of these problems are small and the impact of local errors here on the flow immediately around the model will be minimal.

It is beneficial to keep domain boundaries well away from the region of interest. Axelsson et al (1998) investigated errors associated with the proximity of the domain inlet to vehicle models both in terms of distance and number of cells along the stagnation streamline. For vehicle simulations with pressure correction solvers it is usual to use a velocity inlet and static pressure outlet; if insufficient distance is provided between the model and the inlet so that the model has a significant potential influence on the inlet static pressure then the inlet stagnation pressure will be uneven over the inlet. Axelsson et al (1998) found a distance of three model lengths between the inlet and the front of the geometry was appropriate. Using this distance in the present work resulted in an inlet stagnation pressure non-uniformity of less than 1% of the dynamic pressure. The approximately square domain resulted in low effective blockage levels and static pressure boundaries were used for the sides of the domain in order to further minimise blockage errors.

The near wall cell spacing is a very important grid parameter. When using two-layer turbulence modelling, Computational Dynamics (1999a) recommend a y+ value

(defined in equation 4.1) of around 3 for the first cell. Alternatively, when using "wall-functions" (whereby the entire boundary layer is modelled rather than resolved) Computational Dynamics (1999b) recommend y+ values between 30 and 150. Near wall grid spacings of 0.06mm and 0.95mm were selected with two-layer turbulence modelling and wall-functions respectively, based on a measured boundary layer thickness of 2.3mm at mid-length on the Docton model. Figure 4.2.3 shows pressure distributions obtained with two grids of identical design but with different near wall spacing and boundary layer handling and reveals a very marked difference in the prediction of the separation at the rear of the model. Runs with other geometries, turbulence models and including unsteadiness provided similar results, with lower pressures obtained at the rear of the model when wall-functions were used. Surprisingly, when wall-functions were tested with the fine grid they resulted in an effectively identical solution to that obtained with the Norris-Reynolds near wall turbulence model. Figure 4.2.4 shows the y+ distribution with a near wall cell spacing of 0.06mm. In order to verify grid density independence for the grid designed for two-layer turbulence modelling, both cell dimensions were halved and an additional simulation was performed. Figure 4.2.5 illustrates that the surface pressure distribution is unaffected by this quadrupling of the number of cells.

$$y+ = \frac{y}{\upsilon}\sqrt{\frac{\tau_w}{\rho}} \tag{4.1}$$

where y is the normal distance from the wall to the centroid of the first cell, τ_w is the wall shear stress, ν is kinematic viscosity and ρ is density

4.2.2 Unsteadiness

In order to minimise computational time, the majority of the modelling parameter studies employed steady simulations. In order to obtain converged solutions it was necessary to use an inviscid "splitter plate" on the centreline behind the model in order to suppress instabilities, although in some cases a half grid was generated with an inviscid wall (symmetry plane) on the centreline. Steady simulations performed

on a full grid with a centreline splitter plate were used as the starting point for unsteady simulations, the splitter plate being removed and the solver being switched from the steady SIMPLE algorithm to the time-accurate PISO algorithm.

The PISO algorithm uses a full implicit formulation (ie: flow variables are taken to have their new-time value) which greatly reduces the severity of restrictions on the Courant-Friedricks-Lewy (CFL) number (given in equation 4.2) and hence on the permitted time step for stability when compared with explicit methods. Computational Dynamics recommend that CFL number, based conventionally on local cell size and velocity, be less than 100 and that it be less than 500 based on an overall characteristic dimension of the domain and an average velocity whereas explicit time-marching methods restrict CFL number to be of order 1. Unfortunately this increase in permitted CFL number is not without penalty because the implicit solution at each time step is performed iteratively. For the simulations performed here, these restrictions on CFL number translate to a maximum time step of around 0.007s but in practice smaller time steps were adopted in order to provide good temporal resolution of the vortex shedding.

$$CFL\ number = \frac{|u|\Delta t}{\Delta x} \tag{4.2}$$

where u is velocity, Δt is the time step and Δx is the cell dimension

Figure 4.2.6 shows time-histories at the reference location in the wake of the PARAD1 model for different time steps. In all cases vortex shedding developed without any external perturbation and the flow had settled into essentially pure periodicity within 0.8s simulated time. This time corresponds to approximately 30 shedding periods or 5.5 times the time scale corresponding to the length of the domain divided by the free-stream velocity. Perzon et al (1999), in their simulation of the unsteady flow behind an idealised truck, allowed 1-2 times this time scale for the unsteady flow to develop but expressed concern that a longer settling time might

be required since Direct Numerical Simulations (DNSs) are often performed allowing 10 of these time scales to elapse.

Surface pressures on the PARAD1 model, averaged over one shedding period, are shown in figure 4.2.7 and are compared with the pressure distribution obtained from a steady simulation. We see a large reduction in the pressure at the rear of the model due to the unsteadiness (as expected based on discussions in section 1.4.1). We also see that we do not achieve time step independence even with approximately 100 time steps per shedding period. The choice of time step also affected the predicted Strouhal number (shown in figure 4.2.8) and level of unsteadiness (shown in figure 4.2.9). As will be discussed in section 4.2.3, the impacts of unsteadiness and turbulence model are interrelated. The turbulence models used were designed for use with steady state simulations and although it is common to use conventional turbulence models in unsteady simulations this is not physically correct. If fine grids and small time steps are used then it may be possible to resolve some small scale unsteady structures whose effects have already been included in the turbulence modelling. This double accounting could be partially responsible for the lack of time step independence at small time steps.

4.2.3 Turbulence Model

Simulations were performed with the well known k-ε turbulence model as well as with the k-ε/Chen and k-ε/RNG variants. Figure 4.2.10 shows the effect of turbulence model on the surface pressure distribution around the PARAD1 model for steady simulations. The basic k-ε model is well known to under-predict separations and here it predicts the latest separation of the three models. However, as discussed in section 4.2.2, the inclusion of unsteadiness in the simulation can have a profound effect on the predicted pressure distribution. Figure 4.2.11 shows the time-averaged pressure distributions from unsteady simulations using the same geometry and turbulence models. The unsteadiness has the greatest impact when combined with the k-ε/RNG turbulence model and the smallest impact when combined with the k-ε model; this results in the highest time-averaged surface pressures in the case

of the k-ε model. The k-ε model also results in a slightly higher Strouhal number (S=0.22 vs 0.21) and level of total pressure coefficient unsteadiness at the reference location in the wake (Cpo'=0.21 vs 0.19) compared with the other models.

4.2.4 Inlet Turbulence Parameters

The effect of inlet turbulence intensity and length scale on the predicted surface pressure distributions for steady simulations using the k-ε turbulence model was investigated. Figure 4.2.12 shows that inlet turbulence intensity has no significant impact on the prediction in the range between 1% and 10% (2.5% inlet turbulence intensity was adopted as the standard inlet condition). Turbulence will include a range of length scales so the selection of a single inlet turbulence length scale is difficult. Figure 4.2.13 shows the impact of a broad range of length scales. The smallest scale used, 0.00042m, corresponds to a characteristic dimension of the wire mesh screens in the wind tunnel settling chamber divided by the wind tunnel contraction ratio and the largest scale, 0.68m corresponds to the square root of the tunnel working section cross-sectional area. This length is obviously much larger than the grid spacing and so is really too large to be handled by a turbulence model. A popular "rule of thumb" is to use the tunnel hydraulic diameter multiplied by 0.07 which results in a length scale of around 0.027m. This length scale is again larger than the cells near the model and so is not really appropriate for inclusion in the turbulence model. At free stream velocity the time-scale associated with this length scale is 0.0011s which is larger than the time step used in the unsteady simulations so this scale could arguably be resolved. The length scale adopted as standard was 0.001m; this was chosen mainly as it was a realistic sub-grid scale for the cells in the vicinity of the model. The pressure distribution difference for different sub-grid length scales was small.

4.2.5 Differencing Schemes

Star-CD allows the user to select from a range of schemes for spatial differencing of the momentum and turbulence terms. There is generally a trade off between computational speed, stability and accuracy. Figure 4.2.14 shows the impact of the

various schemes on the surface pressure distribution on the PARAD1 model for a steady simulation. Figure 4.2.15 shows some corresponding results for the time-average of an unsteady simulation. The only scheme which stands out in either case is the first order accurate upwind differencing scheme (UD), all of the higher order schemes were indistinguishable. The Self-Filtered Centred Differencing scheme (SFCD) was adopted as standard for hexahedral meshes. This scheme blends centred and upwind differencing schemes according to the local flow conditions. It is second order accurate in practice but is more robust than more conventional second order schemes such as Centred Differencing (CD) and Linear Upwind Differencing (LUD). The Monotone Adjective and Reconstruction Scheme (MARS) provides second order accuracy but is sufficiently robust to cope with highly skewed grids, it was therefore used for some solutions using tetrahedral / prism meshes. This accuracy and robustness comes at the expense of computational efficiency.

Figure 4.2.15 shows the impact of the differencing scheme used for the turbulence quantities. In this case the UD scheme provided results which were indistinguishable from the higher order SFCD scheme so UD was adopted as standard practice for turbulence quantities.

4.2.6 Standard Practices Adopted

Based on the work outlined above, a number of standard practices were adopted for the two-dimensional geometries, as outlined in table 4.1 below. Because the choice of turbulence model and the inclusion of unsteadiness had significant impacts on the solution, steady and unsteady simulations were performed with a range of turbulence models wherever possible. Obviously the grid structure had to be adapted somewhat in the case of the 2D Ahmed model in ground proximity. In the case of the three-dimensional Ahmed model, resources were insufficient to use a grid meeting the specification outlined below. In that case a combined prism and tetrahedral grid was used, the prisms being used near the wall to minimise the cell normal dimension without adding an unacceptable number of cells. Simulations were generally started using the simple UD scheme on the momentum terms and then, once a “converged”

steady solution had been obtained the simulation was restarted from this point using the SFCD scheme.

Modelling Parameter	**Adopted Practice**
Domain Size	7 model lengths × 6 model lengths
Grid Topology	Hexahedral O-Type Grid
Near Wall Treatment	Norris-Reynolds (Two-Layer) Model
First Cell Height	0.06mm (for a model 522mm long)
Cell normal dimension expansion ratio	1.08
Inlet Turbulence Intensity	2.5%
Inlet Turbulent Length Scale	0.001m
Momentum Differencing Scheme	SFCD
Turbulence Differencing Scheme	UD
Time Step for Unsteady Simulations	0.0005s
Time Allowed for Periodic Flow to Develop	1.0s = 2000 iterations (> ~30shedding periods)

Table 4.1 – Adopted modelling parameters

4.3 Comparisons with Experiment

4.3.1 PARAD1 and PARAD2 Models

Figures 4.3.1 and 4.3.2 compare predicted and measured pressure distributions for the PARAD1 model based on steady and time-accurate simulations respectively. Agreement between the simulations and measurements without boundary layer trips around the front of the model is good. This supports the theory that the apparent effects of the trips are due to the local flow around the trip itself (see section 3.2.1.2). Pressures on the side of the model are generally underpredicted, this could be due to the effect of blockage in the wind tunnel. In an open-jet tunnel we would expect the streamlines at the periphery of the jet to be over-deflected by the model compared with an infinite test section, this results in lower velocities and hence

higher pressures near the model. At the rear of the model the steady simulations generally predict pressures which are too high while the (time-averaged) unsteady simulations result in pressures which are too low. The k-ε model is the closest to the experimental distribution for both steady and unsteady simulations both for the suction peak at the rear of the model and for the base pressure. This is surprising since the RNG and Chen variants are developments from the original k-ε model.

Figures 4.3.3 and 4.3.4 show the corresponding pressure distributions for the PARAD2 model. The results are generally similar to those for the PARAD1 model. Agreement around the front radius is slightly less good, pressures on the side of the model are again underpredicted and the k-ε/Chen and k-ε/RNG models predict a spurious pressure dip on the base. The unsteady simulations in this case appear to be closer to the experimental data for the suction spike at the rear of the model.

Figures 4.3.5 and 4.3.6 show velocity vectors and total pressure coefficient in the wake of the PARAD1 model based on steady and time-averaged (unsteady) simulations using the k-ε turbulence model. The data has been mapped onto the grid used for the wake traverses in the wind tunnel and the same contour shades have been used in order to allow comparison with the equivalent experimental data presented in figure 3.2.13. Figures 4.3.7 and 4.3.8 show the equivalent data for the PARAD2 model, the experimental data in this case was presented in figure 3.2.14. For both geometries, we see a dramatic difference between the steady and time-averaged (unsteady) simulations. The wake closes much more quickly for the unsteady simulation, as we would expect from the discussions in section 1.4.1. The unsteady mixing with the surrounding fluid results in a much wider wake, at the same axial location. In the same way that the surface pressure distributions from steady and unsteady simulations seemed to bracket the experimental surface pressure distribution, the experimental wake measurements seem to fall between those predicted by steady and unsteady simulations.

Figure 4.3.9 shows the Strouhal number predicted with the different turbulence models for the two PARAD models, compared with the value measured in the wind tunnel. Figure 4.3.10 compares the predicted and measured levels of fluctuating total pressure coefficient near the shedding frequency at x/W=0.3, z/W=2.0. Figure 4.3.11 makes the same comparison for the static pressure fluctuation near the suction spike at the rear of the two models. The predicted Strouhal numbers were very similar for the three-turbulence models and were about 50% below the measured values. Work summarised in Basu (1986) indicates that, for subcritical Reynolds number, the finite span of the experimental bodies should result in significantly lower Strouhal numbers than for a true two-dimensional case (as we have in the CFD simulations). The tunnel blockage would be also be expected to lower the measured Strouhal number. The discrepancy seems therefore to be due to inaccuracies in the numerics or turbulence modelling. We saw in figure 4.2.8 that reducing the computational time step increases the predicted Strouhal number but this effect is small compared with the size of the Strouhal number discrepancy. The level of fluctuating total pressure coefficient in the wake at the shedding frequency was quite well predicted in all cases, as shown in figure 4.3.10. Surface pressure fluctuations were dramatically overpredicted however. Furthermore, the level of surface pressure fluctuation varied inconsistently between turbulence models. Again work summarised in Basu (1986) for subcritical Reynolds numbers provides some indication of the possible effect of the finite span of the experimental models. We would expect the level of pressure unsteadiness for the finite-span models to be less than half of the level for a true two-dimensional case as simulated by the CFD. Although this could go some way to accounting for the difference in measured and predicted surface pressure fluctuation, the similarity between measured and predicted total pressure fluctuations, the fact that the scaling given in Basu (1986) did not account for the Strouhal number discrepancy seen here, and very variable results between simulations all suggest that this is not the correct explanation. It seems that the CFD simulations generally predicted much stronger coupling between the unsteady wake flow and the model surface than was observed in practice.

Figures 4.3.12 through 4.3.14 provide sequences showing the unsteady flow (velocity vectors, vorticity and total pressure coefficient) in the wake of the PARAD1 model. Figures 4.3.15 through 4.3.17 provide the equivalent sequences for the PARAD2 model. These sequences can be compared with the reconstructed sequences based on experimental data presented as figures 3.2.47 through 3.2.52. The qualitative agreement is very good. The periodic structure is slightly stronger in the simulated flows but still does not contain reversed flow vectors. Note that very similar packets of excess total pressure are visible at either side of the wake in the simulations and experimental reconstructions. Figures 4.3.18 and 4.3.19 show total pressure coefficient sequences over a larger area. These make it possible to see that the regions of excess total pressure originate at a position to the side of the model/wake approximately level with the rear of the model. A weak zone of high total pressure projects a considerable distance upstream. The excess total pressure packets are convected along beside the wake in a position slightly lagging that of the vortex on the same side. The physics behind the formation of these regions will be discussed in section 5.2.

4.3.2 Two-Dimensional Ahmed Model

Simulations were performed for the two-dimensional Ahmed model at a number of backlight angles. As for the PARAD models, a two-dimensional simulation was performed so any three-dimensionality present in the experimental case will not be captured. The design of the grid was based on the same parameters as the PARAD grids (as in table 4.1), with some adaptation to include the ground boundary.

Figures 4.3.20 through 4.3.24 compare simulated and experimental pressure distributions as backlight angle is increased from 20º to 30º in steps of 2.5º. The agreement between CFD and experiment was generally reasonable around the front of the model, assuming that the low pressure spike in the experimental data is due to the local flow over the trip (as discussed in section 3.2.1.2). Pressures on the flat roof of the model are underpredicted, again as discussed above this could be due to blockage effects in the wind-tunnel. At 20º (figure 4.3.20) the k-ε and k-ε/RNG

models correctly predict attached flow over the backlight while the k-ε/Chen model predicts a separation (figure 4.3.25 presents the velocity vectors from the k-ε run). At 22.5º only the k-ε model continues to correctly predict attached flow. At 25º the k-ε model correctly predicts the change-over to separated flow. The separated flow velocity vectors in the 30º case are illustrated in figure 4.3.26. Again somewhat surprisingly, the k-ε model surpassed the more sophisticated models; it would generally be expected to predict separation erroneously late however in this case its later prediction of separation, compared with the other models, agrees with experiment. Figures 4.3.25 through 4.3.28 illustrate the wake flow in terms of velocity vectors and total pressure coefficient for the 20º and 30º cases. The data has been mapped onto a grid similar to that used in the presentation of experimental results although the grid spacing has been halved and it has been extended forward compared with the experimental data. When comparing with the experimental data (figures 3.4.6-3.4.9) we see that the rate of wake closure is lower in the case of the CFD simulations. This is in line with the PARAD results where steady simulations resulted in slow wake closure compared with experiment. Unsteady simulations were performed for the two-dimensional Ahmed model but, unlike for the PARAD simulations, the predicted levels of unsteadiness were small compared with the experimental data and the inclusion of unsteadiness did not have a significant impact on the pressure distribution or critical backlight angle.

4.3.3 Ahmed Model (Three-Dimensional)

Ideally the experience gained in the two-dimensional simulations would be applied for three-dimensional simulations. A three dimensional O-type grid with the same radial and longitudinal resolutions as the two-dimensional simulations (at least 100×300 cells) with comparable resolution in the third dimension to the longitudinal resolution (approximately 200 cells) would result in a total grid size of 6×10^6 cells. Simulations of this scale are now common in some settings however the memory requirement for such a simulation would be an order of magnitude beyond the resource available for the current project. A comparatively crude simulation of the three-dimensional Ahmed model (30º backlight) was undertaken nevertheless to see

what could be achieved. A primarily tetrahedral grid was used, with prism cells near the wall to improve the near wall spacing. Nevertheless, it was necessary to use wall functions rather than a two-layer turbulence model. The outer bounds of the domain were based on the two-dimensional runs. The full geometry was modelled without a symmetry plane resulting in a total number of grid cells of 3.6×10^5. The k-ε turbulence model was used. Initial solutions were obtained with UD on the momentum terms and then the simulation was restarted with the MARS differencing scheme. Unsteady simulations were performed using a time-step of 0.0005s; this is the same as the value used for the two-dimensional simulations since the frequencies observed in the wind tunnel were similar for the two and three-dimensional geometries. However, no unsteadiness was observed and, reassuringly, the inclusion of unsteadiness therefore had no impact on the time-averaged solution.

Figure 4.3.29 shows the predicted surface pressure distribution on the model centreline, compared with experiments. We see that the pressure distribution around the front and roof of the model agree well with the experimental data for the high drag flow regime. The pressure distribution on the backlight matches with this initially but the flow structure here is clearly not predicted correctly. The CFD simulation predicts attached flow at the top of the backlight with a low pressure spike before the flow separates near the top of the backlight, producing a corresponding increase in surface pressure to an approximately constant value (close to that for fully separated flow). The closed "turbulent separation bubble" observed in practice which maintains a low pressure over the entire backlight is therefore not predicted. Velocity vectors on the centreline (figure 4.3.30) illustrate the predicted flow and provide a comparison with the equivalent experimental data of figure 3.5.13. Figures 4.3.31 and 4.3.32 indicate the total and static pressure on the centreline respectively. Comparing these with the equivalent experimental data (figure 3.5.14 and 3.5.15) we see that the wake closes more rapidly initially in the experimental data but leaves a larger far wake. This is in keeping with the observations made for the two-dimensional models where unsteadiness produced wakes whose core closed quickly but which left a more diffuse far wake. Figures

4.3.33, 4.3.34 and 4.3.35 show secondary flow vectors, vorticity and total pressure coefficient for a number of cross planes in the wake corresponding to the experimental traverse planes presented in figures 3.5.16, 3.5.17 and 3.5.18. Qualitative agreement is reasonable, considering the crudeness of the simulation. The vortices seem to form slightly later in the simulated case, indicated by the incompleteness of the vortices at the most upstream location (figure 4.3.33a). The secondary flow velocities between the vortices and the ground are lower in the simulation and as a consequence the vortices remain rounder and are not drawn down to the groundplane and outwards as much as in the experimental case. The flow on the wake centreline is markedly different, with a high level of loss predicted by the CFD simulation, presumably associated with the separation from the backlight. This separation also reduces the downwash velocity on the centreline which results in reverse vortices visible in the vorticity plots between the c-pillar vortices and the centreline. Also of interest are the small reversed vortices outboard of the c-pillar vortices since reversed vortices are observed in this location in the experimental results (figures 3.5.17a, b).

5. DISCUSSION

The first chapter of this thesis sought to summarise our current level of understanding of large scale aerodynamic unsteadiness relevant to passenger cars. Subsequent chapters presented the detailed results obtained during the course of this work, highlighting important observations. This chapter will seek to tie together the results obtained from the different geometries tested and to present the key additions to our knowledge resulting from this work.

5.1 Extensions to our Time-Averaged Understanding of the Flow around Passenger Cars

Typical flow structures for passenger cars, and fastbacks in particular, were reviewed in section 1.2.3. The Rover 200 model, being a relatively modern design which benefited from considerable aerodynamic development, avoids separations at the front of the bonnet and roof and at the base of the windscreen (see section 3.6.1.2). It demonstrates conventional a-pillar and c-pillar trailing vortices as well as a typical sensitivity to the flow over the backlight through which the pressure on the backlight may be increased by producing a separation from the rear of the roof. As well as directly affecting the flow on the centreline, this weakens the c-pillar vortices and hence increases the pressure in the region of the c-pillars.

5.1.1 A-Pillar Vortices

As the flow from in front of the windscreen separates as it rounds the a-pillar, it forms the a-pillar trailing vortices. As discussed in sections 3.6.1.2 and 3.6.1.5, these vortices trail along the side glass and then move over the roof. They continue to move towards the centreline and appear in the wake above and between the c-pillar vortices. Although this behaviour seems typical, Goh (1994) reports that the path of the a-pillar vortices for the Honda Accord follows the edge of the roof to the apex of the c-pillar so that they wrap around the c-pillar vortex and are absorbed by it. The behaviour of the a-pillar vortices therefore appears to be geometry dependent.

5.1.2 Secondary Vortices Outboard of C-Pillar Vortices

As discussed in section 3.5.1.2, two secondary vortices are formed between the main c-pillar vortices and the backlight for the Ahmed model and these are not included in Ahmed et al's (1984) wake schematics. Similar secondary vortices are formed at the leading edge of delta wings, as illustrated by figure 5.1.1 based on a figure from Gad-el-Hak and Blackwelder (1985). These may be the same vortices which appear in the wake outboard of the c-pillar vortices as discussed in section 3.5.1.5.

For the Rover 200 model these vortices are absent. The flow separates at the c-pillar and then does not come into contact with the backlight (ie: does not produce impingement or separation lines) either with or without the spoiler.

5.1.3 Effect of Spoiler at Top of Backlight

As seen in section 3.6.1.1, the change in forces due to the spoiler at the top of the backlight on the Rover 200 model was not as distinct as that associated with the switch from high drag to low drag flow for the Ahmed model. Increasing the size of the spoiler had a progressive effect on both rear lift and drag This behaviour can be attributed in a general sense to the curved surfaces of the Rover 200 model. Firstly, the flow does not form a closed separation bubble on the backlight (which is largely responsible for the Ahmed high drag flow) and secondly, when we change the size of the spoiler, separations and reattachments are likely to move progressively around a curve rather than to suddenly switch structure.

The spoiler significantly increases the pressure near the c-pillar and around the intersection of the roof and backlight where curvature of the body is greatest but it actually results in a slightly lower pressure over much of the backlight. This is presumably due to the greater curvature of the streamlines around the outside of the separation compared with the streamlines over the backlight in the unseparated case. This varied effect of the spoiler on backlight pressures and the sensitivity of drag and rear lift to spoiler design (section 3.6.1.1) indicate that the effect of a spoiler at

the top of the backlight is not as straightforward as might be imagined and considerable effort may be required to achieve an optimal design.

In the same way that the change from high to low drag flow for the Ahmed model had negligible effect on the pressures on the front half of the model (figure 3.5.8), the spoiler on the Rover 200 model had no effect on the pressures on the front of the model or on the underfloor.

5.1.4 Vortex Breakdown

Sedney (1979) hypothesised that the sudden change in drag at the critical backlight angle demonstrated by the Morel body (a predecessor to the Ahmed body) could be explained by a vortex breakdown occurring in the c-pillar vortex. Also, Goh (1994) speculates on the possibility of a vortex breakdown for c-pillar vortices of the Honda Accord.

The present investigation indicates that vortex breakdown does not occur for the Ahmed model or the Rover 200 model with or without spoiler. As discussed in section 1.4.2.6, a requirement for vortex breakdown is a swirl angle (based on tangential and axial velocities) in excess of around 40°. The peak swirl angles at z/sqrt(A)=1.0 did not exceed 20° and 30° for the Rover 200 model with and without spoiler respectively. For the Ahmed model there were local regions around the vortex where angle of the flow to the axial achieved slightly over 40° however this was largely due to the strong downwash at the centreline and this angle was only maintained for about half of the circumference of the vortex.

The strongest indications that vortex breakdown does not occur are that we do not see a sudden growth in size of the vortices which would accompany a breakdown and we do not see reversed flow at the cores. In fact the minimum velocity at the core of the c-pillar vortices of the Rover 200 without spoiler was around 40% of the free stream velocity.

5.2 The Phenomenon of Transient Increasing Total Pressure

5.2.1 CFD Observations

Simulations of the unsteady flow around two-dimensional models presented in section 4.3 demonstrate large areas to either side of the body and wake where the transient total pressure coefficient increases to values well above unity. These regions of excess total pressure are then convected downstream next to the wake. Note that the time-averaged total pressure does not exceed unity, however.

Numerical errors resulting in total pressures and sometimes surface static pressures in excess of the free-stream total pressure are a common problem for CFD. These errors have been discussed in some detail by Axelsson et al (1998). However, the effect that we are seeing here is not a numerical error but a genuine fluid flow phenomenon.

5.2.2 Theory

The fact that total pressure cannot increase along a streamline is a well known corollary of Bernoulli's equation for steady flow. However, if we remove the assumption of steady flow we find that transient total pressure may increase or decrease.

Consider the momentum equation for one-dimensional, inviscid, incompressible, unsteady flow:

$$\rho \frac{Du}{Dt} + \frac{\partial P}{\partial s} = 0 \qquad (5.1)$$

where ρ is density, u is velocity, t is time, P is static pressure and s is streamwise distance

From the viewpoint of a particle travelling with the flow, changes in u will occur both as a result of the particle travelling through the current u field and due to the variation of u in time at a fixed point in space:

$$\frac{Du}{Dt} = u\frac{\partial u}{\partial s} + \frac{\partial u}{\partial t} \tag{5.2}$$

substituting 5.2 into 5.1:

$$\rho u\frac{\partial u}{\partial s} + \rho\frac{\partial u}{\partial t} + \frac{\partial P}{\partial s} = 0 \tag{5.3}$$

now perform an integration between two positions along a pathline:

$$\rho\int u\frac{\partial u}{\partial s}ds + \rho\int\frac{\partial u}{\partial t}ds + \int\frac{\partial P}{\partial s}ds = 0 \tag{5.4}$$

which simplifies to:

$$\rho\int u\partial u + \rho\int\frac{\partial u}{\partial t}ds + \int dP = 0 \tag{5.5}$$

$$\Delta\left(P + \frac{\rho u^2}{2}\right) + \rho\int\frac{\partial u}{\partial t}ds = 0 \tag{5.6}$$

Equation 5.6 is Bernoulli's equation with an additional time-derivative term which is generally assumed to be zero. The implication of equation 5.6 physically is that, when the flow along a pathline is slowing down *in time*, the stagnation pressure ($P+\rho u^2/2$) can increase along the pathline. He (1996b) discusses the uncoupling of entropy and stagnation pressure in unsteady flows and comes to a similar

conclusion: that it is possible to obtain transient variations in total pressure with constant entropy (ie: isentropic flow).

It is not difficult to imagine situations where this effect must exist, consider a tank car full of air being pushed by a locomotive, as the train accelerates, the pressure on the inside rear surface of the tank must increase in order to accelerate the fluid within it. Now consider the same situation but with the front face of the tank removed so that the fluid inside it is simply stagnant air. With the vehicle travelling at constant speed the pressure acting on the inside face of the vessel will be $(P+\rho u^2/2)$. If the vehicle is accelerating, however, it must accelerate the stagnant fluid inside the vessel and in order to do this the pressure on the inside face of the vessel must increase above $(P+\rho u^2/2)$ (where u is the instantaneous velocity). The same effect will occur with a less contrived geometry where the stagnant fluid is simply the fluid near the stagnation point in front of the body. A practical demonstration of this phenomenon is the operation of valves in long pipelines. Consider a pipe supplied with a constant total head from a large reservoir. A fixed obstruction in the pipe (eg: the face of a partially closed gate valve) will experience a total pressure equivalent to the head of the reservoir. Now if we close the valve then the fluid in the pipe must come to rest and this will require a force to overcome the momentum of all of the moving fluid within the pipe (note that the force will therefore increase with the length of the pipe). This force is provided by an increase in the pressure on the face of the valve beyond the total head of the reservoir while the deceleration takes place. For this reason, valves on long distance pipelines must be closed very slowly (over several minutes) in order to avoid rupturing the pipe.

In the flows considered in this investigation, where the transient is due to intrinsic unsteadiness rather than externally imposed transients, the downstream flow effectively applies a transient blockage similar to the closing gate valve.

5.2.3 Experimental Verification

The verification of the existence of total pressure above the upstream value can only be performed with a probe able to measure transient total pressure, which is probably part of the reason why this phenomenon has remained obscure.

Figure 5.2.1 shows total pressure time-traces from a CFD simulation and a time-accurate five-hole probe measurement just outside the wake of the PARAD1 model. Although the two methods do not show perfect agreement (CFD has overpredicted the level of unsteadiness and underpredicted the frequency and the probe trace contains some noise) they both show that the total pressure coefficient is oscillating about a value of unity.

All of the reconstructed fluctuating total pressure fields presented in Chapter 3 show oscillations in total pressure outside the wake which result in transient total pressure coefficients above unity. The behaviour of these regions is in agreement with the CFD predictions presented in chapter 4.

5.3 Two-Dimensional Geometries

5.3.1 Two-Dimensional Vortex Shedding

5.3.1.1 Reynolds Number and Flow Regime

The benchmark case for the study of two-dimensional bluff bodies is the circular cylinder and its various flow regimes have been discussed in section 1.4.2.1. The Reynolds number for the PARAD models as tested here was 2.3×10^5 based on width. For a circular cylinder this Reynolds number would fall into the critical regime (in which vortex shedding does not occur) however vortex shedding was obviously present for the PARAD models. The lack of shedding for circular cylinders in this regime seems to be linked to the transition of the boundary layers on the cylinder via a laminar separation bubble (see section 1.4.2.1). The bodies studied here do produce boundary layer transition in this way (as discussed in section 3.2.1.1) but the position of the reattachment appears to be constant (in time

and over the span) and tests performed with and without boundary layer trips produced indistinguishable results. The Reynolds number based on model length was 8.9×10^5 which would correspond to the supercritical regime however the presence of such obvious anti-symmetric shedding (albeit less distinct than for the "Pure Karman" regime) suggests that the flow probably fits best into the transcritical regime.

The Reynolds number for the wing with Gurney flap was 3.1×10^5 based on free-stream velocity and wing chord or 1.7×10^4 based on the base dimension. The former corresponds to the critical regime for circular cylinders while the latter corresponds to the subcritical regime. The distinct vortex shedding observed for this geometry is in keeping with the subcritical regime.

5.3.1.2 Universality of Strouhal Number

As discussed in section 1.4.2.1, various researchers have defined universal Strouhal numbers and the approach of Griffin (1981) produced the best collapse of experimental data for different geometries. His method uses a measured wake width (d') defined as the width between points of maximum velocity unsteadiness at the axial position corresponding to minimum static pressure on the wake centreline. In the present investigation, the static pressure decreased as we moved close to the rear of the body until reliable measurements could no longer be made. The width between points of maximum total pressure unsteadiness was therefore substituted for Griffin's (1981) definition of d'. Universal Strouhal numbers (S*) based on this wake width d' and U_b (defined in equation 1.3) provided good collapse of the experimental data obtained here (see table 5.1) although the values determined were well above those obtained by Griffin (1981) at similar Reynolds number (0.16 to 0.17 typically).

	C_P(base)	U_b (m/s)	d' (m)	f (hz)	St	St*
PARAD1	-0.170	29.7	0.090	65	0.313	0.197
PARAD2	-0.141	29.3	0.081	75	0.361	0.207
Gurney Flap	-0.4 (est.)	24.8	0.016	316	0.181	0.204

Table 5.1 – Universal Strouhal numbers for vortex shedding

(Note that the base pressure for the Gurney flap was estimated by extrapolating from the suction surface pressure distribution based on the results of Jeffrey et al (1998) in which the suction surface pressure distribution was continuous with the Gurney base pressure.)

5.3.1.3 Three Dimensionality

The flow around nominally two-dimensional geometries can exhibit three-dimensionality either due to the finite span of any real body and the consequent end effects or due to instabilities in the flow itself.

The PARAD models tested in this investigation have quite a low aspect ratio (span/width = 2.72, span/length = 0.69) and so end effects are to be expected. Observed levels of three-dimensionality for time-averaged and unsteady aspects of the flow for these models were presented in sections 3.2.1.4 and 3.2.2.3 respectively. The same vortex shedding frequency was found to dominate over the entire span and did not undergo the step changes reported by several researchers and reviewed in Basu (1986). In fact, the unsteady parameters (eg: the coherence at the shedding frequency) appeared more two-dimensional than the time-averaged parameters.

It was not the aim of these models to produce a purely two-dimensional flow however it is useful to relate the results from these models to the equivalent results for truly two-dimensional versions (eg: for comparison with two-dimensional CFD simulations). Figures 1.4.2 and 5.3.1 reproduced from Basu (1986) allow us to make

a rough estimate of the impact of the finite span used here on the measured level of unsteadiness and Strouhal number. These figures are based on experiments at subcritical Reynolds numbers, however, so the estimates should be viewed with some trepidation. For a span/width of 2.7, the measured Strouhal number will be some 30% below the value for a true two-dimensional case while the measured pressure unsteadiness will be less than 50% of the two-dimensional value. The expected Strouhal numbers for 2D versions of the PARAD1 and PARAD2 models will therefore be approximately 0.45 and 0.52. These values seem very high, which might suggest that aspect ratio is more important at lower (subcritical) Reynolds number where the flow is otherwise more two-dimensional than for the flow regime of these experiments. As discussed in section 4.3, the Strouhal numbers predicted by the CFD simulations were significantly below the measured values rather than above.

5.3.2 Two-Dimensional Ahmed Model

As discussed in section 3.4, the two-dimensional Ahmed model demonstrates broadly similar behaviour to the conventional, three-dimensional Ahmed model. A suction spike on the backlight increases in intensity as backlight angle is increased up to a critical point. Above the critical backlight angle the entire backlight becomes separated, this separation merges with the recirculation behind the model and the suction spike disappears. For the three-dimensional model the switch occurs at a higher backlight angle (30°) compared with the two-dimensional model (22.5°) because the c-pillar trailing vortices tend to delay the final separation on the centreline. A closed separation bubble is present on the backlight of the three-dimensional model in the high drag state and this produces a minimum static pressure at mid-height on the backlight. The point of minimum pressure on the two-dimensional model is close to the intersection between the roof and backlight and any separation bubble seems to be confined to the top of the backlight.

For the two-dimensional model we see clear periodicity for the high-drag flow (subcritical backlight angle) at a Strouhal number of 0.50 (based on free stream

velocity and square root of equivalent frontal area for a 3D model of the same scale). However, for the fully separated, low-drag flow, dominant periodicity is lost (despite the fact that levels of broadband unsteadiness increase). The flow structure for the high drag flow is not unlike vortex shedding in that the shear layers from the top and bottom edges of the model alternately strengthen and weaken. However, the asymmetry of the time-averaged flow results in only one packet of total pressure loss being released from the wake during each cycle. Very little unsteadiness was predicted by the CFD simulations, irrespective of backlight angle.

5.4 Effects of Geometry on Unsteadiness

5.4.1 PARAD Models (Effect of Corner Radii)

The PARAD1 and PARAD2 models are essentially identical except that the corners on the PARAD2 model are considerably larger. The airflow around these models is presented in section 3.2. It is often assumed that larger radius corners will be more prone to aerodynamic unsteadiness however the results obtained from these models show that this is an oversimplification. In fact many of the effects of increasing the corner radii are by no means obvious.

Increasing the corner radii moved the final separation further around the trailing radius which produced a lower minimum surface pressure and a narrower wake at the point of separation, as would be expected. In keeping with this narrower wake, the shedding frequency was increased by about 15%. This is consistent with results in the literature which indicate higher Strouhal numbers for circular cylinders (0.20 typ.) compared with square cylinders (0.13 typ.) and normal flat plates (0.14 typ.).

It is tempting to connect a higher shedding frequency with stronger shedding however, the periodicity for the PARAD2 model was considerably weaker than that for the PARAD1 model. This is reflected in much lower proportions of pressure unsteadiness due to the shedding band both in the wake and on the surface as well as significantly lower coherence between the reference hot-wire and the fluctuating

total pressure in the wake (0.8 vs 0.9 typically). Total levels of unsteadiness in the wake were very similar and the larger corners produced only a slight reduction in surface pressure unsteadiness. One argument for higher unsteadiness with smaller corners could be that they produce higher shear in the wake however the PARAD2 model (with larger corners) actually produced higher levels of vorticity in the shear layers. Unfortunately, data in the literature on levels of unsteadiness is too sparse to make any generalisations on the effect of corner geometry on levels of unsteadiness in order to compare with the observations made here. When levels of unsteadiness are quoted they may be in terms of fluctuating forces, surface pressures or wake fluctuations and the data is invariably based on measurements at different Reynolds number and aspect ratio. While the data is too limited to corroborate the observation of stronger shedding with sharper corners, there is no data to refute it.

5.4.2 Fastback Passenger Cars

As for the two-dimensional bodies, it may seem intuitive to assume that models with more corner rounding will be more prone to unsteadiness since the point of separations from curved surfaces will not be fixed in the same way that it is from sharp corners.

We can gain some insight by comparing the observations for the Ahmed and Rover 200 models although it is obviously impossible to make generalisations based on case studies for only two (very different) geometries. As for the two-dimensional models, the observations are more complicated than might be assumed. Strouhal numbers for the two models are comparable as shown in table 5.2, factors other than model shape (eg: tunnel used) exerting a larger influence. Levels of unsteadiness are also very similar for the two models, as shown in table 5.3 as are levels of periodicity in terms of coherence and levels of band limited unsteadiness presented in sections 3.5 and 3.6.

The differences between the two models tested here stretch far beyond differences in corner radii. For instance, although the sharp corners of the Ahmed model may fix the separation points, reattachment of the closed separation bubble on the backlight

(in the high drag flow regime) will not be fixed. This provides a degree of freedom which is absent for the Rover 200 model which does not exhibit this closed bubble.

The main conclusion that can be drawn from these observations is that corner radii and even some details of the time-averaged flow do not appear to have an overwhelming effect on frequency or levels of unsteadiness for fastback passenger cars.

	Wake Durham	Wake MIRA	Wake MIRA (same Re. no. as Durham)	Surface Durham
Ahmed (high drag)	0.35	0.08, 0.58	-	0.30
Ahmed (low drag)	-	-	-	0.30
Rover 200 (no spoiler)	0.12, 0.30, ~0.47	-	-	0.12, 0.57, 1.14
Rover 200 (with spoiler)	0.12, 0.32	0.10, 0.50	0.57	0.12, 0.57, 1.14

Table 5.2 – Principal Strouhal numbers for the Ahmed and Rover 200 models

Based on the same intuitive arguments about sharp corners fixing separation points and hence reducing unsteadiness, it is generally assumed that a backlight spoiler such as that fitted to the Rover 200 model will reduce unsteadiness. As summarised in table 5.3, the spoiler does decrease the levels of unsteadiness on the rear surfaces of the model. However, we see no reduction in levels of unsteadiness in the wake and Strouhal numbers are very similar (table 5.2). In fact the unsteady flow for the model with spoiler is slightly more periodic than without, in terms of sharpness of spectral peaks and levels of band limited unsteadiness in the wake and on the surface. The reduced level of pressure fluctuation on the model surface in the case with spoiler can probably be considered to be a result of the reduced time-averaged pressure gradients on the surface of the model. Again we see that the intuitive

assumption that fixing separation points will reduce unsteadiness is an oversimplification.

	Wake Cpostd Durham	Wake Cpostd MIRA	Backlight Cpstd Durham	Base Cpstd Durham
Ahmed (high drag)	0.25	0.28*	0.06-0.11	0.07
Ahmed (low drag)	-	-	0.05	0.05
Rover 200 (no spoiler)	0.27	0.28	0.03-0.08	0.11
Rover 200 (with spoiler)	0.28	0.28	0.03-0.06	0.07

Table 5.3 – Peak levels of fluctuating total pressure coefficient one base dimension behind the Ahmed and Rover 200 models and static pressure coefficient fluctuation on the models (* 0.79 base dimensions behind model)

The possibility of a link between the central unsteady frequency (Strouhal number ~0.3) and the rear lift was considered since we know that there is a strong link between the base pressure and shedding frequency for two-dimensional bodies. For the three-dimensional models and the two-dimensional Ahmed model, Strouhal number was often higher for geometries with lower pressures on the backlight. However, the effect was not strong enough to be distinguished from the experimental variation of Strouhal number for a given geometry, even though backlight pressures were significantly different. Any effect was certainly not as strong as the relationship between Strouhal number and base pressure for two-dimensional vortex-shedding bodies.

5.5 Effects of Scale and Velocity on Unsteadiness for Fastbacks

For two-dimensional bodies exhibiting vortex shedding, the frequency of the shedding is generally related to the free-stream velocity and body size through an approximately constant Strouhal number over wide Reynolds number ranges (see section 1.4.2.1). Simple dimensional analysis tells us that we should expect frequency to increase in proportion to velocity and decrease in proportion to dimension for a given geometry. The prominent frequencies in the wake of the Ahmed and Rover 200 models were found to increase with velocity and decrease with scale generally but the Strouhal number at different scales in different tunnels varied significantly. It was generally found that testing at larger scales in the MIRA tunnel produced higher Strouhal numbers but no definite trend with model scale or Reynolds number could be observed. The two tunnels do have significantly different levels of free stream turbulence and the spectral makeup of the background tunnel unsteadiness is also different (see section 2.1.1). The periodicity for these three-dimensional models is quite weak and the Strouhal number varied by up to 0.05 from run to run for the same model in the same tunnel. We observe that the background unsteadiness in the Durham tunnel dominates the unsteady wake structure for the Rover 200 model at S=0.12 (see section 3.6) so it is reasonable to assume that the weak periodicity of these models makes them sensitive to external influences. The unsteady structure (which will be discussed in sections 5.6 and 5.7) is quite intricate so it seems possible that the unsteady flow exhibits a complex sensitivity to the tunnel unsteadiness and this results in the apparently random Strouhal number variation in the different tunnels.

Unfortunately this unclear scaling of the predominant frequencies with scale and velocity makes it difficult to predict accurately the unsteady frequencies for a real car, although the assumption of constant Strouhal number would probably provide at least a crude estimate.

5.6 Observed Unsteady Flow for Fastback Passenger Cars

5.6.1 Levels of Unsteadiness

Peak levels of unsteadiness in the wake and on the rear surfaces of the three-dimensional models were given is table 5.3. The levels of unsteadiness were surprisingly similar for different geometries despite much larger differences in the time-averaged flow. Levels of unsteadiness were also very similar when measured in the Durham and MIRA tunnels despite differences in the time-averaged flow in these two tunnels and despite differences in the background tunnel unsteadiness. Again, care should be taken drawing generalised conclusions from only a couple of case studies.

We see peak total pressure unsteadiness in the wake corresponding to slightly more than 25% of the dynamic pressure both at one base dimension behind the model, as indicated in table 5.3 but also immediately behind the models. Levels of fluctuating pressure on the rear surface of the models was much lower than in the wake, generally below 10% of the dynamic head.

5.6.2 Periodicity

Although every effort was made in the present work to identify and observe periodic flow structures, periodicity for the three-dimensional models was weak. In cases where other researchers have made instantaneous measurements in an entire plane (Wang et al (1996) using PIV, Ishihara and Takagi (1999) using a rake of 200 probes) they were unable to observe any repeating structure. The spectral methods used here present observations of the unsteady structure based on frequency but it is probably best to consider this to be simply an indication of the mean time-scale.

Even in the most periodic regions of the wake, the fluctuation due to a frequency band around the most dominant unsteady frequency never amounted to more than 40% of the local unsteadiness. If we normalise this value by dividing by the

bandwidth and multiplying by the principal frequency as in equation 5.7 then we obtain an index with which to assess the sharpness of the spectral peak.

$$PeakSharpness = \frac{Cpo'(f_1 - f_2)}{Cpo'} \bullet \frac{(f_1 + f_2)}{2(f_1 - f_2)} \tag{5.7}$$

Table 5.4 compares this and other parameters for the three-dimensional and two-dimensional models and hence provides a summary of the various plots of band limited unsteadiness and coherence in chapter 3. Observe that the levels of periodicity are much lower for the three-dimensional models than for the two-dimensional models (between a factor of 2 and 10 on the sharpness of spectral peaks).

Also given in table 5.4 are peak coherence values at the principal frequency in the wake. For the three-dimensional models this was generally less then 0.5 and in some cases as low as 0.2. This compares with peak coherence values around 0.9 for the two dimensional models and, in the case of vortex shedding from the Gurney flap, the coherence was above 0.95 throughout much of the wake and surroundings. Note that the parameters in table 5.4 are dependent on the background tunnel unsteadiness, values of coherence in particular being much higher in the MIRA tunnel than in the Durham tunnel.

The overwhelming observation on the subject of periodicity is that the unsteadiness for the three-dimensional models is much less periodic than for two-dimensional (vortex shedding) cases. We can also see that the shedding behind the Gurney flap is much more periodic than for the other vortex shedding cases, as discussed in section 5.3.1.1, this has been attributed to the difference in Reynolds number and hence flow regime. One interesting observation is the lack of periodicity for the two-dimensional Ahmed model in low drag flow. This is in contrast to observations by Morel (1980) and Xia and Bearman (1983) (discussed in section 1.4.2.2) who found

	S	Max. $\frac{Cpo'(band)}{Cpo'}$	Peak Sharpness Index (eq. 5.7)	Max. Wake Coherence
Rover 200 no spoiler 15% - Durham	0.30	0.34	1.4	0.2
Rover 200 with spoiler 15% - Durham	0.32	0.37	1.5	0.5
Rover 200 with spoiler 40% - MIRA	0.50	0.50	1.1	0.7
Ahmed high drag 1/8 – Durham	0.35	0.35	1.9	0.2
Ahmed high drag ¼ - MIRA	0.58	-	-	0.6
2D Ahmed 20°	0.49	0.65	5.9	0.92
2D Ahmed 22.5°	0.50	0.55	5.0	0.88
2D Ahmed 30°	0.27	0.32	1.6	0.45
Gurney Flap	0.18	0.92	9.7	0.96
PARAD1	0.31	0.6	3.6	0.93
PARAD2	0.36	0.45	3.2	0.80

Table 5.4 - Parameters for periodicity

strong periodicity for their three-dimensional slant based body only in the low drag configuration.

5.6.3 Structure Observations

Observations of the structure of the large scale unsteadiness for the Ahmed and Rover 200 models are based largely on the animations produced by the unsteady reconstruction technique. This technique makes it possible to visualise the combined information contained in the time-averaged plots, the standard deviation magnitude plots, the standard deviation contribution plots and the cross-spectral phase plots.

The most universal unsteady structure observed consisted of the alternate strengthening and weakening of the two c-pillar vortices in a symmetric fashion. This alternating vortex strength is apparent both in terms of the velocity field and also in terms of total pressure loss at the vortex cores. As well as oscillating in strength the vortices also move up and down in the wake. This structure was observed for the Ahmed model and for the Rover 200 model with and without spoiler in both the Durham and MIRA tunnels. Reconstructions of this mode were presented as figures 3.5.33, 3.6.103, 3.6.104 and 3.6.155. The Strouhal number for this structure for the various geometries in the Durham tunnel was between 0.30 and 0.36 but was higher (0.51 to 0.58) in the MIRA tunnel. This frequency was also apparent on the wake centreline near the bottom of the rear bumper. This structure seems to come into being in the wake, it's characteristic frequency is not visible in unsteady pressure or shear stress measurements on the model surfaces. The spectrum for the Rover 200 model without spoiler in the Durham tunnel had a broad plateau connected to the main peak at S=0.30 and spanning to around S=0.47 (see figure 3.6.70). All of the evidence indicates that the entire plateau corresponds to the same symmetric unsteady structure.

Another structure was observed at lower Strouhal number (0.10 to 0.12). The Durham tunnel exhibited a high level of background unsteadiness at this frequency (as discussed in section 2.1.1.1) and this made observations difficult. In the case of

the Rover 200 model it is believed that the unsteady wake structure of the model "locked-in" to the tunnel unsteadiness however for the Ahmed model there was less evidence of any structure due to the model itself. The strongest argument for wake unsteadiness at this frequency produced by the model is the fact that the structure appears very clearly in the tests performed at the MIRA tunnel on the Rover 200 model with spoiler. In the MIRA tunnel this structure is anti-symmetric and involves the alternate strengthening of the two c-pillar vortices. This alternate strengthening of the vortices occurs both in terms of the velocity field and total pressure loss at the vortex cores. Because of the influence of background unsteadiness in the Durham tunnel, the analyses at this frequency indicated a confusing combination of symmetric and antisymmetric behaviour. The presence of an antisymmetric structure is important for CFD because it cannot be resolved by a simulation using a conventional symmetry plane on the centreline. This frequency was observed on the model surface in the Durham tunnel but this seems likely to be due more to background tunnel unsteadiness than anything else.

Higher frequencies were observed on the surface of the Rover 200 model, at S=0.57, S=1.14 and above. These frequencies seemed to be associated with the rear of the model. There was very little coherence across the backlight at S=1.14, indicating that unsteadiness at this frequency was not coupled between the sides of the model. This is not really surprising given that the length scale in a separated flow at such a high frequency can be expected to be much less than the width of the model.

5.7 A Proposed Unsteady Structure for Fastback Passenger Cars

The observations made in the wake of the Ahmed and Rover 200 models has already been discussed in sections 3.5, 3.6 and 5.6. We will now attempt to identify the reasons why the flow behaves the way it does and to speculate on further details of the flow based on these results and the experience of other researchers.

Any self-excited unsteadiness implies the presence of some sort of instability. The unsteadiness in the wake involves the alternate strengthening and weakening of the c-pillar vortices, either symmetrically or antisymmetrically. Increasing the strength of a vortex on one side of the wake will increase the centreline downwash and hence increase the strength of the vortex on the other side. It is not difficult to imagine feedback across the centreline in this way could lead to a symmetric mode instability. As we progress downstream in the wake the vortices move towards the groundplane and apart from each other. It is therefore not unreasonable to imagine that the coupling between the vortices on either side of the wake will be stronger closer to the model. If a perturbation causes the strengthening of one of the vortices at an axial location in the wake we could expect that this will strengthen the vortex progressively further upstream. As the strengthening moves upstream it exerts a greater influence on the vortex on the opposite side of the wake and this vortex then progressively strengthens moving downstream. The passing of the information upstream for communication across the wake and then downstream again to reach the original axial position provides a time delay which could account for the anti-symmetric structure.

As indicated previously, we see spectral peaks at higher frequencies on the model surface than in the wake. Interestingly, the different frequencies on the model surface and the frequency of the symmetric structure in the wake are related by factors of two. Duell and George (1992, 1999) found similar factors of two between dominant frequencies moving downstream in the shear layers behind a squareback model and attributed this to vortex pairing (as described by Winant and Brownland (1974)). The time-averaged flow structure in our case is much more complex so the details of their mechanism could not apply here, however. As discussed in section 1.4.2.5, Squire et al (1963) and Payne et al (1991) observed that the trailing vortices on a delta wing were formed by the combining of many smaller contributory vortices (see figure 1.4.15 from Squire et al (1963)). Gad-el-Hak and Blackwelder (1985) also observed that the trailing vortices on a delta wing were produced from

smaller contributory vortices but unlike Squire et al (1963) and Payne et al (1991) they found that the contributory vortices were generated in an unsteady fashion, being shed along the length of the wing leading edge. Gad-el-Hak and Blackwelder (1985) observed pairs of the contributory vortices to undergo repeated vortex pairing until they reached the size of the final trailing vortices. It seems reasonable to imagine a similar mechanism for fastback passenger cars, with the contributory vortices shed unsteadily either along the entire c-pillar (as in Gad-el-Hak and Blackwelder (1985)) or separately along the c-pillar (as in Squire et al (1963)) at around S=1.14. The first vortex pairing then results in the S=0.57 peak on the model surface and an additional pairing corresponds to the spectral peak near S=0.3 in the wake. Here we potentially see a coupling between this mechanism and a separate instability in the wake which is sensitive to frequencies in this region. Only once the contributory vortices have rolled into the main c-pillar vortices do we see coupling (and hence higher cross-spectral coherence) across the wake. The formation of the c-pillar vortices through unsteady contributory vortices would be in keeping with the observations of Wang et al (1996) in the wake of a Honda Accord; they saw apparently random packets of vorticity in instantaneous PIV images which, when averaged out, were equivalent to the c-pillar vortices. CFD simulations hoping to capture this unsteady flow would have to use a sufficiently small time-step and a fine enough grid density to resolve the contributory vortices and this could potentially explain the apparent inability of CFD simulations to capture larger unsteady structures in the wake of fastbacks.

Goh (1994) and Bearman (1997) observed a fairly conventional vortex shedding mechanism behind a Honda Accord model. The vortices were shed alternately from the bottom of the rear bumper and separated region at the top of the base/bottom of the backlight. Goh (1994) points out that the flow from under the car and the geometry in this region are fairly two-dimensional. We see high levels of periodicity behind the bottom of the rear bumper at the frequency corresponding to the symmetric wake structure. It is therefore proposed that this structure involves two-

dimensional transverse vortices being shed along the line of the bottom of the bumper opposed not by another transverse vortex but by the strengthening of the two c-pillar vortices.

Another possible unsteady mechanism in the vertical oscillation of the c-pillar vortex could be an unsteady vortex bounce phenomenon. Vortex bounce is used to describe the behaviour of aircraft trailing vortices at take-off and landing (Harvey and Perry (1971)). The wing tip trailing vortices are drawn towards the ground where they induce secondary vortices of opposite sign on the ground-plane. These secondary vortices move outboard of the main trailing vortices and then act to lift the trailing vortices away from the ground. So, as we move downstream along the trailing vortices from the aircraft wing, the vortices initially move close to the ground and then away from it, hence the term "vortex bounce". An unsteady version of this mechanism would "bounce" the c-pillar vortices off the ground plane at the bottom of their trajectory. Although the reconstructions indicate periodic regions of high loss on the groundplane, consistent with the existence of secondary vortices, no secondary vortices were actually observed so there is no real evidence for this mechanism.

5.8 Impacts of Unsteadiness

As discussed in section 1.4.1, aerodynamic unsteadiness can have both unsteady and time-averaged effects. The latter due to non-linearities in the behaviour of fluid flows.

5.8.1 Unsteady Forces on Vehicle

It is difficult to obtain a force balance system with sufficient frequency response for the measurements of unsteady forces on a wind tunnel model. Although some attempt was made to measure unsteady forces with a conventional strain-gauge balance through the use of a transfer-function correction approach this was ultimately abandoned (see section 2.2.6.1). Nouzawa et al (1992) do report unsteady drag measurements for their sharp-edged notchback geometry. Estimating from their

raw time-traces indicates a fluctuation of around 0.015 on C_D. Nguyen et al (1997) made unsteady side force measurements and found levels of fluctuating side force coefficient of around 0.01 for a sharp edged model and 0.06 for a real car shape at similar levels of turbulence to those used here. Based on pressure fluctuations on the surface of the Rover 200 model (section 3.6.2.1), rough estimates indicate that the maximum possible level of lift and drag fluctuation could be in the region of $C_D'=C_L'=0.015$ but the presence of multiple frequencies and the limited coherence at each frequency (see section 3.6.2.4) means that actual levels of lift and drag fluctuation can be expected to be below 0.010 on C_D or C_L.

5.8.2 Unsteady Forces on Following Vehicles

The wake traverse planes in the present work are all within just over one car length of the back of the model and so are too close to represent a realistic following distance at high speed on the road. However, the unsteadiness seems to die out quite slowly in the far wake (see figures 3.6.58 and 3.6.59), indicating that even at more realistic following distances it would not be inconceivable to see velocity fluctuations of up to 10% of the vehicle velocity, which is at least twice that expected under "normal" natural wind conditions (see Watkins and Saunders (1995)). The small area over which the unsteadiness would attain this level (perhaps 10% of the vehicle frontal area) will limit its importance, however.

5.8.3 Estimation of Time-Averaged Effects

As discussed in section 1.4.1, unsteadiness can be expected to affect the time-averaged flow-field. The ability of turbulence to delay separation or to promote reattachment of boundary layers is well known. The turbulence achieves this by mixing high velocity fluid from the outside of the boundary layer with the low velocity (or reversed) fluid near the wall. Large scale unsteadiness at the rear of bluff bodies acts in much the same way, it mixes high velocity fluid from the periphery of the wake into the lower energy regions towards the centre of the wake, thereby shortening the recirculation length. A shorter recirculation length is synonymous with higher turning of the high velocity fluid around the wake and this

in turn leads to lower pressures on the rear surfaces of the body. For a fastback passenger car this is likely to increase not only the drag but also the rear lift.

The effect of vortex shedding on the base pressure and drag of two-dimensional symmetric bodies can be quantified by placing a splitter plate on the centreline in the wake (see section 1.4.1). For more complicated unsteady structures and geometries where the unsteadiness is no longer based on fluid crossing a symmetry plane the use of a splitter plate is no longer appropriate. CFD could provide a method of assessing the impact of the unsteadiness since it is possible to suppress the unsteady structures numerically. However, attempts to predict unsteadiness for fastback passenger car shapes using CFD have not had much success so far.

One method of estimating the impact of the unsteadiness is to look at the Reynolds stresses acting to entrain fluid from outside the wake (ie: the shear stresses with components in the axial direction) (Hinze (1959) derives and discusses the Reynolds stress terms in the time-averaged Navier-Stokes equations). The level of stress generated due to the predominant unsteady structures behind the two-dimensional symmetric models and the Rover 200 model were calculated by first applying a narrow band digital filter to the fluctuating velocities and then calculating the Reynolds (shear) stresses from the remaining velocity fluctuations. Comparing the results for the two-dimensional symmetric models (figures 3.2.42 and 3.2.43) with those for the Rover 200 (figures 3.6.97 through 3.6.100) we see that the stresses due to the unsteady structure are higher by an order of magnitude for the two-dimensional models. For low aspect ratio (three-dimensional) bodies the relative area over which the stresses can act is larger (ie: the wake can close from all directions) however this effect is overwhelmed by the difference in the magnitude of the stresses. We know from splitter plate experiments that vortex shedding can be responsible for over 30% of the drag for two-dimensional bodies (Roshko 1954) so we could make a very crude estimate that one of the unsteady structures in the wake of the Rover 200 model could be responsible for 3% of its drag (ie: 10 drag counts).

5.8.4 Rear Lift Implications

Howell (1998) and Howell and Le Good (1999) discuss the apparent link between rear lift and adverse vehicle handling at high speed, based on track tests. Rear lift will tend to produce oversteer as velocity is increased however the actual force changes they observed seemed insufficient to produce a significant effect on handling through oversteer (decreasing understeer). This suggests that high rear lift may be an indicator for something else. As discussed in section 5.8.3, high rear lift is a symptom of unsteadiness at the rear of the vehicle. We have observed that the unsteady structures in the wake are only weakly periodic and are sensitive to external influences and so could be manifest as a high sensitivity to natural wind fluctuations. Therefore, high rear lift could effectively be an indicator for both increased self-excited unsteadiness and increased sensitivity to the natural wind.

6. CONCLUSIONS

6.1 Transfer-Function Correction Technique

The transfer function correction technique has been successfully applied in the investigation of large scale aerodynamic unsteadiness relevant to passenger cars. It has been used to measure time-accurate surface pressures and to obtain time-accurate pressure and velocity measurements using conventional five-hole probes. The application of the technique to five-hole probes was validated against a hot-wire anemometer.

For a typical static tapping connected to 1m of 1mm internal diameter tubing and a scanivalve, this technique could provide acceptable results up to a frequency of 1 or 2kHz. The maximum frequency response that could be achieved for a five-hole probe will be dependent on the geometry of the tubing between the probe head and the pressure transducer but will ultimately be limited to around 1.2kHz by hysteresis in the flow around the probe head (for typical test velocity and probe size).

6.2 Unsteady Reconstruction Method

A method has been developed which makes it possible to visualise periodic flow structures from quantitative measurements made sequentially in the wake or on the model surface. In the present work this method was applied to time-accurate five-hole probe measurements in the wake and time-accurate surface pressures measured by means of a scanivalve. The reconstruction method complements established spectral and cross-spectral methods by reducing the burden of interpreting results for complicated unsteady flow structures. Initially the technique was used to visualise nominally two-dimensional vortex shedding structures as a validation exercise, the technique was then used in the investigation of previously unobserved unsteady structures in the wake of fastback car shapes.

The technique is spectral based and uses a convolution in the complex frequency domain to effectively synchronise the measurements relative to the unsteady structure of interest through the use of a stationary reference signal (eg: a reference probe in the wake). A key element of this approach is the ability to synchronise not only the fundamental frequency but also its harmonics. Digital filtering operations make it possible to focus on the unsteady structure of interest and hence to investigate even weak periodic structures.

6.3 Increasing Transient Total Pressure

Transient total pressure has been observed to fluctuate (increase and decrease) due to inviscid unsteady effects. This was demonstrated to be possible analytically using the one-dimensional, inviscid, unsteady momentum equation. The phenomenon was predicted using CFD and verified experimentally.

6.4 Periodic Unsteadiness for Fastback Car Shapes

Unsteady flows for fastback passenger cars were found to be much less periodic than for two-dimensional vortex shedding cases. This was demonstrated by less sharp spectral peaks and reduced cross-spectral coherence. Strouhal numbers for the fastback shapes were not constant between tunnels and no obvious pattern (eg: Reynolds number dependence) could be observed. The unsteady structures were observed to lock-in to background tunnel unsteadiness and it is believed that this may be responsible for variations in Strouhal number, particularly between tunnels. The sensitivity of the unsteady flow to external influences could be expected to appear as sensitivity to natural wind fluctuations in an on-road situation.

6.5 Unsteady Forces due to Aerodynamic Unsteadiness

Pressure fluctuations were significantly lower on the model surface than in the wake. This results in limited unsteady forces. Although unsteady forces were not measured, estimates from the fluctuating surface pressures suggest that fluctuating forces will be less than 0.01 on C_D or C_L. This is in keeping with unsteady force measurements reported by other researchers.

Unsteady pressures of up to 10% of the dynamic head could be experienced by following vehicles but only over an area equivalent to approximately 10% of the vehicle frontal area.

6.6 Effects of Geometry on Unsteadiness

The effects of geometry were not straightforward.

For the two-dimensional symmetric models, increasing corner radius increased Strouhal number but decreased the level of periodicity and had little effect on the overall level of unsteadiness.

Unsteady flow structures, Strouhal numbers and levels of unsteadiness were very similar for the Rover 200 model with and without spoiler and for the Ahmed model (high drag state). The spoiler did reduce the level of surface pressure fluctuations but this appears to be a knock-on effect of the much larger impact which it had on the time-averaged flow since it did not reduce unsteadiness in the wake. In fact the level of periodicity was actually increased slightly by the addition of the spoiler to the Rover 200 model.

These results suggest that sharp corners (eg: on the Ahmed model or the Rover 200 spoiler) do not have a dominant effect on unsteadiness.

This also suggests that it is reasonable to use idealised models in the investigation of unsteady flow structures for fastback passenger cars.

6.7 Unsteady Flow Structures for Fastback Passenger Cars

Two principal structures were observed in the wake of the fastback shapes (the Ahmed model in the high drag state and the Rover 200 model with and without backlight spoiler).

In some cases, a structure was observed in the wake at around S=0.1 which involves the alternate strengthening of the two c-pillar vortices in an antisymmetric mode. This has the important implication that unsteady CFD simulations should be of the full car since the use of a centreline symmetry plane would suppress this unsteady structure.

At Strouhal numbers between 0.30 and 0.35 in the Durham tunnel (0.5-0.6 in the MIRA tunnel) an unsteady structure was observed in the wake consisting of the oscillation of the strength of the two c-pillar vortices in a symmetric mode. At the same time the location of the vortices oscillates in the vertical direction with the vortices spreading outwards as they approach the ground plane. It has been proposed that the fluctuating downwash of the c-pillar vortices is opposed by the shedding of nominally two-dimensional transverse vortices from the bottom of the rear bumper. The Strouhal number corresponding to these fluctuations in the wake was not observed on the model surface but fluctuations were observed at higher Strouhal numbers, related by factors of approximately 2 and 4. It has been proposed that small trailing vortices are shed from the c-pillar at S>1 and that these vortices undergo repeated pairing with each other in order to form the c-pillar vortices.

7. FURTHER WORK

7.1 Tow Tank Visualisation with Dye from the C-Pillars

Gad-el-Hak and Blackwelder (1985) observed the shedding of discrete vortices from the leading edge of a delta wing and subsequent vortex pairing by releasing dye from the surface of their wing in a tow tank. Since a similar unsteady mechanism has been proposed for the formation of the c-pillar vortices on fastbacks, it would be appropriate to perform a similar experiment with a fastback passenger car model.

7.2 Investigation Inside Separated Regions

Although the five-hole probes used were designed to operate over a wide incidence range and although local nulling of the probe with respect to the time-averaged flow was employed, very little work was performed within the separated region behind the car.

Investigations in this region could be accomplished using a probe designed for the purpose. The probe would need to be of small size in order to avoid disturbing the flow in this sensitive region. A probe without sting would make it possible to rotate the probe for local nulling more easily in order to accommodate reversed flows; the facility to null the probe in the second rotational axis might also be a benefit. Alternatively, a probe with rearward facing holes could eliminate the need for local nulling.

An arguably better way to look at the separated regions would be to use PIV or LDA, since the intrusivity of these methods is minimal and they are better suited to low velocity measurements in separated regions.

7.3 Validation against other Methods of Measurement

Many of the techniques used in this work are novel, so validation using other methods would be appropriate wherever possible. In some cases the techniques used

are effectively the only means of making the measurements, for example the measurement of unsteady pressures in the wake, in these cases a comparison of some other quantity (eg: fluctuating velocity) with that determined from another technique would nevertheless provide a useful validation.

7.4 Additional Unsteady Data on Wake Centreline for Fastbacks

Although time-accurate hot-wire measurements were made on the centreline in the wake of the Ahmed and Rover 200 models, time-accurate five-hole probe measurements were only made for the cross-wake traverse planes. Time-accurate five-hole probe measurements on the centreline combined with a stationary reference probe would provide a valuable additional insight. Reconstructions on the centreline could confirm the shedding of transverse vortices from the bottom of the rear bumper. The usefulness of five-hole probe measurements on the centreline would be enhanced by the use of probe nulling within the recirculation region as discussed above.

7.5 Measurement of Unsteady Forces

The measurement of unsteady forces is not straightforward, however this is potentially the measurement of greatest practical importance. This could be accomplished either by making direct force measurements with a high response balance or by integrating unsteady pressures from a large number of tappings covering the model surface. The pressures could be measured simultaneously using an electronically scanned pressure transducer system or measured sequentially using a scanivalve, after which the data could be processed using the unsteady reconstruction method before instantaneous pressure distributions could be integrated.

7.6 Additional Fastback Geometries

The investigation of the flow around fastback car shapes in this study has essentially adopted a case study approach, performing detailed investigations on a small

number of geometries. This approach was chosen in order to focus sufficient experimental effort on each geometry to determine the unsteady flow field. Testing multiple geometries made it possible to obtain some perspective on the general applicability of the observations made. This perspective could be improved by making measurements for a larger number of fastback car shapes. The results from the present work seem to indicate that geometric details such as sharp c-pillar corners or the fitting of a spoiler at the top of the backlight have a surprisingly limited effect on the unsteadiness, the best way to confirm this would be with parametric models, for instance allowing c-pillar corner radius to be modified.

7.7 Use of Additional Scales and Additional Tunnels

One of the surprising observations made in this work was the absence of a linear relationship between model scale and period of unsteadiness. This could be due to the effect of different tunnels on the unsteadiness since different model scales were tested in different wind tunnels. The testing of multiple model scales within a single tunnel would therefore be appropriate. Testing in additional tunnels would make it possible to obtain a more accurate assessment of the impact of the tunnel used on the unsteadiness. Perhaps the best test to perform, however, would be a track test, including the measurement of unsteady surface pressures and ideally some unsteady wake measurements. Care would have to be taken to monitor natural wind fluctuations in order to distinguish between high sensitivity to external influences and self-excited unsteadiness.

7.8 Remove Subjectivity in Unsteady Reconstruction Method

The unsteady reconstruction method currently requires the user to specify the width of spectral bands to attribute to the unsteady structure of interest. This is done by inspecting the width of the spectral peaks and by performing test reconstructions and inspecting raw and reconstructed time-traces. As well as allowing subjectivity to have a significant effect on the results, this approach is time consuming. An automatic approach could be implemented which assesses the level of background

unsteadiness around the frequency of interest and therefore determines the additional unsteadiness due to the peak.

7.9 Quantification of Unsteady Effects on Time-Averaged Forces

Two-dimensional symmetric models make it possible to asses the impact of vortex shedding on time-averaged pressures and forces by comparing measurements with and without a splitter plate on the wake centreline. If detailed unsteady wake measurements were made with and without a splitter plate for a number of two-dimensional symmetric models it might be possible to relate the impact of the unsteadiness on time-averaged effects on the model (eg: surface pressures) through the Reynolds stresses in the wake. By assessing the magnitude of the Reynolds stresses in the wake of a three-dimensional body we could then make an estimate of the impact of the unsteadiness on the time-averaged surface pressures (and hence forces).

7.10 Accurate CFD Simulation of Unsteady Flow for Fastbacks

Several of the questions raised above could be answered if a reliable CFD simulation of the unsteady flow around fastback shapes were available. Such a simulation would provide the best visualisation of the unsteady flow structure, it would provide details of the unsteady forces and could also make it possible to assess the impact of the unsteadiness on the time-averaged forces (by numerically suppressing the unsteadiness). So far simulations of the unsteady flow around fastback passenger cars have not been achieved, however. If the unsteady structure proposed in this work, including the shedding of vortices from the c-pillar at high frequency, were correct then the simulation would have to employ a small time step and fine grid spacing around the c-pillar. The time-step in particular would have to be smaller than those employed to date. This would make the simulation computationally expensive but not impossible with current equipment.

REFERENCES

Abernathy, FH, Kronauer, RE (1961) The Formation of the Vortex Street, Journal of Fluid Mechanics v13 pp1-20, 1962.

Ahmed, SR (1998) Computational Fluid Dynamics, in Hucho, W-H, ed. Aerodynamics of Road Vehicles, Fourth Edition, Society of Automotive Engineers, Warrendale Pa, 1998.

Ahmed, SR, Ramm, G, Faltin, G (1984) Some Salient Features of the Time-Averaged Ground Vehicle Wake, SAE Paper 840300.

Axelsson, N, Ramnefors, M, Gustafsson, R (1998) Accuracy in Computational Aerodynamics Part 1: Stagnation Pressure, SAE Paper 980037 in Developments in Vehicle Aerodynamics (SAE SP-1318), 1998.

Axon, L, Garry, K, Howell, J (1999) The Influence of Ground Condition on the Flow Around a Wheel Located Within a Wheelhouse Cavity, SAE Paper 1999-01-0806 in Vehicle Aerodynamics and Wind Noise (SP-1441).

Bandyopadhyay, PR, Stead, DJ, Ash, RL (1991) Organised Nature of a Turbulent Trailing Vortex, AIAA Journal vol 29 no 10 pp1627-1633, 1991.

Basu, RI (1986) Aerodynamic Forces on Structures of Circular Cross-Section, Part 2, The Influence of Turbulence and Three-Dimensional Effects, Journal of Wind Engineering and Industrial Aerodynamics 24.

Bearman, PW (1984a) Vortex Shedding from Oscillating Bluff Bodies, Annual Review of Fluid Mechanics 1984.

Bearman, PW (1984b) Some Observations on Road Vehicle Wakes, SAE Paper 840301, 1984.

Bearman, PW (1997) Near Wake Flows Behind Two-Dimensional and Three-Dimensional Bluff Bodies, Journal of Wind Engineering 69-71 pp33-54, 1997.

Bearman, PW, Harvey, JK, Stewart, JN (1997) Two and Three Component Velocity Measurements in a Wind Tunnel using PIV, RAES Proceedings, Wind Tunnels and Wind Tunnel Test Techniques. 14-16 April 1997, Cambridge, UK.

Bellhouse, BJ, Schultz, DL (1966) Determination of Mean and Dynamic Skin Friction, Separation and Transition in Low Speed Flow with a Thin-Film Heated Element, Journal of Fluid Mechanics, vol. 24, part 2, pp379-400, 1966.

Bendat, JS, Piersol, AG (1980) Engineering applications of correlation and spectral analysis, ISBN 0471058874 m, Wiley, New York, 1980.

Berger, E, Scholz, D, Schumm, M (1990) Coherent Vortex Structures in the Wake of a Sphere and Circular Disk at Rest and Under Forced Vibrations, Journal of Fluids and Structures 4 pp231-257, 1990.

Brown, GL, Roshko, A (1974) On Density Effects and Large Structures in Turbulent Mixing Layers, Journal of Fluid Mechanics vol 64, 1974.

Brown, MA, Baxendale, AJ, Hickman, D (1998) Recent Enhancements of the MIRA Model Wind-Tunnel, Second MIRA International Conference on Vehicle Aerodynamics, Coventry, 20-21 October, 1998.

Bruun, HH (1995) Hot-Wire Anemometry, Principles and Signal Analysis, Oxford University Press, 1995.

Bruun, HH, Khan, MA, Al-Kayiem, HH, Fardad, AA (1988) Velocity Calibration Relationships for hot-wire anemometry, Journal of Phys. E.: Sci. Instr., 21, 225-232, 1988.

Bruun, HH, Nabhani, N, Al-Kayiem, AA, Fardad, AA, Khan, MA, Hogarth, E (1990) Calibration and analysis of X hot-wire probe signals, Meas. Sci. Technol. 1, 782-785, 1990.

Bruun HH, Tropea, C (1980) Calibration of normal, inclined and X-array hot-wire probes, Technical Report SFB80/M/170 Sonderforschungs-bereich 80, Universität Karlsruhe, 1980.

Bruun HH, Tropea, C (1985) The calibration of inclined hot-wire probes, Journal of Phys. E. Sci. Instr. 18 405-413, 1985.

Carmody, T (1964) Establishment of the Wake Behind a Disk, Journal of Basic Engineering vol 86 pp869-882.

Carr GW (1997) Developments in Wind Tunnel Testing of Road Vehicles, RAES Proceedings, Wind Tunnels and Wind Tunnel Test Techniques. 14-16 April 1997, Cambridge, UK.

Carr, GW, Eckert, W (1994) A Further Evaluation of the Ground-Plane Suction Method for Ground Simulation in Automotive Wind Tunnels, SAE Paper 940418 in Analysis of Vehicle Aerodynamics (SP-1036)

Casey, M (1996) CFD for Fluid Machinery, IMechE Presentation, London, 1996.

Cherrett, MA, Bryce, JD, Hodson, HP (1992) 3D Pneumatic and 2D Dynamic Probes: Their Development and Subsequent Use in a Transonic Fan, 11th Symposium on Measurement Techniques for Transonic and Supersonic Flows in Cascades and Turbomachines, Munich 14-15 September 1992.

Cogotti, A (1997) Aeroacoustics Development at Pininfarina, SAE Paper 970402 in SP-1232, presented at the SAE International Congress and Exposition, Detroit, 1997.

Cometta, C (1957) An Investigation of the Unsteady Flow Pattern in the Wake of Cylinders and Spheres Using a Hot-Wire Probe, Brown University Div. Engineering Report WT 21 October 1957.

Computational Dynamics (1999a) Methodology, Star-CD Version 3.10A, Computational Dynamics Ltd. 1999.

Computational Dynamics (1999b) User Guide, Star-CD Version 3.10A, Computational Dynamics Ltd. 1999.

Cook, SCP (1989) The Development of a High Response Aerodynamic Wedge Probe and use on a High-Speed Research Compressor, Proceedings of the Ninth International Symposium on Air Breathing Engines, Athens. Vol 1 pp1113-1125, 1989.

Crossland, SC, Sims-Williams, DB, Dominy, RG (2000) The Reconstruction of Bluff-Body Unsteady Flow Fields, 9th International Symposium on Flow Visualization, Edinburgh, August 22-25, 2000

Davis, JP (1982) Wind Tunnel Investigation of Road Vehicle Wakes, PhD Theses, Imperial College London, Department of Aeronautics, 1982.

Dobbeling, K, Lenze, B, Leuckel, W (1990) Computer-Aided Calibration and Measurements with a Quadruple Hot-Wire Probe, Experiments in Fluids 9, 1990.

Docton, MKR (1997) The Simulation of Transient Cross Winds on Passenger Vehicles, PhD Thesis, University of Durham.

Dominy, RG (1995a) Flow Unsteadiness over Passenger Vehicle Rear Surfaces, Autotech 95 paper C498/36/181

Dominy, RG (1995b) Private Communication

Dominy, RG, Hodson, HP (1993) An Investigation of Factors Influencing the Calibration of 5-Hole Probes for 3-D Flow Measurements, ASME Journal of Turbomachinery 115, 513-518, 1993.

Dominy, RG, Ryan, A (1999) An Improved Wind Tunnel Configuration for the Investigation of Aerodynamic Cross Wind Gust Response, SAE Paper 1999-01-0808 in Vehicle Aerodynamics and Wind Noise, SP-1441.

Duell, EG, George, AR (1992) Unsteady Near Wake Flows of Ground Vehicle Bodies, AIAA Paper 92-264-CP, AIAA 10th Applied Aerodynamics Conference, June 1992.

Duell, EG, George, AR (1999) Experimental Study of a Ground Vehicle Body Unsteady Near Wake, SAE Paper 1999-01-0814 in Vehicle Aerodynamics and Wind Noise (SP –1441).

Emerson, DR (1996) Implementing Codes for Thermofluid Simulation on MPP Systems, IMechE Specialist Meeting on Parallel Computing for Flow Simulation, 26 September 1996, Rugby.

Emmelmann, H-J, Hucho, W-H (1998) Performance of Light Cars and Trucks in Hucho, W-H, ed. Aerodynamics of Road Vehicles, Fourth Edition, Society of Automotive Engineers, Warrendale Pa, 1998.

Fackrell, JE (1974) The Aerodynamic Characteristics of an Isolated Wheel Rotating in Contact with the Ground, PhD Thesis, Imperial College, University of London, 1974.

Fago, B, Lindner, H, Marenholtz, O (1991) The Effect of Ground Simulation on the Flow Round Vehicles in Wind Tunnel Testing, Journal of Wind Engineering and Industrial Aerodynamics 38, 1991, 47-57

Fuchs, H.V. Mercker, E, Michel, U (1979) Large Scale Coherent Structures in the Wake of Axisymmetric Bodies, Journal of Fluid Mechanics 93, pp189-211.

Gad-el-Hak, M, Blackwelder, RF (1985) The Discrete Vortices from a Delta Wing, AIAA Journal, vol 23, no 6, pp961-962, 1985.

Gad-el-Hak, M, Blackwelder, RF (1987) Control of the Discrete Vortices from a Delta Wing, AIAA Journal, vol 25, no 8, pp 1042-1049, 1987.

Garry KP, Cooper KR, Fediw A, Wallis SB, Wilsden DJ (1994) The Effect on Aerodynamic Drag of the Longitudinal Position of a Road Vehicle Model in a Wind Tunnel Section, SAE Paper 940414 in Vehicle Aerodynamics, 1994.

Gaylard, AP, Bickerton, JE, Howell, JP (1998) Current Issues in the Use of CFD to Predict Aerodynamic Characteristics of Car Shapes, Second MIRA International Conference on Vehicle Aerodynamics, Coventry, 20-21 October, 1998.

Gerrard, JH (1966) The Mechanics of the Formation Region of Vortices Behind Bluff Bodies, Journal of Fluid Mechanics Vol 25 pp401-413, 1966.

Goh, EK (1994) An Experimental Study into the Time-Dependent Characteristics of a Road Vehicle Wake Flow, PhD Thesis, Department of Aeronautics, Imperial College, London, 1994.

Gossweiler CR, Kupferschmied P, Gyarmathy G (1995) On Fast Response Probes: Part 1 - Technology, Calibration and Application to Turbomachinery, Journal of Turbomachinery Vol 117 October 1995.

Griffin, OM (1981) Universal Similarity in the Wakes of Stationary and Vibrating Bluff Structures, ASME Journal of Fluids Engineering V 103 March 1981.

Hall, MG (1972) Vortex Breakdown, Annual Review of Fluid Mechanics vol 4, 1972.

Hamidy, E (1991) The Structure of Wakes of 3-D Bluff Bodies in Proximity to the Ground, PhD Theses, Department of Aeronautics, Imperial College, London, 1990.

Harvey, JK (1962) Some Observation of the Vortex Breakdown Phenomenon, Journal of Fluid Mechanics vol 14 part 4, 1962.

Harvey, JK, Perry, FJ (1971) Flow Field Produced by Trailing Vortex in the Vicinity of the Ground, AIAA Journal vol 9 pp1659-1660, 1971.

Hinze, JO (1959) Turbulence. An introduction to its mechanism and theory, McGraw-Hill, New-York, 1959.

He, L (1996a) Modelling Issues for Computation of Unsteady Turbomachinery Flows, Von Karman Institute for Fluid Dynamics, Lecture Series 1996-05, Unsteady Flows in Turbomachines, 1996.

He, L (1996b) Time-Marching Calculations of Unsteady Flows, Blade Row Interaction and Flutter, Von Karman Institute for Fluid Dynamics, Lecture Series 1996-05, Unsteady Flows in Turbomachines, 1996.

Hooper, JD, Musgrove, AR (1991) Multi-Hole Pressure Probes for the Determination of the Total Velocity Vector in Turbulent Single-Phase Flow, 4th International Symposium Transport Phenomena in Heat and Mass Transfer, The University of New South Wales, Sydney, Australia, ed. JA Reizes, July, 1991.

Howell, JP (1998) The Influence of Aerodynamic Lift on Lane Change Manoeuvrability, 2nd MIRA International Conference on Vehicle Aerodynamics, Coventry, 1998.

Howell, JP, Goodwin, JC (1995) The Influence of Ground Simulation on the Aerodynamics of Simple Car Like Shapes with Under Body Roughness, Autotech C498/36/158, 1995.

Howell, JP, Hickman, D (1997) The Influence of Ground Simulation on the Aerodynamics of a Simple Car Model, SAE Paper 970134.

Howell, JP, Le Good, G (1999) The Influence of Aerodynamic Lift on High Speed Stability, SAE Paper 1999-01-0651 in SP-1441

Hucho, W-H (1998a) Introduction to Automobile Aerodynamics, in Hucho, W-H, ed. Aerodynamics of Road Vehicles, Fourth Edition, Society of Automotive Engineers, Warrendale Pa, 1998.

Hucho, W-H (1998b) Wind Tunnels, in Hucho, W-H, ed. Aerodynamics of Road Vehicles, Fourth Edition, Society of Automotive Engineers, Warrendale Pa, 1998.

Hucho, WH, Janssen, JL, Emmelmann, H-J (1976) The Optimisation of Body Details - A Method for Reducing the Aerodynamic Drag of Road Vehicles, SAE Paper 760185 Detroit.

Hucho, W, Sovran, G (1993) Aerodynamics of Road Vehicles, Annual Review of Fluid Mechanics vol 25 pp485-537, 1999.

Irwin, HPAH, Cooper, KR, Girard, R (1979) Correction of Distortion Effects Caused by Tubing Systems in Measurements of Fluctuating Pressures, Journal of Industrial Aerodynamics 5, 1979.

Ishihara, Y, Takagi, M (1999) Unsteady Pressure Analysis of the Wake Flow Behind a Passenger Car Model, 1999.

Jeffrey, D, Zhang, X, Hurst, DW (1998) Some Aspects of the Time-Averaged and Unsteady Aerodynamics of Gurney Flaps, Second MIRA International Conference on Vehicle Aerodynamics, Coventry, 20-21 October, 1998.

Jørgensen, FE (1971) Directional sensitivity of wire and fibre-film probes, DISA Info. No 11, 31-37, 1971.

King, LV (1914) On the convection of heat from small cylinders in a stream of fluid: Determination of the convection of constants of small platinum wires with applications to hot-wire anemometry, Phil. Transactions of the Royal Society, A214, 373-432, 1914.

Klein, RH, Jex, HR (1980) Development and Calibration of an Aerodynamic Disturbance Test Facility, SAE Paper 800143

Kohl, W (1998) Upgrade of Aerodynamic Windtunnel, Ford-Werke AG, for Aeroacoustic Measurement, Second MIRA International Conference on Vehicle Aerodynamics, Coventry, 20-21 October, 1998.

Koike, T, Hase, N, Koide, E, Murakami, Y, Izawa, S, Ohhira, T, Nagasaka, O, Tanaka, Y, Suzuki, T (1999) Development of a Rear Spoiler with Built-in Antenna, SAE Paper 1999-01-0807 in Vehicle Aerodynamics and Wind Noise (SP-1441)

Kuenstner R, Deutenbach K-R, Vagt J-D (1992) Measurement of Reference Dynamic Pressure in Open-Jet Automotive Wind Tunnels, Vehicle Aerodynamics: Wake Flows, Computational Fluid Dynamics, and Aerodynamic Testing SAE SP-908, 1992.

Lambourne, NC, Bryer, DW (1961) The Bursting of Leading Edge Vortices - Some Observations and Discussion of the Phenomenon, Aeronautical Research Council R&M 3282, 1961.

Macklin, AR, Garry, KP, Howell, JP (1996) Comparing static and dynamic testing techniques for the crosswind sensitivity of road vehicles, SAE Paper 960674

McCroskey, WJ (1977) Some Current Research in Fluid Dynamics, ASME Journal of Fluids Engineering, Vol 99, 1977, pp8-39; ASME Freeman Scholar Lecture.

Mercker, E, Wickern, G, Weidemann, J (1997) Contemplation of Nozzle Blockage in Open Jet Wind-Tunnels in View of Different 'Q' Determination Techniques, SAE Paper 970136.

Mercker, E, Wiedemann, J (1990) Comparison of Different Ground Simulation Techniques for use in Automotive Wind Tunnels, SAE Paper 900321.

Milne-Thompson, LM (1948) Theoretical Aerodynamics pp195-179, Dover Publications Inc, New York, 1948.

Morel, T (1980) The Effect of Base Slant on the Flow Pattern and Drag of Three-Dimensional Bodies with Blunt End, Aeronautical Quarterly, vol 31, 1980.

Morkovin, MV (1964) Flow Around Circular Cylinder - A Kaleidoscope of Challenging Fluid Phenomena, ASME Symposium on Fully Separated Flows 1964 p102

Müller, UR (1983) A Hot-Wire Method for High-Intensity Turbulent Flows, ICIASF '83 Record. Proc. Int. Congr. Instrum. in Aerospace Simulation Facilities, ISL, St Louis, France pp298-304, 1983.

Nguyen, TM, Saunders, JW, Watkins, S (1997) The Sideways Dynamic Force on Passenger Cars in Turbulent Winds, SAE Paper 970405 in SAE SP-1232

Nouzawa, T, Haruna, S, Hiasa, K, Nakamura, T, Sato, H (1990) Analysis of Wake Pattern for Reducing Aerodynamic Drag of Notchback Model, SAE Paper 900318, 1990.

Nouzawa, T, Hiasa, K, Nakamura, T, Kawamoto, A, Sato, H (1992) Unsteady Analysis of the Aerodynamic Drag of Notchback Model with Critical Afterbody Geometry, SAE Paper 920202 in Vehicle Aerodynamics: Wake Flows, Computational Fluid Dynamics and Aerodynamic Testing (SP-908).

Payne, FM, Ng, TT, Nelson, RC (1991) Visualisation of Leading Edge Vortices on a Series of Flat Plate Delta Wings, NASA Contractor Report 4320, 1991.

Pearce, W, Baker, CJ (1998) Measurement of the Unsteady Crosswind Forces and Moments on Ground Vehicles, Second MIRA International Conference on Vehicle Aerodynamics, Coventry, 20-21 October, 1998.

Peric, C, Watkins, S, Lindqvist, E, Saunders, J (1997) Effects of On-Road Turbulence on Automotive Wind Noise: Comparing Wind-Tunnel and On-Road Tests, SAE Paper 970406.

Perry, AE, Watmuff, JH (1981) The Phase-Averaged Large-Scale Structures in Three-Dimensional Turbulent Wakes, Journal of Fluid Mechanics, 103, 33-51, 1981.

Perzon, S, Janson, J, Höglin, L (1999) On Comparisons Between CFD Methods and Wind Tunnel Tests on a Bluff Body, SAE Paper 1999-01-0805 in Vehicle Aerodynamics and Wind Noise (SP-1441).

Press, WH, Teukolsky, SA, Vetterling, WT, Flannery, BP (1992) Numerical Recipes in Fortran second edition, Cambridge University Press, 1992.

Reichert, JK, Azad, RS (1977) Wall Shear Stress Measurement with a Hot Film in Variable Temperature Flow, Rev. Sci. Instr. 48 pp341-345, 1977.

Roberts, JB (1973) Coherence Measurements in an Axisymmetric Wake, AIAA Journal 11, 1569-1571.

Roshko, A (1954) On the drag and shedding frequency of two-dimensional bluff bodies, NACA TN no 3169, July 1954.

Roshko, A (1993) Perspectives on Bluff Body Aerodynamics, Journal of Wing Engineering and Industrial Aerodynamics 49 pp79-100.

Ryan, A (2000) The Simulation of Transient Cross-Wind Gusts and their Aerodynamic Influence on Passenger Cars, PhD Thesis, University of Durham, 2001.

Ryan, A, Dominy, RG (1998) The Aerodynamic Forces Induced on a Passenger Vehicle in Response to a Transient Cross-Wind Gust at a Relative Incidence of 30°, SAE Paper 980392 in Developments in Vehicle Aerodynamics (SAE SP-1318).

Sandham, ND, Howard, RJA, Clark, DG (1996) Use of Direct Numerical Simulation for the Study of Near-Wall Turbulence, IMechE Specialist Meeting on Parallel Computing for Flow Simulation, 26 September 1996, Rugby.

Sedney, R (1979) A Flow Model for the Effect of a Slanted Base on Drag, Aerodynamics of Transportation, ASME-CSME Conference, Niagara Falls June 18-20, 1979.

Sims-Williams, DB (1994) The Initial Development of a Pressure Probe for Active Measurement of Unsteady Flows, Project Report, Part II Engineering Tripos, Cambridge University, 1994.

Sims-Williams, DB, Dominy, RG (1998a) The Validation and Application of a 5 Hole Pressure Probe with Tubing Transfer Correction for Time-Accurate Measurements in Unsteady Flows, Second MIRA International Conference on Vehicle Aerodynamics, Coventry, 20-21 October, 1998.

Sims-Williams, DB, Dominy, RG (1998b) Experimental Investigation into Unsteadiness and Instability in Passenger Car Aerodynamics, SAE Paper 980391 in Developments in Vehicle Aerodynamics (SAE SP-1318), 1998.

Sims-Williams, DB, Dominy, RG (1999) The Reconstruction of Periodic Pressure Fields from Point Measurements, SAE Paper 1999-01-0809 in Vehicle Aerodynamics and Wind Noise (SP-1441)

Sims-Williams, DB, White, AJ, Dominy, RG (1999) Gurney Flap Aerodynamic Unsteadiness, Sports Engineering, Motorsport Edition, 1999.

Singh, G, Walker, PJ, Haller, BR (1995) Development of Three-Dimensional Stage Viscous Time Marching Method for Optimisation of Short Height Stages, 1st European Conference on Turbomachinery-Fluid Dynamic and Thermodynamic Aspects, Erlangen, 1-3 March 1995.

Sovran, G (1983) Tractive Energy Based Formulae for the impact of Aerodynamics over the EPA driving Schedules, SAE Paper 830304

Squire, LC, Jones, JG, Stanbrook, A (1963) An Experimental Investigation of the Characteristics of some Plane and Cambered 65° Delta Wings at Mach Numbers 0.7 to 2.0, Aeronautical Research Council R&M No 3305, London, 1963.

Taneda, S (1978) Visual Observation of a Flow Past a Sphere at Re between 10000 and 1000000, Journal of Fluid Mechanics vol 85 part 1, 1978.

Tromp, JC, Beran, PS (1996) Temporal Evolution of Three-Dimensional Vortex Breakdown from Steady Axisymmetric Solutions, AIAA Journal Vol 34 No 3 March 1996.

Tsuboi, K, Shirayama, S, Oana, M, Kunio, K (1988) Computational Study of the Effect of Base Slant, Proceedings of the 2nd International Conference on Super Computing in the Automotive Industry

Tudeman, H (1975) On the Propagation of Sound Waves in Cylindrical Tubes, Journal of Sound and Vibration Vol 39 No 1, 1975.

Uchida, K, Okumura, K, Kuriyama, T (1997) Aerodynamic Simulations by Using Discontinuous Interface Grid and Solution Adaptive Grid Method, SAE Paper 970141.

Ukita, T, China, H, Kanie, K (1997) Analysis of Vehicle Wind Throb using CFD and Flow Visualisation, SAE Paper 970407 in SAE SP-1232

Wang, Q, Bearman, P, Harvey, J (1996) A Study of Instantaneous Flow Structure Behind a Car by Particle Image Velocimetry, Optical Methods and Data Processing in Heat and Fluid Flow, IMechE, London, 1996.

Wark, CE, Nagib, HM, Jennings, MJ (1990) A Rotating Hot-Wire Technique for Spatial Sampling of Disturbed and Manipulated Duct Flows, Experiments in Fluids 9, 1990.

Watkins, S, Oswald, G (1999) The Flow Field of Automobile Add-Ons - With Particular Reference to the Vibration of External Mirrors, Journal of Wind Engineering and Industrial Aerodynamics 83 pp541-554, 1999.

Watkins, S, Saunders, J (1995) Turbulence Experienced by Road Vehicles under Normal Driving Conditions, SAE Paper 950997, 1995.

Watmuff, JH, Perry, AE, Chong, MS (1983) A Flying Hot-Wire System, Experiments in Fluids 1, 63-71, 1983.

Wickern, G, Zwicker, K, Pfadenhauer, M (1997) Rotating Wheels - Their Impact on Wind Tunnel Test Techniques and on Vehicle Drag Results, SAE Paper 970133.

Winant CD, Browand, FK (1974) Vortex Pairing: The Mechanism of Turbulent Mixing Layer Growth at Moderate Reynolds Number, Journal of Fluid Mechanics Vol 63, 1974.

Xia, XJ, Bearman, PW (1983) An Experimental Investigation of the Wake of an Axisymmetric Body with a Slanted Base, Aeronautical Quarterly vol 34 pp24-45, 1983.

Yamane, K, Hase, N, Fujita, Sadao, Isomura, R, Takeda, I, Sumitani, K, Murayama, T (1997) Concurrent CFD Analysis for Development of Rear Spoiler for Hatchback Vehicles, SAE Paper 970410.

Self-Excited Aerodynamic Unsteadiness Associated with Passenger Cars

Volume 2 of 2

David B. Sims-Williams

A Thesis submitted for the degree of Doctor of Philosophy

University of Durham

School of Engineering

2001

CONTENTS

VOLUME 2

FIGURES FOR CHAPTER 1 - INTRODUCTION

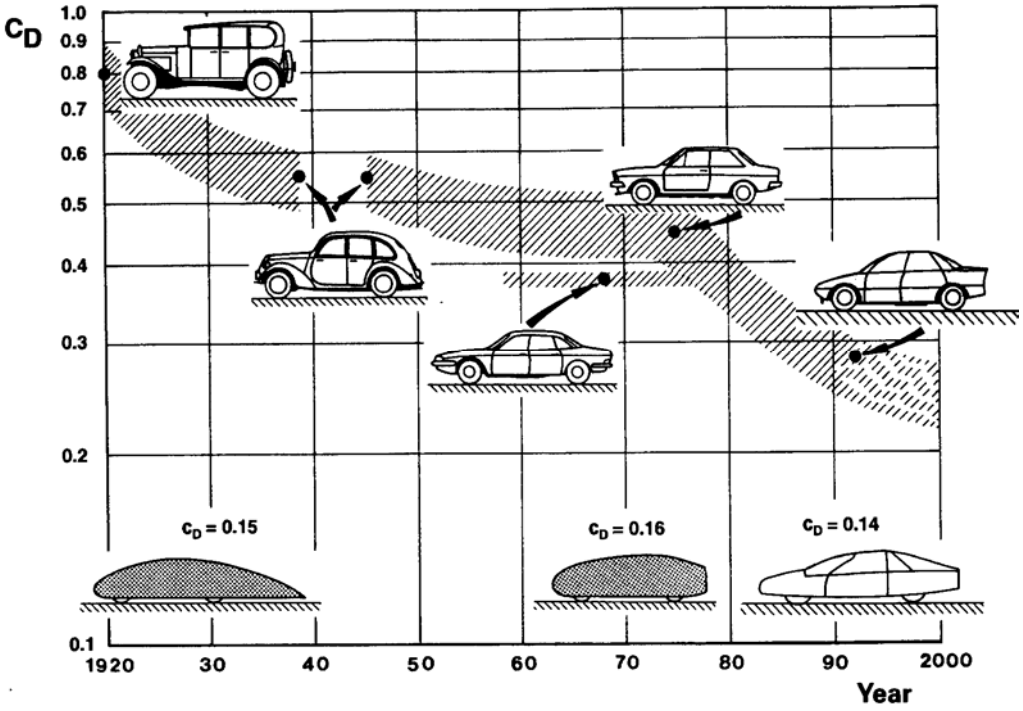

Figure 1.2.1 - History of C_D of European passenger cars (from Hucho (1998a))

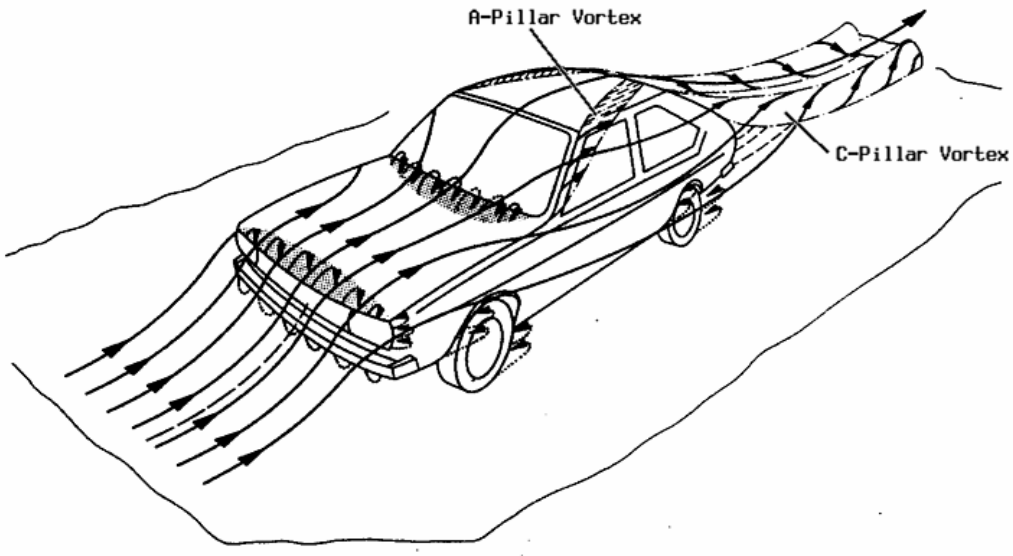

Figure 1.2.2 - Flow structure for a typical passenger car (from Hucho (1998a))

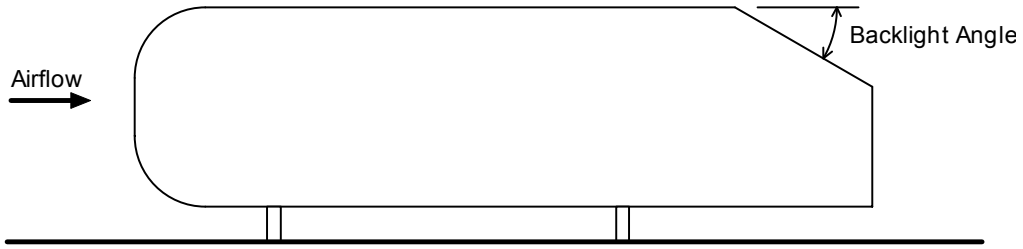

Figure 1.2.3 - Definition of backlight angle

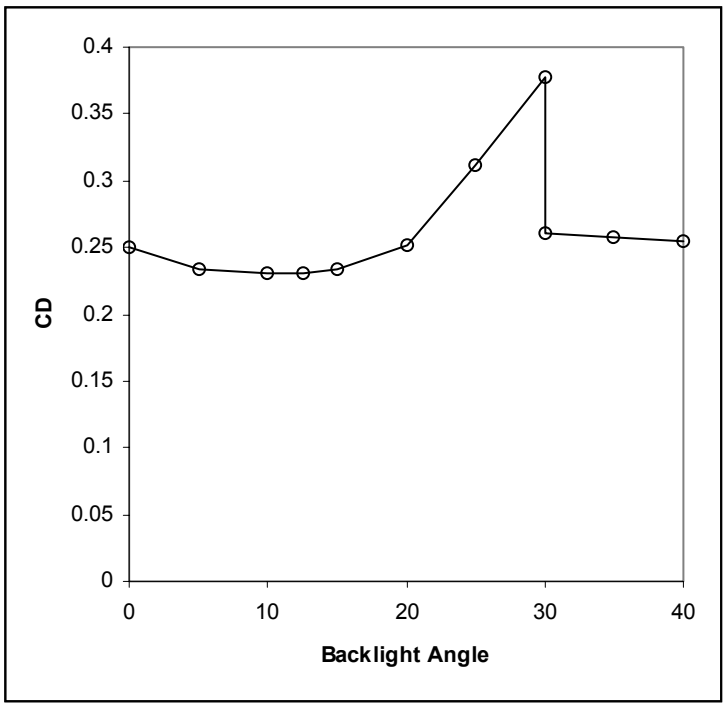

Figure 1.2.4 - The effect of backlight angle on C_D (data from Ahmed et al (1984))

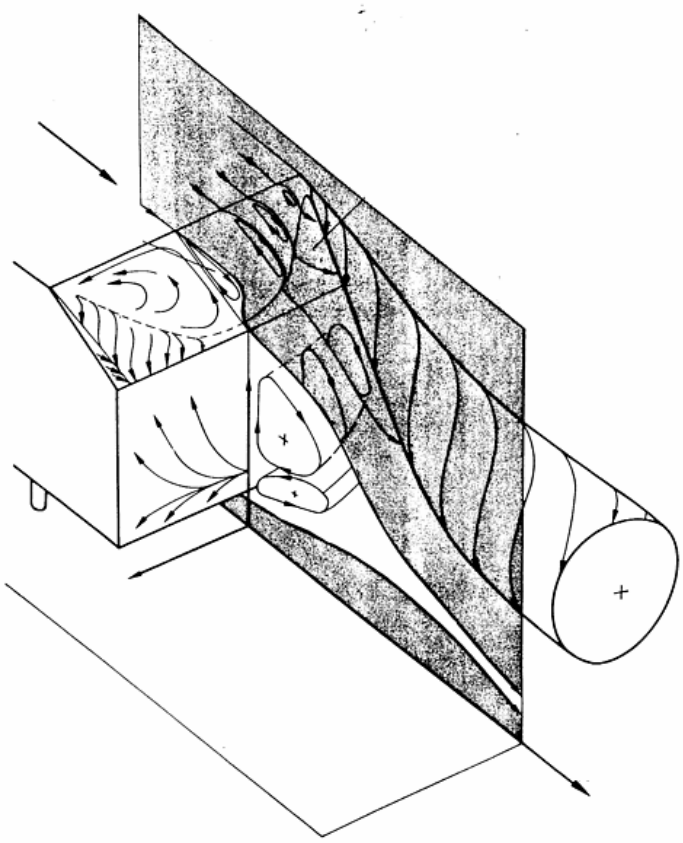

Figure 1.2.5 - Schematic representation of high drag flow (30° backlight) (from Ahmed et al (1984))

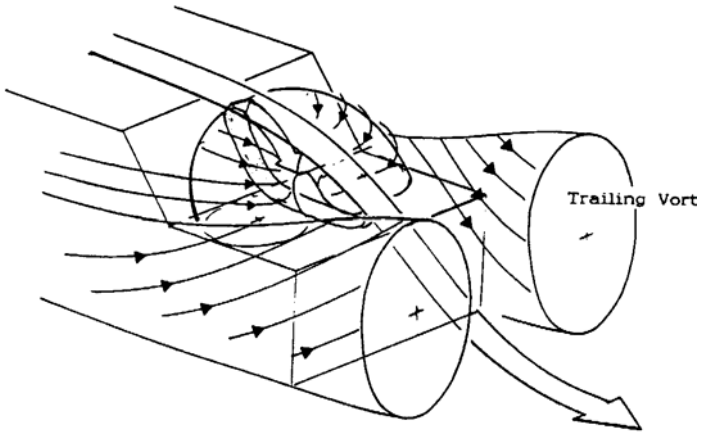

Figure 1.2.6 - High drag flow behind notchback (from Nouzawa et al (1990))

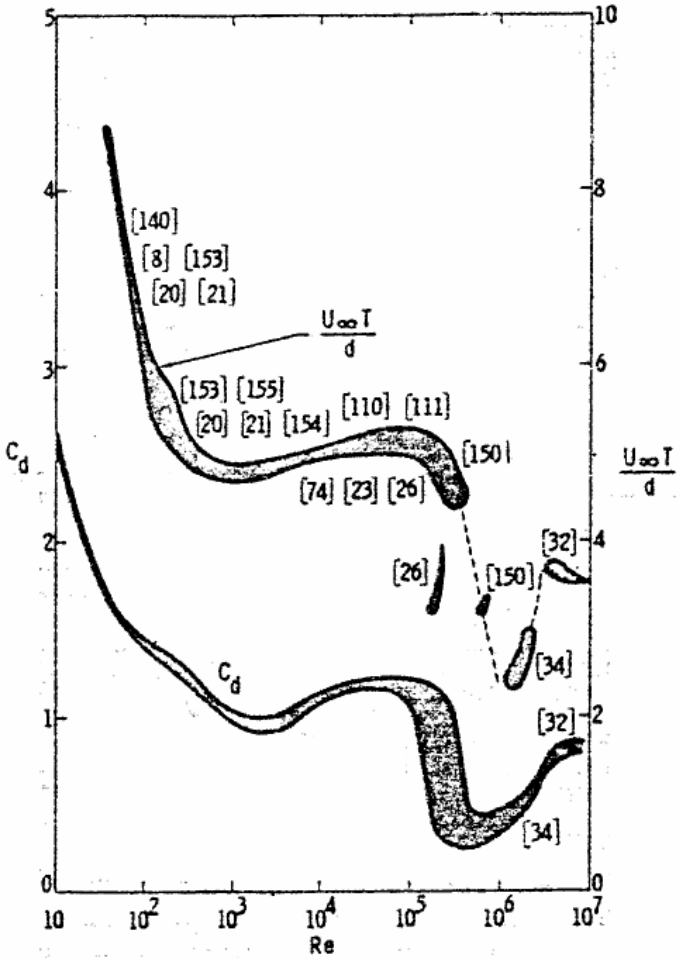

Figure 1.4.1 - Effect of Reynolds number on mean drag coefficient and inverse of Strouhal number for the circular cylinder (from Morkovin (1964))

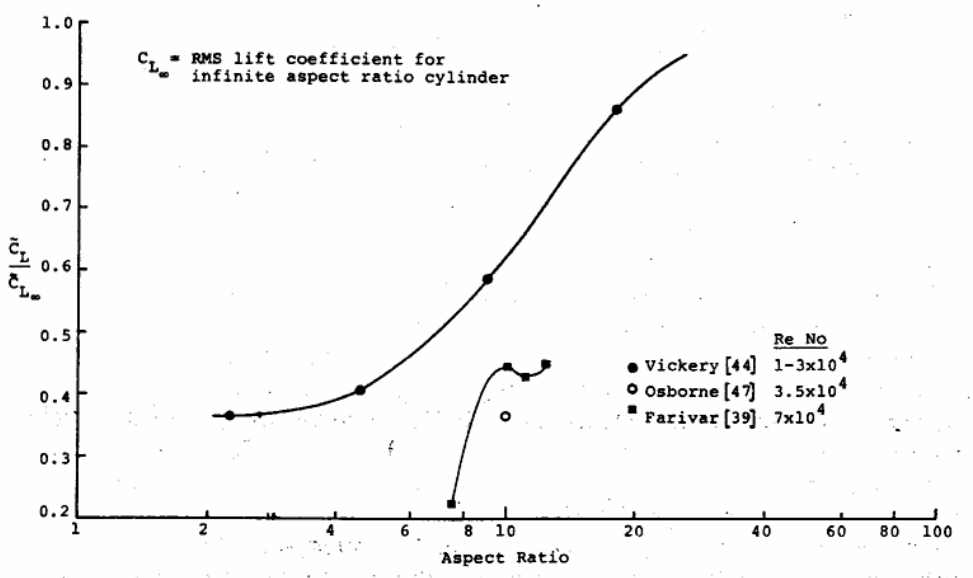

Figure 1.4.2 - Effect of aspect ratio on fluctuating lift for circular cylinders (from Basu (1986))

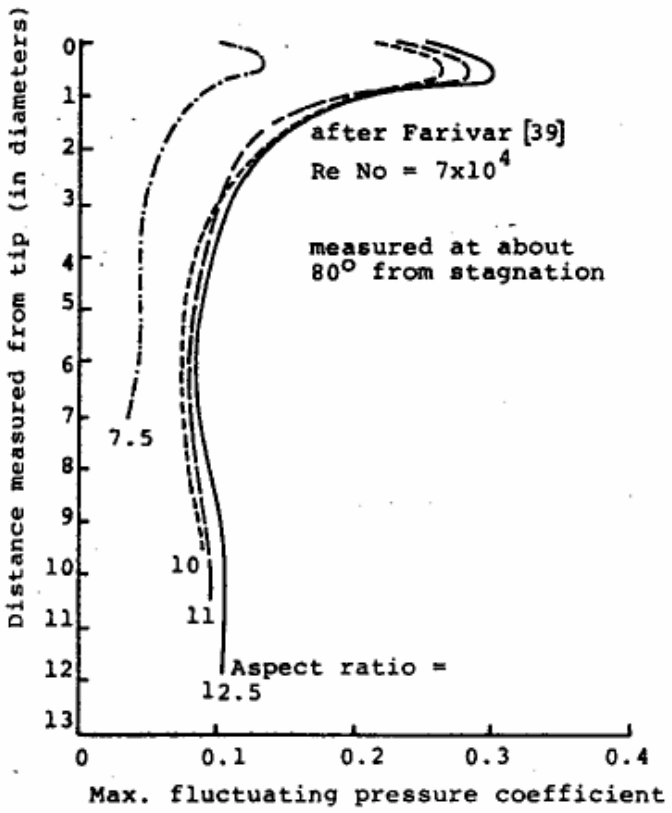

Figure 1.4.3 - Spanwise distribution of local fluctuating pressure coefficient for circular cylinders (from Basu (1986))

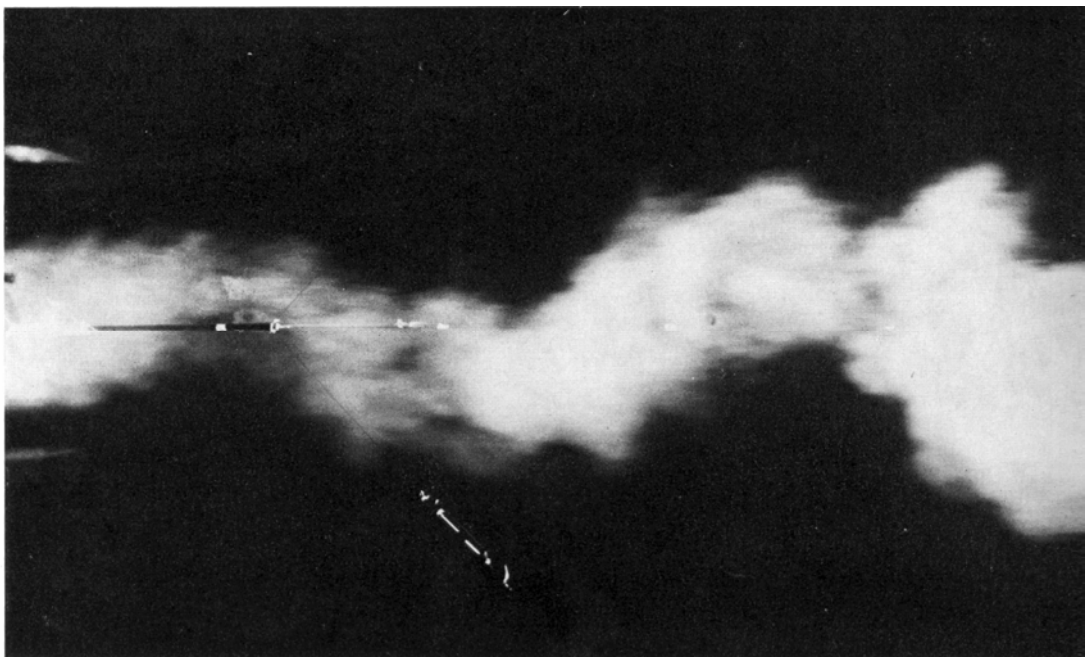

Figure 1.4.4 - Sphere smoke photograph from above (from Taneda (1978)) (simultaneous with figure 1.4.5)

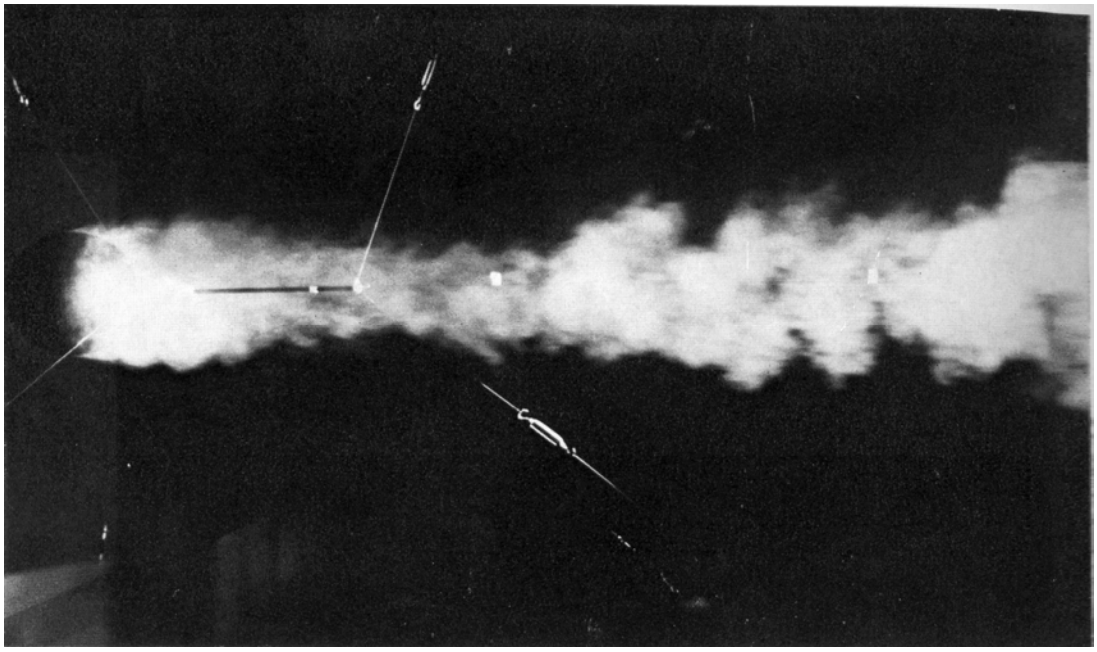

Figure 1.4.5 - Sphere smoke photograph from the side (from Taneda (1978)) (simultaneous with figure 1.4.4)

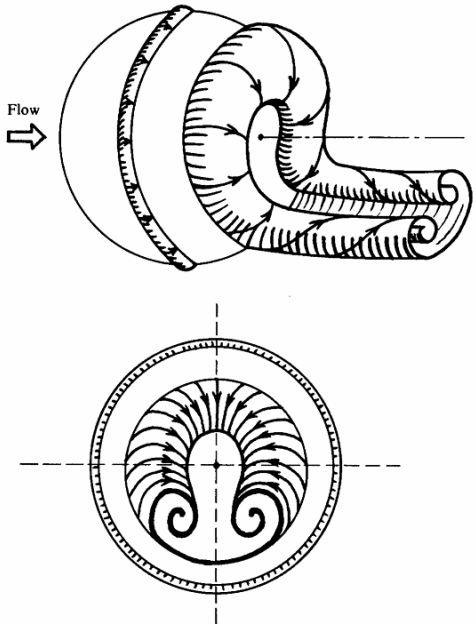

Figure 1.4.6 - Schematic representation of flow in the range $3.8x10^5<Re<10^6$ (from Taneda (1978))

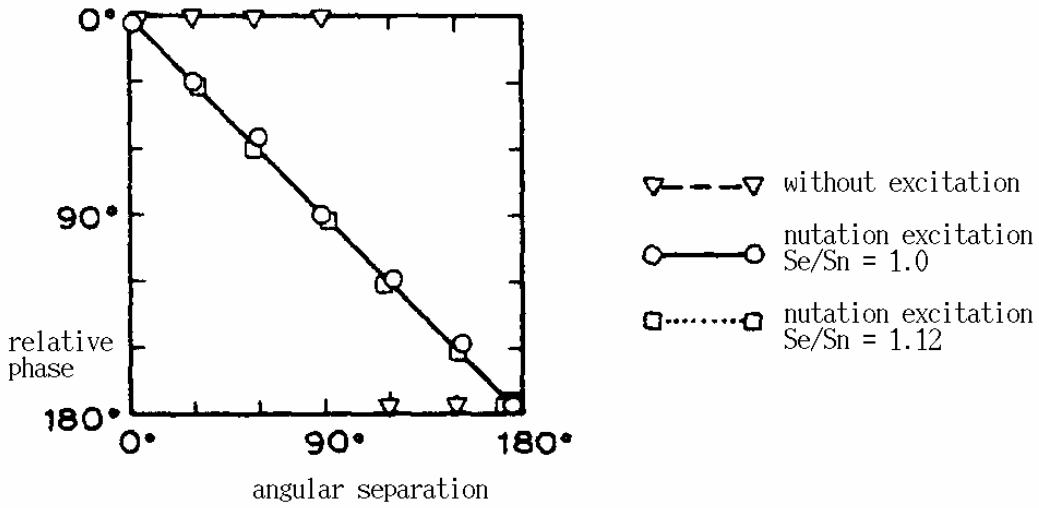

Figure 1.4.7 - Phase shift between probes vs angular separation (from Berger et al (1990))

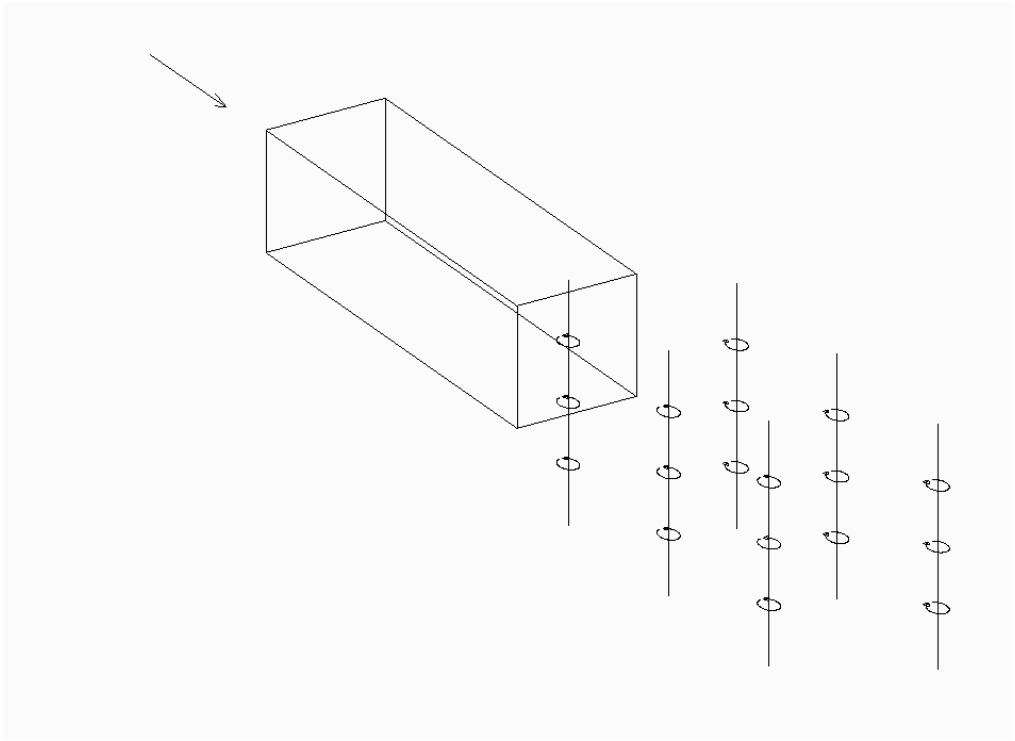

Figure 1.4.8 - Schematic illustration of essentially 2D antisymmetric shedding

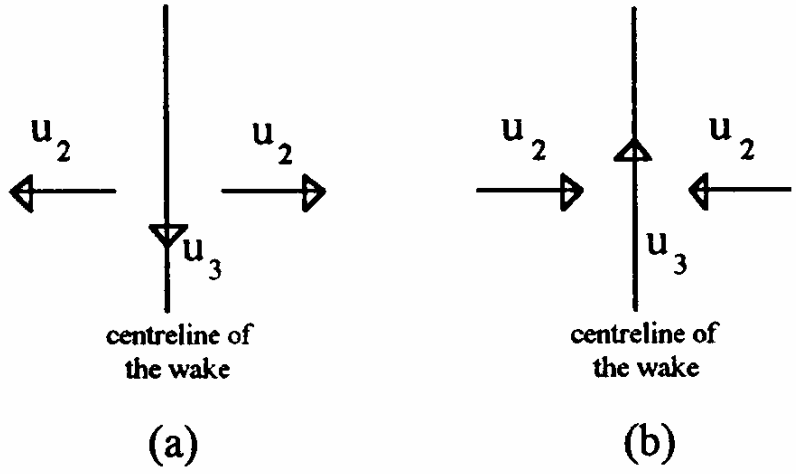

Figure 1.4.9 - Schematic of proposed motion of vortex cores and flow at centreline (from Goh (1994))

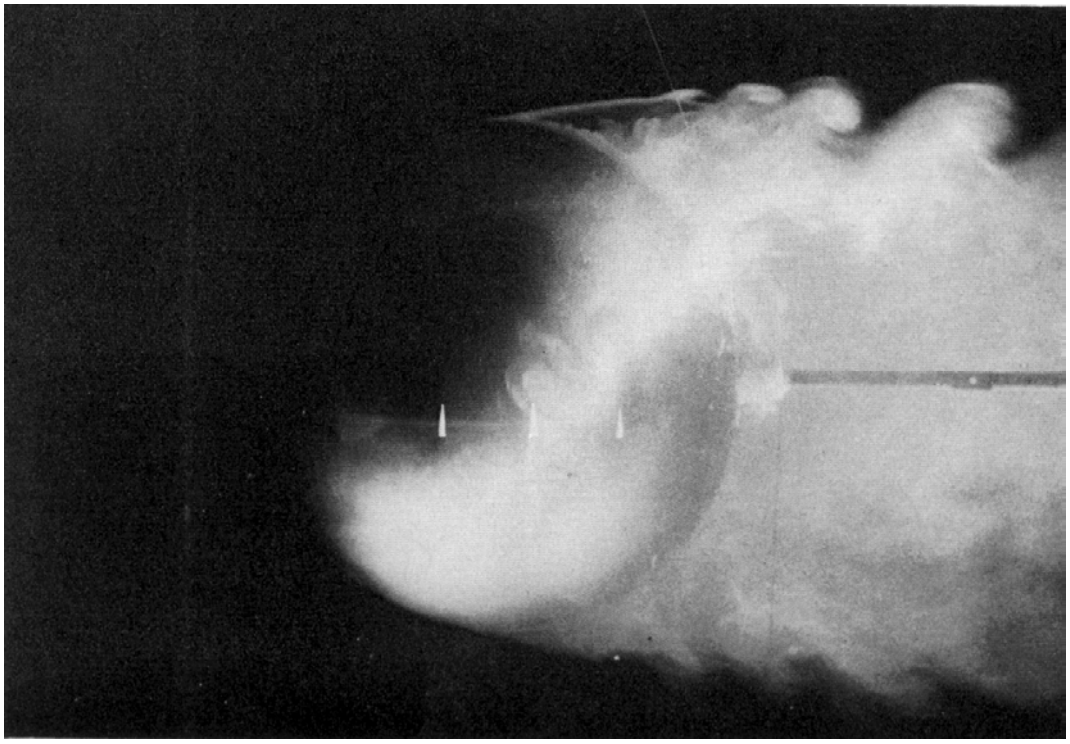

Figure 1.4.10 - Shear layer instability (from Taneda (1978))

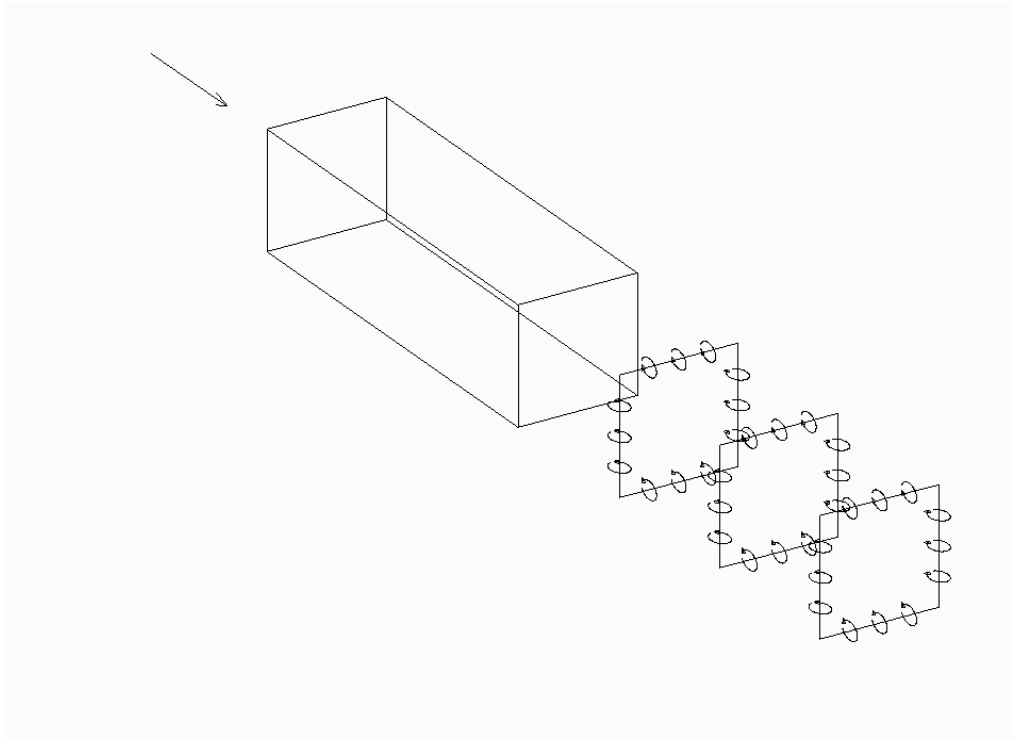

Figure 1.4.11 - Schematic illustration of shedding of ring vortices

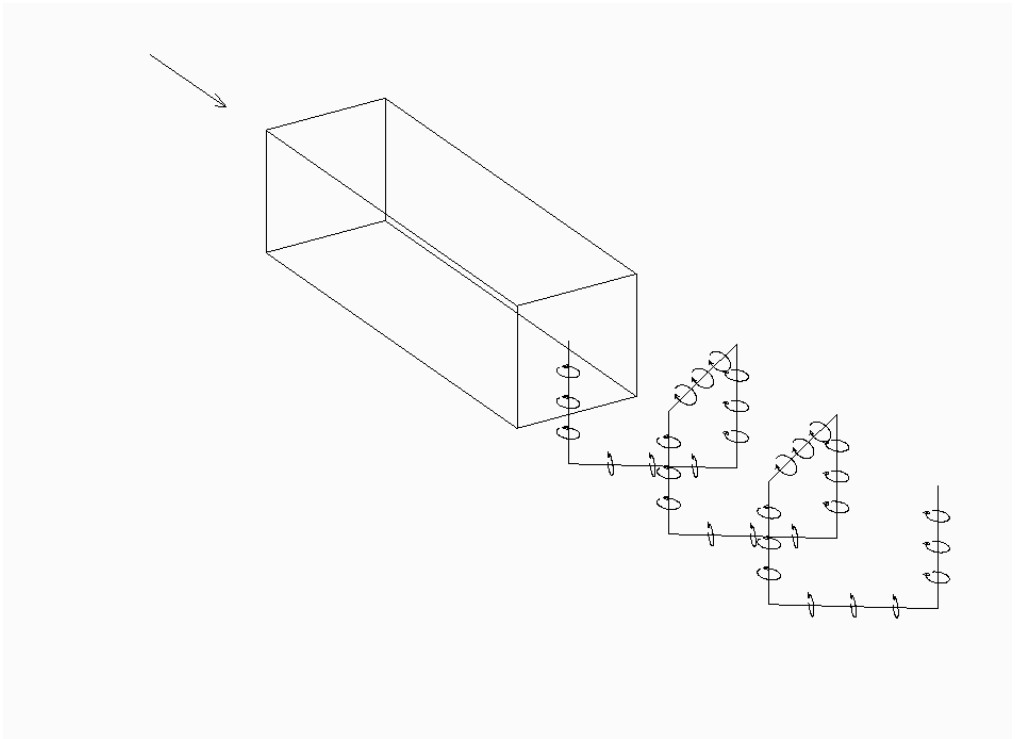

Figure 1.4.12 - Schematic illustration of pseudo-helical structure described by Duell and George (1999)

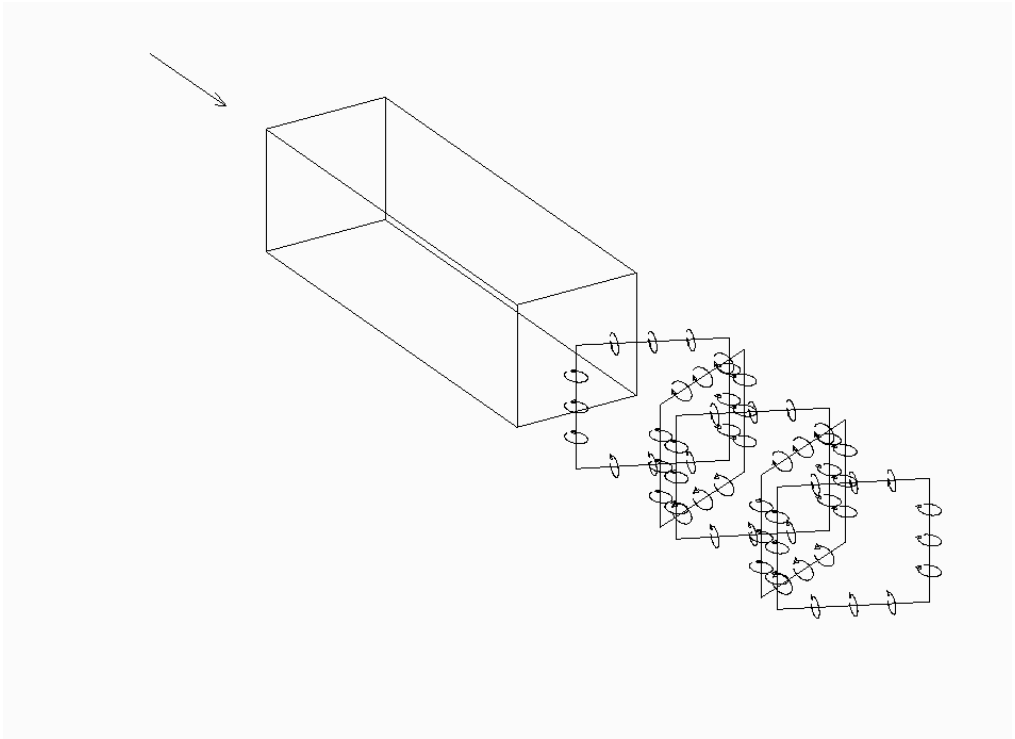

Figure 1.4.13 - Schematic illustration of shedding of inclined ring vortices

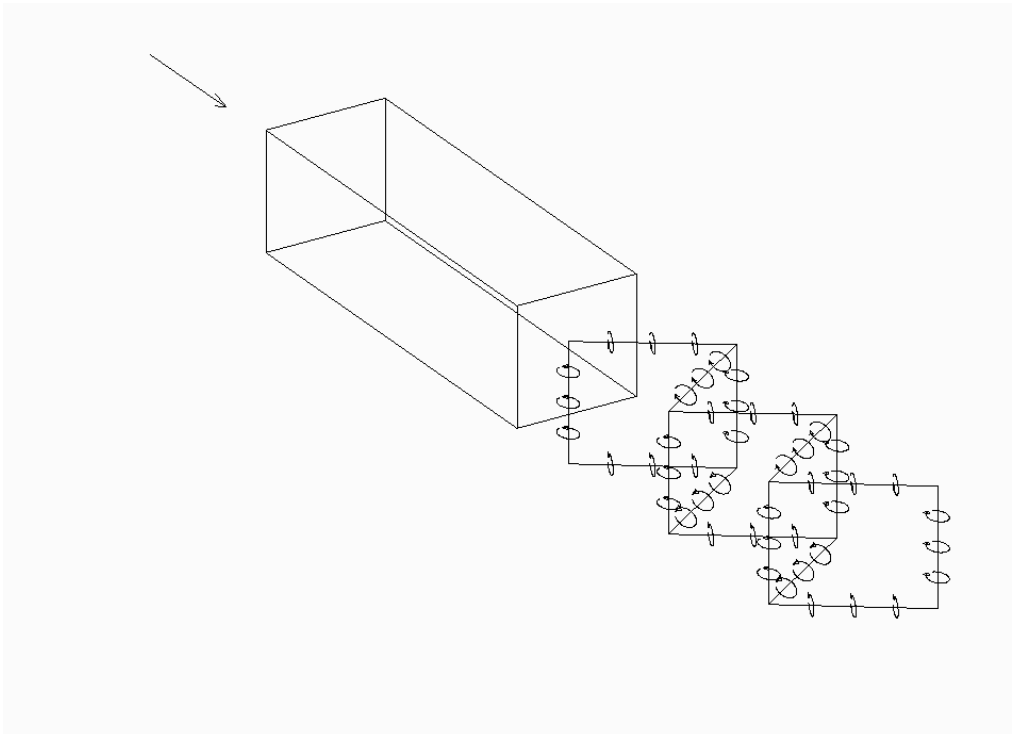

Figure 1.4.14 - Schematic illustration of shedding of linked inclined ring vortices

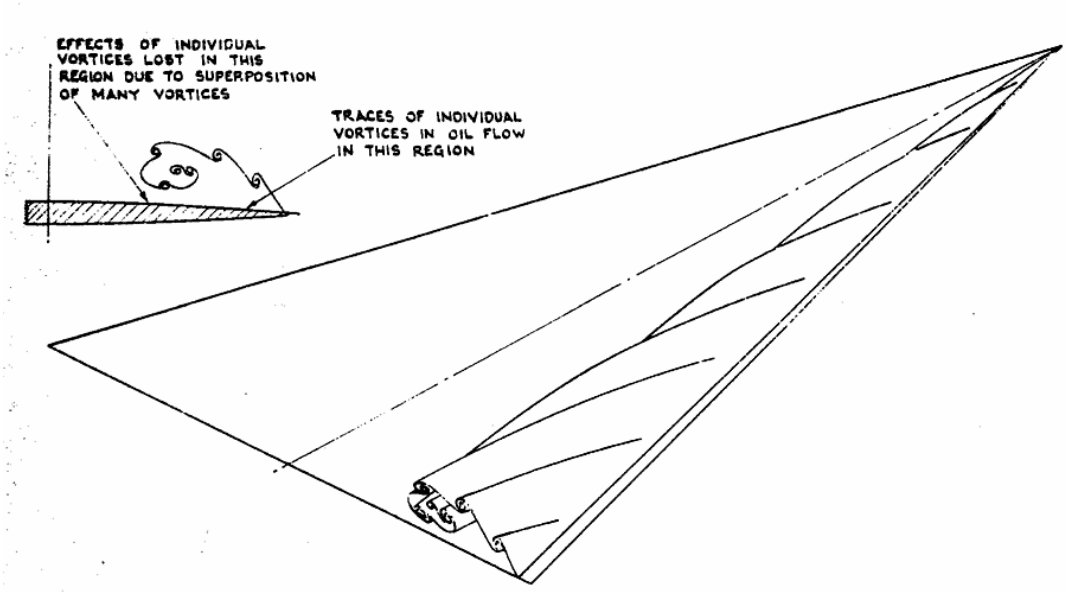

Figure 1.4.15 - Streamwise vortices in the separated sheet (from Squire et al (1963))

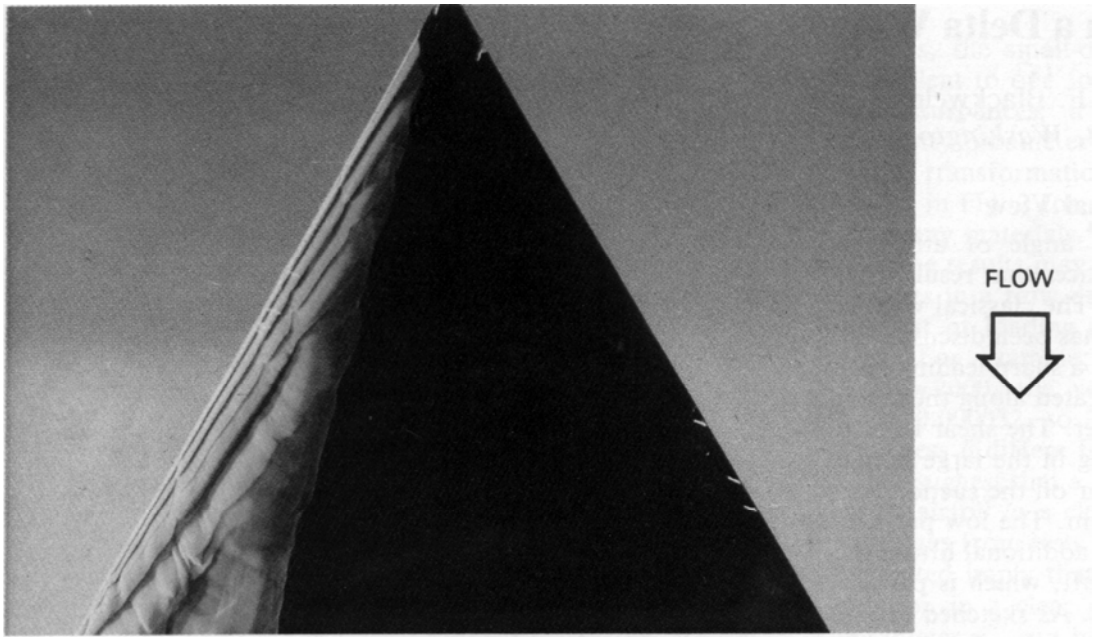

Figure 1.4.16 - Dye-injection flow visualisation of vortices shed along leading edge of delta wing (from Gad-el-Hak and Blackwelder (1985))

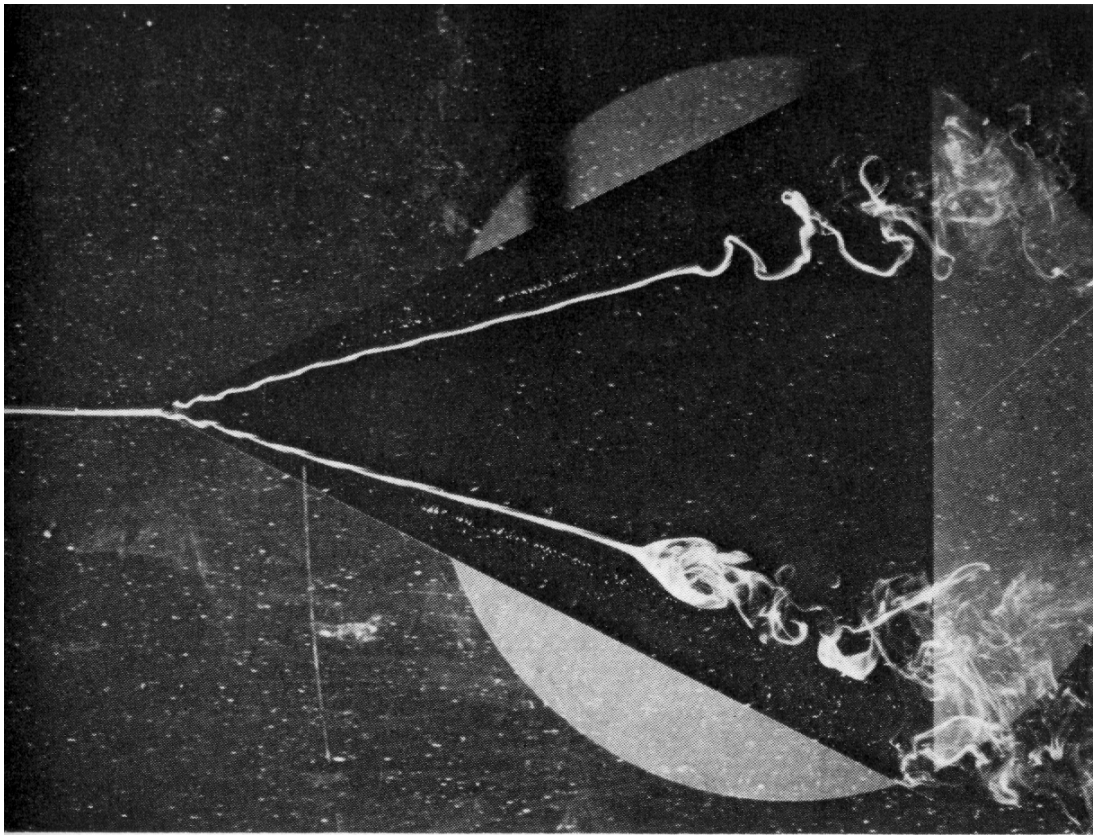

Figure 1.4.17 - Spiral and bubble vortex breakdown over a delta wing (from Lambourne and Bryer (1961))

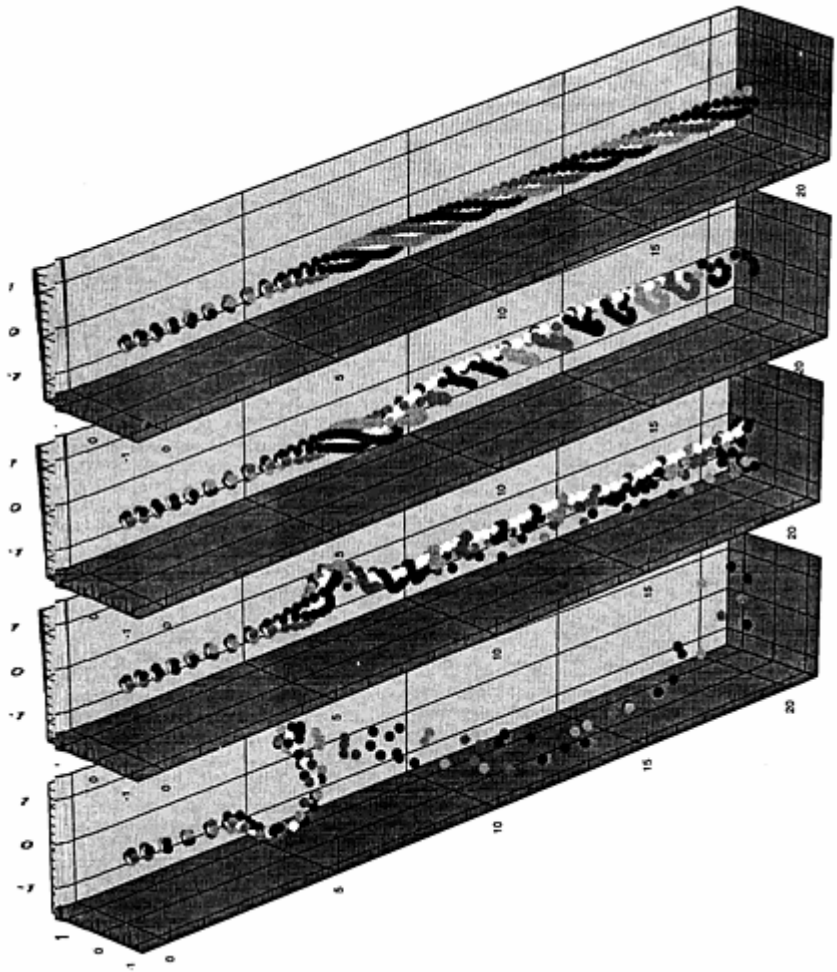

Figure 1.4.18 - Particle traces showing vortex breakdown with increasing vortex strength (from Tromp and Beran (1996))

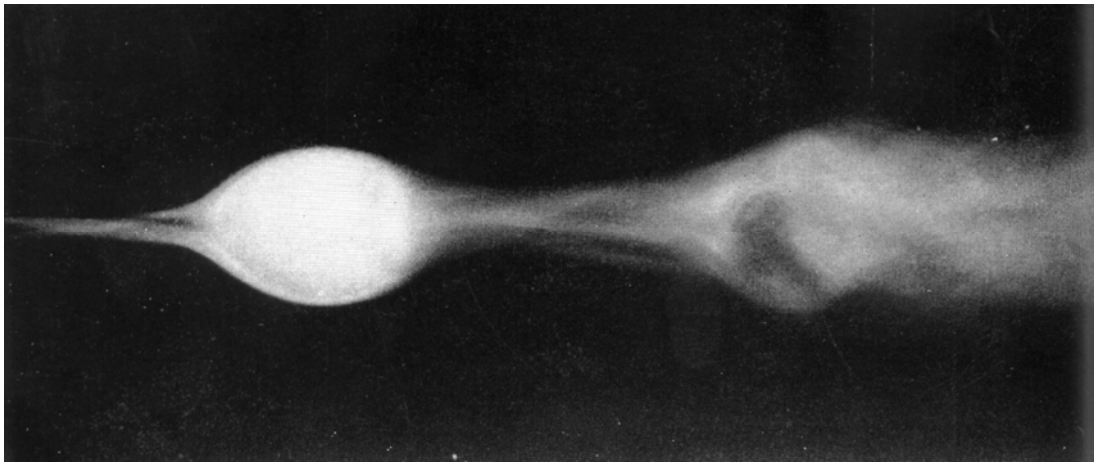

Figure 1.4.19 - Laminar to turbulent transition and vortex breakdown (from Harvey (1962))

FIGURES FOR CHAPTER 2 – EXPERIMENTAL TECHNIQUES

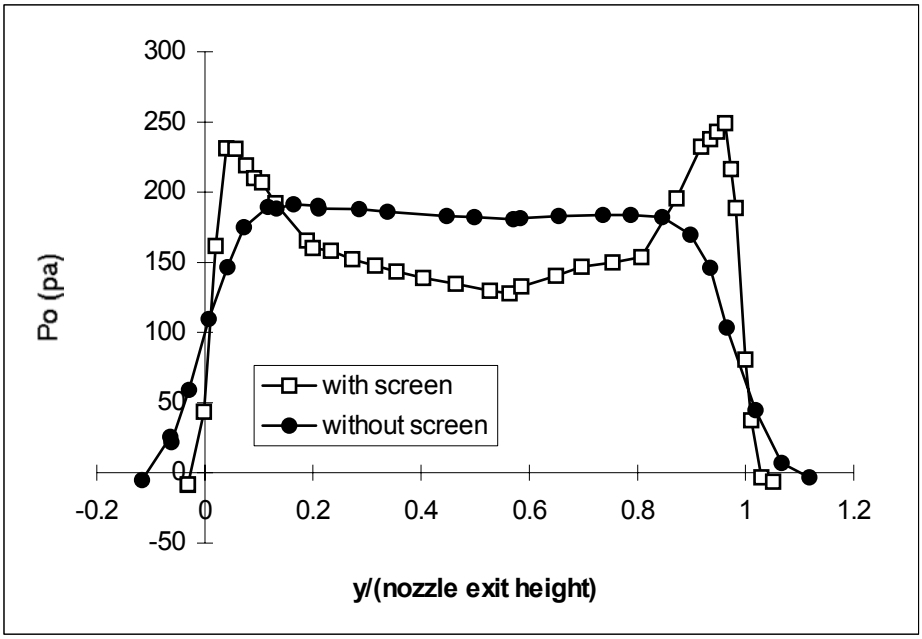

Figure 2.1.1 - Effect of removing screen immediately upstream of contraction on total pressure distribution in working section of Durham 0.85mx0.55m tunnel

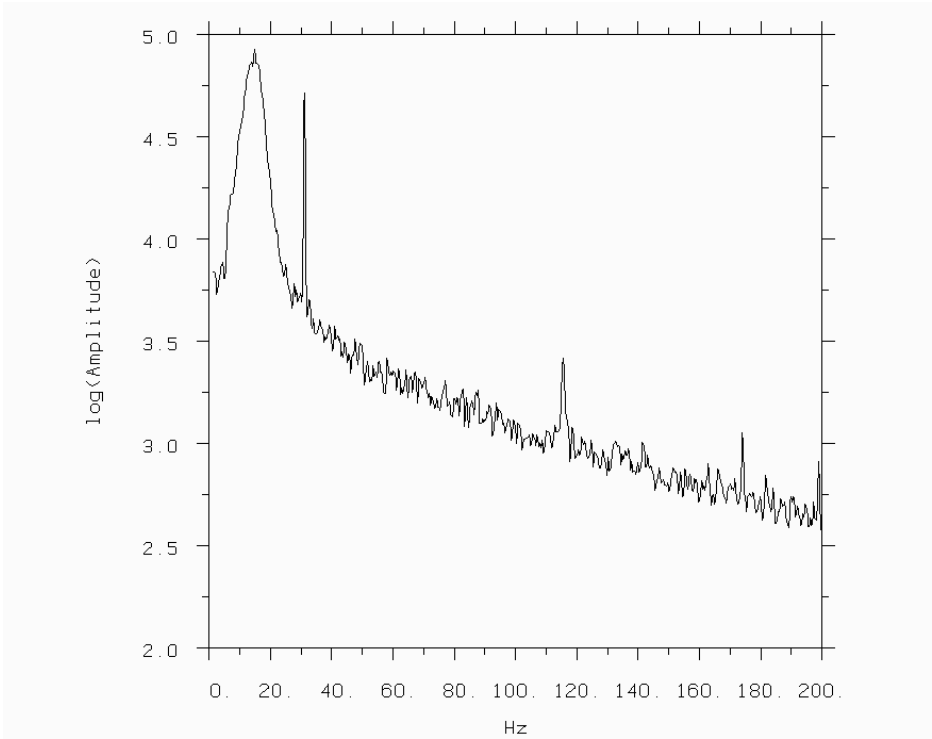

Figure 2.1.2 - Hot-wire velocity spectrum in Durham tunnel empty working section

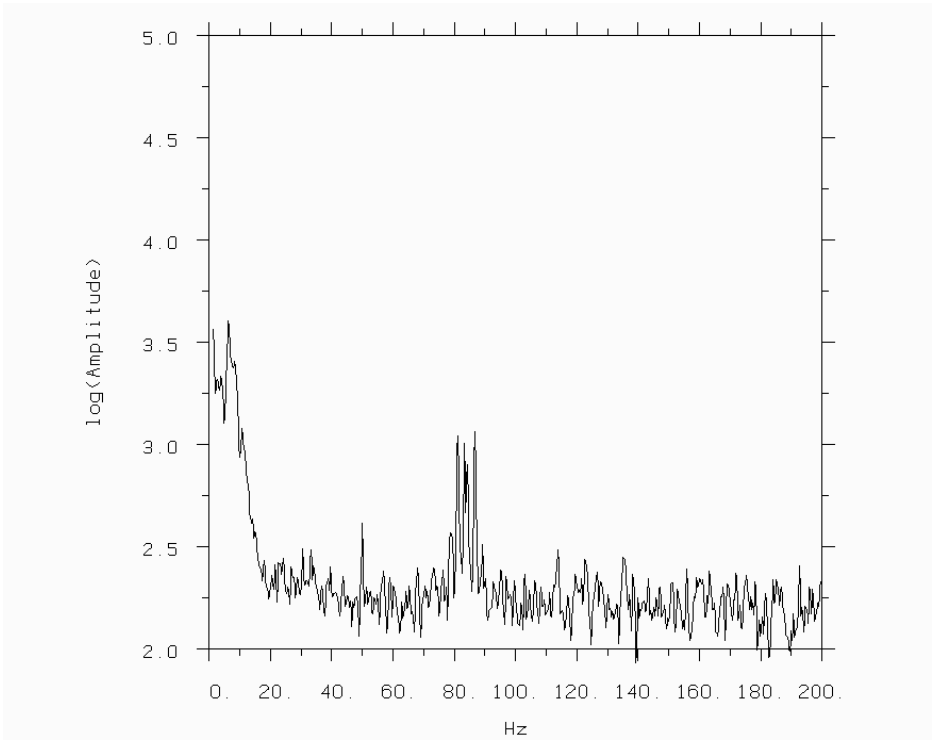

Figure 2.1.3 - Hot-wire velocity spectrum in MIRA model tunnel empty working section

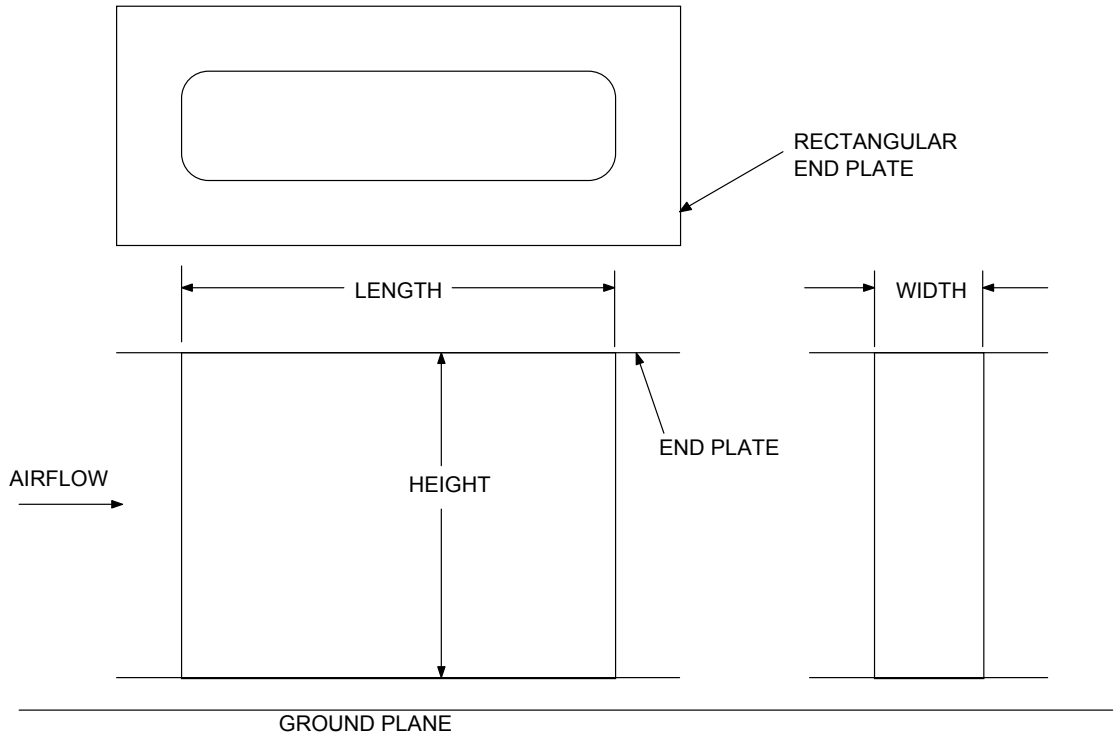

Figure 2.1.4 - Orthographic projection of PARAD type model

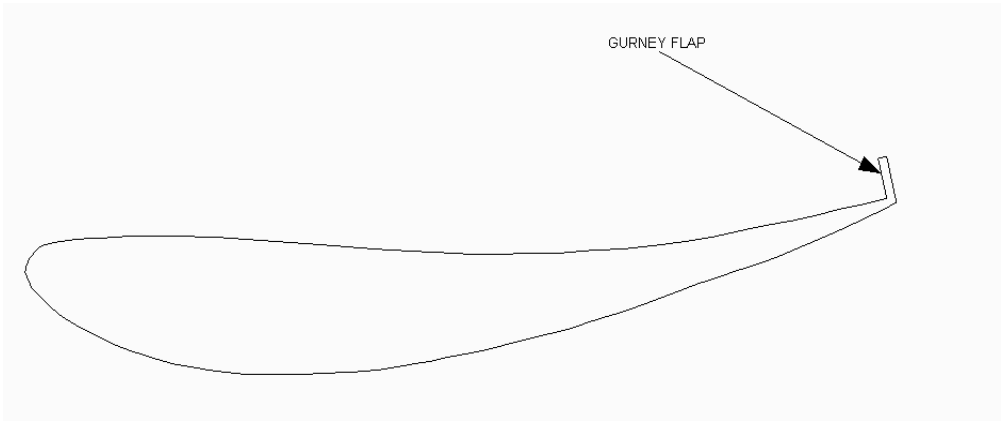

Figure 2.1.5 - Profile of racing car wing with Gurney flap

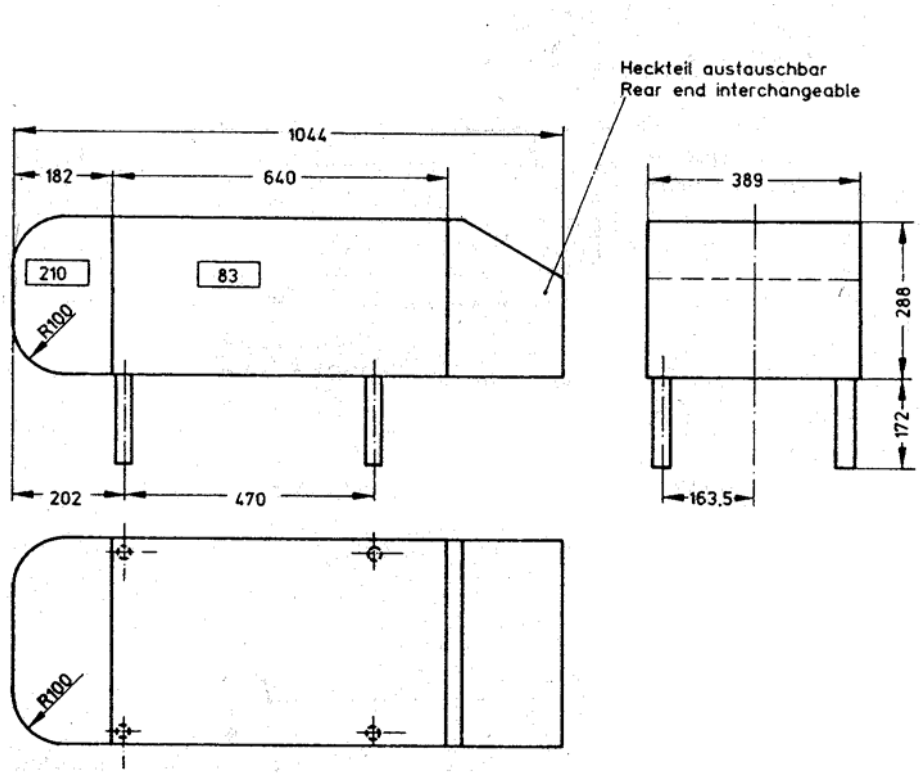

Figure 2.1.6 - The Ahmed model (1/4 scale) (from Ahmed et al (1984))

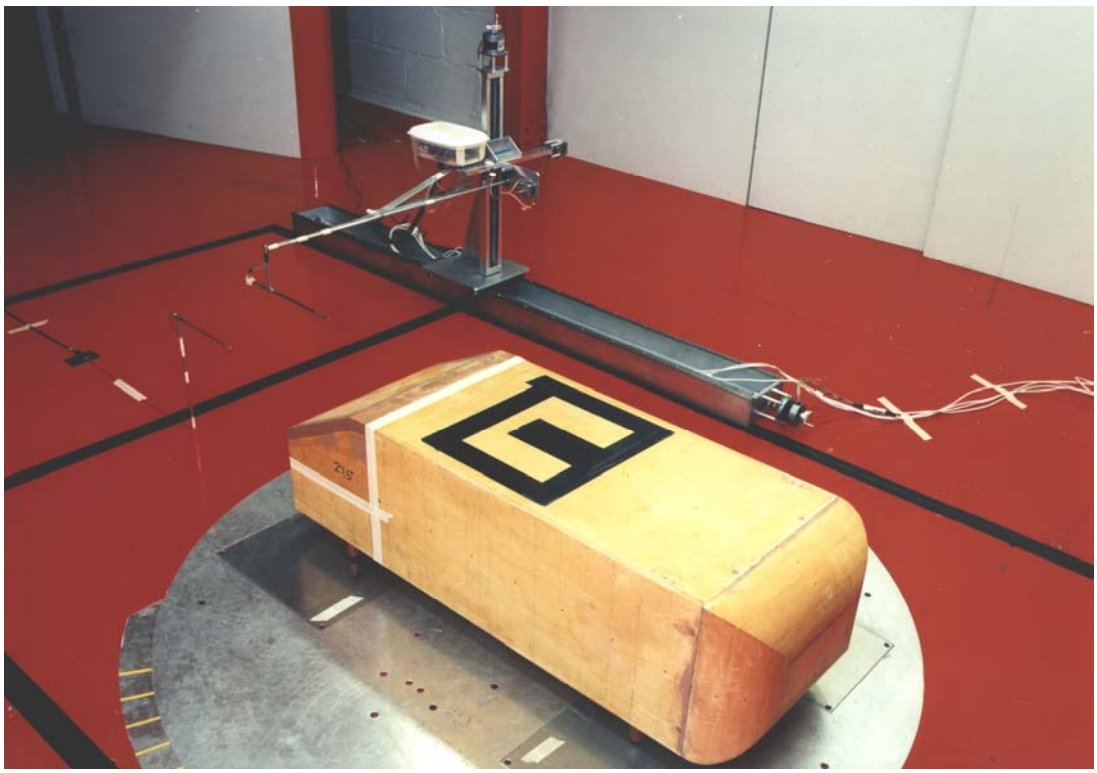

Figure 2.1.7 – The four-axis traverse installed in the MIRA model tunnel

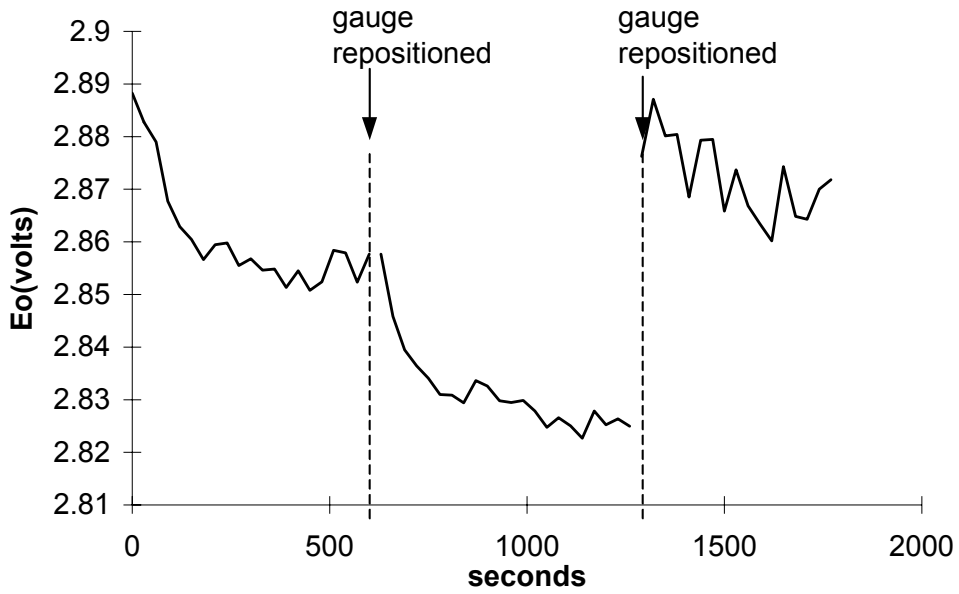

Figure 2.2.1 - Transient hot-film voltage after repositioning (zero flow conditions) (gauge repositioned at 0s, 600s and 1290s)

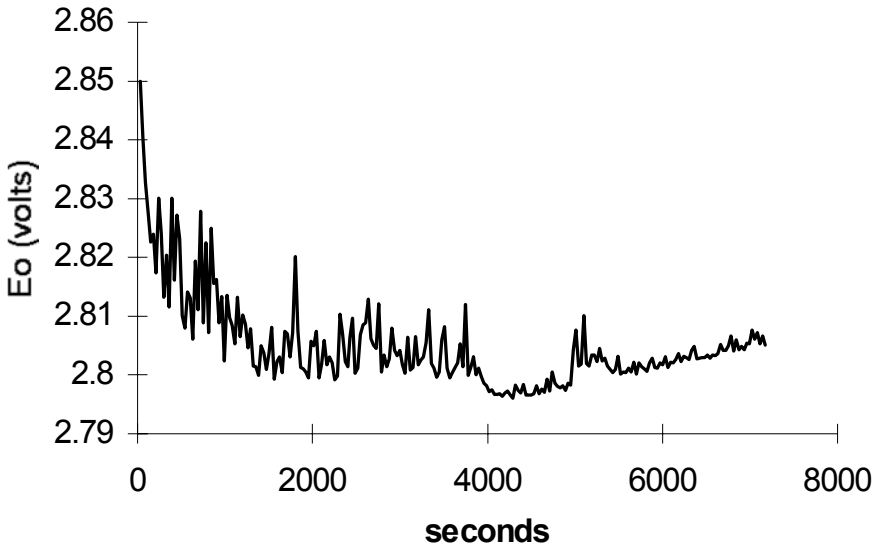

Figure 2.2.2 - Transient hot-film voltage after activation from cold (zero flow conditions)

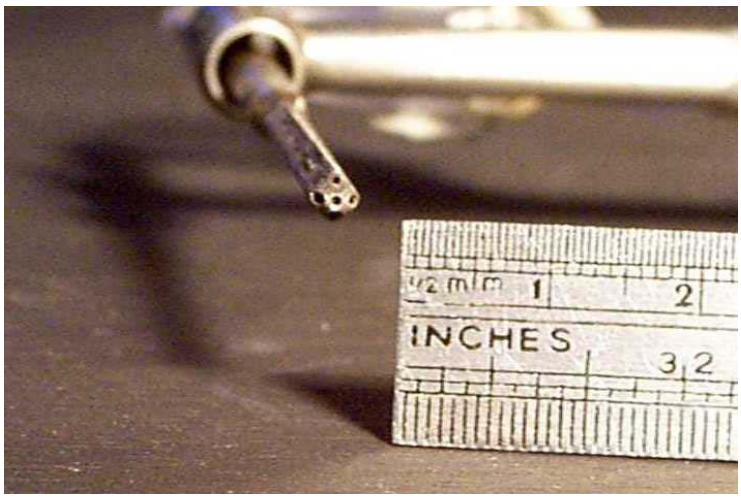

Figure 2.2.3 - The head of a 5-hole probe (probe 5h_03)

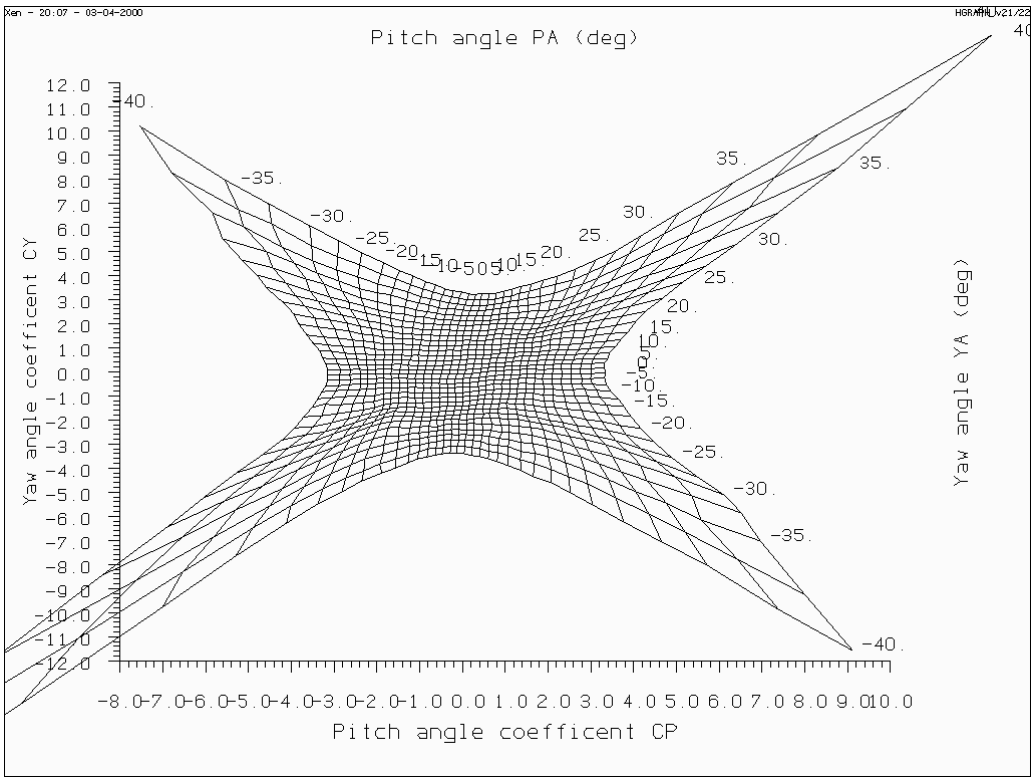

Figure 2.2.4 - Pitch and yaw angle calibration map for a 5-hole probe (probe 5h_03)

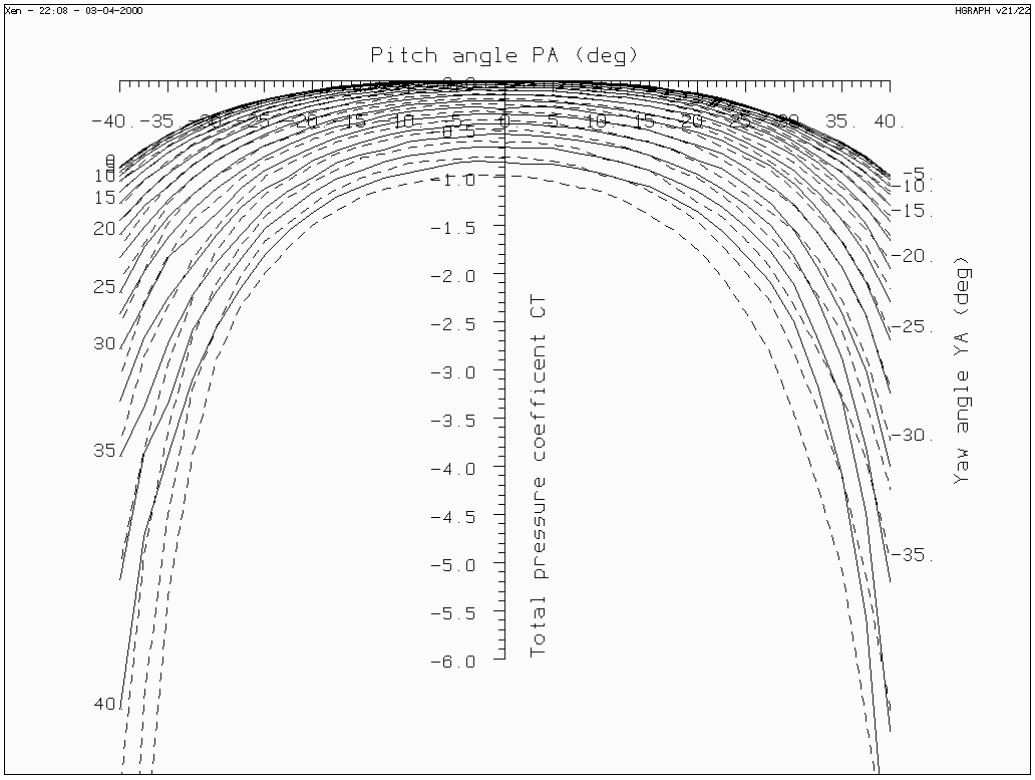

Figure 2.2.5 - Total pressure calibration for a 5-hole probe (probe 5h_03)

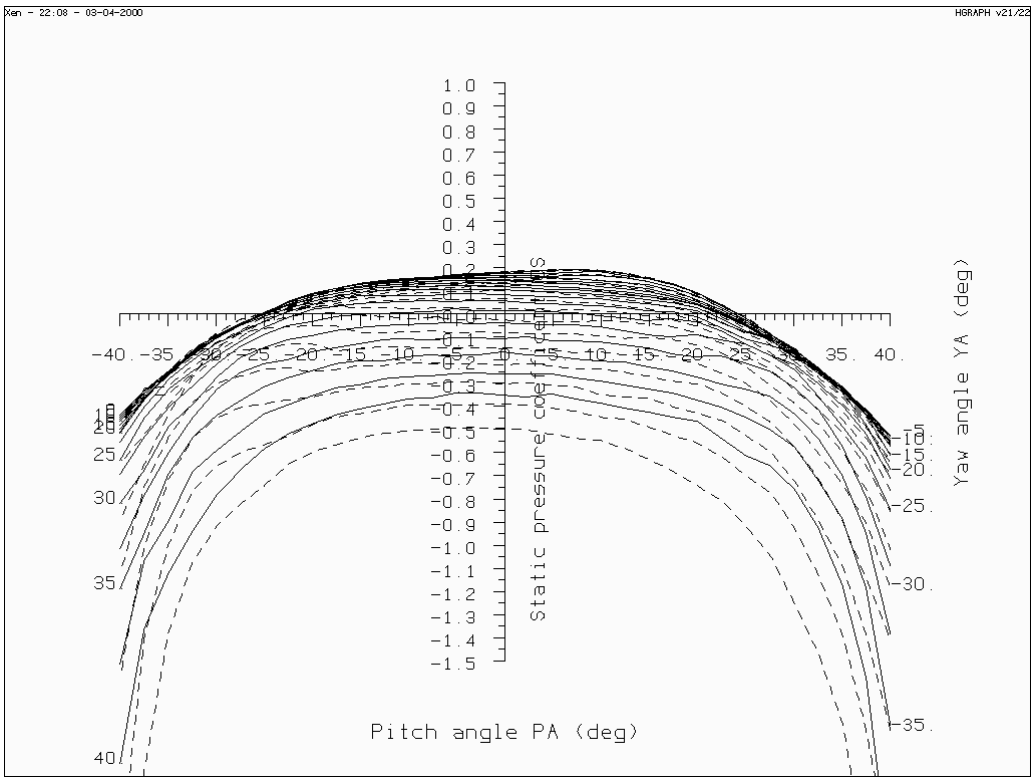

Figure 2.2.6 - Static pressure calibration for a 5-hole probe (probe 5h_03)

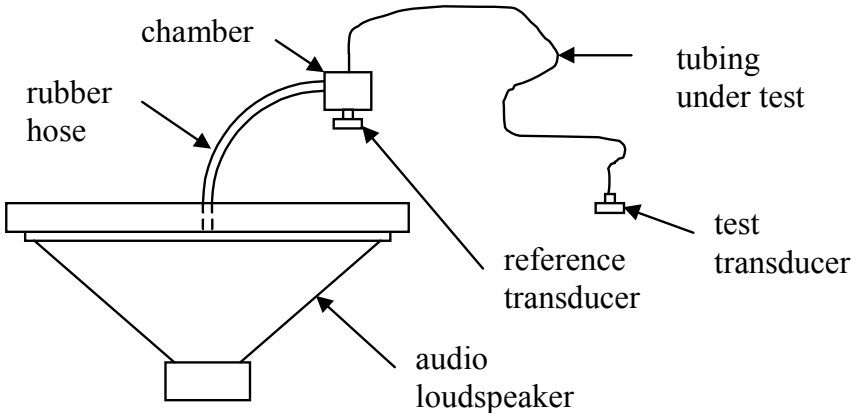

Figure 2.2.7 - Transfer-function correction apparatus

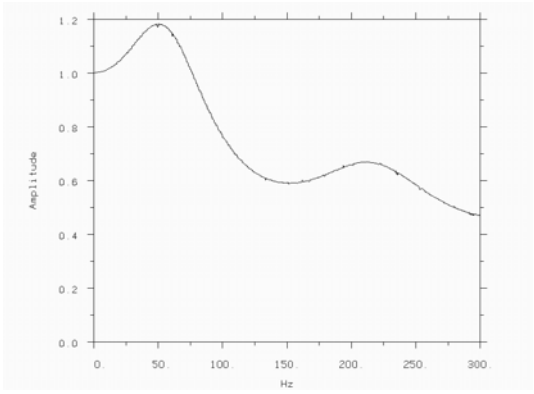

Figure 2.2.8a) Transfer function for 450mmx1mm plastic tube - amplitude

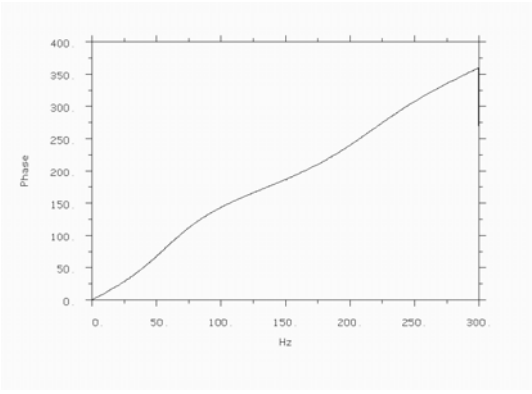

Figure 2.2.8b) Transfer function for 450mmx1mm plastic tube - phase

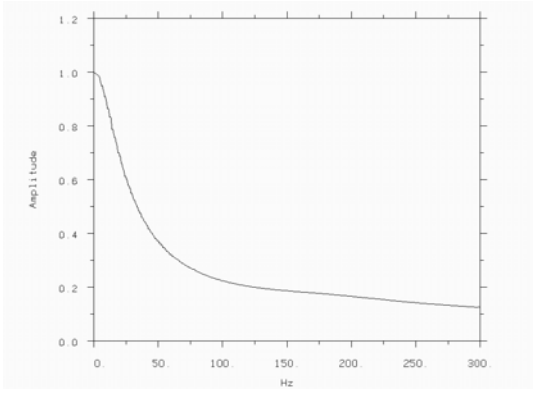

Figure 2.2.9a) Transfer function for tube 1 of 5-hole probe 5h_01 - amplitude

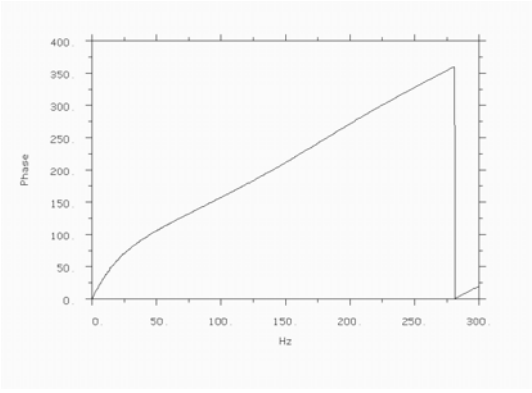

Figure 2.2.9b) Transfer function for tube 1 of 5-hole probe 5h_01 - phase

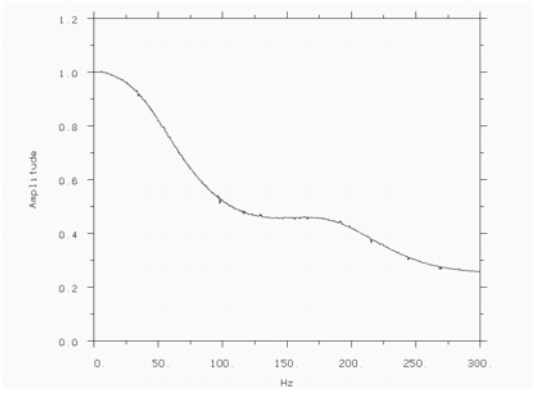

Figure 2.2.10a) Transfer function for tube 1 of 5-hole probe 5h_03 - amplitude

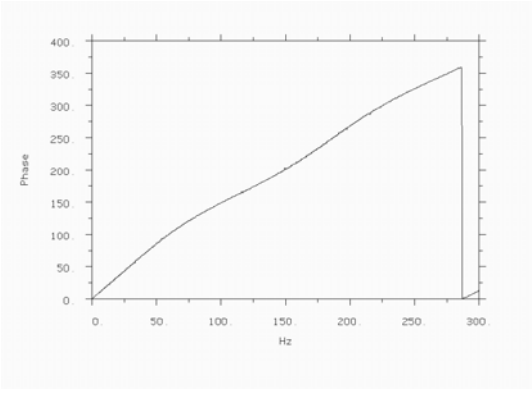

Figure 2.2.10b) Transfer function for tube 1 of 5-hole probe 5h_03 - phase

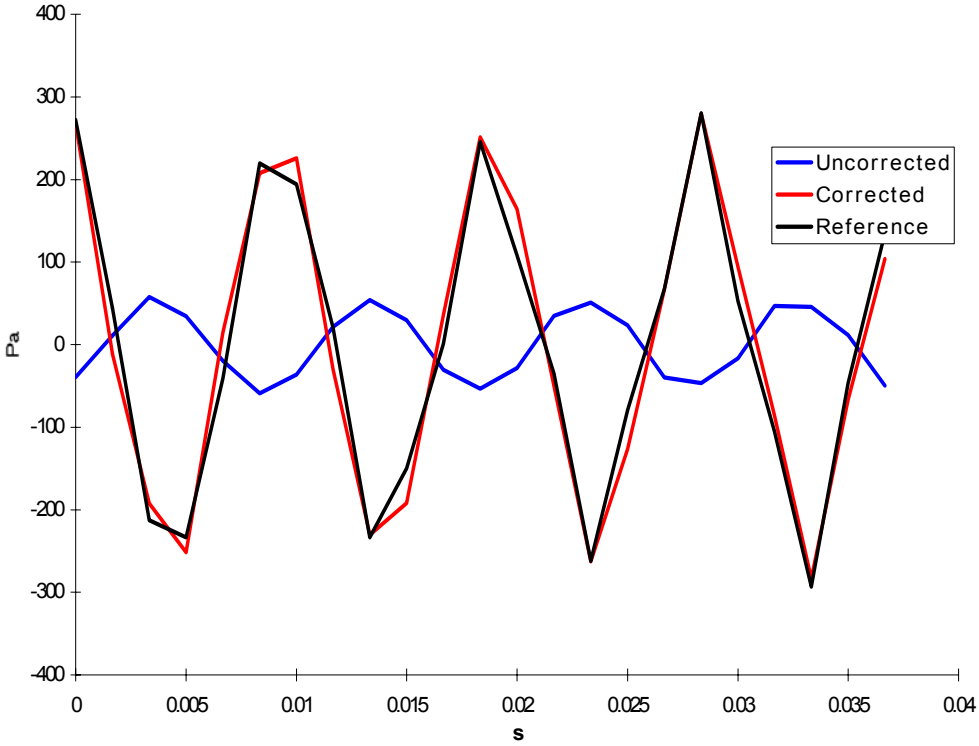

Figure 2.2.11 - Demonstration of transfer function correction using 100hz saw wave (5h_01 tube 1)

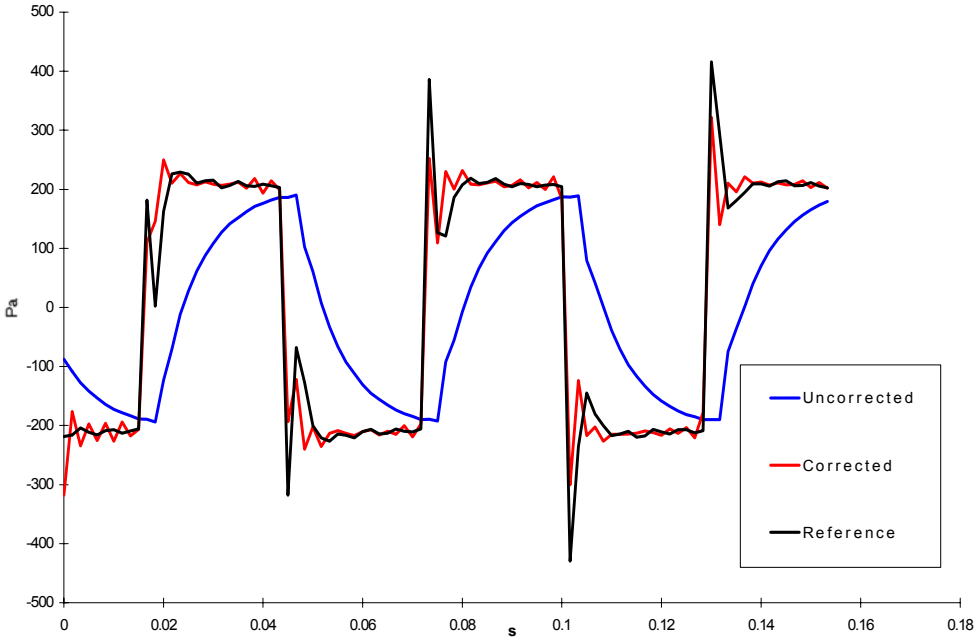

Figure 2.2.12 - Demonstration of transfer function correction using 20hz square wave (5h_01 tube 1)

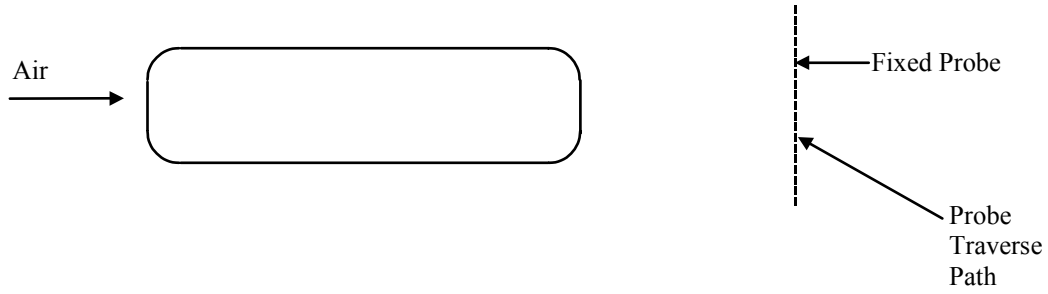

Figure 2.2.13 – Arrangement of model and probes

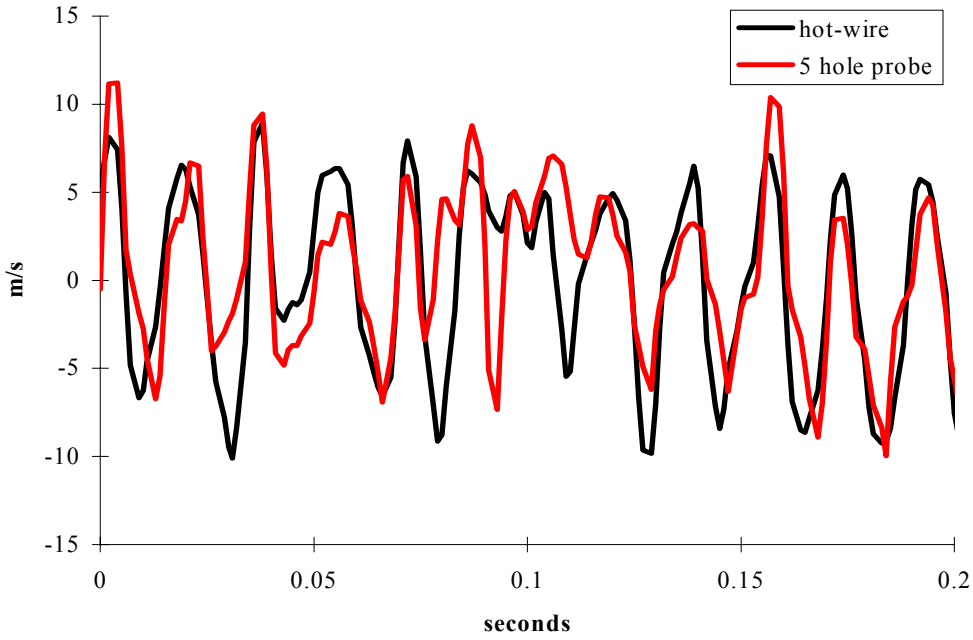

Figure 2.2.14 – Time-traces of fluctuating hot-wire effective velocity from hot-wire and 5-hole probe with transfer function correction

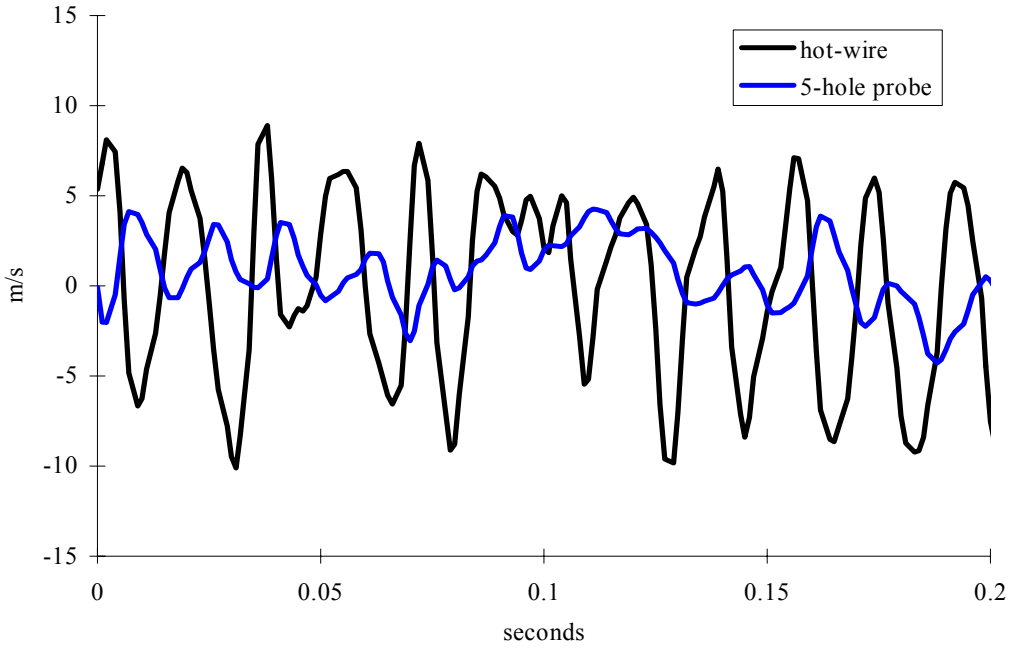

Figure 2.2.15 – Time-traces of fluctuating hot-wire effective velocity from hot-wire and 5-hole probe without transfer function correction

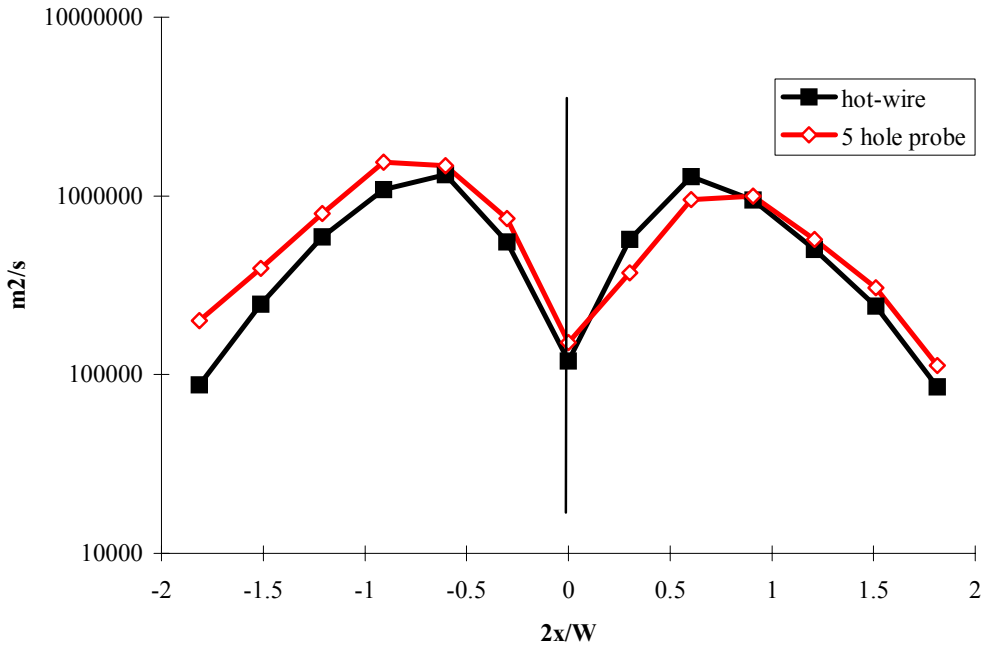

Figure 2.2.16 - Hot-wire effective velocity autospectral density across the wake of the PARAD2 model

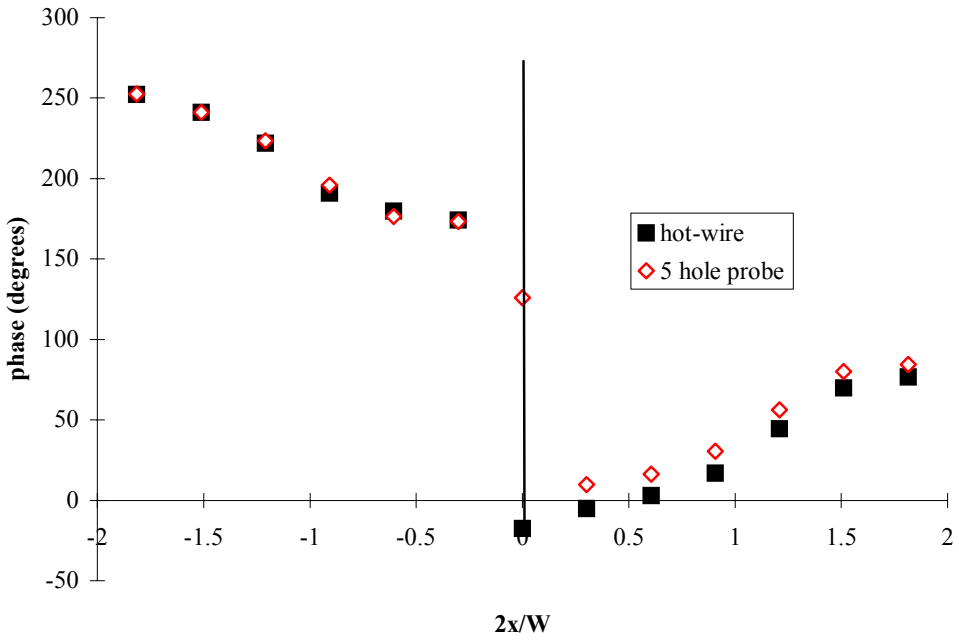

Figure 2.2.17 - Phase between stationary and traversing probes across the wake of the PARAD2 model (hot-wire effective velocity)

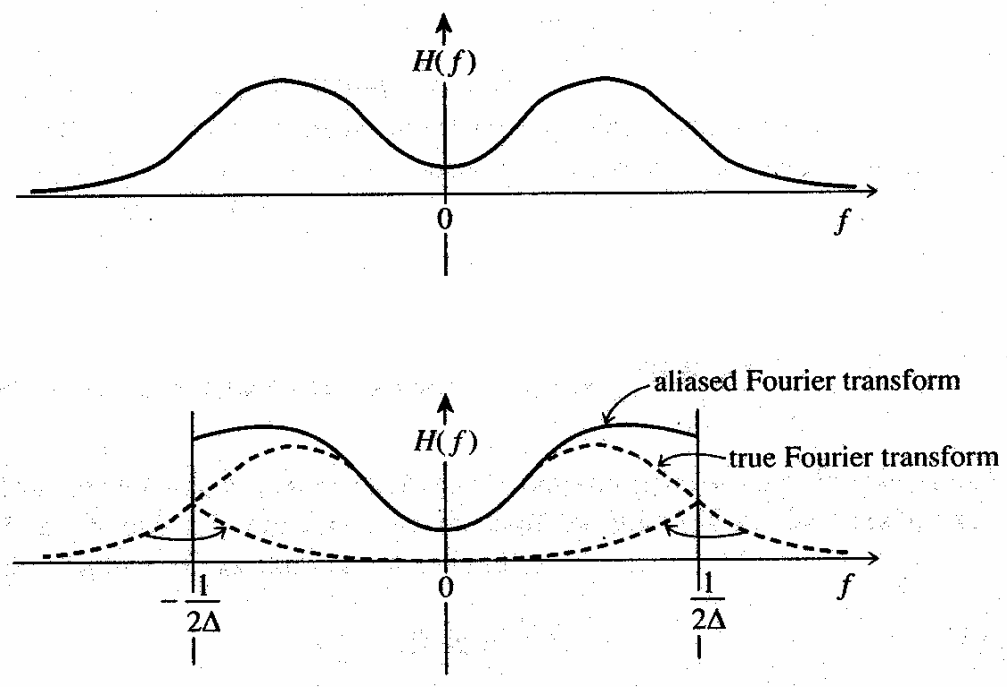

Figure 2.3.1 - Aliasing for double-sided Fourier transform (from Press et al (1992))

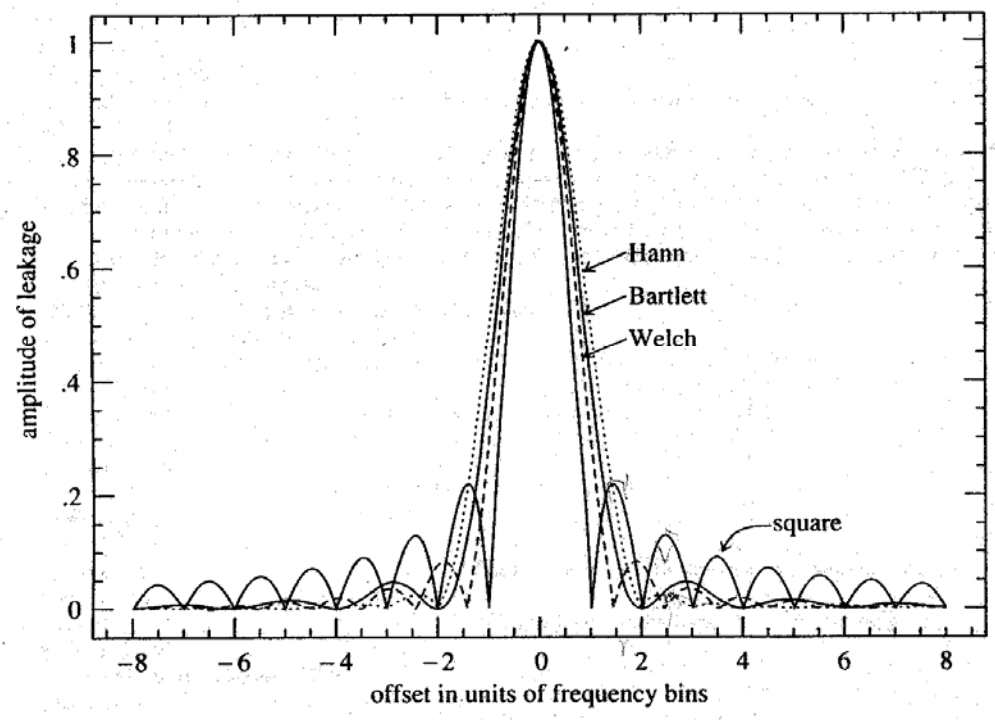

Figure 2.3.2 - Leakage functions for some common windowing functions (from Press et al (1992))

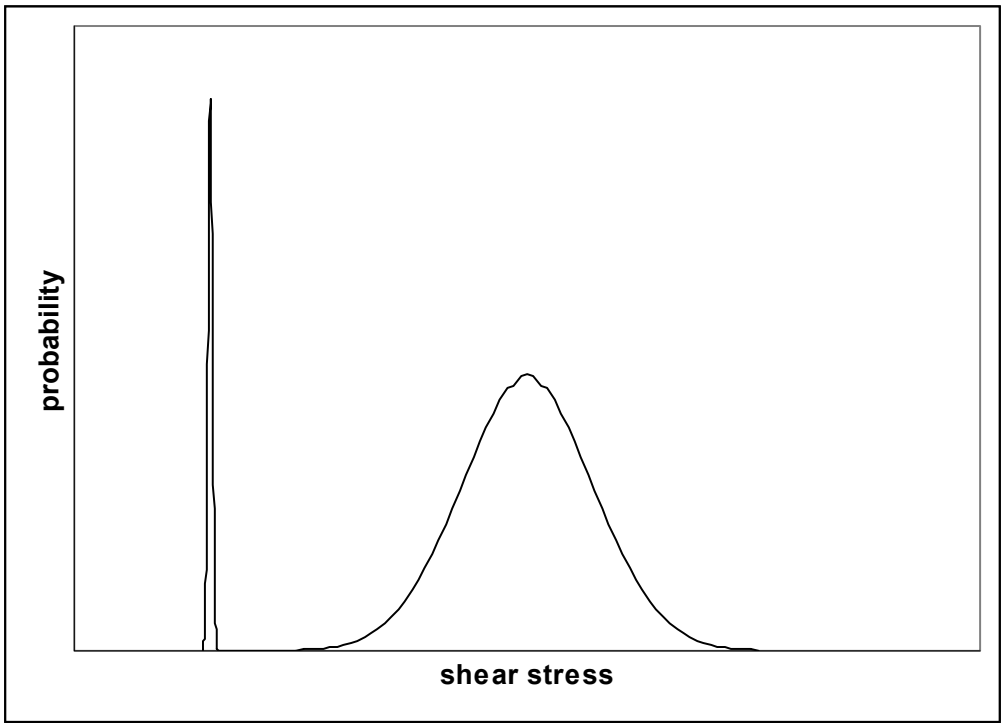

Figure 2.3.3 - Idealised probability density function for skin friction in transitional boundary layer

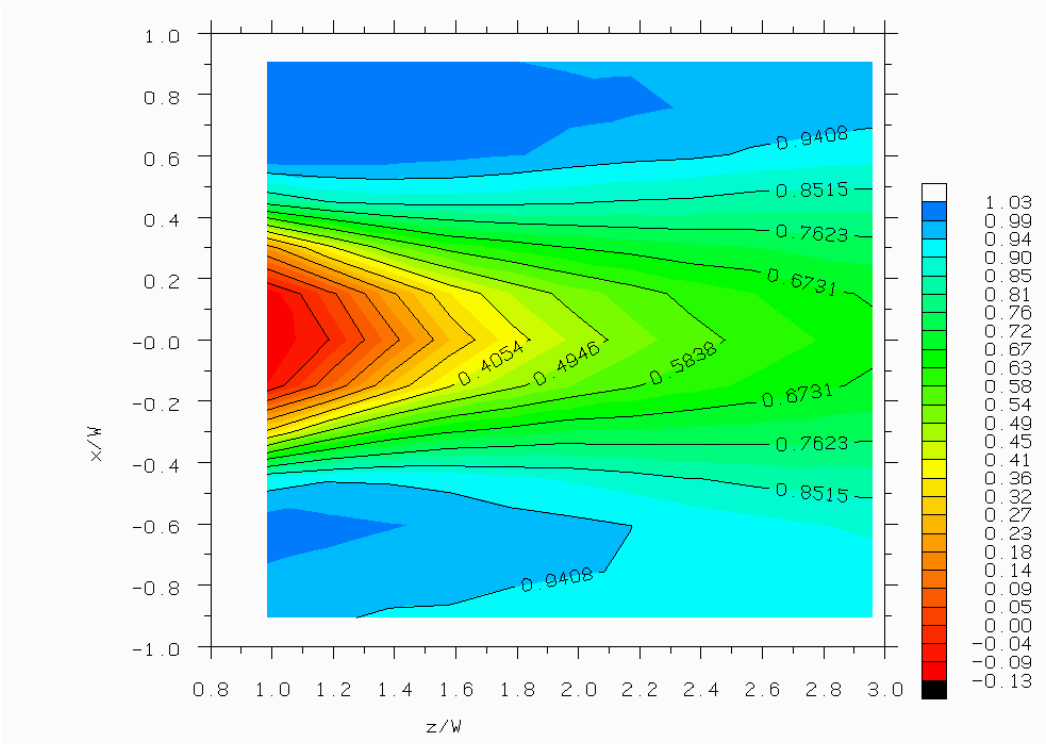

Figure 2.3.4 - Total pressure coefficient in the wake of the PARAD2 model – time-averaging applied after probe calibration – (with transfer function correction)

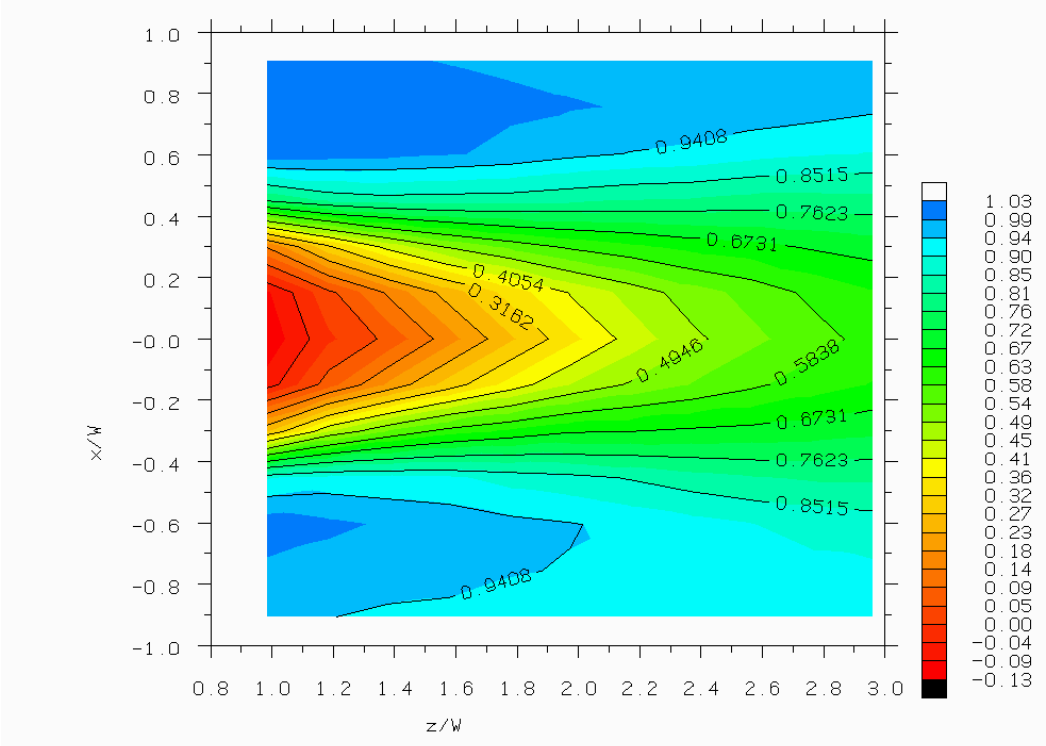

Figure 2.3.5 - Total pressure coefficient in the wake of the PARAD2 model – time-averaging applied before probe calibration – (no transfer function correction)

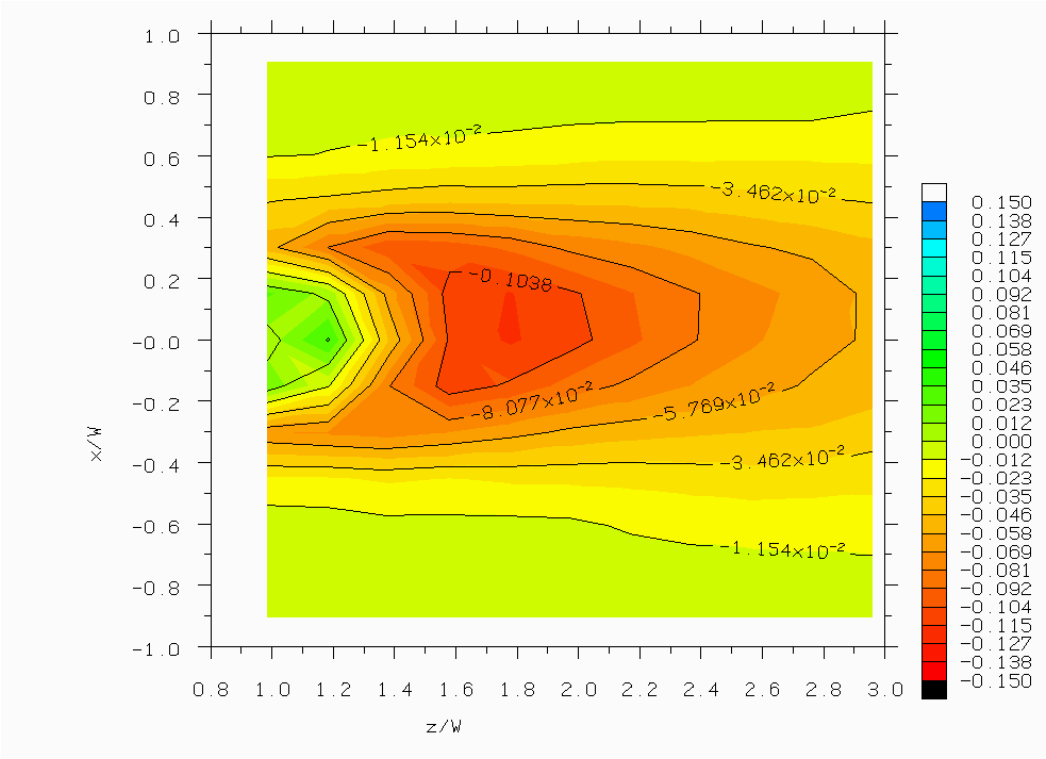

Figure 2.3.6 - Effect of time-averaging before probe calibration
(ie: figure 2.3.5 - figure 2.3.4)

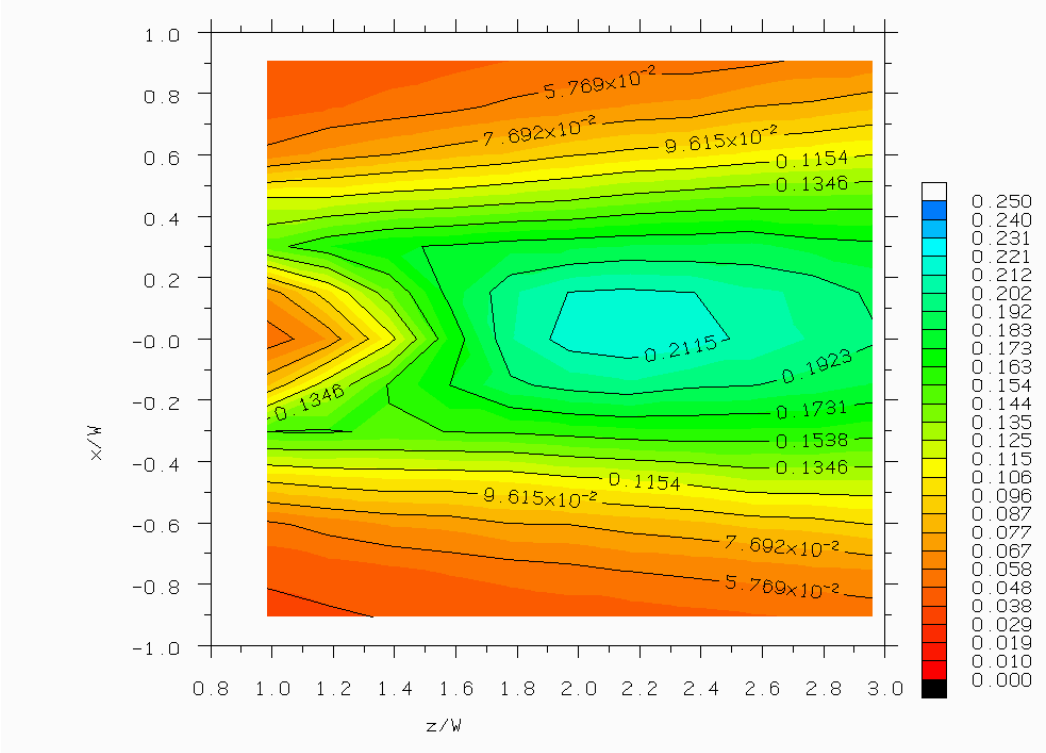

Figure 2.3.7 - Fluctuating cross flow velocity (ux') non-dimensionalised by free stream velocity in the wake of the PARAD2 mode

FIGURES FOR CHAPTER 3 – EXPERIMENTAL RESULTS

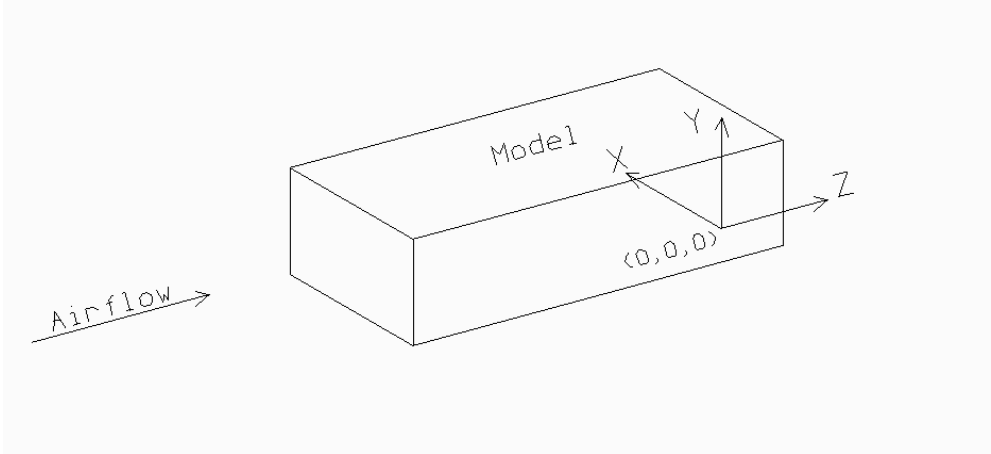

Figure 3.1.1 - Coordinate system

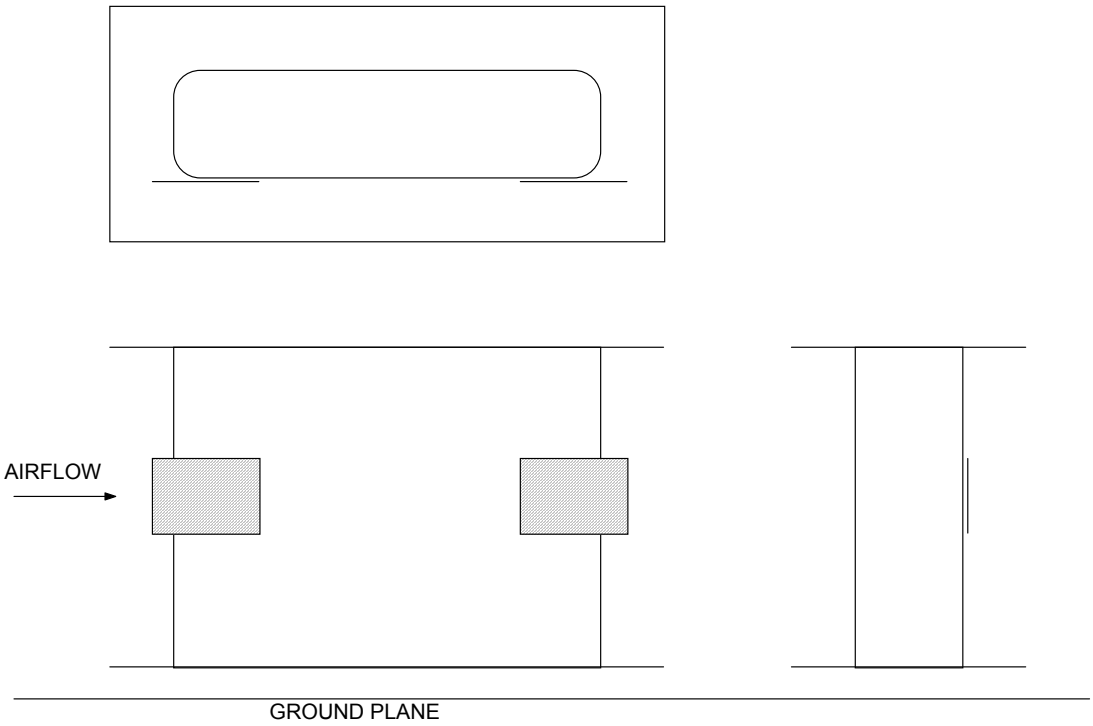

Figure 3.2.1 - Locations of surface oil photographs

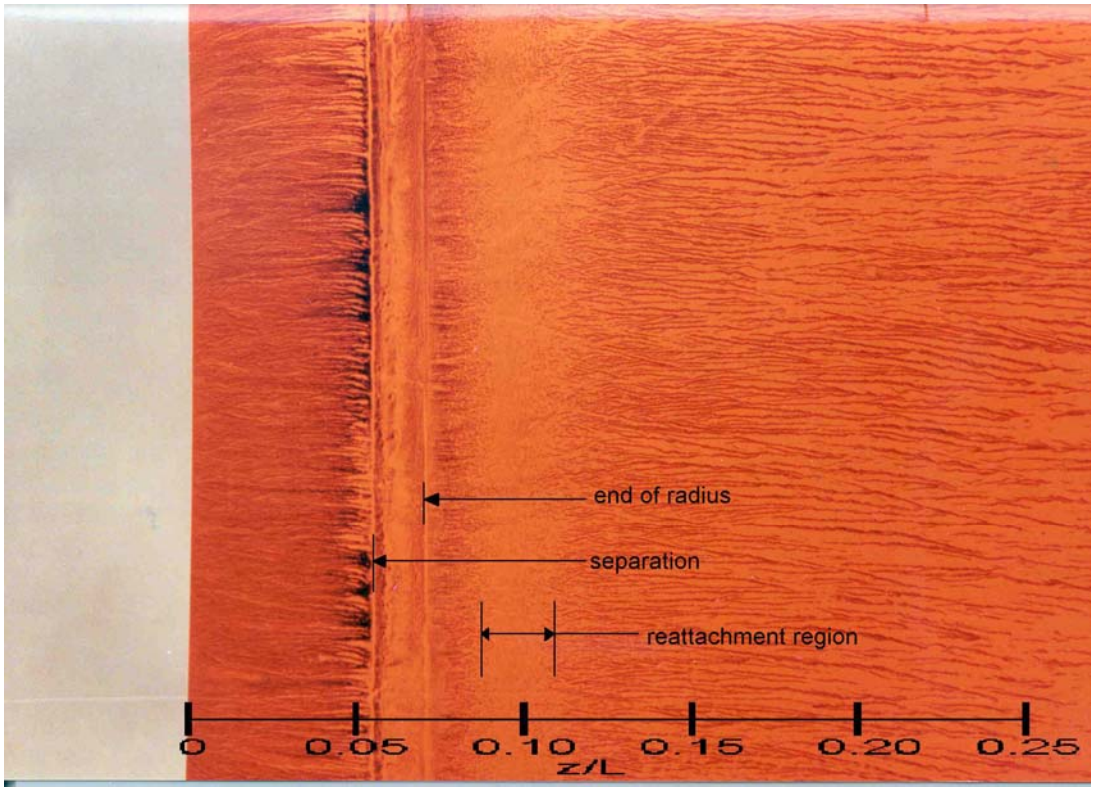

Figure 3.2.2 - Forward radius separation bubble on PARAD1 model

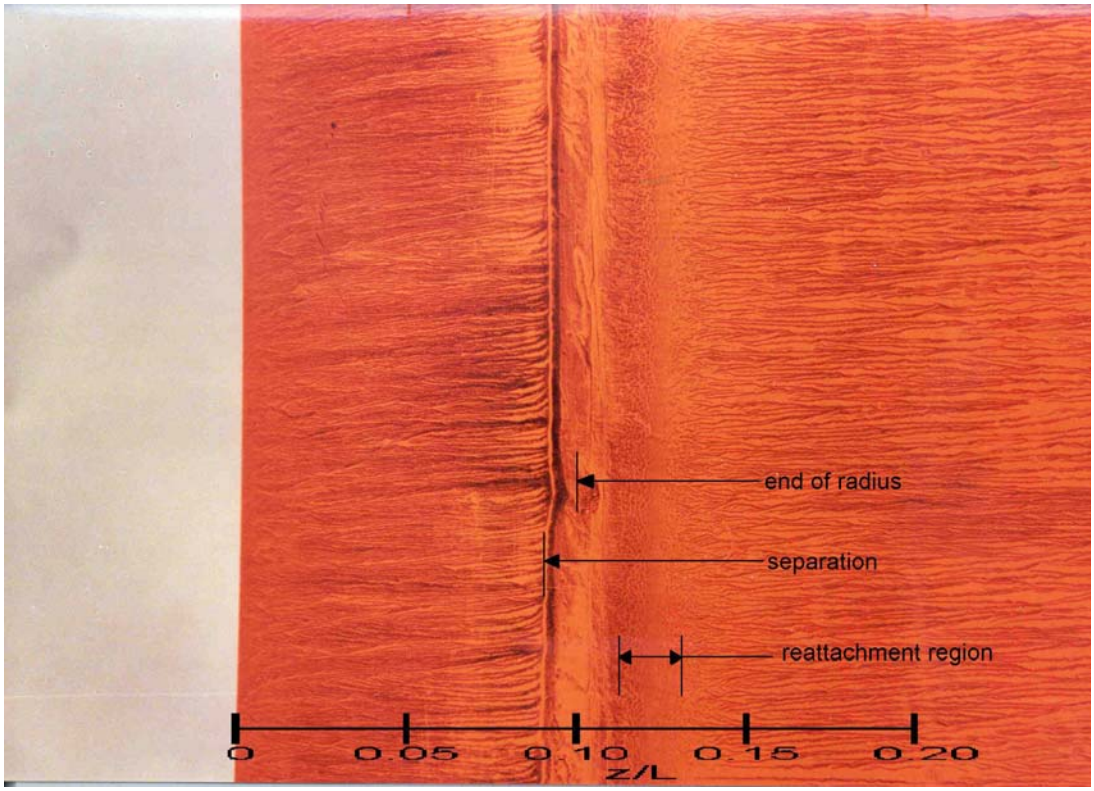

Figure 3.2.3 - Forward radius separation bubble on PARAD2 model

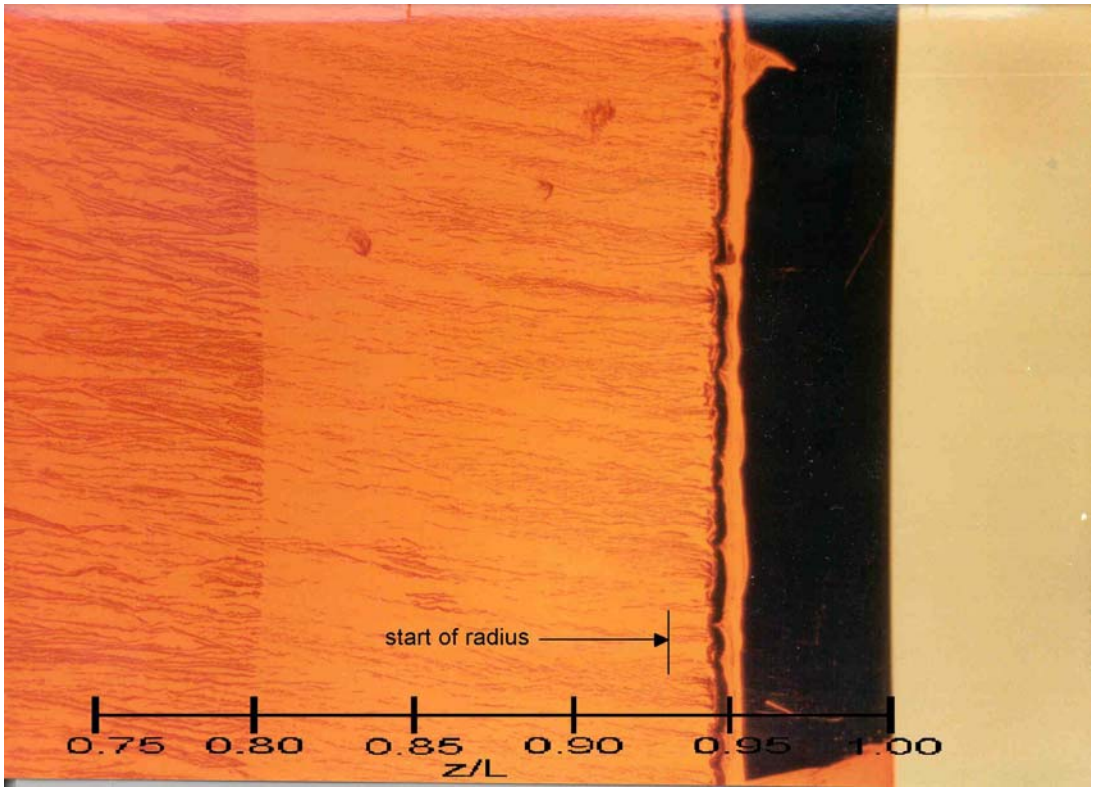

Figure 3.2.4 - Rear separation on PARAD1 model

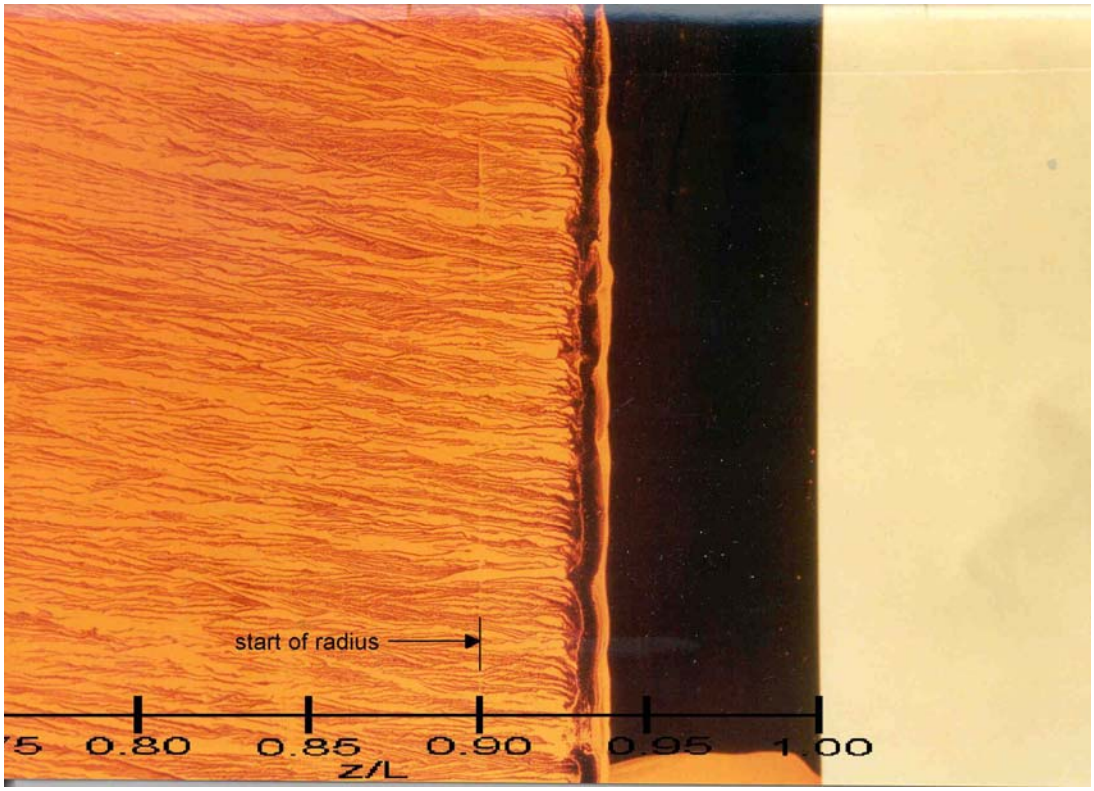

Figure 3.2.5 - Rear separation on PARAD2 model

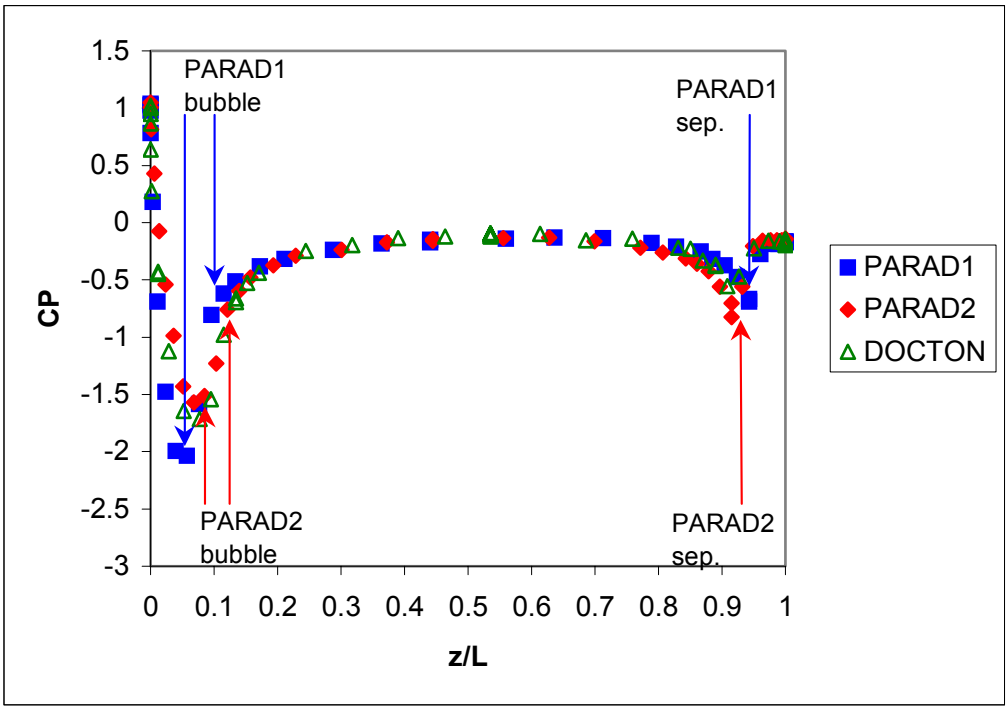

Figure 3.2.6 - Surface pressure distributions for the 2D symmetric models - no trips (separation points from flow visualisation indicated)

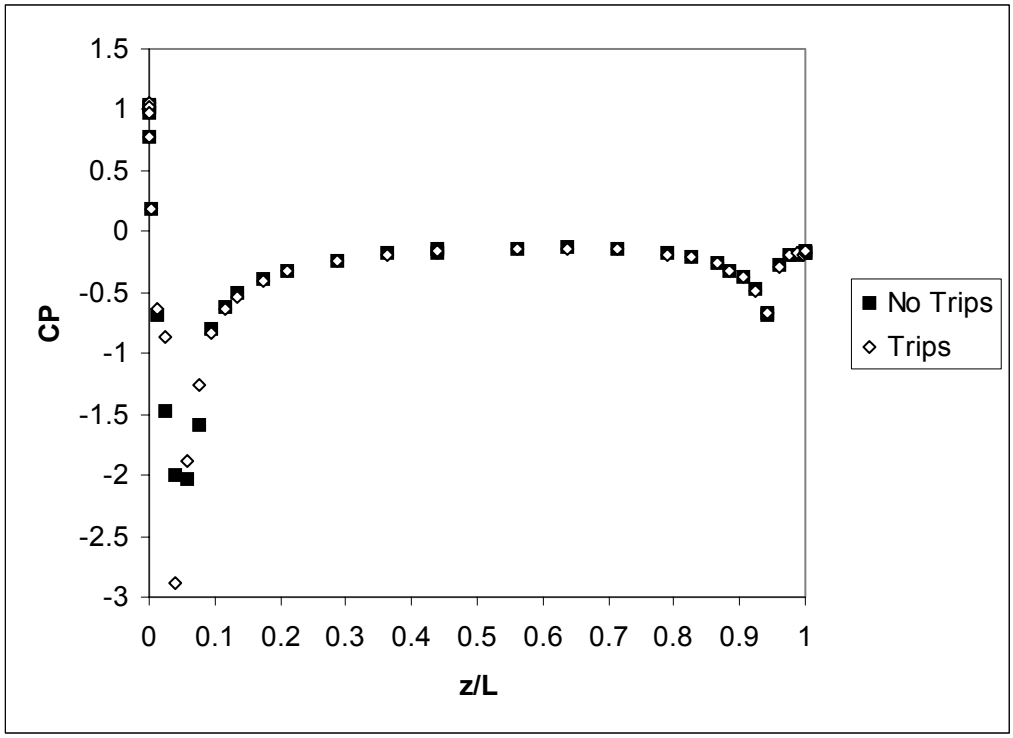

Figure 3.2.7 - Surface pressure distribution for the PARAD1 model – with and without trips

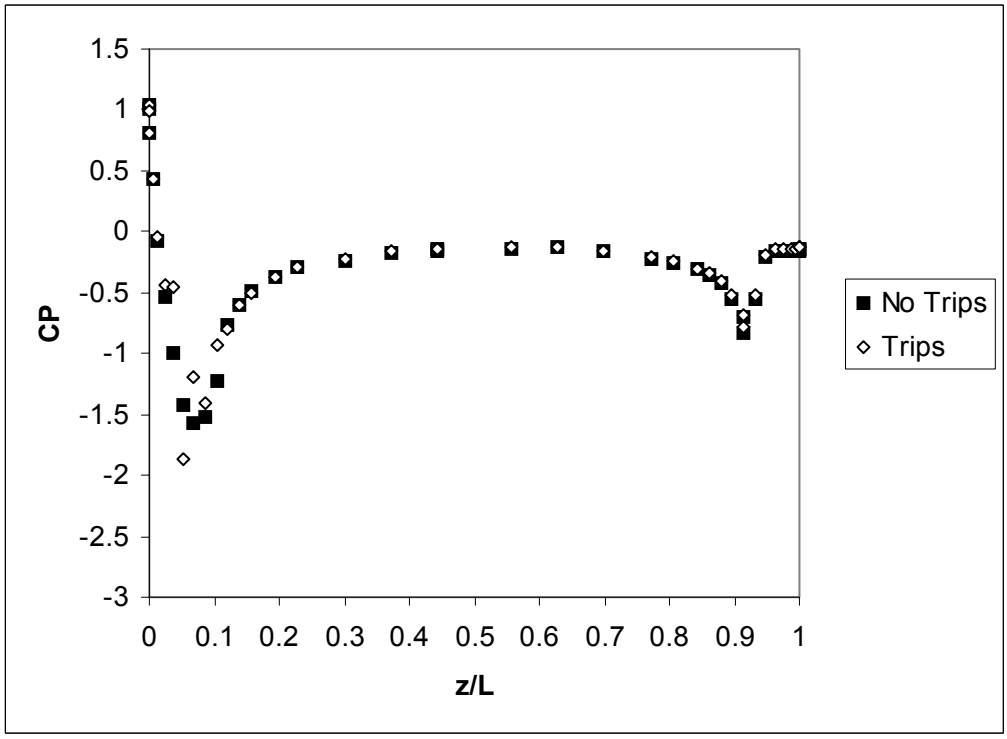

Figure 3.2.8 - Surface pressure distribution for the PARAD2 model – with and without trips

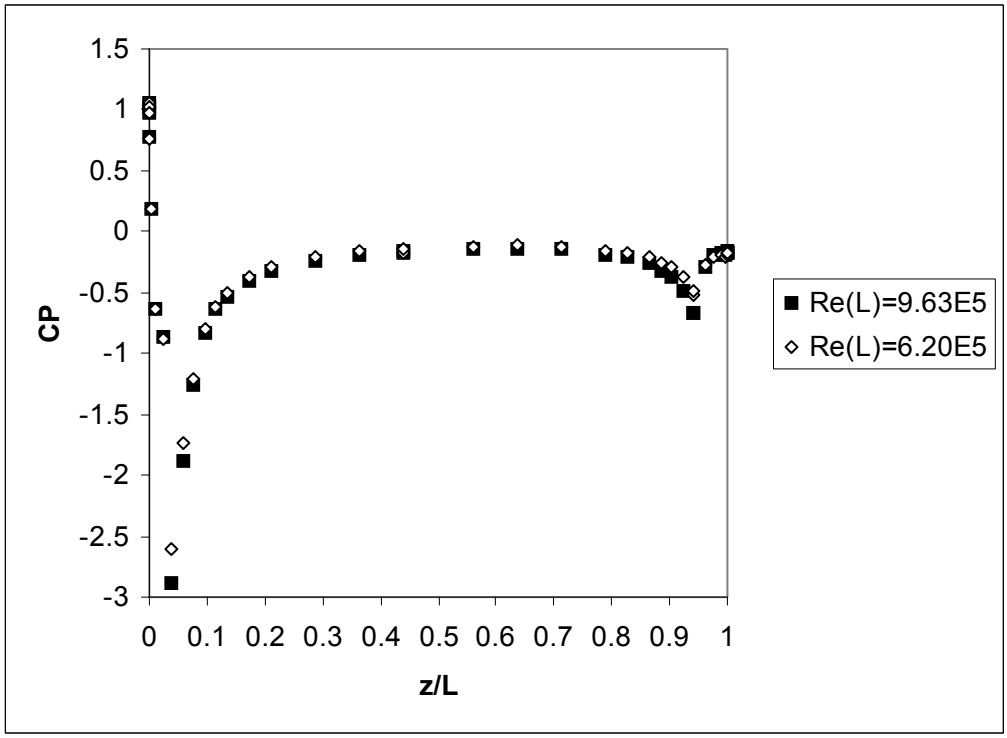

Figure 3.2.9 - Effect of velocity on surface pressure distribution – PARAD1 - with trips

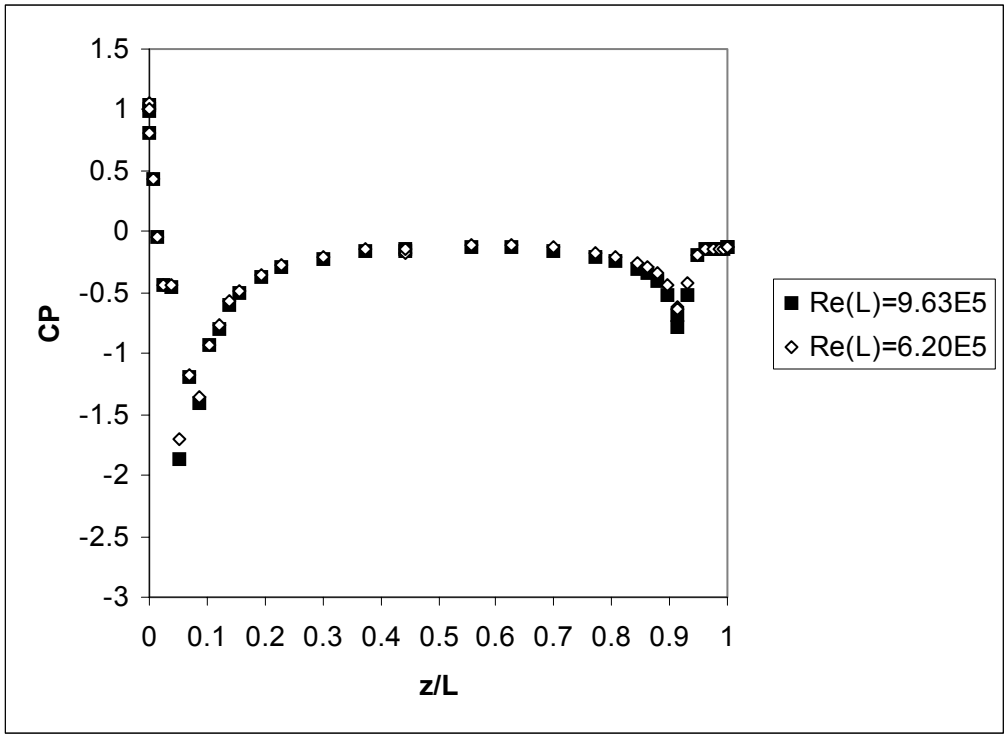

Figure 3.2.10 - Effect of velocity on surface pressure distribution – PARAD2 - with trips

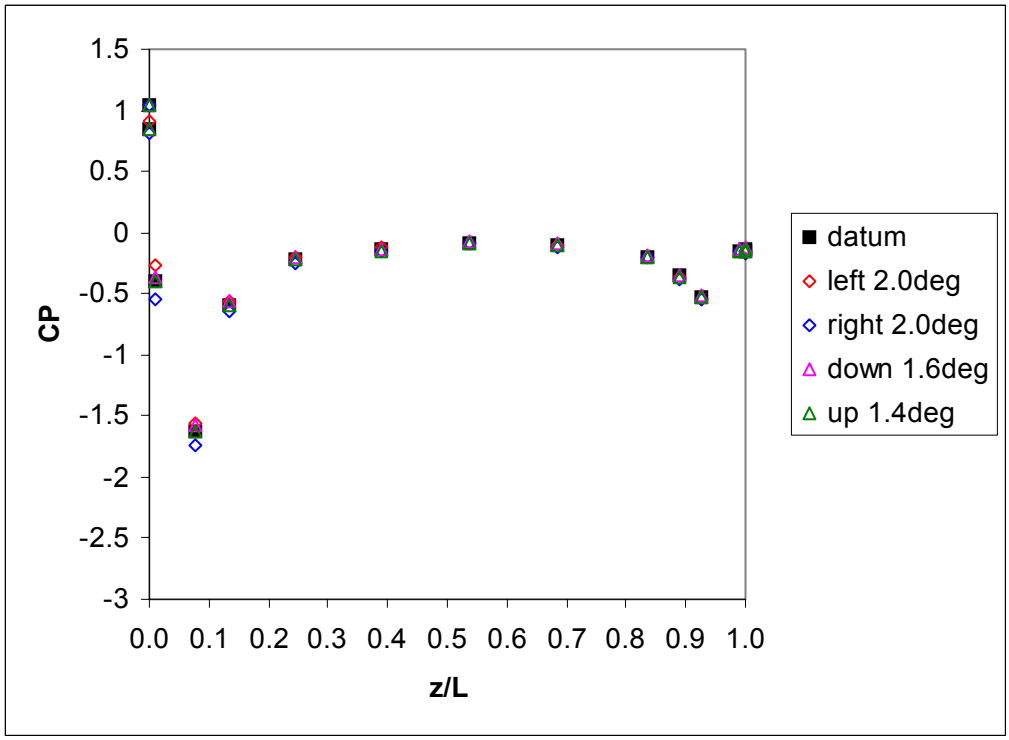

Figure 3.2.11 - Effect of model misalignment on surface pressure distribution – Docton - no trips

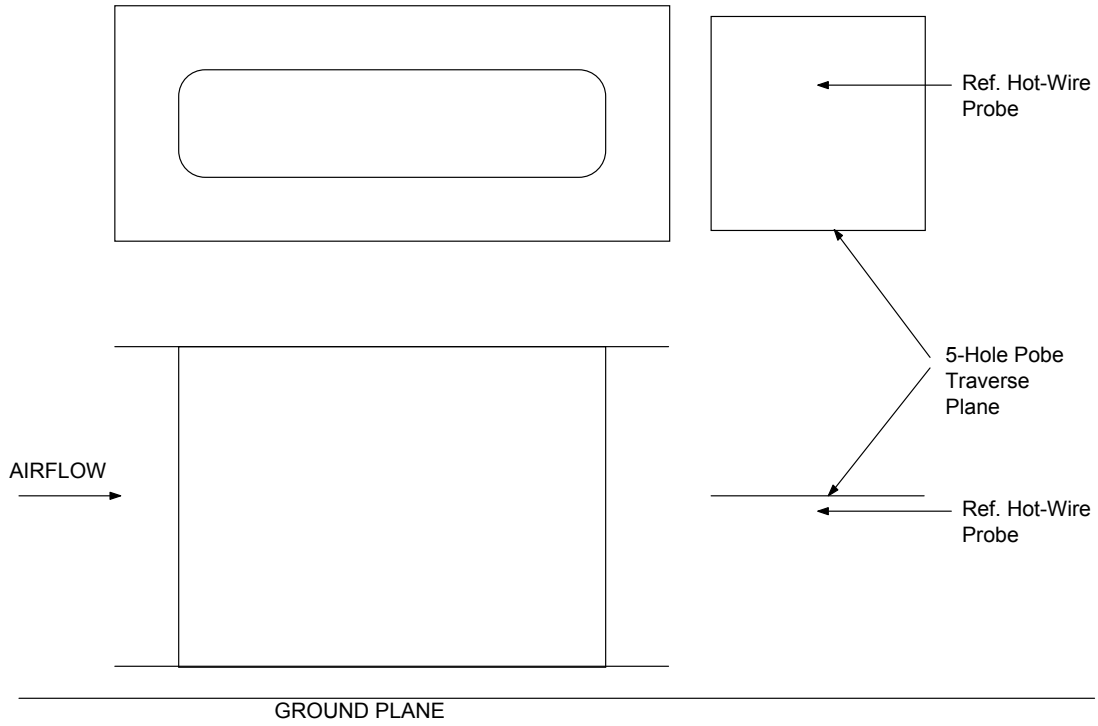

Figure 3.2.12 - Traverse plane and reference hot-wire location (for unsteady work)

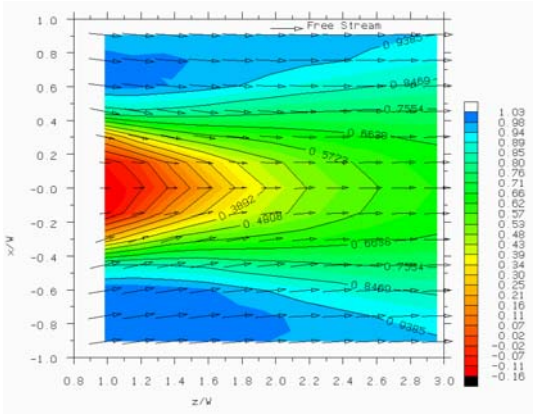

Figure 3.2.13 - Total pressure coefficient and velocity vectors in the wake of the PARAD1 model

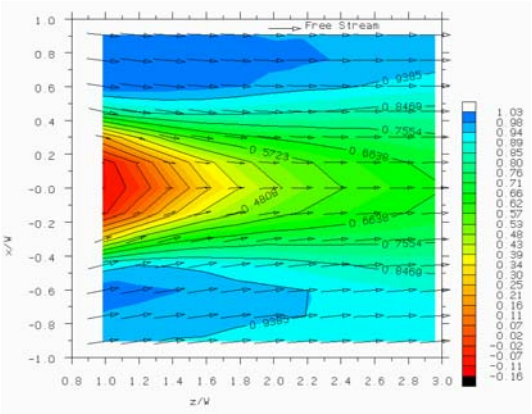

Figure 3.2.14 - Total pressure coefficient and velocity vectors in the wake of the PARAD2 model

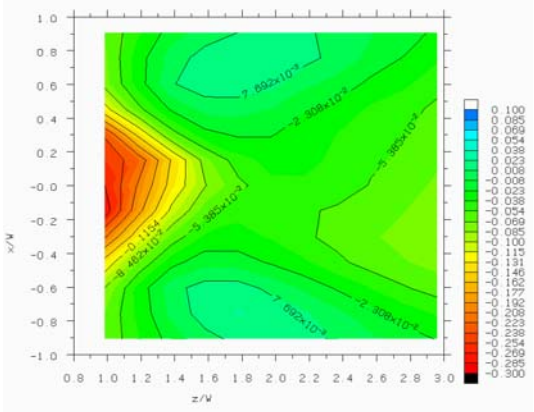

Figure 3.2.15 - Static pressure coefficient in the wake of the PARAD1 model

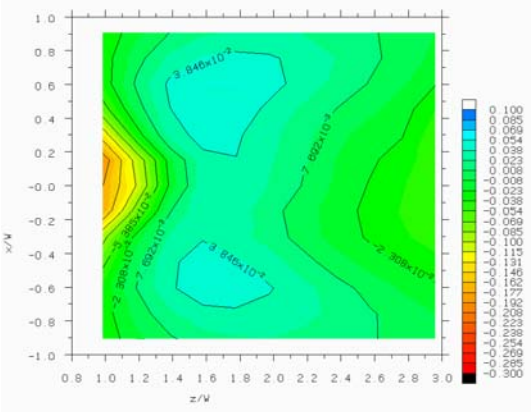

Figure 3.2.16 - Static pressure coefficient in the wake of the PARAD2 model

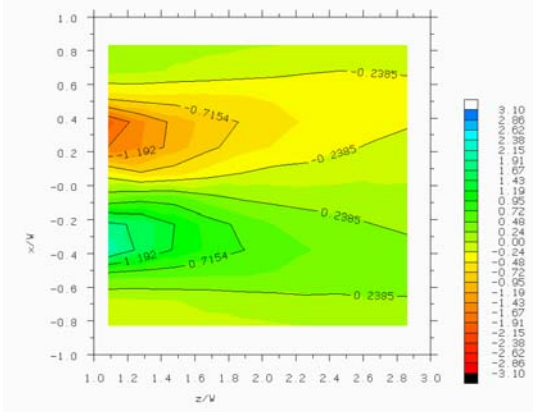

Figure 3.2.17 - Vorticity contours in the wake of the PARAD1 model (non-dimensionalised by free-stream velocity and W)

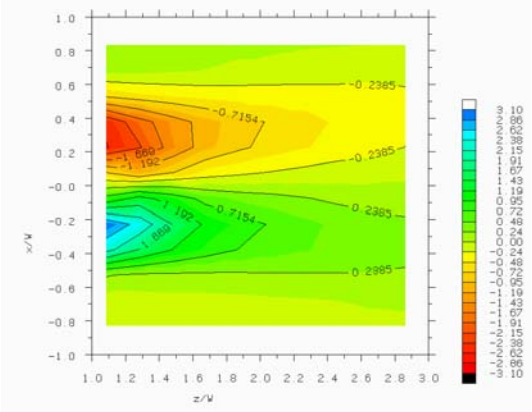

Figure 3.2.18 - Vorticity contours in the wake of the PARAD2 model (non-dimensionalised by free-stream velocity and W)

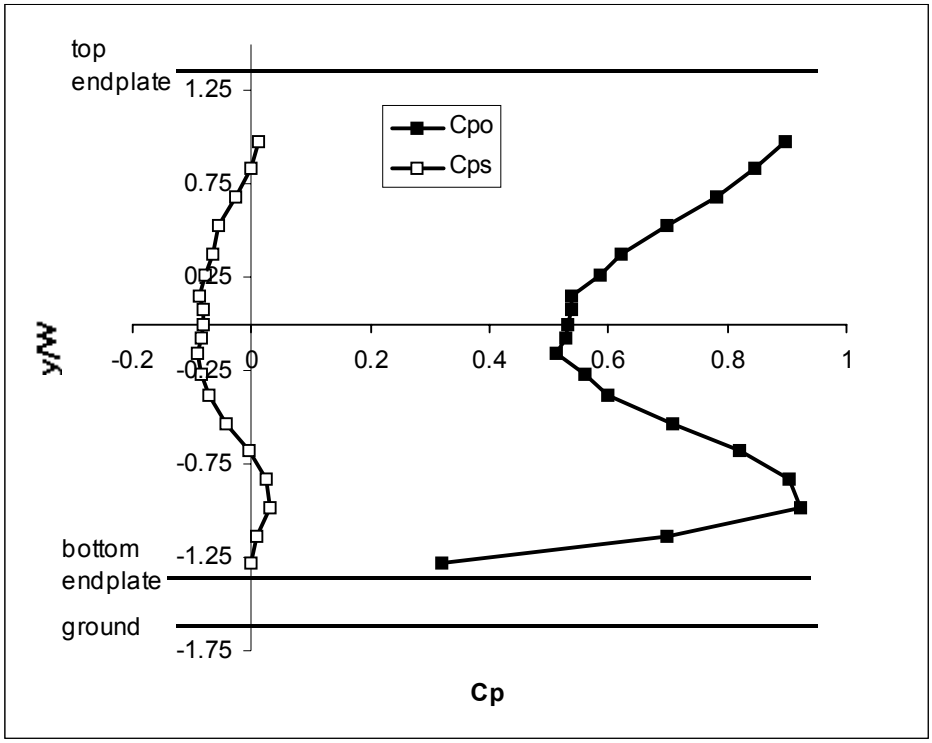

Figure 3.2.19 - Total and static pressure distributions in "spanwise" direction at x/W=-0.3, z/W=2.0 in the wake of the PARAD1 model

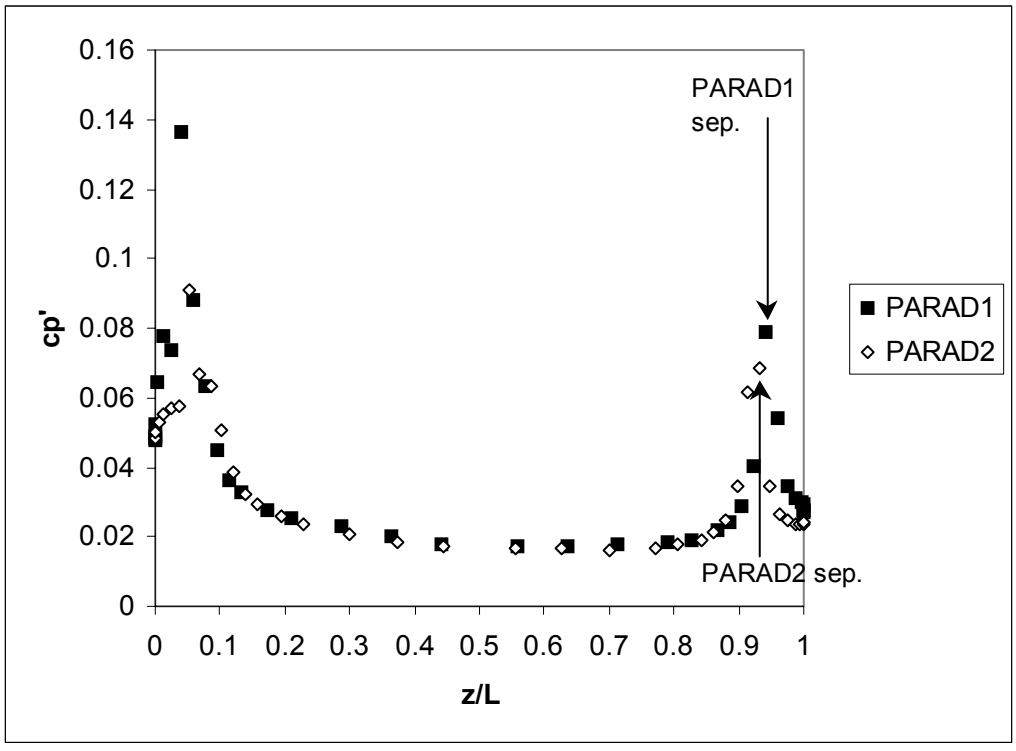

Figure 3.2.20 - Surface pressure coefficient fluctuation (standard deviation) for the PARAD models (separation points from oil-flow visualisation indicated

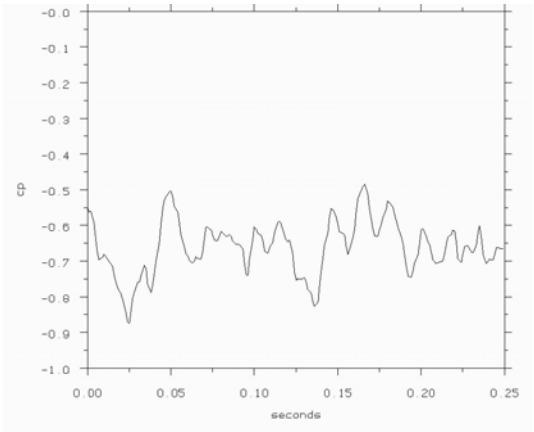

Figure 3.2.21 - Time-trace of fluctuating pressure coefficient at z/L=0.94 on the surface of the PARAD1 model

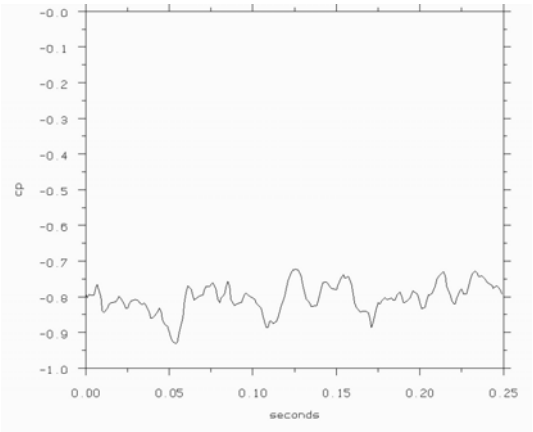

Figure 3.2.22 - Time-trace of fluctuating pressure coefficient at z/L=0.91 on the surface of the PARAD2 model

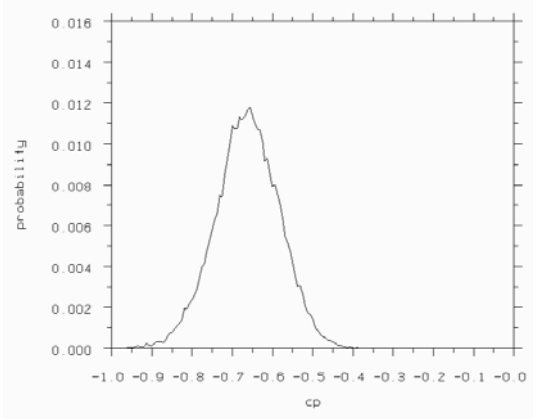

Figure 3.2.23 - Probability density function for fluctuating pressure coefficient at z/L=0.94 on the surface of the PARAD1 model

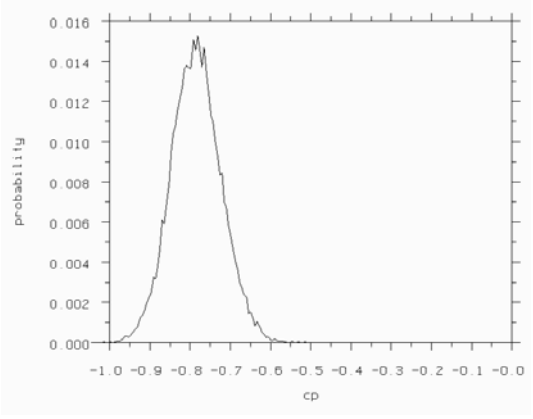

Figure 3.2.24 - Probability density function for fluctuating pressure coefficient at z/L=0.91 on the surface of the PARAD2 model

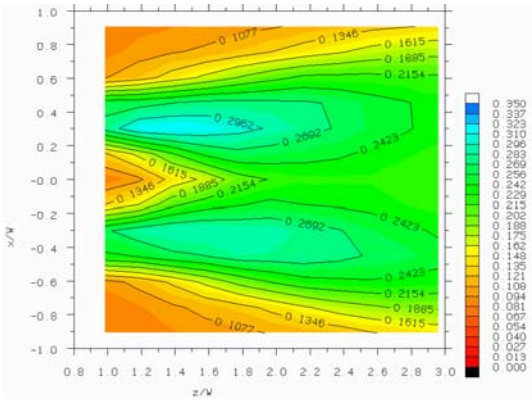

Figure 3.2.25 - Fluctuating total pressure coefficient (standard deviation) in the wake of the PARAD1 model

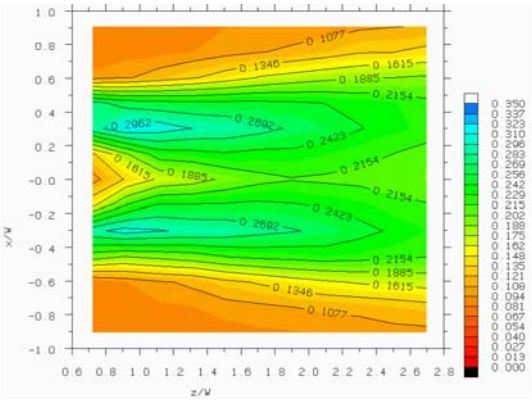

Figure 3.2.26 - Fluctuating total pressure coefficient (standard deviation) in the wake of the PARAD2 model

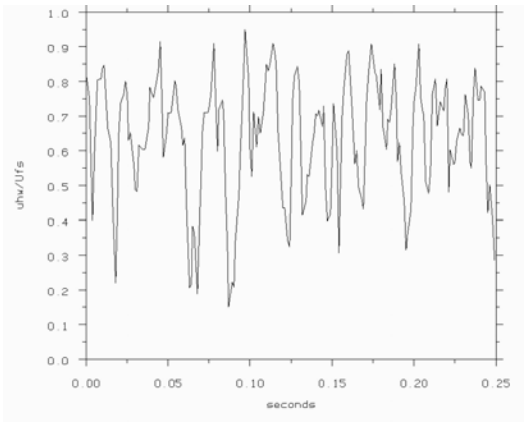

Figure 3.2.27 - Time-trace of hot-wire velocity in the wake of the PARAD1 model at x/W= 0.3, z/W = 2.0

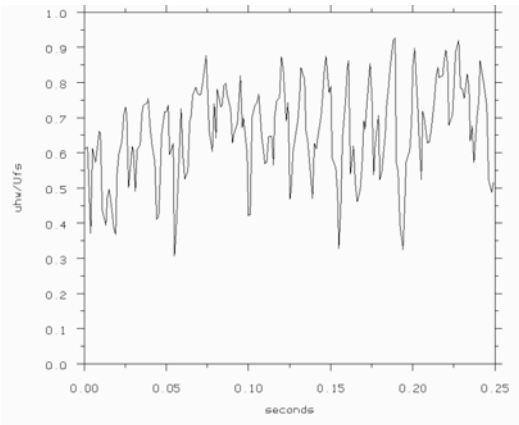

Figure 3.2.28 - Time-trace of hot-wire velocity in the wake of the PARAD2 model at x/W= 0.3, z/W = 2.0

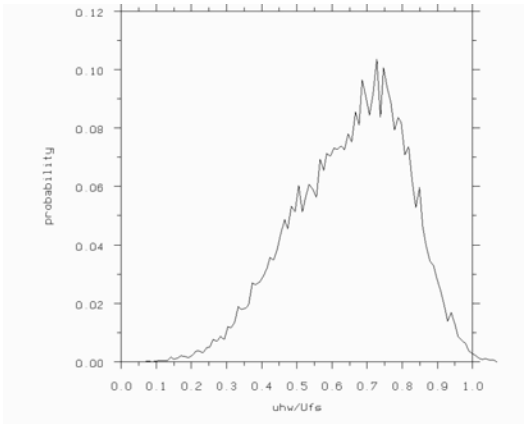

Figure 3.2.29 - Probability density function for fluctuating hot-wire velocity in the wake of the PARAD1 model at x/W= 0.3, z/W = 2.0

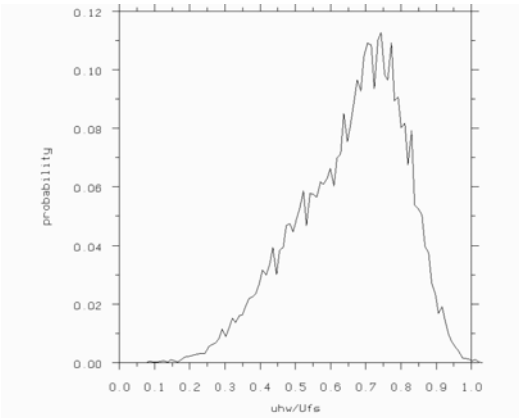

Figure 3.2.30 - Probability density function for fluctuating hot-wire velocity in the wake of the PARAD2 model at x/W= 0.3, z/W = 2.0

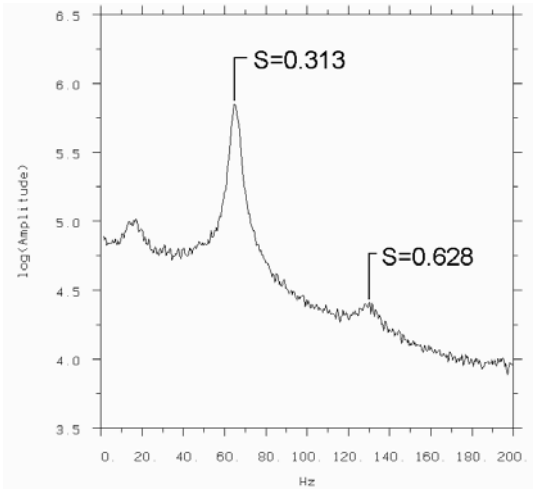

Figure 3.2.31 - Autospectral density of hot-wire velocity in the wake of the PARAD1 model at x/W= 0.3, z/W = 2.0

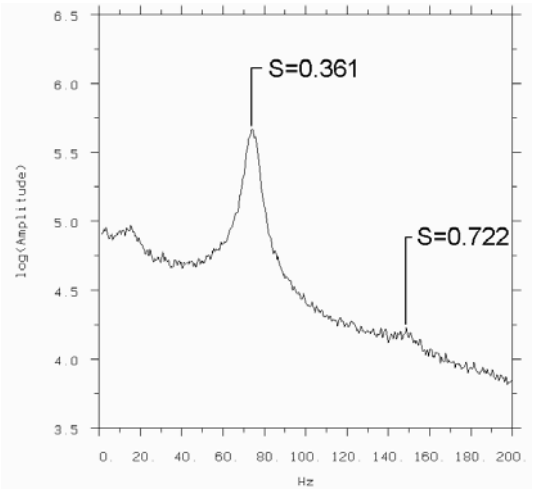

Figure 3.2.32 - Autospectral density of hot-wire velocity in the wake of the PARAD2 model at x/W= 0.3, z/W = 2.0

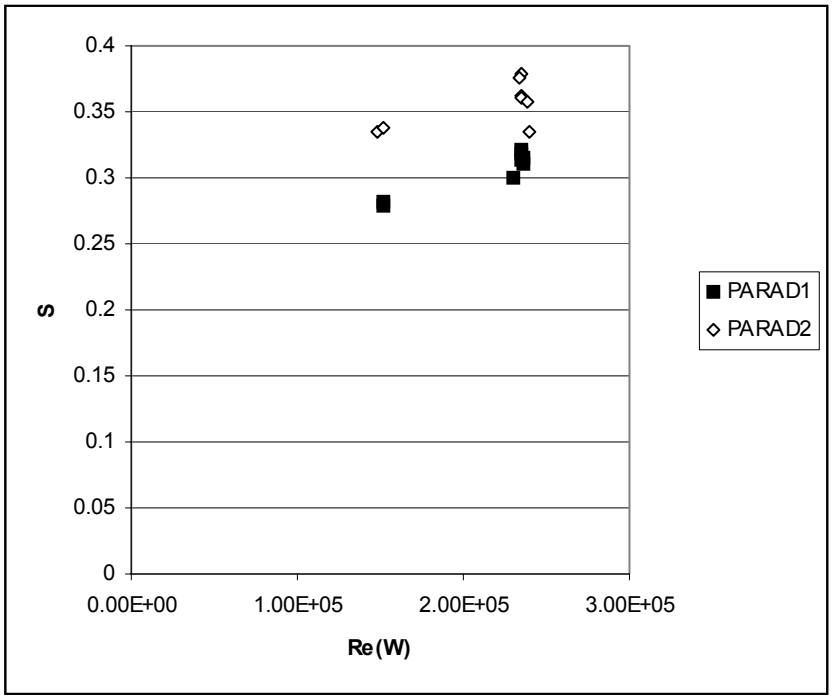

Figure 3.2.33 - Effect of Reynolds number on Strouhal number for PARAD models

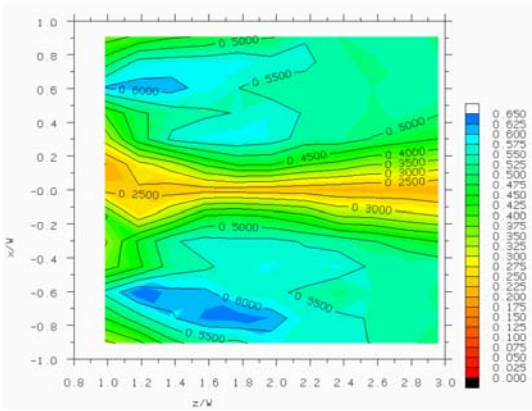

Figure 3.2.34 - Fraction of total pressure coefficient fluctuation due to unsteadiness near S=0.31 (shedding frequency) (S=0.281-0.332, f=55-65hz) in the wake of the PARAD1 model

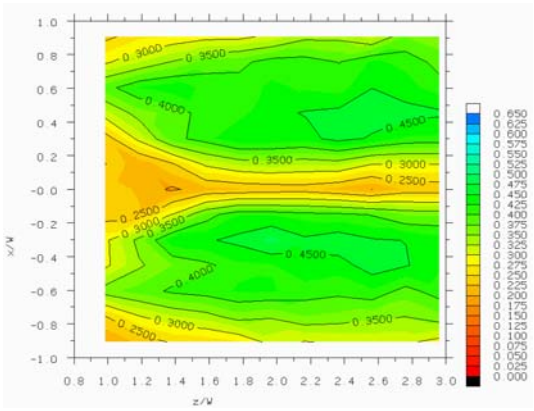

Figure 3.2.36 - Fraction of total pressure coefficient fluctuation due to unsteadiness near S=0.34 (shedding frequency) (S=0.312-0.361, f=65-75hz) in the wake of the PARAD2 model

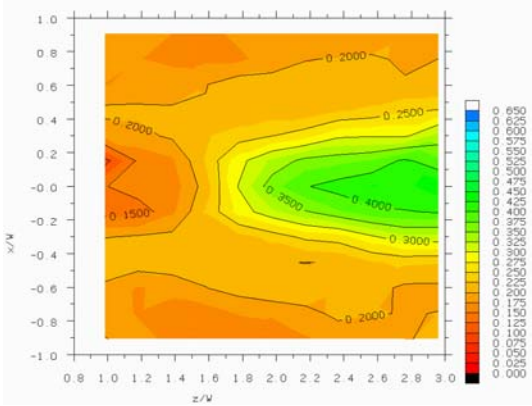

Figure 3.2.35 - Fraction of total pressure coefficient fluctuation due to unsteadiness near S=0.62 (twice shedding frequency) (S=0.562-0.664, f=110-130hz) in the wake of the PARAD1 model

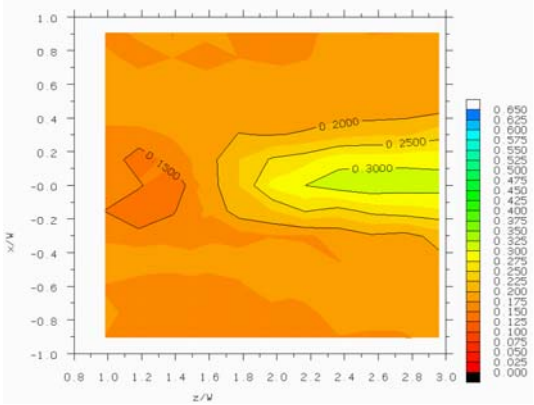

Figure 3.2.37 - Fraction of total pressure coefficient fluctuation due to unsteadiness near S=0.68 (twice shedding frequency) (S=0.624-0.722, f=130-150hz) in the wake of the PARAD2 model

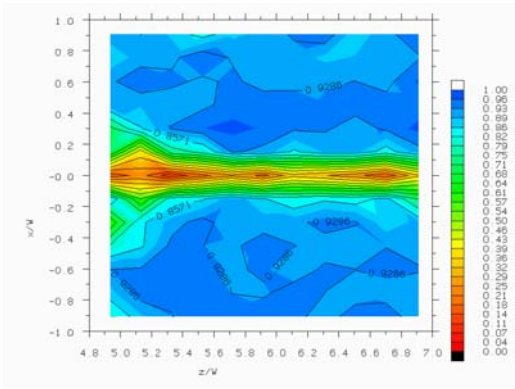

Figure 3.2.38 - Coherence at the shedding frequency between fixed hot-wire and total pressure in the wake of the PARAD1 model

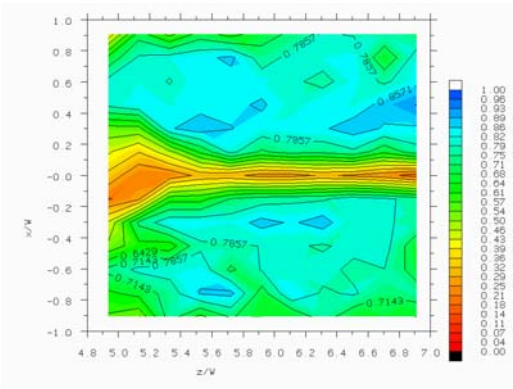

Figure 3.2.39 - Coherence at the shedding frequency between fixed hot-wire and total pressure in the wake of the PARAD2 model

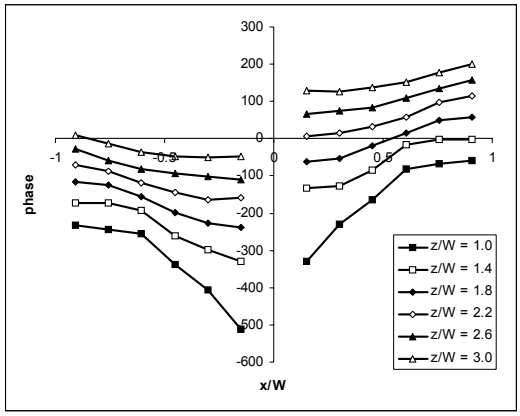

Figure 3.2.40 - Cross-spectral phase at the shedding frequency between fixed hot-wire and total pressure in the wake of the PARAD1 model

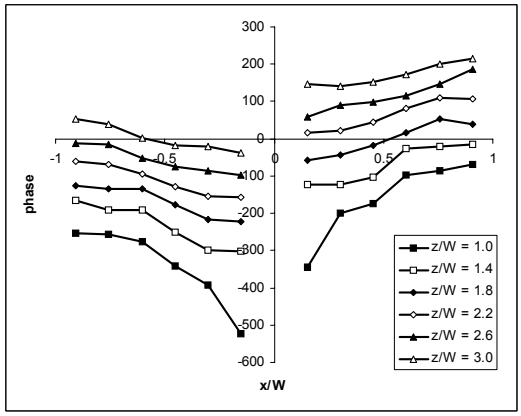

Figure 3.2.41 - Cross-spectral phase at the shedding frequency between fixed hot-wire and total pressure in the wake of the PARAD2 model

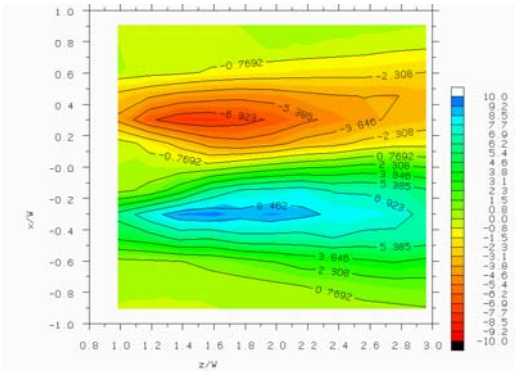

Figure 3.2.42 - $\overline{ux'uz'}$ near S=0.31 (shedding frequency) (S=0.281-0.332, f=55-65hz) in the wake of the PARAD1 model

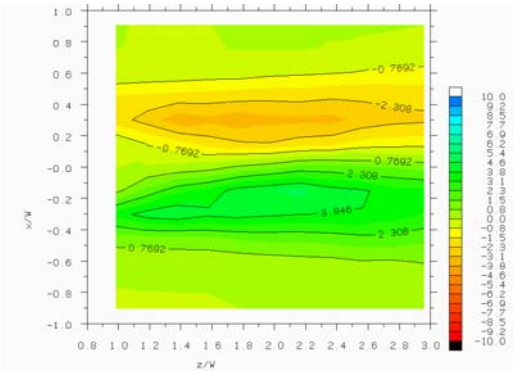

Figure 3.2.43 - $\overline{ux'uz'}$ near S=0.34 (shedding frequency) (S=0.312-0.361, f=65-75hz) in the wake of the PARAD2 model

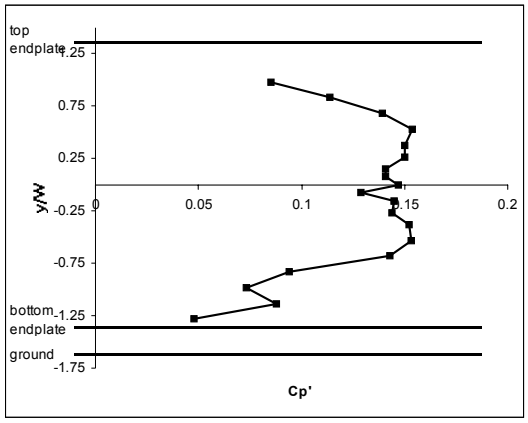

Figure 3.2.44 – Spanwise distribution of fluctuating pressure coefficient at centre hole of 5-hole probe (not corrected for transfer function) along x=-0.30, z/2.0 in the wake of the PARAD1 model

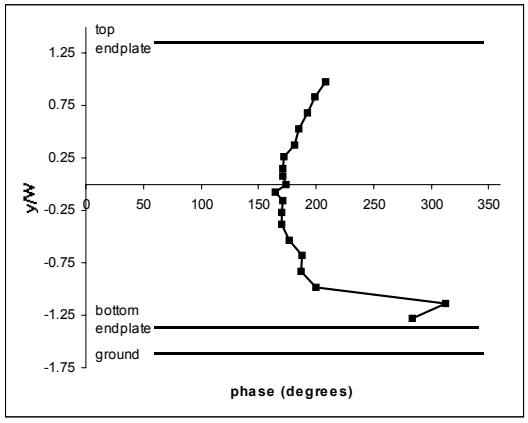

Figure 3.2.45 – Spanwise distribution of cross-spectral phase between total pressure along x/W=-0.30, z/W=2.0 and hot-wire at x/W=0.30, y/W=0.0, z/W=2.0 in the wake of the PARAD1 model

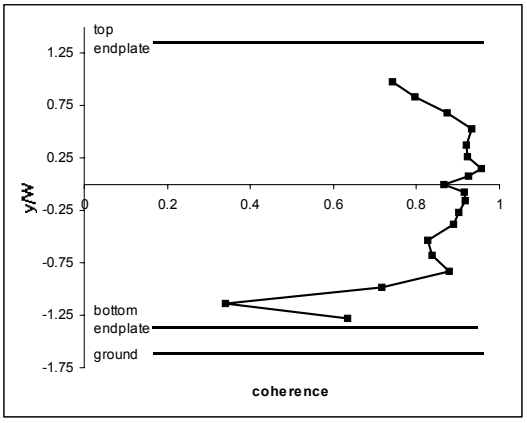

Figure 3.2.46 - Spanwise distribution of coherence between total pressure along x/W=-0.30, z/W=2.0 and hot-wire at x/W=0.30, y/W=0.0, z/W=2.0 in the wake of the PARAD1 model

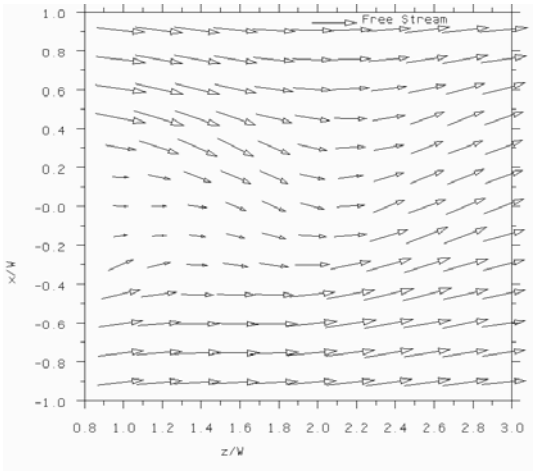

a) t=0.0s, t/T=0.0

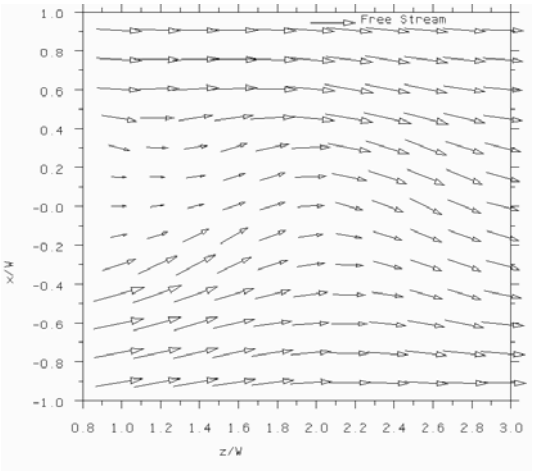

d) t=0.0077s, t/T=0.462

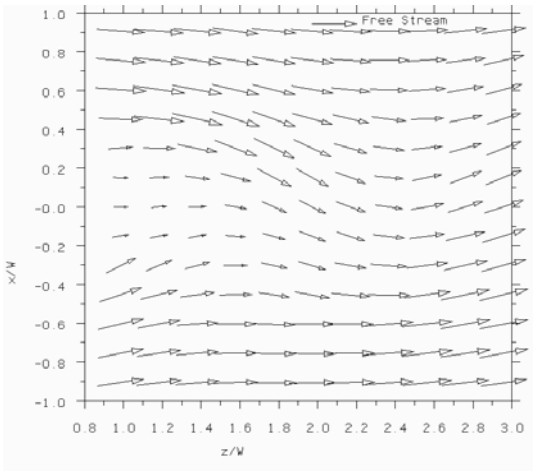

b) t=0.0026s, t/T=0.154

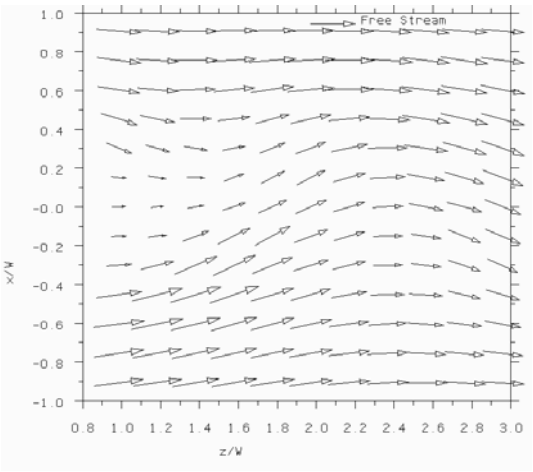

e) t=0.0103s, t/T=0.615

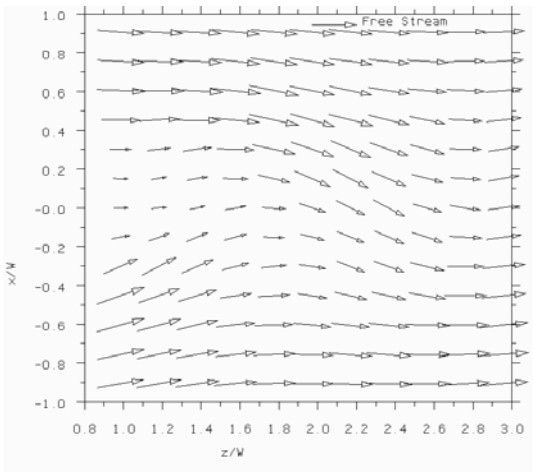

c) t=0.0051s, t/T=0.308

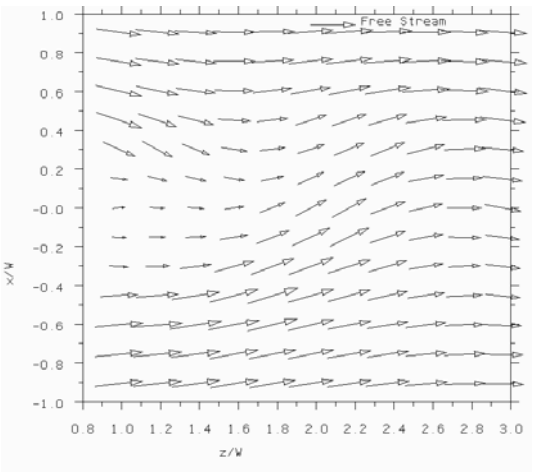

f) t=0.0128s, t/T=0.769

Figure 3.2.47 - Sequence showing velocity vectors reconstructed from shedding frequency and first harmonic (1.5hz bands) in the wake of the PARAD1 model

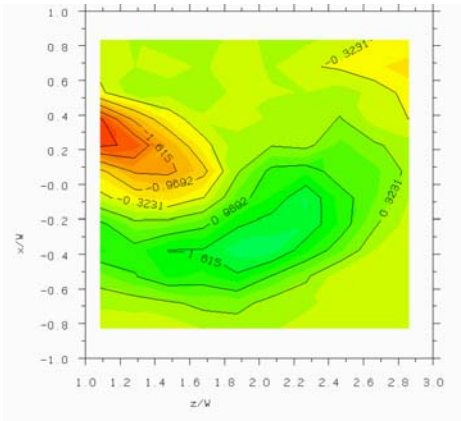

a) t=0.0s, t/T=0.0

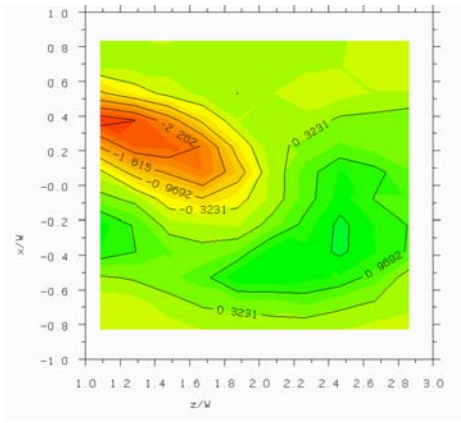

b) t=0.0026s, t/T=0.154

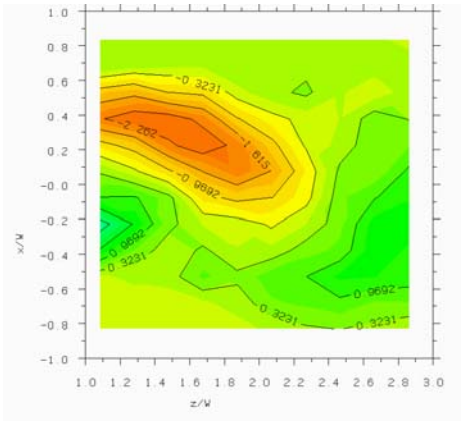

c) t=0.0051s, t/T=0.308

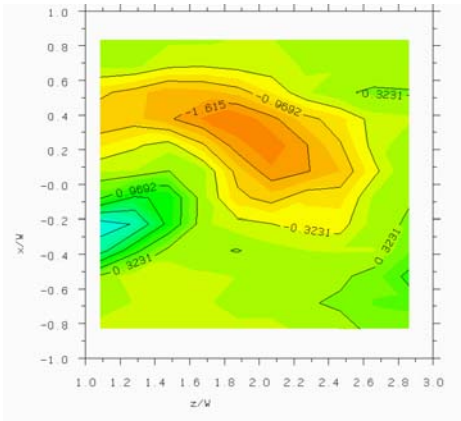

d) t=0.0077s, t/T=0.462

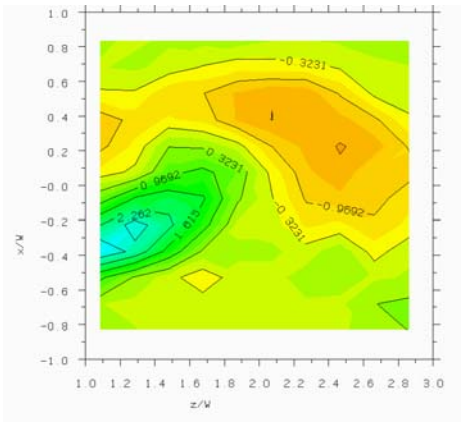

e) t=0.0103s, t/T=0.615

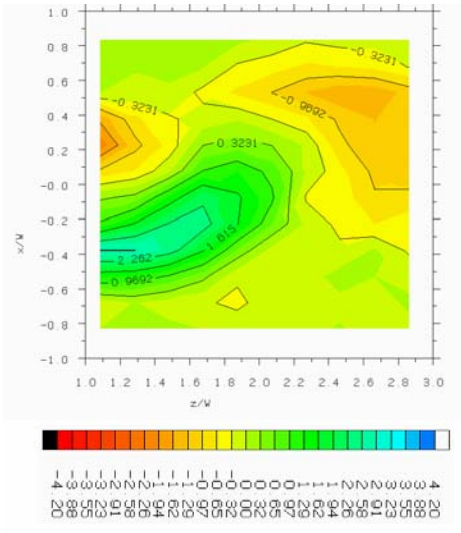

f) t=0.0128s, t/T=0.769

Figure 3.2.48 - Sequence showing vorticity (non-dimensionalised by free stream velocity and model width) reconstructed from shedding frequency and first harmonic (1.5hz bands) in the wake of the PARAD1 model

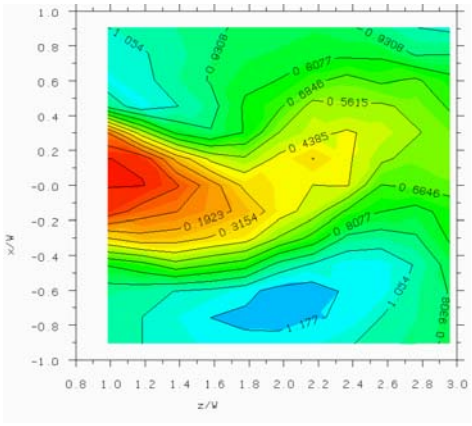

a) t=0.0s, t/T=0.0

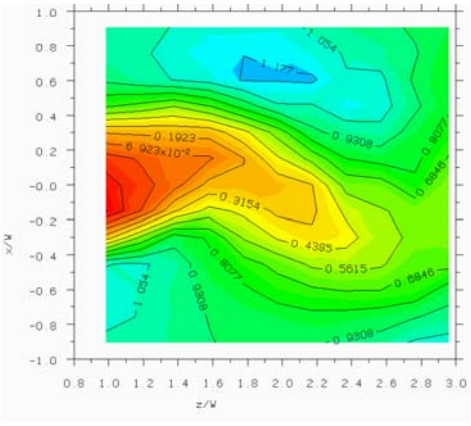

d) t=0.0077s, t/T=0.462

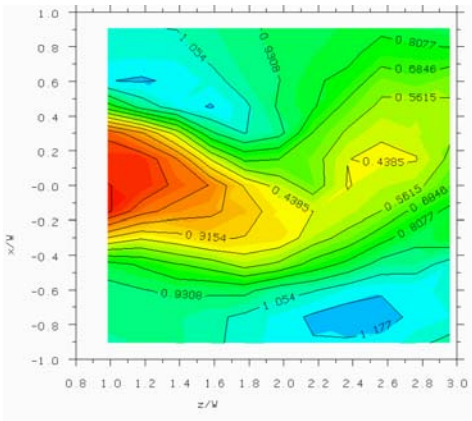

b) t=0.0026s, t/T=0.154

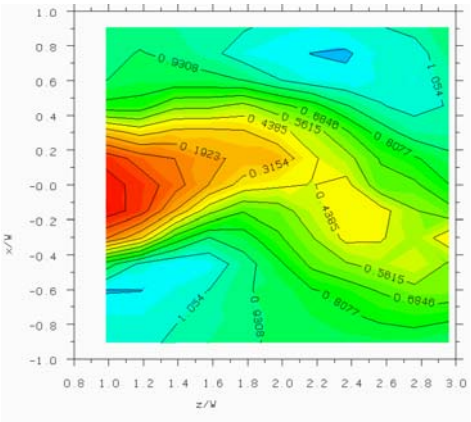

e) t=0.0103s, t/T=0.615

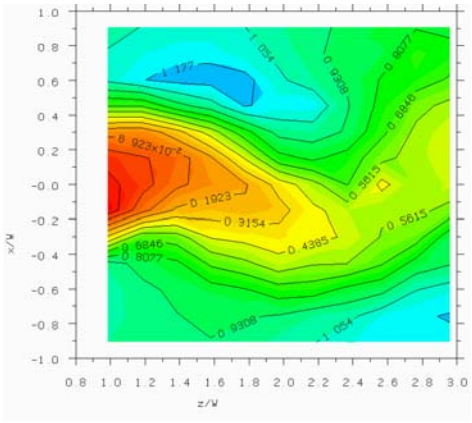

c) t=0.0051s, t/T=0.308

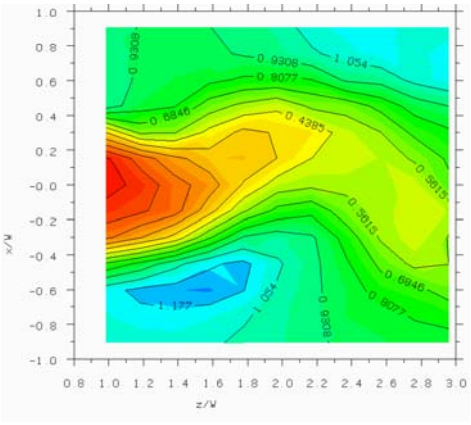

f) t=0.0128s, t/T=0.769

Figure 3.2.49 - Sequence showing total pressure coefficient reconstructed from shedding frequency and first harmonic (1.5hz bands) in the wake of the PARAD1 model

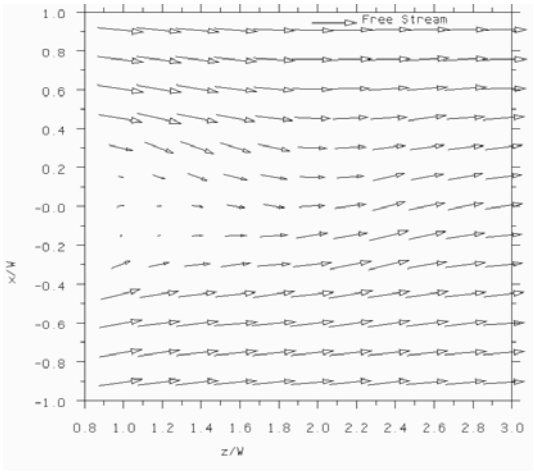

a) t=0.0s, t/T=0.0

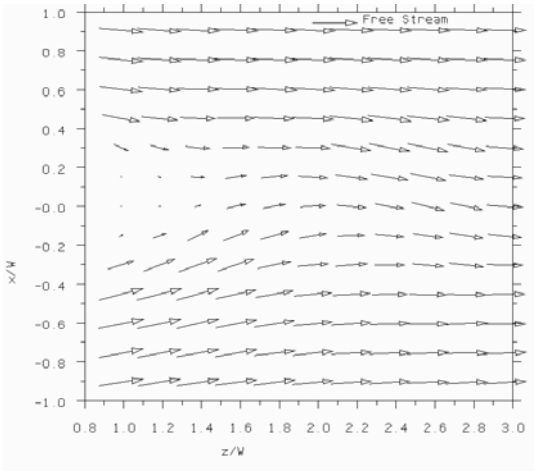

d) t=0.0078s, t/T=0.545

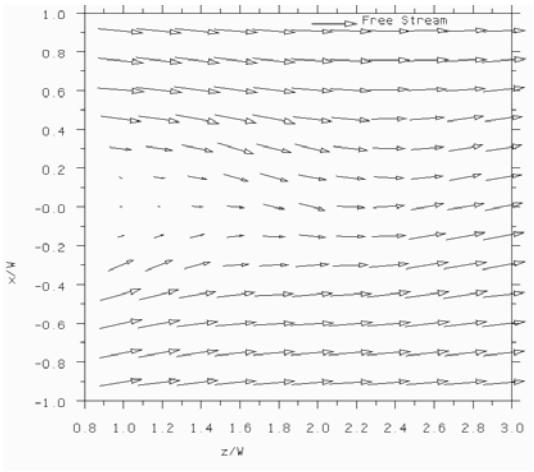

b) t=0.0026s, t/T=0.182

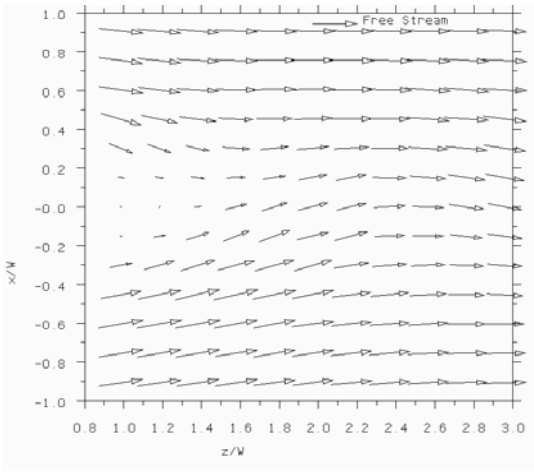

e) t=0.0104s, t/T=0.727

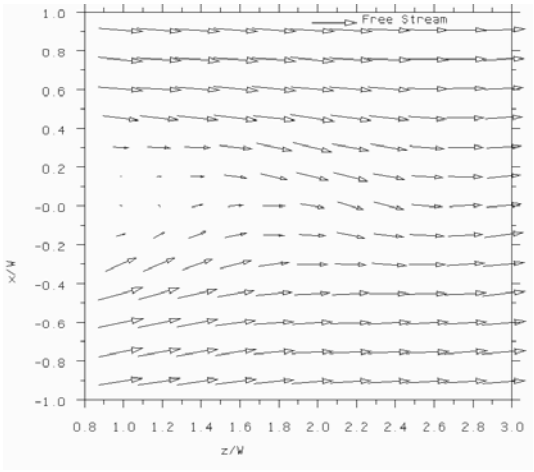

c) t=0.0052s, t/T=0.364

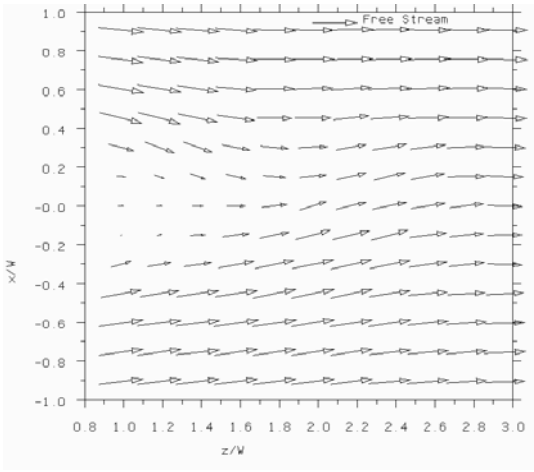

f) t=0.0130s, t/T=0.909

Figure 3.2.50 - Sequence showing velocity vectors reconstructed from shedding frequency and first harmonic (1.5hz bands) in the wake of the PARAD2 model

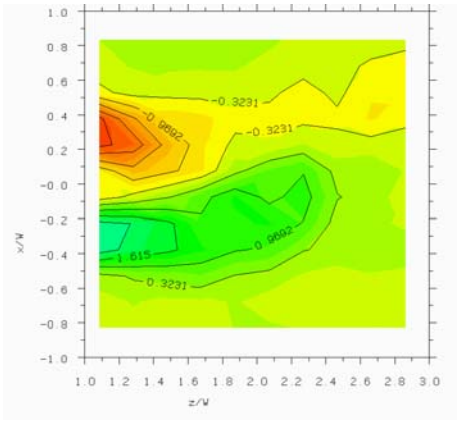

a) t=0.0s, t/T=0.0

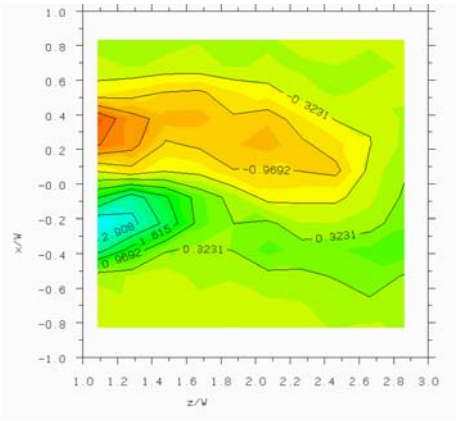

d) t=0.0078s, t/T=0.545

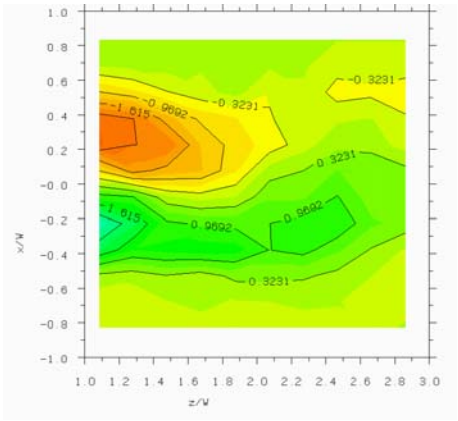

b) t=0.0026s, t/T=0.182

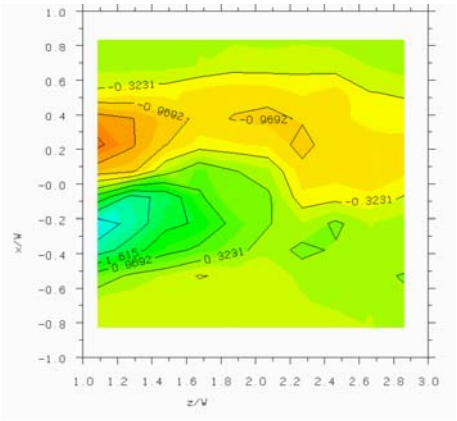

e) t=0.0104s, t/T=0.727

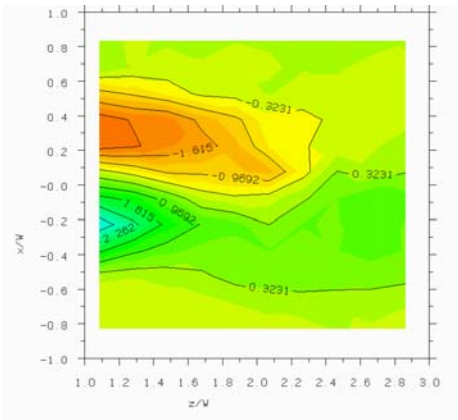

c) t=0.0052s, t/T=0.364

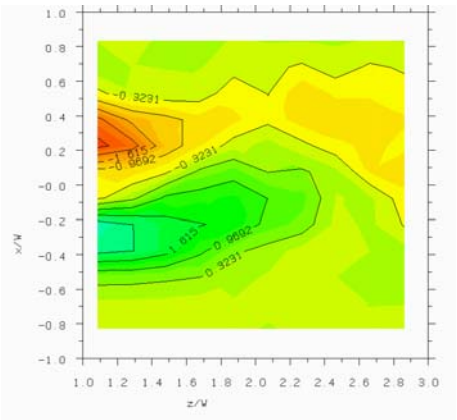

f) t=0.0130s, t/T=0.9

Figure 3.2.51 - Sequence showing vorticity (non-dimensionalised by free stream velocity and model width) reconstructed from shedding frequency and first harmonic (1.5hz bands) in the wake of the PARAD2 model

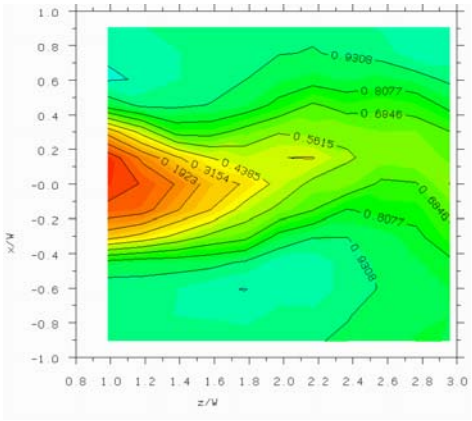

a) t=0.0s, t/T=0.0

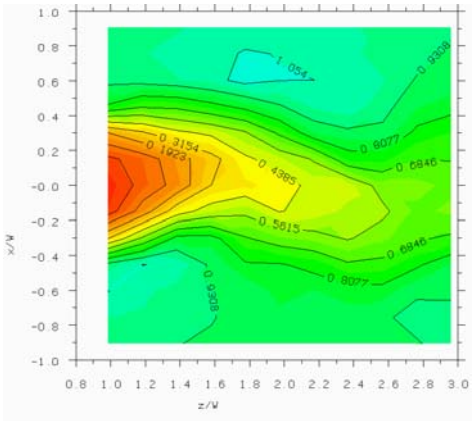

d) t=0.0078s, t/T=0.545

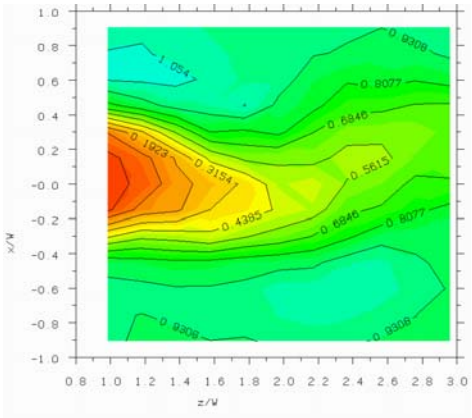

b) t=0.0026s, t/T=0.182

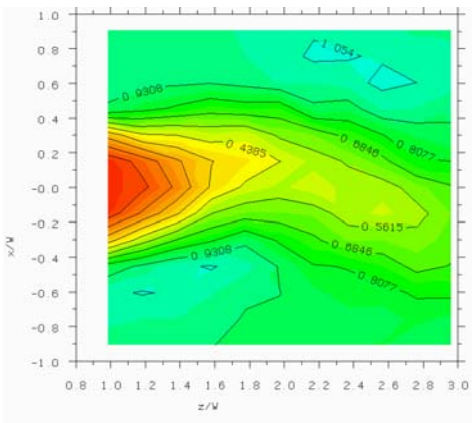

e) t=0.0104s, t/T=0.727

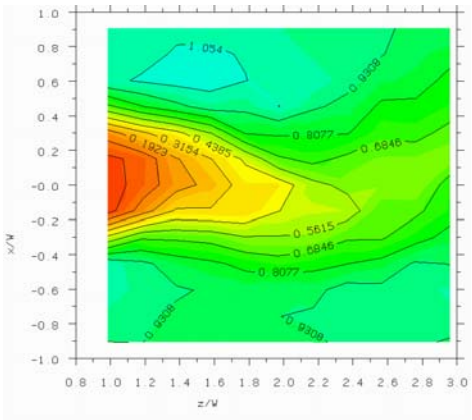

c) t=0.0052s, t/T=0.364

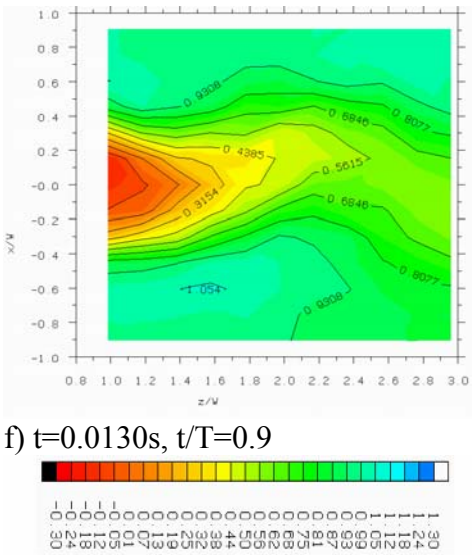

f) t=0.0130s, t/T=0.9

Figure 3.2.52 - Sequence showing total pressure coefficient reconstructed from shedding frequency and first harmonic (1.5hz bands) in the wake of the PARAD2 model

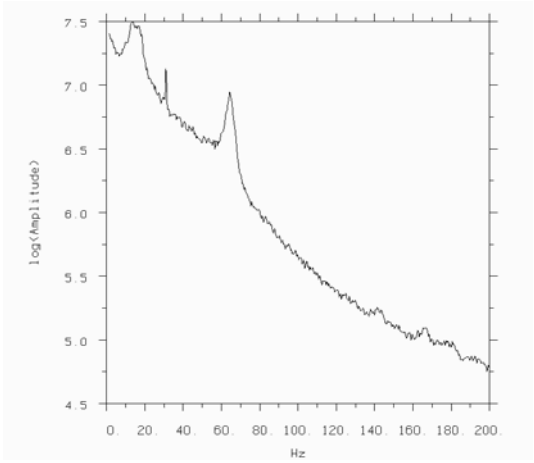

Figure 3.2.53 - Autospectral density of fluctuating pressure coefficient at z/L=0.94 on the surface of the PARAD1 model

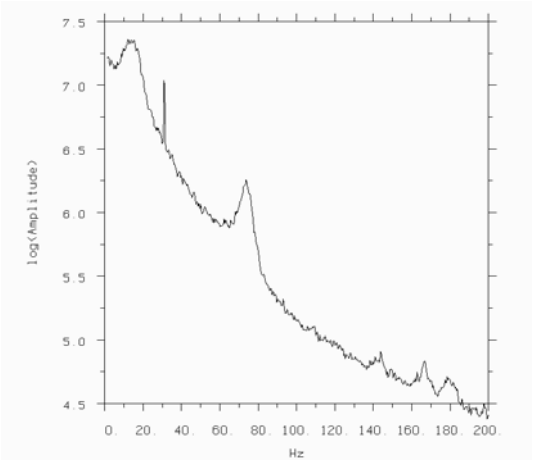

Figure 3.2.54 - Autospectral density of fluctuating pressure coefficient at z/L=0.91 on the surface of the PARAD2 model

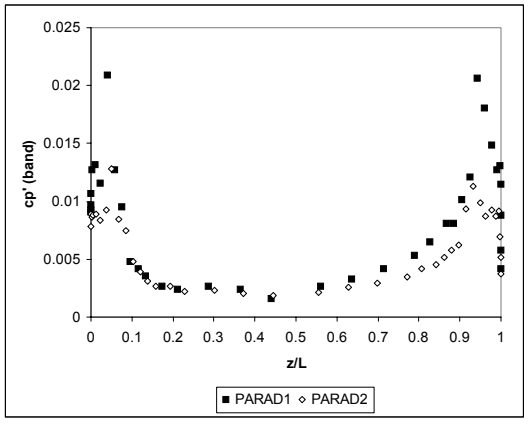

Figure 3.2.55 - Contribution of unsteadiness near shedding frequency to fluctuating surface pressure coefficient on the PARAD models
(PARAD1: S=0.29-0.34, f=60-70hz)
(PARAD2: S=0.34-0.39, f=70-80hz)

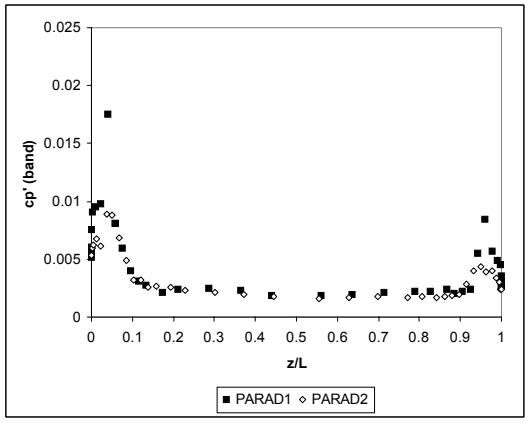

Figure 3.2.56 - Contribution of unsteadiness at twice shedding frequency to fluctuating surface pressure coefficient on the PARAD models
(PARAD1: S=0.58-0.68, f=120-140hz)
(PARAD2: S=0.68-0.78, f=140-160hz)

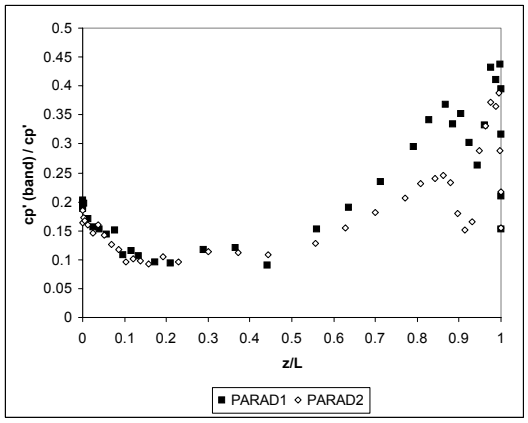

Figure 3.2.57 - Fraction of surface pressure coefficient unsteadiness due to band near shedding frequency for the PARAD models
(PARAD1: S=0.29-0.34, f=60-70hz)
(PARAD2: S=0.34-0.39, f=70-80hz)

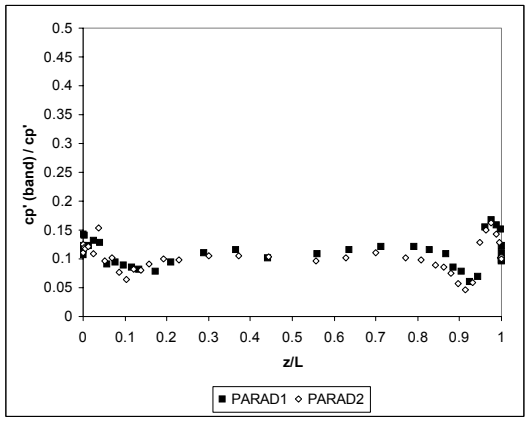

Figure 3.2.58 - Fraction of surface pressure coefficient unsteadiness due to band near twice shedding frequency for the PARAD models
(PARAD1: S=0.58-0.68, f=120-140hz)
(PARAD2: S=0.68-0.78, f=140-160hz)

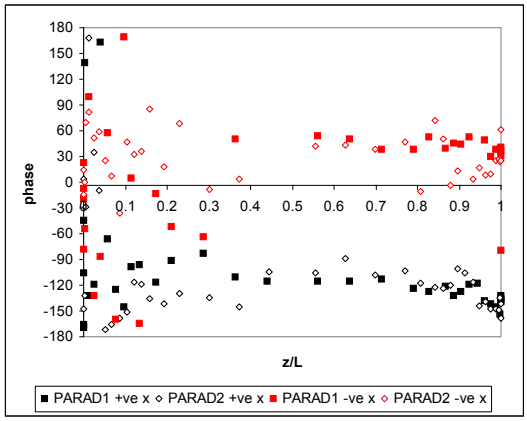

Figure 3.2.59 - Cross-spectral phase at the shedding frequency between pressure on the surface of the PARAD models and reference hot-wire in the wake (at x/W=0.3, z/W=2.0)

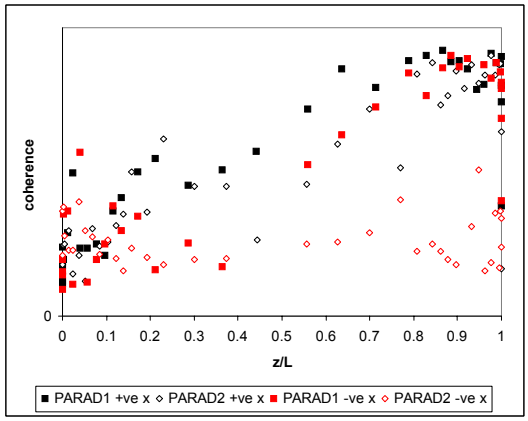

Figure 3.2.60 - Coherence at the shedding frequency between pressure on the surface of the PARAD models and reference hot-wire in the wake (at x/W=0.3, z/W=2.0)

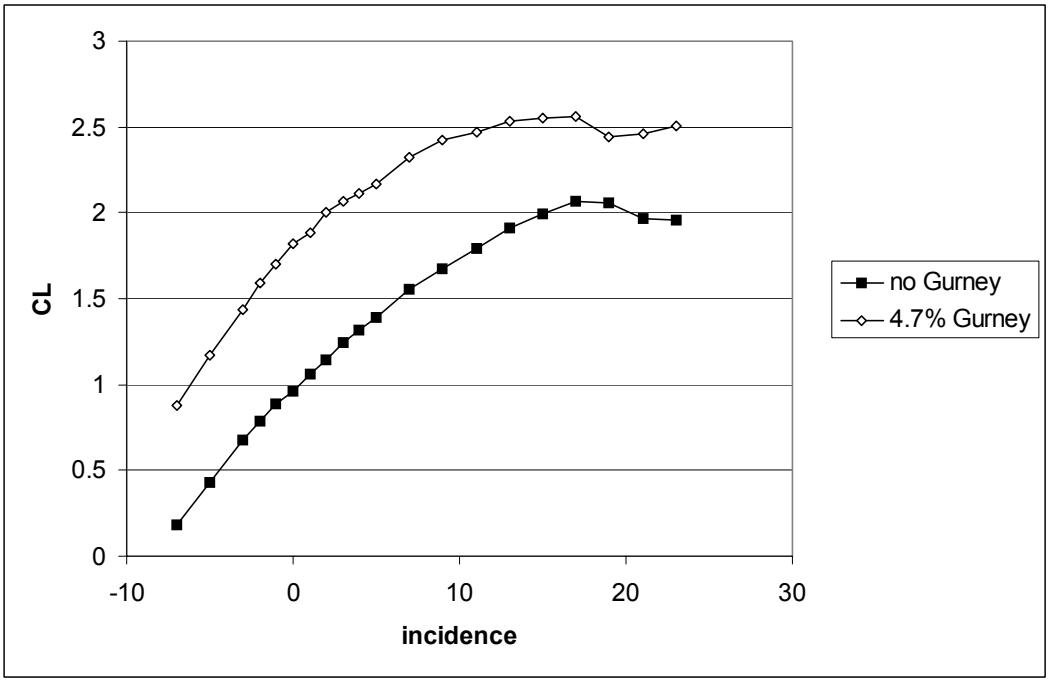

Figure 3.3.1 - Lift versus incidence with and without 4.7% Gurney flap

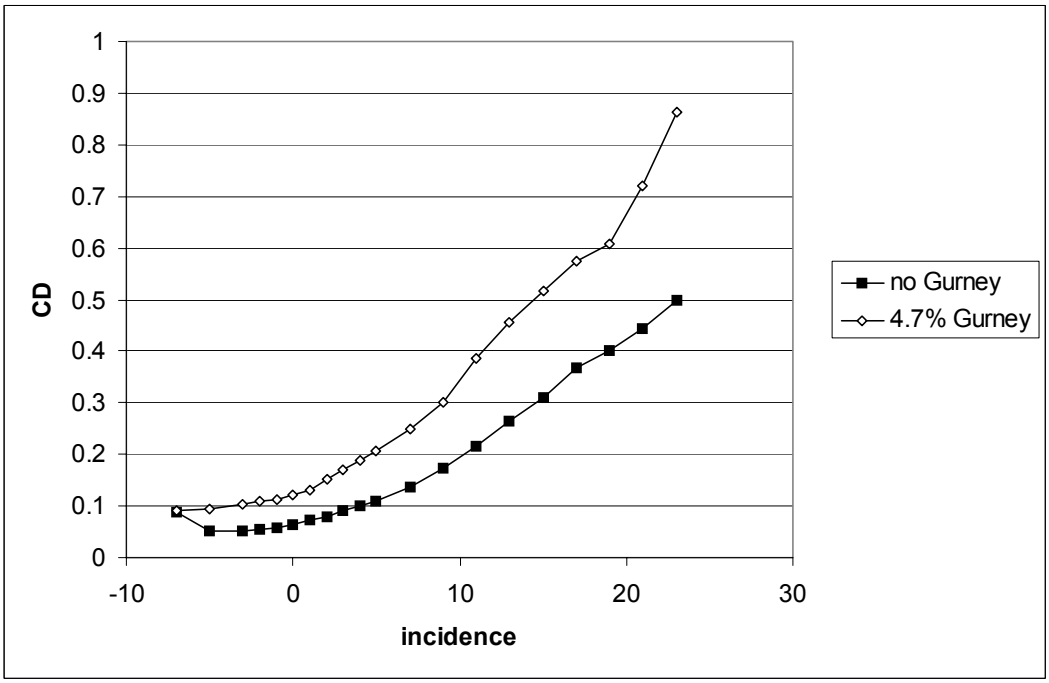

Figure 3.3.2 - Drag versus incidence with and without 4.7% Gurney flap

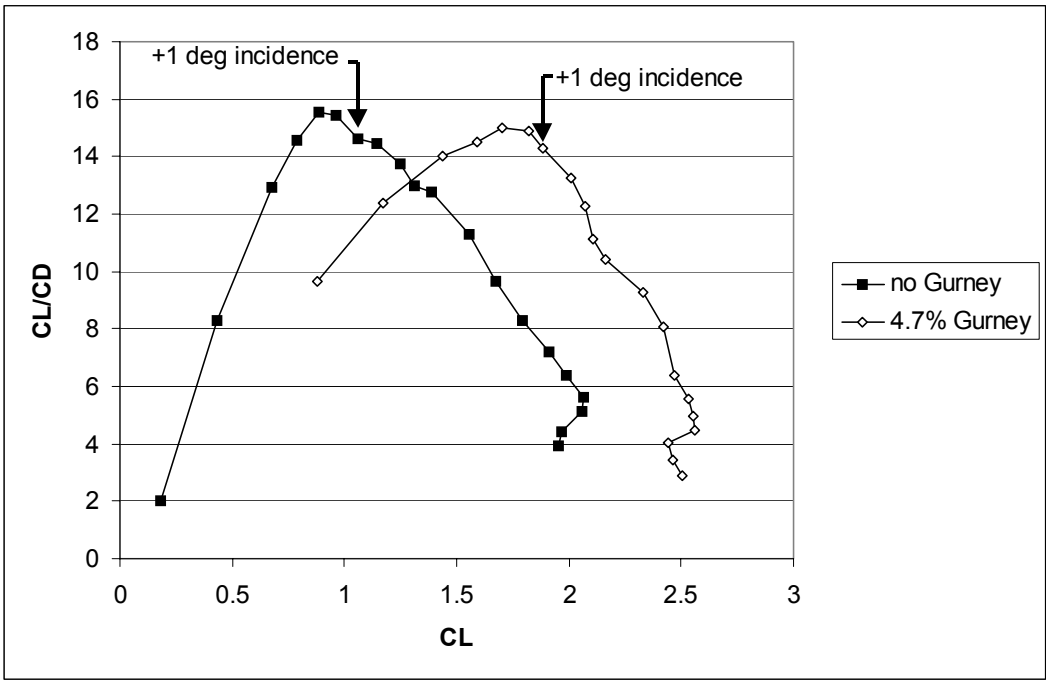

Figure 3.3.3 - Lift/Drag versus lift with and without 4.7% Gurney flap

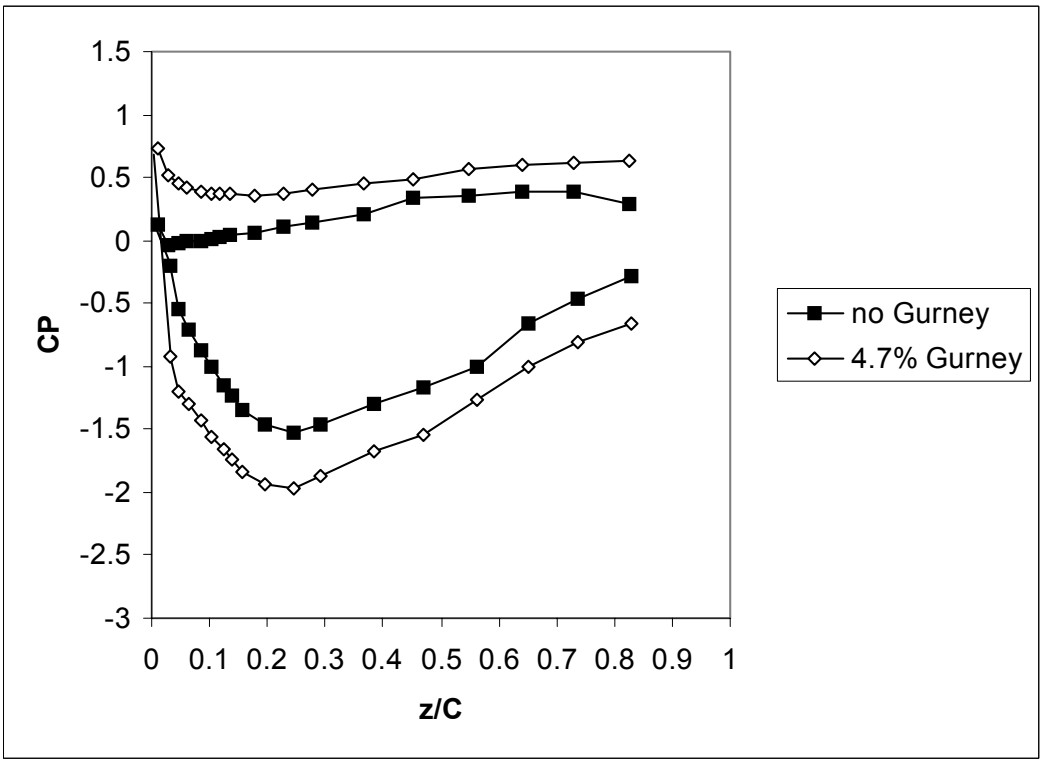

Figure 3.3.4 - Surface pressure distributions at mid-span with and without 4.7% Gurney flap (+1° incidence)

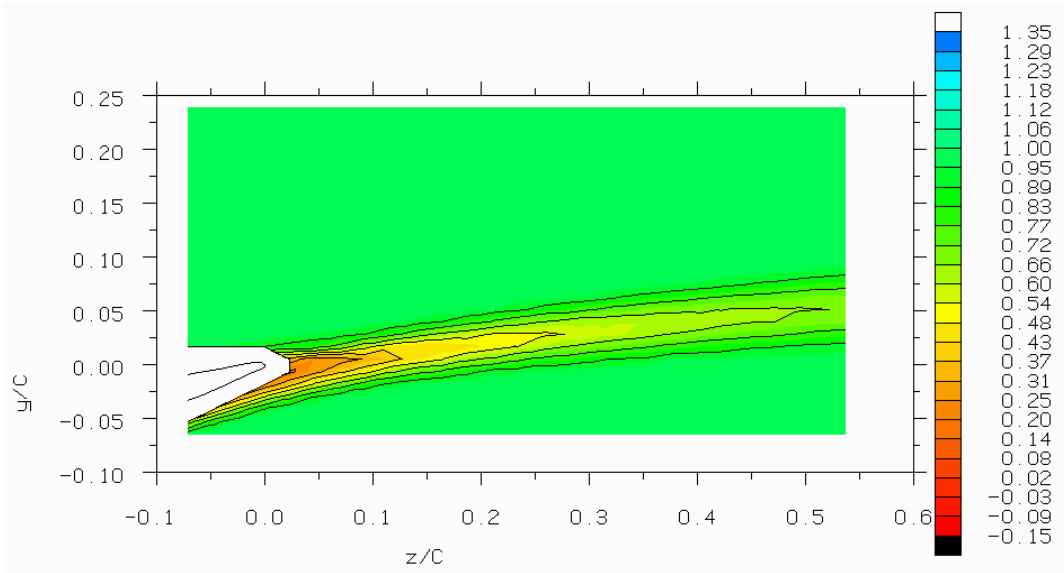

Figure 3.3.5 - Time-averaged total pressure coefficient and velocity vectors in the wake centreline without Gurney flap (+1° incidence)

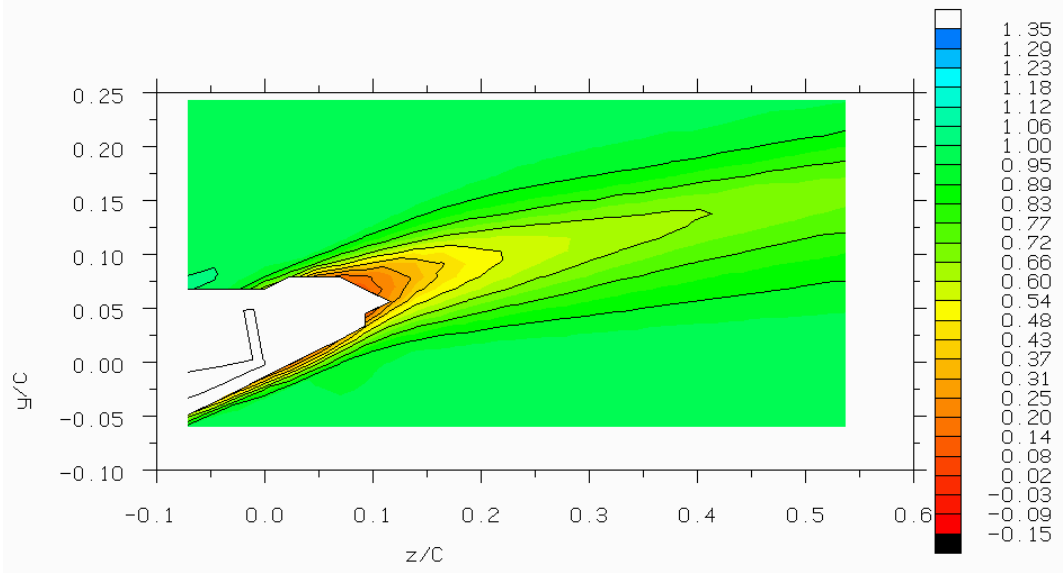

Figure 3.3.6 - Time-averaged total pressure coefficient and velocity vectors in the wake centreline with 4.7% Gurney flap (+1° incidence)

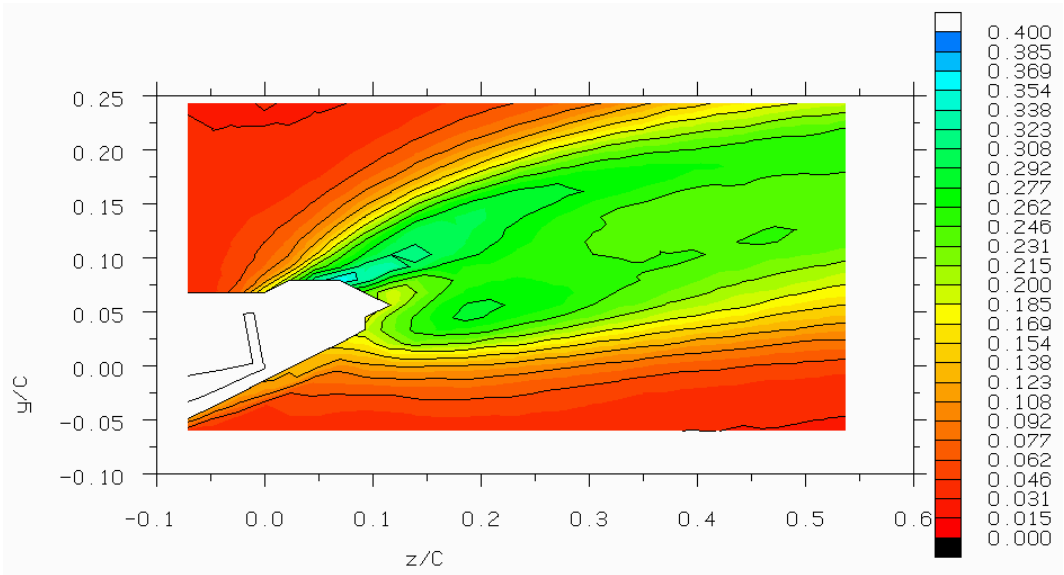

Figure 3.3.7 - Fluctuating total pressure coefficient (standard deviation) in the wake of the wing with Gurney flap (+1° incidence)

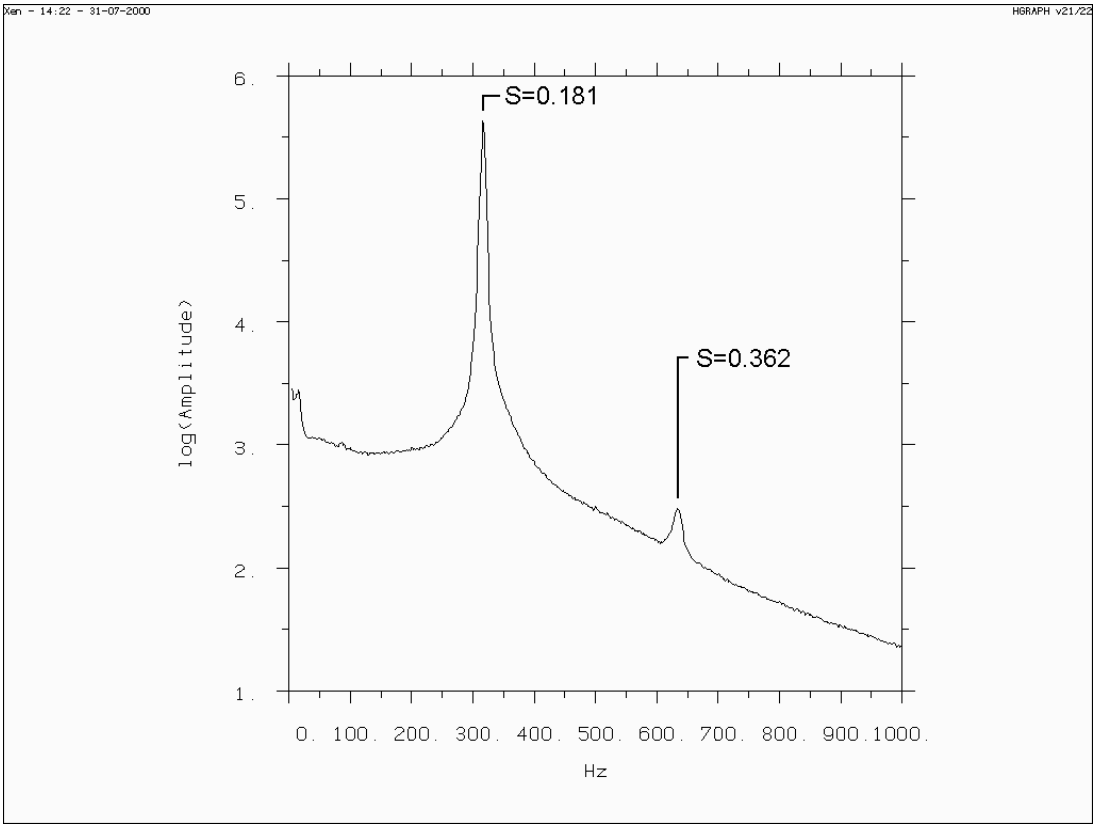

Figure 3.3.8 - Autospectral density of hot-wire velocity in the downstream of the wing with Gurney flap (+1° incidence)

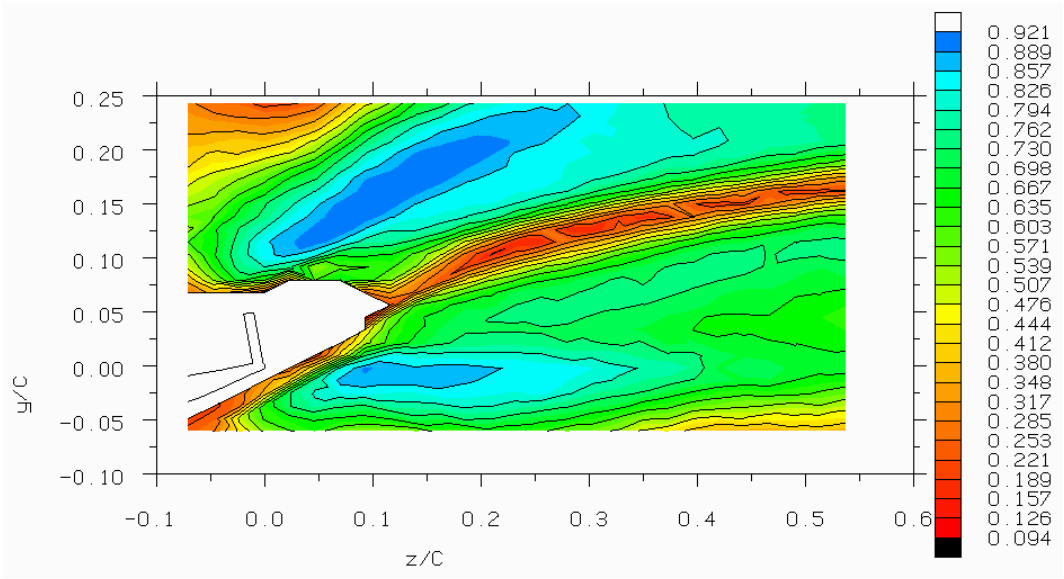

Figure 3.3.9 - Contribution of unsteadiness near shedding frequency (S=0.18) to fluctuating total pressure coefficient in the wake of the wing with Gurney flap (S=0.172-0.189, 301-331hz) (+1° incidence)

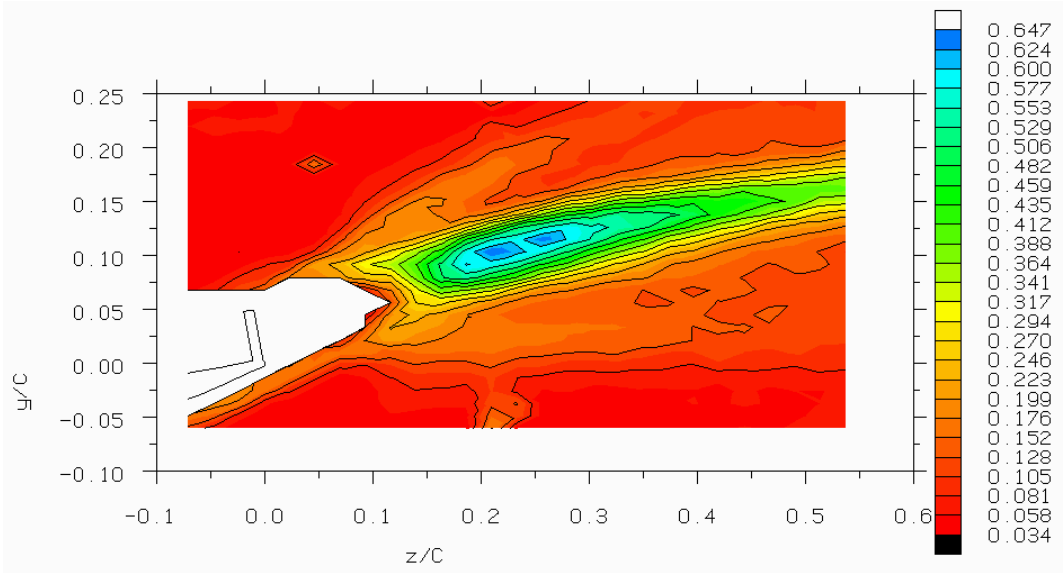

Figure 3.3.10 - Contribution of unsteadiness at twice shedding frequency (S=0.36) to fluctuating total pressure coefficient in the wake wing with Gurney flap (S=0.353-0.370, 618-648hz) (+1° incidence)

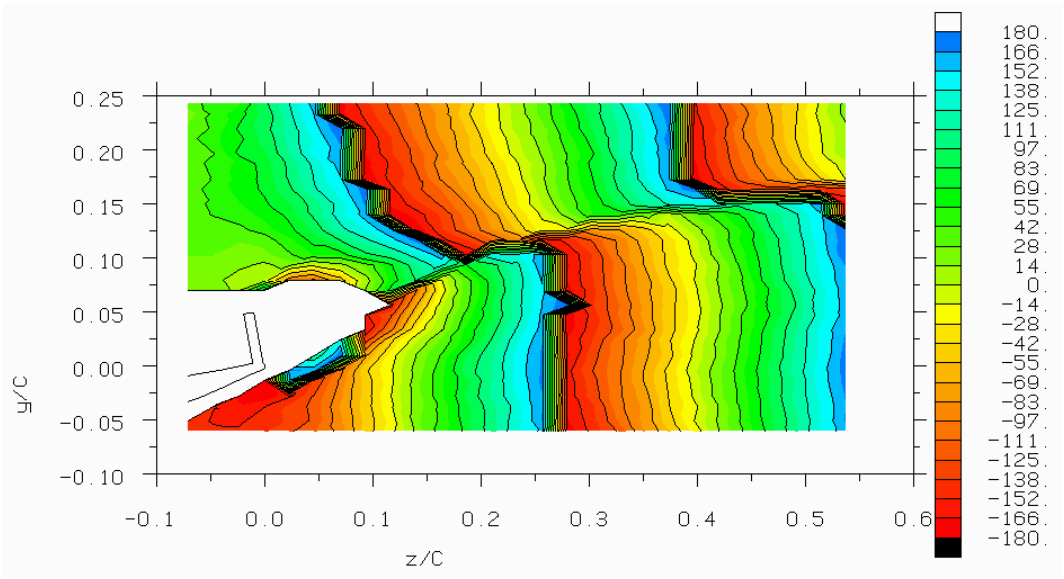

Figure 3.3.11 - Cross-spectral phase at the shedding frequency (S=0.18) between fixed hot-wire and total pressure on the centreline in the wake of the wing with Gurney flap (+1° incidence)

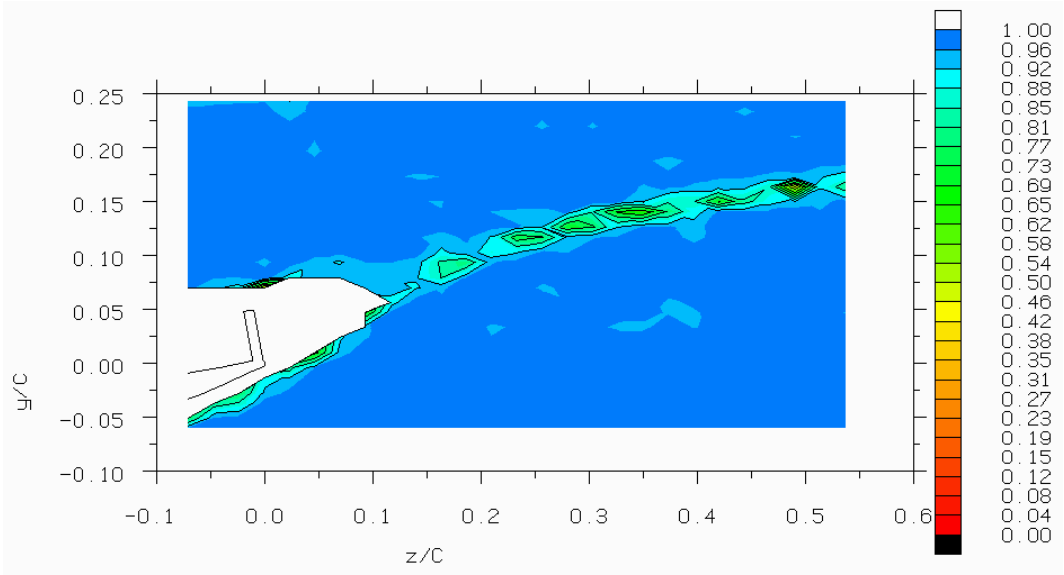

Figure 3.3.12 - Coherence at the shedding frequency (S=0.18) between fixed hot-wire and total pressure on the centreline in the wake of the wing with Gurney flap (+1° incidence)

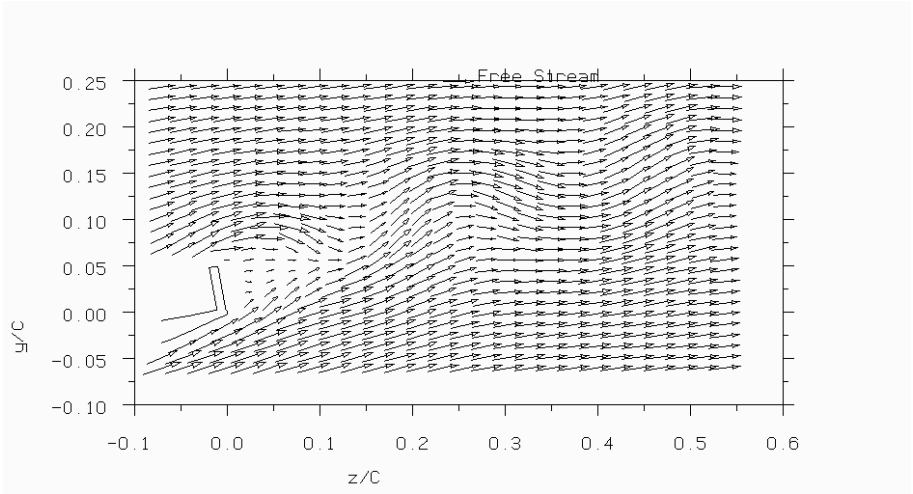

Figure 3.3.13a) t=0.0s, t/T=0.0

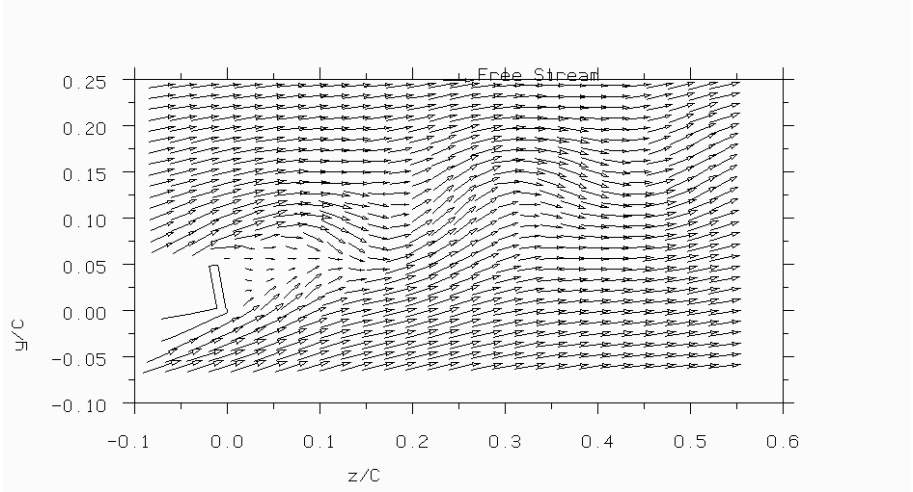

Figure 3.3.13b) t=0.0007s, t/T=0.22

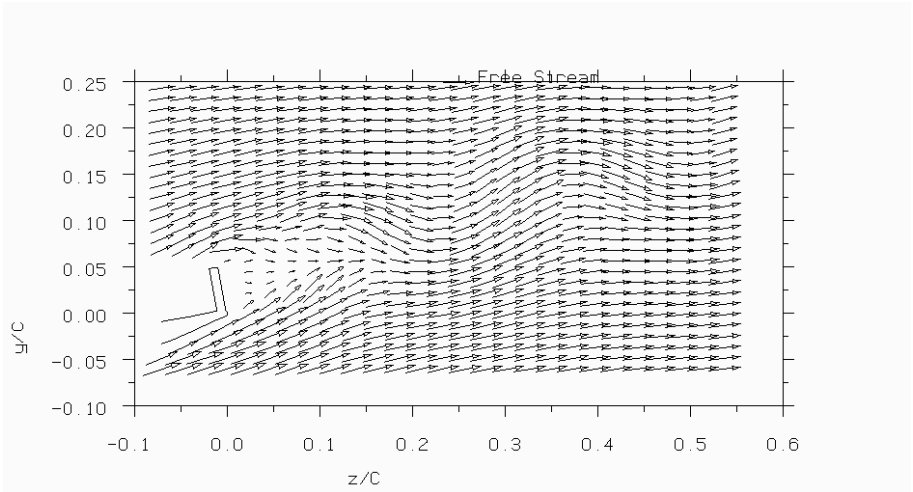

Figure 3.3.13c) t=0.0014s, t/T=0.44

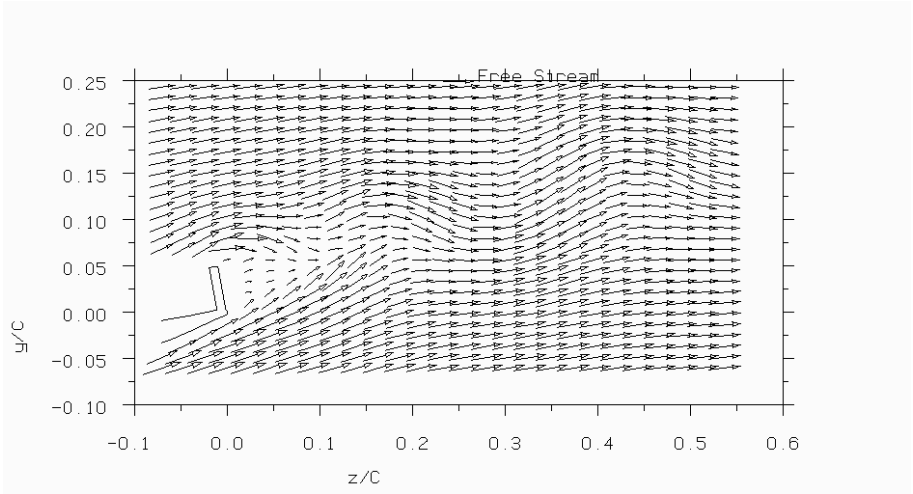

Figure 3.3.13d) t=0.0021s, t/T=0.66

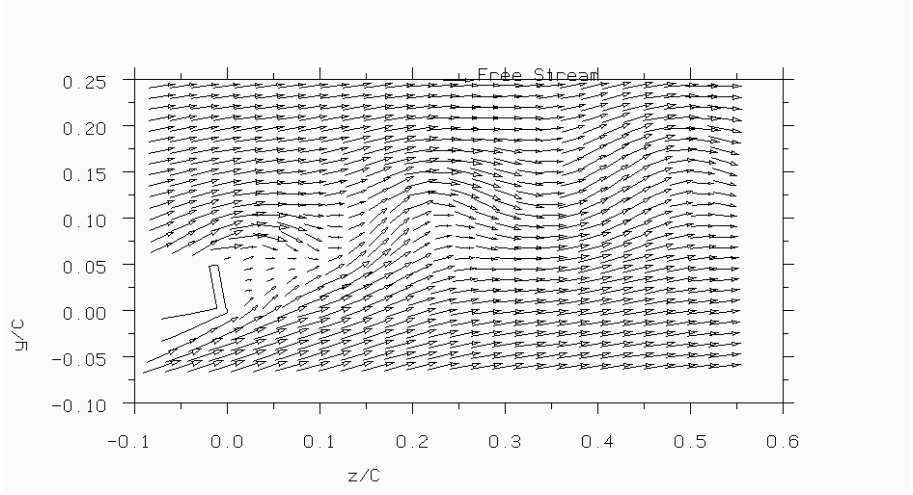

Figure 3.3.13e) t=0.0028s, t/T=0.88

Figure 3.3.13 - Sequence showing velocity vectors reconstructed from shedding frequency and first higher harmonic (1.5hz bands) in the wake of the wing with Gurney flap (+1° incidence)

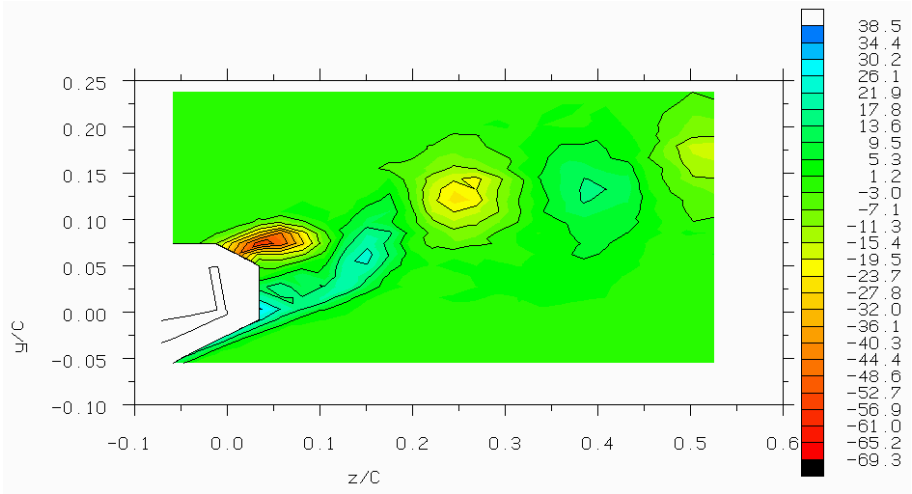

Figure 3.3.14a) t=0.0s, t/T=0.0

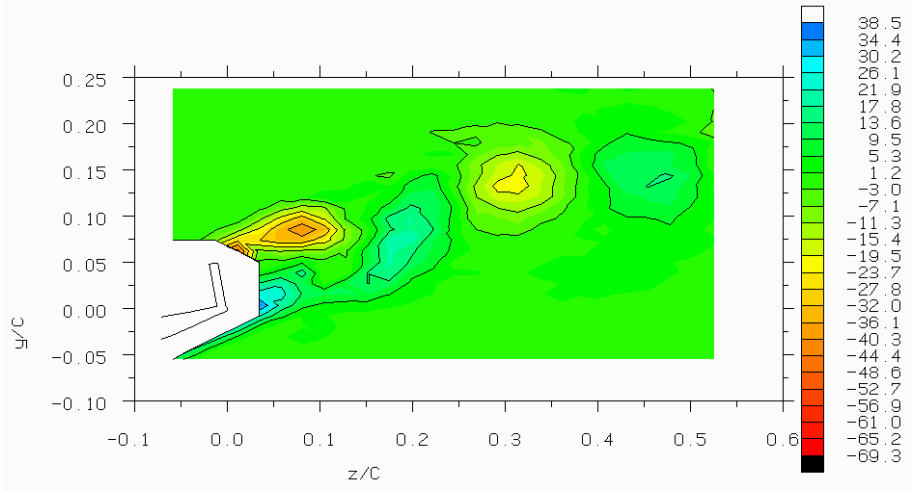

Figure 3.3.14b) t=0.0007s, t/T=0.22

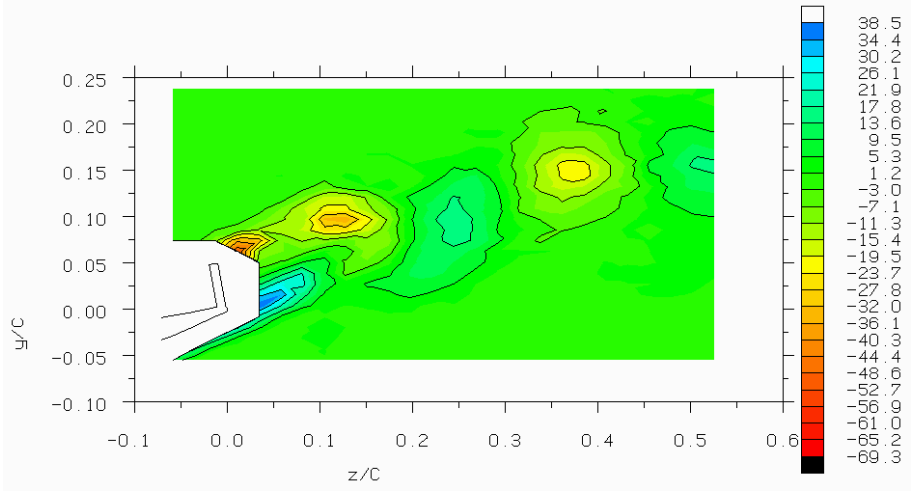

Figure 3.3.14c) t=0.0014s, t/T=0.44

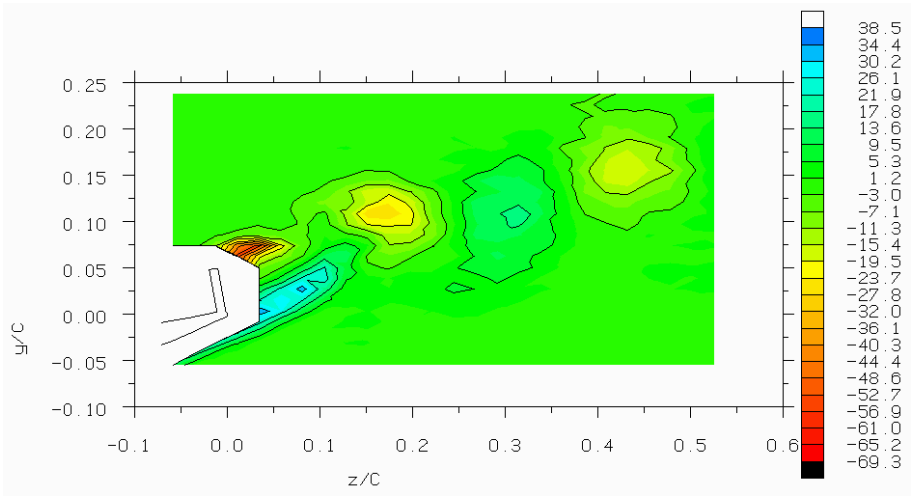

Figure 3.3.14d) t=0.0021s, t/T=0.66

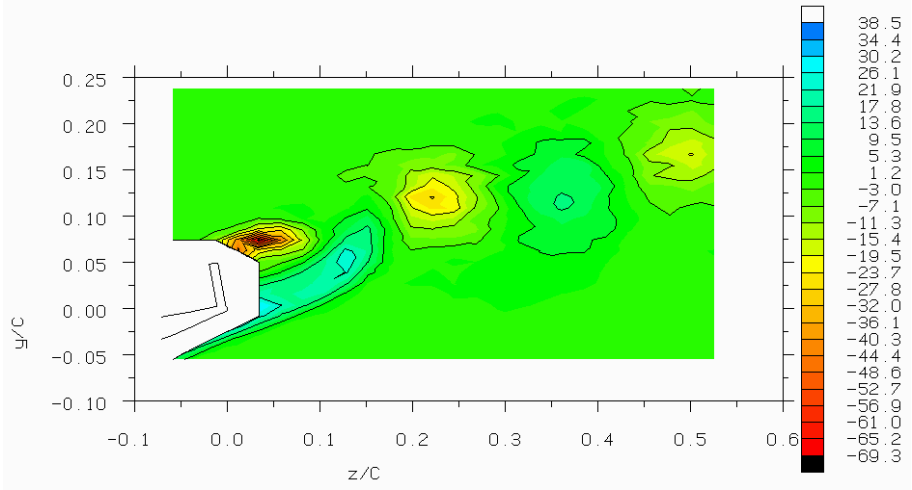

Figure 3.3.14e) t=0.0028s, t/T=0.88

Figure 3.3.14 1- Sequence showing vorticity reconstructed from shedding frequency and first higher harmonic (1.5hz bands) in the wake of the wing with Gurney flap (+1° incidence)

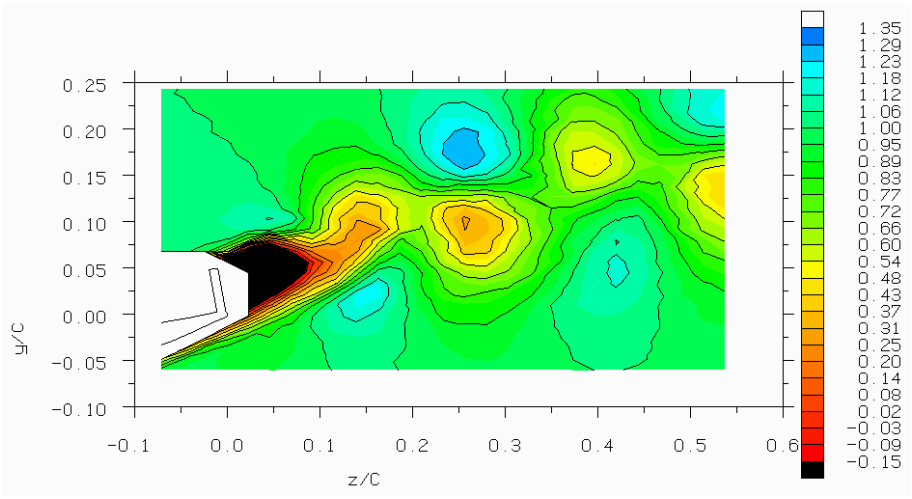

Figure 3.3.15a) t=0.0s, t/T=0.0

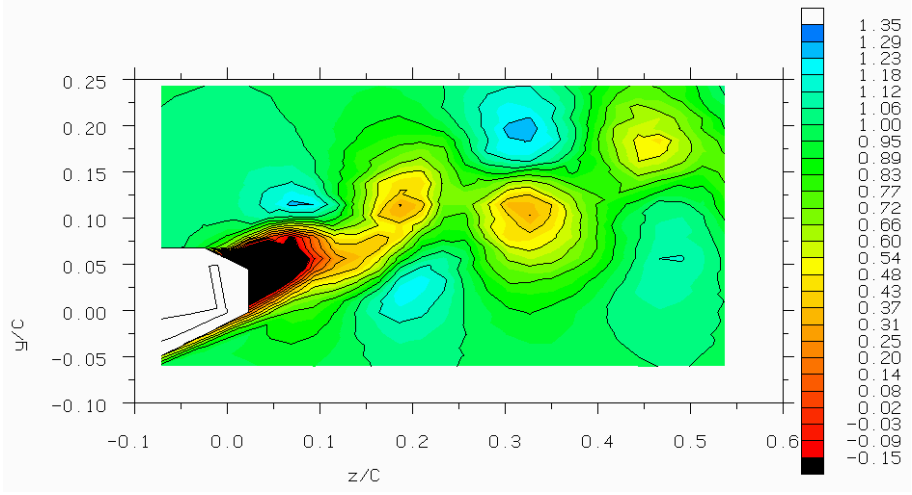

Figure 3.3.15b) t=0.0007s, t/T=0.22

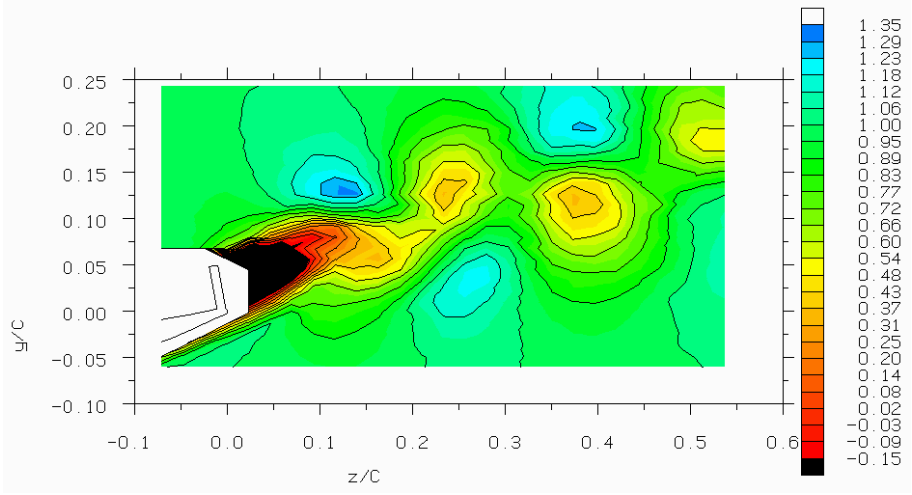

Figure 3.3.15c) t=0.0014s, t/T=0.44

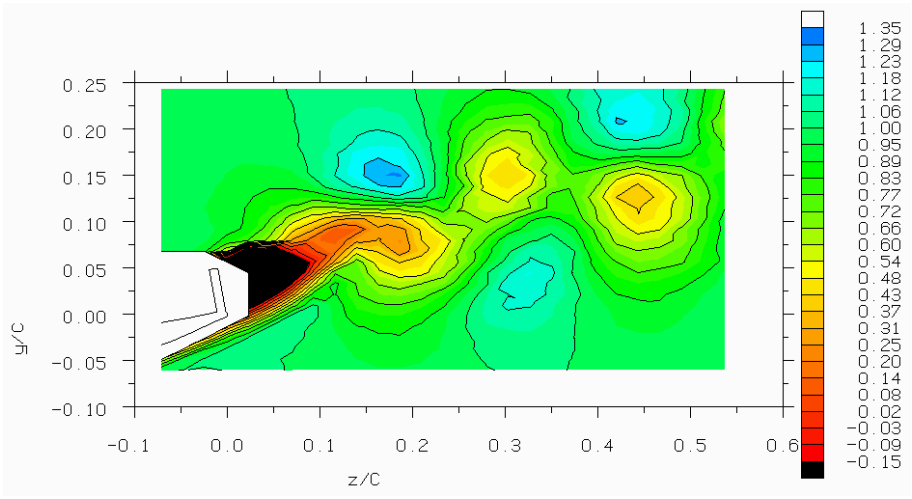

Figure 3.3.15d) t=0.0021s, t/T=0.66

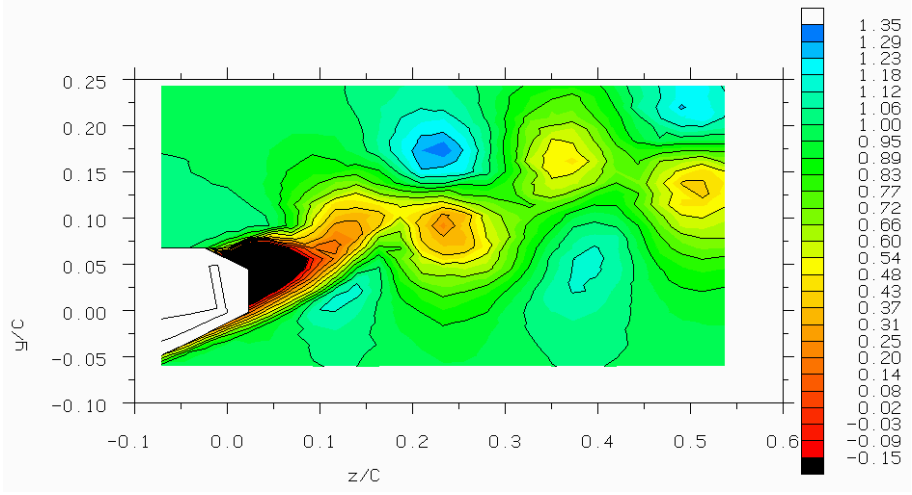

Figure 3.3.15e) t=0.0028s, t/T=0.88

Figure 3.3.15 - Sequence showing total pressure coefficient reconstructed from shedding frequency and first higher harmonic (1.5hz bands) in the wake of the wing with Gurney flap (+1° incidence)

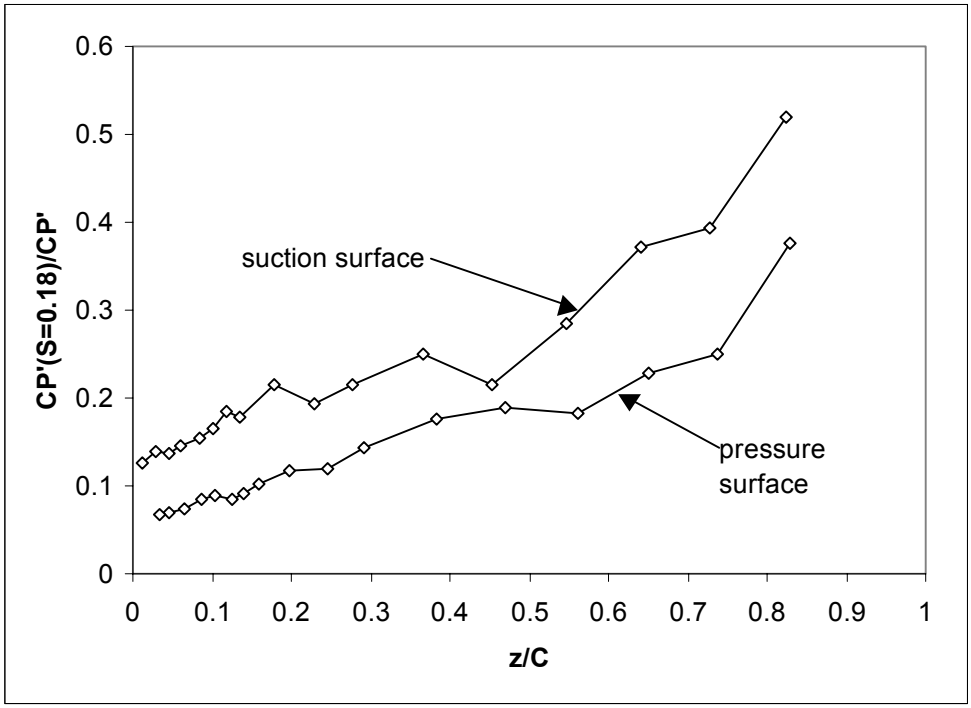

Figure 3.3.16 - Contribution of unsteadiness near shedding frequency (S=0.18) to fluctuating pressure coefficient at mid-span on the surface of the wing with Gurney flap (S=0.172-0.189, 301-331hz) (+1° incidence)

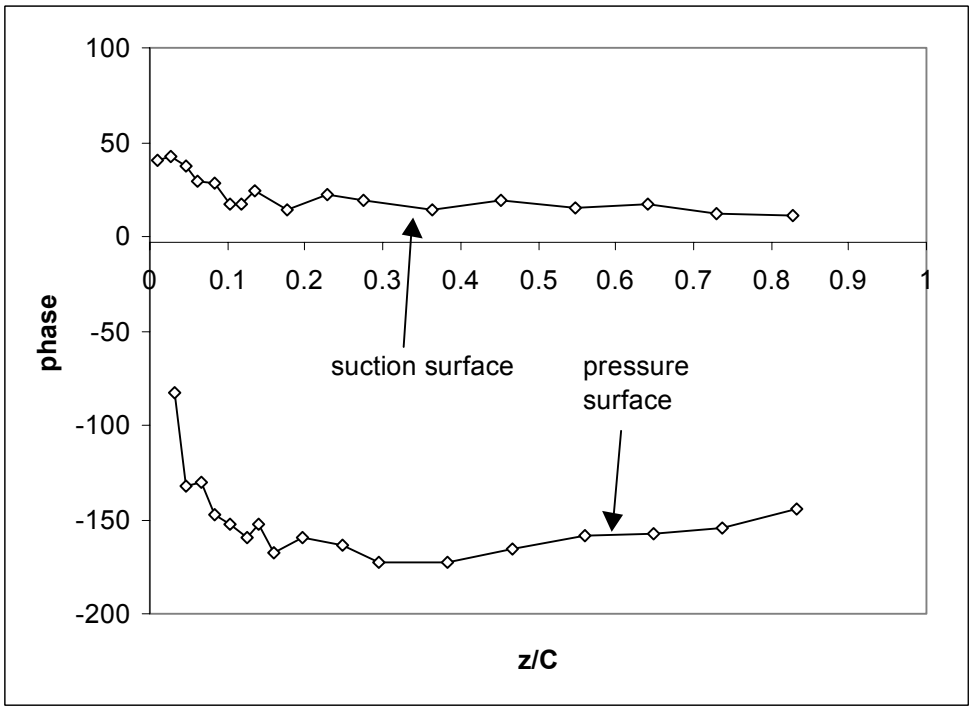

Figure 3.3.17 - Cross-spectral phase at the shedding frequency (S=0.18) between fluctuating pressure coefficient at mid-span on the surface of the wing with Gurney flap and the reference hot-wire downstream (+1° incidence)

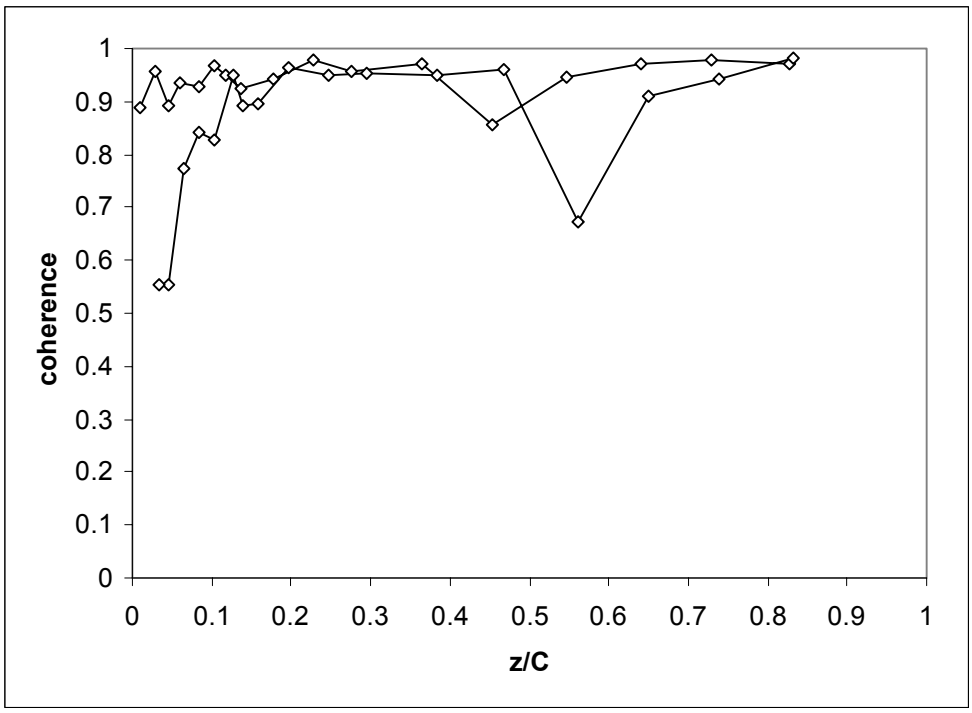

Figure 3.3.18 - Coherence at the shedding frequency (S=0.18) between fluctuating pressure coefficient at mid-span on the surface of the wing with Gurney flap and the reference hot-wire (+1° incidence)

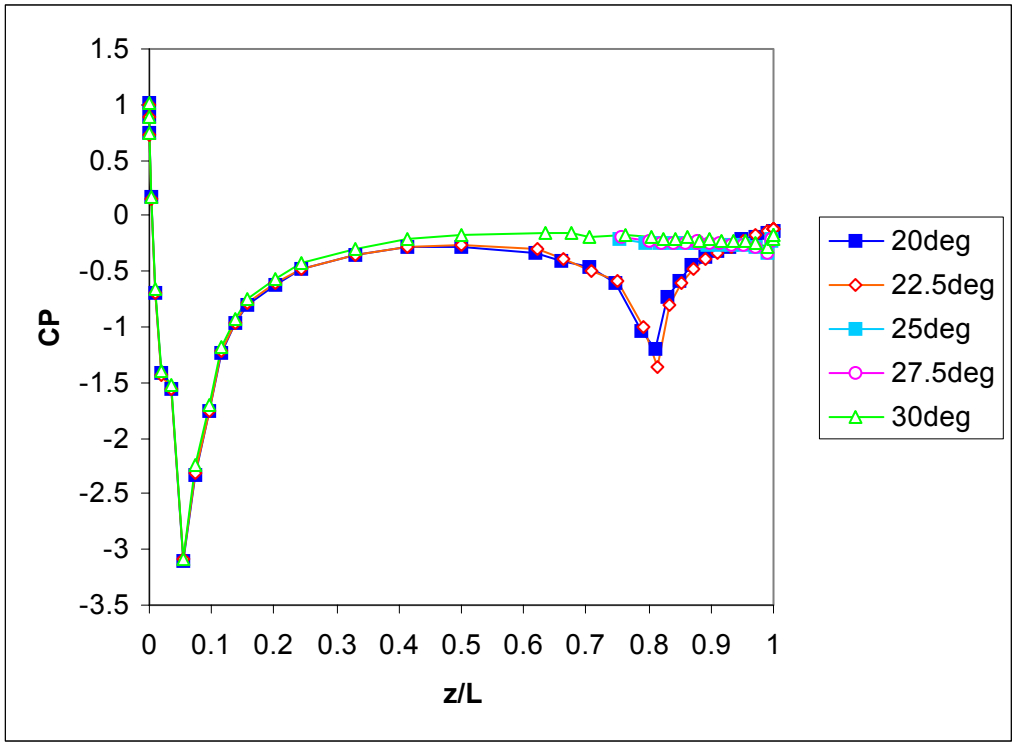

Figure 3.4.1 - Surface pressure distributions on the two-dimensional Ahmed model

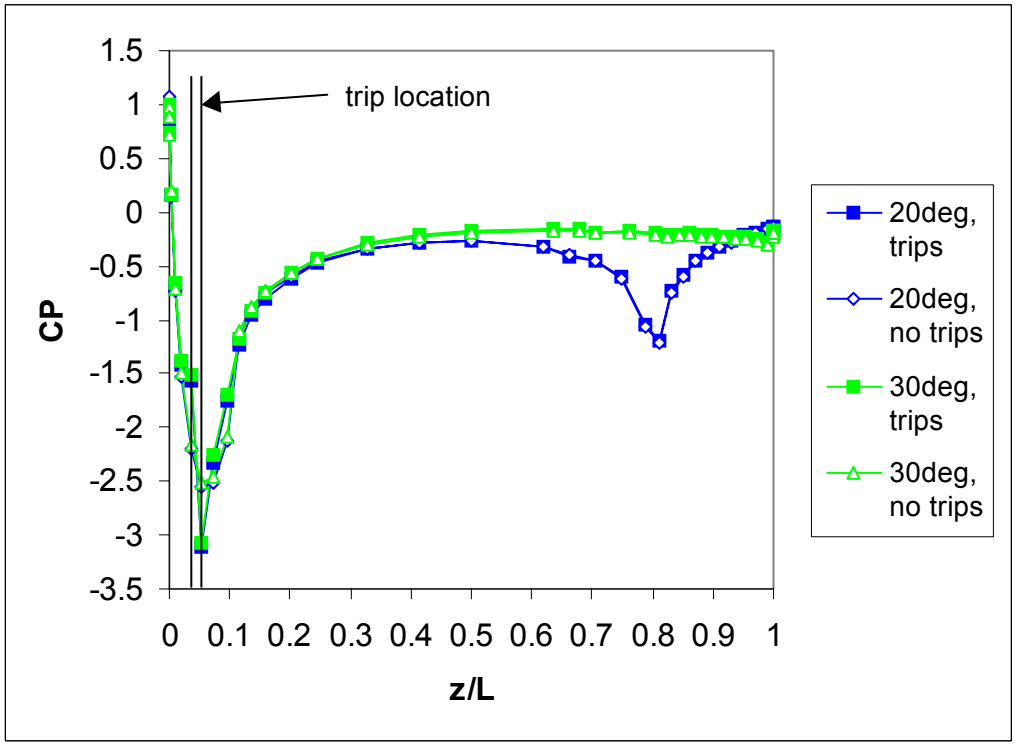

Figure 3.4.2 - Effect of trips on surface pressures for the two-dimensional Ahmed model (trip location and width shown)

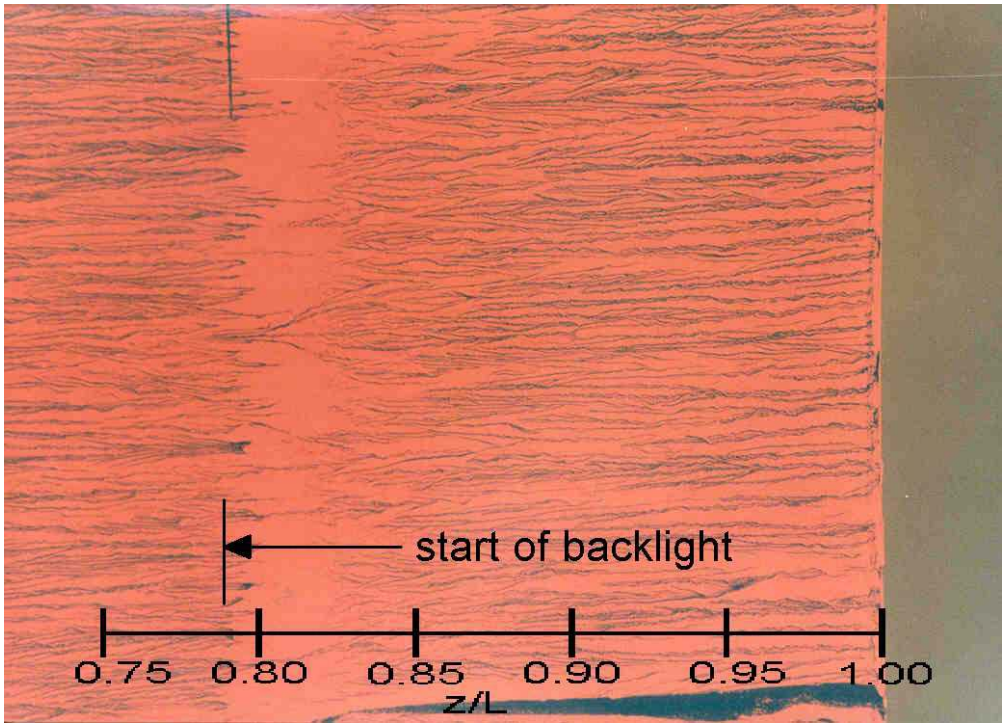

Figure 3.4.3 - Surface oil flow on the backlight of the two-dimensional Ahmed model (10 degree backlight)

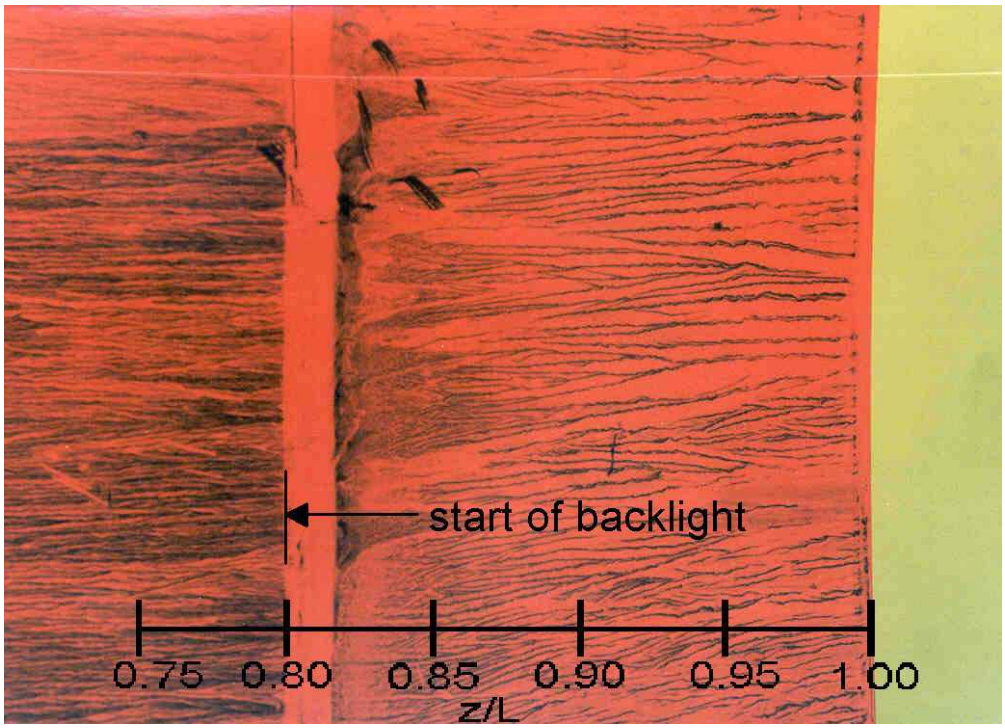

Figure 3.4.4 - Surface oil flow on the backlight of the two-dimensional Ahmed model (20 degree backlight)

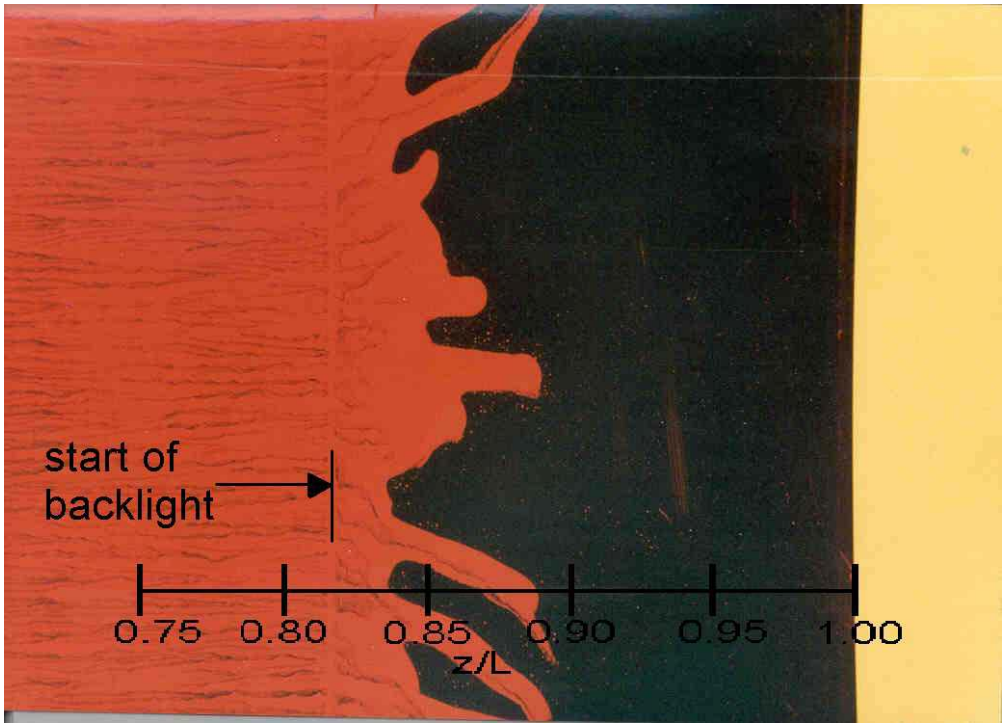

Figure 3.4.5 - Surface oil flow on the backlight of the two-dimensional Ahmed model (30 degree backlight)

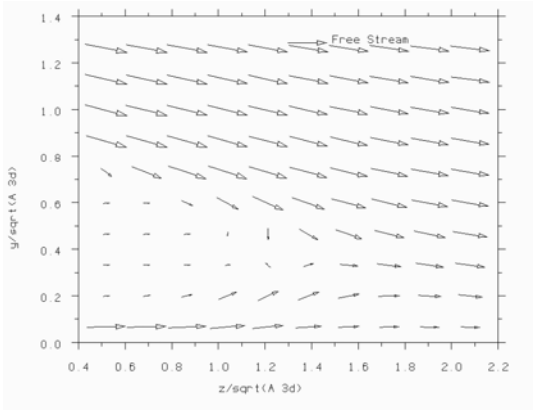

Figure 3.4.6 - Centre-plane velocity vectors behind the two-dimensional Ahmed model (20 degree backlight)

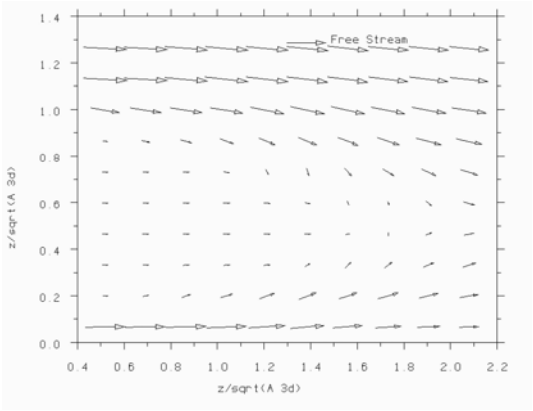

Figure 3.4.7 - Centre-plane velocity vectors behind the two-dimensional Ahmed model (30 degree backlight)

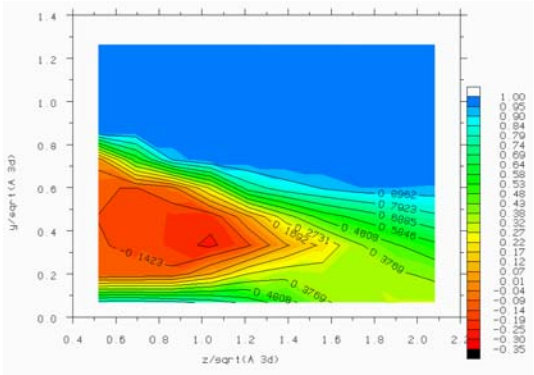

Figure 3.4.8 - Centre-plane total pressure coefficient behind the two-dimensional Ahmed model (20 degree backlight)

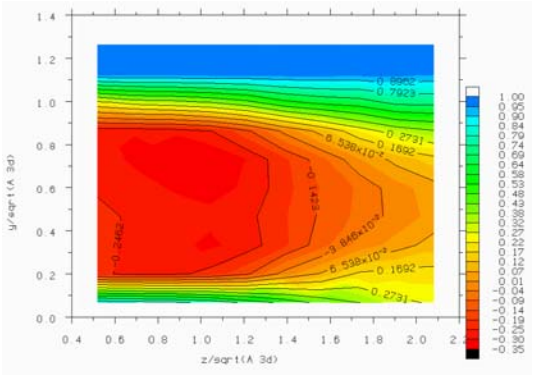

Figure 3.4.9 - Centre-plane total pressure coefficient behind the two-dimensional Ahmed model (30 degree backlight)

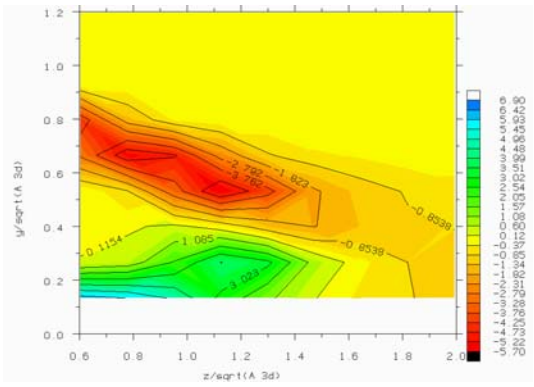

Figure 3.4.10 - Centre-plane vorticity behind the two-dimensional Ahmed model (20 degree backlight) (vorticity non-dimensionalised by free-stream velocity and square-root of frontal area for equivalent 3D model)

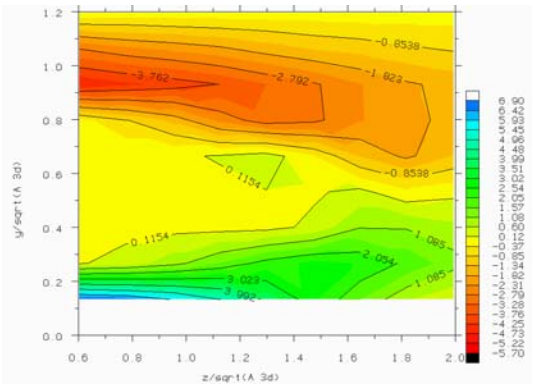

Figure 3.4.11 - Centre-plane vorticity behind the two-dimensional Ahmed model (30 degree backlight) (vorticity non-dimensionalised by free-stream velocity and square-root of frontal area for equivalent 3D model)

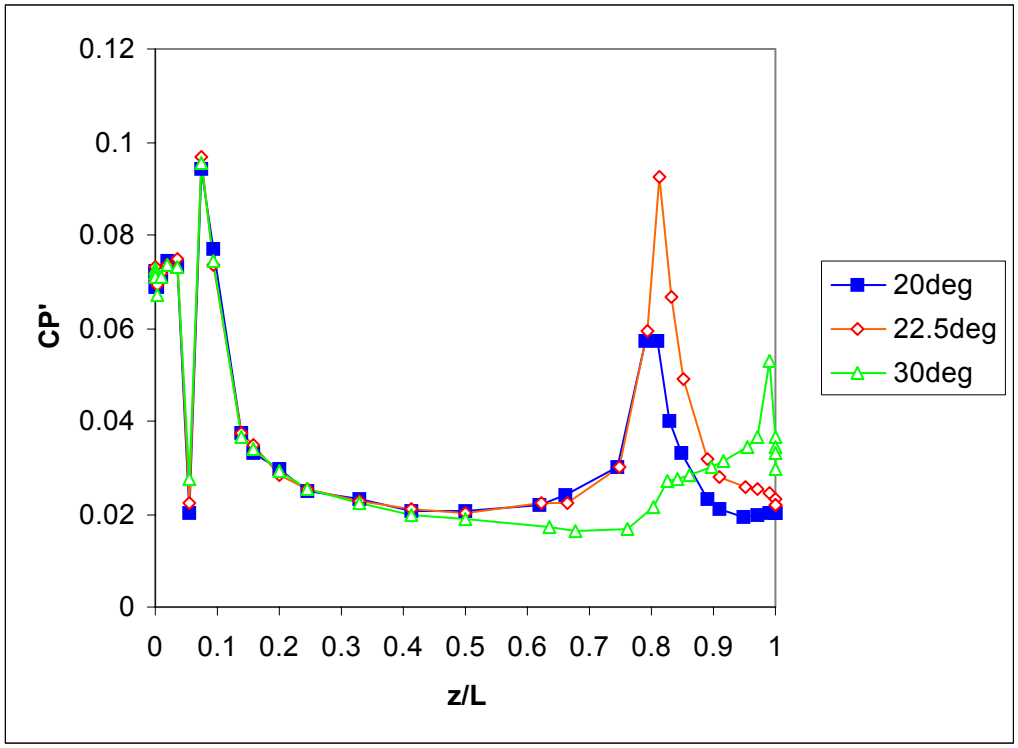

Figure 3.4.12 - Fluctuating pressure coefficient (standard deviation) on the surface of the 2D Ahmed model

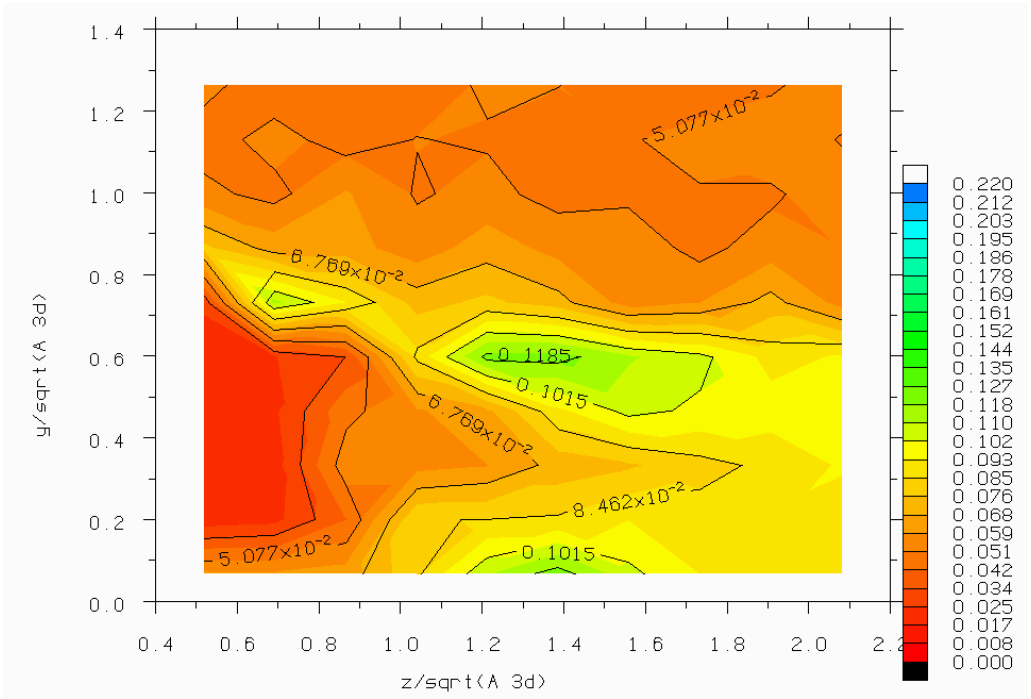

Figure 3.4.13 - Centre-plane centre-hole pressure coefficient unsteadiness (standard deviation) in the wake of the two-dimensional Ahmed model (20 degree backlight)

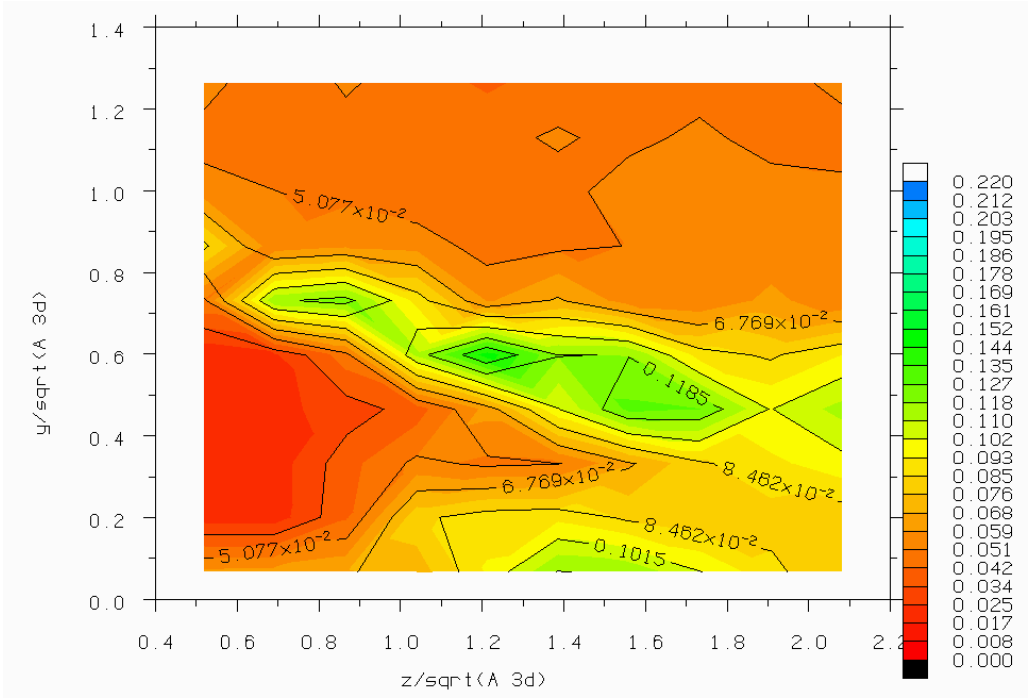

Figure 3.4.14 - Centre-plane centre-hole pressure coefficient unsteadiness (standard deviation) in the wake of the two-dimensional Ahmed model (22.5 degree backlight)

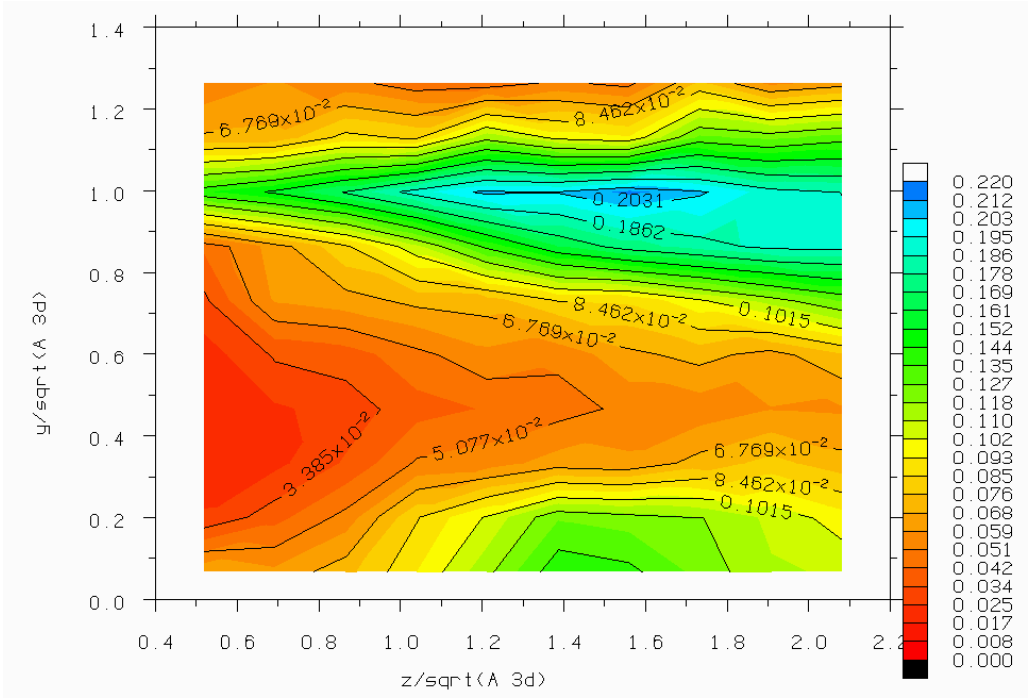

Figure 3.4.15 - Centre-plane centre-hole pressure coefficient unsteadiness (standard deviation) in the wake of the two-dimensional Ahmed model (30 degree backlight)

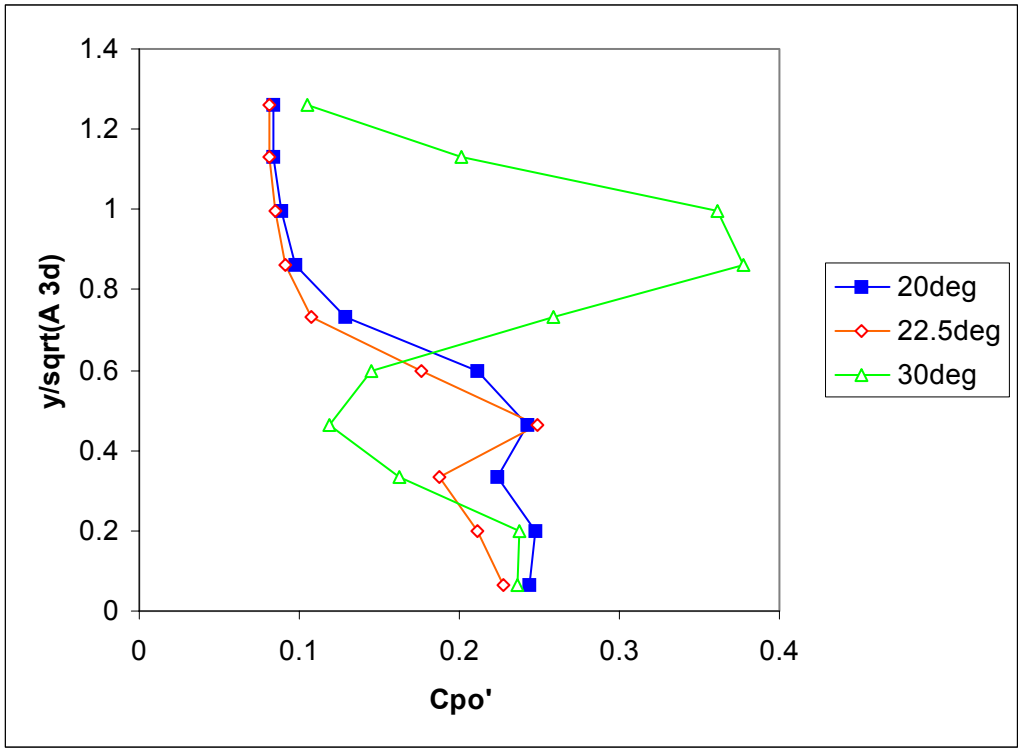

Figure 3.4.16 - Fluctuating total pressure coefficient at z/sqrt(A_{3D})=1.73 in the wake of the 2D Ahmed model

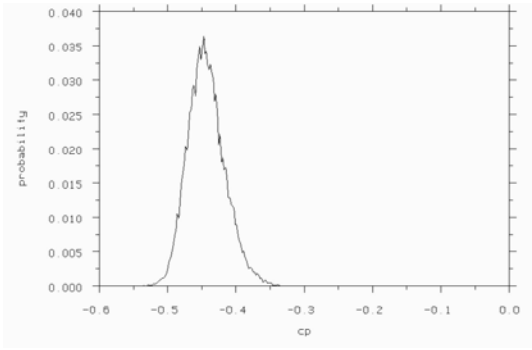

Figure 3.4.17 - Probability density function for pressure coefficient at z/L=0.87 on the backlight of the 2D Ahmed model (20 degree backlight)

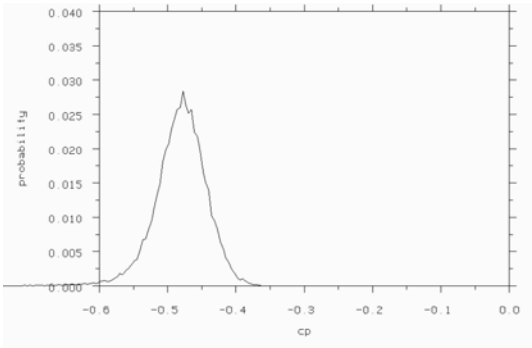

Figure 3.4.18 - Probability density function for pressure coefficient at z/L=0.87 on the backlight of the 2D Ahmed model (22.5 degree backlight)

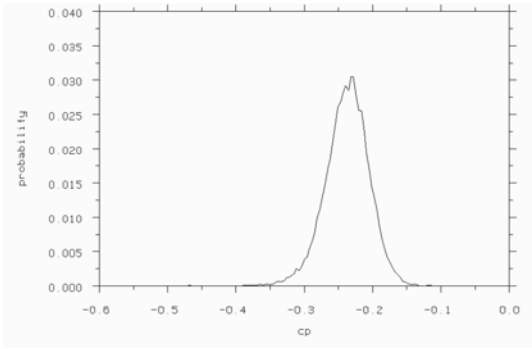

Figure 3.4.19 - Probability density function for pressure coefficient at z/L=0.94 on the backlight of the 2D Ahmed model (30 degree backlight)

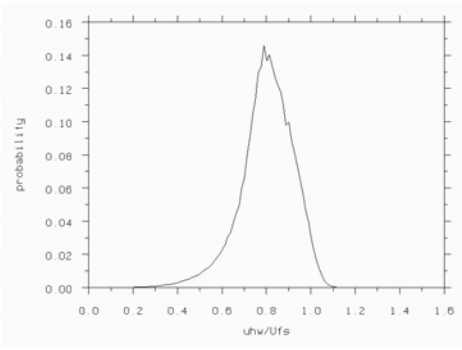

Figure 3.4.20 - Probability density function for hot-wire velocity in the wake of the two-dimensional Ahmed model (20 degree backlight) at $z/\sqrt{A_{3D}}=1.73$, $y/\sqrt{A_{3D}}=0.60$

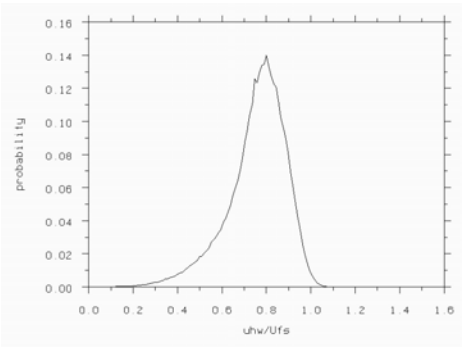

Figure 3.4.21 - Probability density function for hot-wire velocity in the wake of the two-dimensional Ahmed model (22.5 degree backlight) at $z/\sqrt{A_{3D}}=1.73$, $y/\sqrt{A_{3D}}=0.53$

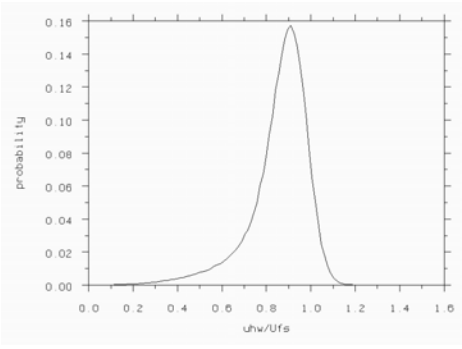

Figure 3.4.22 - Probability density function for hot-wire velocity in the wake of the two-dimensional Ahmed model (30 degree backlight) at $z/\sqrt{A_{3D}}=1.73$, $y/\sqrt{A_{3D}}=1.00$

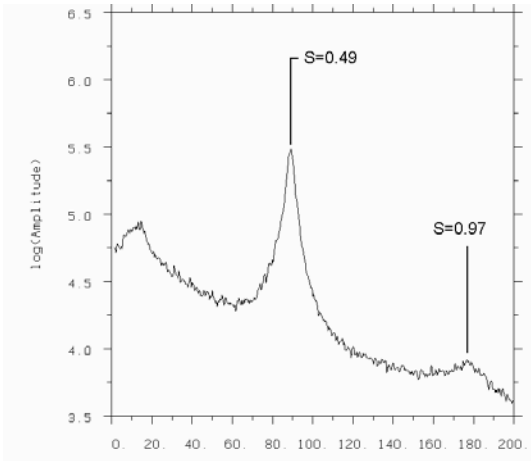

Figure 3.4.23 - Autospectral density for hot-wire velocity in the wake of the two-dimensional Ahmed model (20 degree backlight) at z/sqrt(A_{3D})=1.73, y/sqrt(A_{3D})=0.60

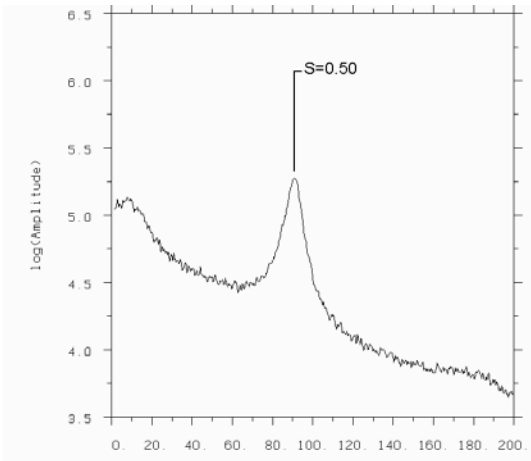

Figure 3.4.24 - Autospectral density for hot-wire velocity in the wake of the two-dimensional Ahmed model (22.5 degree backlight) at z/sqrt(A_{3D})=1.73, y/sqrt(A_{3D})=0.53

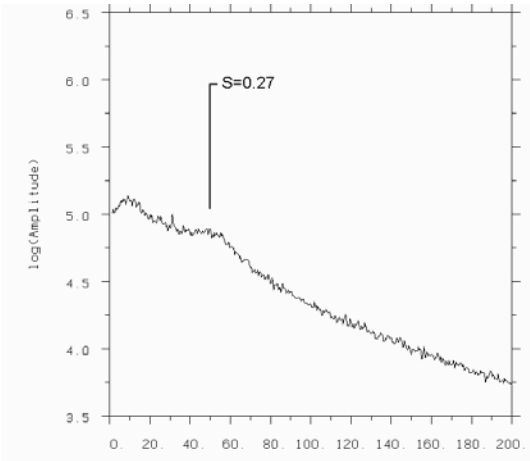

Figure 3.4.25 - Autospectral density for hot-wire velocity in the wake of the two-dimensional Ahmed model (30 degree backlight) at z/sqrt(A_{3D})=1.73, y/sqrt(A_{3D})=1.00

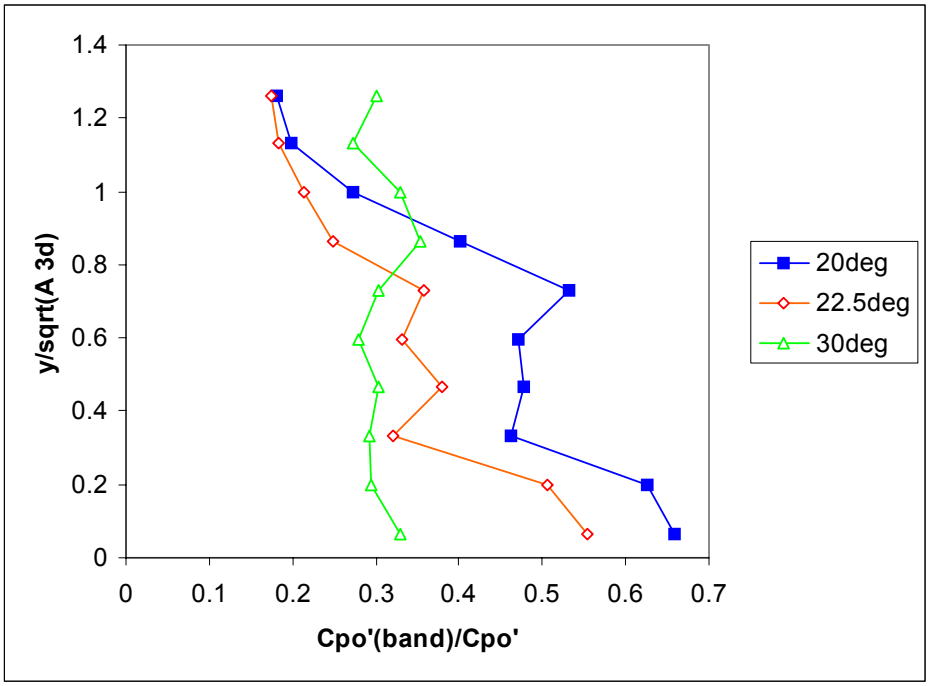

Figure 3.4.26 - Fraction of total pressure unsteadiness due to specified frequency band at z/sqrt(A_{3D})=1.73 in the wake of the 2D Ahmed model
20deg and 22.5deg: S=0.47-0.52 (f=85-95hz), 30deg: S=0.25-0.30 (f=45-55hz)

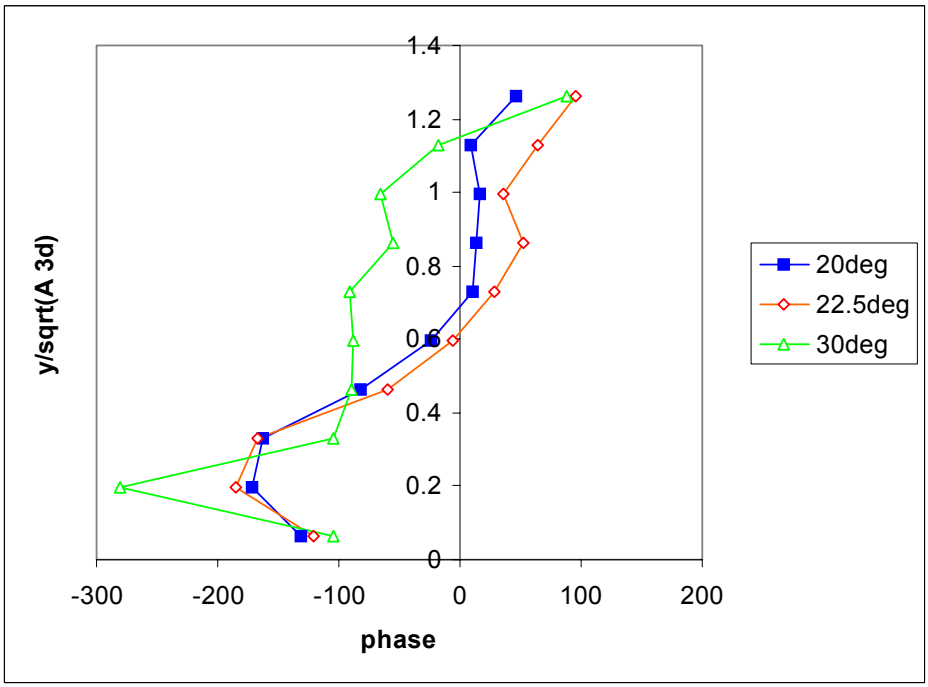

Figure 3.4.27 - Cross-spectral phase near S=0.50 (20deg, 22.5deg) and S=0.27 (30deg) between fixed hot-wire and total pressure fluctuations at z/sqrt(A_{3D})=1.73 in the wake of the 2D Ahmed model (hot-wire at z/sqrt(A_{3D})=1.73 and y/sqrt(A_{3D})=0.60 (20deg), y/sqrt(A_{3D})=0.53 (22.5deg) y/sqrt(A_{3D})=1.00 (30deg))

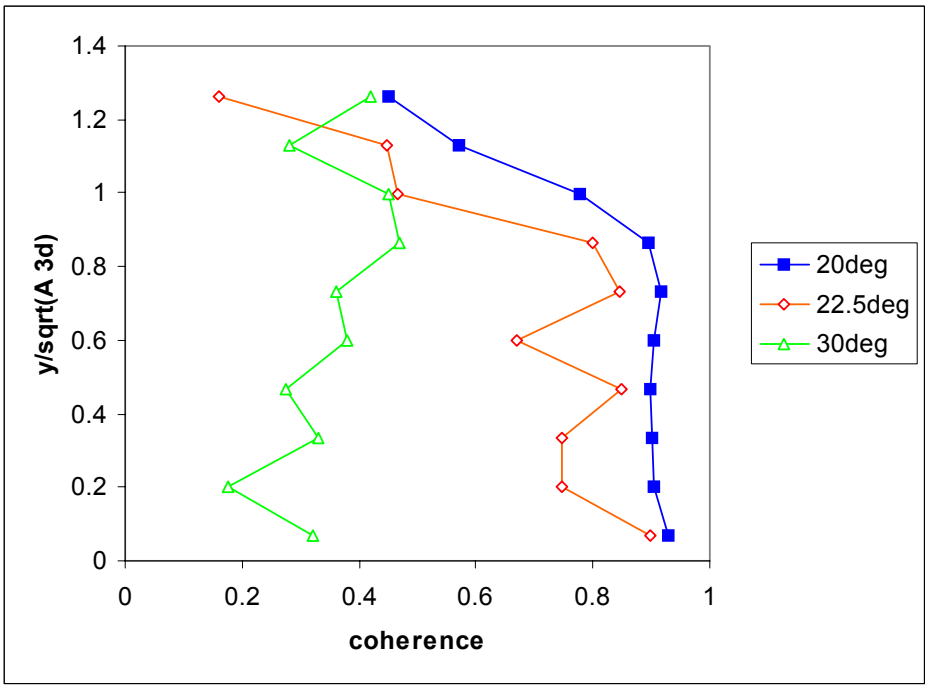

Figure 3.4.28 - Coherence near S=0.50 (20deg, 22.5deg) and S=0.27 (30deg) between fixed hot-wire and total pressure fluctuations at z/sqrt(A_{3D})=1.73 in the wake of the 2D Ahmed model (hot-wire at z/sqrt(A_{3D})=1.73 and y/sqrt(A_{3D})=0.60 (20deg), y/sqrt(A_{3D})=0.53 (22.5deg) y/sqrt(A_{3D})=1.00 (30deg))

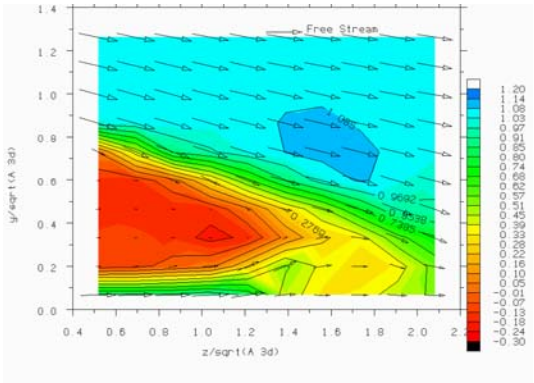

Figure 3.4.29a) t=0.0000s, t/T=0.0

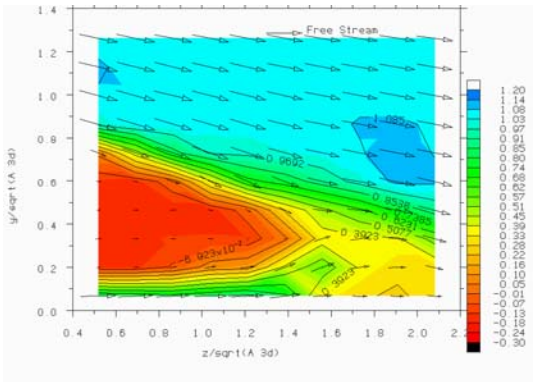

Figure 3.4.29b) t=0.0025s, t/T=0.22

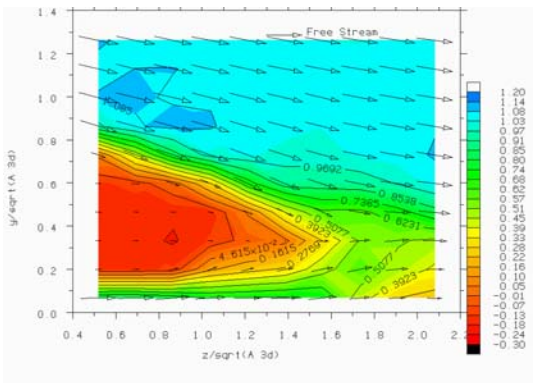

Figure 3.4.29c) t=0.0049s, t/T=0.44

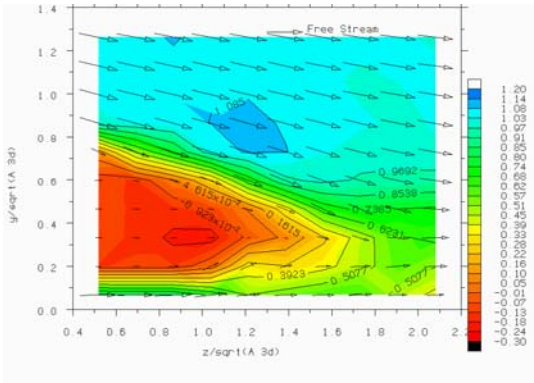

Figure 3.4.29d) t=0.0074s, t/T=0.67

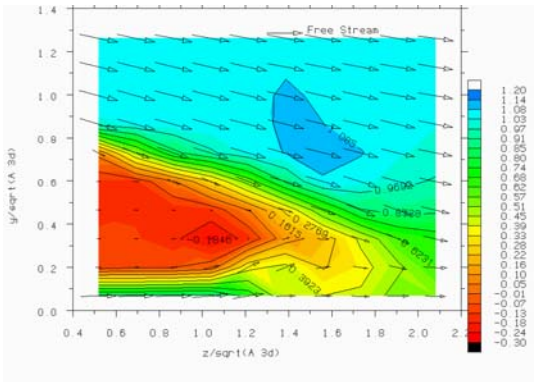

Figure 3.4.29e) t=0.0099s, t/T=0.89

Figure 3.4.29 - Sequence showing total pressure and velocity vectors reconstructed from S=0.5 and S=1.0 (2x1.5hz bands) in the wake of the 2D Ahmed model (22.5 degree backlight)

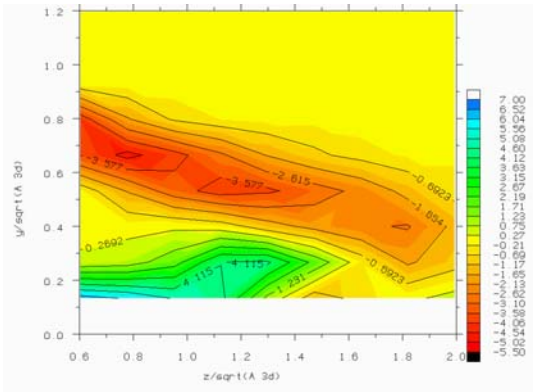

Figure 3.4.30a) t=0.0000s, t/T=0.0

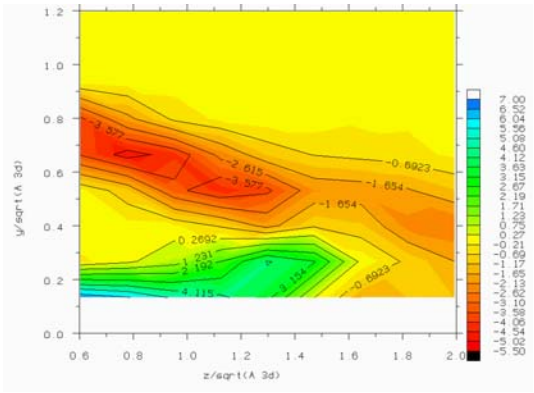

Figure 3.4.30b) t=0.0025s, t/T=0.22

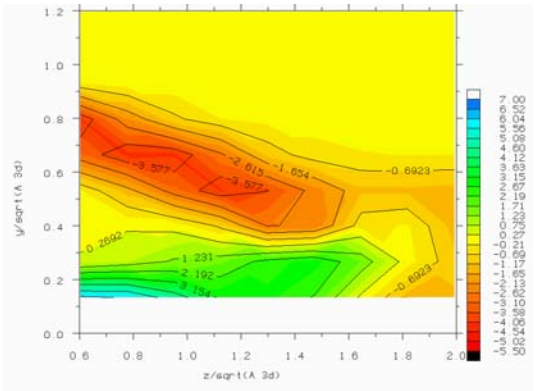

Figure 3.4.30c) t=0.0049s, t/T=0.44

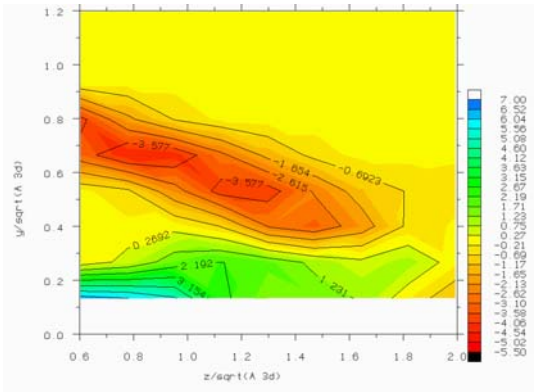

Figure 3.4.30d) t=0.0074s, t/T=0.67

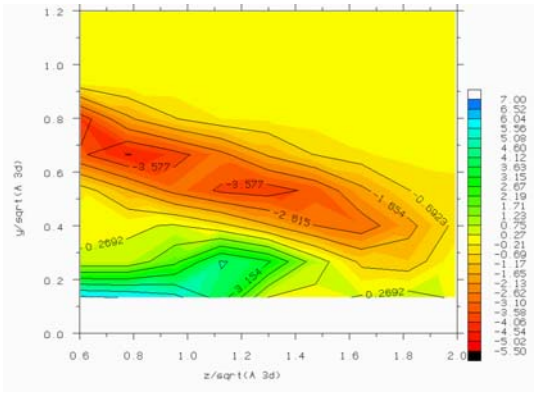

Figure 3.4.30e) t=0.0099s, t/T=0.89

Figure 3.4.30 - Sequence showing vorticity and velocity vectors reconstructed from S=0.5 and S=1.0 (2x1.5hz bands) in the wake of the 2D Ahmed model (22.5 degree backlight)

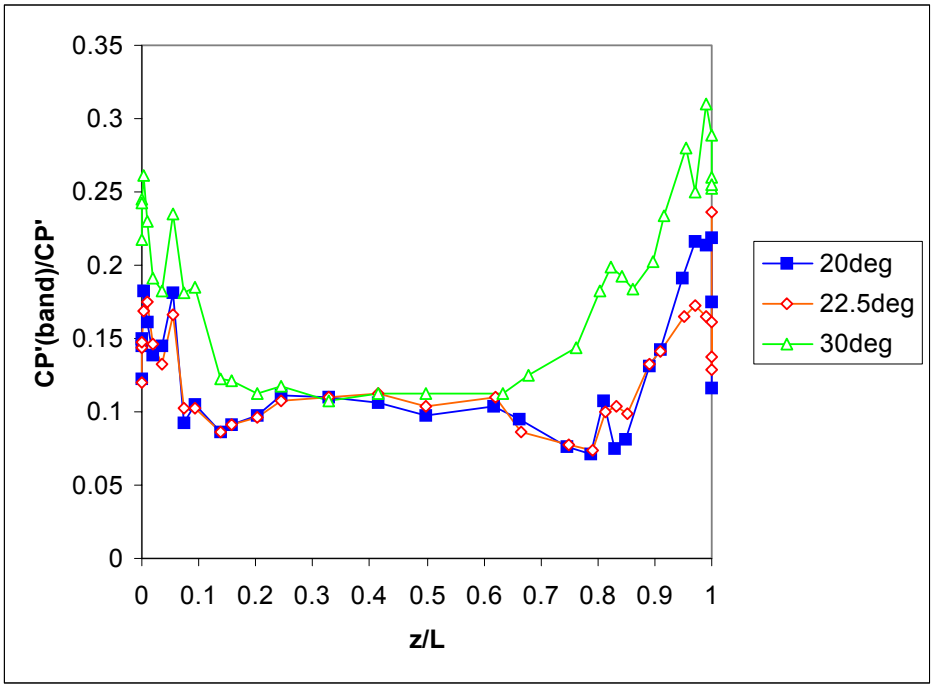

Figure 3.4.31 - Fraction of surface pressure unsteadiness due to specified frequency band on the 2D Ahmed model
20deg and 22.5deg: S=0.47-0.52 (f=85-95hz), 30deg: S=0.25-0.30 (f=45-55hz)

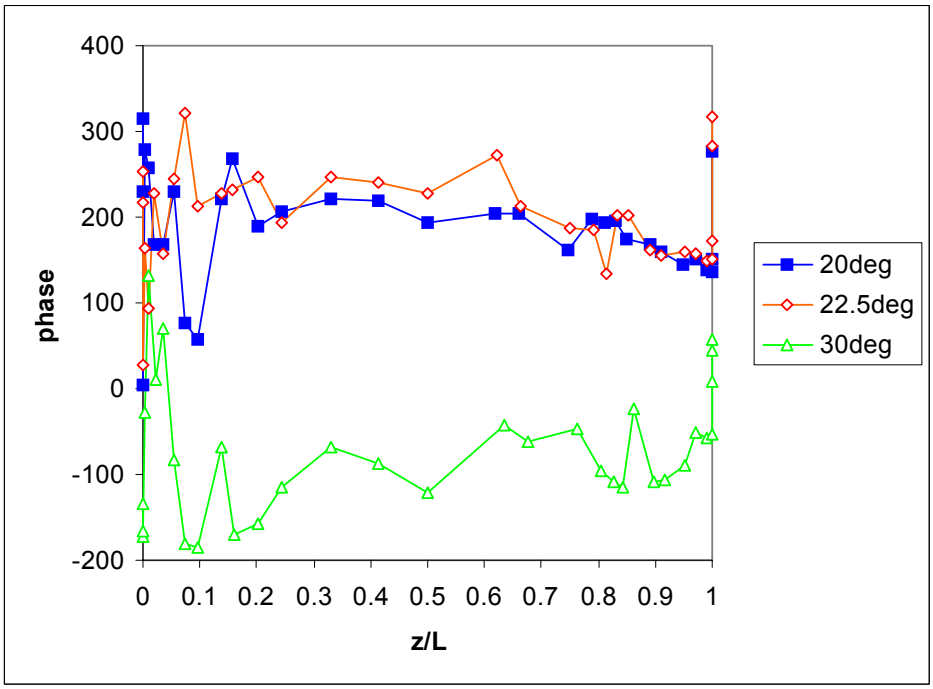

Figure 3.4.32 - Cross-spectral phase near S=0.50 (20deg, 22.5deg), S=0.27 (30deg) between fixed hot-wire and pressure on the surface of the 2D Ahmed model (hot-wire at z/sqrt(A_{3D})=1.73 and y/sqrt(A_{3D})=0.60 (20deg), y/sqrt(A_{3D})=0.53 (22.5deg) y/sqrt(A_{3D})=1.00 (30deg))

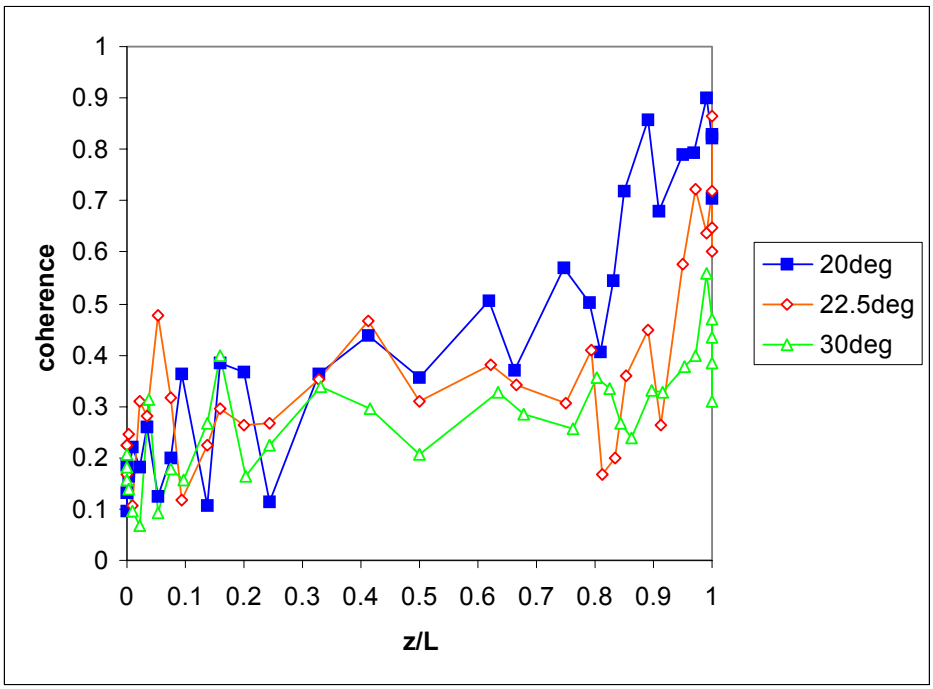

Figure 3.4.33 - Coherence near S=0.50 (20deg, 22.5deg), S=0.27 (30deg) between fixed hot-wire and pressure on the surface of the 2D Ahmed model (hot-wire at $z/\sqrt{A_{3D}}=1.73$ and $y/\sqrt{A_{3D}}=0.60$ (20deg), $y/\sqrt{A_{3D}}=0.53$ (22.5deg) $y/\sqrt{A_{3D}}=1.00$ (30deg))

Figure 3.5.1 - Smoke flow visualisation on Ahmed backlight (30º backlight - high drag flow) ($Re(A^{1/2})=4.4x10^4$)

Figure 3.5.2 - Smoke flow visualisation on Ahmed backlight (30º backlight - low drag flow) ($Re(A^{1/2})=4.4x10^4$)

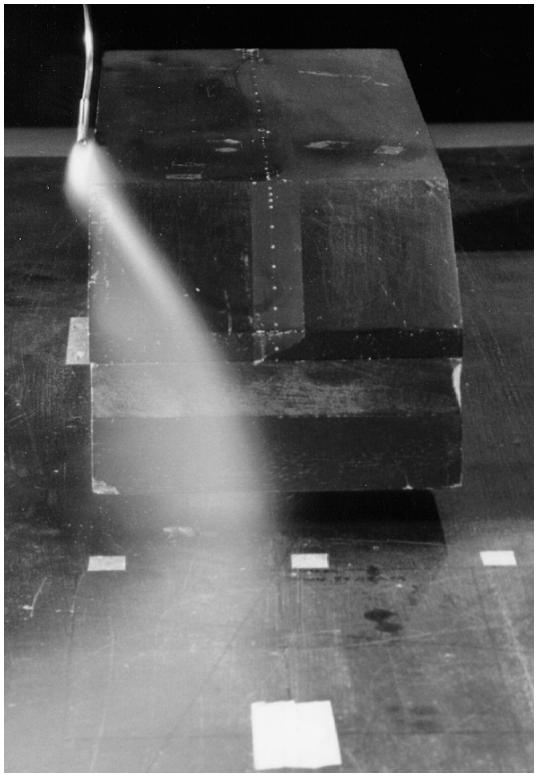

Figure 3.5.3 - Smoke flow visualisation for Ahmed model showing trailing vortex (30º backlight - high drag flow) ($Re(A^{1/2})=4.4x10^4$)

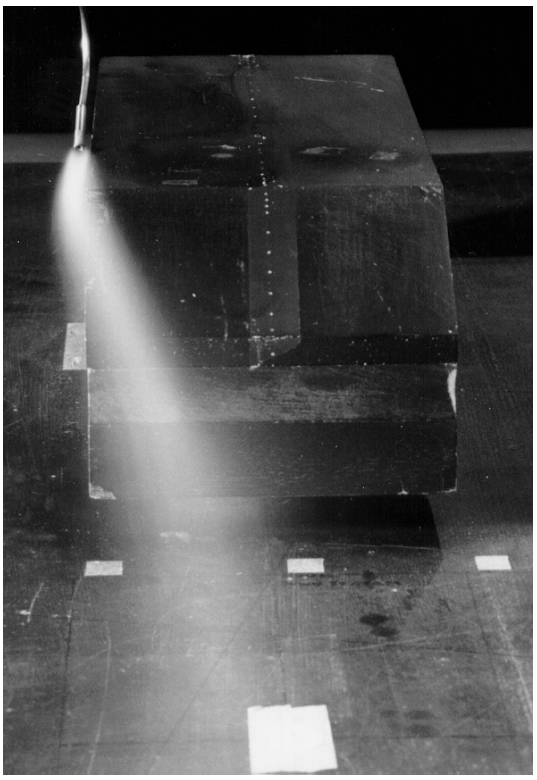

Figure 3.5.4 - Smoke flow visualisation for Ahmed model showing trailing vortex (30º backlight - low drag flow) ($Re(A^{1/2})=4.4x10^4$)

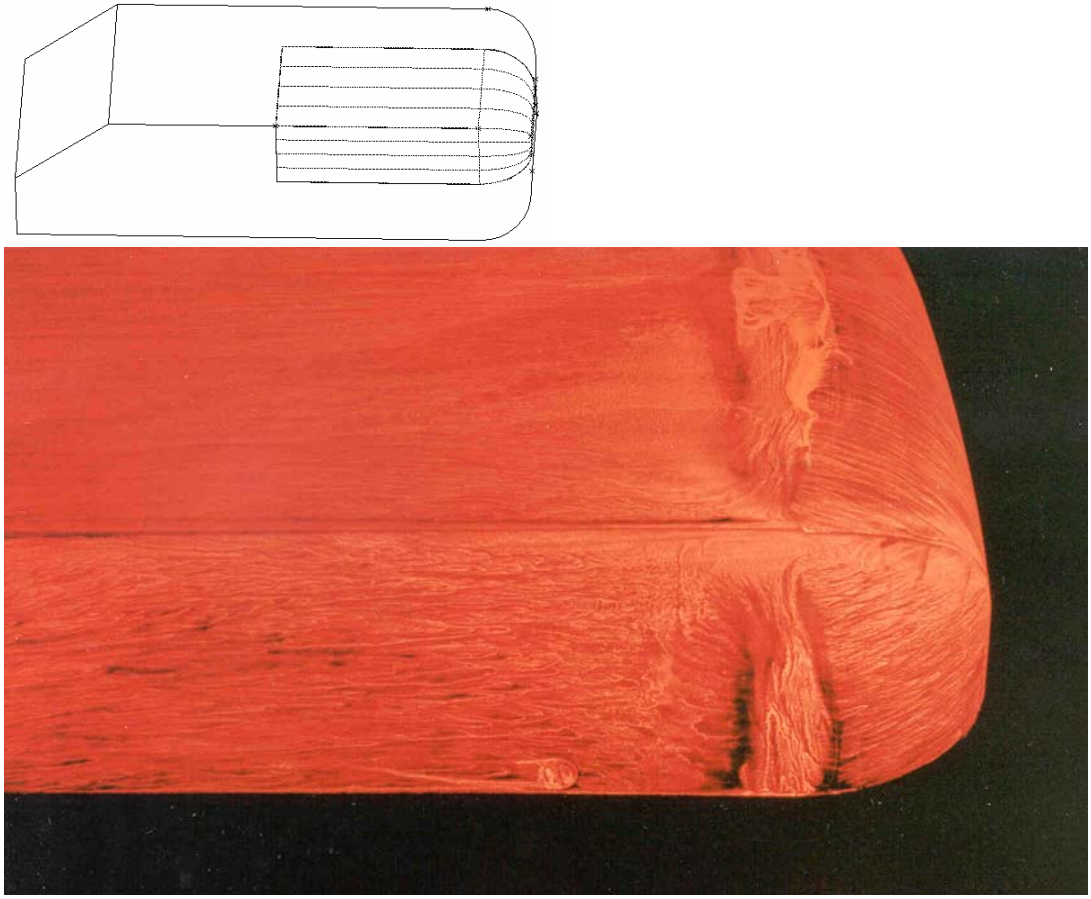

Figure 3.5.5 - Surface oil flow showing forward radius laminar separation bubble on Ahmed model (Dominy (1995b))

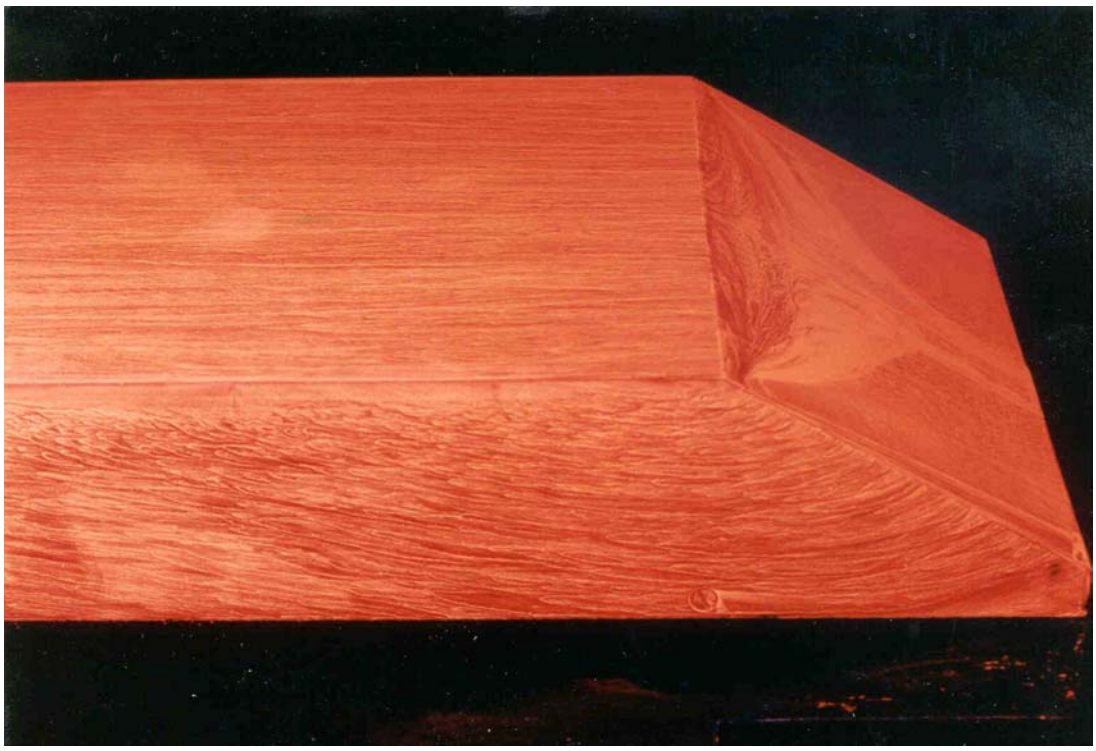

Figure 3.5.6 - Surface oil flow on upper rear of Ahmed model - 30° backlight – high drag flow (Dominy (1995b))

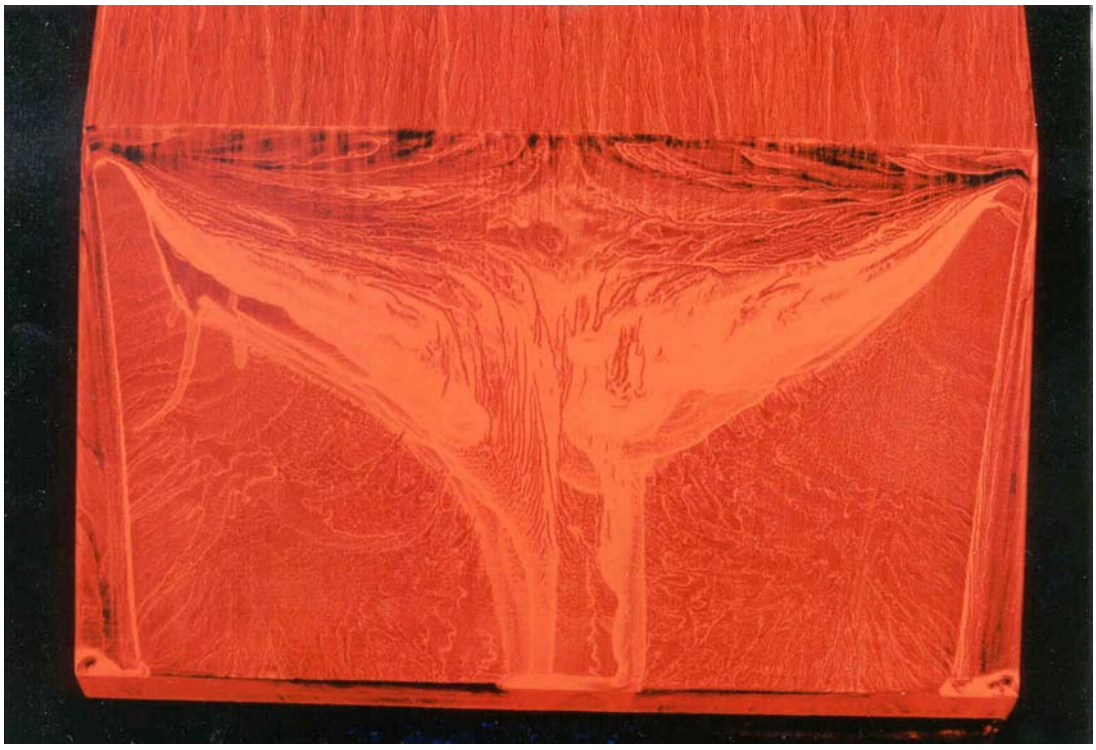

Figure 3.5.7 - Surface oil flow on backlight of Ahmed model - 30° backlight – high drag flow (Dominy (1995b))

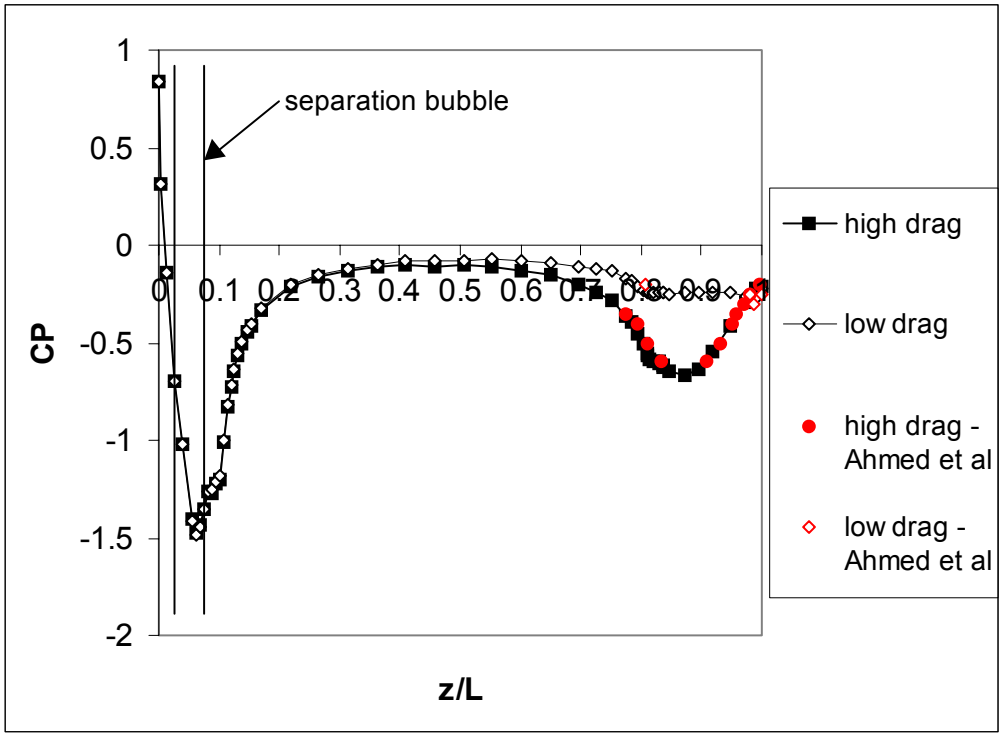

Figure 3.5.8 - Centreline pressure distribution on Ahmed model (30º backlight) for high drag and low drag flow including data from Ahmed et al (1984) (approximate extent of separation bubble indicated)

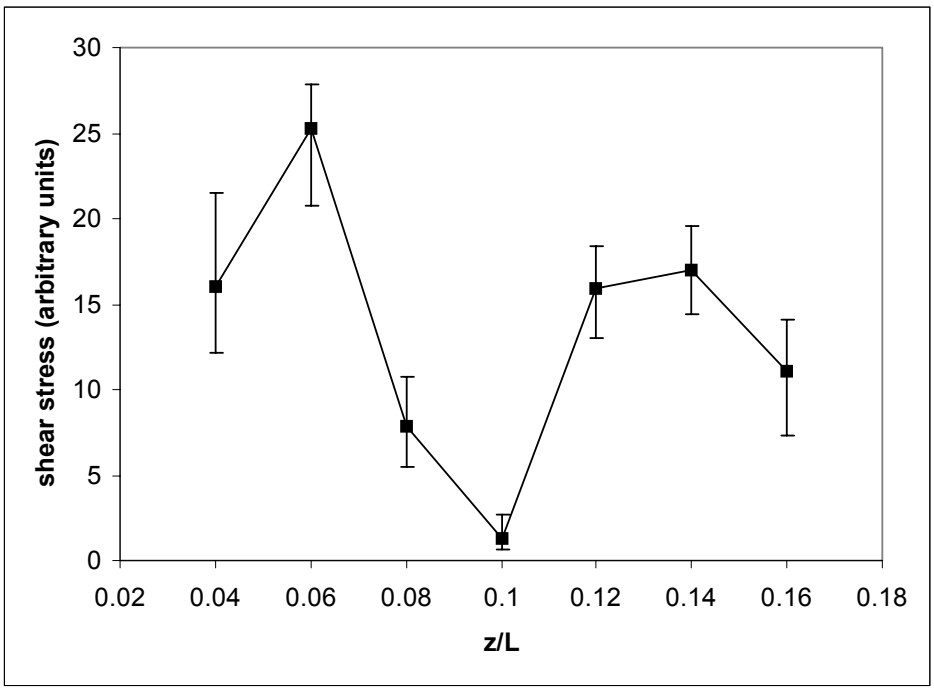

Figure 3.5.9 - Time-averaged shear stress on the forward radius of the Ahmed model measured using surface mounted hot-film gauges

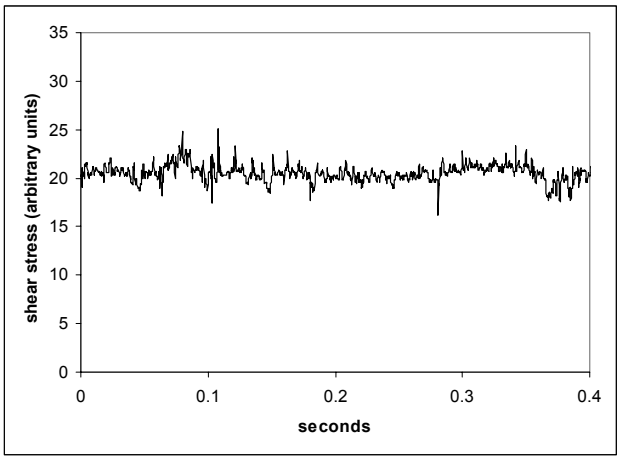

Figure 3.5.10 - Time-trace of shear stress on the forward radius of the Ahmed model at z/L=0.04

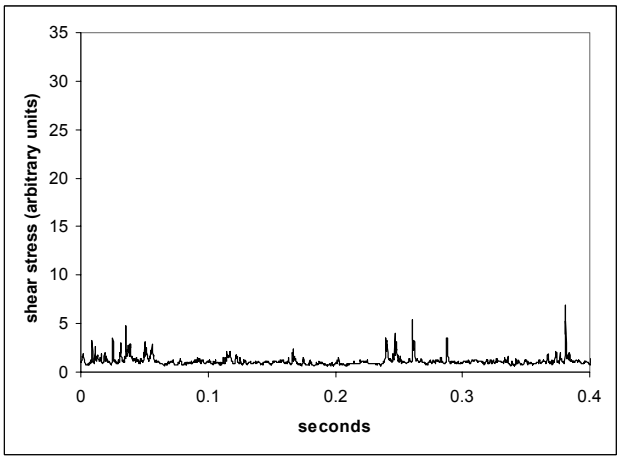

Figure 3.5.11 - Time-trace of shear stress on the forward radius of the Ahmed model at z/L=0.10

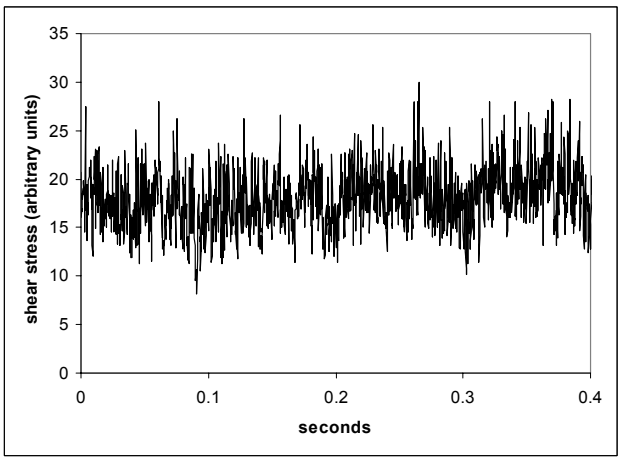

Figure 3.5.12 - Time-trace of shear stress on the forward radius of the Ahmed model at z/L=0.14

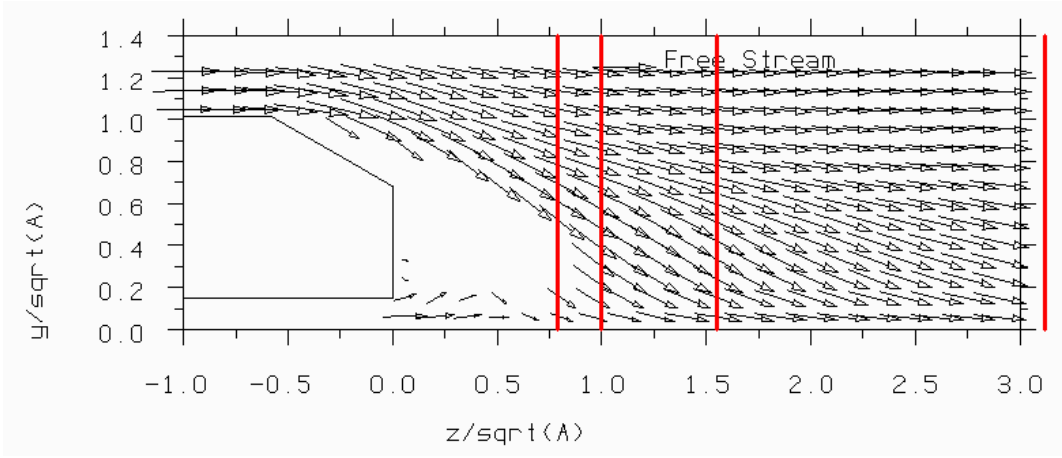

Figure 3.5.13 - Velocity vectors on the centre-plane of the Ahmed model - 30° backlight – high drag flow (1/8 scale) (traverse planes indicated)

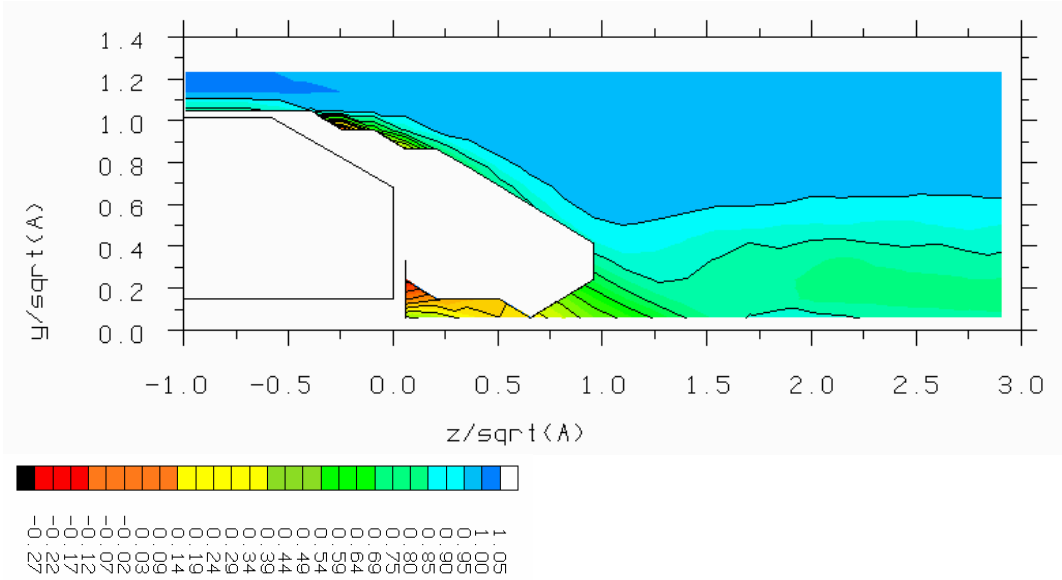

Figure 3.5.14 - Total pressure coefficient on the centre-plane of the Ahmed model - 30° backlight – high drag flow (1/8 scale)

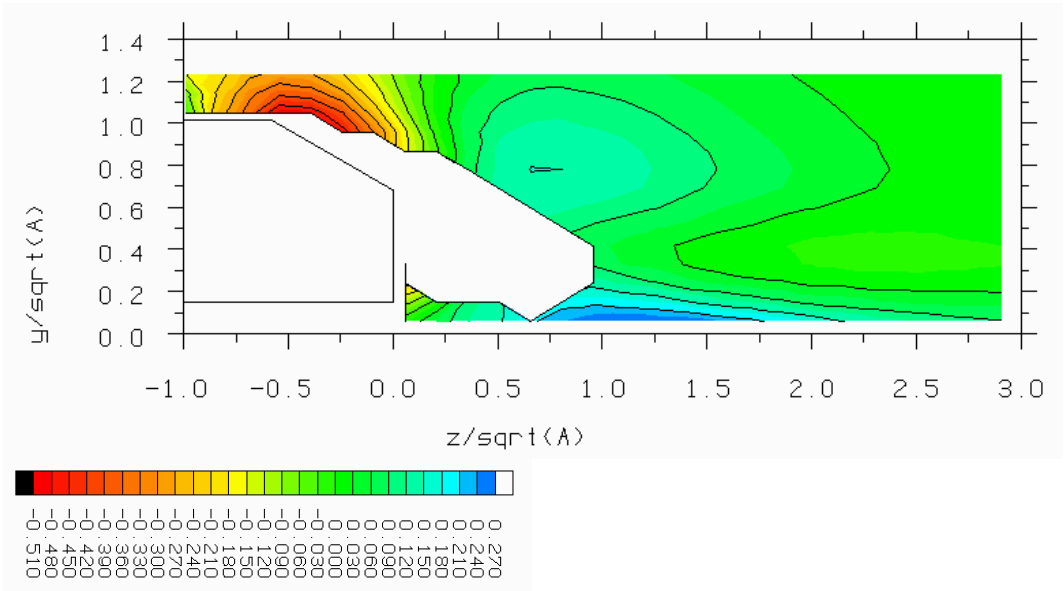

Figure 3.5.15 - Static pressure coefficient on the centre-plane of the Ahmed model - 30° backlight – high drag flow (1/8 scale)

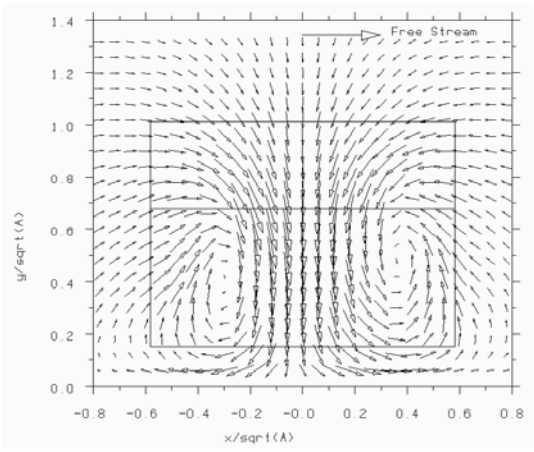

Figure 3.5.16a) z/sqrt(A) = 0.78

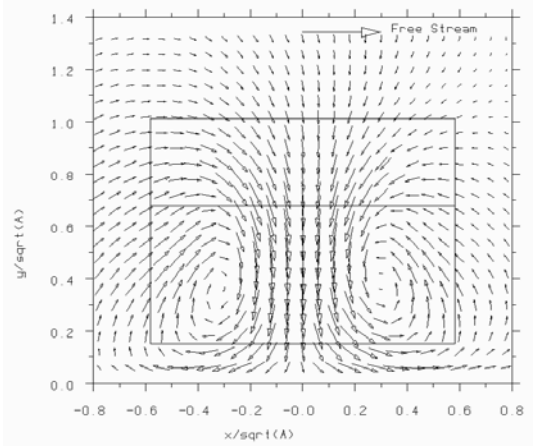

Figure 3.5.16b) z/sqrt(A) = 1.0

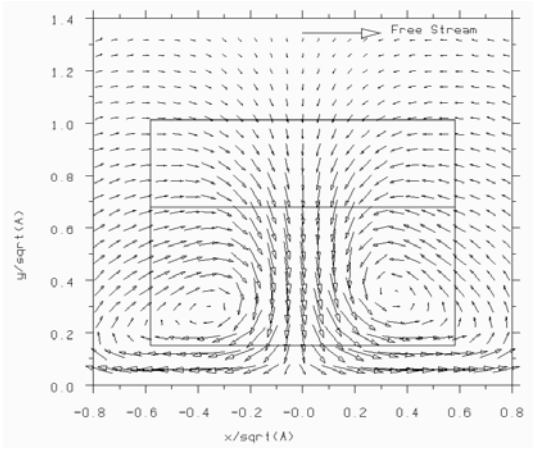

Figure 3.5.16c) z/sqrt(A) = 1.56

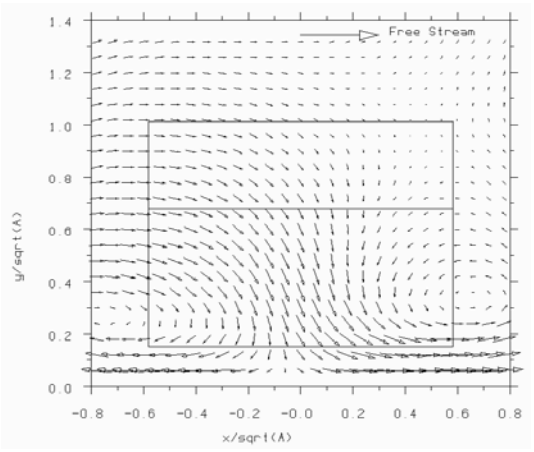

Figure 3.5.16d) z/sqrt(A) = 3.13

Figure 3.6.16 - Velocity vectors in the wake of the Ahmed model - 30° backlight – high drag flow (1/8 scale)

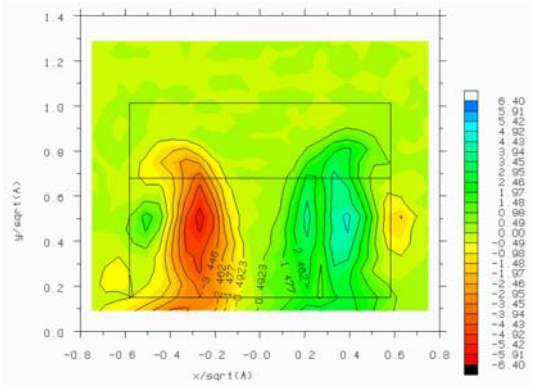

Figure 3.5.17a) z/sqrt(A) = 0.78

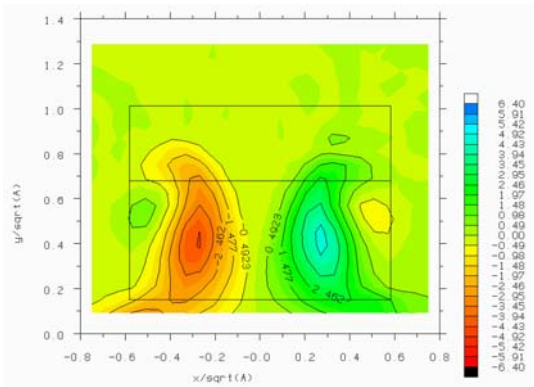

Figure 3.5.17b) z/sqrt(A) = 1.0

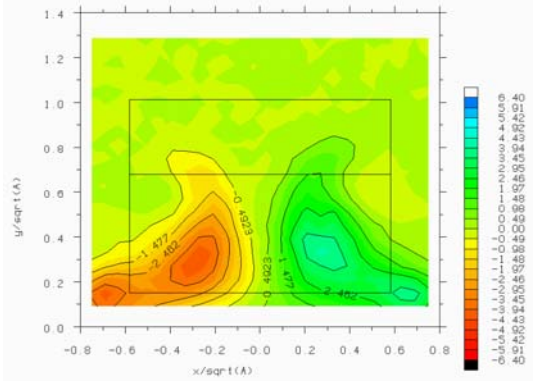

Figure 3.5.17c) z/sqrt(A) = 1.56

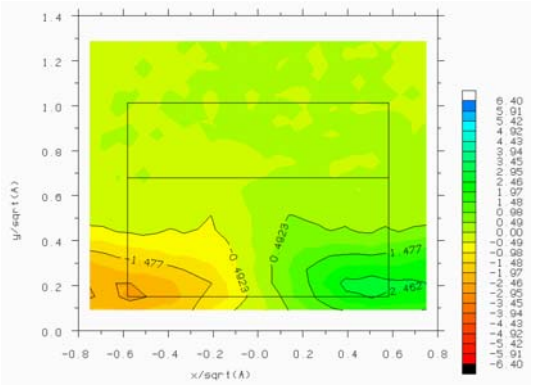

Figure 3.5.17d) z/sqrt(A) = 3.13

Figure 3.6.17 - Streamwise vorticity in the wake of the Ahmed model - 30° backlight – high drag flow (1/4 scale)

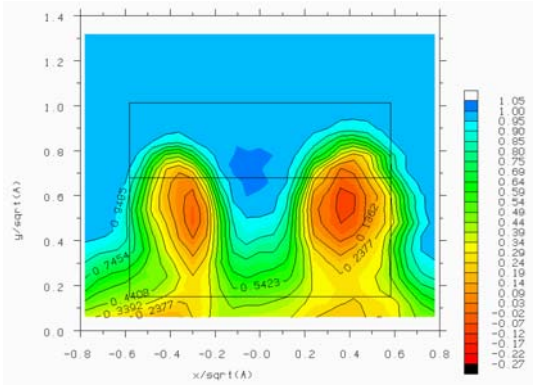

Figure 3.5.18a) z/sqrt(A) = 0.78

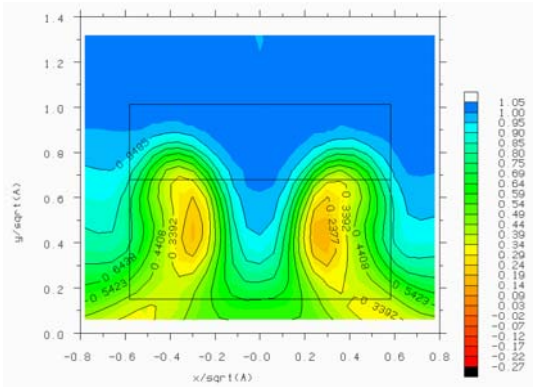

Figure 3.5.18b) z/sqrt(A) = 1.00

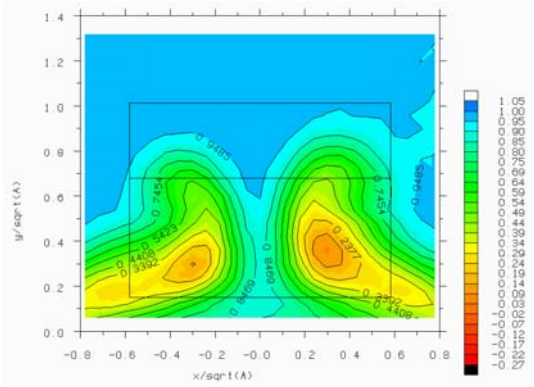

Figure 3.5.18c) z/sqrt(A) = 1.56

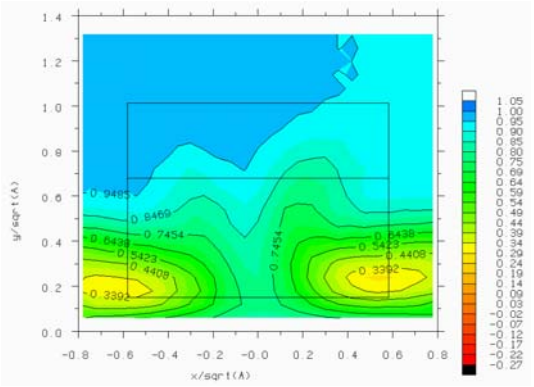

Figure 3.5.18d) z/sqrt(A) = 3.13

Figure 3.6.18 - Total pressure coefficient in the wake of the Ahmed model - 30° backlight – high drag flow (1/4 scale)

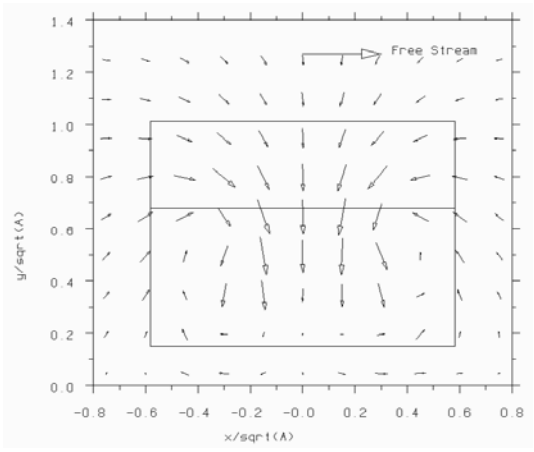

Figure 3.5.19 - Velocity vectors at z/sqrt(A)=0.78 in the wake of the Ahmed model – 27.5° backlight – high drag flow (1/4 scale)

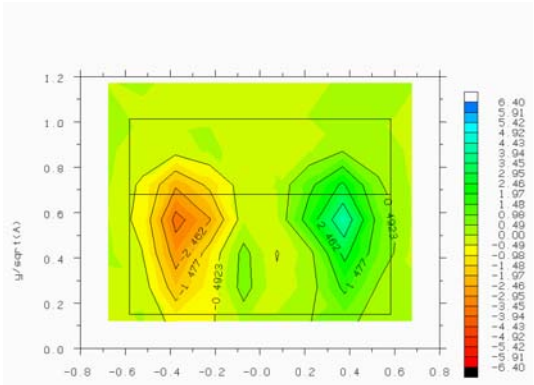

Figure 3.5.20 - Streamwise vorticity at z/sqrt(A)=0.78 in the wake of the Ahmed model – 27.5° backlight – high drag flow (1/4 scale)

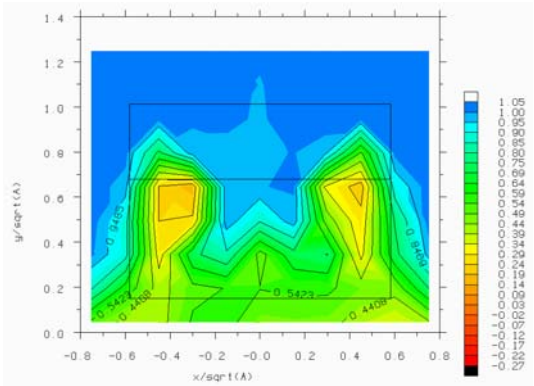

Figure 3.5.21 - Total pressure coefficient at z/sqrt(A)=0.78 in the wake of the Ahmed model – 27.5° backlight – high drag flow (1/4 scale)

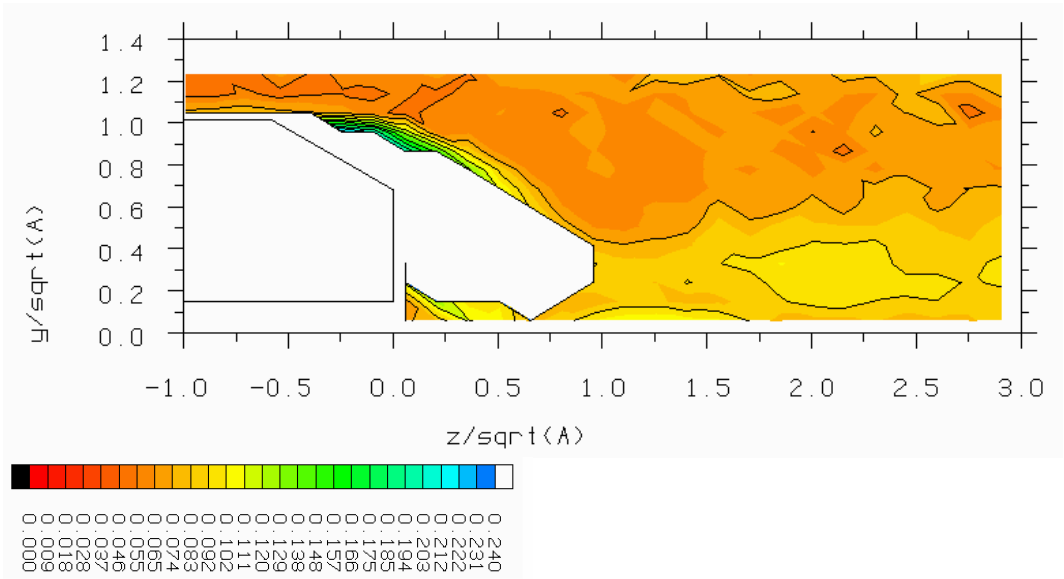

Figure 3.5.22 - Centre-plane centre-hole pressure coefficient unsteadiness (standard deviation) in the wake of the Ahmed model (30° backlight, high-drag flow, 1/8 scale)

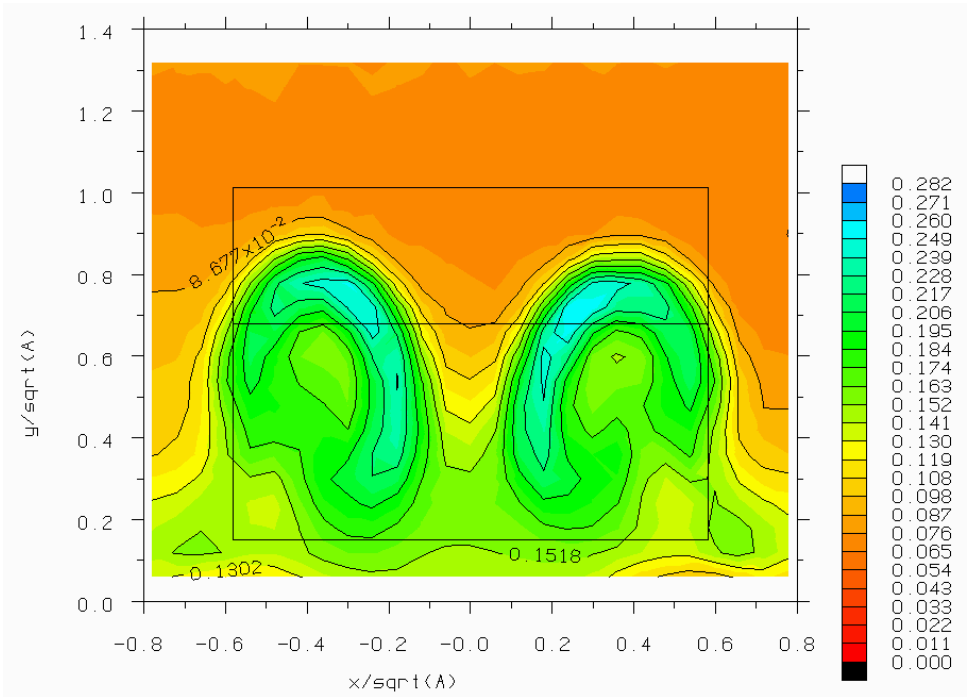

Figure 3.5.23 - Total pressure coefficient unsteadiness (standard deviation) at z/sqrt(A)=1.0 in the wake of the Ahmed model (30° backlight, high-drag flow, 1/8 scale)

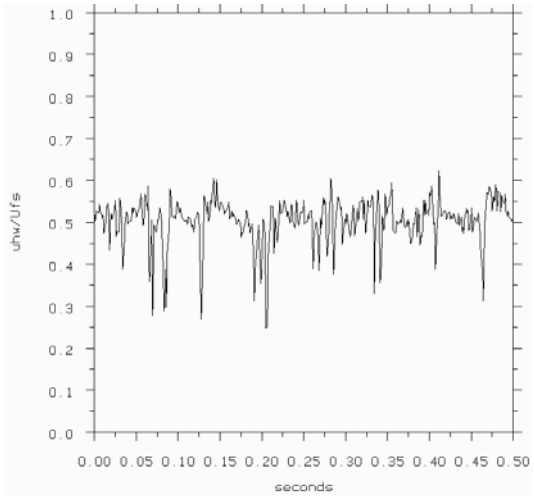

Figure 3.5.24 - Time-trace of hot-wire effective velocity at x/sqrt(A)=0.36, y/sqrt(A)=0.84, z/sqrt(A)=0.78 in the wake of the Ahmed model (30° backlight, high-drag flow, 1/8 scale)

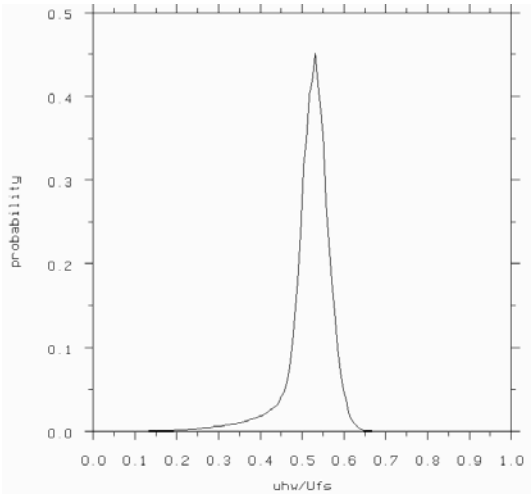

Figure 3.5.25 - Probability density function of hot-wire effective velocity at x/sqrt(A)=0.36, y/sqrt(A)=0.84, z/sqrt(A)=0.78 in the wake of the Ahmed model (30° backlight, high-drag flow, 1/8 scale)

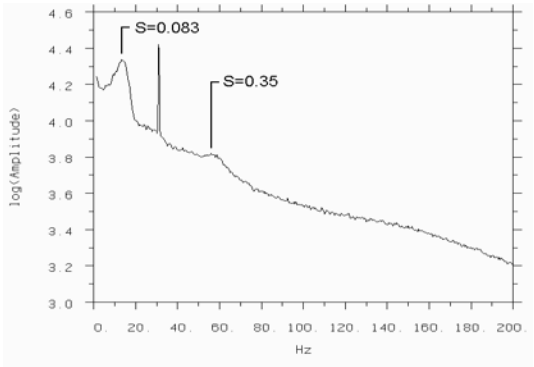

Figure 3.5.26 - Autospectral density function for hot-wire effective velocity at x/sqrt(A)=0.36, y/sqrt(A)=0.84, z/sqrt(A)=0.78 in the wake of the Ahmed model (30° backlight, high-drag flow, 1/8 scale)

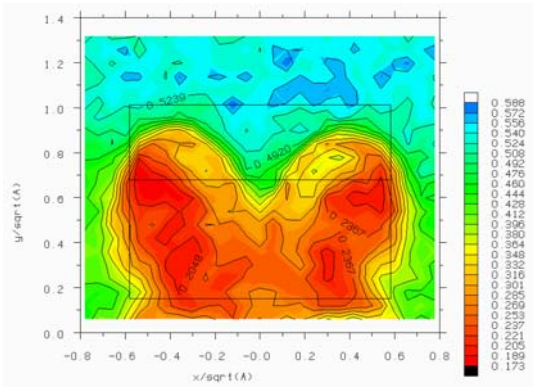

Figure 3.5.27 - Fraction of total pressure unsteadiness due to frequency band near S=0.08 (S=0.07-0.09, f=11-15hz) one base dimension behind the Ahmed model (30° backlight, high-drag flow, 1/8 scale)

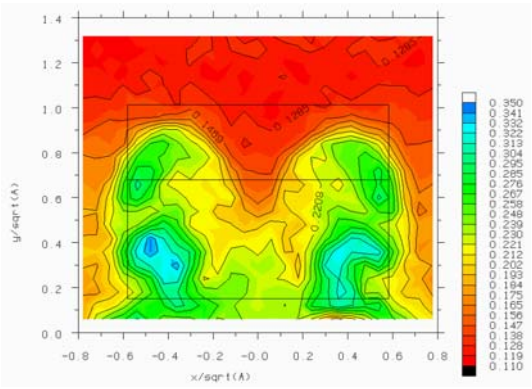

Figure 3.5.28 - Fraction of total pressure unsteadiness due to frequency band near S=0.34 (S=0.31-0.38, f=50-60hz) one base dimension behind the Ahmed model (30° backlight, high-drag flow, 1/8 scale)

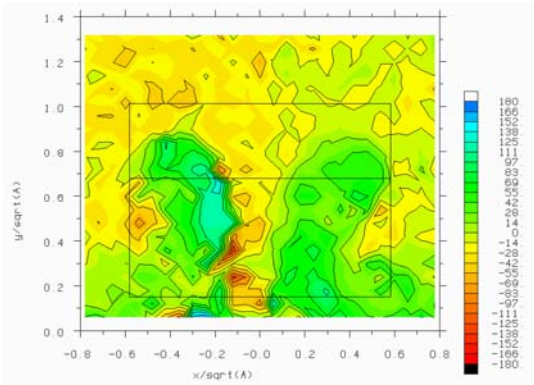

Figure 3.5.29 - Cross-spectral phase between fluctuating total pressure and reference hot-wire velocity near S=0.08 one base dimension behind the Ahmed model (30° backlight, high-drag flow, 1/8 scale) (reference hot-wire at: x/sqrt(A)=0.36, y/sqrt(A)=0.84, z/sqrt(A)=0.78)

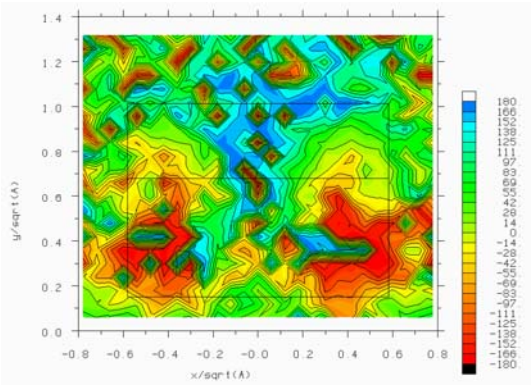

Figure 3.5.30 - Cross-spectral phase between fluctuating total pressure and reference hot-wire velocity near S=0.34 one base dimension behind the Ahmed model (30° backlight, high-drag flow, 1/8 scale) (reference hot-wire at: x/sqrt(A)=0.36, y/sqrt(A)=0.84, z/sqrt(A)=0.78)

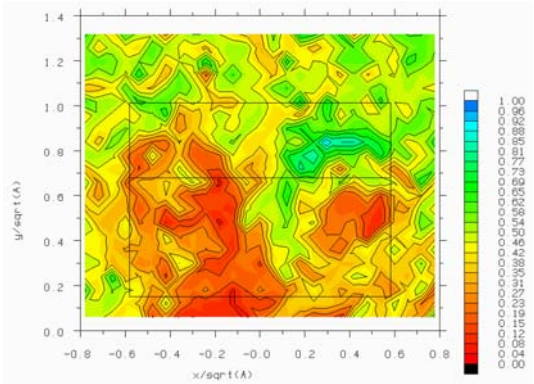

Figure 3.5.31 - Coherence between fluctuating total pressure and reference hot-wire velocity near S=0.08 one base dimension behind the Ahmed model (30° backlight, high-drag flow, 1/8 scale) (reference hot-wire at: x/sqrt(A)=0.36, y/sqrt(A)=0.84, z/sqrt(A)=0.78)

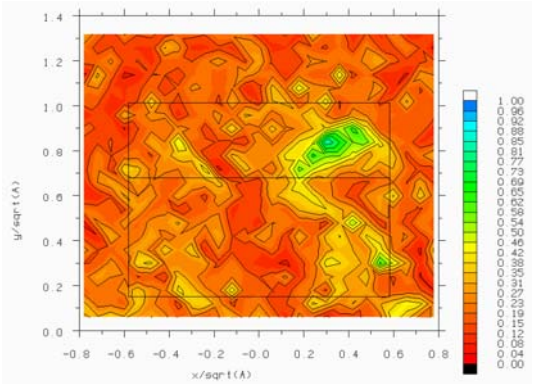

Figure 3.5.32 - Coherence between fluctuating total pressure and reference hot-wire velocity near S=0.34 one base dimension behind the Ahmed model (30° backlight, high-drag flow, 1/8 scale) (reference hot-wire at: x/sqrt(A)=0.36, y/sqrt(A)=0.84, z/sqrt(A)=0.78)

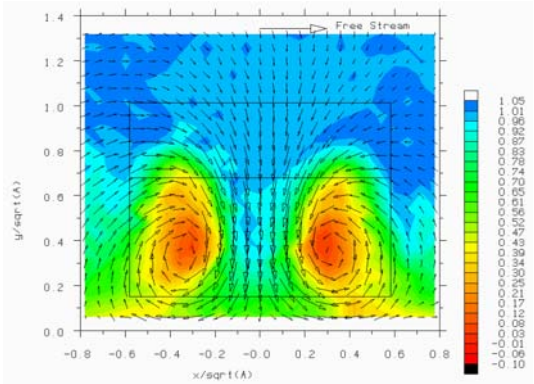

Figure 3.5.33a) t=0.0s, t/T=0.0

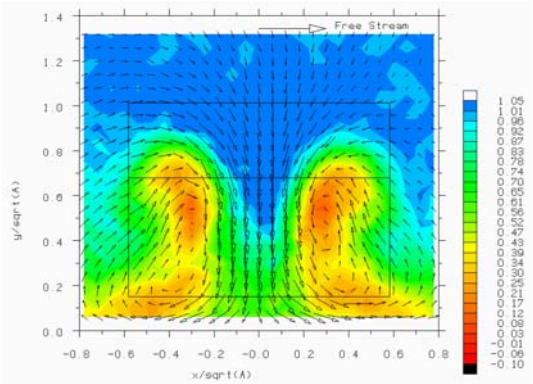

Figure 3.5.33d) t=0.0073s, t/T=0.400

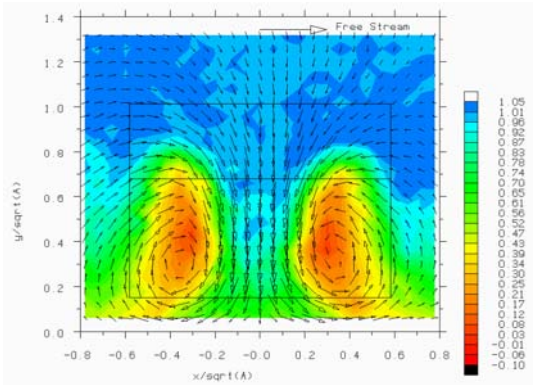

Figure 3.5.33b) t=0.0024s, t/T=0.133

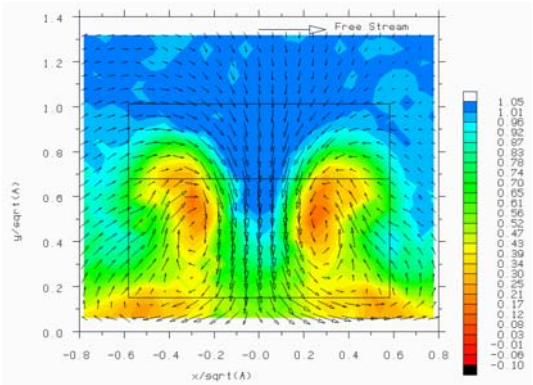

Figure 3.5.33e) t=0.0097s, t/T=0.533

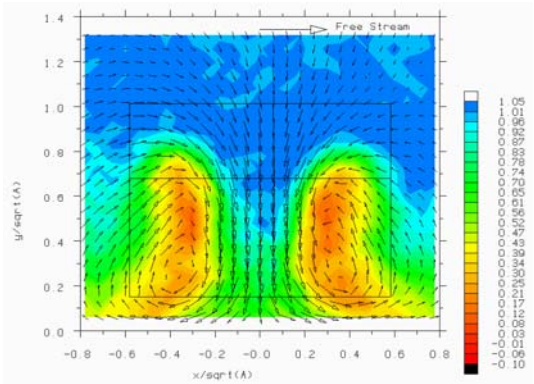

Figure 3.5.33c) t=0.0048s, t/T=0.267

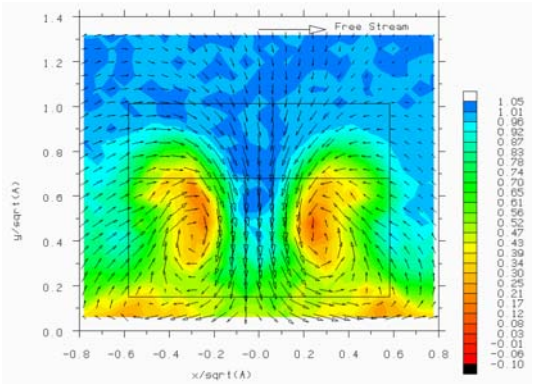

Figure 3.5.33f) t=0.0121s, t/T=0.667

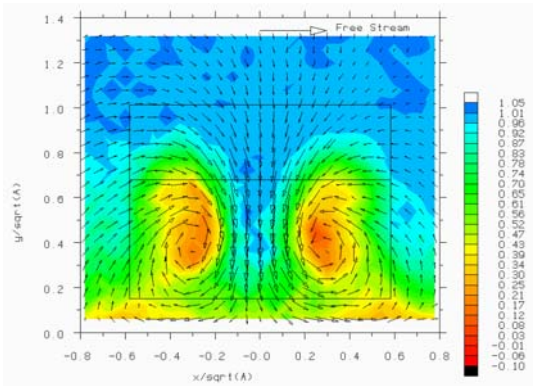

Figure 3.5.33g) t=0.0145s, t/T=0.800

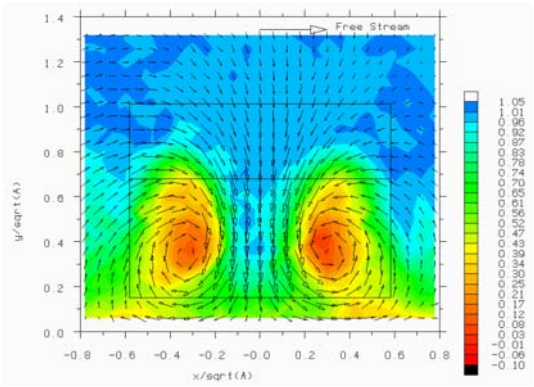

Figure 3.5.33h) t=0.0170s, t/T=0.933

Figure 3.5.33 - Sequence showing total pressure coefficient and velocity vectors reconstructed from S=0.34 (4hz band@~55hz) one base dimension behind the Ahmed model (30° backlight, high-drag flow, 1/8 scale)

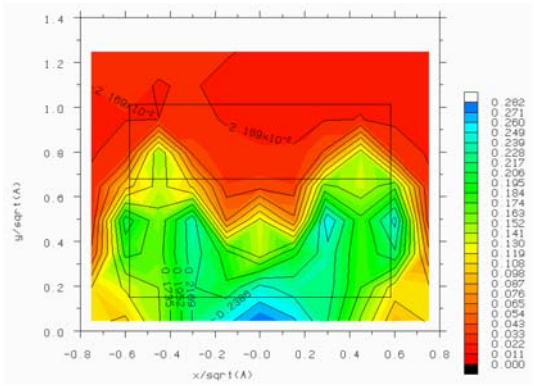

Figure 3.5.34 - Total pressure coefficient unsteadiness (standard deviation) at z/sqrt(A)=0.78 in the wake of the Ahmed model (27.5° backlight, high-drag flow, 1/4 scale)

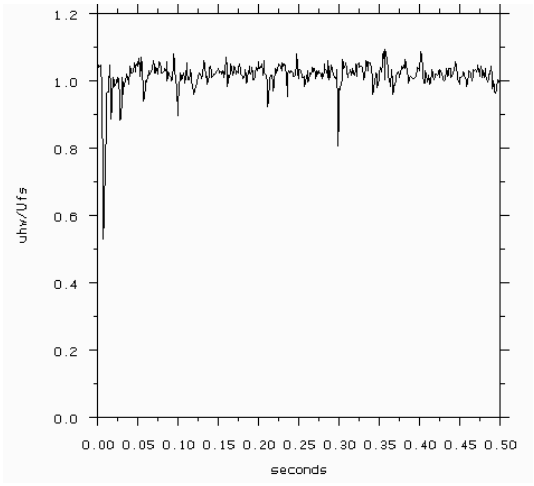

Figure 3.5.35 - Time-trace of hot-wire effective velocity at x/sqrt(A)=0.35, y/sqrt(A)=0.84, z/sqrt(A)=0.78 in the wake of the Ahmed model (27.5° backlight, high-drag flow, 1/4 scale)

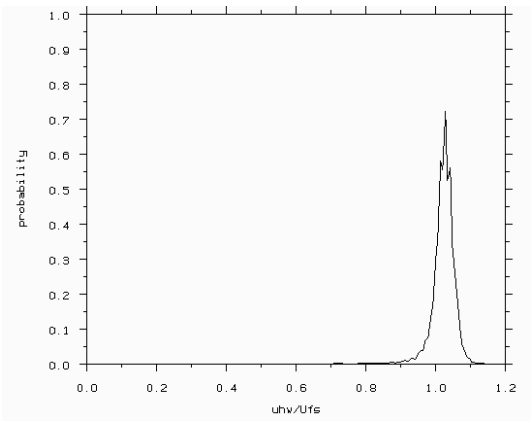

Figure 3.5.36 - Probability density function of hot-wire effective velocity at x/sqrt(A)=0.35, y/sqrt(A)=0.84, z/sqrt(A)=0.78 in the wake of the Ahmed model (27.5° backlight, high-drag flow, 1/4 scale)

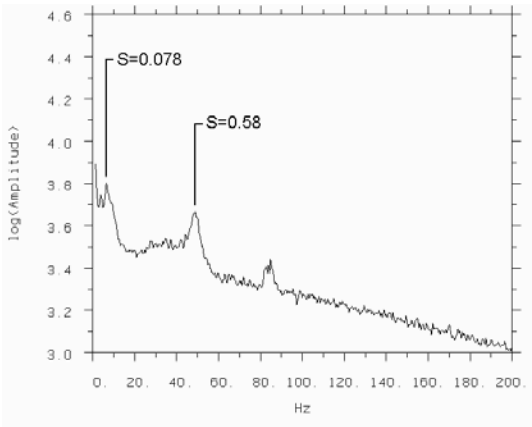

Figure 3.5.37 - Autospectral density function for hot-wire effective velocity at x/sqrt(A)=0.35, y/sqrt(A)=0.84, z/sqrt(A)=0.78 in the wake of the Ahmed model (27.5° backlight, high-drag flow, 1/4 scale)

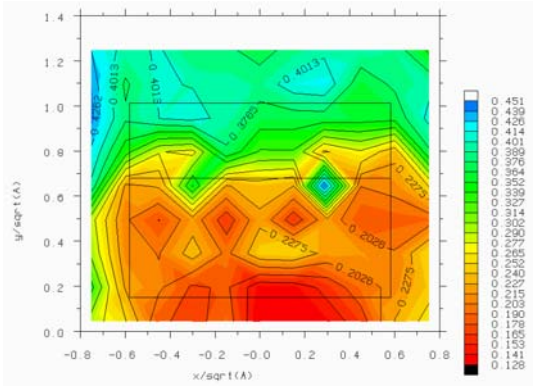

Figure 3.5.38 - Fraction of total pressure unsteadiness due to frequency band near S=0.08 (S=0.06-0.11, f=5-9hz) at z/sqrt(A)=0.78 behind the Ahmed model (27.5° backlight, high-drag flow, 1/4 scale)

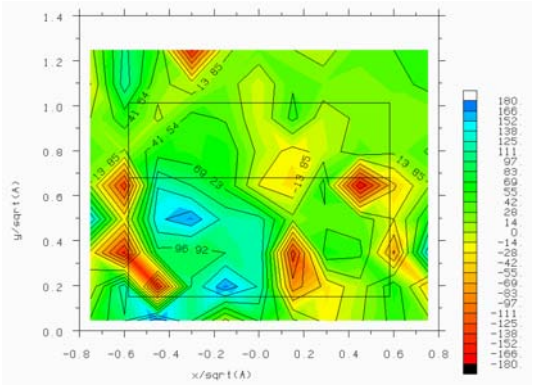

Figure 3.5.40 - Cross-spectral phase between fluctuating total pressure and reference hot-wire velocity near S=0.08 at z/sqrt(A)=0.78 behind the Ahmed model (27.5° backlight, high-drag flow, 1/4 scale) (reference hot-wire at: x/sqrt(A)=0.35, y/sqrt(A)=0.84, z/sqrt(A)=0.78)

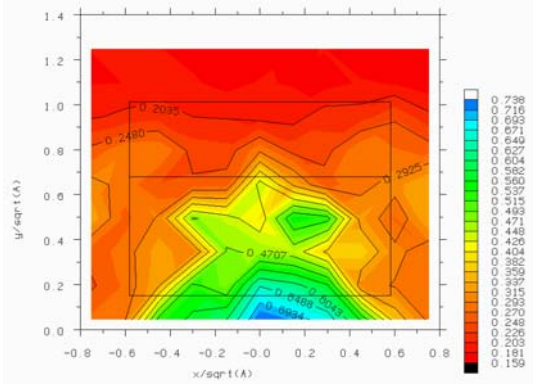

Figure 3.5.39 - Fraction of total pressure unsteadiness due to frequency band near S=0.58 (S=0.54-0.65, f=45-55hz) at z/sqrt(A)=0.78 behind the Ahmed model (27.5° backlight, high-drag flow, 1/4 scale)

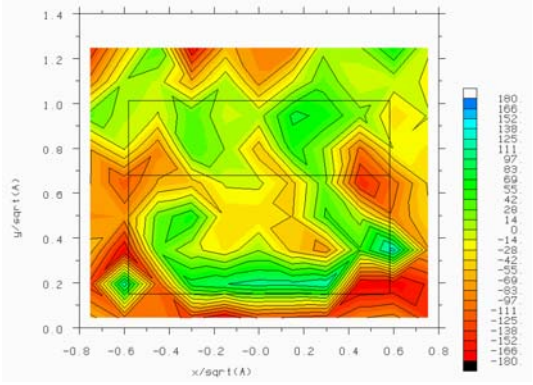

Figure 3.5.41 - Cross-spectral phase between fluctuating total pressure and reference hot-wire velocity near S=0.58 at z/sqrt(A)=0.78 behind the Ahmed model (27.5° backlight, high-drag flow, 1/4 scale) (reference hot-wire at: x/sqrt(A)=0.35, y/sqrt(A)=0.84, z/sqrt(A)=0.78)

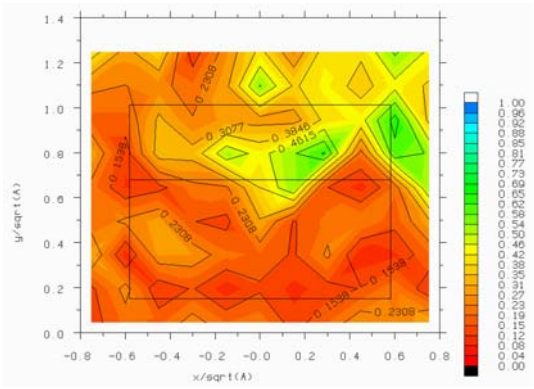

Figure 3.5.42 - Coherence between fluctuating total pressure and reference hot-wire velocity near S=0.08 at z/sqrt(A)=0.78 behind the Ahmed model (27.5° backlight, high-drag flow, 1/4 scale) (reference hot-wire at: x/sqrt(A)=0.35, y/sqrt(A)=0.84, z/sqrt(A)=0.78)

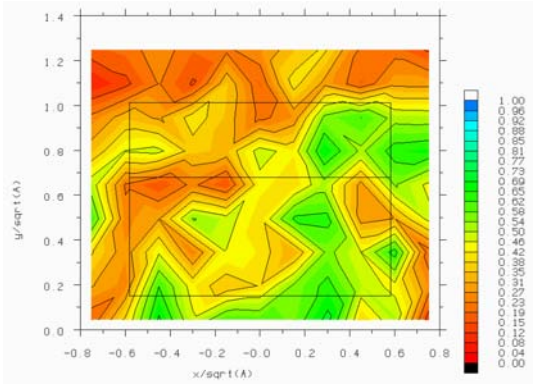

Figure 3.5.43 - Coherence between fluctuating total pressure and reference hot-wire velocity near S=0.58 at z/sqrt(A)=0.78 behind the Ahmed model (27.5° backlight, high-drag flow, 1/4 scale) (reference hot-wire at: x/sqrt(A)=0.35, y/sqrt(A)=0.84, z/sqrt(A)=0.78)

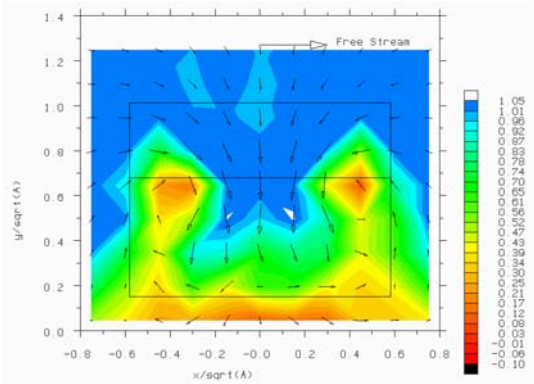

Figure 3.5.44 a) t=0.0s, t/T=0.0

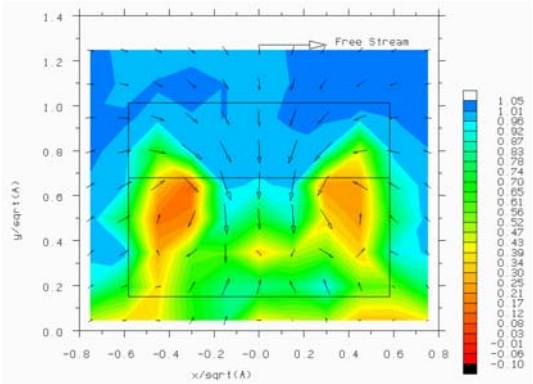

Figure 3.5.44 d) t=0.0075 s, t/T=0.375

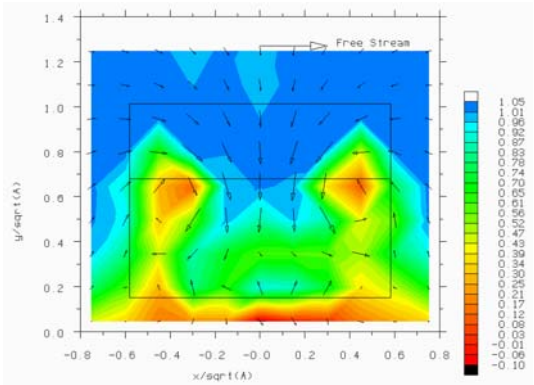

Figure 3.5.44 b) t=0.0025s, t/T=0.125

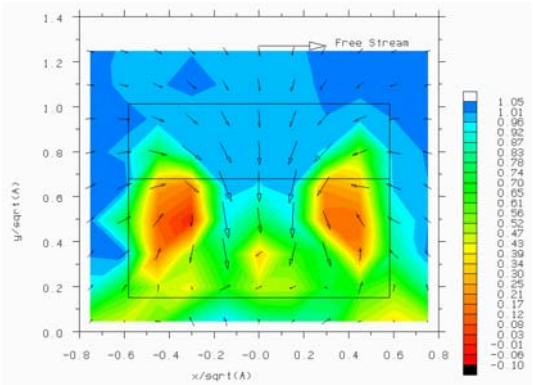

Figure 3.5.44 e) t=0.0100 s, t/T=0.500

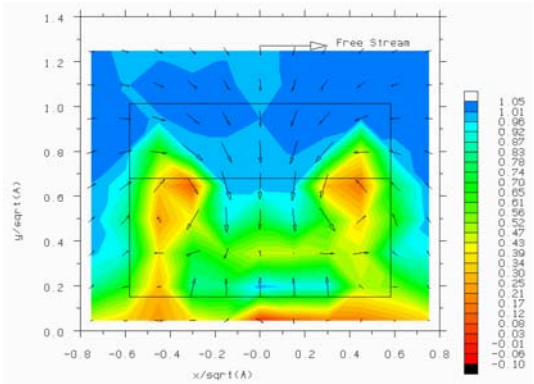

Figure 3.5.44 c) t=0.0050s, t/T=0.250

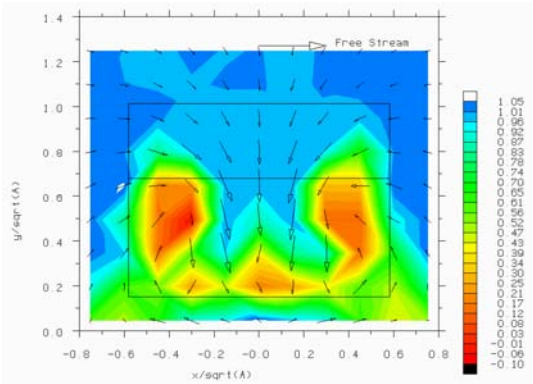

Figure 3.5.44 f) t=0.0125s, t/T=0.6250

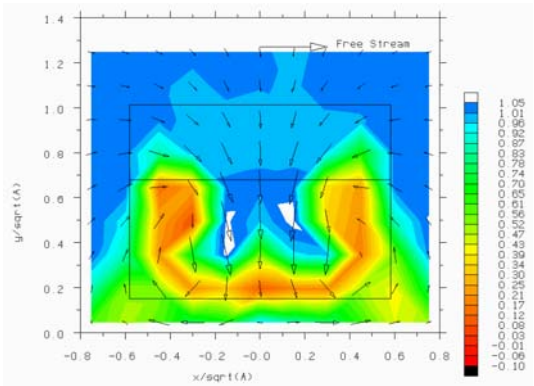

Figure 3.5.44 g) t=0.0150s, t/T=0.7500

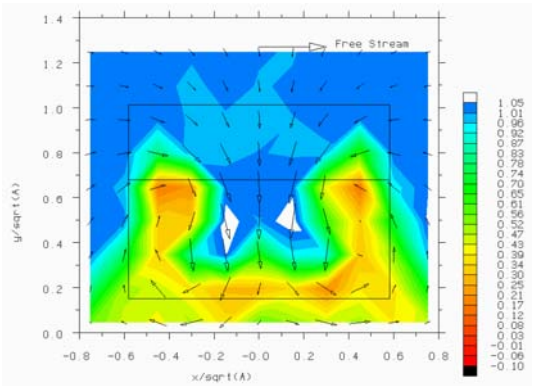

Figure 3.5.44 h) t=0.0175s, t/T=0.8750

Figure 3.5.44 - Sequence showing total pressure coefficient and velocity vectors reconstructed from S=0.58 (4hz band@~50hz) at z/sqrt(A)=0.78 behind the Ahmed model (27.5° backlight, high-drag flow, 1/4 scale)

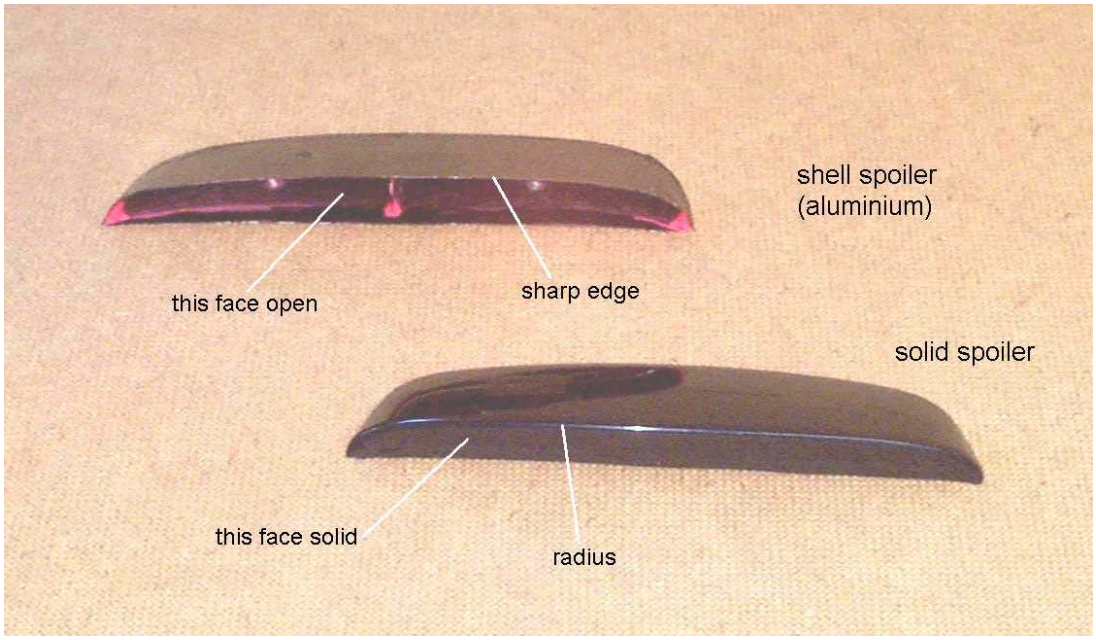

Figure 3.6.1 - Solid and shell spoilers (aluminium) for the 15% R3 model

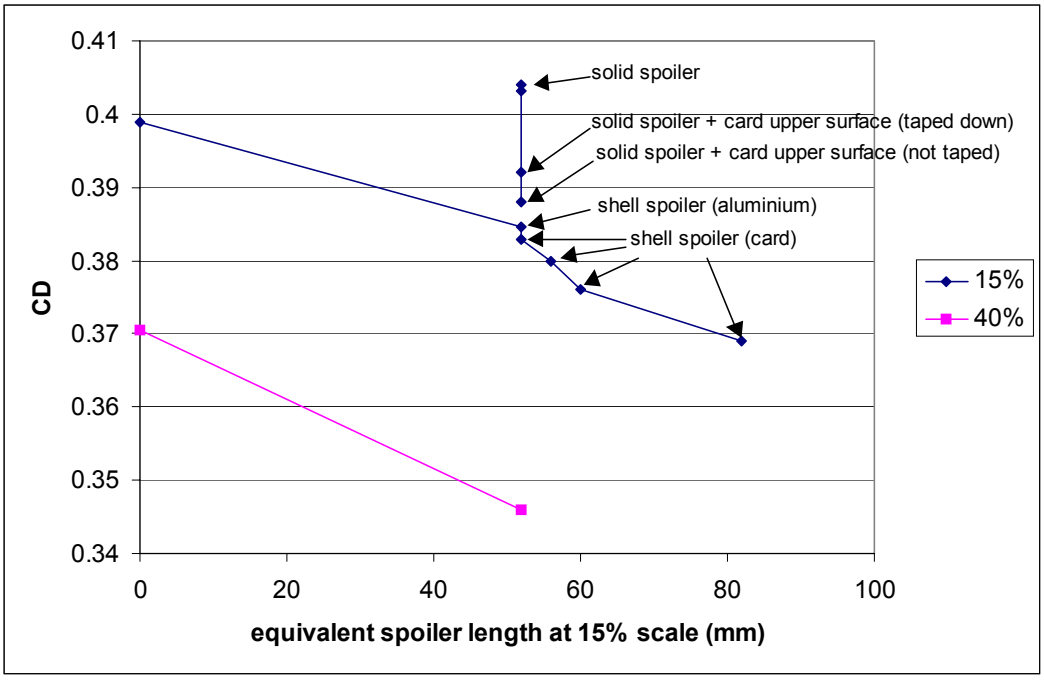

Figure 3.6.2 - Effect of spoiler size and design on drag

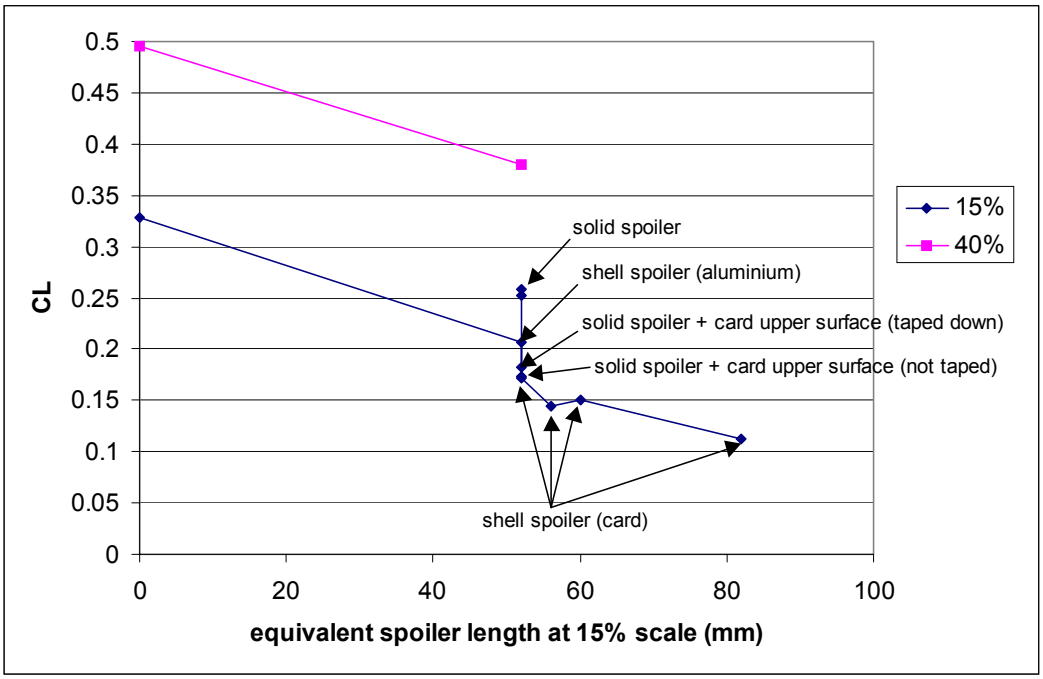

Figure 3.6.3 - Effect of spoiler size and design on total lift

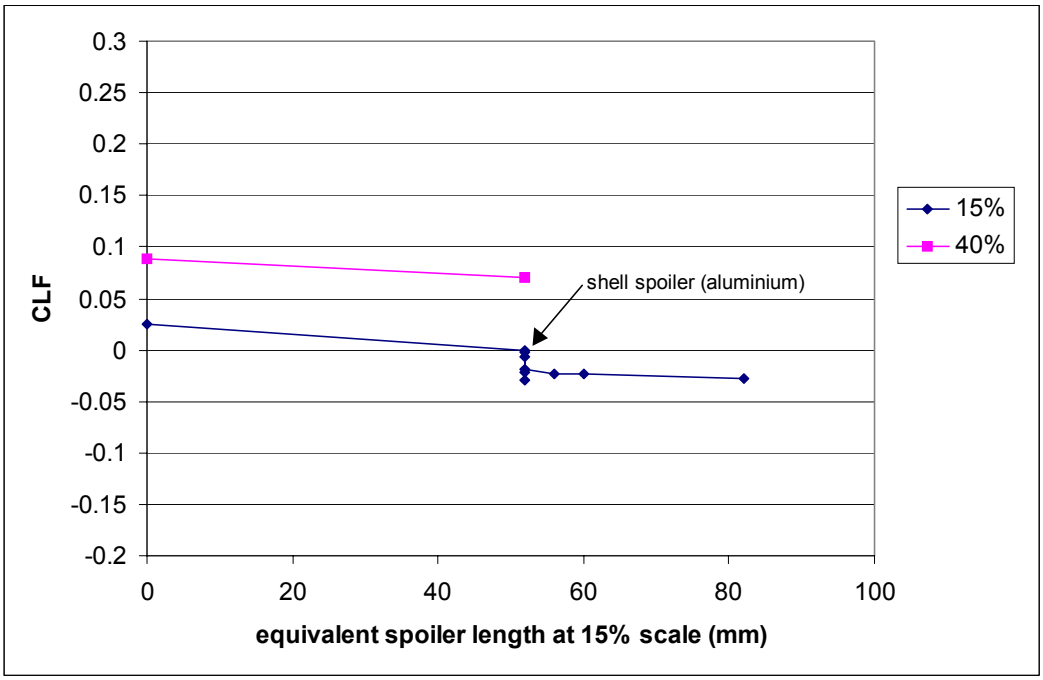

Figure 3.6.4 - Effect of spoiler size and design on front lift

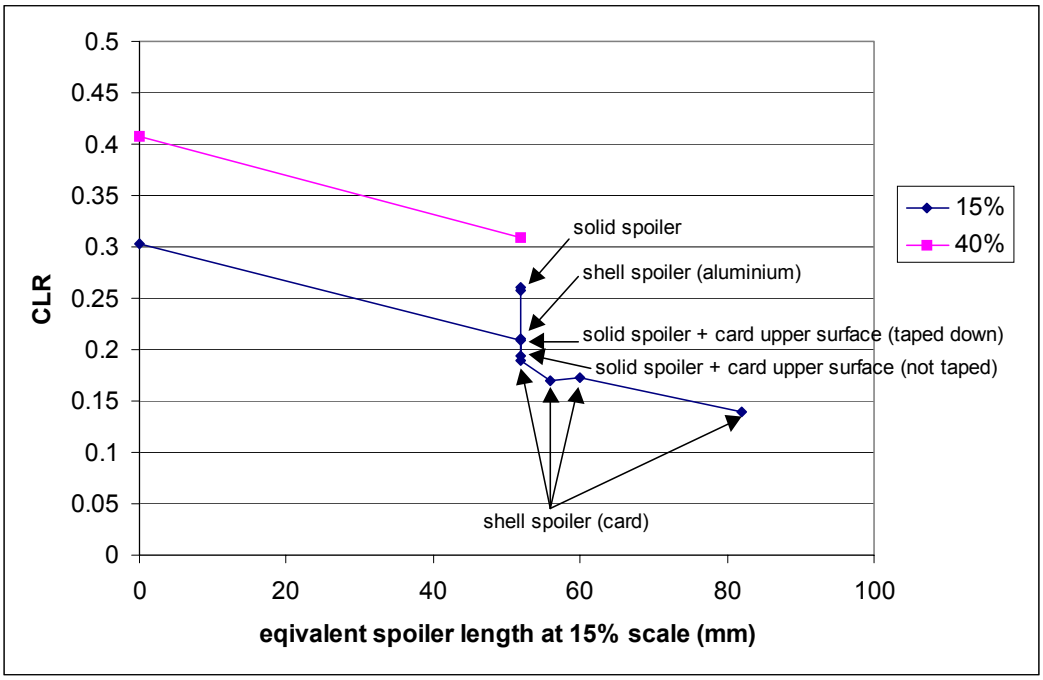

Figure 3.6.5 - Effect of spoiler size and design on rear lift

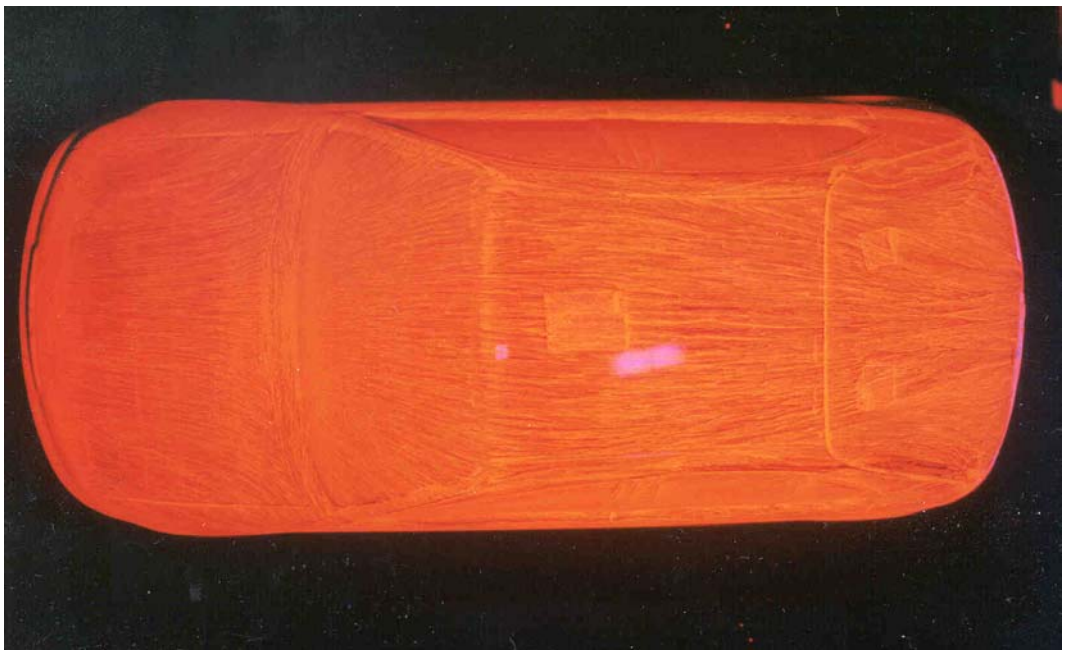

Figure 3.6.6 - Surface oil flow on Rover 200 model without spoiler from above (15% scale)

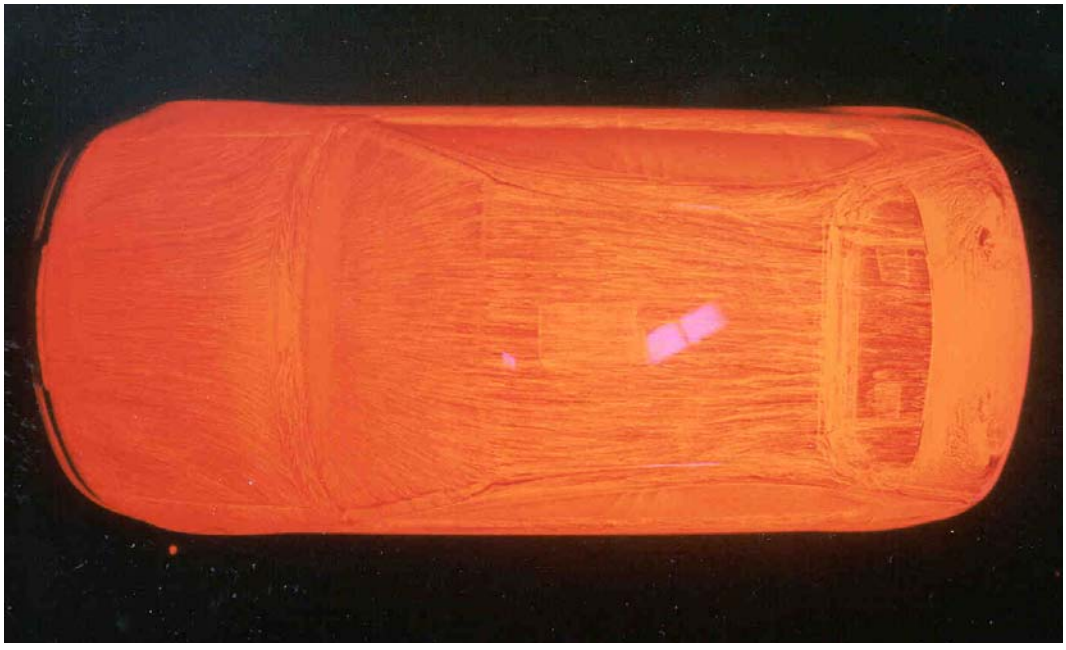

Figure 3.6.7 - Surface oil flow on Rover 200 model with spoiler from above (15% scale)

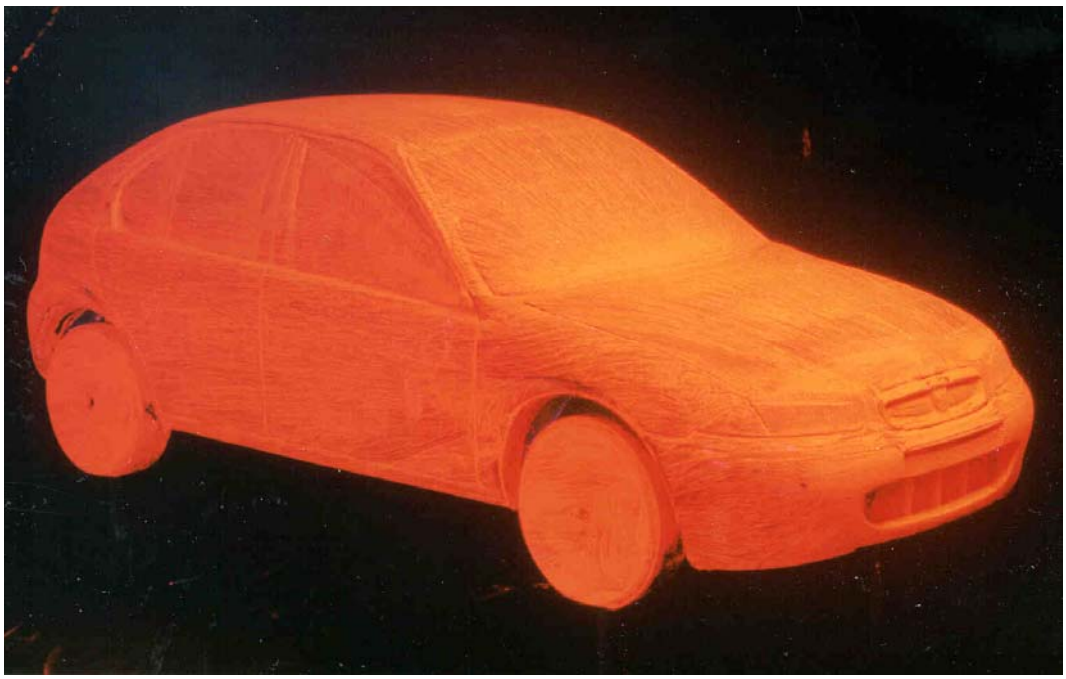

Figure 3.6.8 - Surface oil flow on Rover 200 model without spoiler (15% scale)

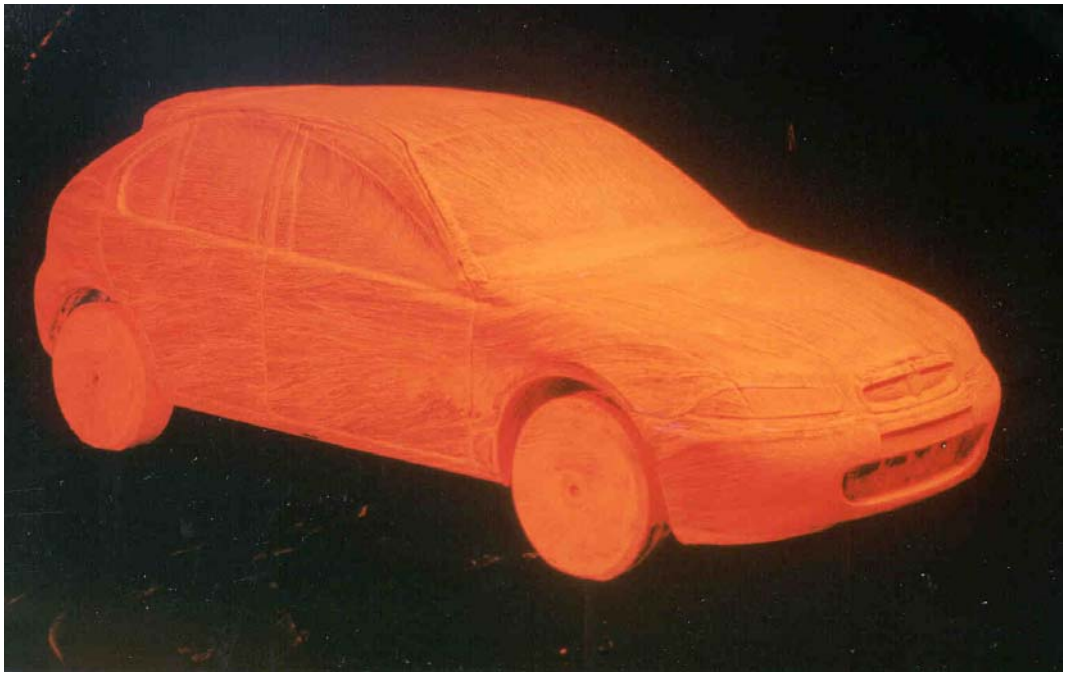

Figure 3.6.9 - Surface oil flow on Rover 200 model with spoiler (15% scale)

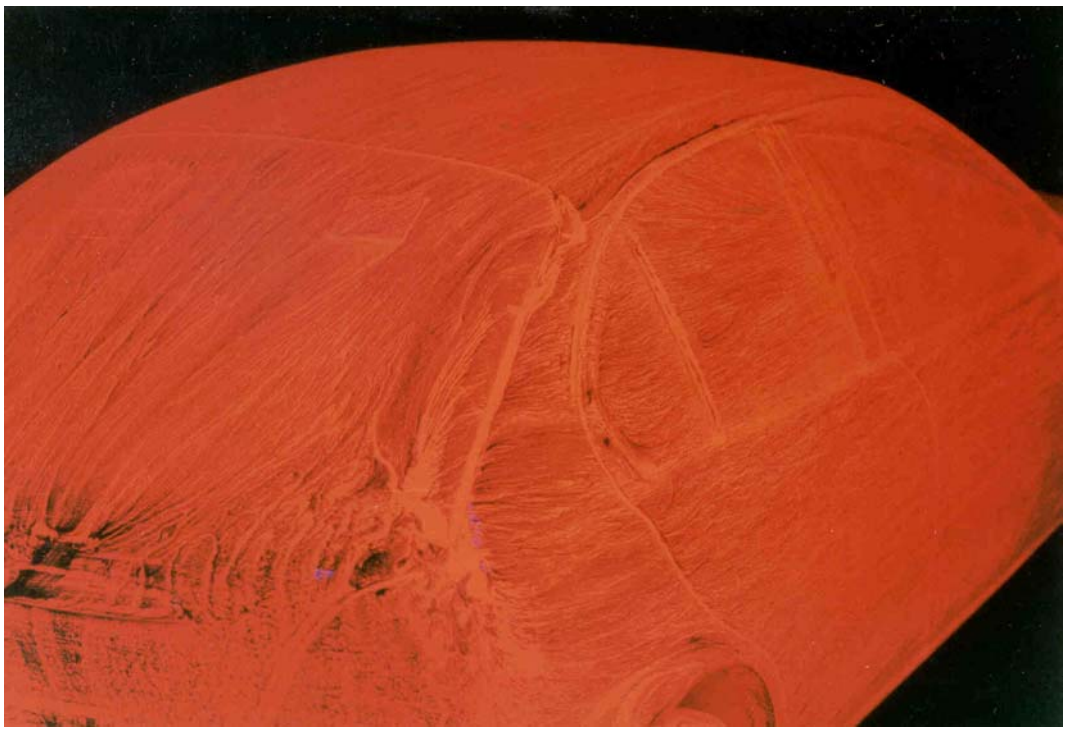

Figure 3.6.10 - Surface oil flow on Rover 200 model without spoiler (15% scale)

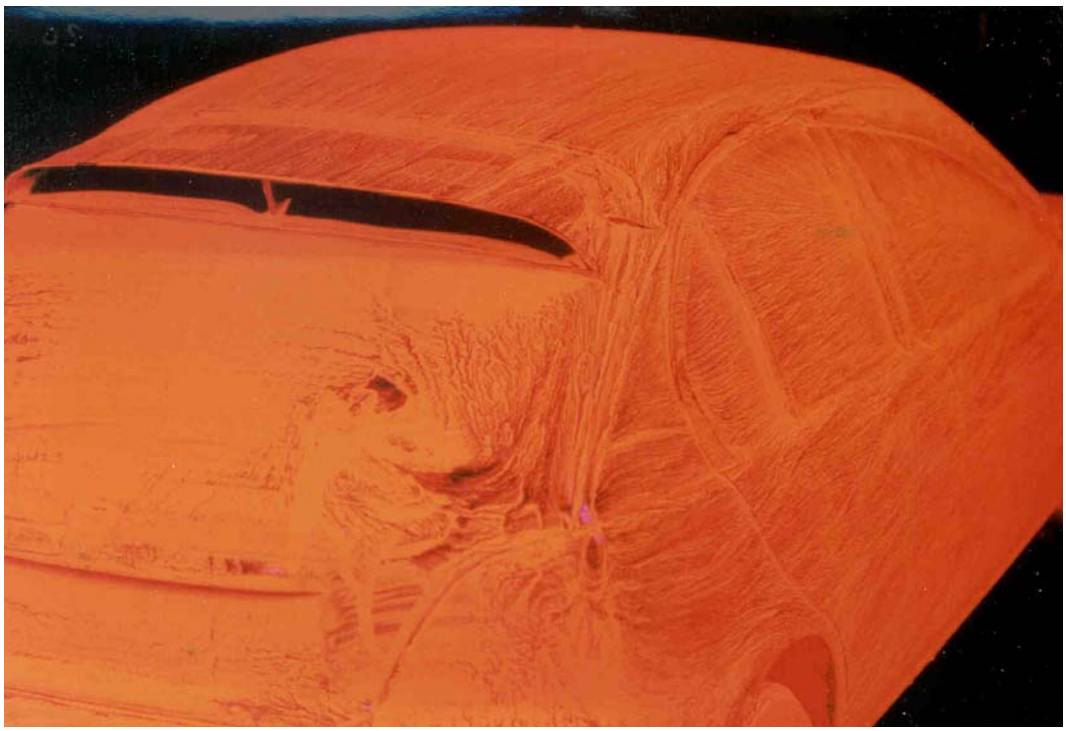

Figure 3.6.11 - Surface oil flow on Rover 200 model with spoiler (15% scale)

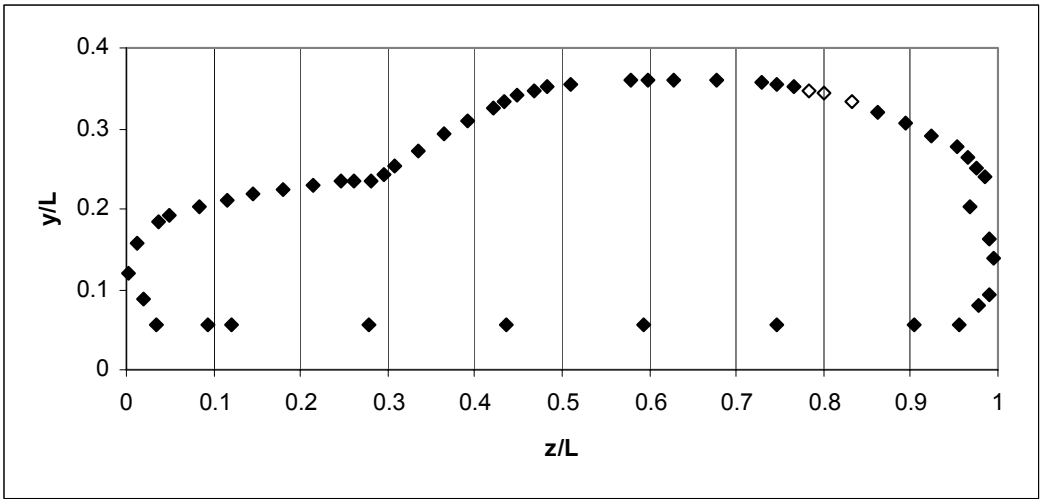

Figure 3.6.12 - Tapping positions on the centreline of the Rover 200 model (tappings covered by the spoiler are indicated by open symbols) (15% scale)

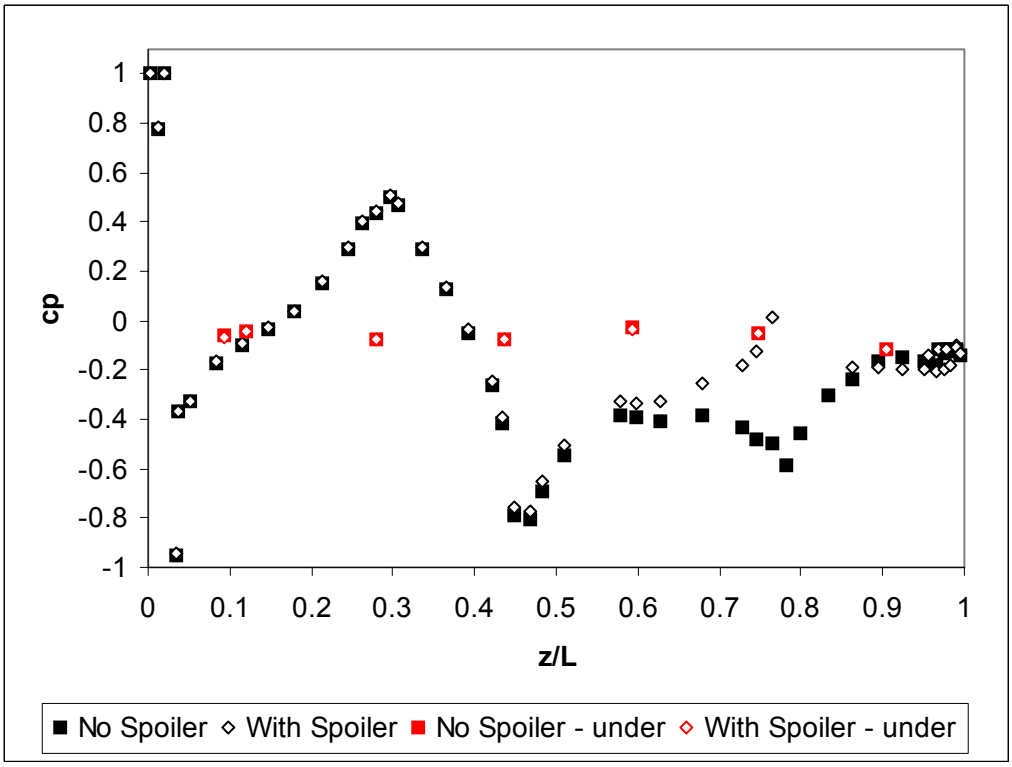

Figure 3.6.13 - Centreline pressure distribution on the Rover 200 model with and without spoiler (15% scale)

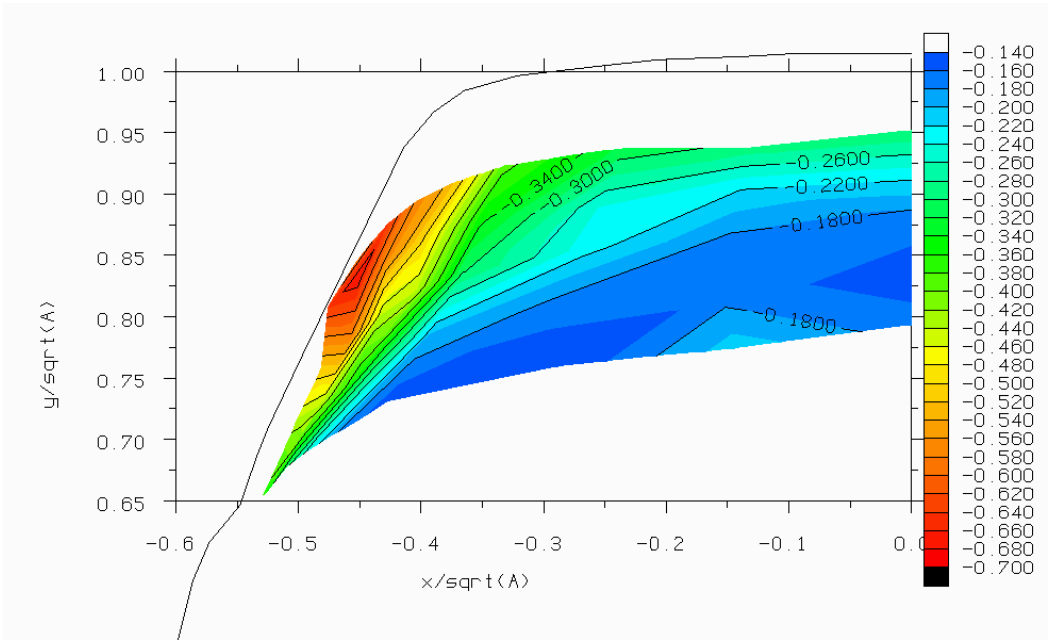

Figure 3.6.14 - Pressure distribution on backlight of Rover 200 model without spoiler (15% scale)

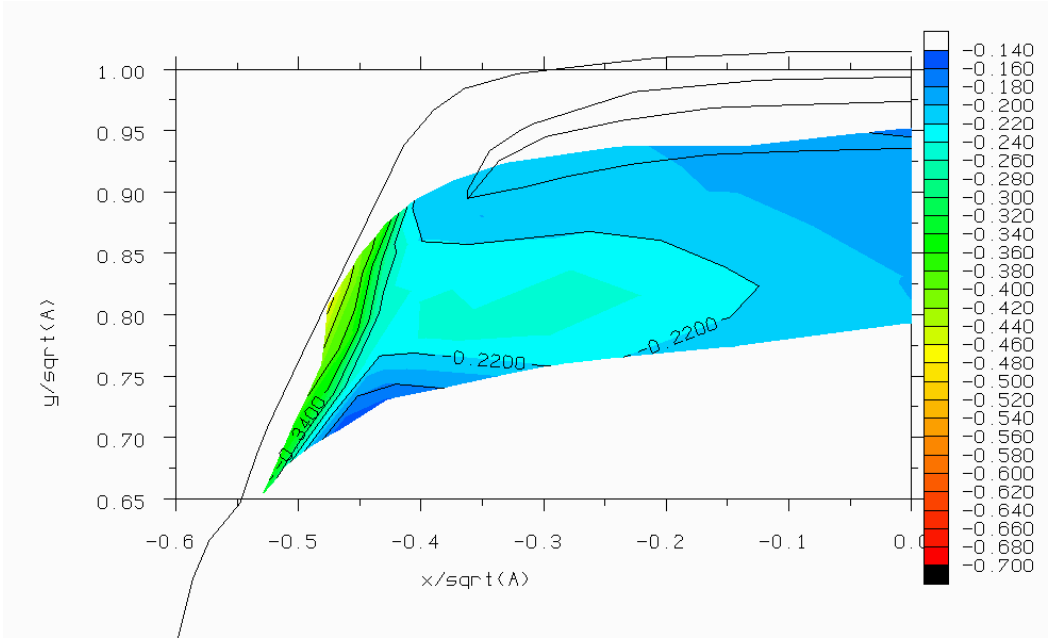

Figure 3.6.15 - Pressure distribution on backlight of Rover 200 model with spoiler (15% scale)

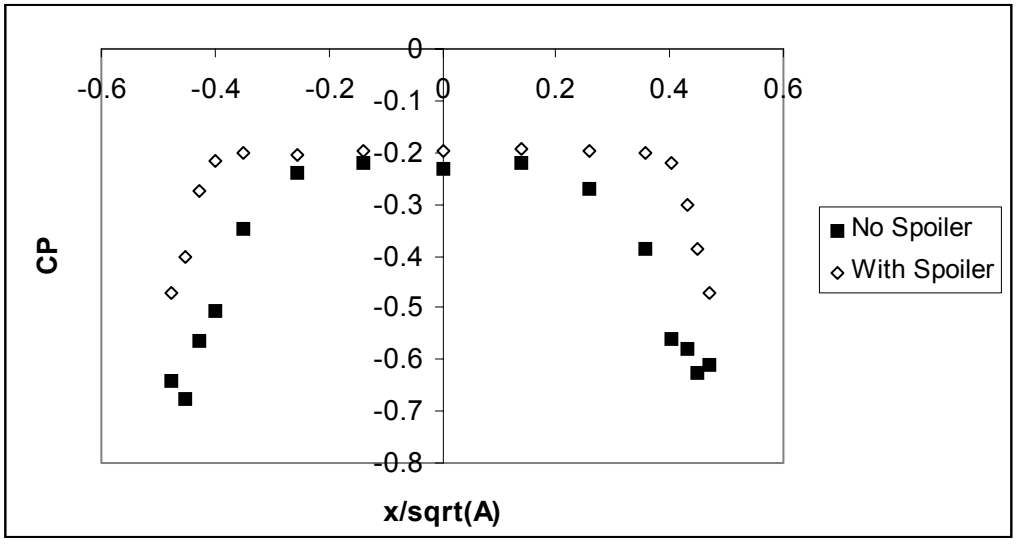

Figure 3.6.16 - Pressure distribution across backlight of Rover 200 model with and without spoiler (15% scale)

Figure 3.6.17 - Smoke flow visualisation on the centreline of the Rover 200 model without spoiler ($Re(A^{1/2})=1.1x10^5$)

Figure 3.6.18 - Smoke flow visualisation on the centreline of the Rover 200 model with spoiler ($Re(A^{1/2})=1.1x10^5$)

Figure 3.6.19 - Smoke flow visualisation on the centreline of the Rover 200 model without spoiler, smoke injected under model ($Re(A^{1/2})=1.1x10^5$)

Figure 3.6.20 - Smoke flow visualisation on the centreline of the Rover 200 model with spoiler, smoke injected under model ($Re(A^{1/2})=1.1x10^5$)

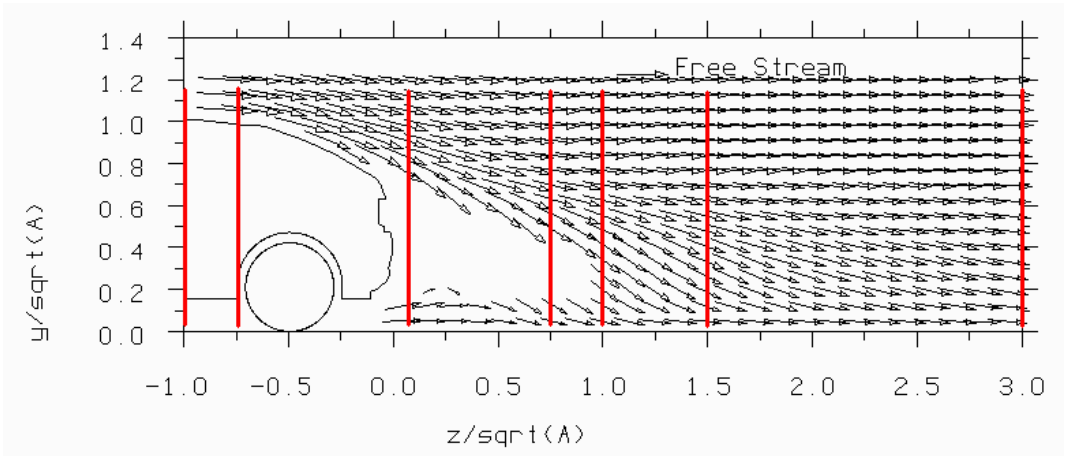

Figure 3.6.21 - Velocity vectors on the centre-plane of the Rover 200 model without spoiler (15% scale) (traverse planes indicated)

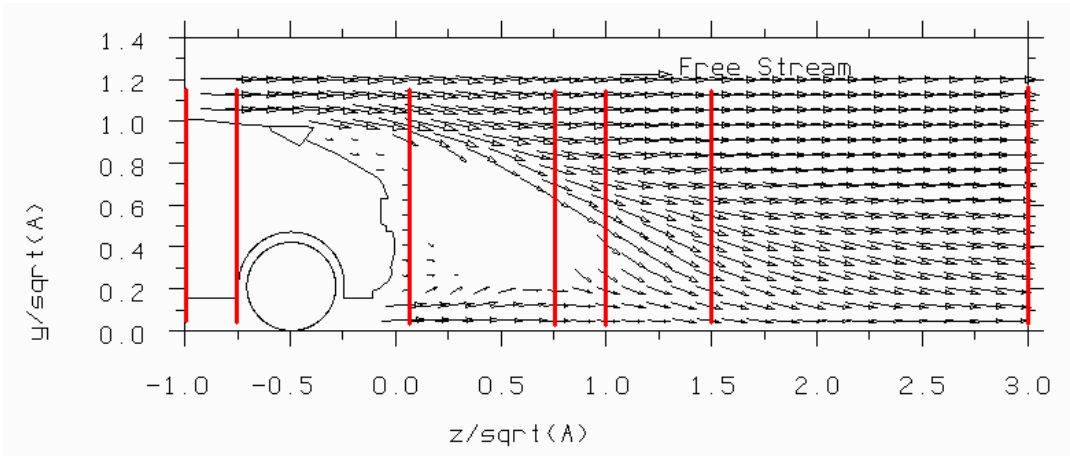

Figure 3.6.22 - Velocity vectors on the centre-plane of the Rover 200 model with spoiler (15% scale) (traverse planes indicated)

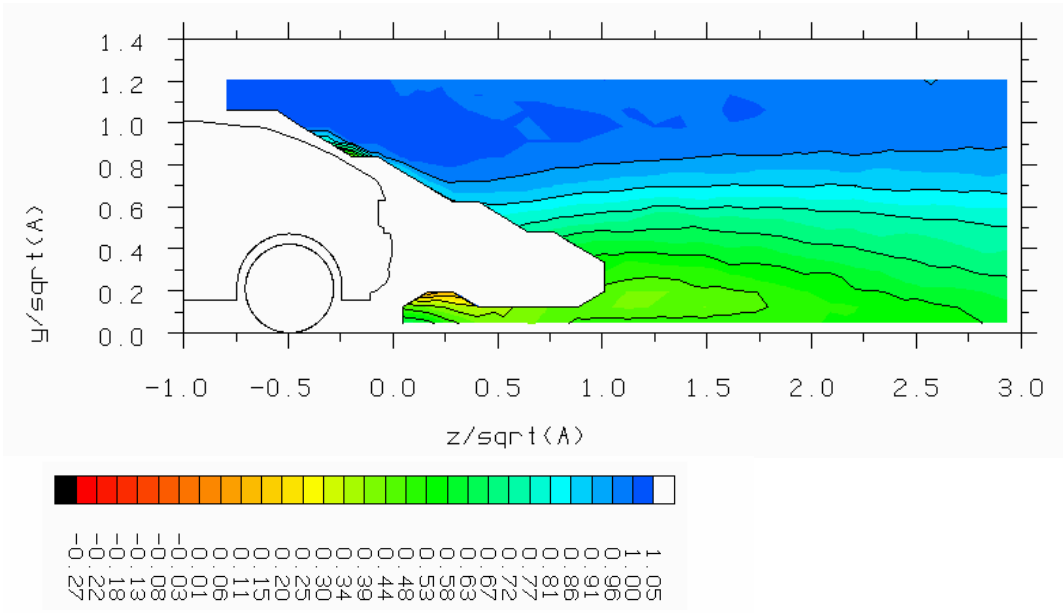

Figure 3.6.23 - Total pressure coefficient on the centre-plane of the Rover 200 model without spoiler (15% scale)

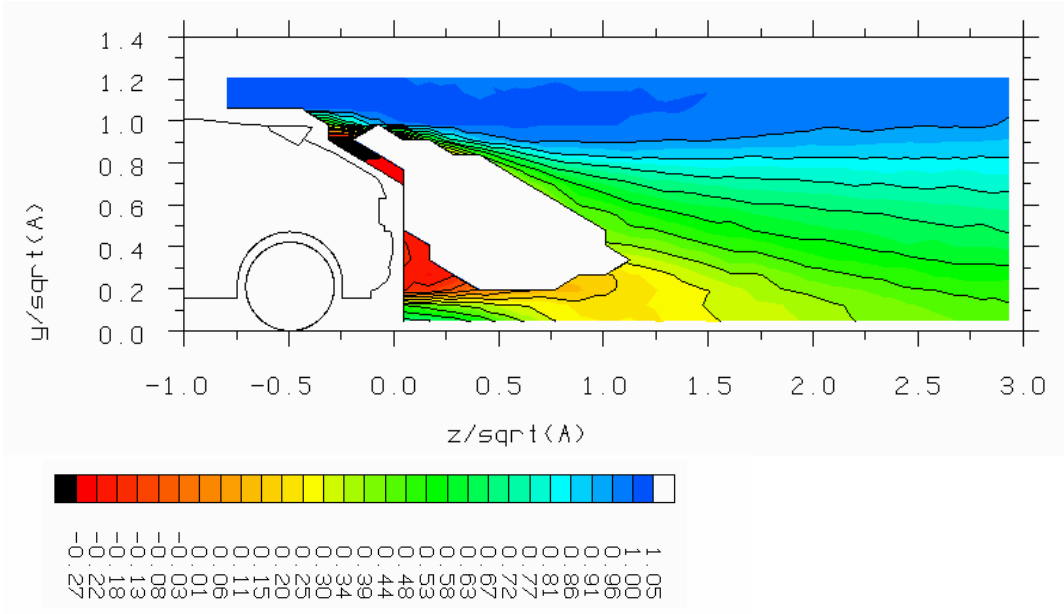

Figure 3.6.24 - Total pressure coefficient on the centre-plane of the Rover 200 model with spoiler (15% scale)

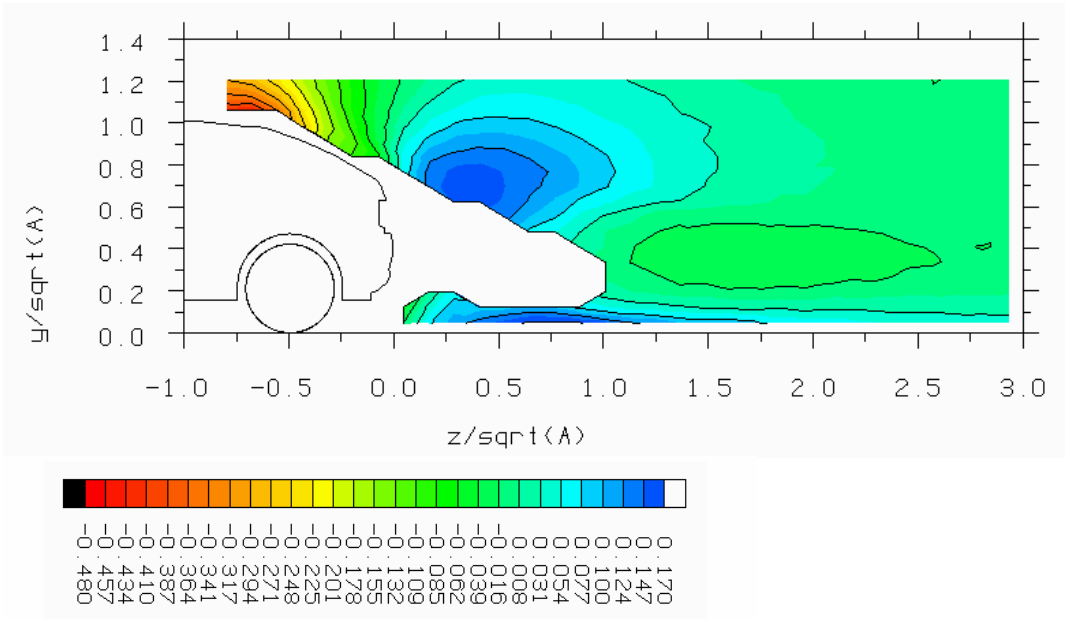

Figure 3.6.25 - Static pressure coefficient on the centre-plane of the Rover 200 model without spoiler (15% scale)

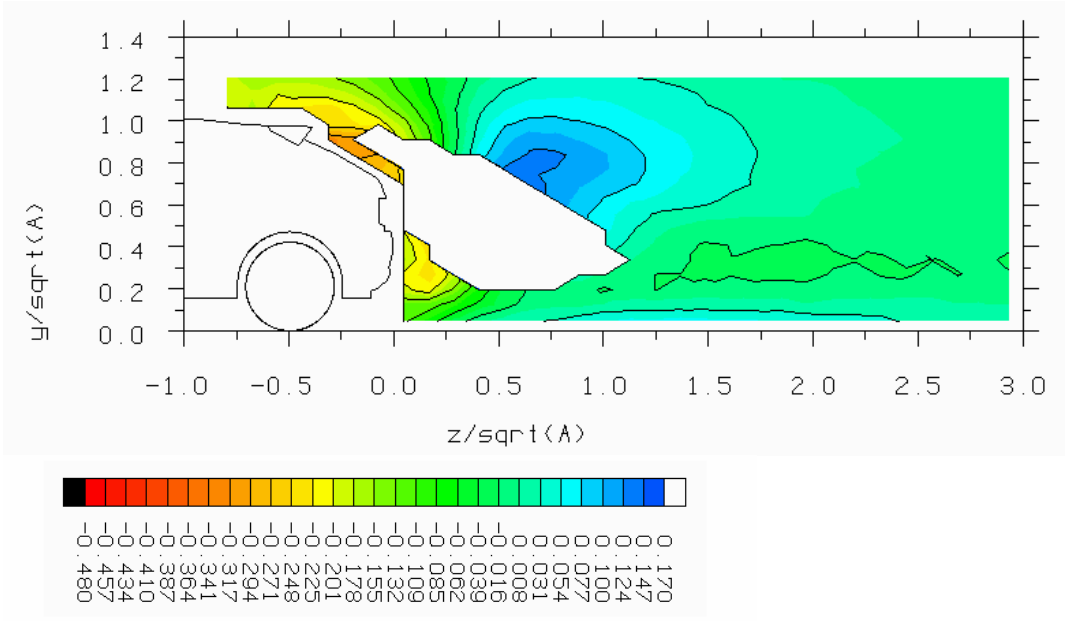

Figure 3.6.26 - Static pressure coefficient on the centre-plane of the Rover 200 model with spoiler (15% scale)

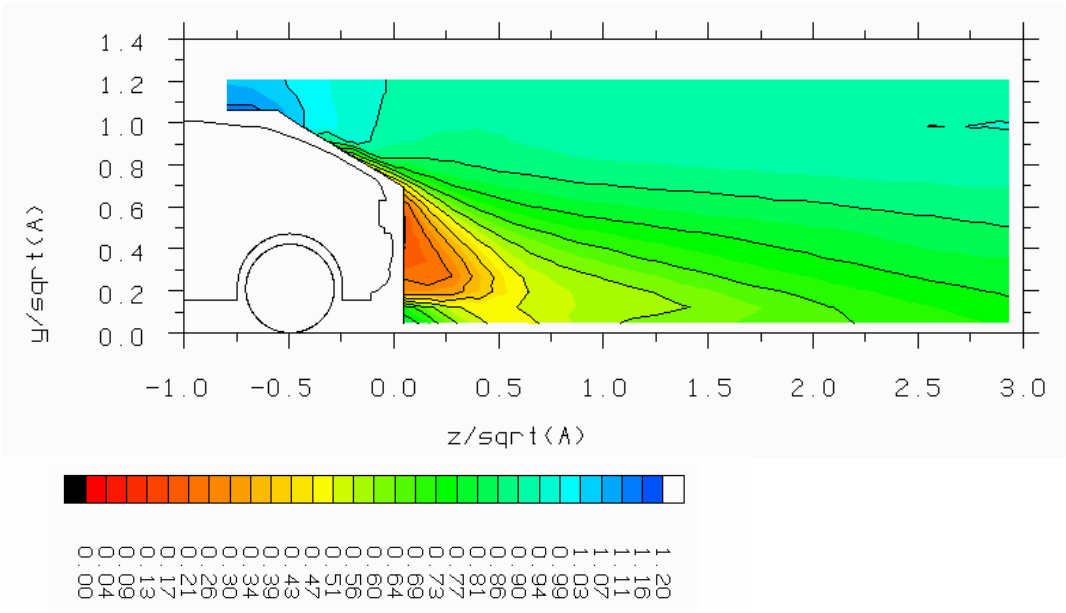

Figure 3.6.27 - Hot-wire effective velocity on the centre-plane of the Rover 200 model without spoiler (non-dimensionalised by free-stream velocity) (wire axis vertical) (15% scale)

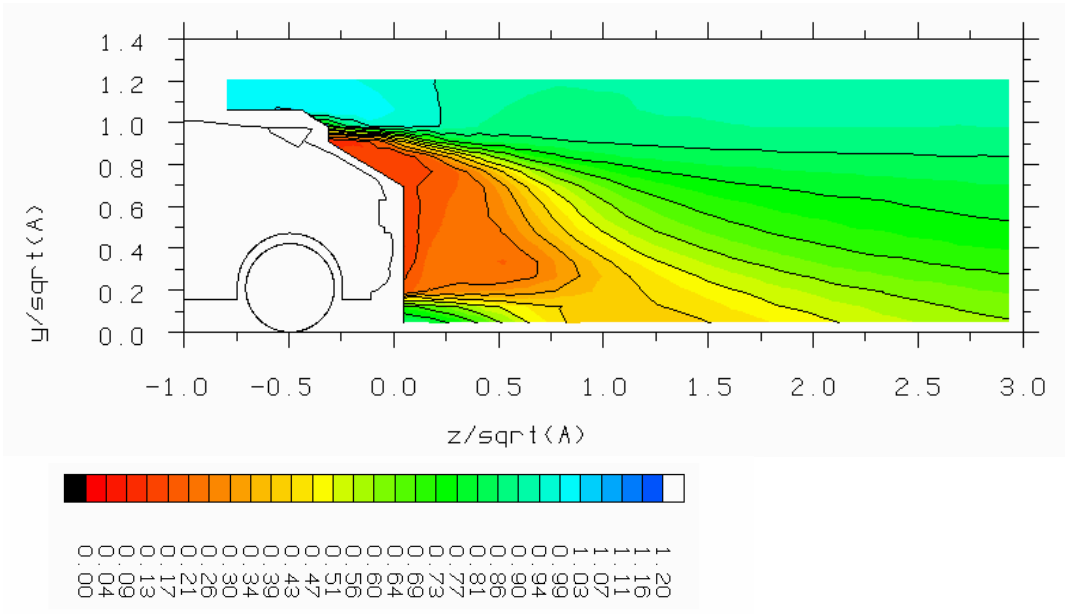

Figure 3.6.28 - Hot-wire effective velocity on the centre-plane of the Rover 200 model with spoiler (non-dimensionalised by free-stream velocity) (wire axis vertical) (15% scale)

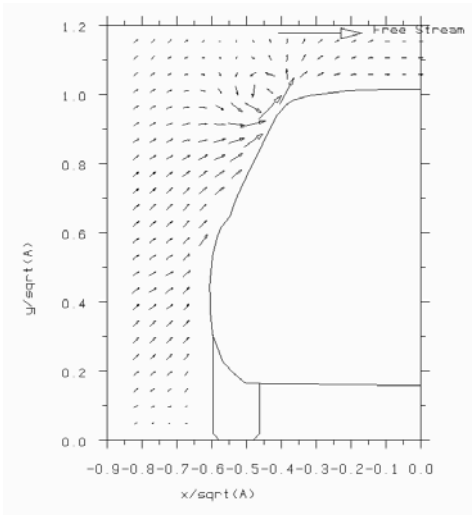

Figure 3.6.29a) z/sqrt(A) = -1.0

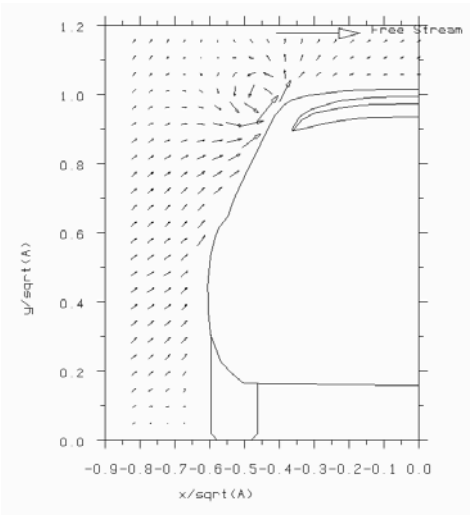

Figure 3.6.30a) z/sqrt(A) = -1.0

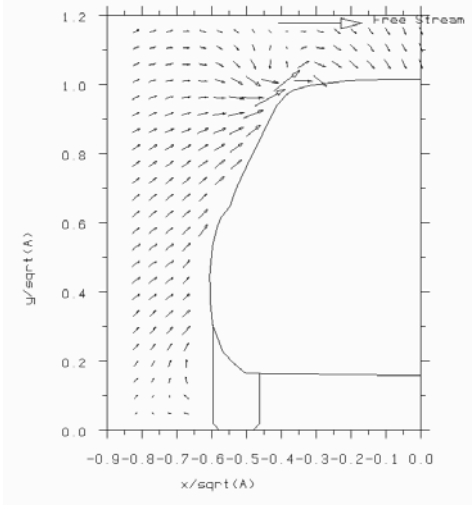

Figure 3.6.29b) z/sqrt(A) = -0.75

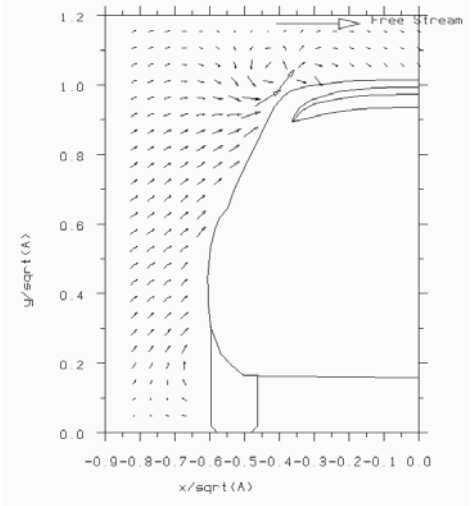

Figure 3.6.30b) z/sqrt(A) = -0.75

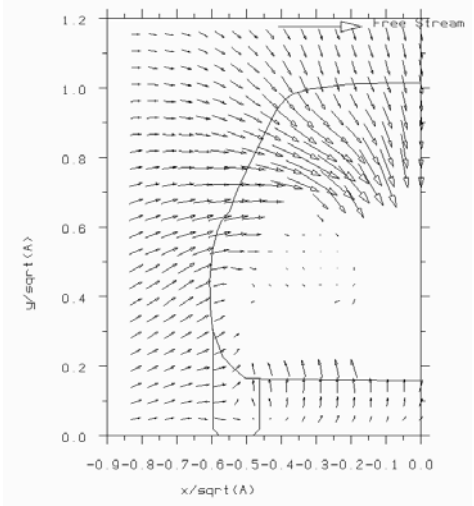

Figure 3.6.29c) z/sqrt(A) = 0.05

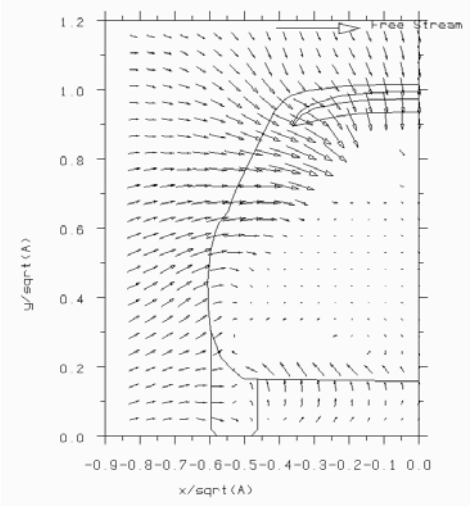

Figure 3.6.30c) z/sqrt(A) = 0.05

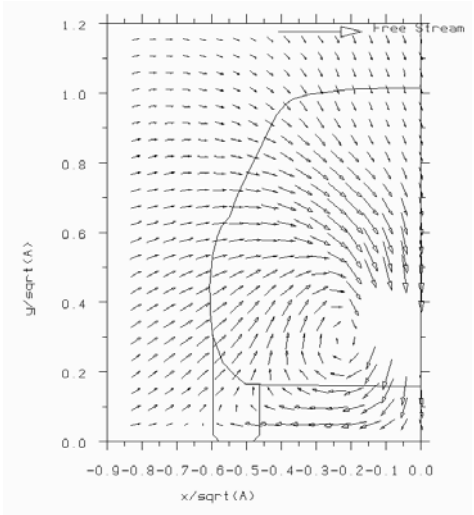

Figure 3.6.29d) z/sqrt(A) = 0.75

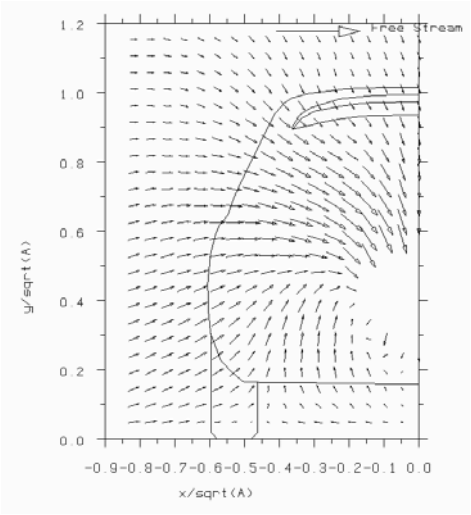

Figure 3.6.30d) z/sqrt(A) = 0.75

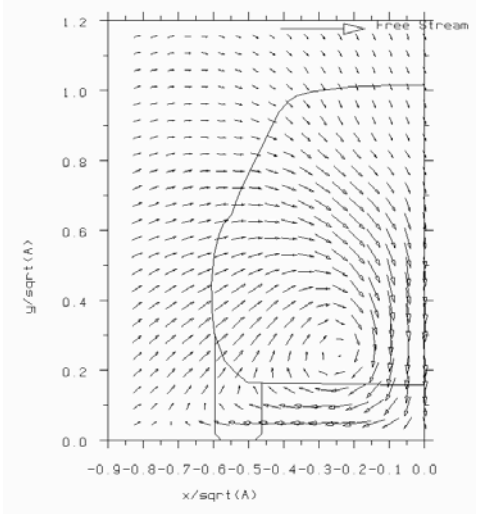

Figure 3.6.29e) z/sqrt(A) = 1.0

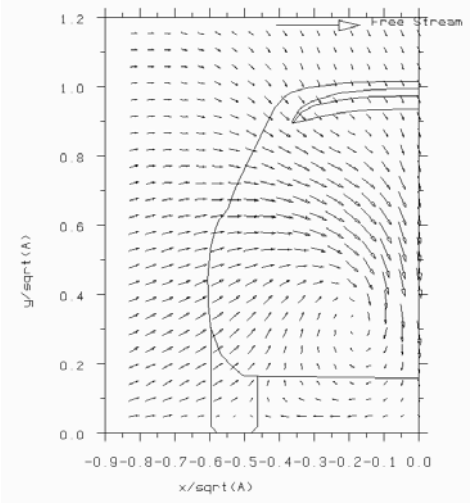

Figure 3.6.30e) z/sqrt(A) = 1.0

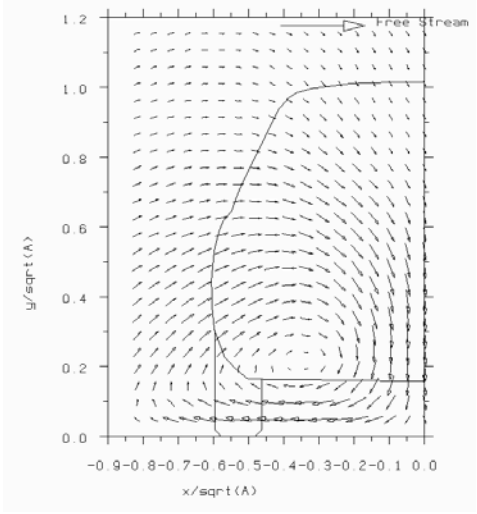

Figure 3.6.29f) z/sqrt(A) = 1.5

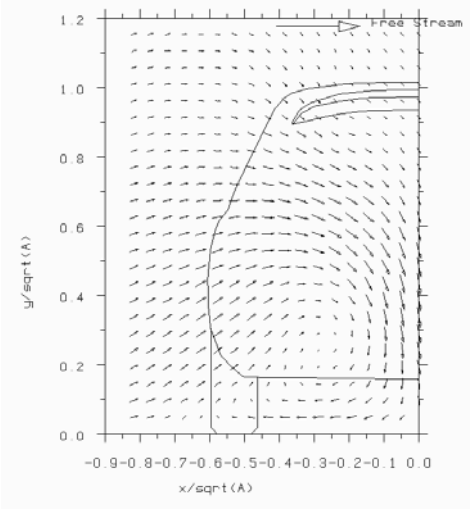

Figure 3.6.30f) z/sqrt(A) = 1.5

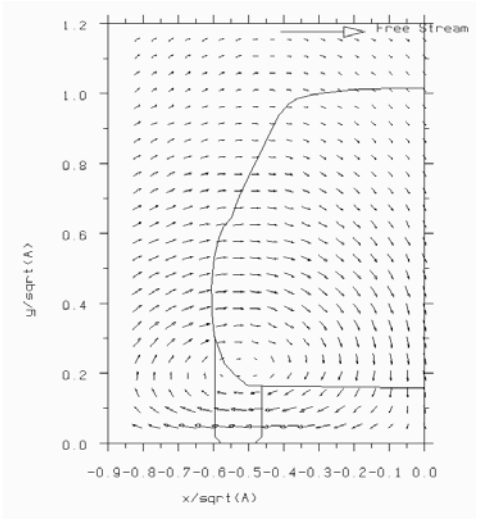

Figure 3.6.29g) z/sqrt(A) = 3.0

Figure 3.6.29 - Velocity vectors in the wake of the Rover 200 model without spoiler (15% scale)

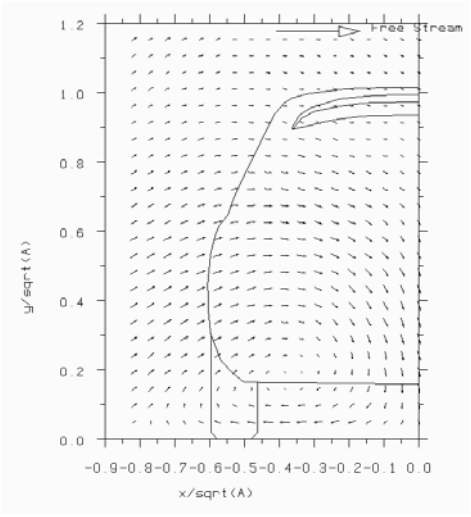

Figure 3.6.30g) z/sqrt(A) = 3.0

Figure 3.6.30 - Velocity vectors in the wake of the Rover 200 model with spoiler (15% scale)

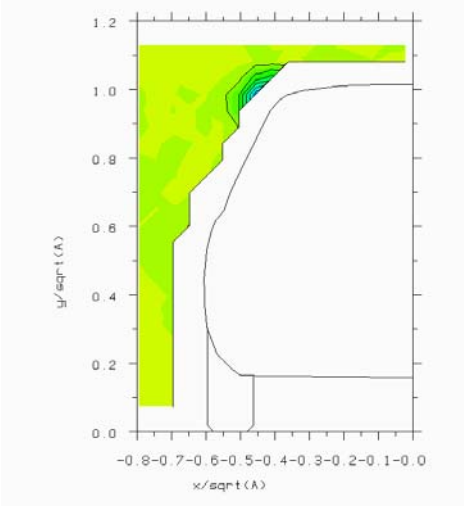

Figure 3.6.31a) z/sqrt(A) = -1.0 (range –12.8-+12.8)

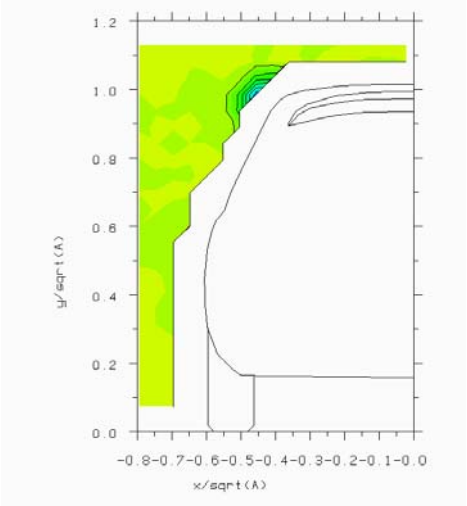

Figure 3.6.32a) z/sqrt(A) = -1.0 (range –12.8-+12.8)

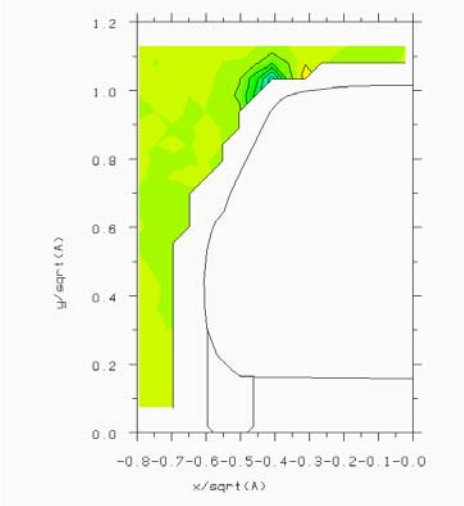

Figure 3.6.31b) z/sqrt(A) = -0.75 (range –12.8-+12.8)

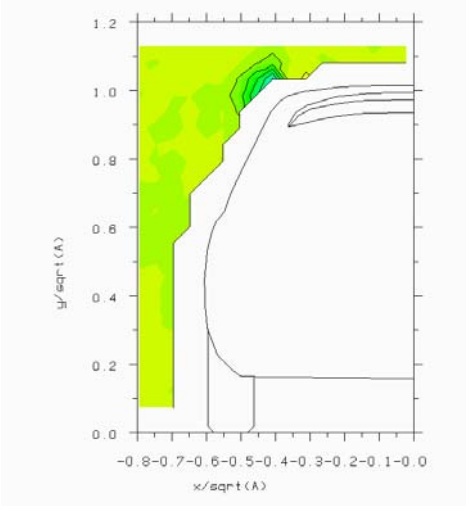

Figure 3.6.32b) z/sqrt(A) = -0.75 (range –12.8-+12.8)

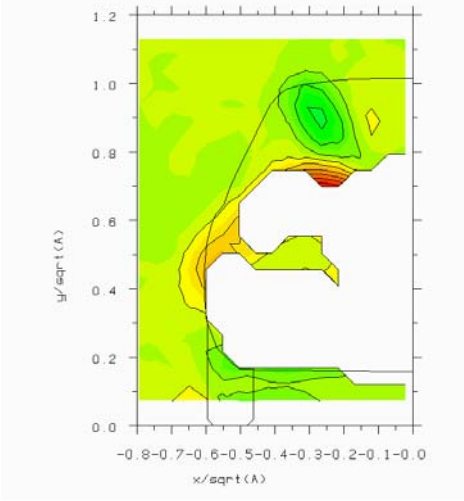

Figure 3.6.31c) z/sqrt(A) = 0.05

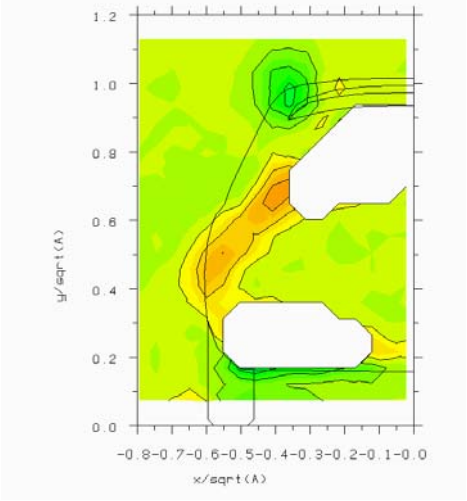

Figure 3.6.32c) z/sqrt(A) = 0.05

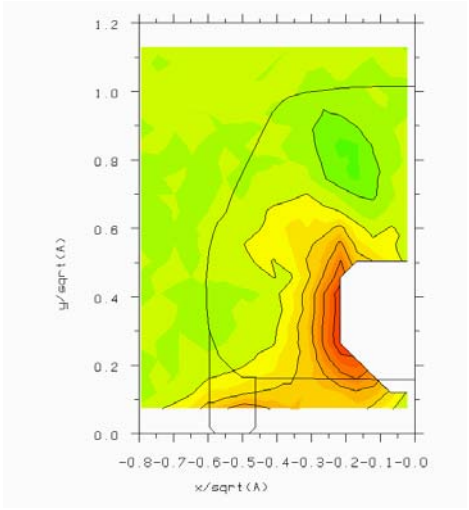

Figure 3.6.31d) z/sqrt(A) = 0.75

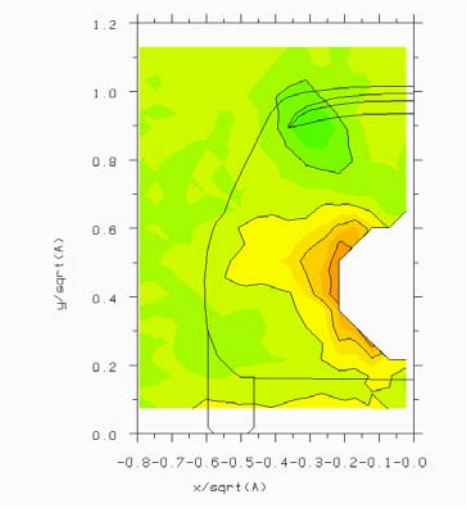

Figure 3.6.32d) z/sqrt(A) = 0.75

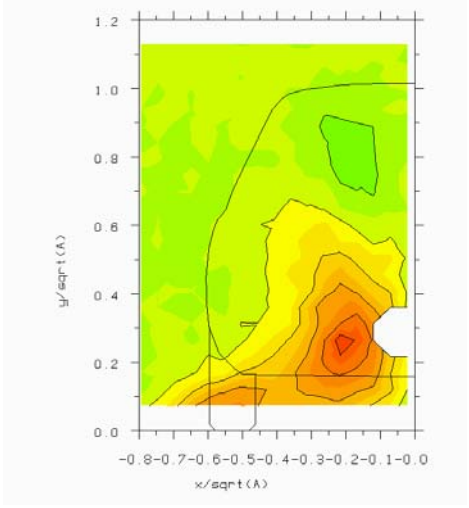

Figure 3.6.31e) z/sqrt(A) = 1.0

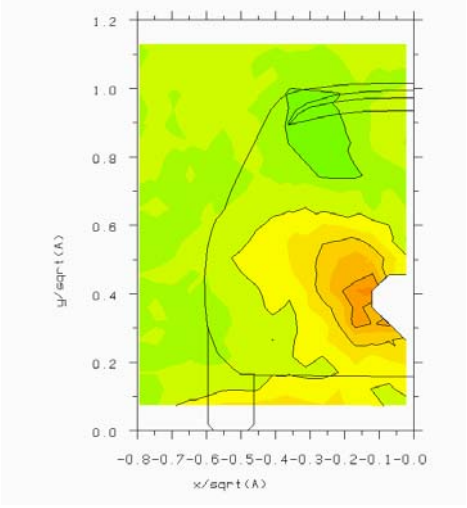

Figure 3.6.32e) z/sqrt(A) = 1.0

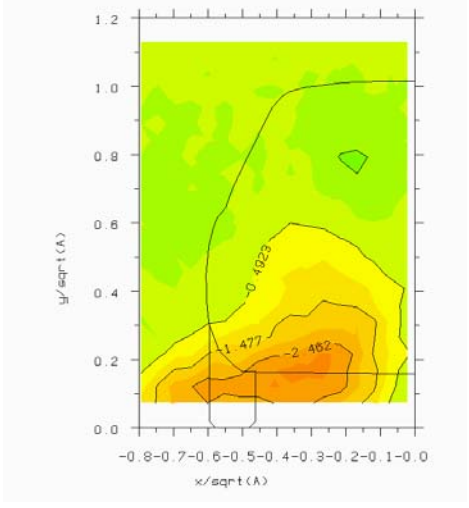

Figure 3.6.31f) z/sqrt(A) = 1.5

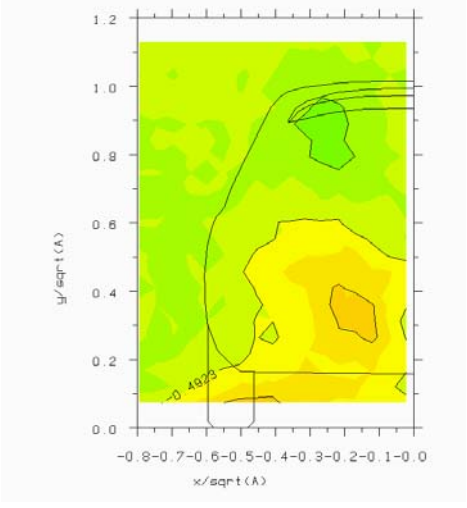

Figure 3.6.32f) z/sqrt(A) = 1.5

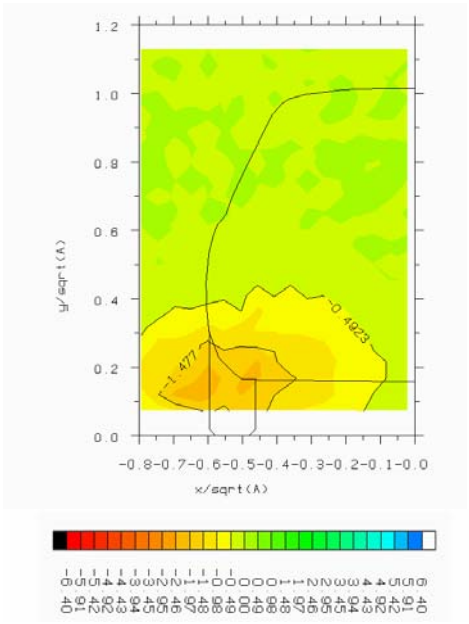

Figure 3.6.31g) z/sqrt(A) = 2.0

Figure 3.6.31 - Vorticity in the wake of the Rover 200 model without spoiler (non-dimensionalised by free-stream velocity and $A^{1/2}$) (15% scale)

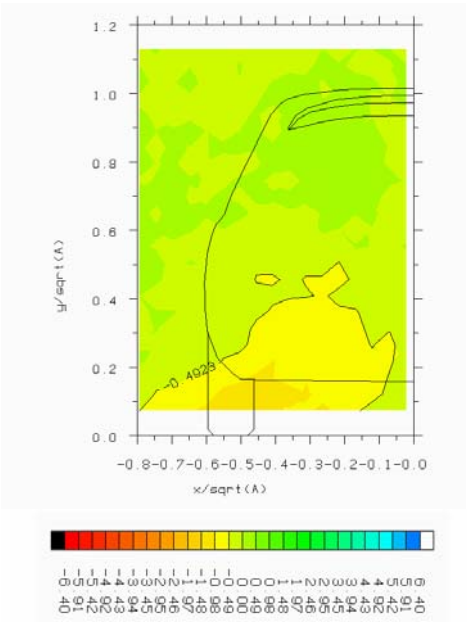

Figure 3.6.32g) z/sqrt(A) = 2.0

Figure 3.6.32 - Vorticity in the wake of the Rover 200 model with spoiler (non-dimensionalised by free-stream velocity and $A^{1/2}$) (15% scale)

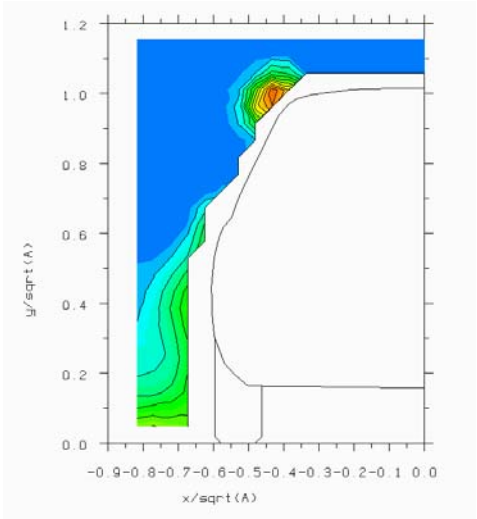

Figure 3.6.33a) z/sqrt(A) = -1.0

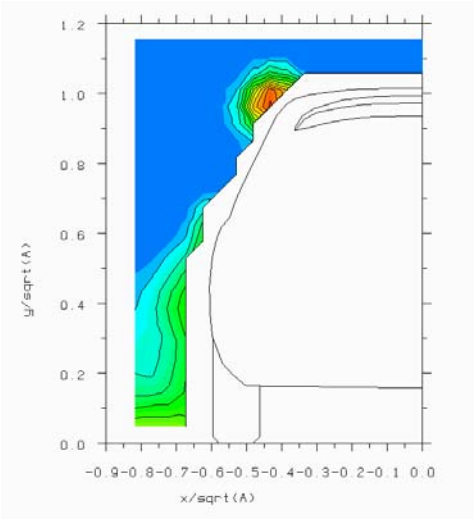

Figure 3.6.34a) z/sqrt(A) = -1.0

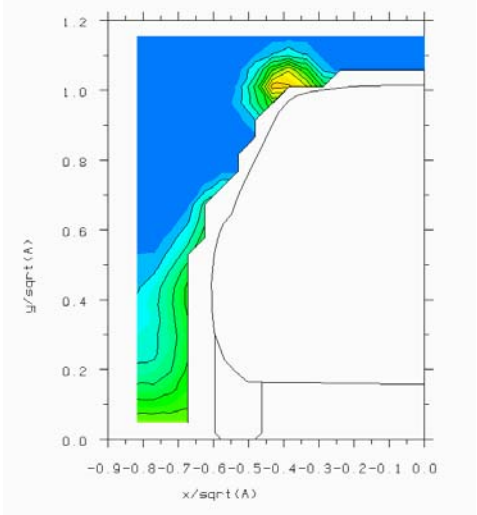

Figure 3.6.33b) z/sqrt(A) = -0.75

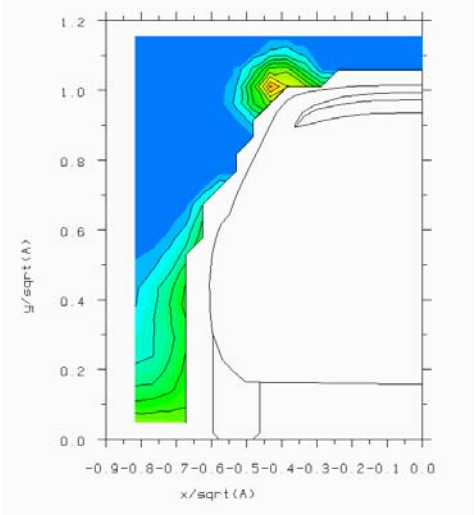

Figure 3.6.34b) z/sqrt(A) = -0.75

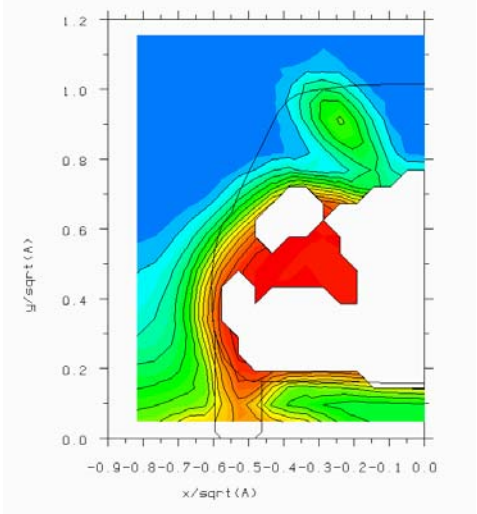

Figure 3.6.33c) z/sqrt(A) = 0.05

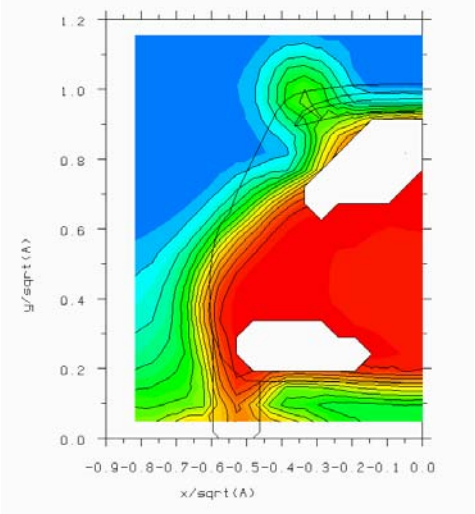

Figure 3.6.34c) z/sqrt(A) = 0.05

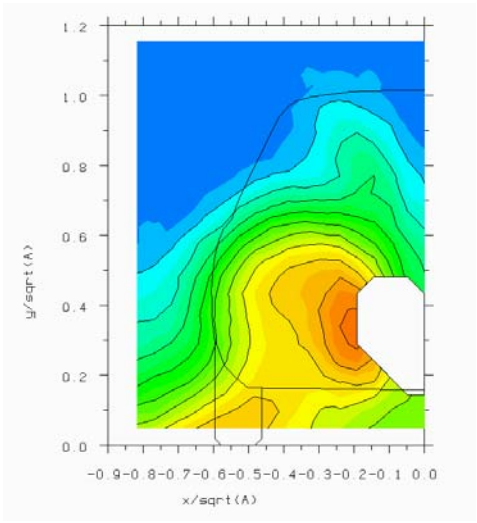

Figure 3.6.33d) z/sqrt(A) = 0.75

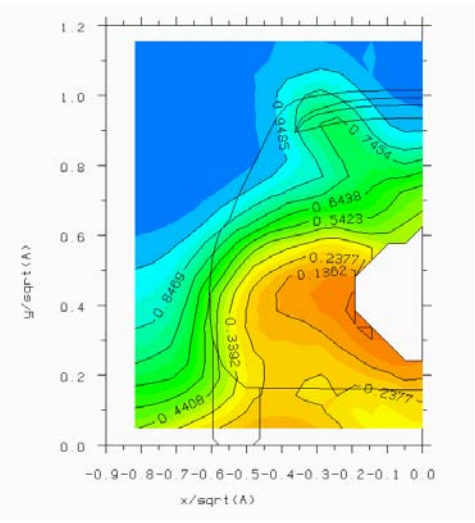

Figure 3.6.34d) z/sqrt(A) = 0.75

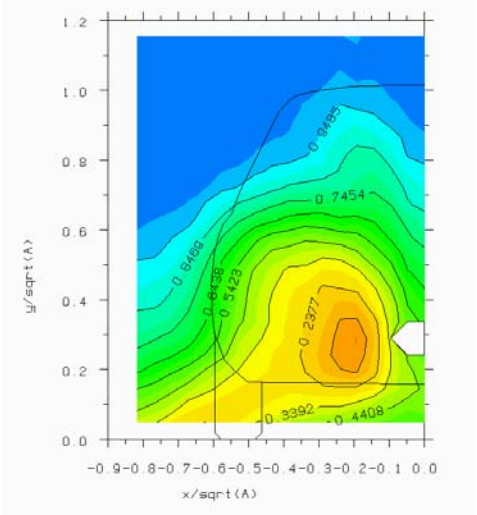

Figure 3.6.33e) z/sqrt(A) = 1.0

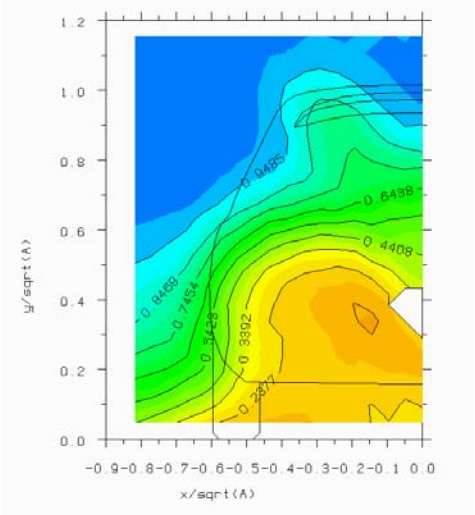

Figure 3.6.34e) z/sqrt(A) = 1.0

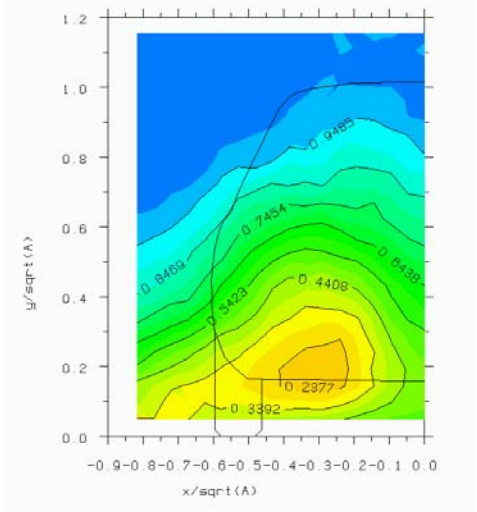

Figure 3.6.33f) z/sqrt(A) = 1.5

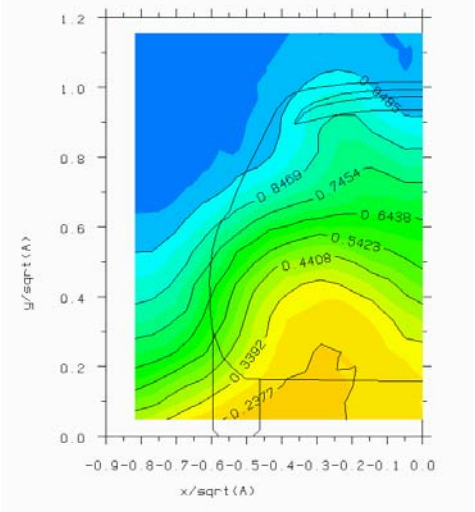

Figure 3.6.34f) z/sqrt(A) = 1.5

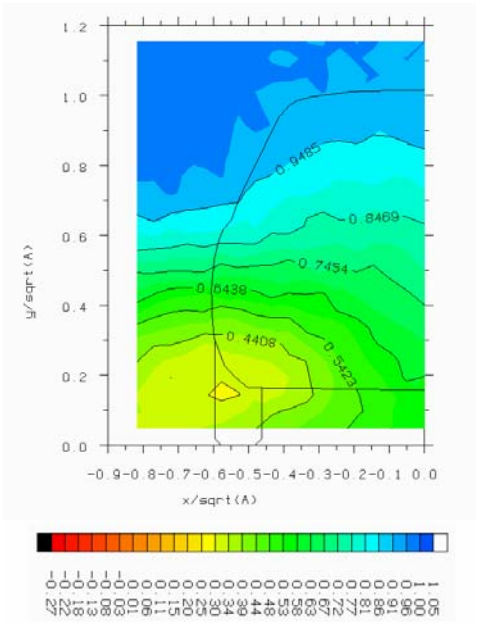

Figure 3.6.33g) z/sqrt(A) = 3.0

Figure 3.6.33 - Total pressure coefficient in the wake of the Rover 200 model without spoiler (15% scale)

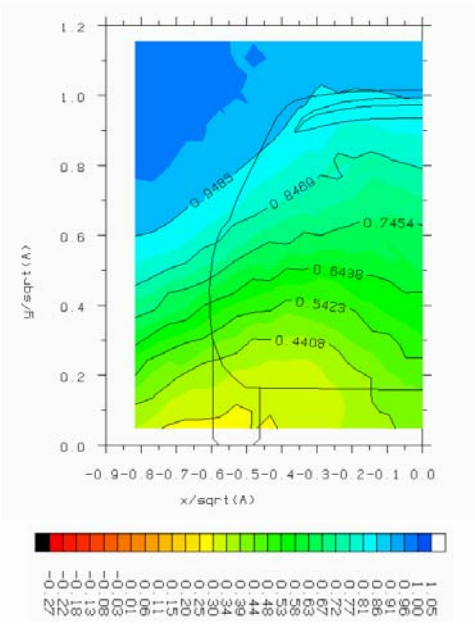

Figure 3.6.34g) z/sqrt(A) = 3.0

Figure 3.6.34 - Total pressure coefficient in the wake of the Rover 200 model with spoiler (15% scale)

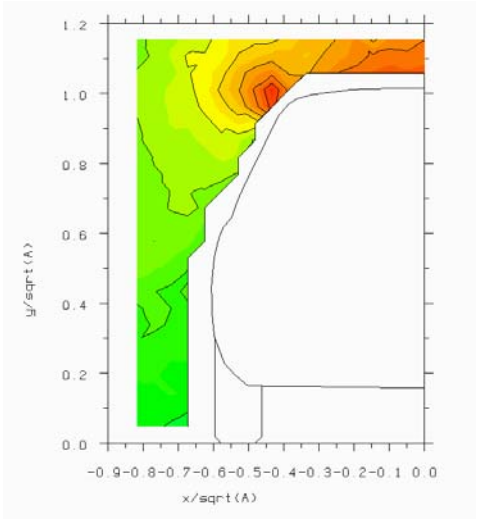

Figure 3.6.35a) z/sqrt(A) = -1.0

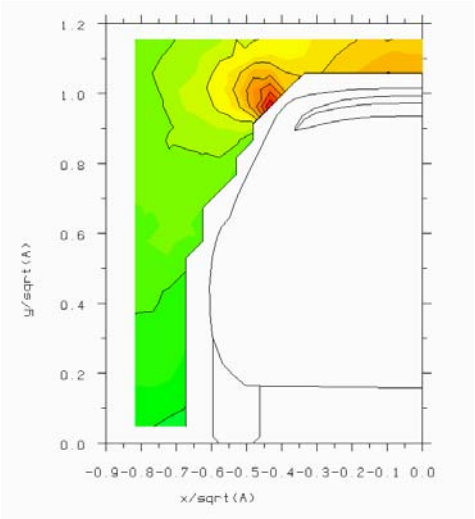

Figure 3.6.36a) z/sqrt(A) = -1.0

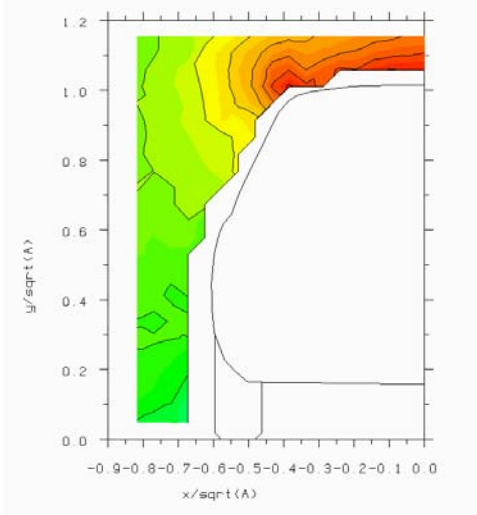

Figure 3.6.35b) z/sqrt(A) = -0.75

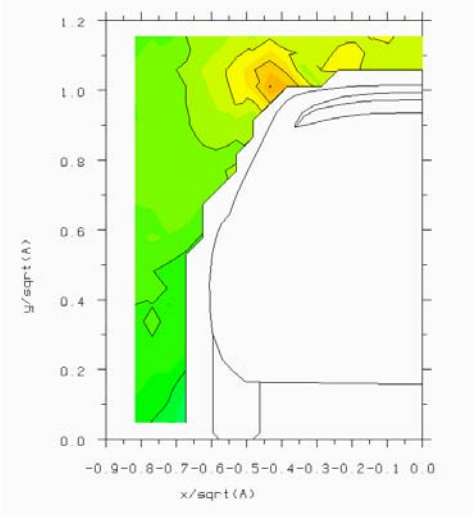

Figure 3.6.36b) z/sqrt(A) = -0.75

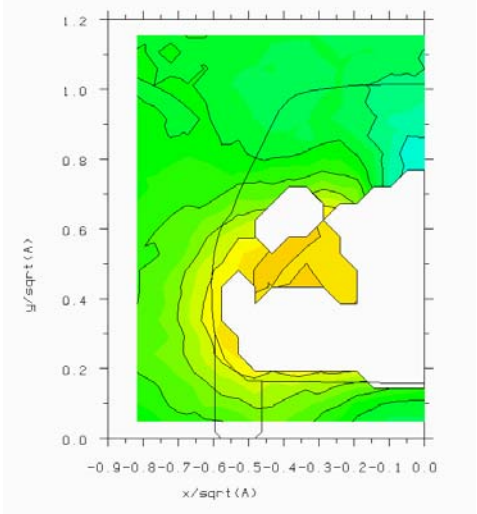

Figure 3.6.35c) z/sqrt(A) = 0.05

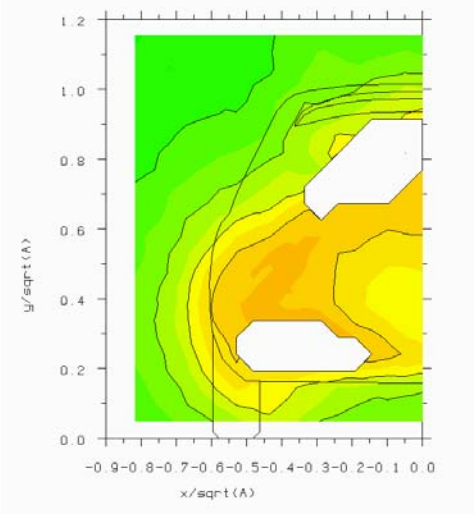

Figure 3.6.36c) z/sqrt(A) = 0.05

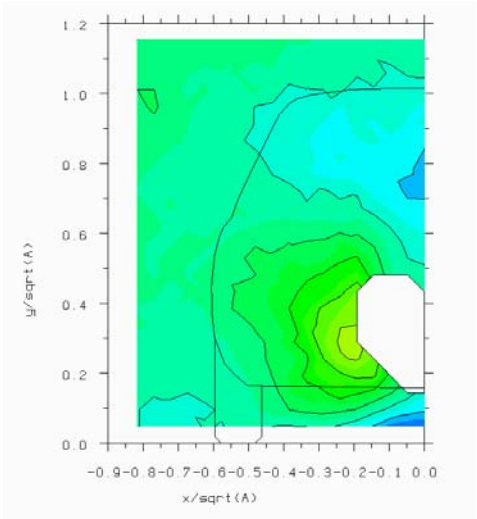

Figure 3.6.35d) z/sqrt(A) = 0.75

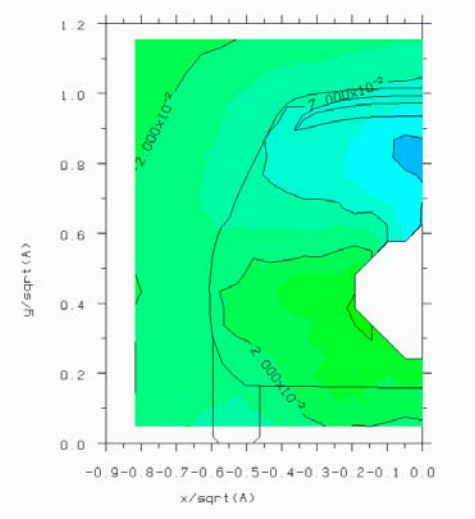

Figure 3.6.36d) z/sqrt(A) = 0.75

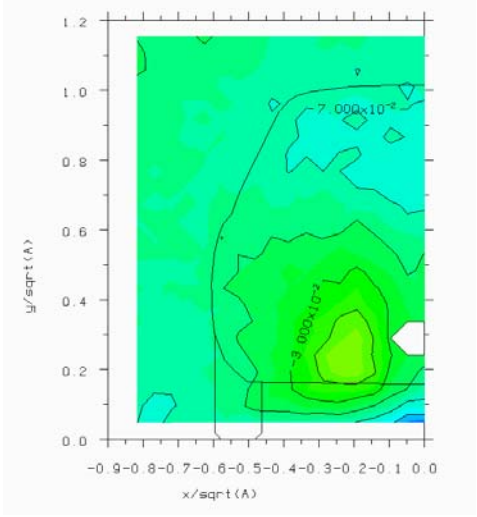

Figure 3.6.35e) z/sqrt(A) = 1.0

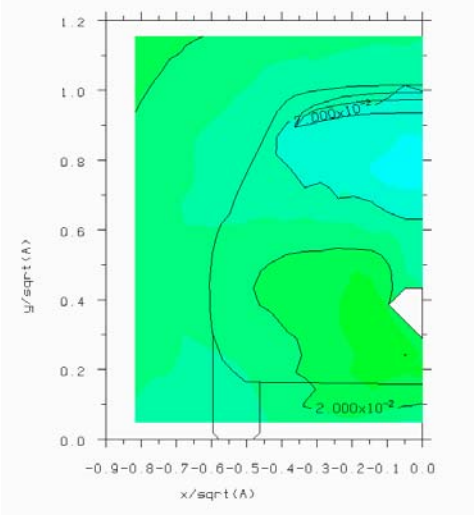

Figure 3.6.36e) z/sqrt(A) = 1.0

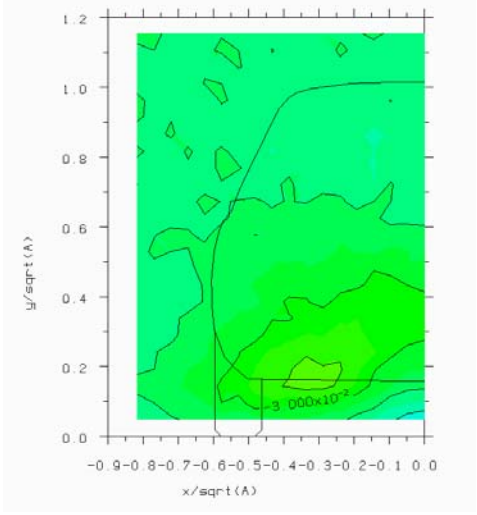

Figure 3.6.35f) z/sqrt(A) = 1.5

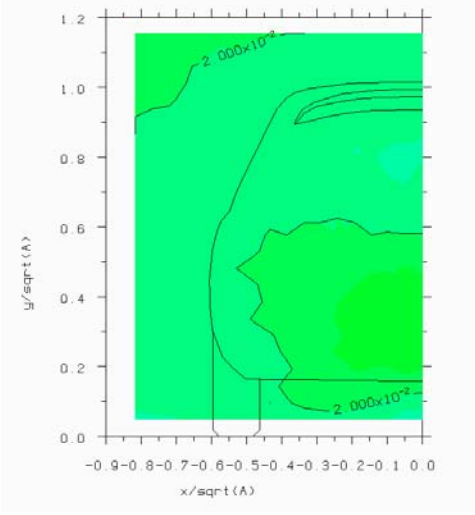

Figure 3.6.36f) z/sqrt(A) = 1.5

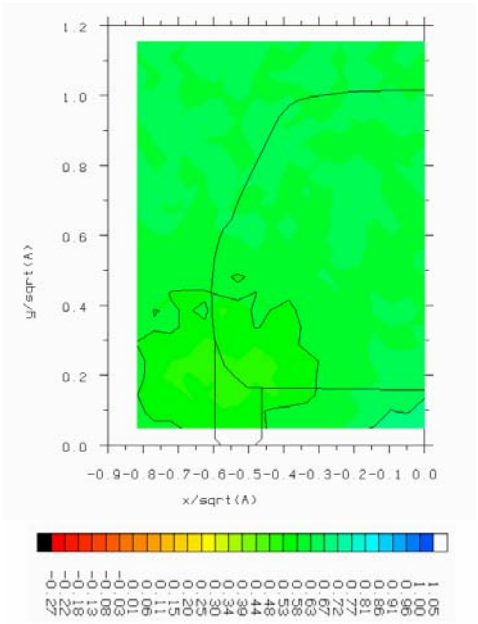

Figure 3.6.35g) z/sqrt(A) = 3.0

Figure 3.6.35 - Static pressure coefficient in the wake of the Rover 200 model without spoiler (15% scale)

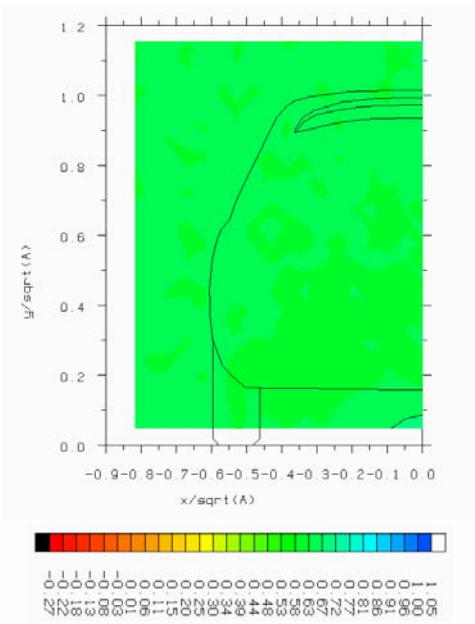

Figure 3.6.36g) z/sqrt(A) = 3.0

Figure 3.6.36 - Static pressure coefficient in the wake of the Rover 200 model with spoiler (15% scale)

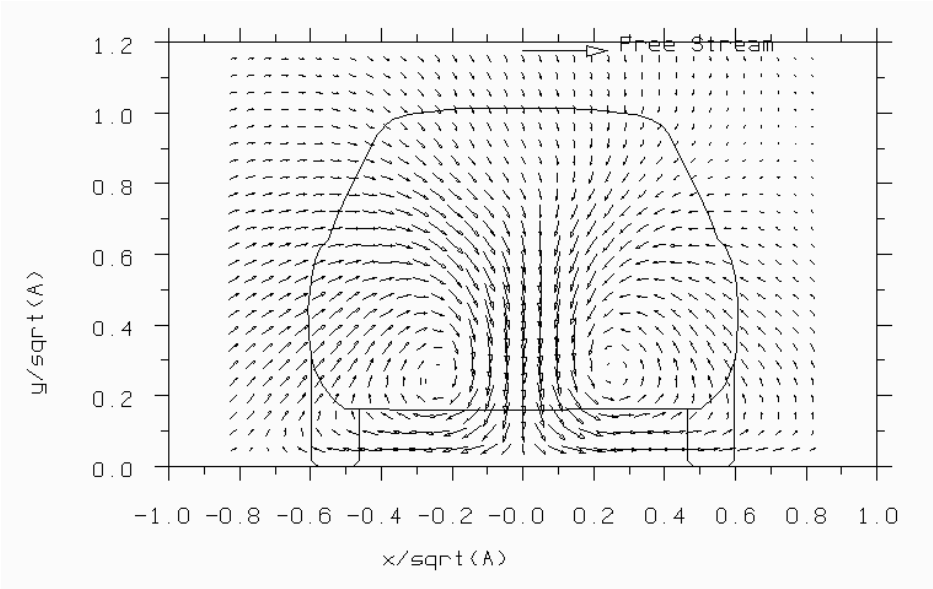

Figure 3.6.37 - Velocity vectors one base dimension behind the Rover 200 model without spoiler (15% scale) (true time-average)

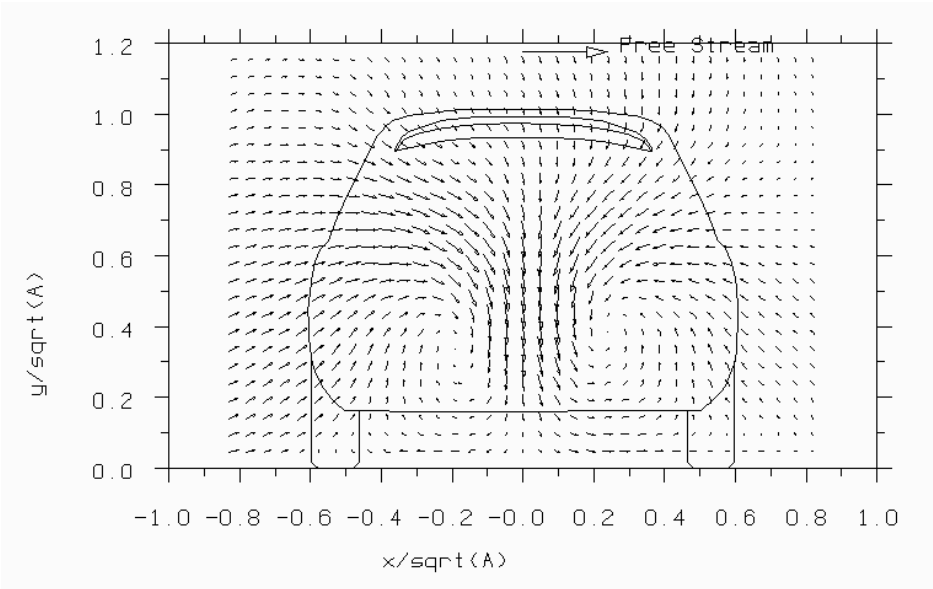

Figure 3.6.38 - Velocity vectors one base dimension behind the Rover 200 model with spoiler (15% scale) (true time-average)

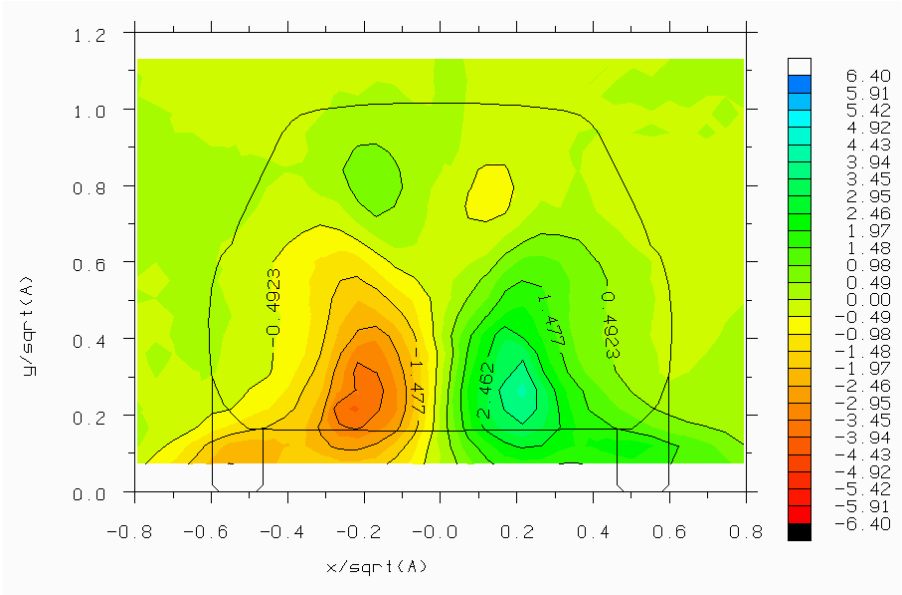

Figure 3.6.39 - Vorticity one base dimension behind the Rover 200 model without spoiler (non-dimensionalised by free-stream velocity and $A^{1/2}$) (15% scale) (true time-average)

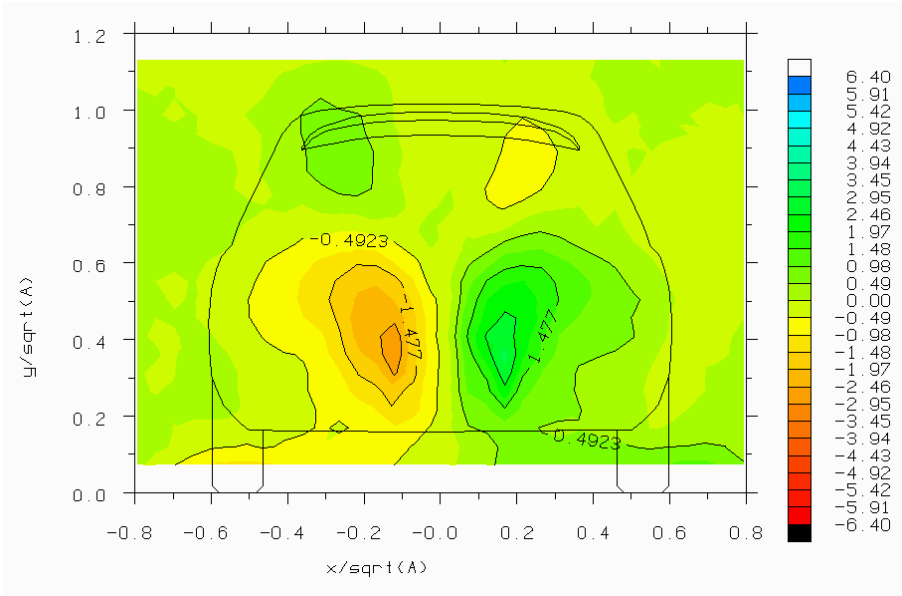

Figure 3.6.40 - Vorticity one base dimension behind the Rover 200 model with spoiler (non-dimensionalised by free-stream velocity and $A^{1/2}$) (15% scale) (true time-average)

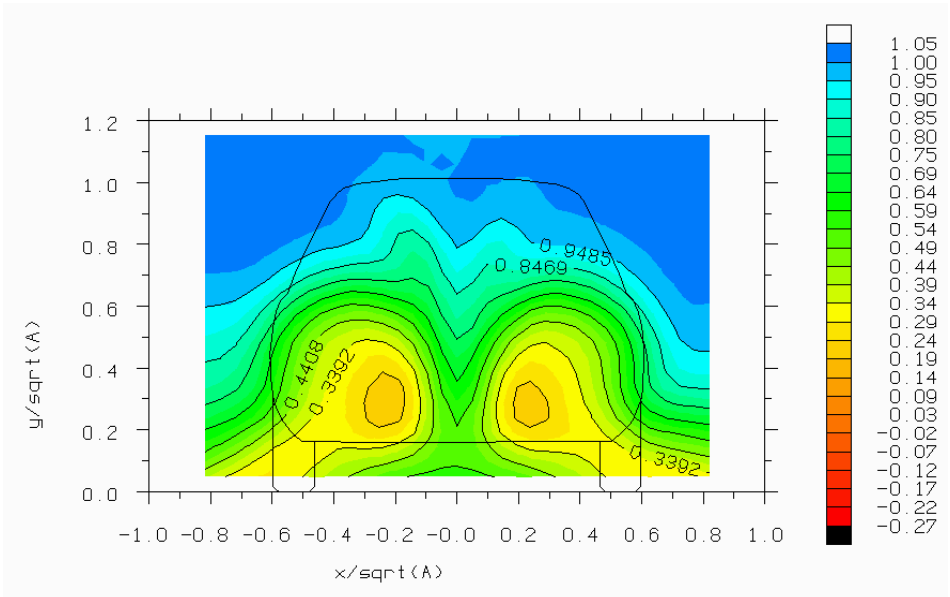

Figure 3.6.41 - Total pressure coefficient one base dimension behind the Rover 200 model without spoiler (15% scale) (true time-average)

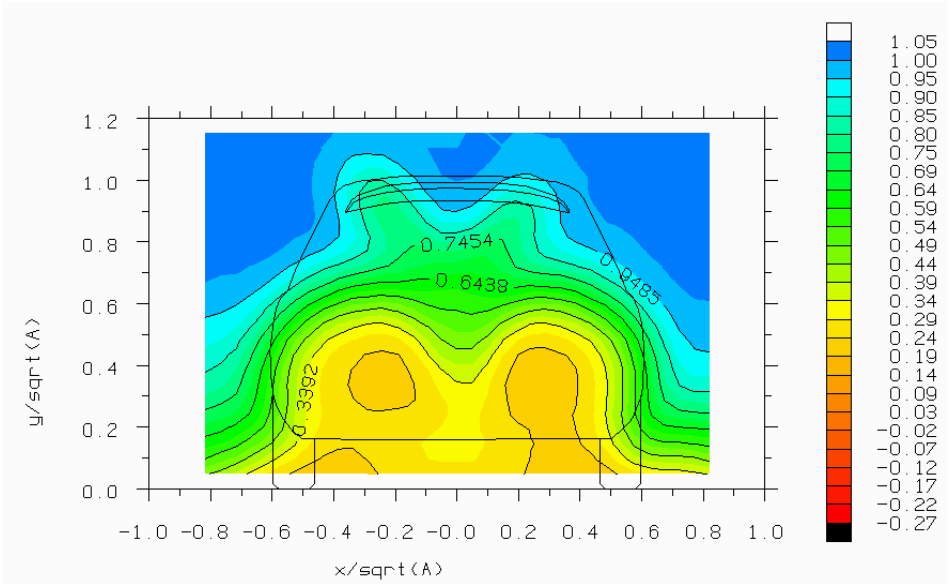

Figure 3.6.42 - Total pressure coefficient one base dimension behind the Rover 200 model with spoiler (15% scale) (true time-average)

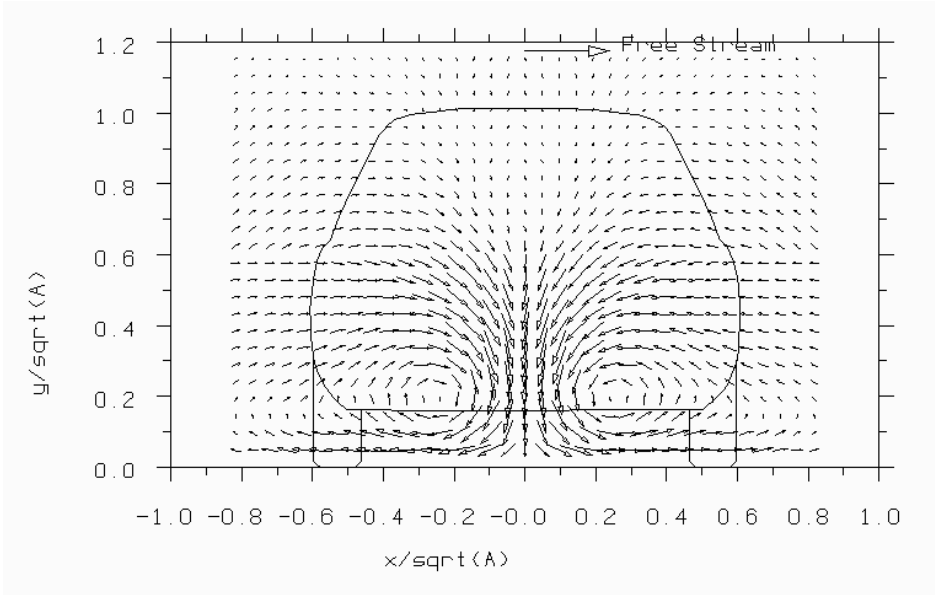

Figure 3.6.43 - Velocity vectors one base dimension behind the Rover 200 model without spoiler (40% scale) (true time-average) (mirrored)

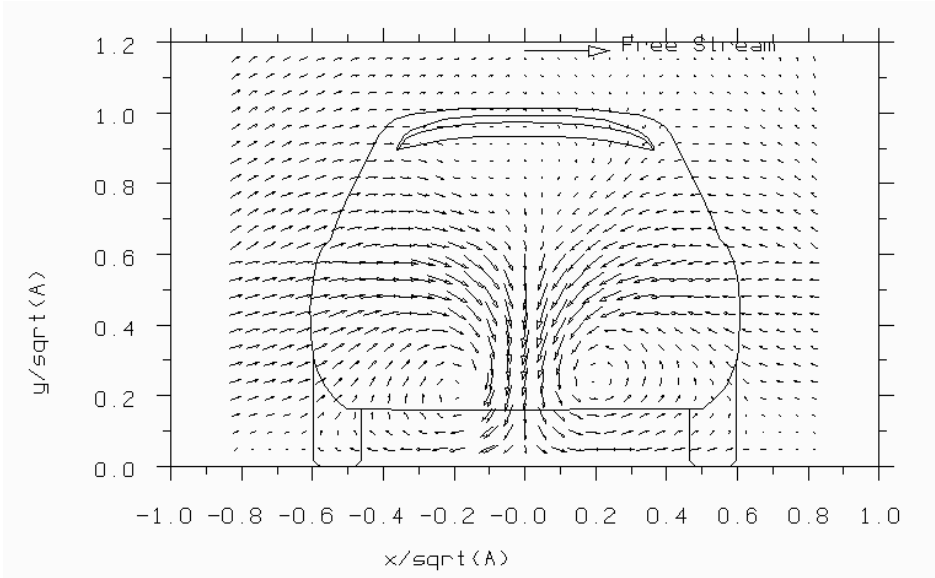

Figure 3.6.44 - Velocity vectors one base dimension behind the Rover 200 model with spoiler (40% scale) (true time-average)

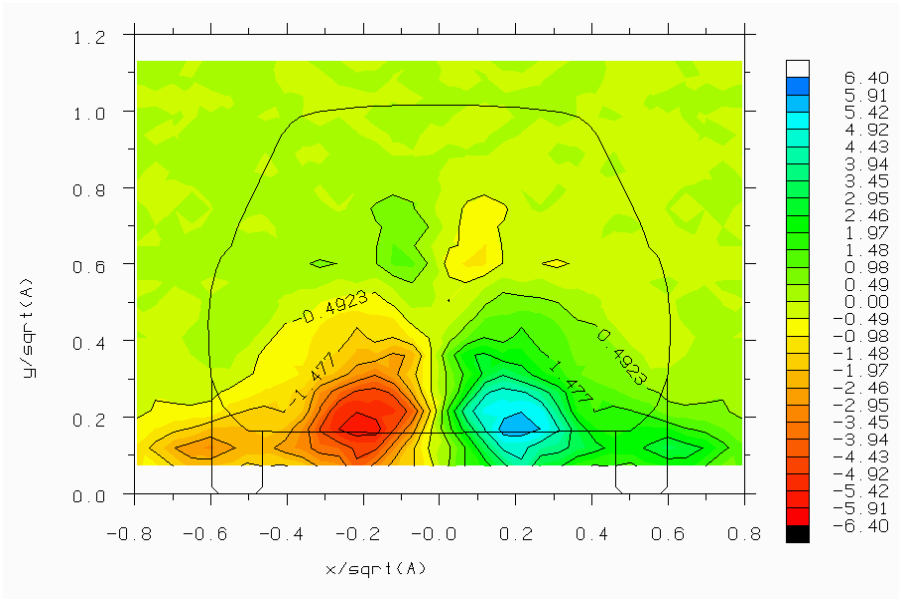

Figure 3.6.45 - Vorticity one base dimension behind the Rover 200 model without spoiler (non-dimensionalised by free-stream velocity and $A^{1/2}$) (40% scale) (true time-average) (mirrored)

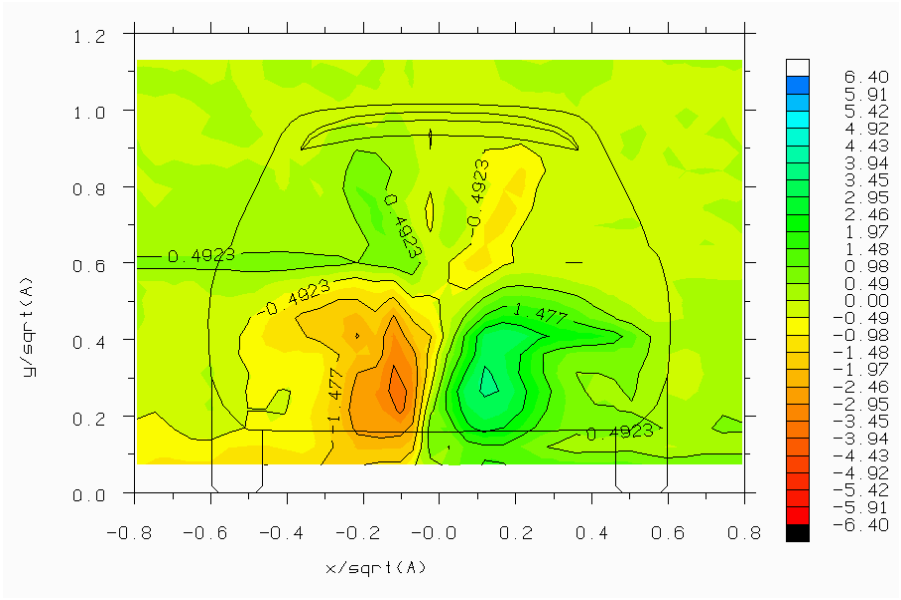

Figure 3.6.46 - Vorticity one base dimension behind the Rover 200 model with spoiler (non-dimensionalised by free-stream velocity and $A^{1/2}$) (40% scale) (true time-average)

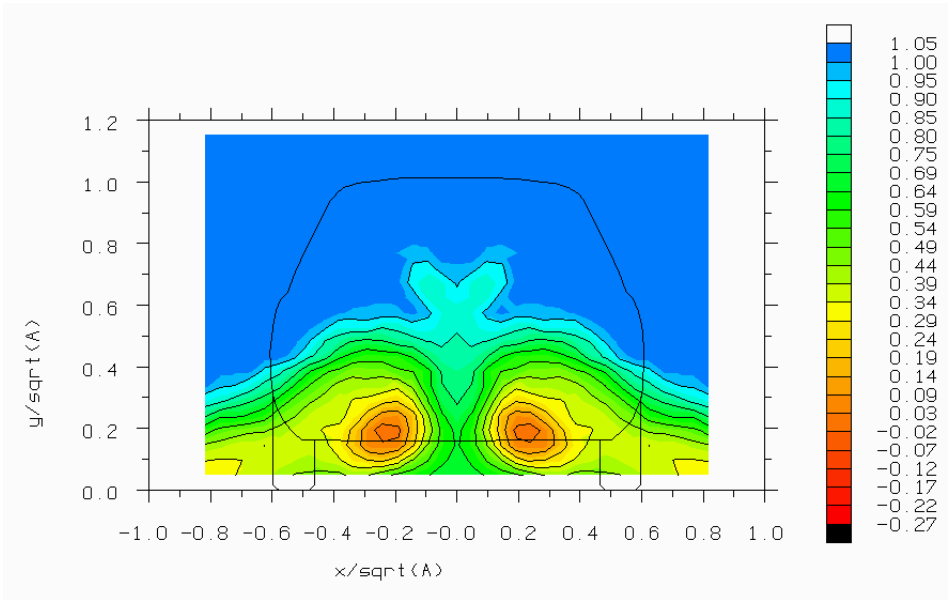

Figure 3.6.47 - Total pressure coefficient one base dimension behind the Rover 200 model without spoiler (40% scale) (true time-average) (mirrored)

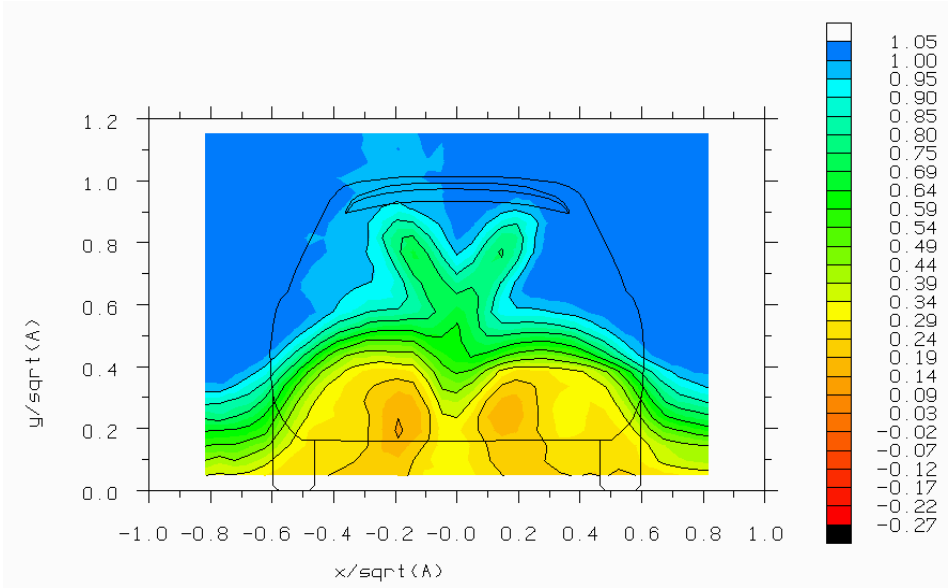

Figure 3.6.48 - Total pressure coefficient one base dimension behind the Rover 200 model with spoiler (40% scale) (true time-average)

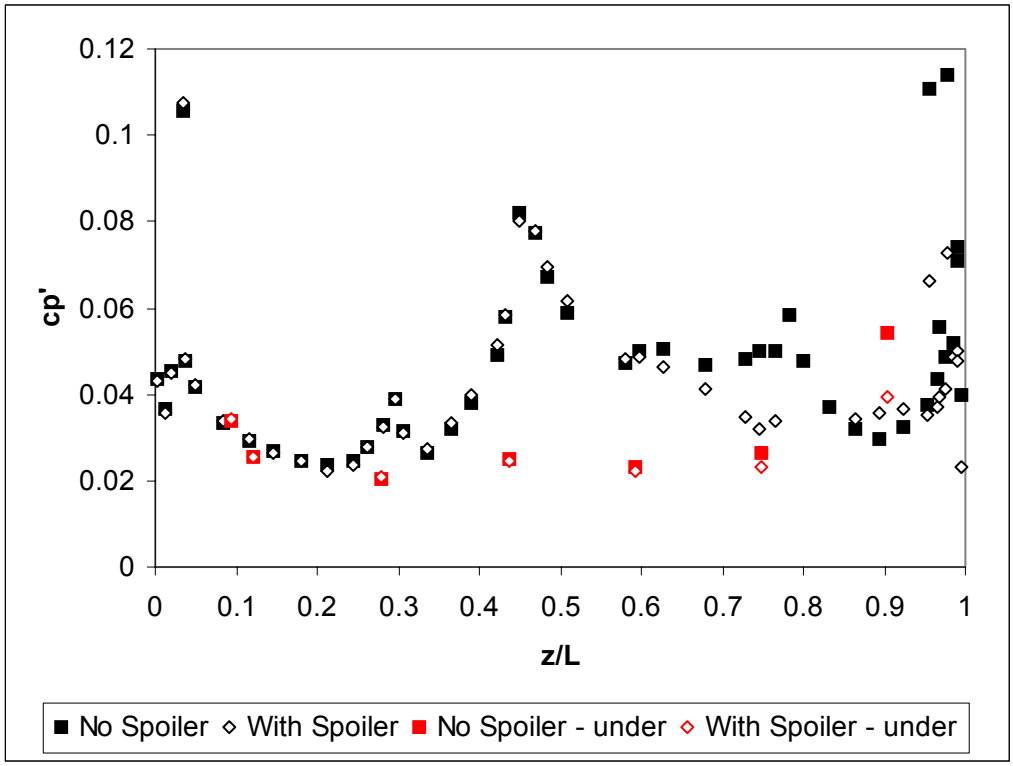

Figure 3.6.49 - Fluctuating pressure coefficient (standard deviation) on the surface of the Rover 200 model with and without spoiler (15% scale)

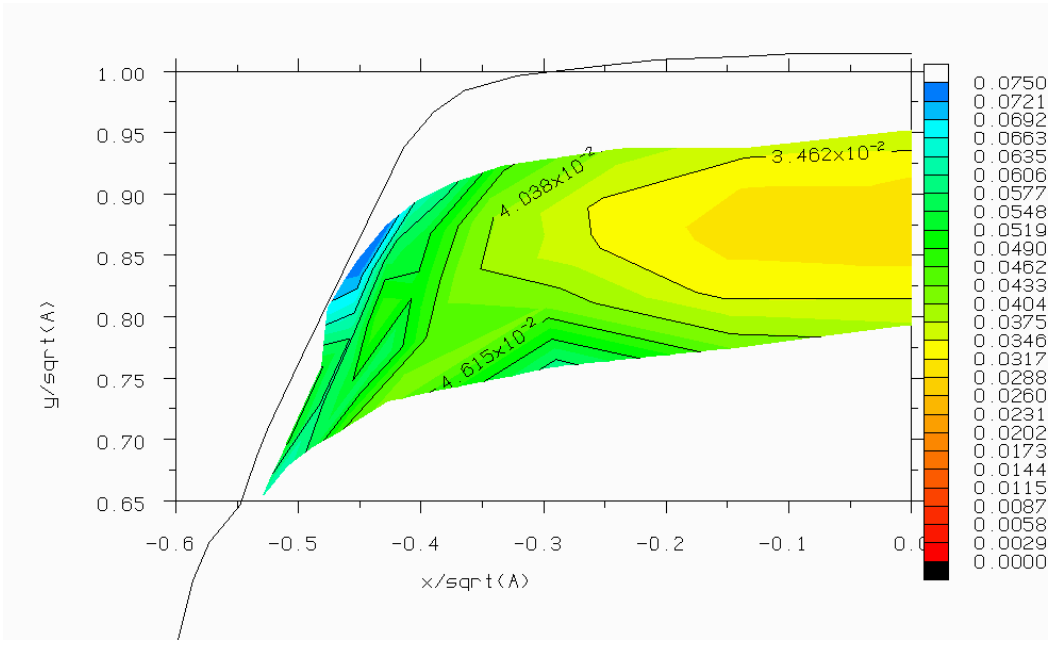

Figure 3.6.50 - Fluctuating pressure coefficient (standard deviation) on the left hand side of the backlight of the Rover 200 model without spoiler (15% scale)

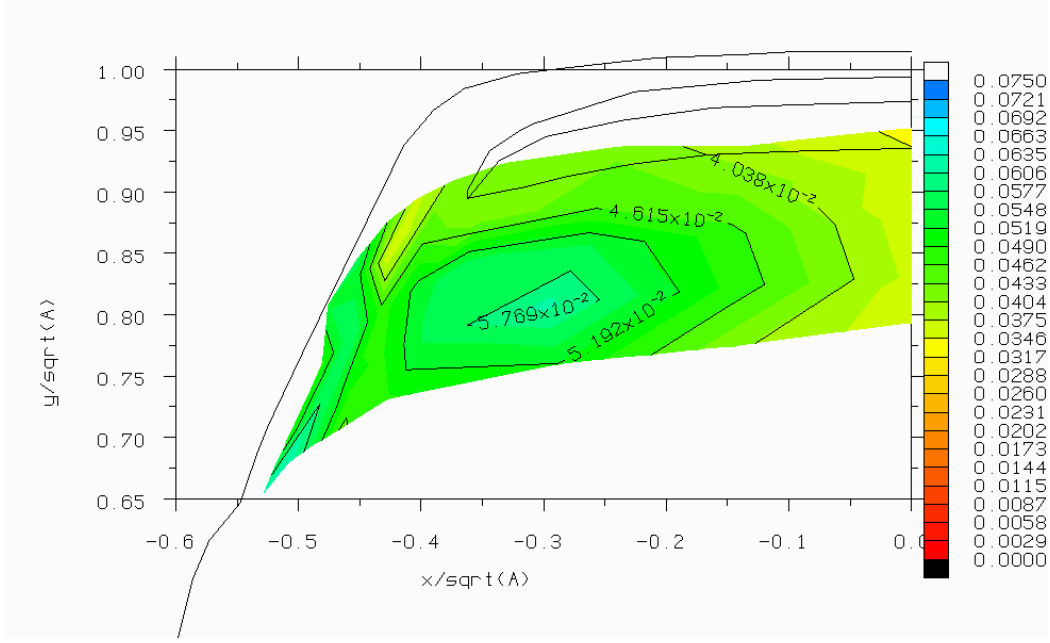

Figure 3.6.51 - Fluctuating pressure coefficient (standard deviation) on the left hand side of the backlight of the Rover 200 model with spoiler (15% scale)

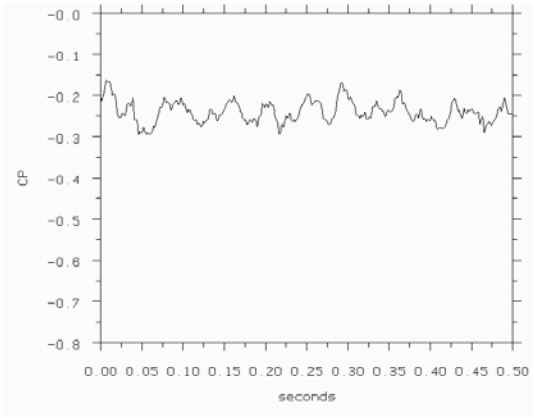

Figure 3.6.52 - Time-trace of surface pressure coefficient at z/L = 0.86 on the centreline of the Rover 200 model without spoiler (15% scale)

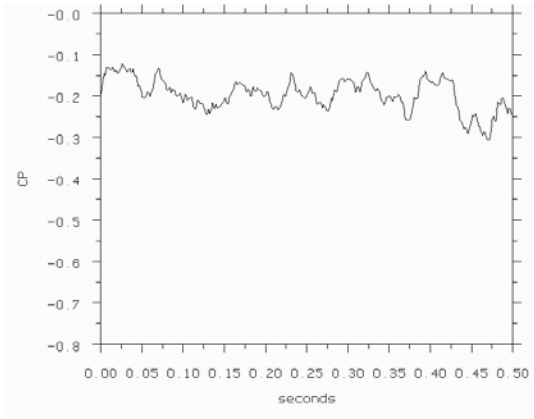

Figure 3.6.53 - Time-trace of surface pressure coefficient at z/L = 0.86 on the centreline of the Rover 200 model with spoiler (15% scale)

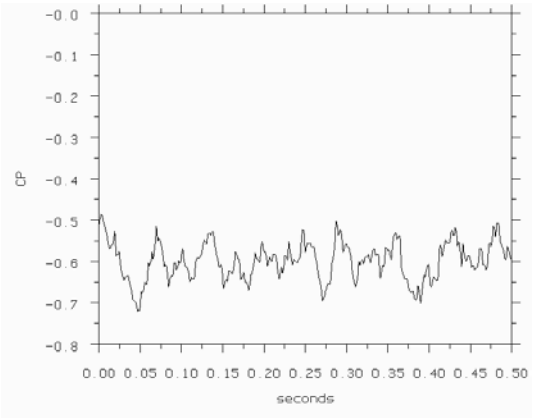

Figure 3.6.54 - Time-trace of surface pressure coefficient at z/L = 0.86 near the c-pillar (x/sqrt(A)=0.43, y/sqrt(A)=0.85) on the Rover 200 model without spoiler (15% scale)

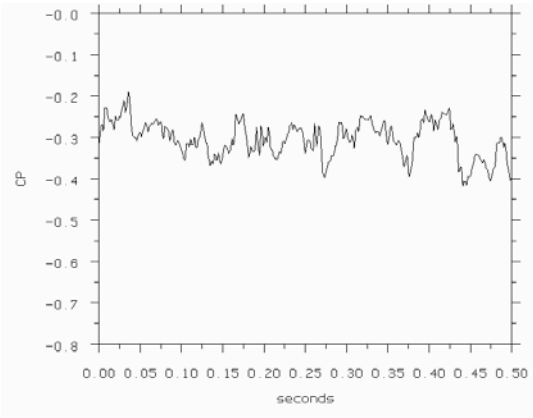

Figure 3.6.55 - Time-trace of surface pressure coefficient at z/L = 0.86 near the c-pillar (x/sqrt(A)=0.43, y/sqrt(A)=0.85) on the Rover 200 model with spoiler (15% scale)

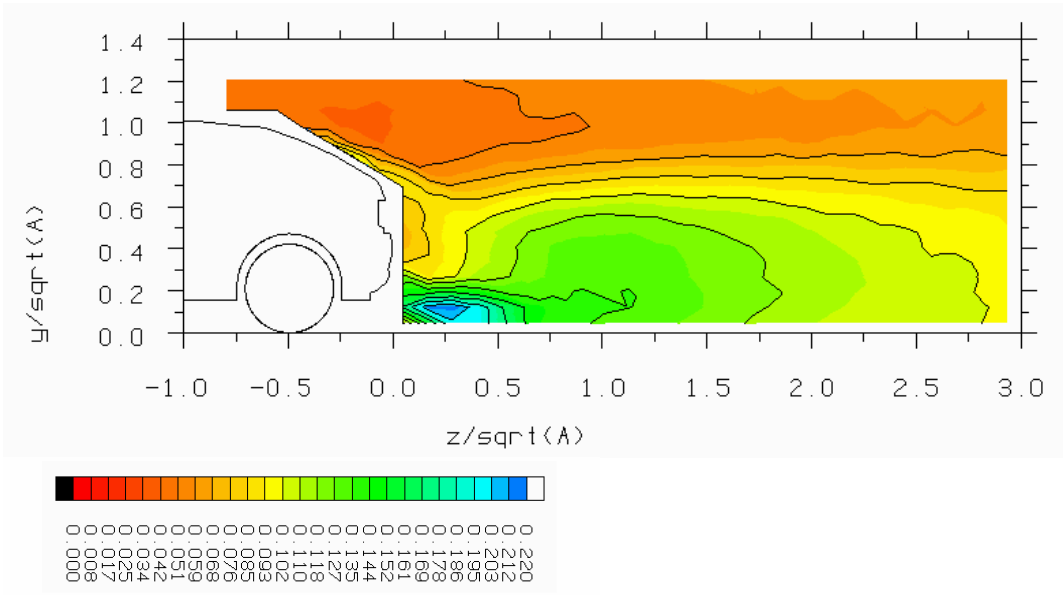

Figure 3.6.56 - Fluctuating hot-wire effective velocity (standard deviation) on the centre-plane of the Rover 200 model without spoiler (non-dimensionalised by free-stream velocity) (wire axis vertical) (15% scale)

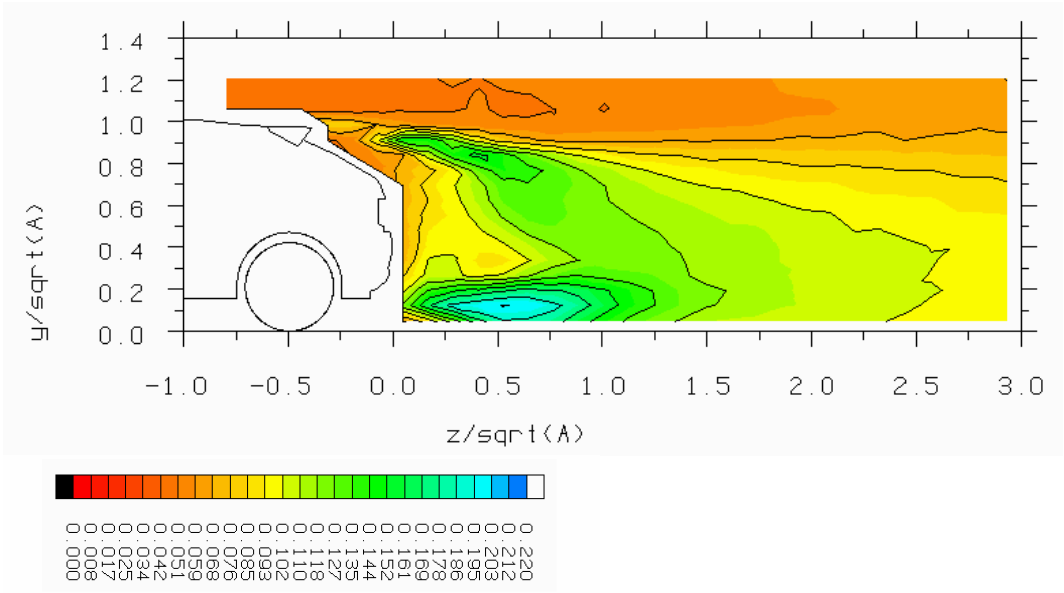

Figure 3.6.57 - Fluctuating hot-wire effective velocity (standard deviation) on the centre-plane of the Rover 200 model with spoiler (non-dimensionalised by free-stream velocity) (wire axis vertical) (15% scale)

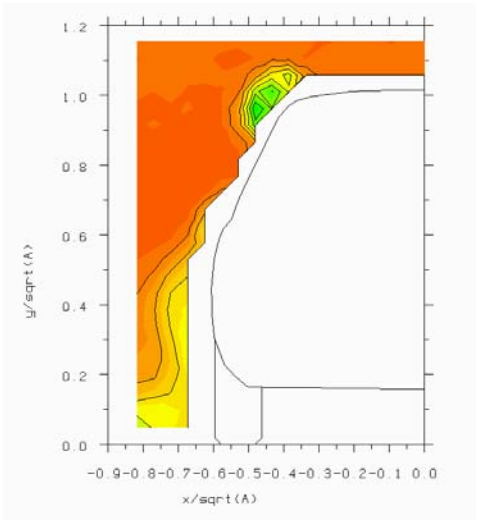

Figure 3.6.58a) z/sqrt(A) = -1.0

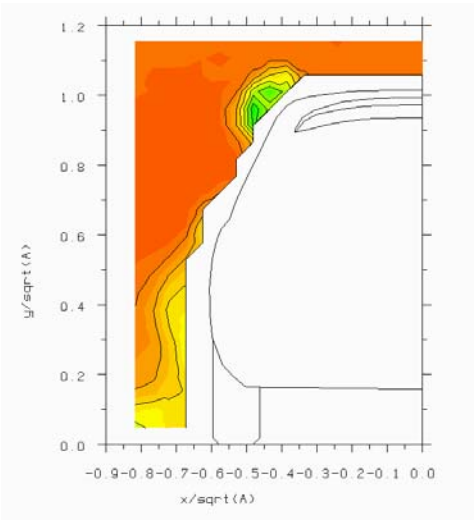

Figure 3.6.59a) z/sqrt(A) = -1.0

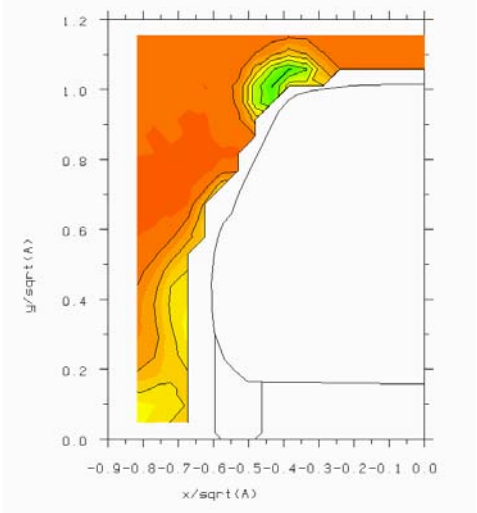

Figure 3.6.58b) z/sqrt(A) = -0.75

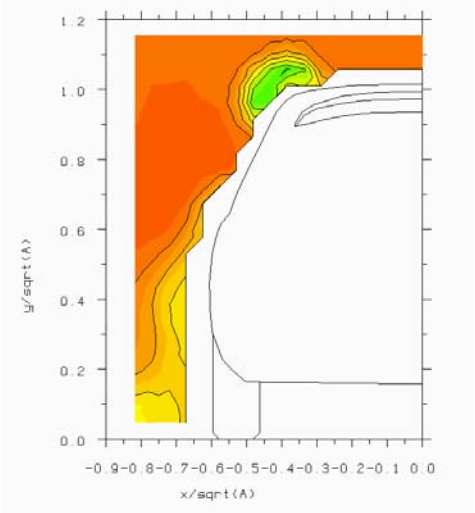

Figure 3.6.59b) z/sqrt(A) = -0.75

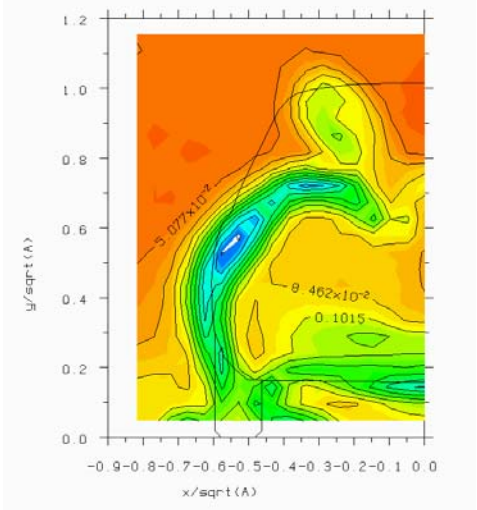

Figure 3.6.58c) z/sqrt(A) = 0.05

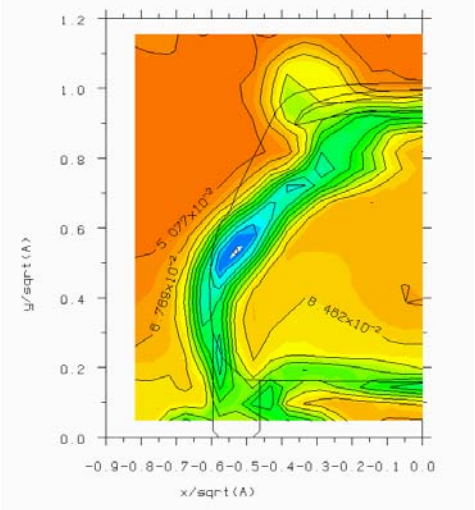

Figure 3.6.59c) z/sqrt(A) = 0.05

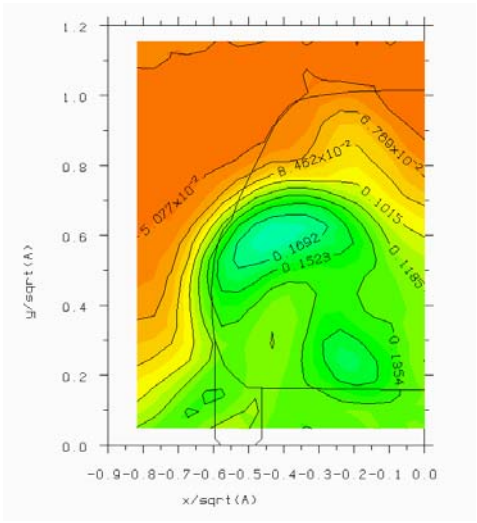

Figure 3.6.58d) z/sqrt(A) = 0.75

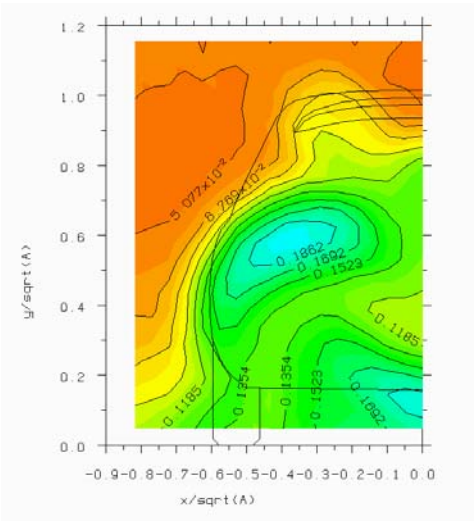

Figure 3.6.59d) z/sqrt(A) = -0.75

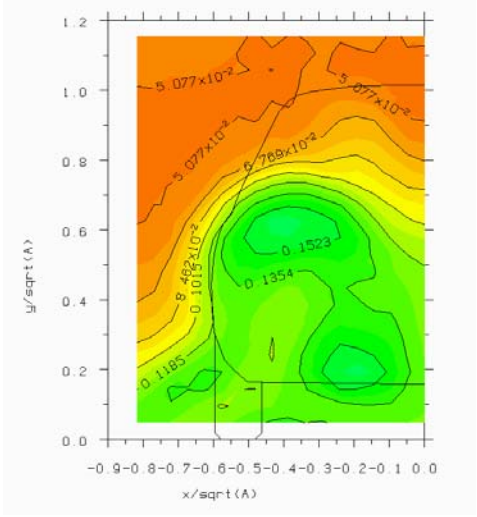

Figure 3.6.58e) z/sqrt(A) = 1.0

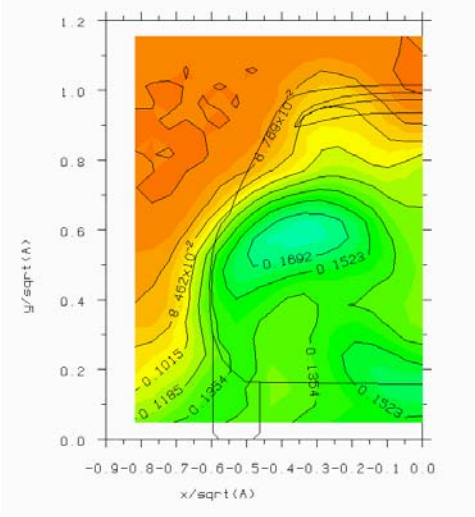

Figure 3.6.59e) z/sqrt(A) = 1.0

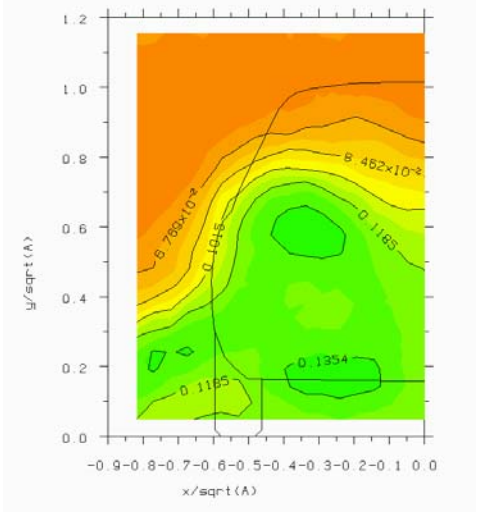

Figure 3.6.58f) z/sqrt(A) = 1.5

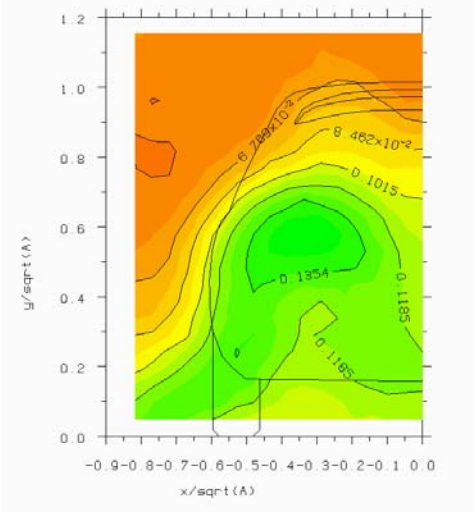

Figure 3.6.59f) z/sqrt(A) = 1.5

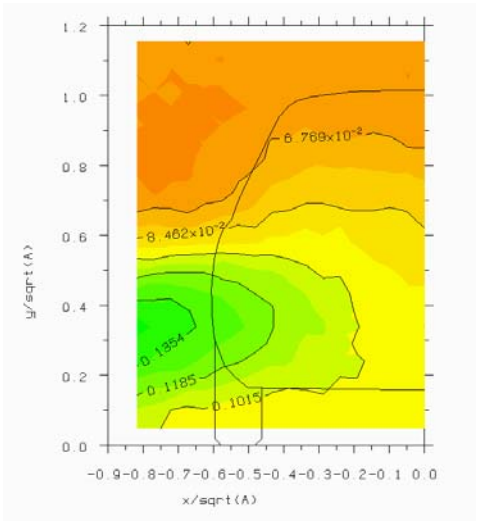

Figure 3.6.58g) z/sqrt(A) = 3.0

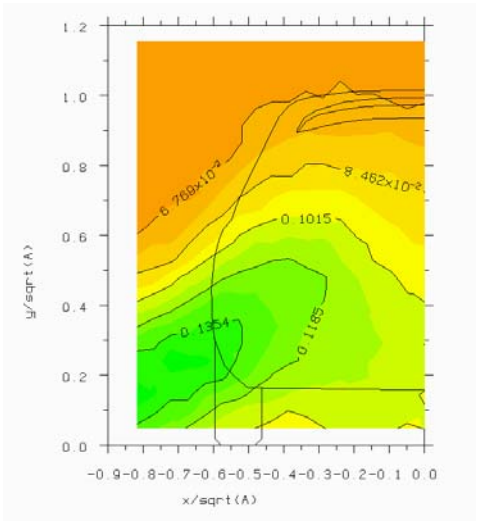

Figure 3.6.59g) z/sqrt(A) = 3.0

Figure 3.6.58 - Fluctuating hot-wire effective velocity (standard deviation) in the wake of the Rover 200 model without spoiler (non-dimensionalised by free-stream velocity) (wire axis vertical) (15% scale)

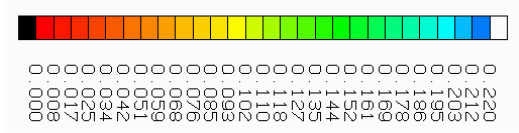

Figure 3.6.59 - Fluctuating hot-wire effective velocity (standard deviation) in the wake of the Rover 200 model with spoiler (non-dimensionalised by free-stream velocity) (wire axis vertical) (15% scale)

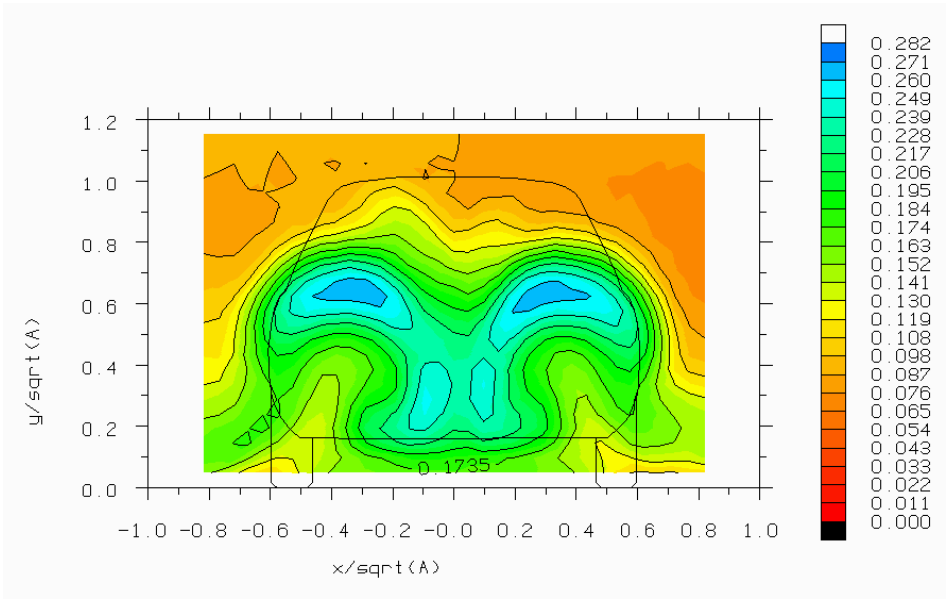

Figure 3.6.60 - Fluctuating total pressure coefficient (standard deviation) one base dimension behind the Rover 200 model without spoiler (15% scale)

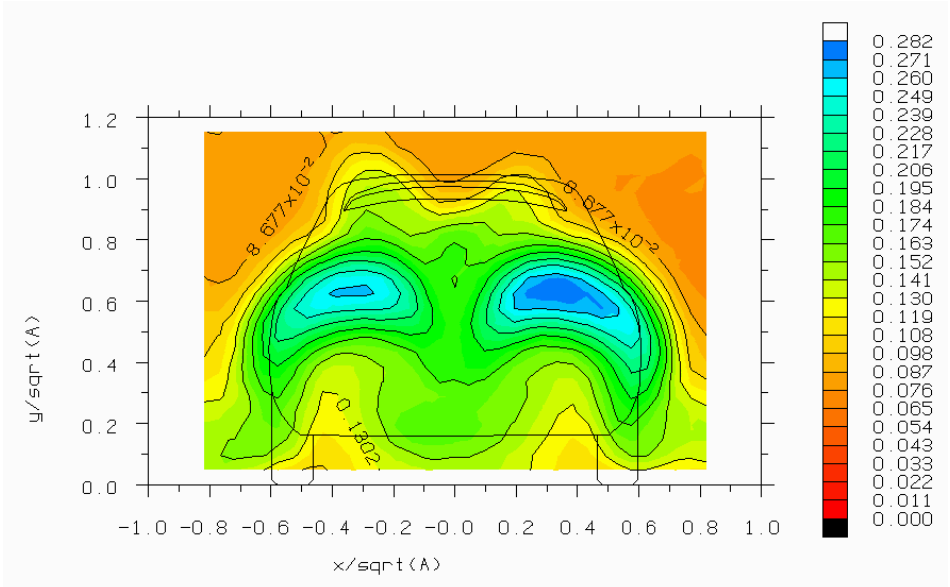

Figure 3.6.61 - Fluctuating total pressure coefficient (standard deviation) one base dimension behind the Rover 200 model with spoiler (15% scale)

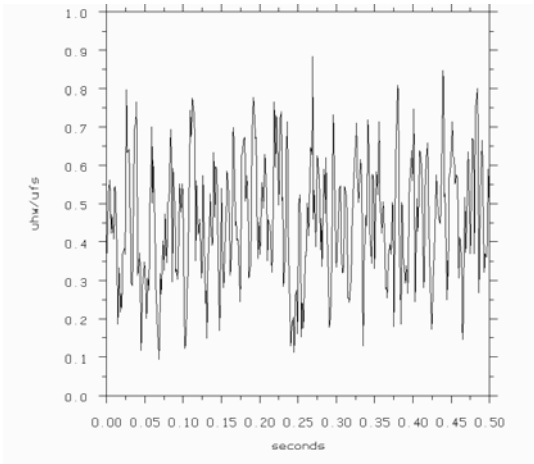

Figure 3.6.62 - Time-trace of hot-wire effective velocity at x/sqrt(A)=-0.24, y/sqrt(A)=0.24, z/sqrt(A)=0.75 in the wake of the Rover 200 model without spoiler (15% scale)

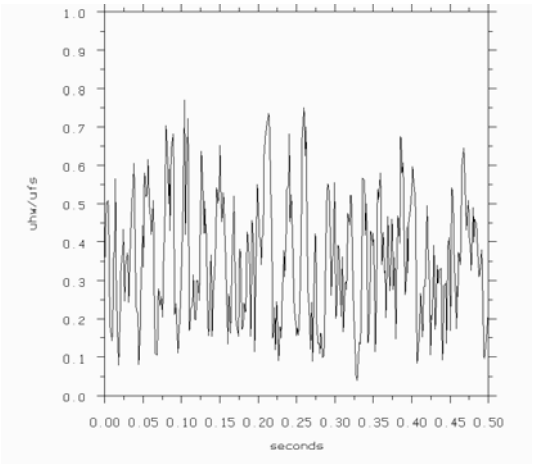

Figure 3.6.63 - Time-trace of hot-wire effective velocity at x/sqrt(A)=-0.14, y/sqrt(A)=0.24, z/sqrt(A)=0.75 in the wake of the Rover 200 model with spoiler (15% scale)

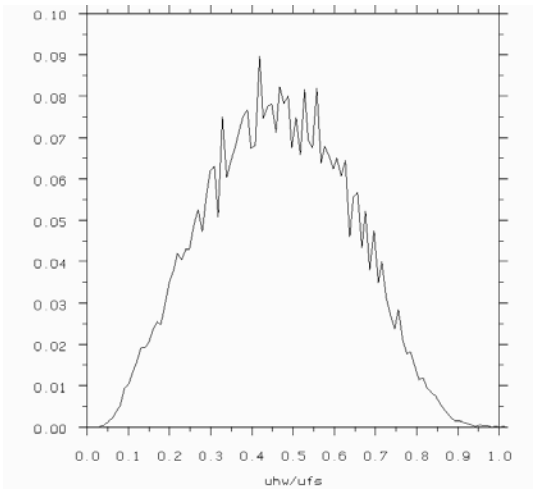

Figure 3.6.64 - Probability density of hot-wire effective velocity at x/sqrt(A)=-0.24, y/sqrt(A)=0.24, z/sqrt(A)=0.75 in the wake of the Rover 200 model without spoiler (15% scale)

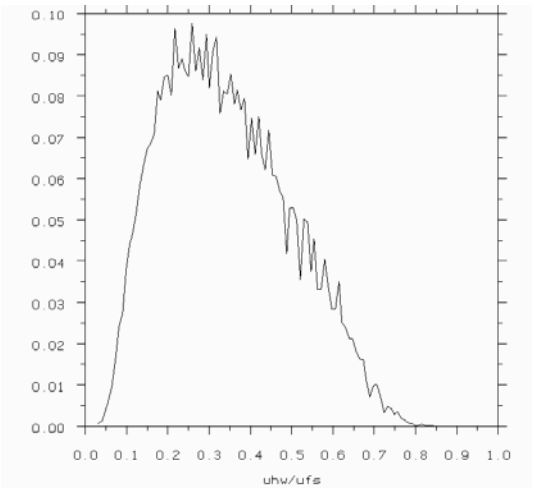

Figure 3.6.65 - Probability density of hot-wire effective velocity at x/sqrt(A)=-0.14, y/sqrt(A)=0.24, z/sqrt(A)=0.75 in the wake of the Rover 200 model with spoiler (15% scale)

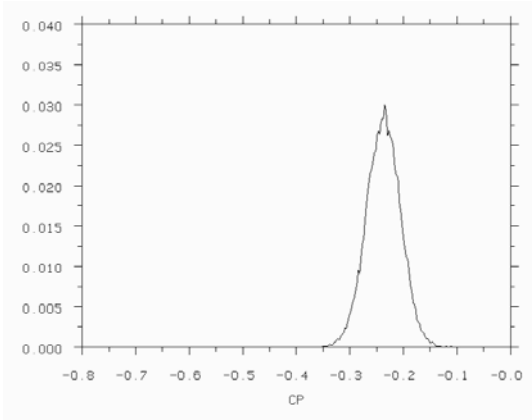

Figure 3.6.66 - Probability density of surface pressure coefficient at z/L = 0.86 on the centreline of the Rover 200 model without spoiler (15% scale)

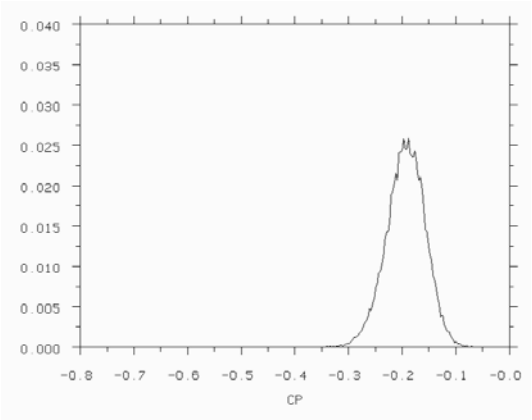

Figure 3.6.67 - Probability density of surface pressure coefficient at z/L = 0.86 on the centreline of the Rover 200 model with spoiler (15% scale)

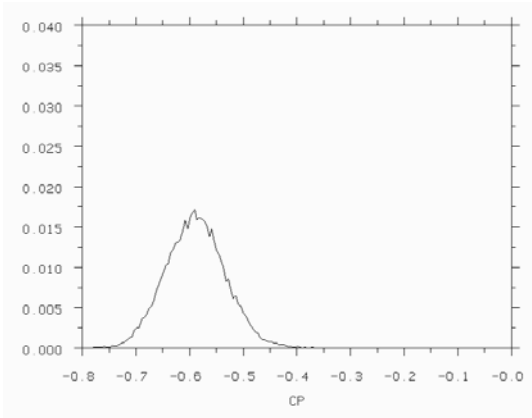

Figure 3.6.68 - Probability density of surface pressure coefficient at z/L = 0.86 near the c-pillar (x/sqrt(A)=0.43, y/sqrt(A)=0.85) on the Rover 200 model without spoiler (15% scale)

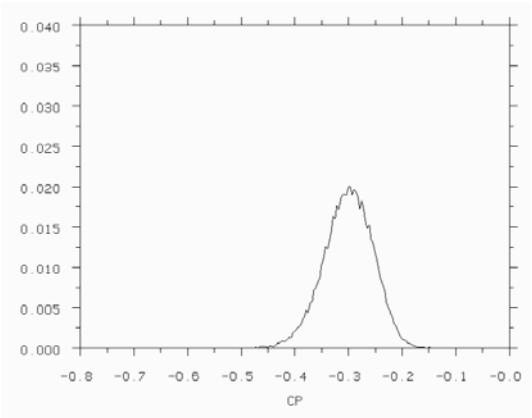

Figure 3.6.69 - Probability density of surface pressure coefficient at z/L = 0.86 near the c-pillar (x/sqrt(A)=0.43, y/sqrt(A)=0.85) on the Rover 200 model with spoiler (15% scale)

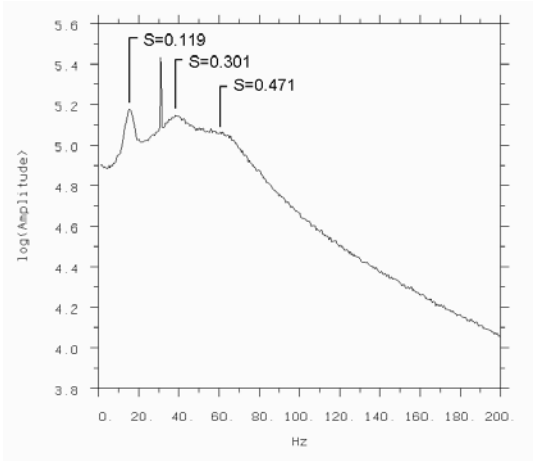

Figure 3.6 70 - Autospectral density of hot-wire effective velocity at x/sqrt(A)=-0.24, y/sqrt(A)=0.24, z/sqrt(A)=0.75 in the wake of the Rover 200 model without spoiler (15% scale)

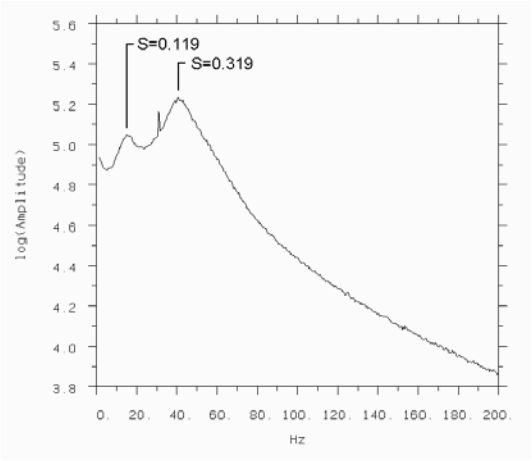

Figure 3.6.71 - Autospectral density of hot-wire effective velocity at x/sqrt(A)=-0.14, y/sqrt(A)=0.24, z/sqrt(A)=0.75 in the wake of the Rover 200 model with spoiler (15% scale)

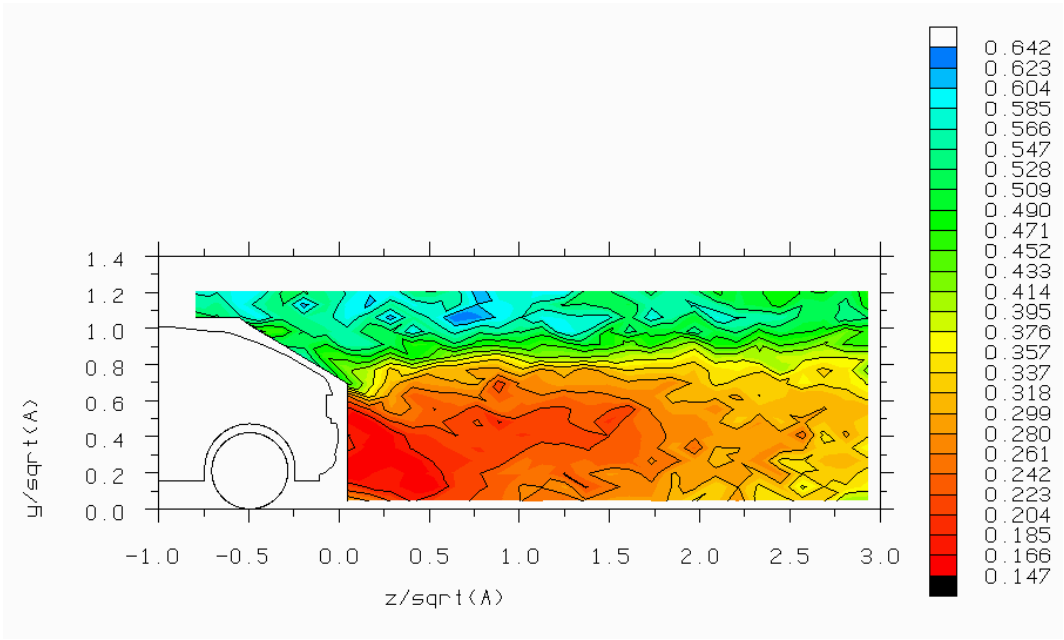

Figure 3.6.72 - Fraction of hot-wire effective velocity fluctuation due to unsteadiness near S=0.12 (S=0.102-0.133, f=13-17hz) on the centreline in the wake of the Rover 200 model without spoiler (15% scale)

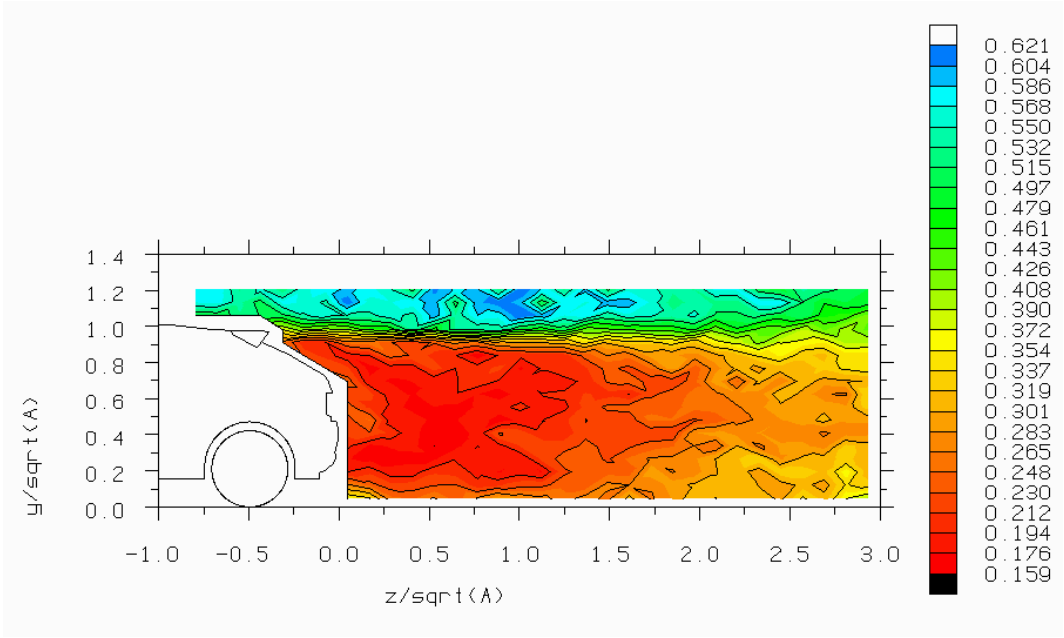

Figure 3.6.73 - Fraction of hot-wire effective velocity fluctuation due to unsteadiness near S=0.12 (S=0.102-0.133, f=13-17hz) on the centreline in the wake of the Rover 200 model with spoiler (15% scale)

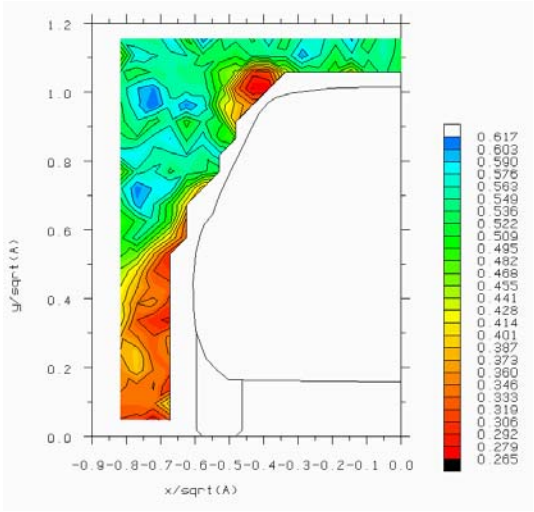

Figure 3.6.74a) z/sqrt(A) = -1.0

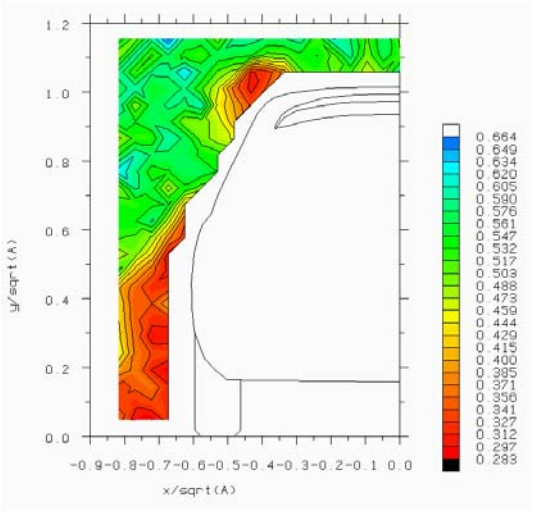

Figure 3.6.75a) z/sqrt(A) = -1.0

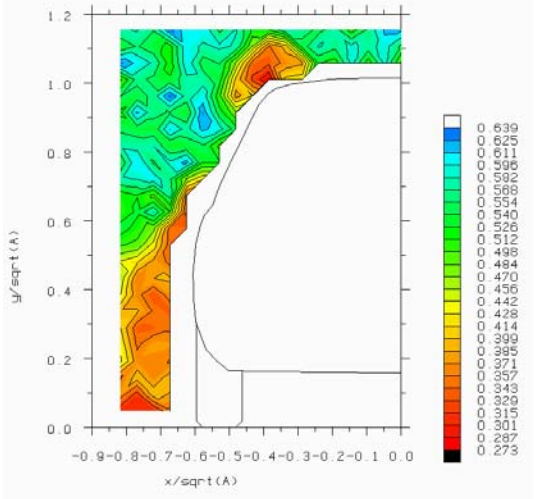

Figure 3.6.74b) z/sqrt(A) = -0.75

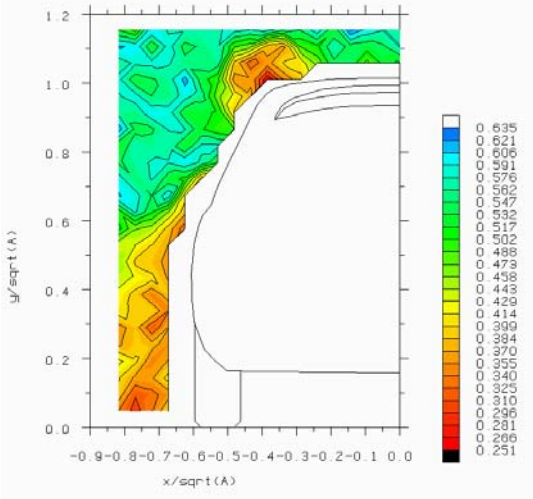

Figure 3.6.75b) z/sqrt(A) = -0.75

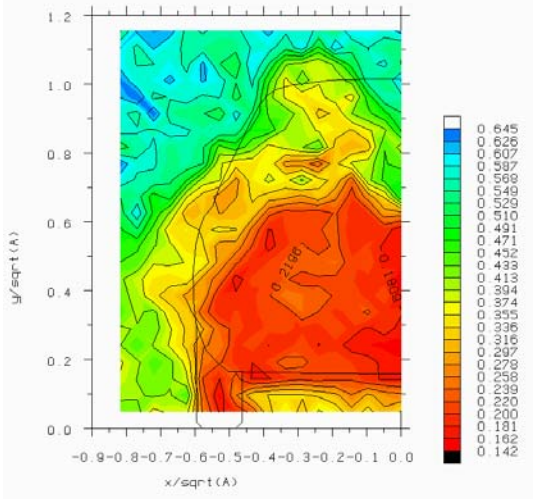

Figure 3.6.74c) z/sqrt(A) = 0.05

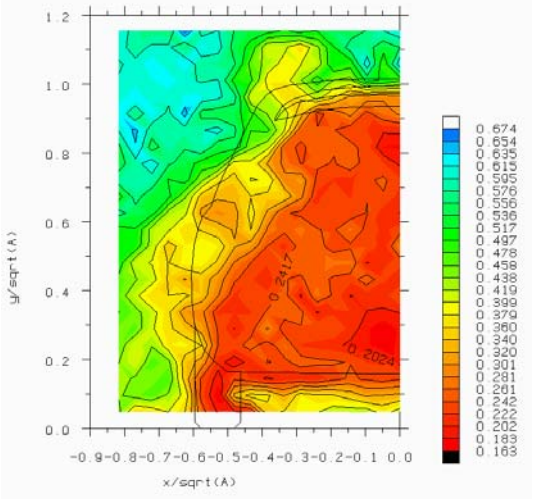

Figure 3.6.75c) z/sqrt(A) = 0.05

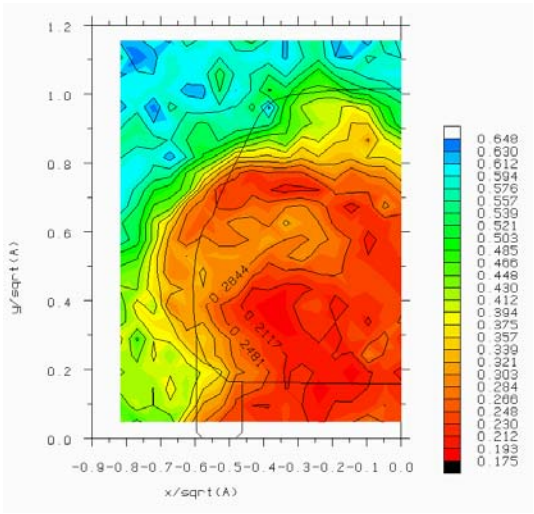

Figure 3.6.74d) z/sqrt(A) = 0.75

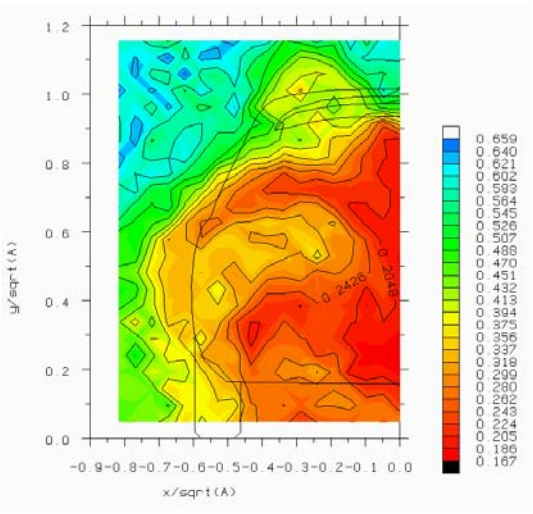

Figure 3.6.75d) z/sqrt(A) = 0.75

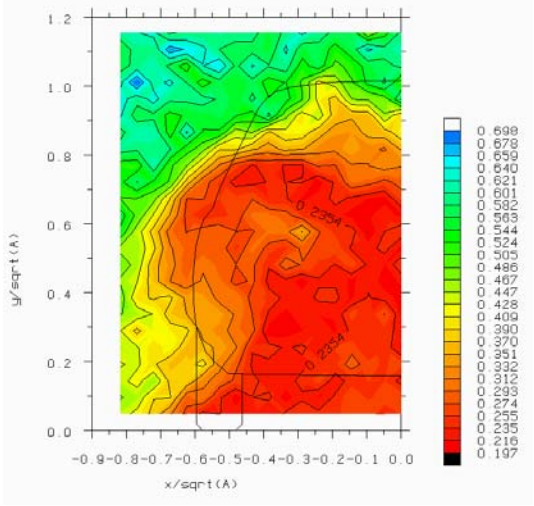

Figure 3.6.74e) z/sqrt(A) = 1.0

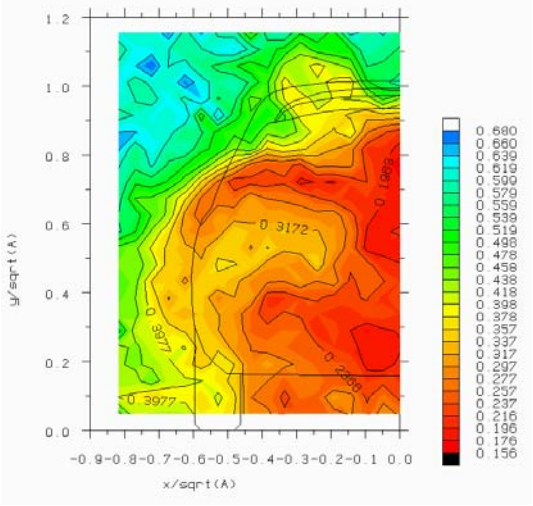

Figure 3.6.75e) z/sqrt(A) = 1.0

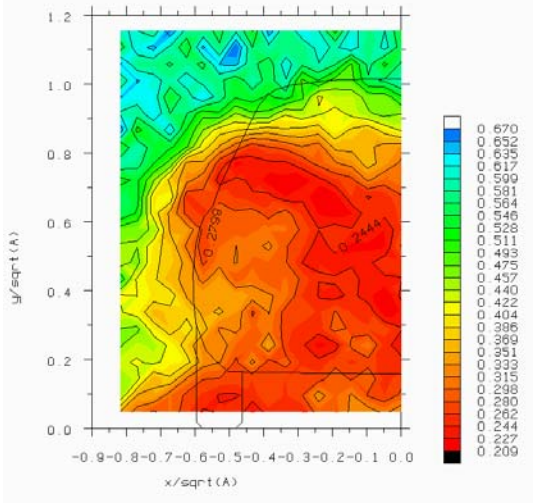

Figure 3.6.74f) z/sqrt(A) = 1.5

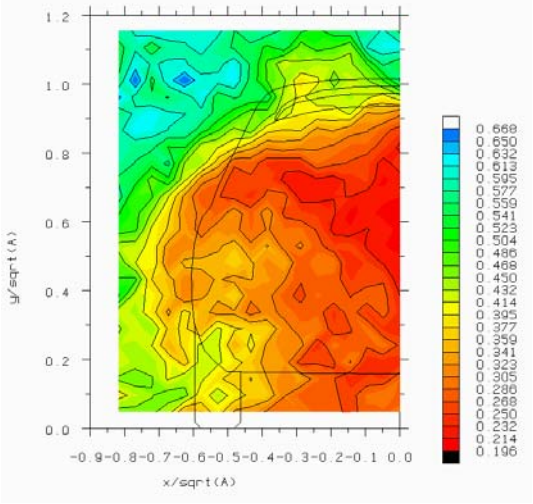

Figure 3.6.75f) z/sqrt(A) = 1.5

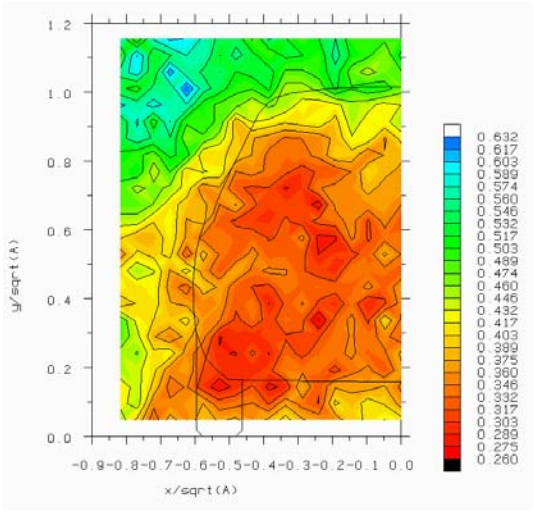

Figure 3.6.74g) z/sqrt(A) = 3.0

Figure 3.6.74 - Fraction of hot-wire effective velocity fluctuation due to unsteadiness near S=0.12 (S=0.102-0.133, f=13-17hz) in the wake of the Rover 200 model without spoiler (15% scale)

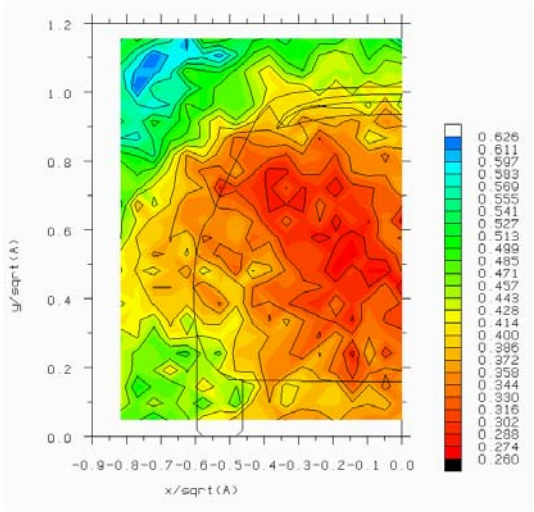

Figure 3.6.75g) z/sqrt(A) = 3.0

Figure 3.6.75 - Fraction of hot-wire effective velocity fluctuation due to unsteadiness near S=0.12 (S=0.102-0.133, f=13-17hz) in the wake of the Rover 200 model with spoiler (15% scale)

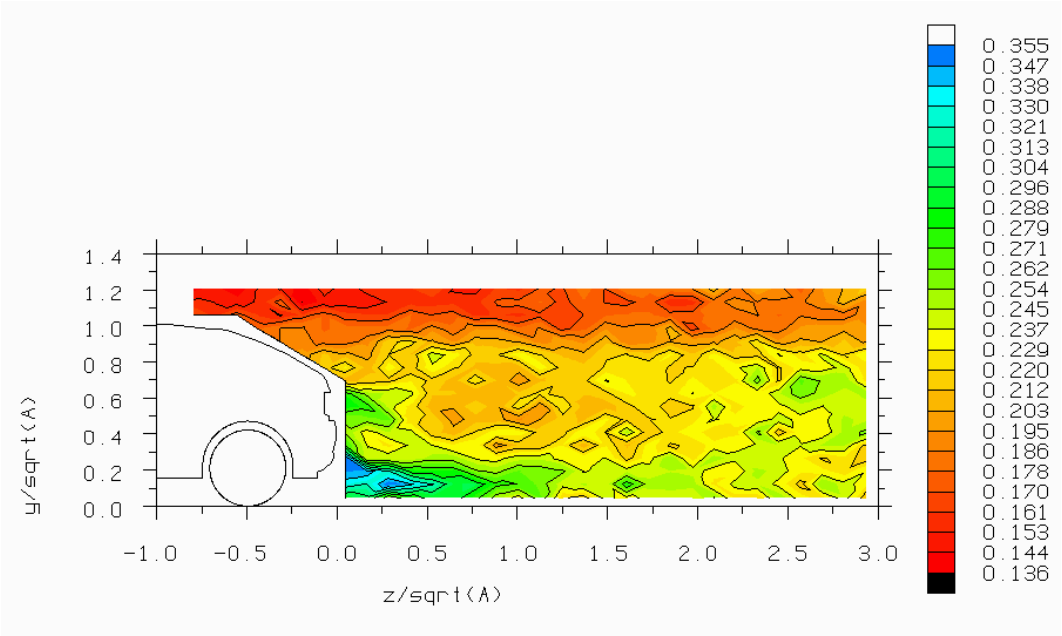

Figure 3.6.76 - Fraction of hot-wire effective velocity fluctuation due to unsteadiness near S=0.31 (S=0.275-0.353, f=35-45hz) on the centreline in the wake of the Rover 200 model without spoiler (15% scale)

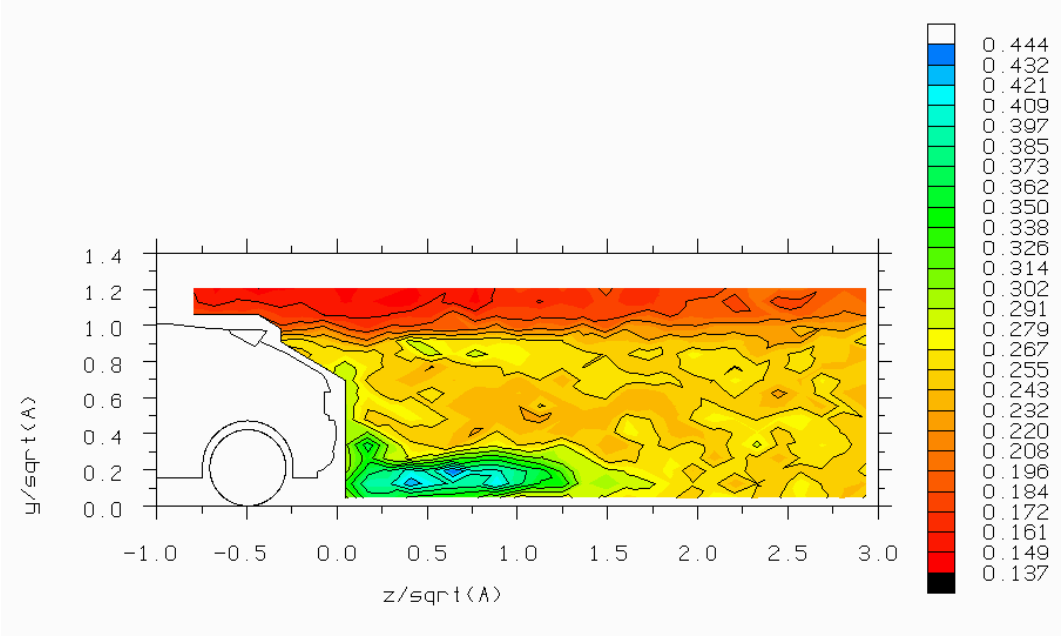

Figure 3.6.77 - Fraction of hot-wire effective velocity fluctuation due to unsteadiness near S=0.31 (S=0.275-0.353, f=35-45hz) on the centreline in the wake of the Rover 200 model with spoiler (15% scale)

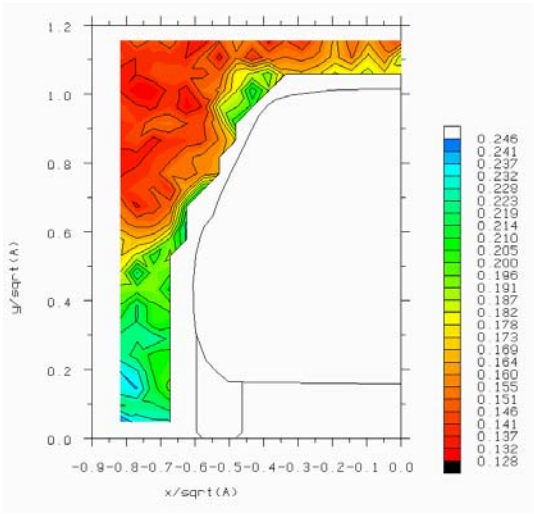

Figure 3.6.78a) z/sqrt(A) = -1.0

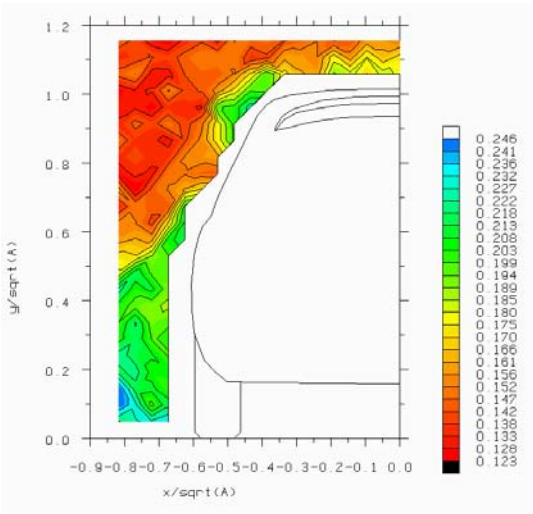

Figure 3.6.79a) z/sqrt(A) = -1.0

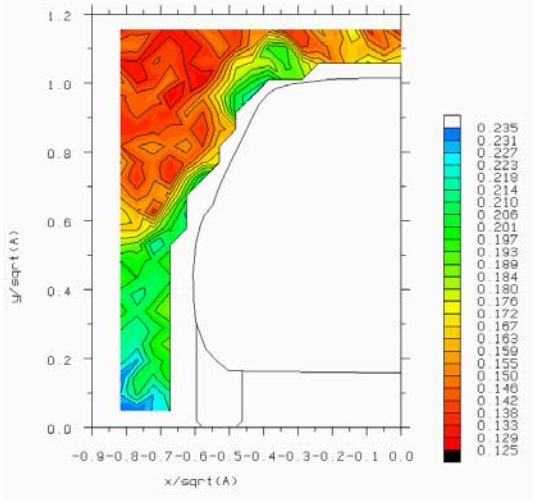

Figure 3.6.78b) z/sqrt(A) = -0.75

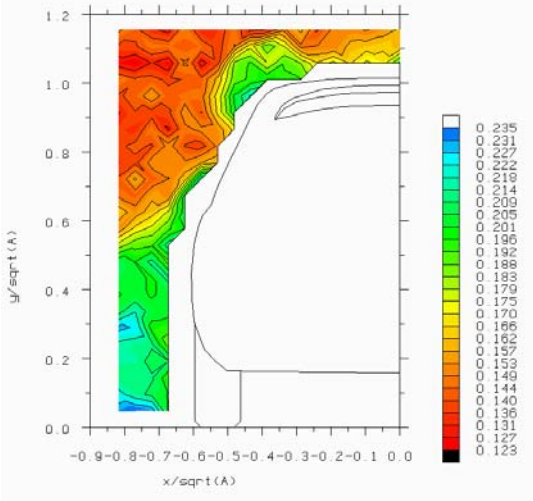

Figure 3.6.79b) z/sqrt(A) = -0.75

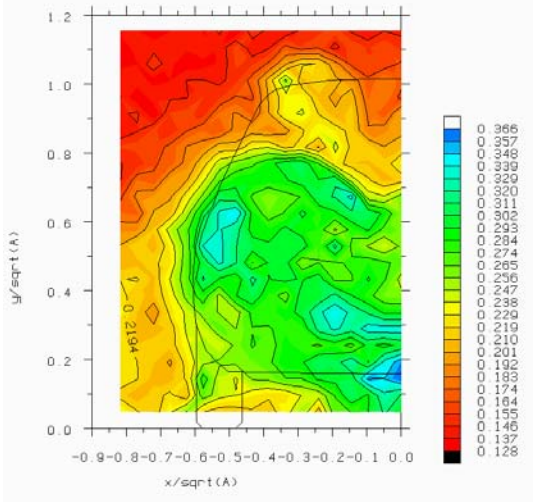

Figure 3.6.78c) z/sqrt(A) = 0.05

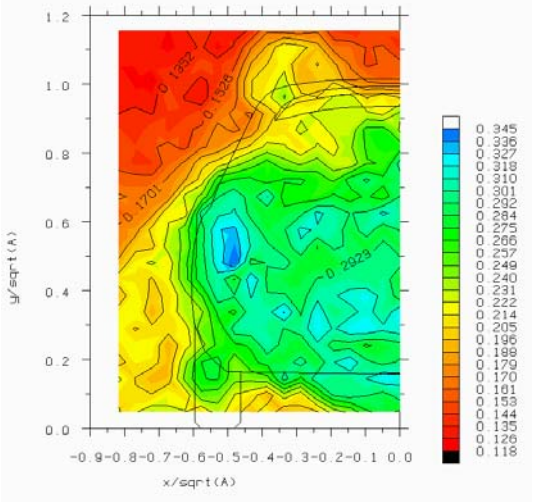

Figure 3.6.79c) z/sqrt(A) = 0.05

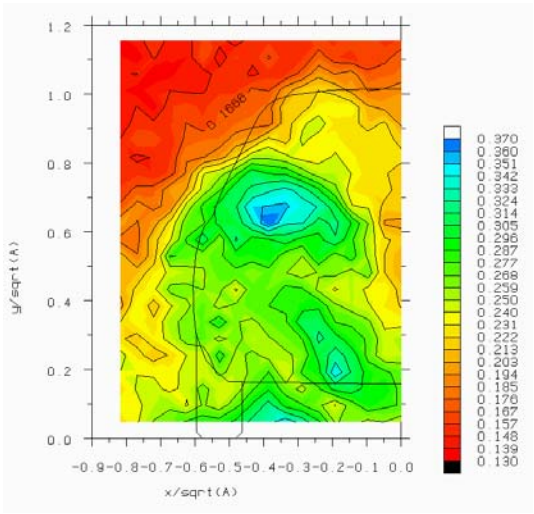

Figure 3.6.78d) z/sqrt(A) = 0.75

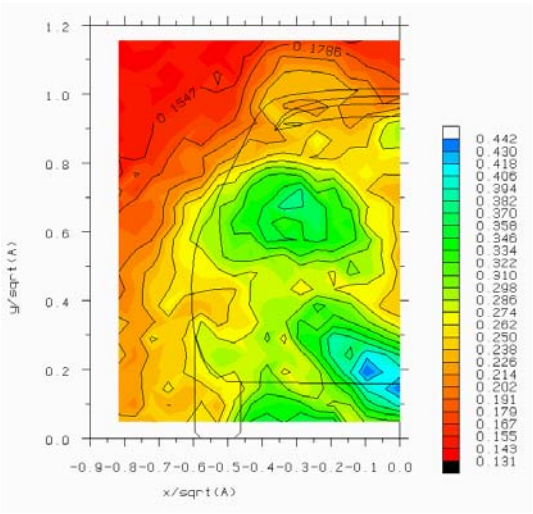

Figure 3.6.79d) z/sqrt(A) = 0.75

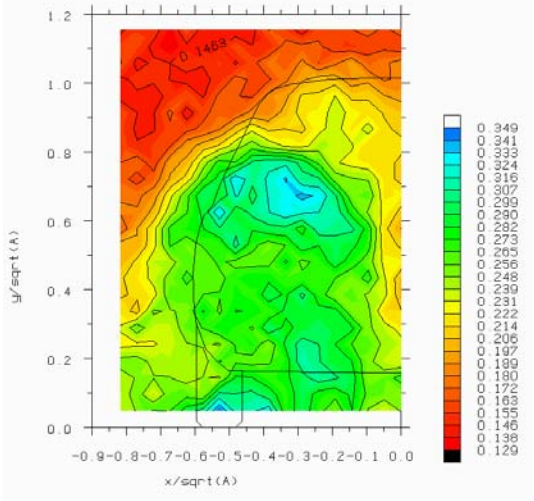

Figure 3.6.78e) z/sqrt(A) = 1.0

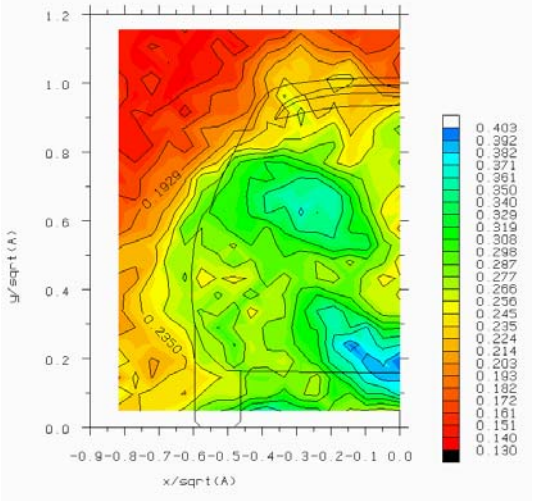

Figure 3.6.79e) z/sqrt(A) = 1.0

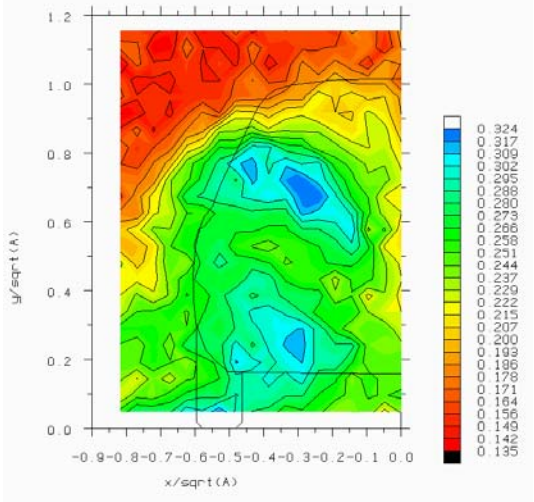

Figure 3.6.78f) z/sqrt(A) = 1.5

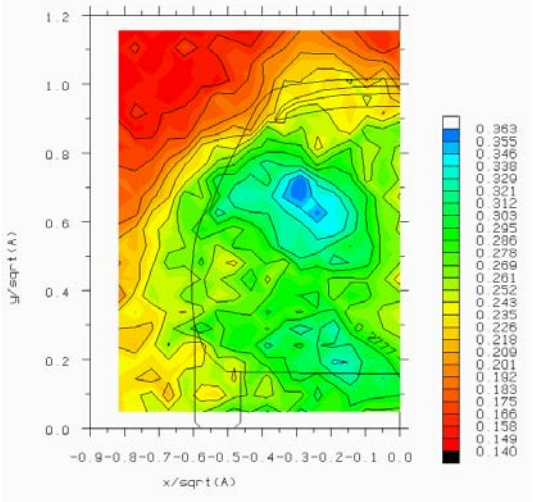

Figure 3.6.79f) z/sqrt(A) = 1.5

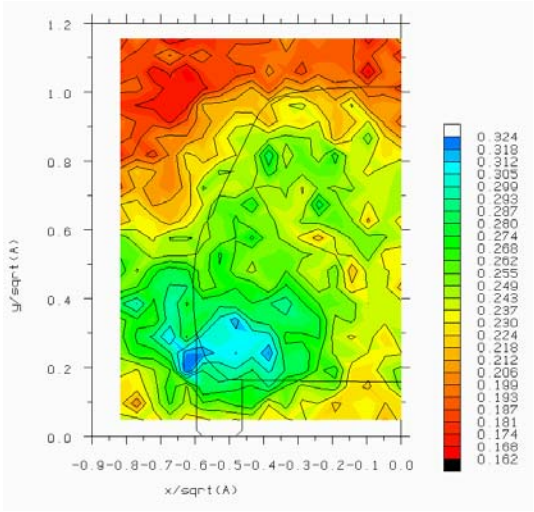

Figure 3.6.78g) z/sqrt(A) = 3.0

Figure 3.6.78 - Fraction of hot-wire effective velocity fluctuation due to unsteadiness near S=0.31 (S=0.275-0.353, f=35-45hz) in the wake of the Rover 200 model without spoiler (15% scale)

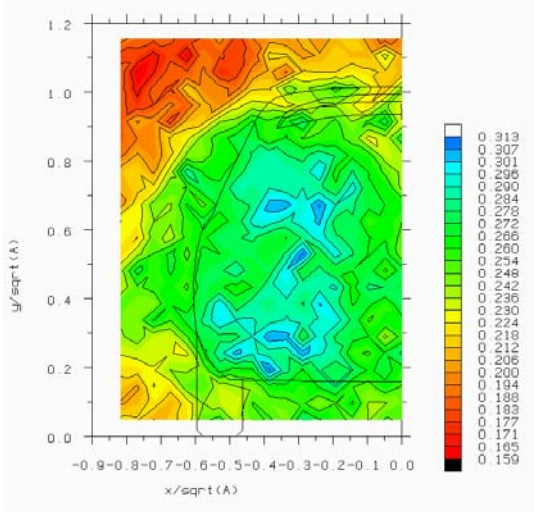

Figure 3.6.79g) z/sqrt(A) = 3.0

Figure 3.6.79 - Fraction of hot-wire effective velocity fluctuation due to unsteadiness near S=0.31 (S=0.275-0.353, f=35-45hz) in the wake of the Rover 200 model with spoiler (15% scale)

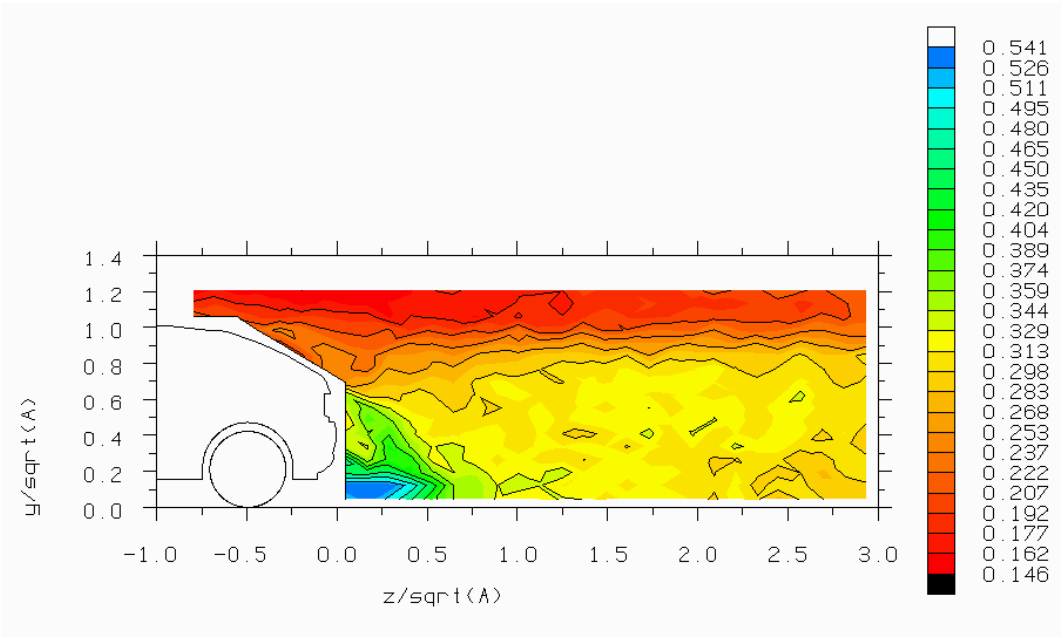

Figure 3.6.80 - Fraction of hot-wire effective velocity fluctuation due to unsteadiness near S=0.47 (S=0.392-0.549, f=50-70hz) on the centreline in the wake of the Rover 200 model without spoiler (15% scale)

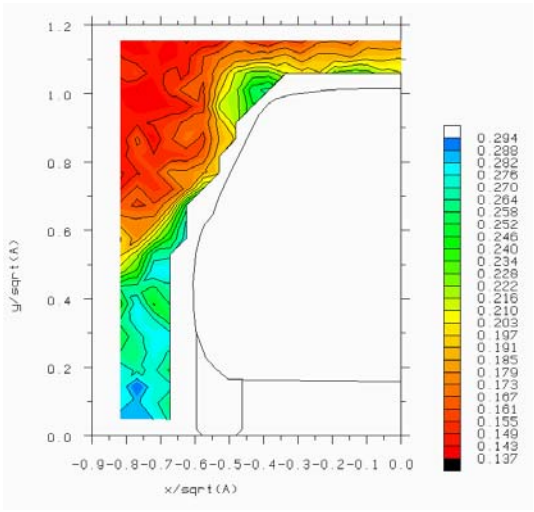

Figure3.6.81a) z/sqrt(A) = -1.0

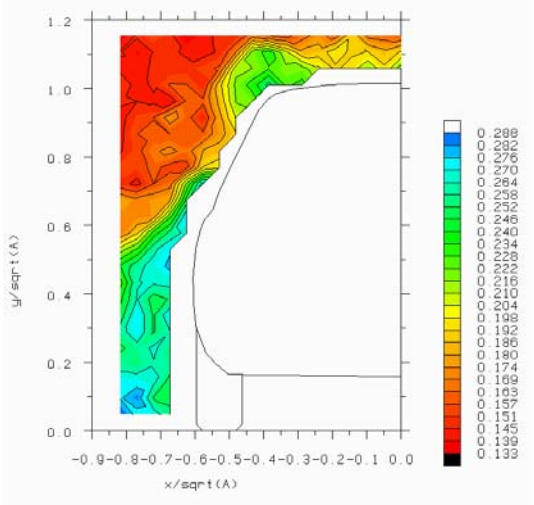

Figure3.6.81b) z/sqrt(A) = -0.75

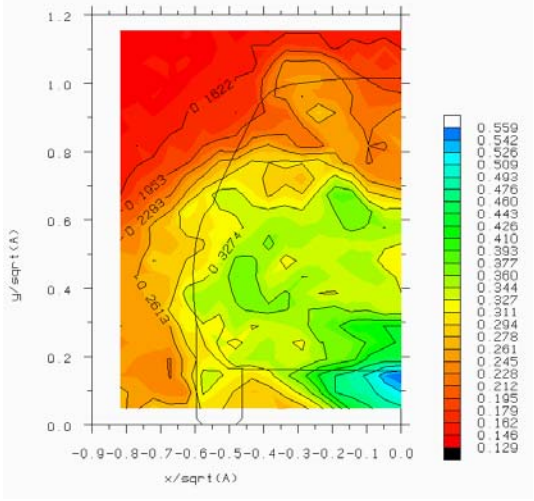

Figure3.6.81c) z/sqrt(A) = 0.05

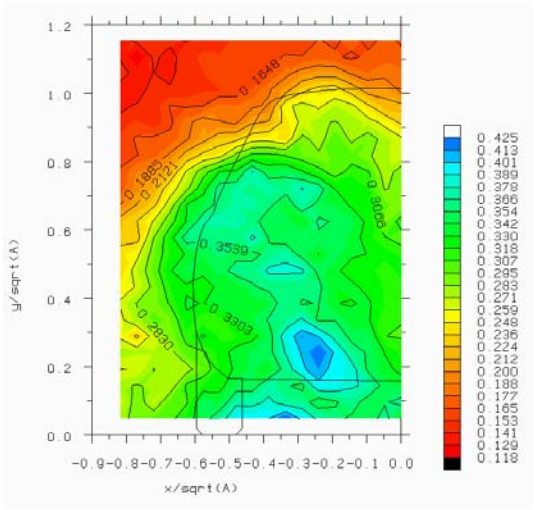

Figure3.6.81d) z/sqrt(A) = 0.75

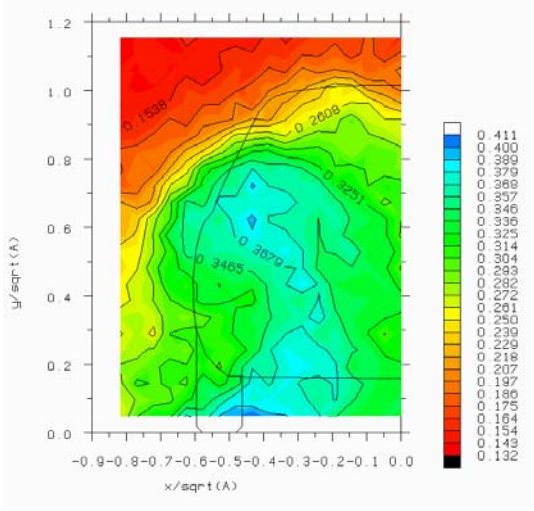

Figure3.6.81e) z/sqrt(A) = 1.0

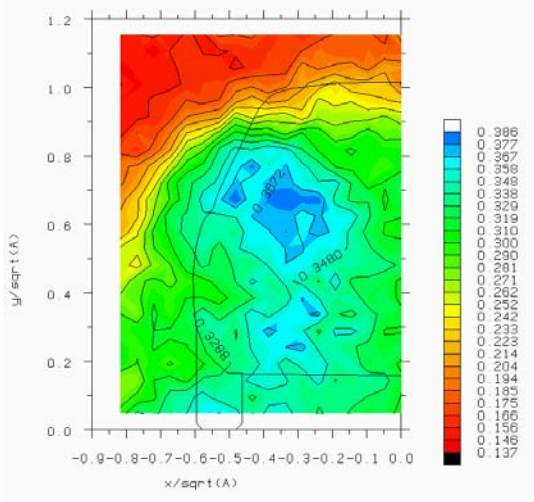

Figure3.6.81f) z/sqrt(A) = 1.5

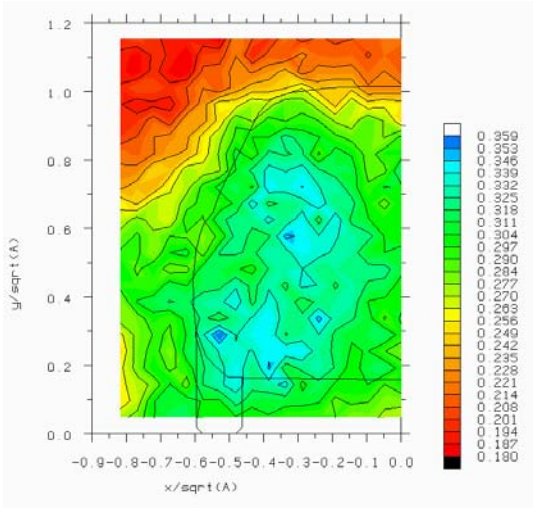

Figure3.6.81g) z/sqrt(A) = 3.0

Figure 3.6.81 - Fraction of hot-wire effective velocity fluctuation due to unsteadiness near S=0.47 (S=0.392-0.549, f=50-70hz) in the wake of the Rover 200 model without spoiler (15% scale)

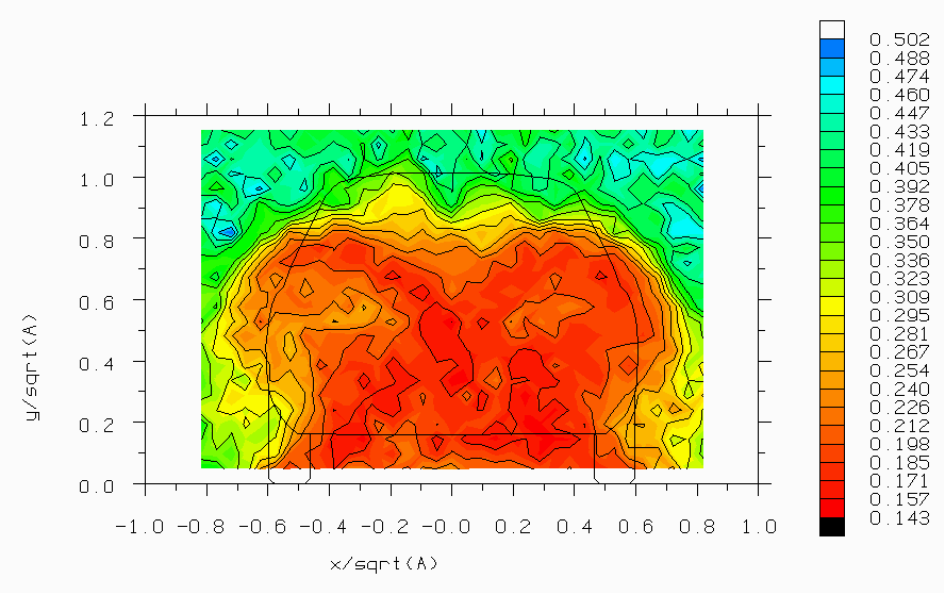

Figure 3.6.82 - Fraction of total pressure coefficient fluctuation due to unsteadiness near S=0.12 (S=0.110-0.126, f=14-16hz) one base dimension behind the Rover 200 model without spoiler (15% scale)

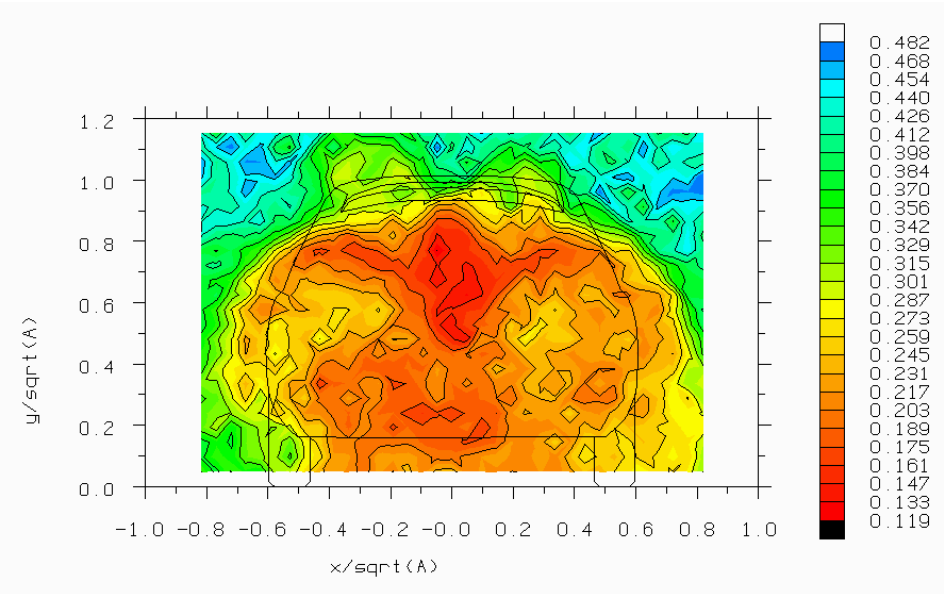

Figure 3.6.83 - Fraction of total pressure coefficient fluctuation due to unsteadiness near S=0.12 (S=0.110-0.126, f=14-16hz) one base dimension behind the Rover 200 model with spoiler (15% scale)

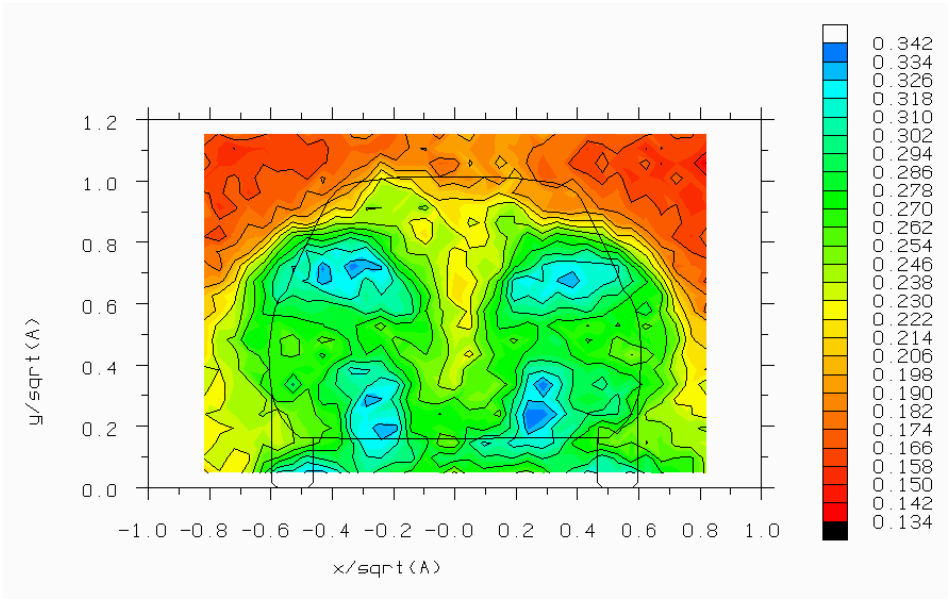

Figure 3.6.84 - Fraction of total pressure coefficient fluctuation due to unsteadiness near S=0.31 (S=0.275-0.353, f=35-45hz) one base dimension behind the Rover 200 model without spoiler (15% scale)

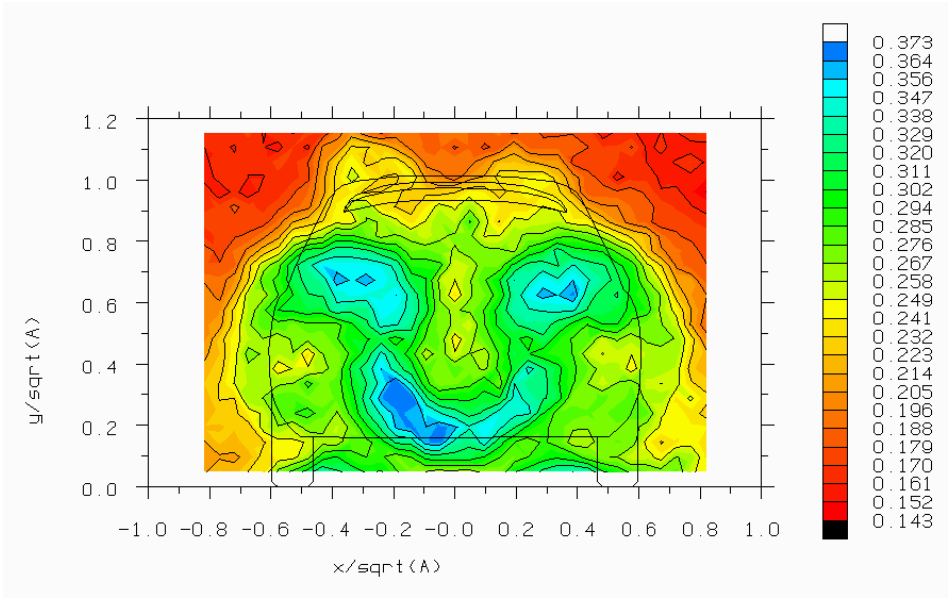

Figure 3.6.85 - Fraction of total pressure coefficient fluctuation due to unsteadiness near S=0.31 (S=0.275-0.353, f=35-45hz) one base dimension behind the Rover 200 model with spoiler (15% scale)

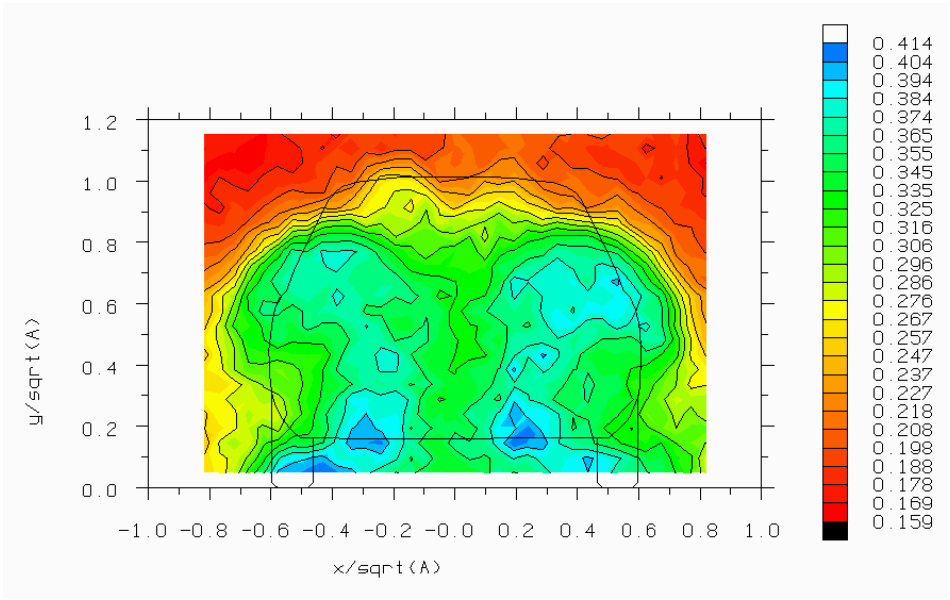

Figure 3.6.86 - Fraction of total pressure coefficient fluctuation due to unsteadiness near S=0.47 (S=0.432-0.510, f=55-65hz) one base dimension behind the Rover 200 model without spoiler (15% scale)

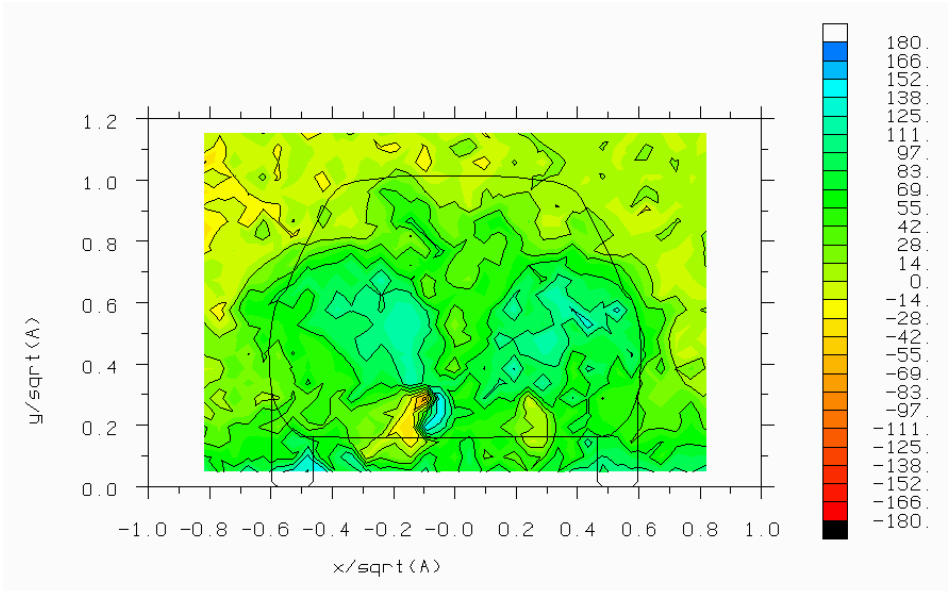

Figure 3.6.87 - Total pressure cross-spectral phase near S=0.12 (f=15hz) one base dimension behind the Rover 200 model without spoiler relative to reference hot-wire (at x/sqrt(A)=-0.24, y/sqrt(A)=0.24, z/sqrt(A)=0.75) (15% scale)

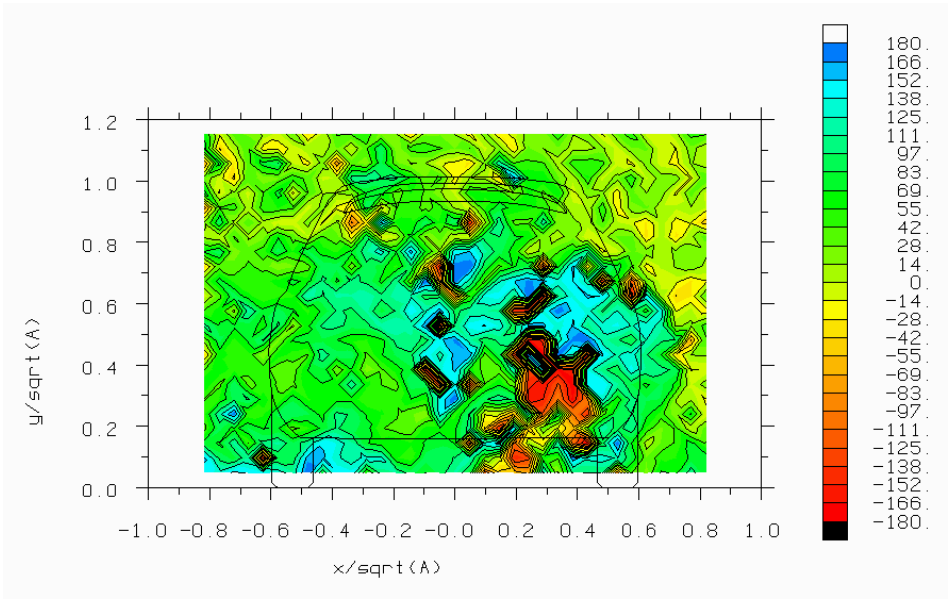

Figure 3.6.88 - Total pressure cross-spectral phase near S=0.12 (f=15hz) one base dimension behind the Rover 200 model with spoiler relative to reference hot-wire (at x/sqrt(A)=-0.14, y/sqrt(A)=0.24, z/sqrt(A)=0.75) (15% scale)

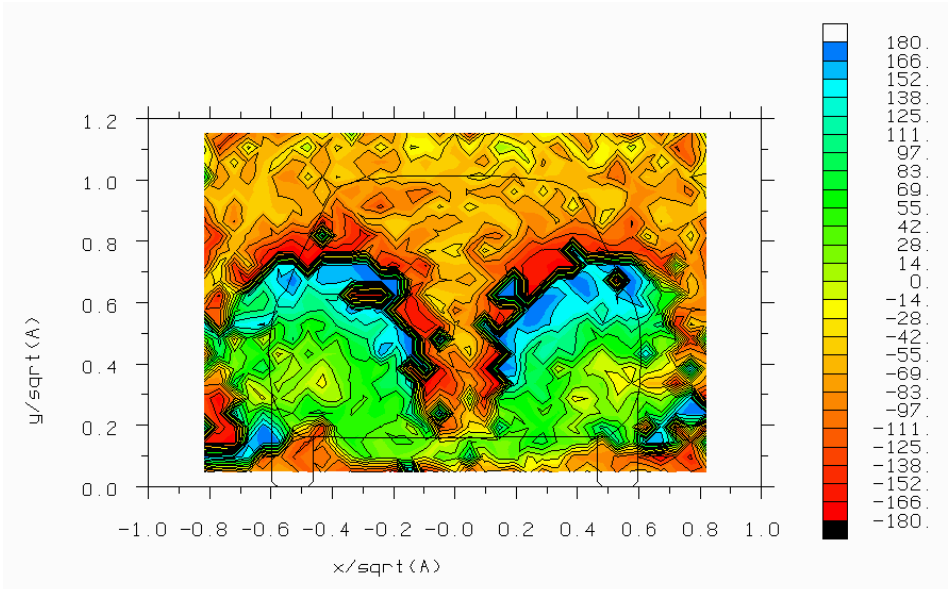

Figure 3.6.89 - Total pressure cross-spectral phase near S=0.31 (f=40hz) one base dimension behind the Rover 200 model without spoiler relative to reference hot-wire (at x/sqrt(A)=-0.24, y/sqrt(A)=0.24, z/sqrt(A)=0.75) (15% scale)

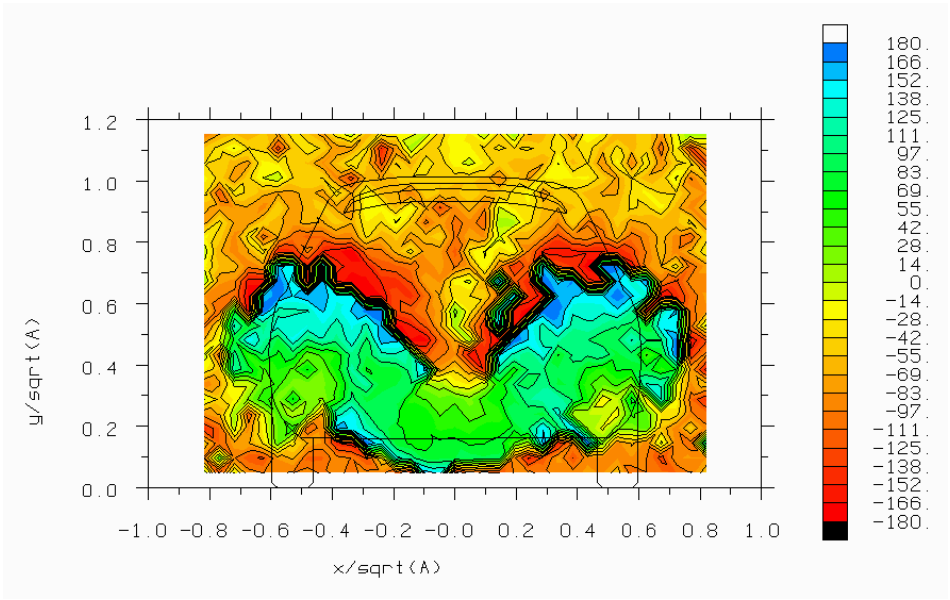

Figure 3.6.90 - Total pressure cross-spectral phase near S=0.31 (f=40hz) one base dimension behind the Rover 200 model with spoiler relative to reference hot-wire (at x/sqrt(A)=-0.14, y/sqrt(A)=0.24, z/sqrt(A)=0.75) (15% scale)

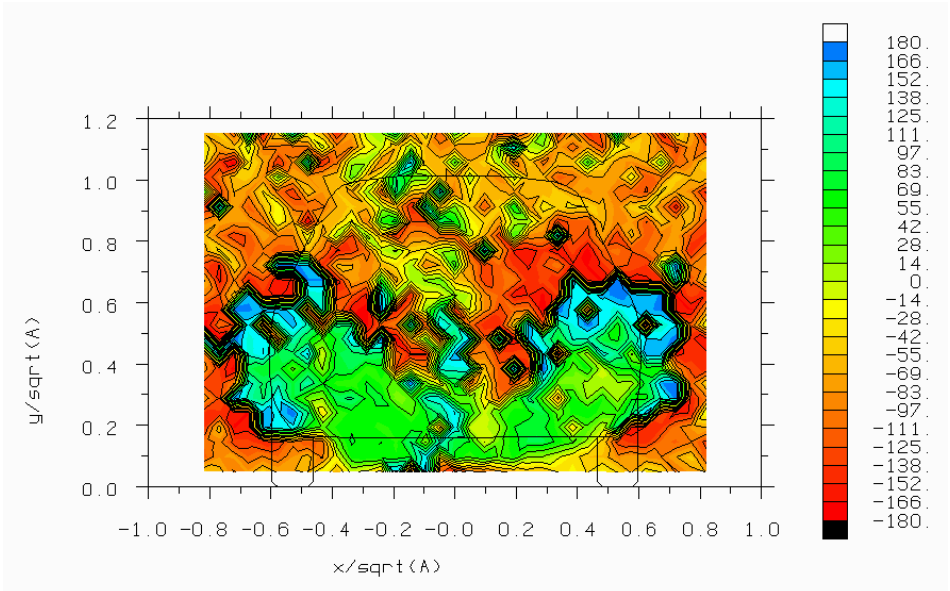

Figure 3.6.91 - Total pressure cross-spectral phase near S=0.47 (f=60hz) one base dimension behind the Rover 200 model without spoiler relative to reference hot-wire (at x/sqrt(A)=-0.24, y/sqrt(A)=0.24, z/sqrt(A)=0.75) (15% scale)

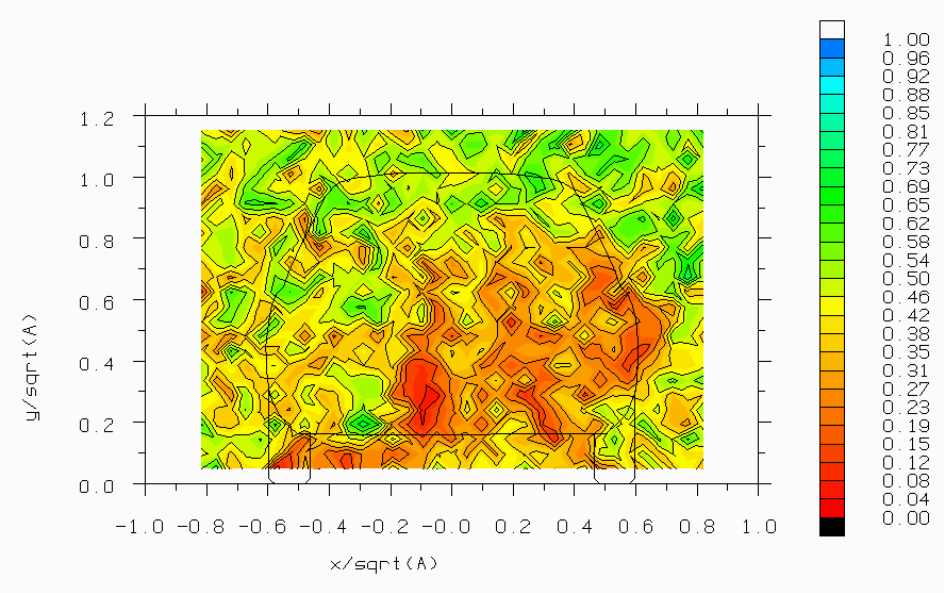

Figure 3.6.92 - Coherence between total pressure and reference hot-wire (at x/sqrt(A)=-0.24, y/sqrt(A)=0.24, z/sqrt(A)=0.75) near S=0.12 (f=15hz) one base dimension behind the Rover 200 model without spoiler (15% scale)

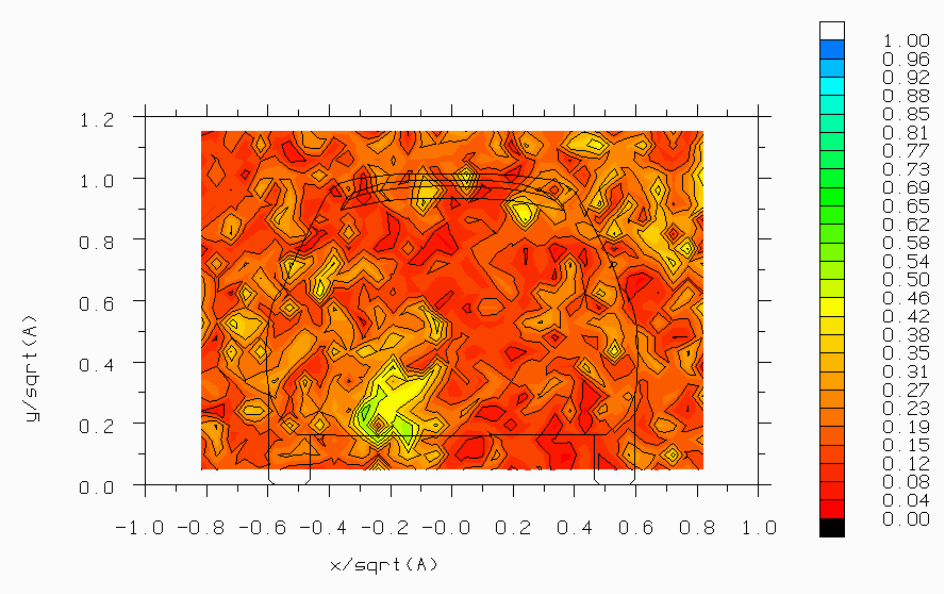

Figure 3.6.93 - Coherence between total pressure and reference hot-wire (at x/sqrt(A)=-0.14, y/sqrt(A)=0.24, z/sqrt(A)=0.75) near S=0.12 (f=15hz) one base dimension behind the Rover 200 model with spoiler (15% scale)

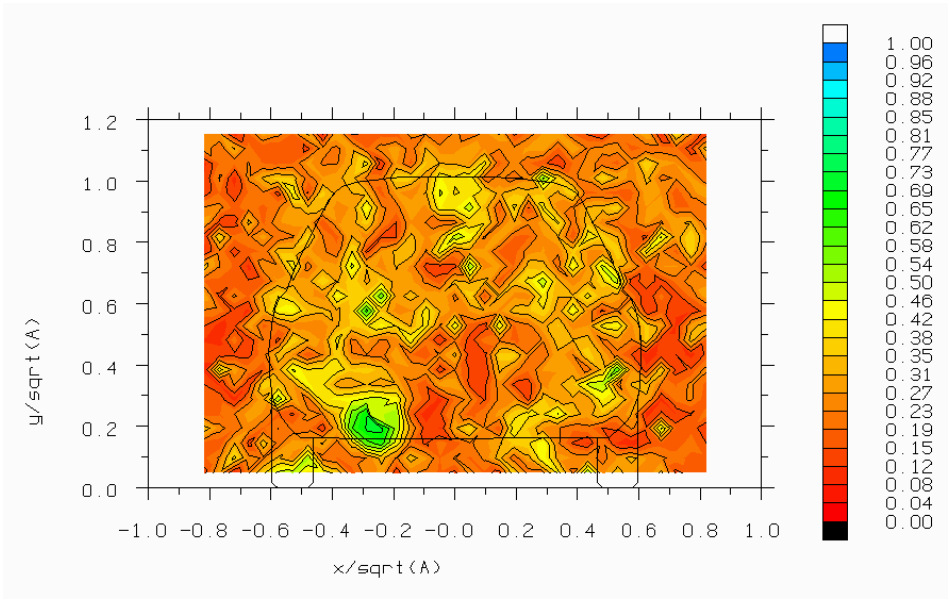

Figure 3.6.94 - Coherence between total pressure and reference hot-wire (at x/sqrt(A)=-0.24, y/sqrt(A)=0.24, z/sqrt(A)=0.75) near S=0.31 (f=40hz) one base dimension behind the Rover 200 model without spoiler (15% scale)

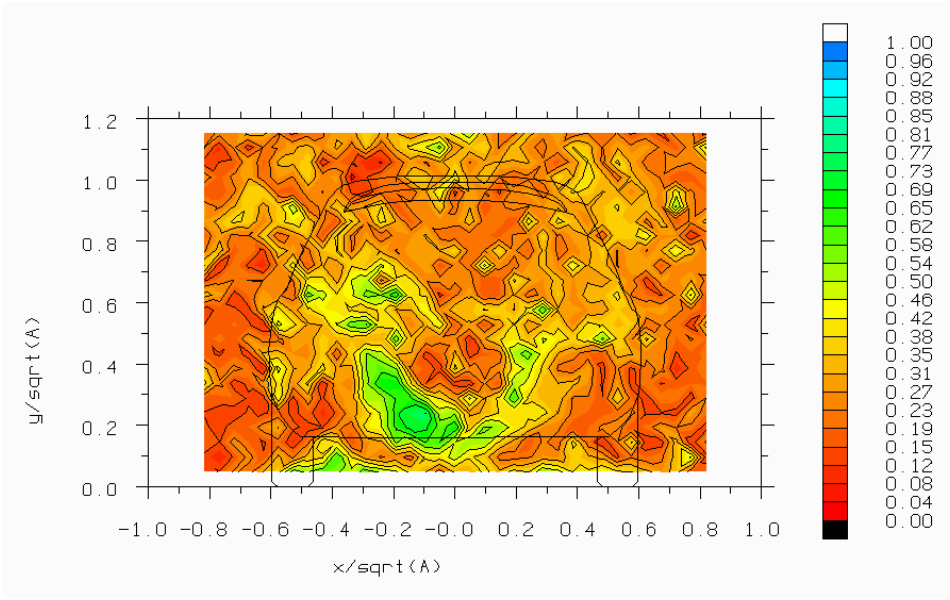

Figure 3.6.95 - Coherence between total pressure and reference hot-wire (at x/sqrt(A)=-0.14, y/sqrt(A)=0.24, z/sqrt(A)=0.75) near S=0.31 (f=40hz) one base dimension behind the Rover 200 model with spoiler (15% scale)

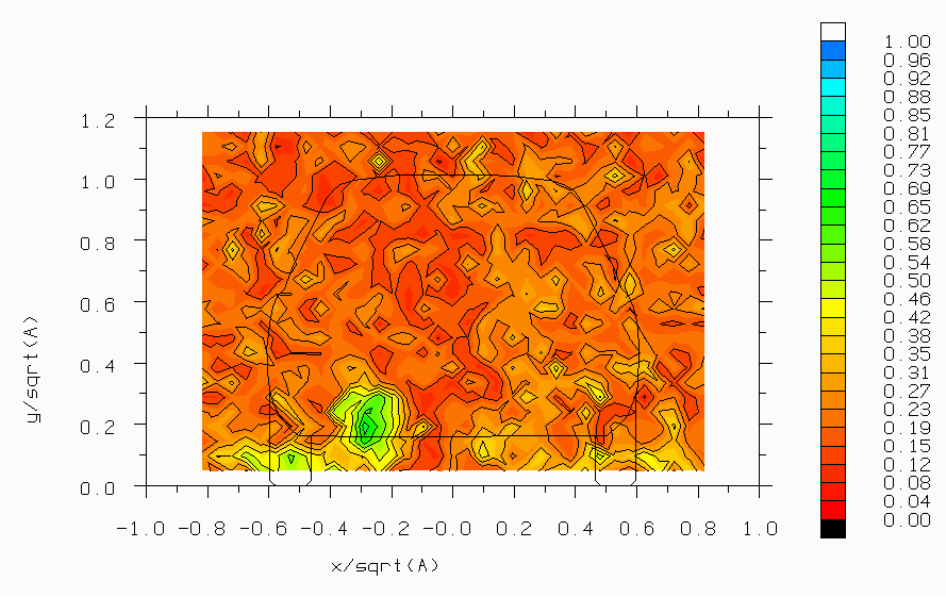

Figure 3.6.96 - Coherence between total pressure and reference hot-wire (at x/sqrt(A)=-0.24, y/sqrt(A)=0.24, z/sqrt(A)=0.75) near S=0.47 (f=60hz) one base dimension behind the Rover 200 model without spoiler (15% scale)

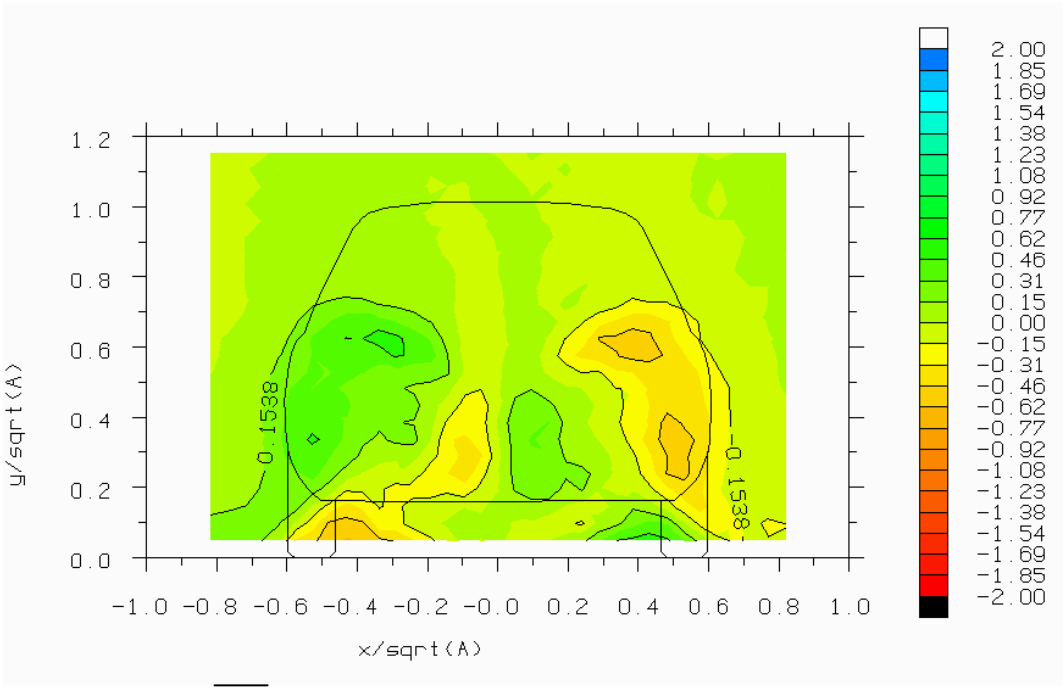

Figure 3.6.97 - $\overline{u'_x u'_z}$ near S=0.31 (S=0.275-0.353, f=35-45hz) one base dimension behind the Rover 200 model without spoiler (15% scale)

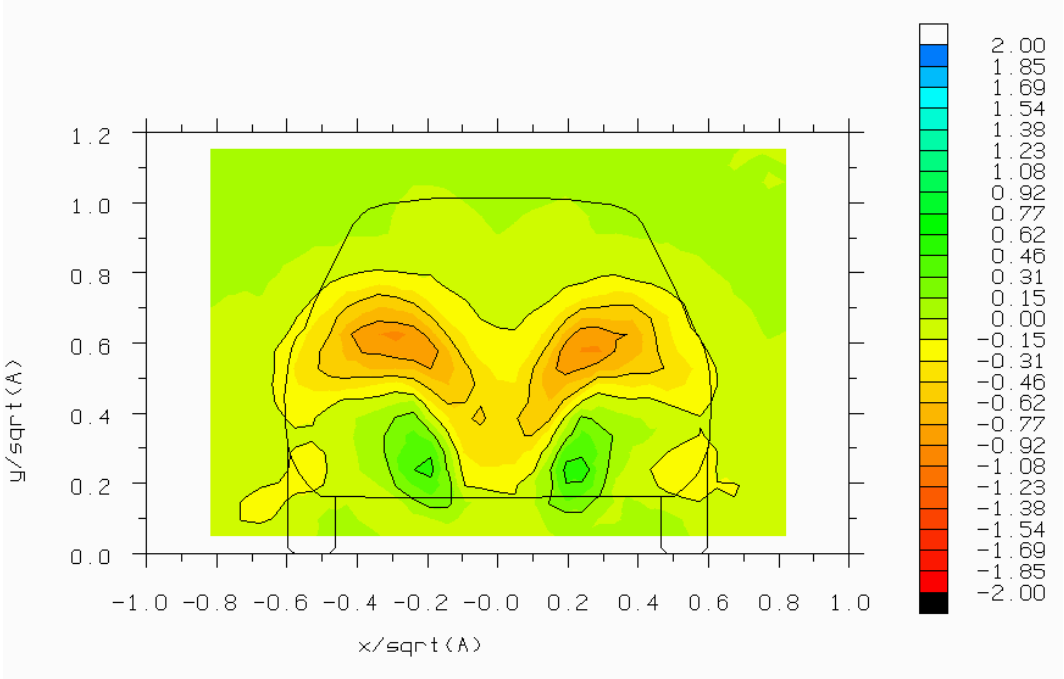

Figure 3.6.98 - $\overline{u'_y u'_z}$ near S=0.31 (S=0.275-0.353, f=35-45hz) one base dimension behind the Rover 200 model without spoiler (15% scale)

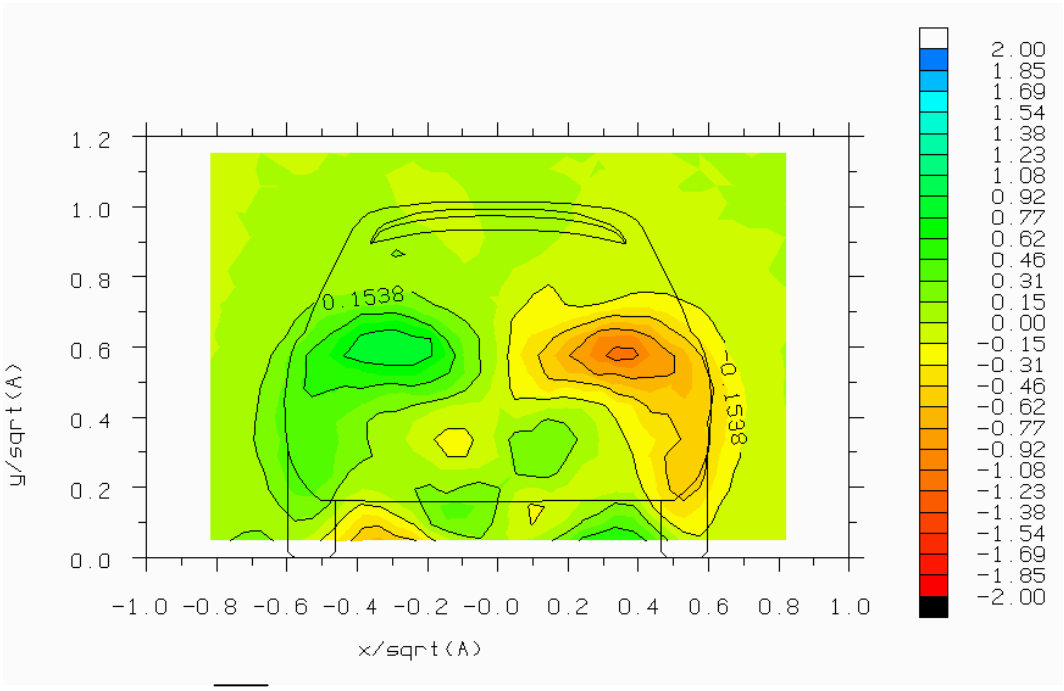

Figure 3.6.99 - $\overline{u'_x u'_z}$ near S=0.31 (S=0.275-0.353, f=35-45hz) one base dimension behind the Rover 200 model with spoiler (15% scale)

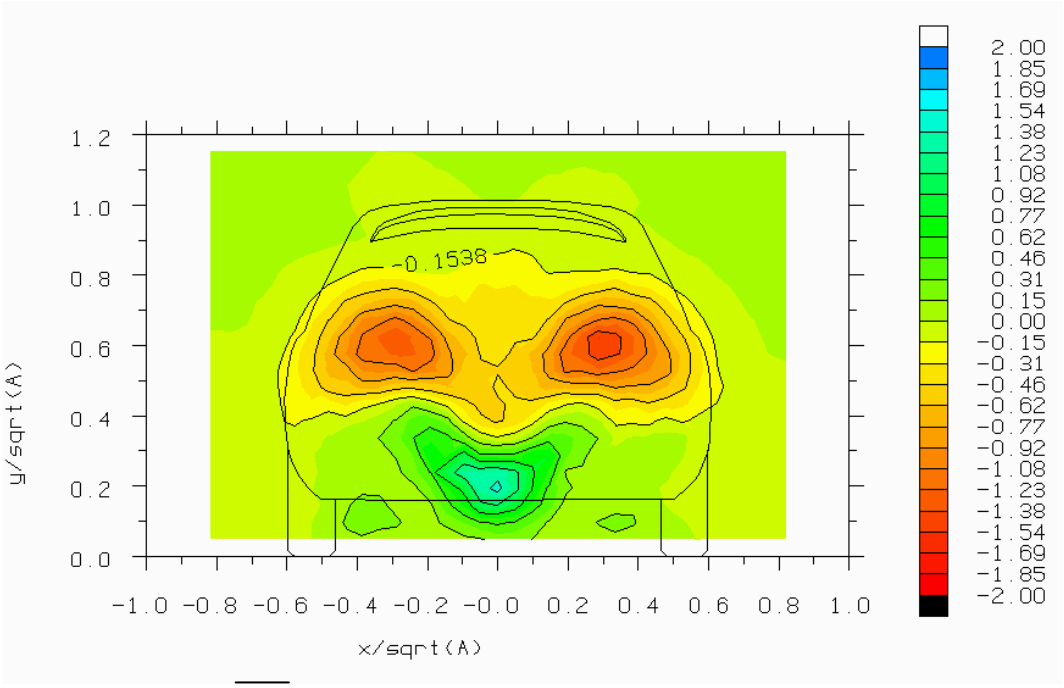

Figure 3.6.100 - $\overline{u'_y u'_z}$ near S=0.31 (S=0.275-0.353, f=35-45hz) one base dimension behind the Rover 200 model with spoiler (15% scale)

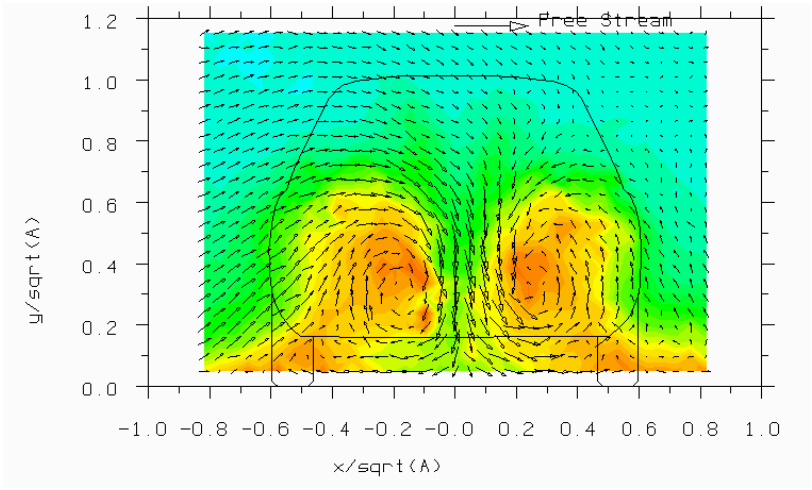

Figure3.6.101a) 0.0s, t/T=0.0

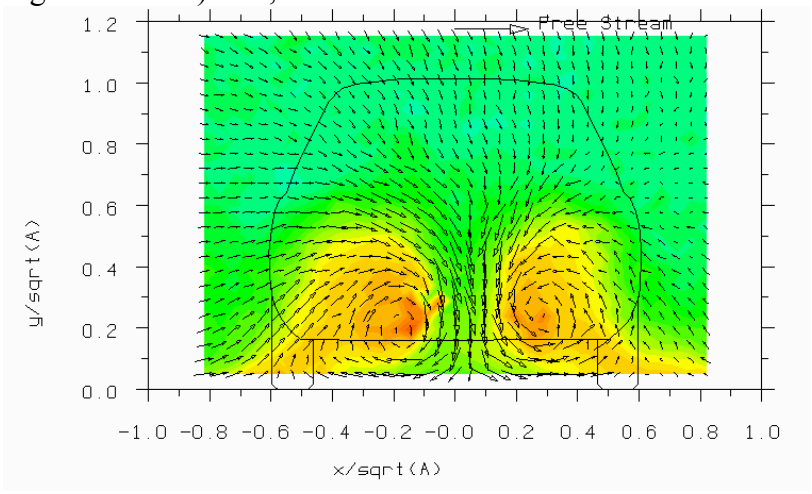

Figure3.6.101b) 0.01s, t/T=0.15

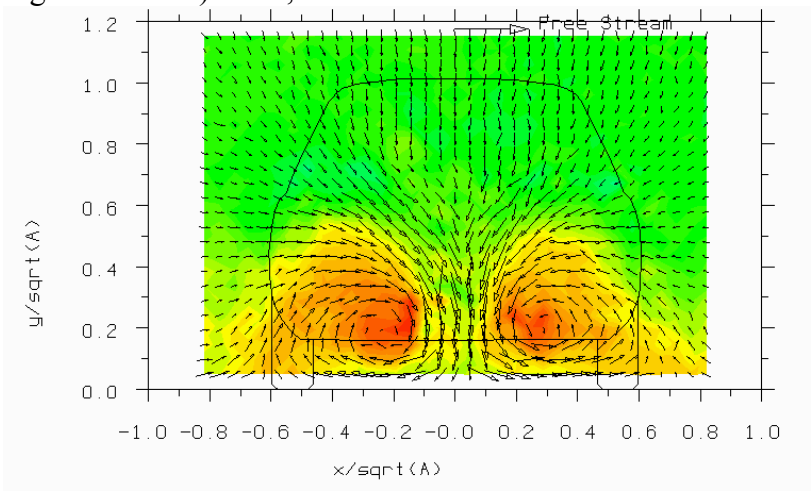

Figure3.6.101c) 0.02s, t/T=0.30

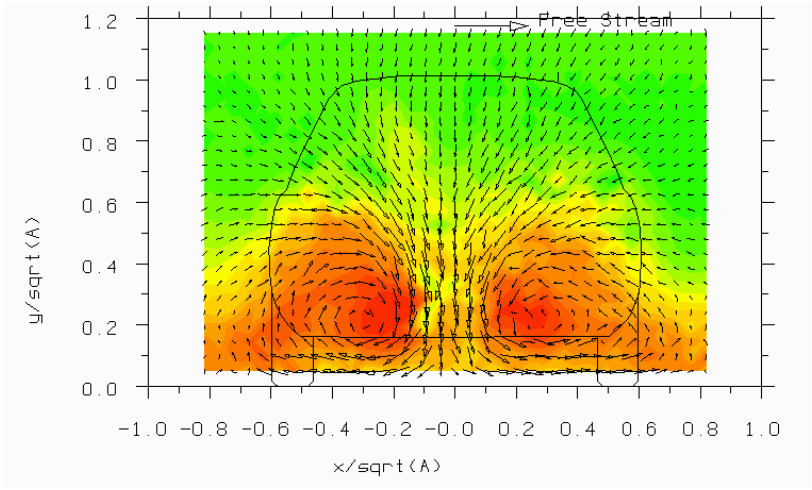

Figure3.6.101d) 0.03s, t/T=0.45

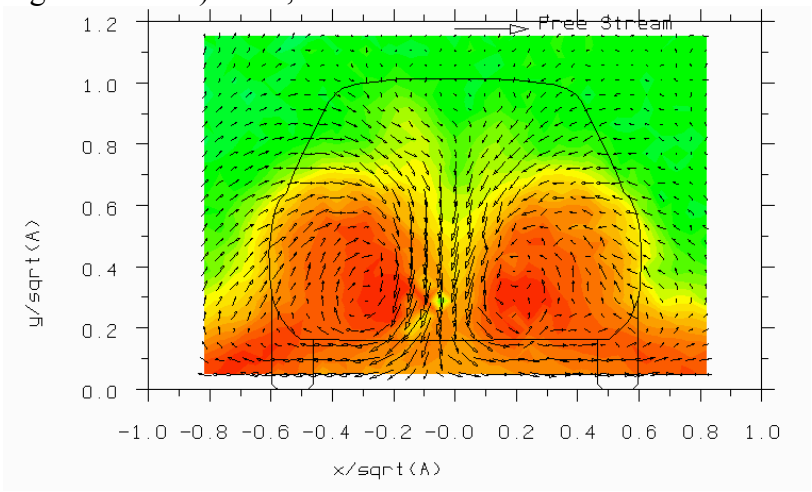

Figure3.6.101e) 0.04s, t/T=0.6

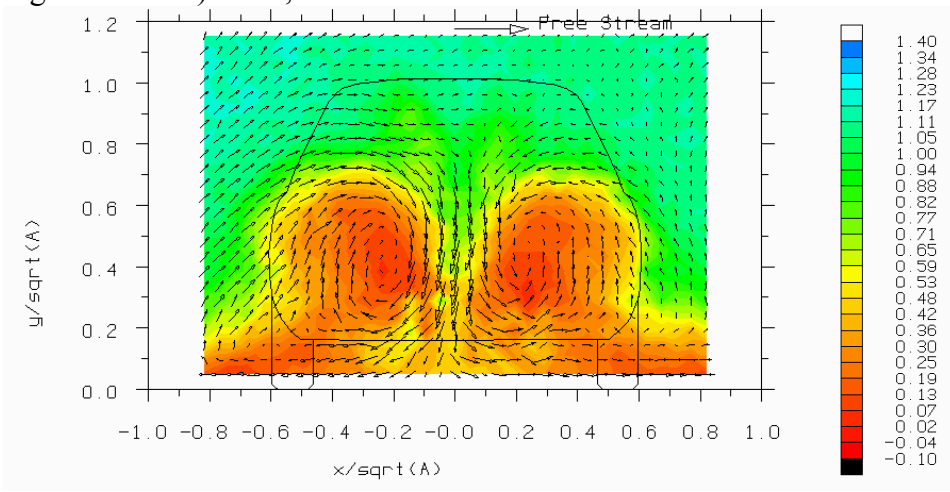

Figure3.6.101f) 0.05s, t/T=0.75

Figure 3.6.101 - Sequence showing total pressure coefficient and velocity vectors reconstructed from S=0.118 (4hz band@~15hz) one base dimension behind the Rover 200 model without spoiler (15% scale)

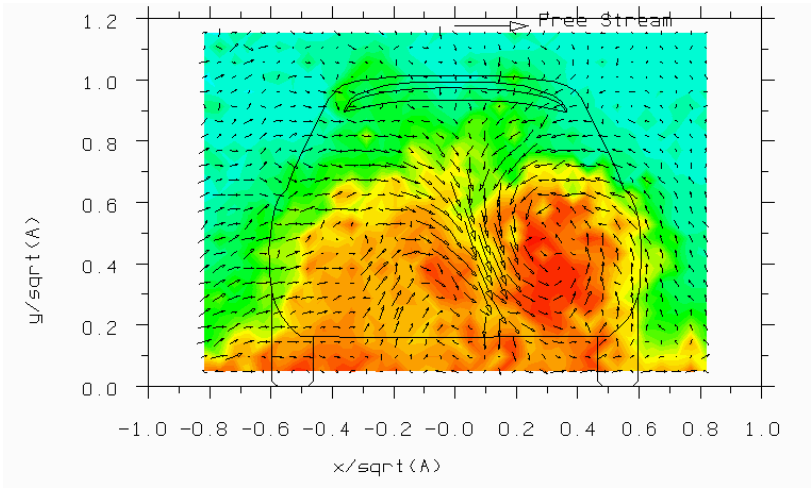

Figure3.6.102a) 0.0s, t/T=0.0

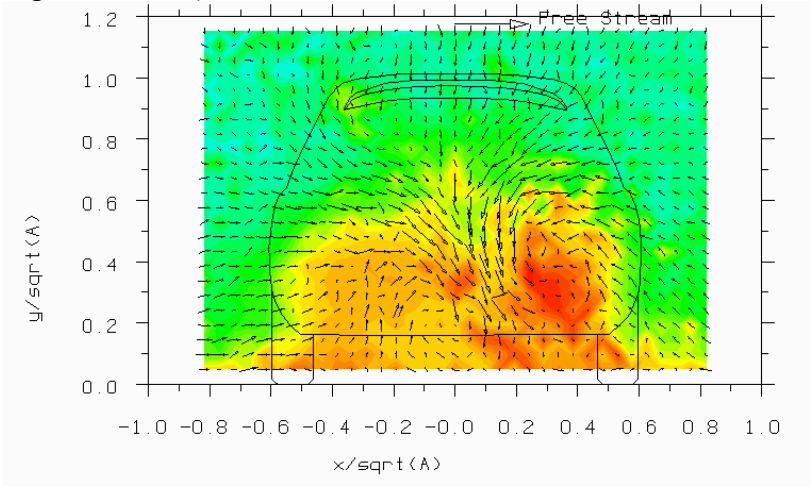

Figure3.6.102b) 0.01s, t/T=0.15

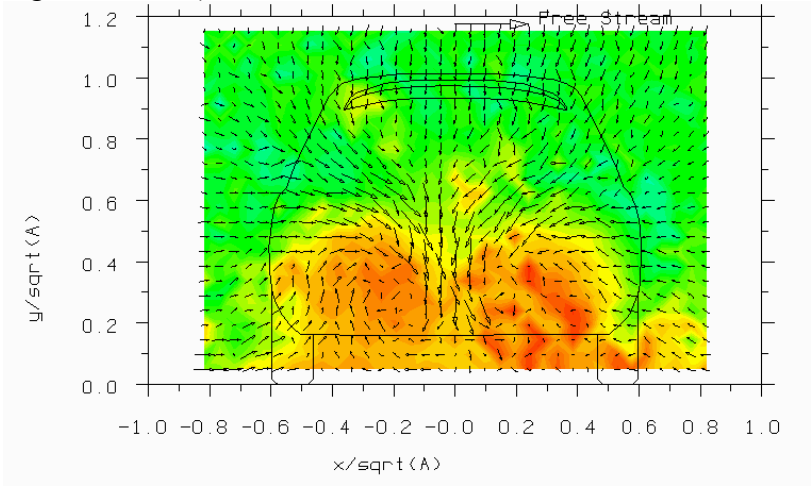

Figure3.6.102c) 0.02s, t/T=0.30

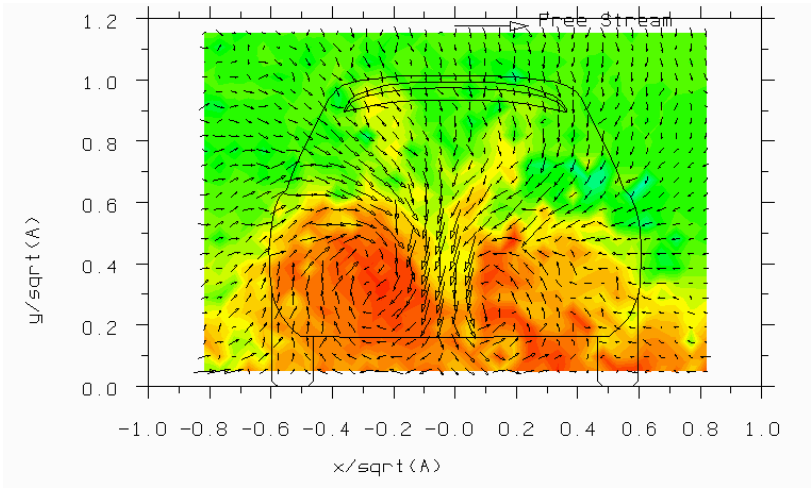

Figure3.6.102d) 0.03s, t/T=0.45

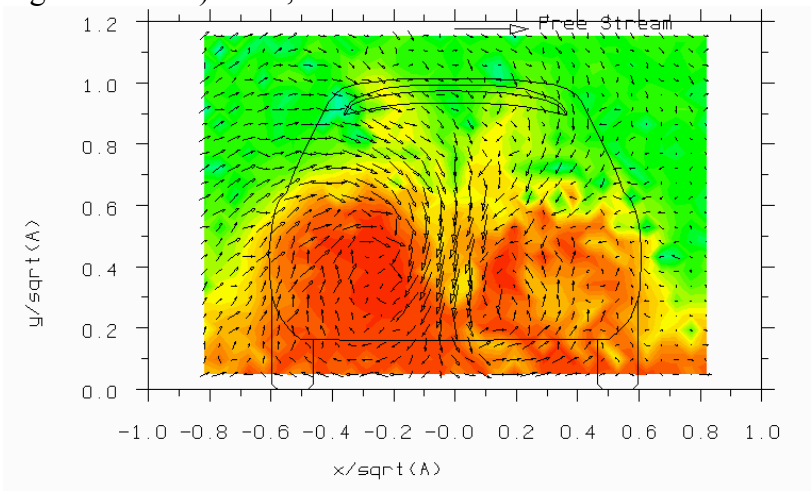

Figure3.6.102e) 0.04s, t/T=0.6

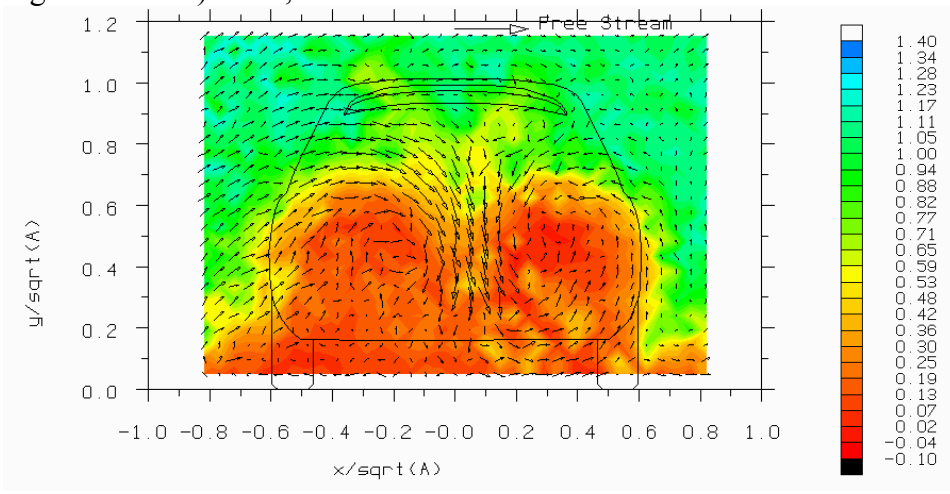

Figure3.6.102f) 0.05s, t/T=0.75

Figure 3.6.102 - Sequence showing total pressure coefficient and velocity vectors reconstructed from S=0.118 (4hz band@~15hz) one base dimension behind the Rover 200 model with spoiler (15% scale)

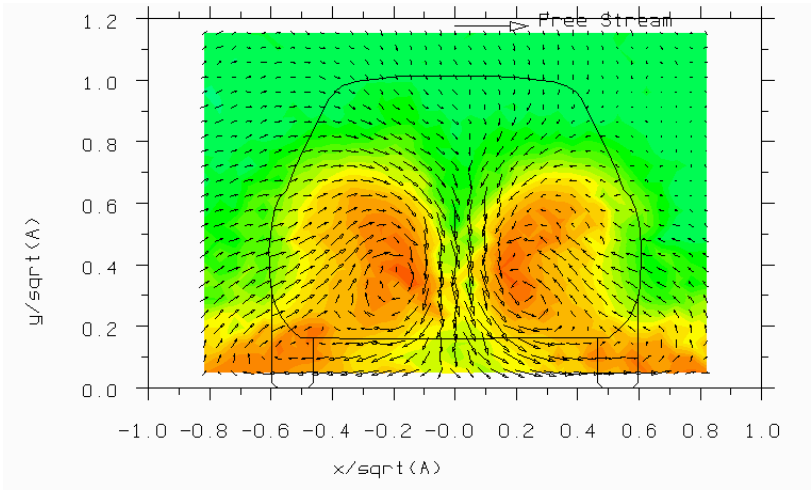

Figure 3.6.103a) 0.0s, t/T=0.0

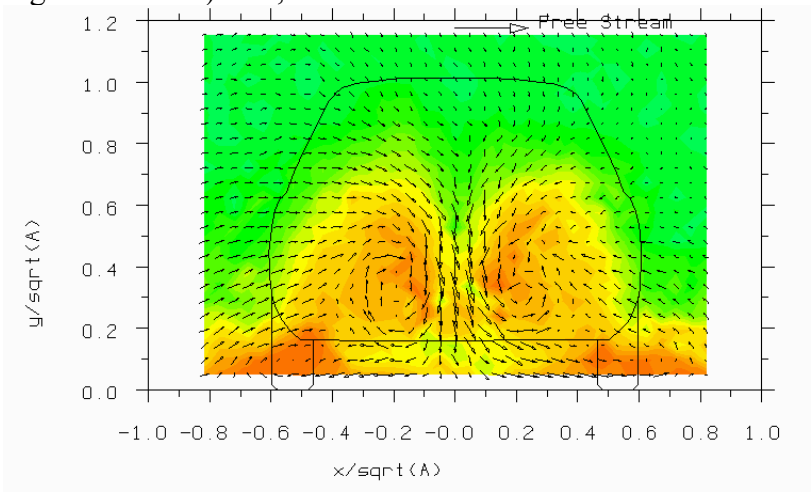

Figure 3.6.103b) 0.00375s, t/T=0.15

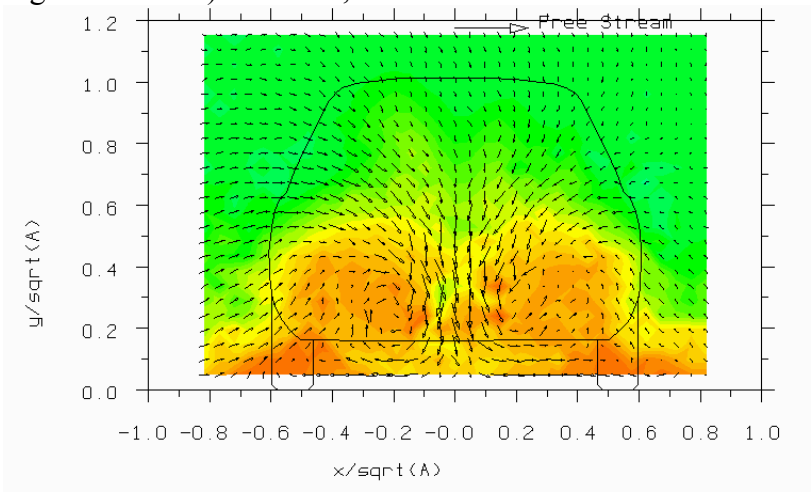

Figure 3.6.103c) 0.00750s, t/T=0.30

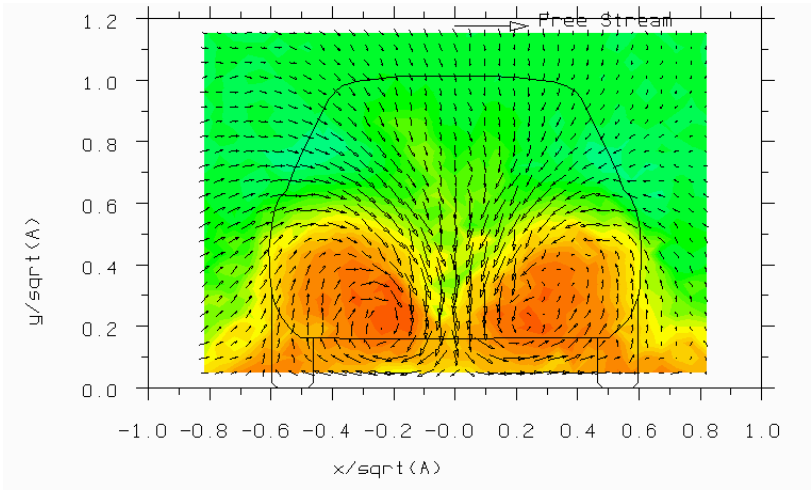

Figure 3.6.103d) 0.01125s, t/T=0.45

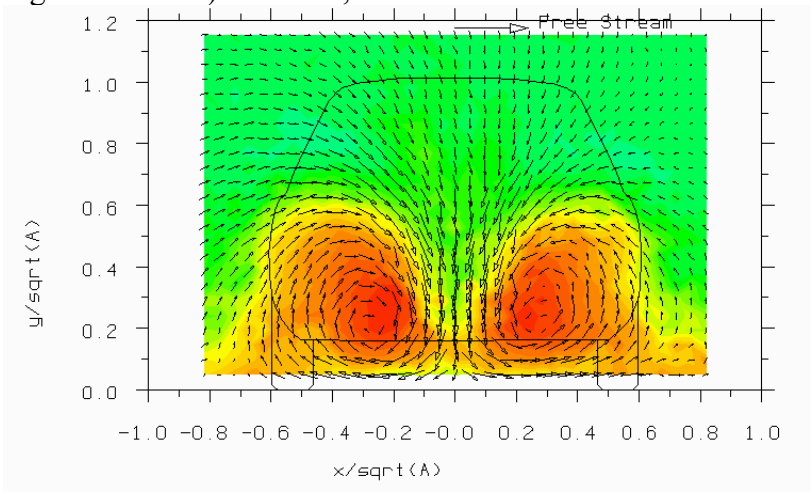

Figure 3.6.103e) 0.01500s, t/T=0.6

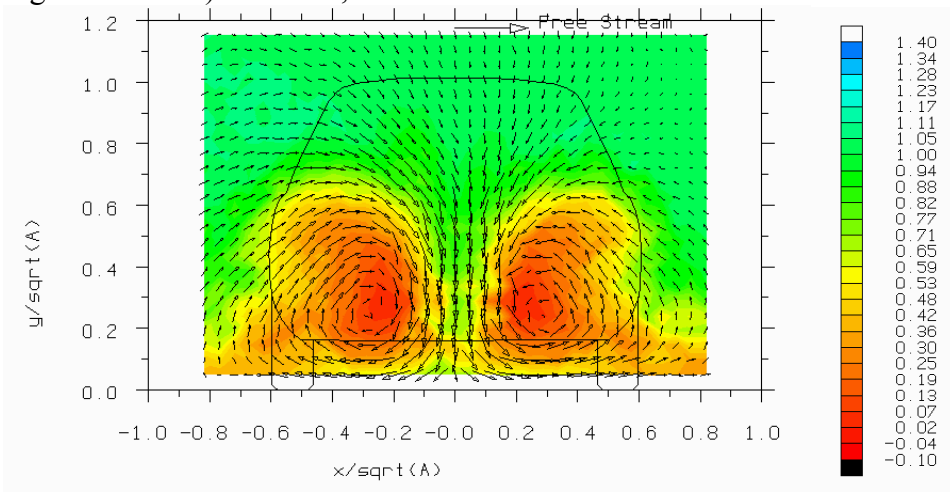

Figure 3.6.103f) 0.01875s, t/T=0.75

Figure 3.6.103 - Sequence showing total pressure coefficient and velocity vectors reconstructed from S=0.314 (4hz band@~40hz) one base dimension behind the Rover 200 model without spoiler (15% scale)

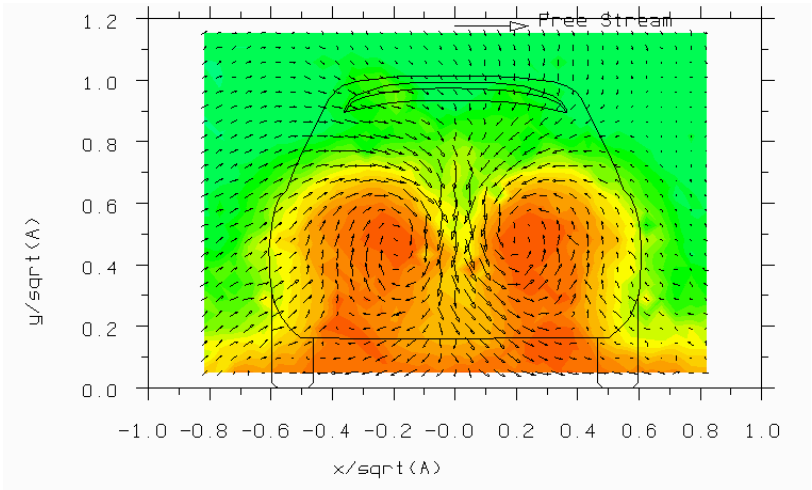

Figure 3.6.104a) 0.0s, t/T=0.0

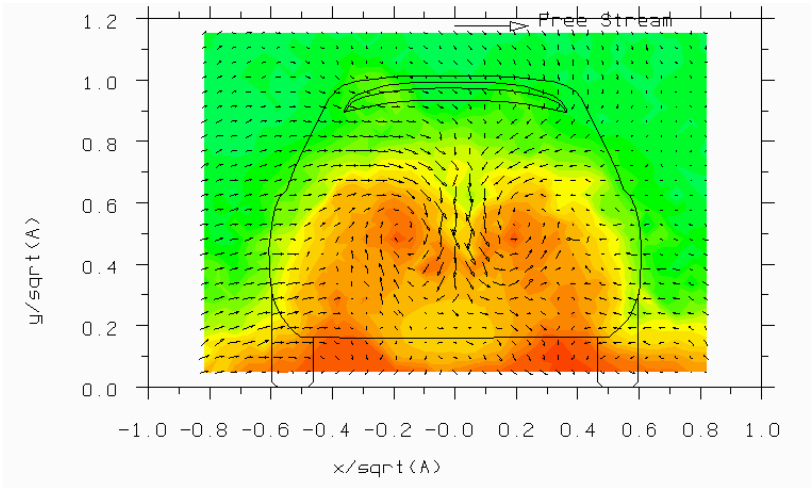

Figure 3.6.104b) 0.00375s, t/T=0.15

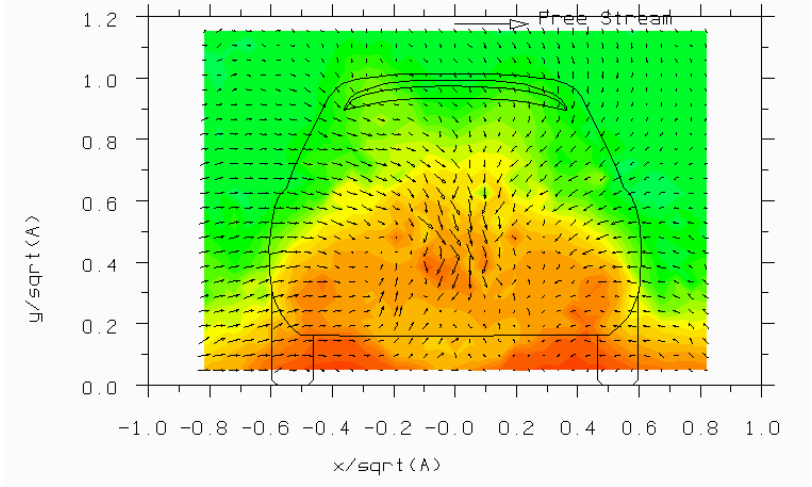

Figure 3.6.104c) 0.00750s, t/T=0.30

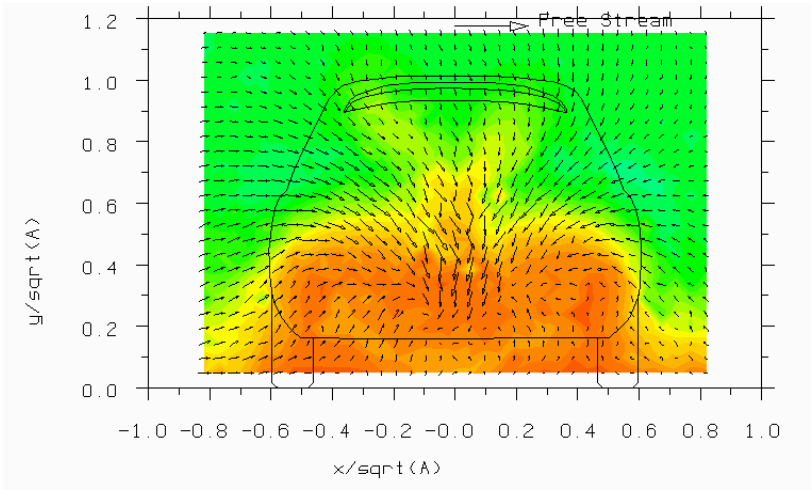

Figure 3.6.104d) 0.01125s, t/T=0.45

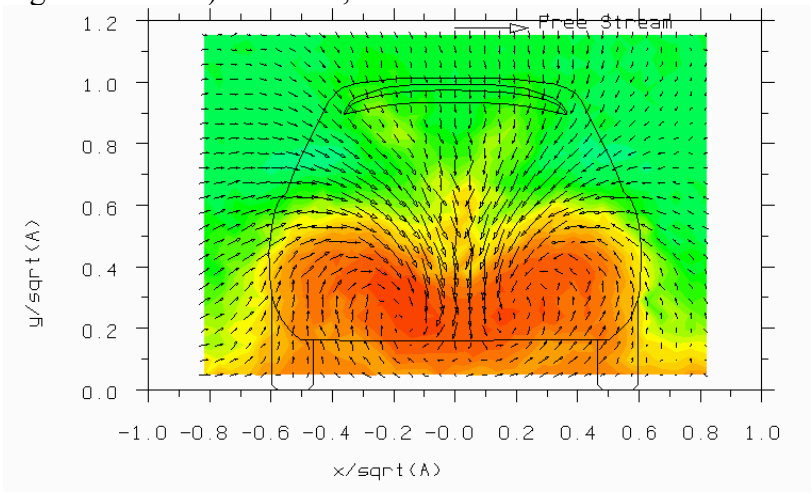

Figure 3.6.104e) 0.01500s, t/T=0.6

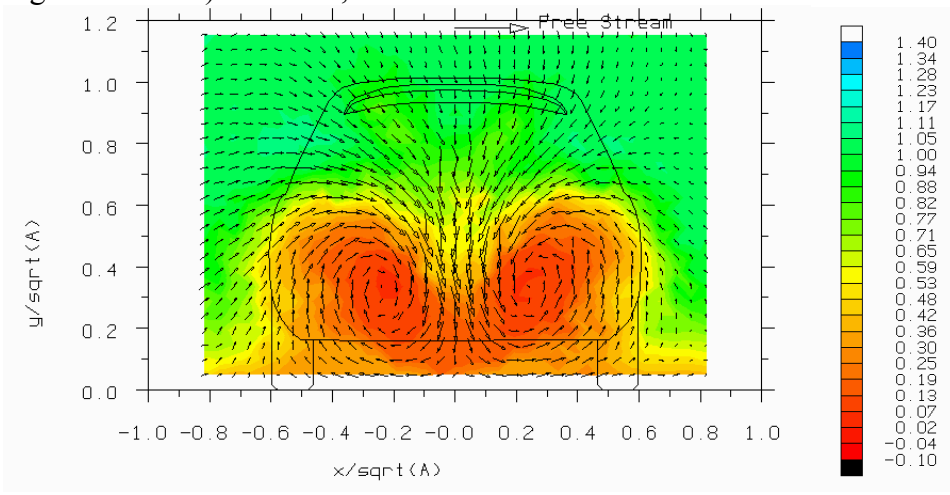

Figure 3.6.104f) 0.01875s, t/T=0.75

Figure 3.6.104 - Sequence showing total pressure coefficient and velocity vectors reconstructed from S=0.314 (4hz band@~40hz) one base dimension behind the Rover 200 model with spoiler (15% scale)

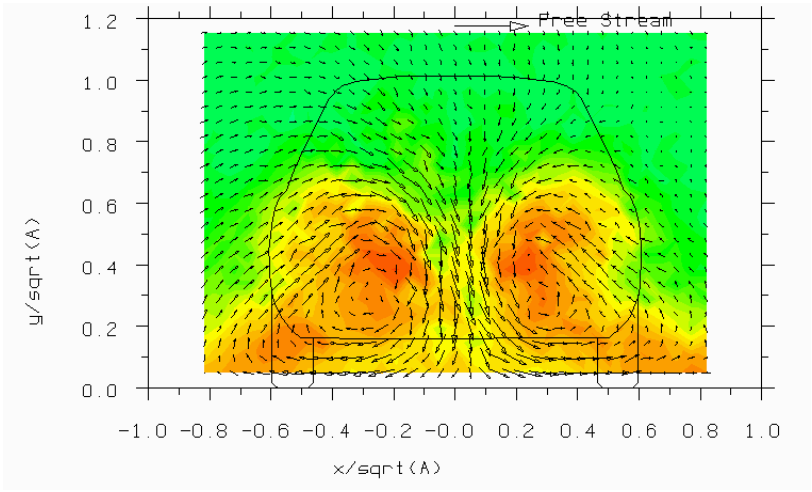

Figure 3.6.105a) 0.0s, t/T=0.0

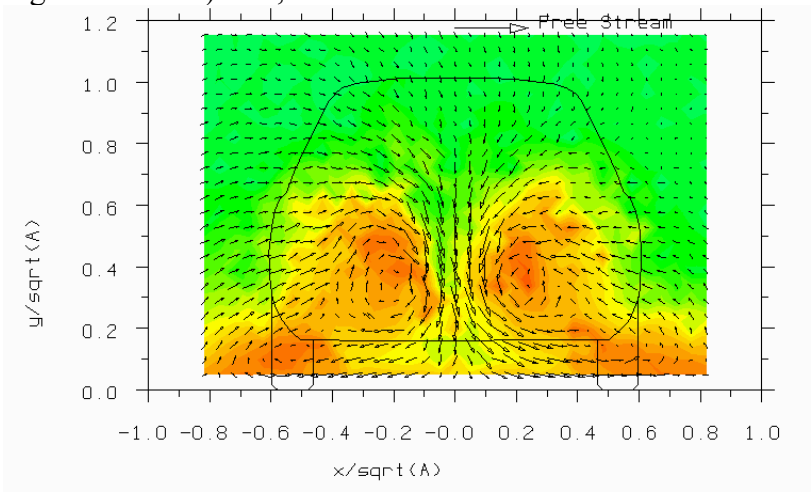

Figure 3.6.105b) 0.0025s, t/T=0.15

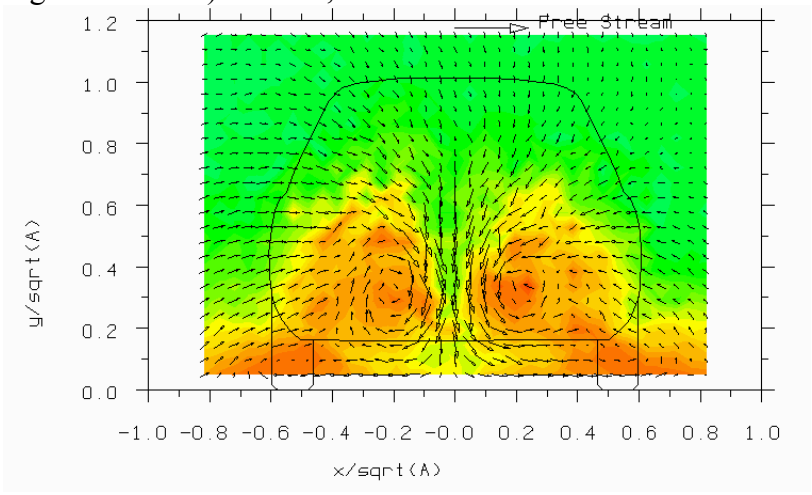

Figure 3.6.105c) 0.0050s, t/T=0.30

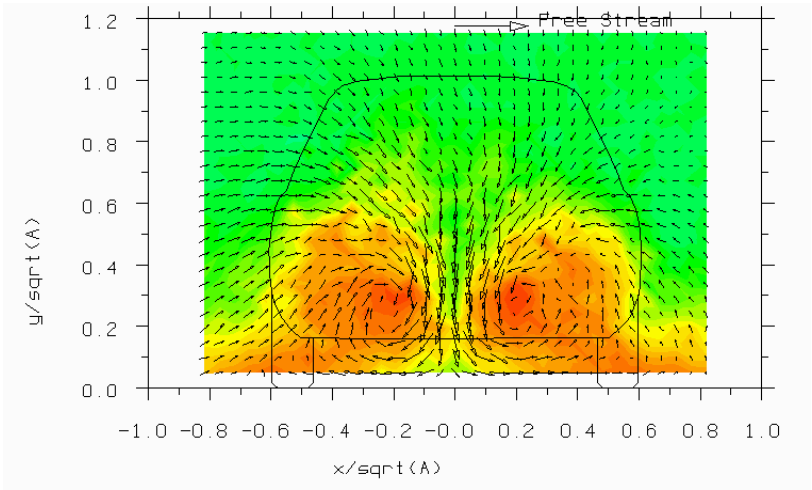

Figure 3.6.105d) 0.0075s, t/T=0.45

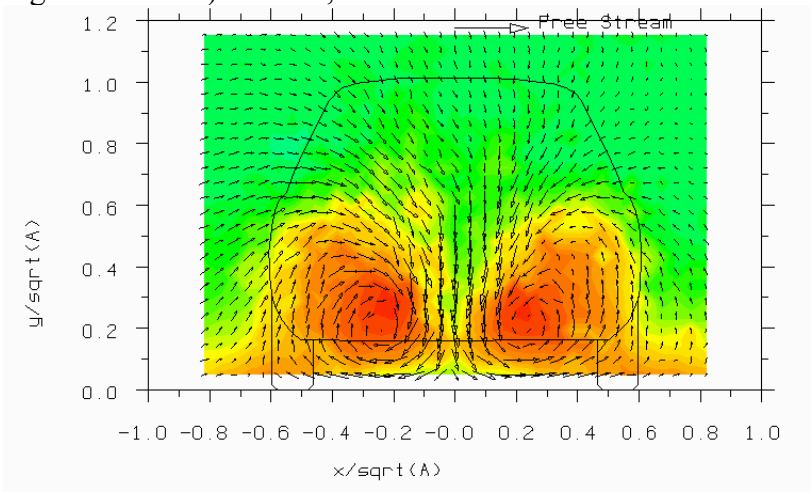

Figure 3.6.105e) 0.0100s, t/T=0.6

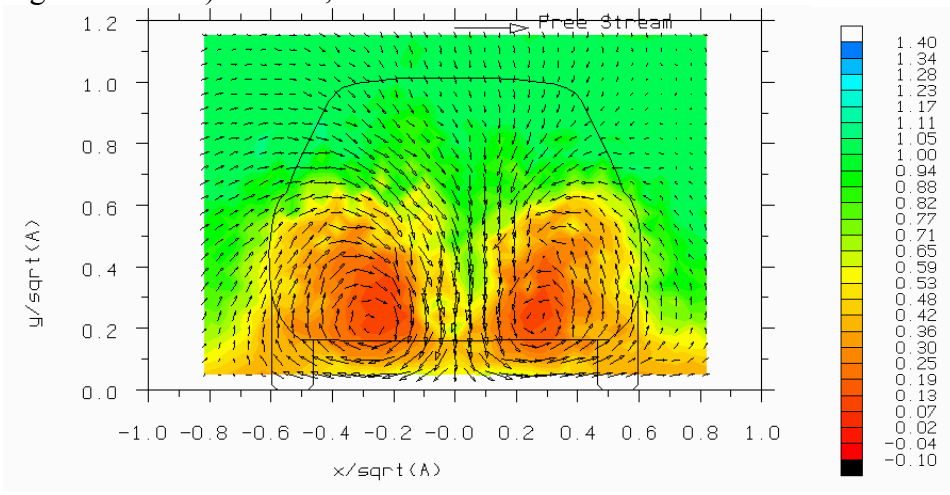

Figure 3.6.105f) 0.0125s, t/T=0.75

Figure 3.6.105 - Sequence showing total pressure coefficient and velocity vectors reconstructed from S=0.471(4hz band@~60hz) one base dimension behind the Rover 200 model without spoiler (15% scale)

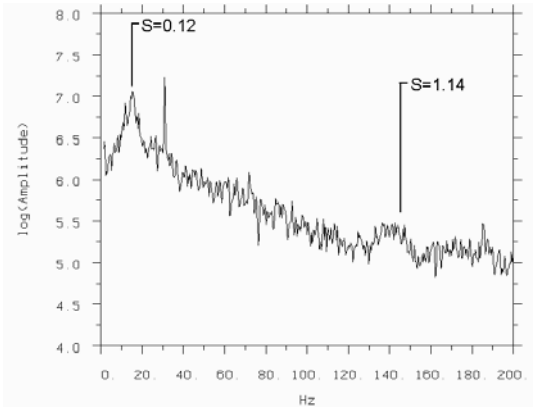

Figure 3.6.106 - Autospectral density of pressure on the centreline at z/L = 0.30 on the surface of the Rover 200 model without spoiler (windscreen stagnation) (15% scale)

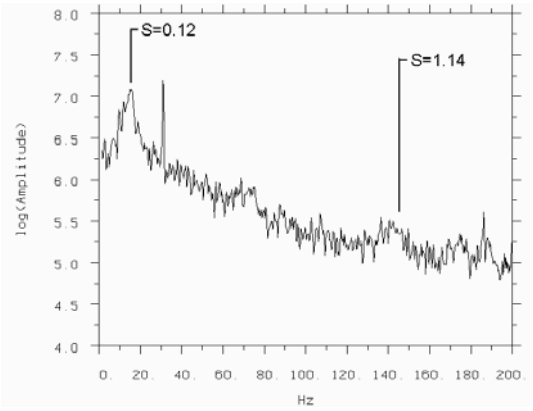

Figure 3.6.107 - Autospectral density of pressure on the centreline at z/L = 0.30 on the surface of the Rover 200 model with spoiler (windscreen stagnation) (15% scale)

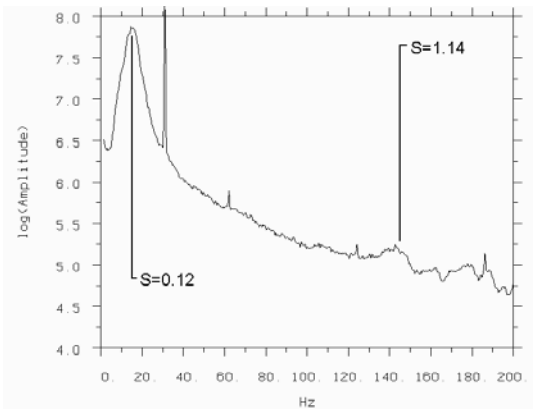

Figure 3.6.108 - Autospectral density of pressure on the centreline at z/L = 0.47 on the surface of the Rover 200 model without spoiler (windscreen suction) (15% scale)

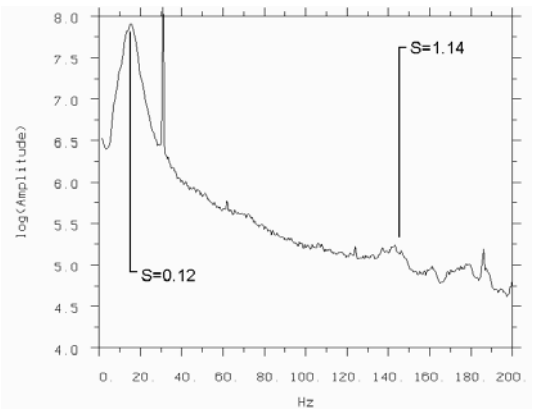

Figure 3.6.109 - Autospectral density of pressure on the centreline at z/L = 0.47 on the surface of the Rover 200 model with spoiler (windscreen suction) (15% scale)

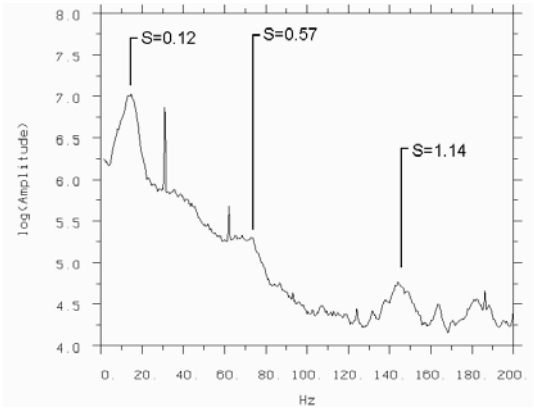

Figure 3.6.110 - Autospectral density of pressure on the centreline at z/L = 0.86 on the surface of the Rover 200 model without spoiler (mid-backlight) (15% scale)

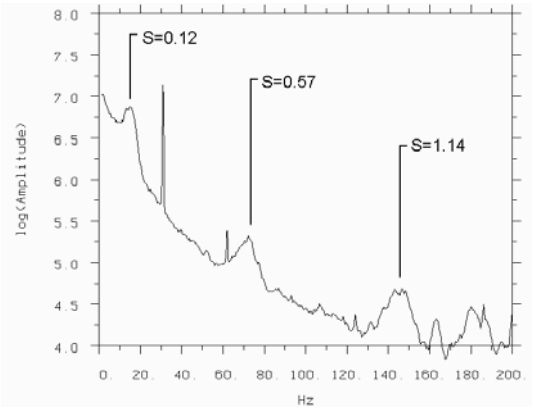

Figure 3.6.111 - Autospectral density of pressure on the centreline at z/L = 0.86 on the surface of the Rover 200 model with spoiler (mid-backlight) (15% scale)

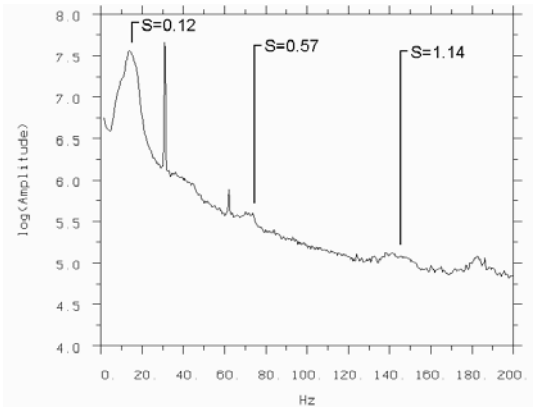

Figure 3.6.112 - Autospectral density of surface pressure at z/L = 0.86 near the c-pillar (x/sqrt(A)=0.43, y/sqrt(A)=0.85) on the Rover 200 model without spoiler (15% scale)

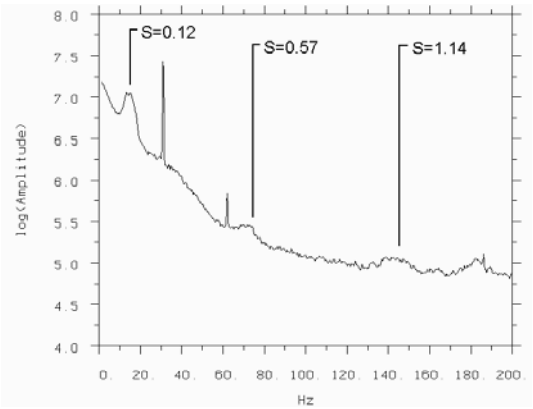

Figure 3.6.113 - Autospectral density of surface pressure at z/L = 0.86 near the c-pillar (x/sqrt(A)=0.43, y/sqrt(A)=0.85) on the Rover 200 model with spoiler (15% scale)

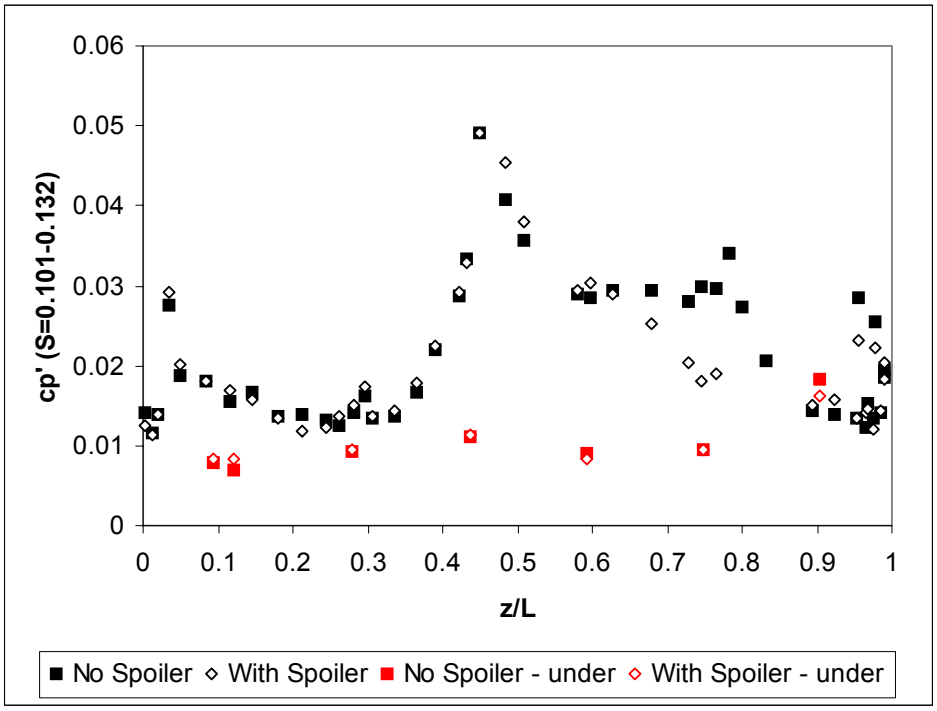

Figure 3.6.114 - Fluctuating surface pressure coefficient on the centreline of the Rover 200 model due to unsteadiness near S=0.12 (S=0.101-S=0.132, f=13-17hz) (15% scale)

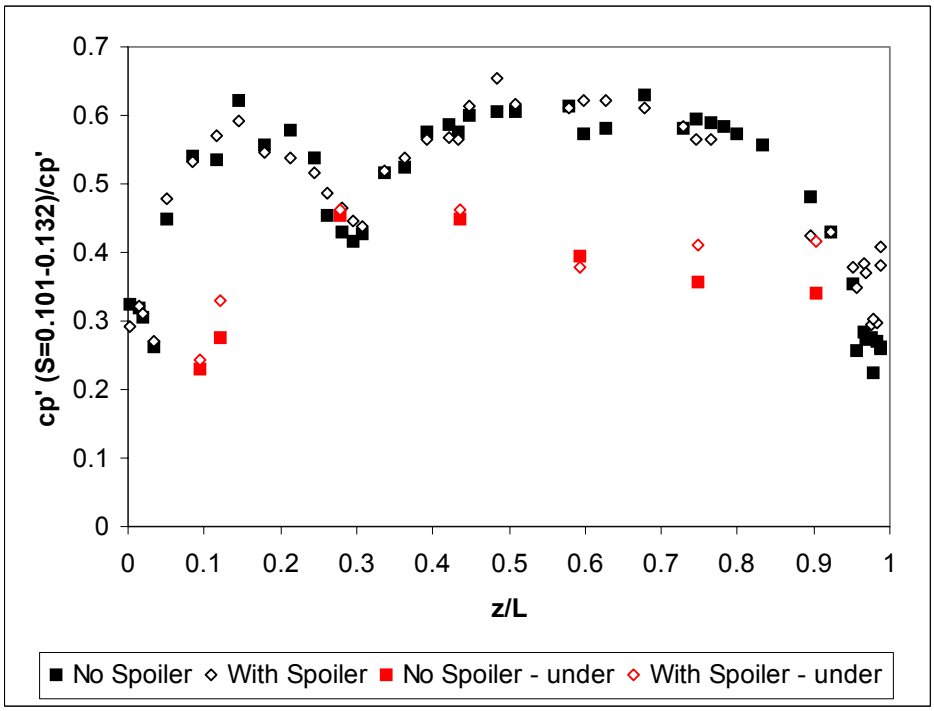

Figure 3.6.115 - Fraction of fluctuating surface pressure coefficient on the centreline of the Rover 200 model due to unsteadiness near S=0.12 (S=0.101-S=0.132, f=13-17hz) (15% scale)

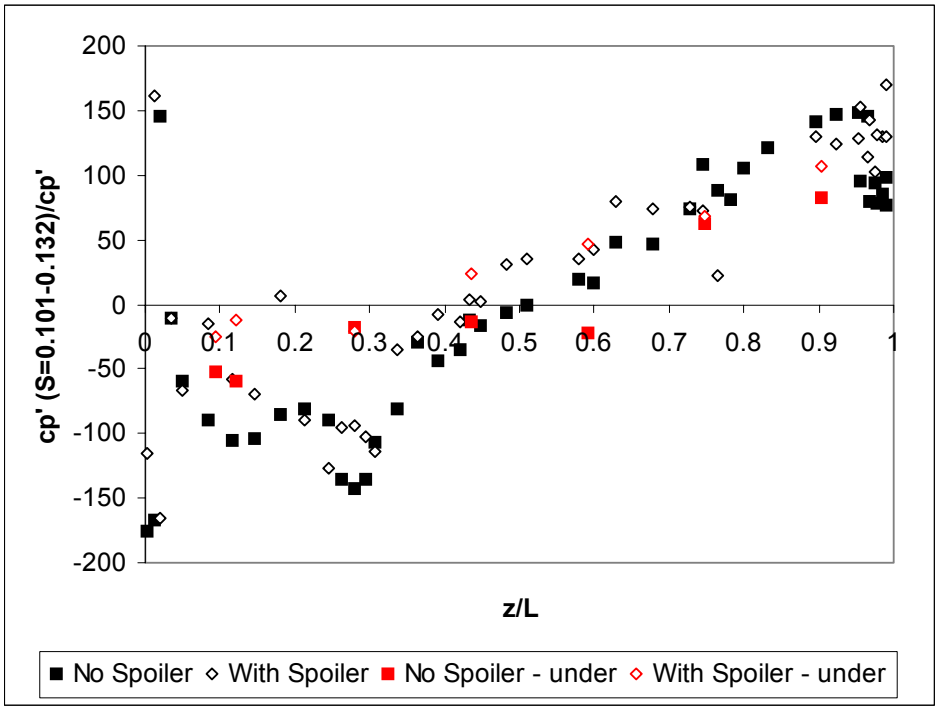

Figure 3.6.116 - Cross-spectral phase between reference hot-wire and fluctuating surface pressure on the centreline of the Rover 200 model near S=0.12 (15% scale)

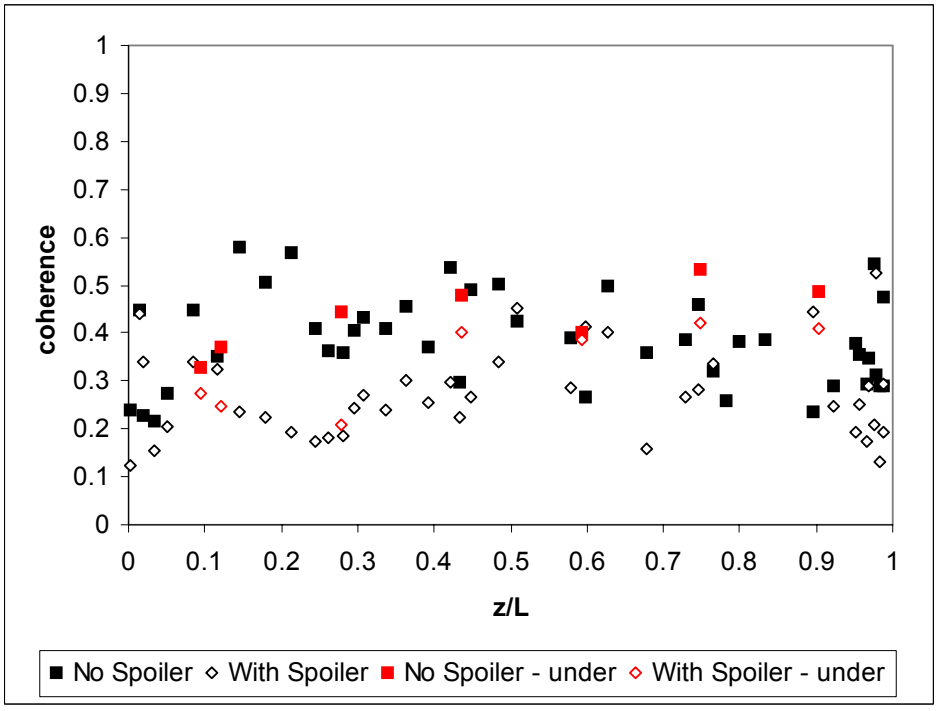

Figure 3.6.117 - Coherence between reference hot-wire and fluctuating surface pressure on the centreline of the Rover 200 model near S=0.12 (15% scale)

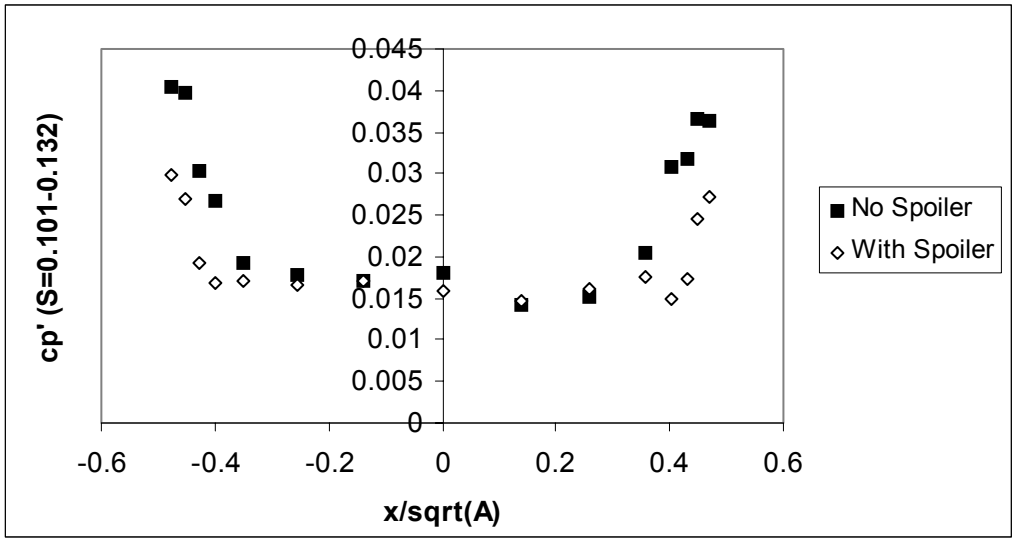

Figure 3.6.118 - Fluctuating surface pressure coefficient across the backlight of the Rover 200 model due to unsteadiness near S=0.12 (S=0.101-S=0.132, f=12-17hz) (15% scale)

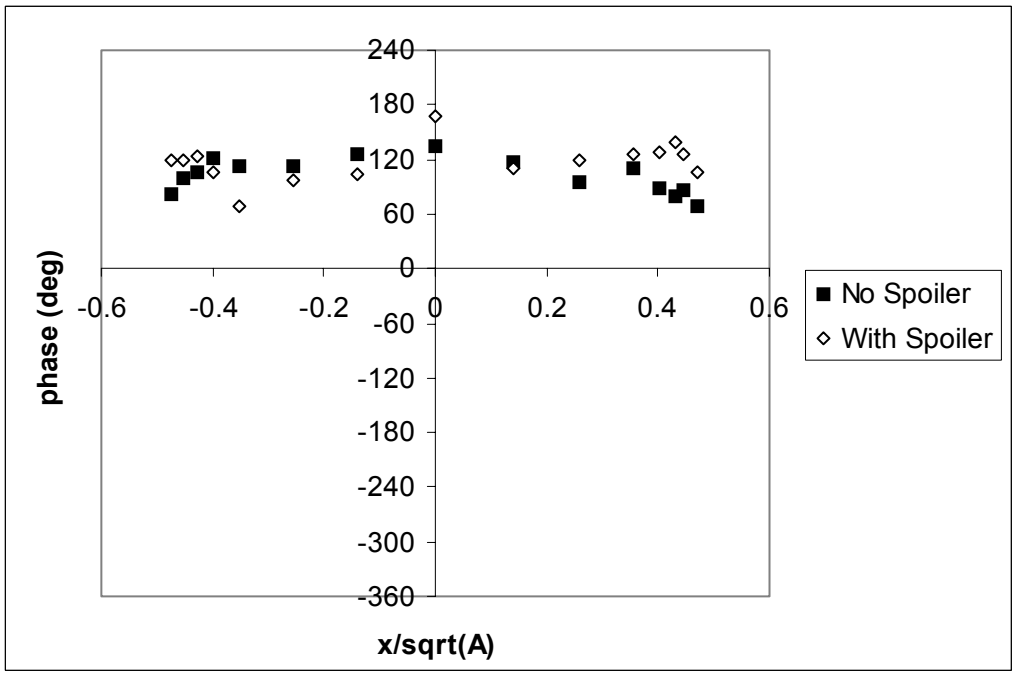

Figure 3.6.119 - Cross-spectral phase between reference hot-wire and fluctuating surface pressure across the backlight of the Rover 200 model near S=0.12 (15% scale)

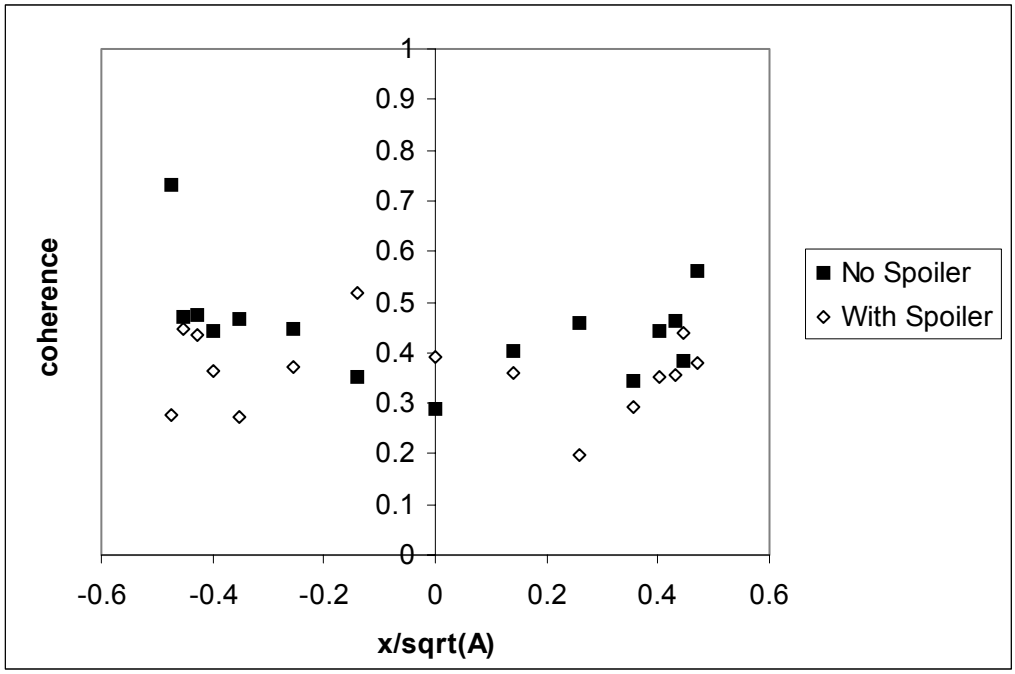

Figure 3.6.120 - Coherence between reference hot-wire and fluctuating surface pressure across the backlight of the Rover 200 model near S=0.12 (15% scale)

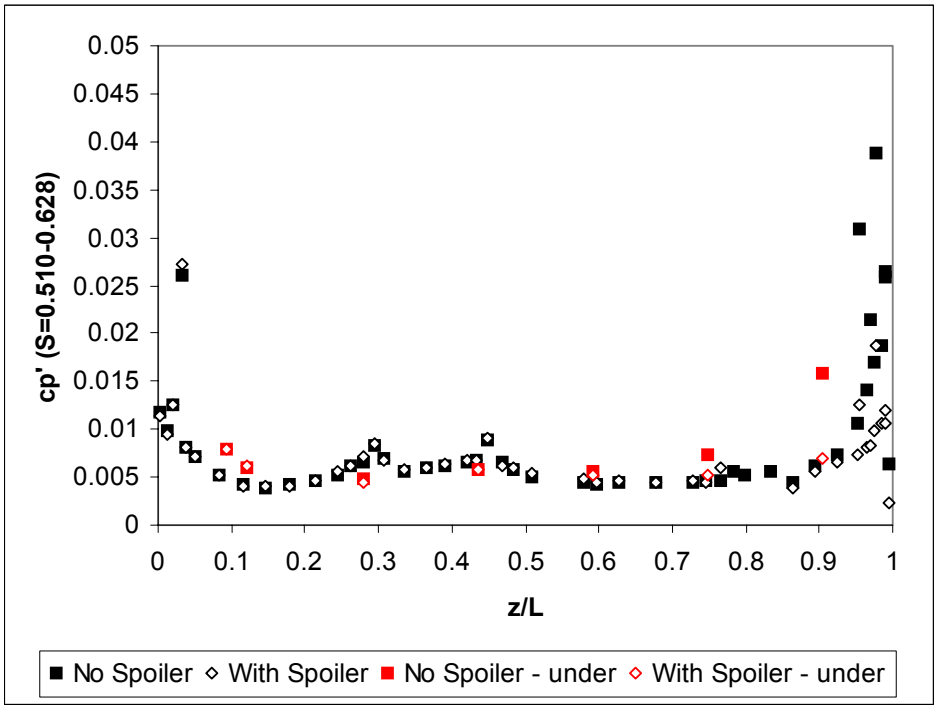

Figure 3.6.121 - Fluctuating surface pressure coefficient on the centreline of the Rover 200 model due to unsteadiness near S=0.57 (S=0.510-0.628, f=65-80hz) (15% scale)

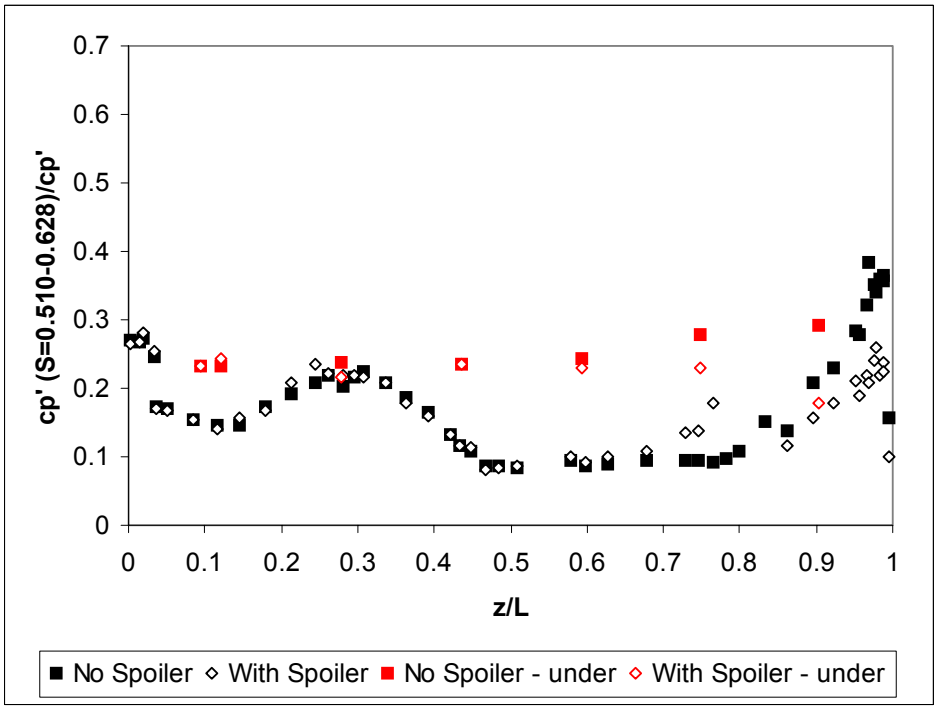

Figure 3.6.122 - Fraction of fluctuating surface pressure coefficient on the centreline of the Rover 200 model due to unsteadiness near S=0.57 (S=0.510-0.628, f=65-80hz) (15% scale)

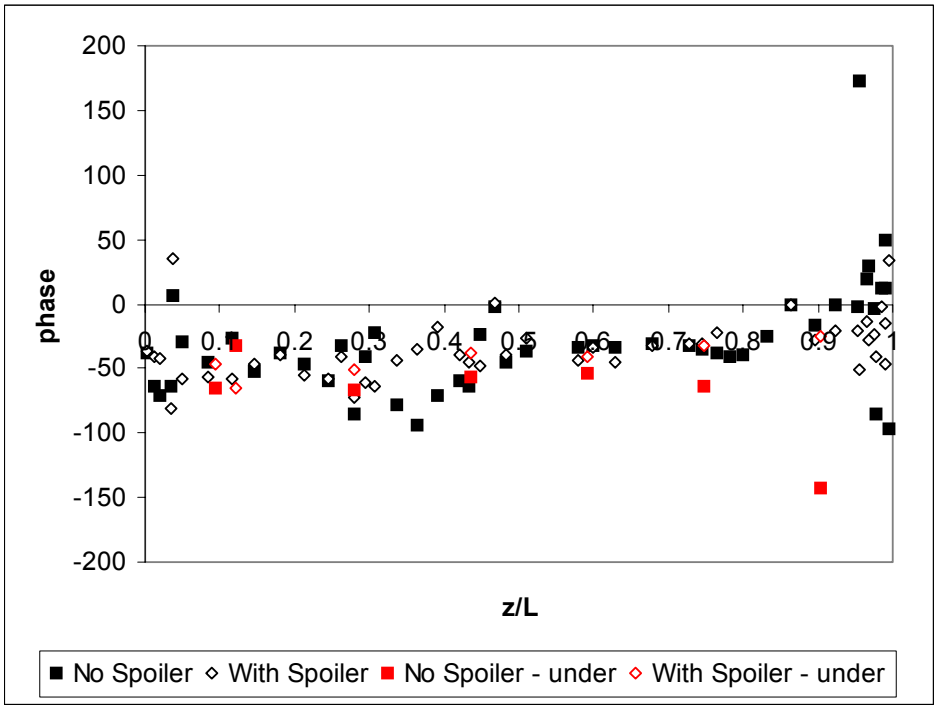

Figure 3.6.123 - Cross-spectral phase between fluctuating surface pressure at z/L=0.86 and elsewhere on the centreline of the Rover 200 model near S=0.57 (15% scale)

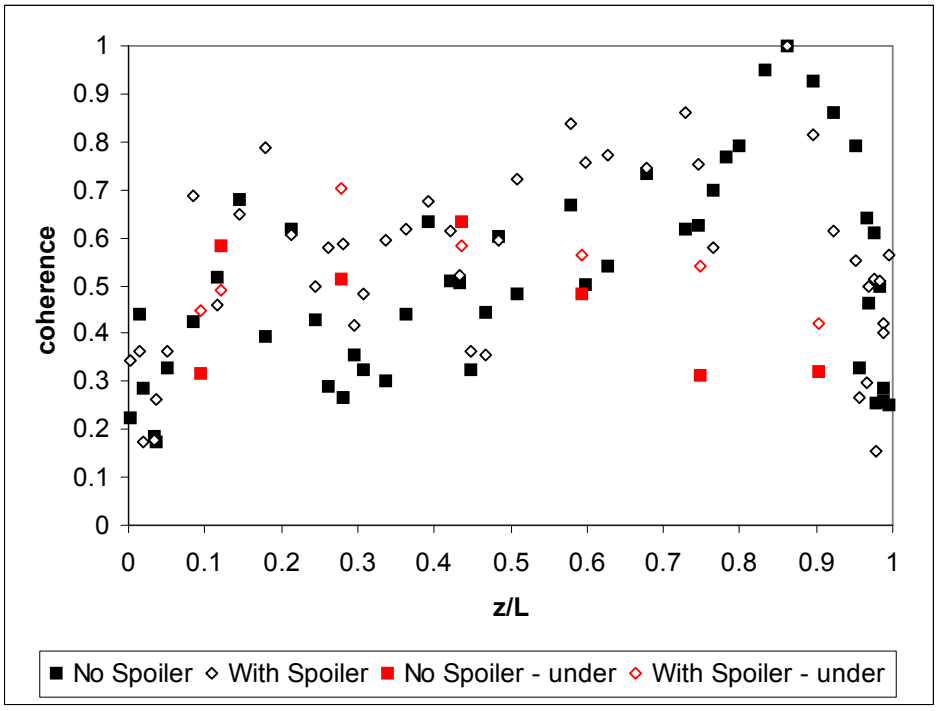

Figure 3.6.124 - Coherence between fluctuating surface pressure at z/L=0.86 and elsewhere on the centreline of the Rover 200 model near S=0.57 (15% scale)

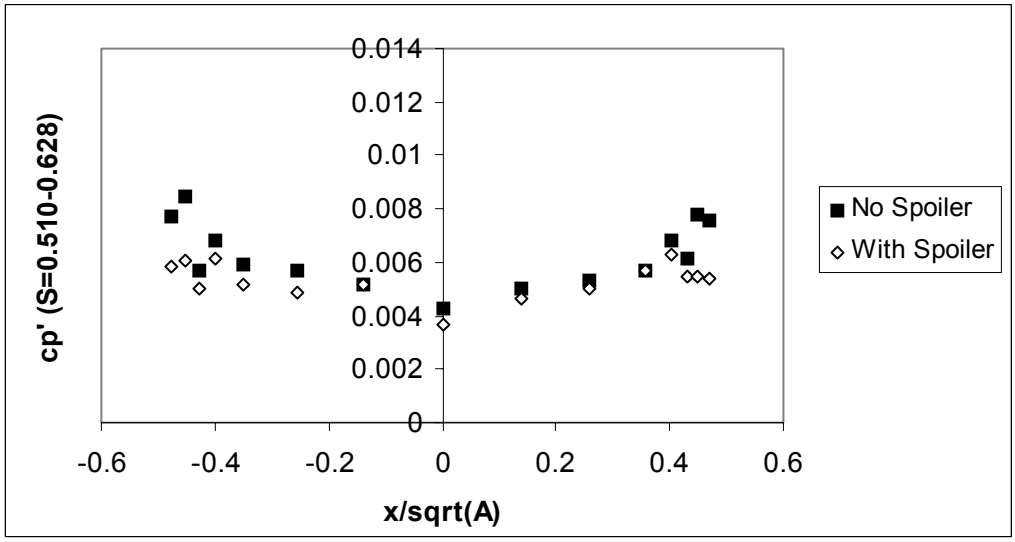

Figure 3.6.125 - Fluctuating surface pressure coefficient across the backlight of the Rover 200 model due to unsteadiness near S=0.57 (S=0.510-0.628, f=65-80hz) (15% scale)

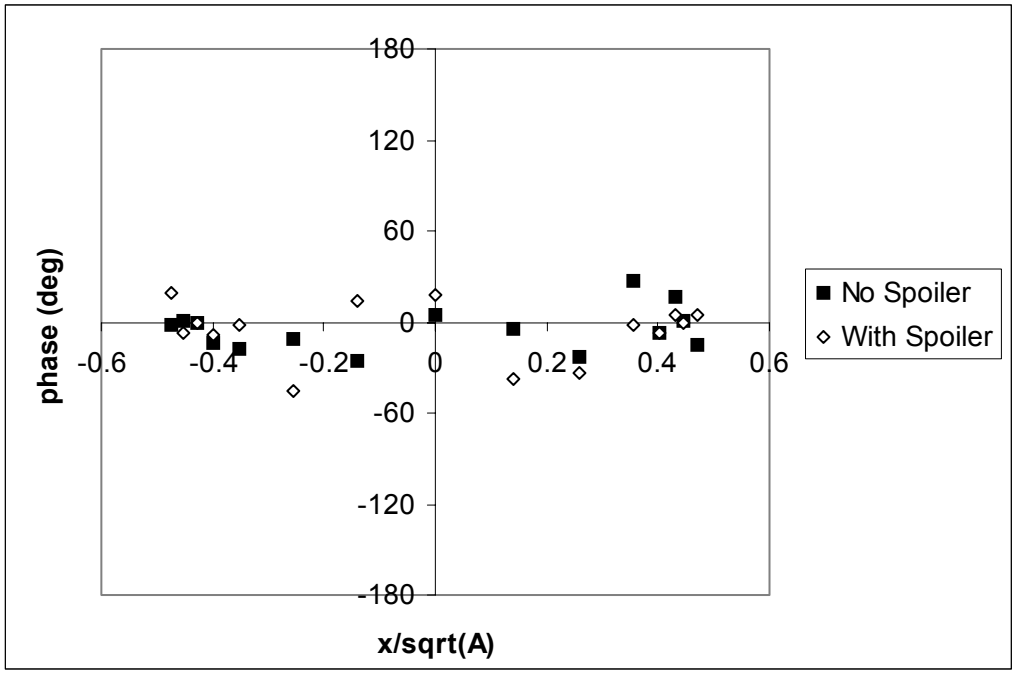

Figure 3.6.126 - Cross-spectral phase between fluctuating surface pressure at c-pillar and across the backlight of the Rover 200 model near S=0.57 (15% scale)

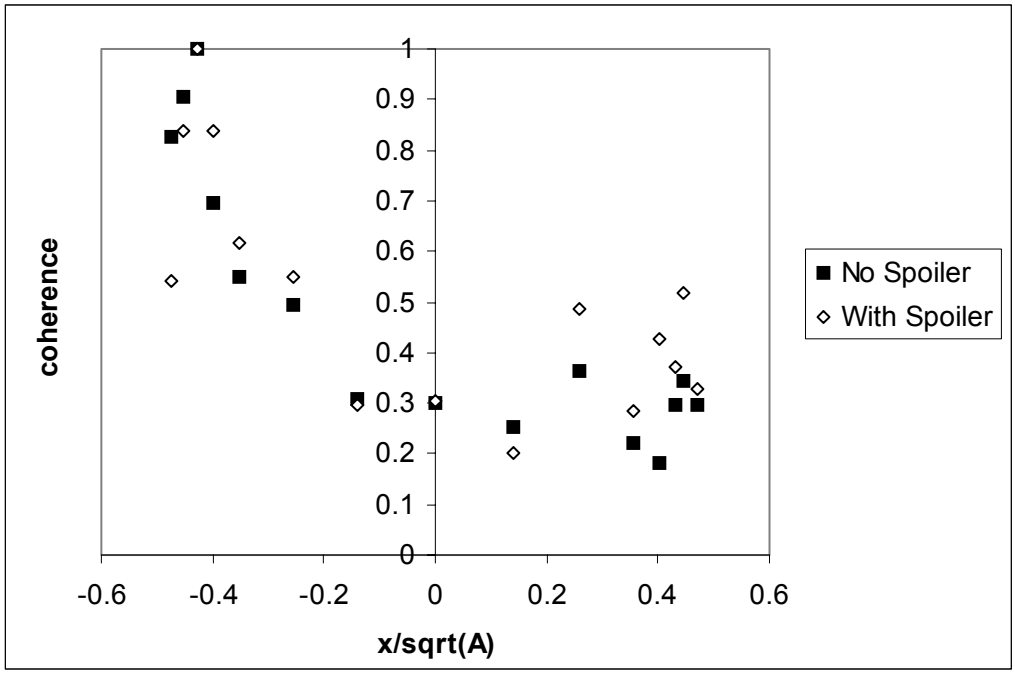

Figure 3.6.127 - Coherence between fluctuating surface pressure at c-pillar and across the backlight of the Rover 200 model near S=0.57 (15% scale)

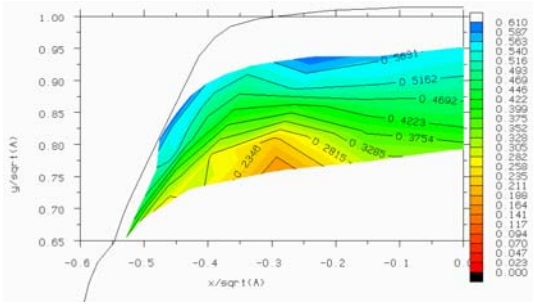

Figure 3.6.128 - Fraction of surface pressure coefficient fluctuation due to unsteadiness near S=0.12 (S=0.101-0.132, f=13-17hz) on the backlight of the Rover 200 model without spoiler

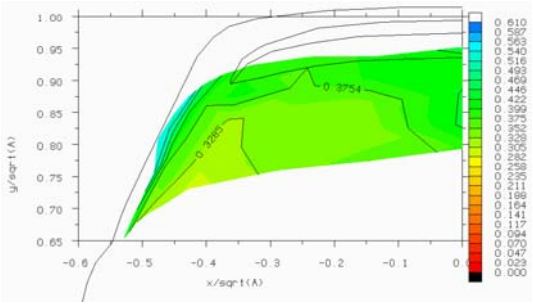

Figure 3.6.129 - Fraction of surface pressure coefficient fluctuation due to unsteadiness near S=0.12 (S=0.101-0.132, f=13-17hz) on the backlight of the Rover 200 model with spoiler (15% scale)

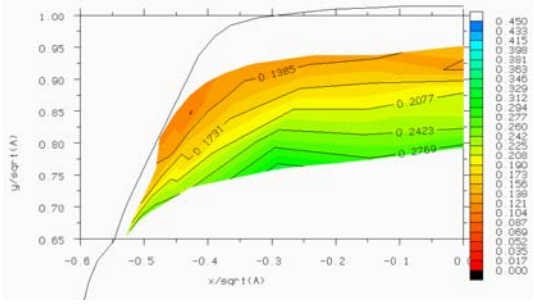

Figure 3.6.130 - Fraction of surface pressure coefficient fluctuation due to unsteadiness near S=0.57 (S=0.510-0.628, f=65-80hz) on the backlight of the Rover 200 model without spoiler

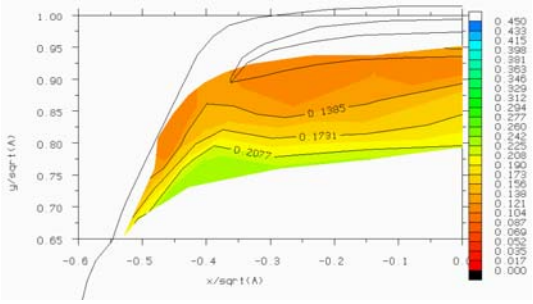

Figure 3.6.131 - Fraction of surface pressure coefficient fluctuation due to unsteadiness near S=0.57 (S=0.510-0.628, f=65-80hz) on the backlight of the Rover 200 model with spoiler (15% scale)

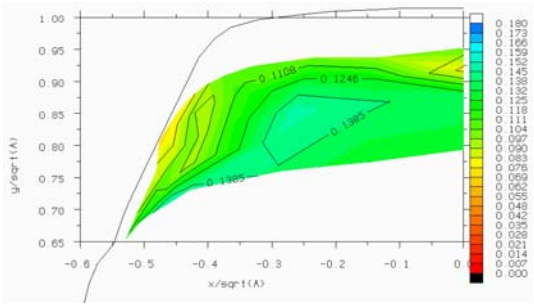

Figure 3.6.132 - Fraction of surface pressure coefficient fluctuation due to unsteadiness near S=1.14 (S=1.06-1.22, f=135-155hz) on the backlight of the Rover 200 model without spoiler (15%)

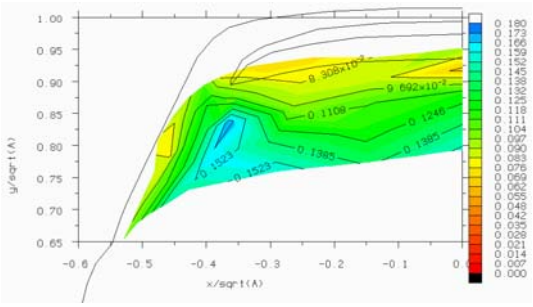

Figure 3.6.133 - Fraction of surface pressure coefficient fluctuation due to unsteadiness near S=1.14 (S=1.06-1.22, f=135-155hz) on the backlight of the Rover 200 model with spoiler (15% scale)

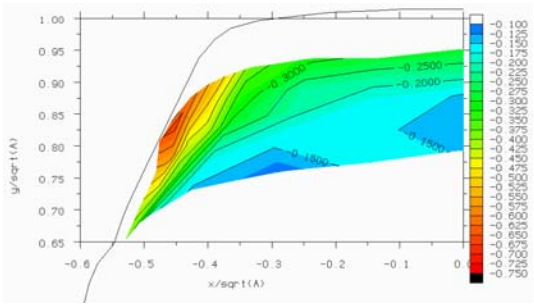

a) 0.0s, t/T=0

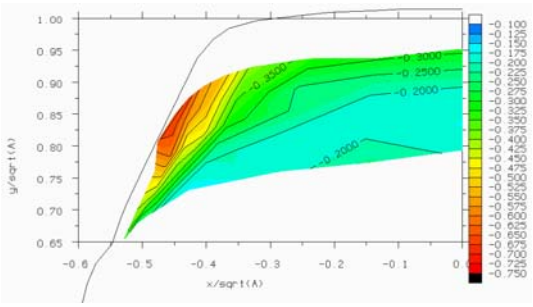

d) 0.0075s, t/T=0.55

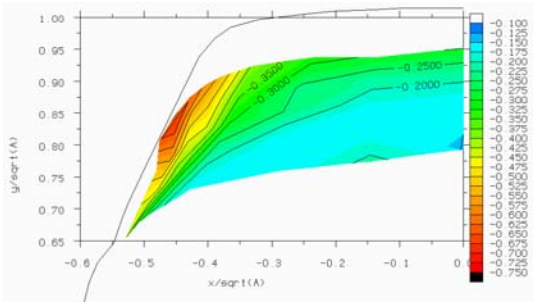

b) 0.0025s, t/T=0.18

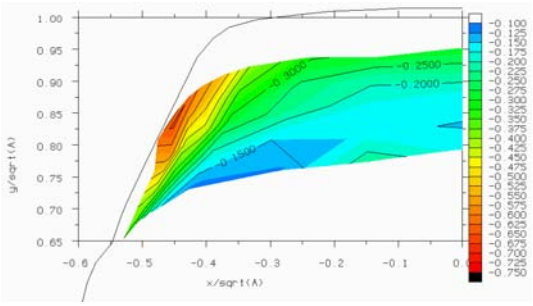

e) 0.0100s, t/T=0.73

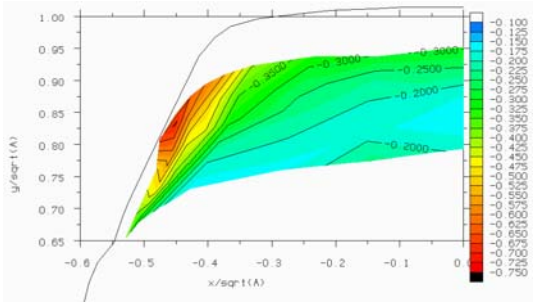

c) 0.0050s, t/T=0.37

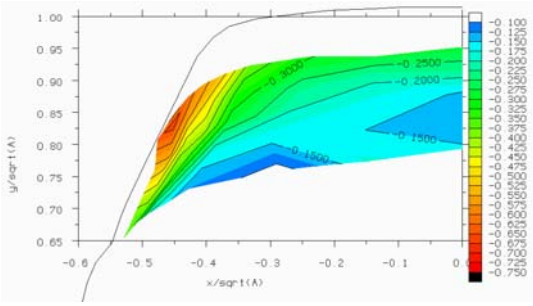

f) 0.00125s, t/T=0.91

Figure 3.6.134 - Sequence showing surface pressure coefficient reconstructed from S=0.57 and S=1.15 (2 × 4hz bands@~72.5hz and harmonic) on the backlight of the Rover 200 model without spoiler (using pressure tap on centreline at z/L=0.86 for phase reference) (15% scale)

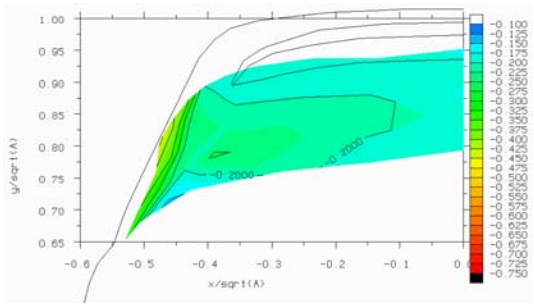

a) 0.0s, t/T=0

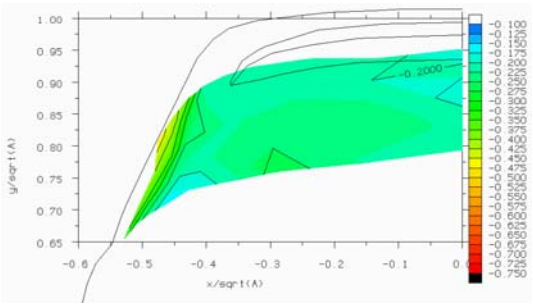

d) 0.0075s, t/T=0.55

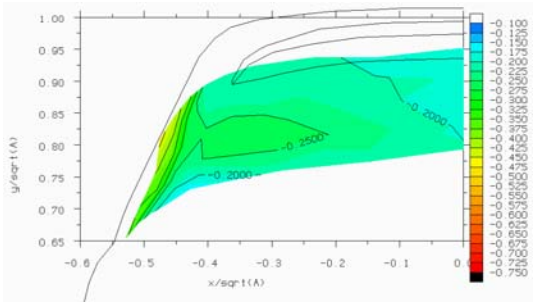

b) 0.0025s, t/T=0.18

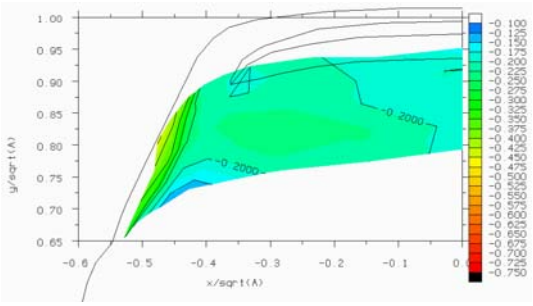

e) 0.0100s, t/T=0.73

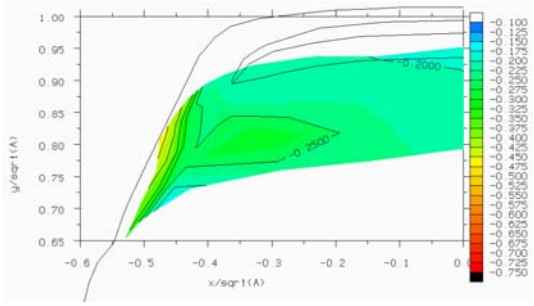

c) 0.0050s, t/T=0.37

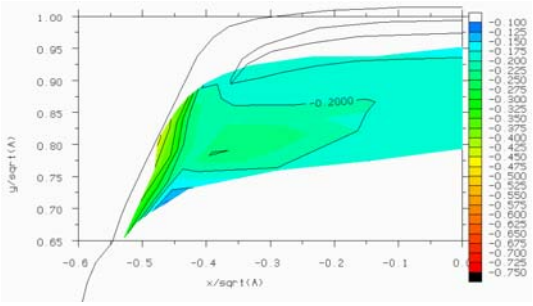

f) 0.00125s, t/T=0.91

Figure 3.6.135 - Sequence showing surface pressure coefficient reconstructed from S=0.57 and S=1.14 (2 × 4hz bands@~72.5hz and harmonic) on the backlight of the Rover 200 model with spoiler (using pressure tap on centreline at z/L=0.86 for phase reference) (15% scale)

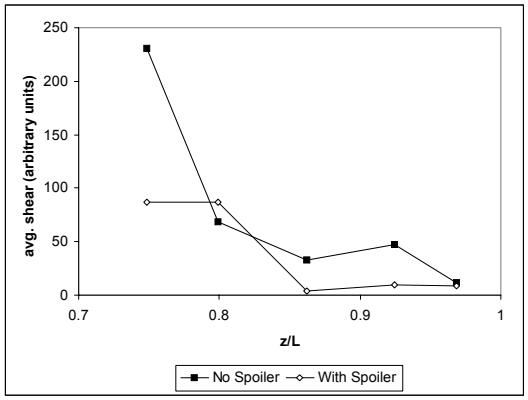

Figure 3.6.136 - Time-averaged shear stress (arbitrary units) on the centreline of the Rover 200 model (15% scale)

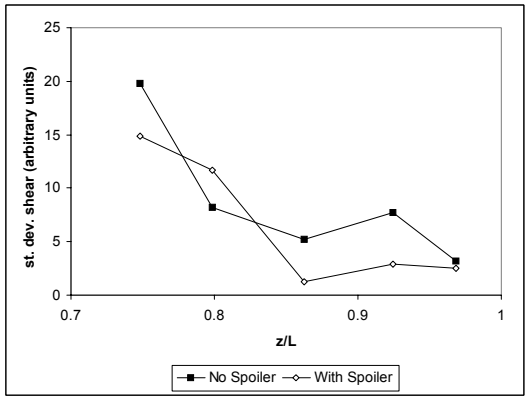

Figure 3.6.137 - Fluctuating shear stress (standard deviation) on the centreline of the Rover 200 model (15% scale)

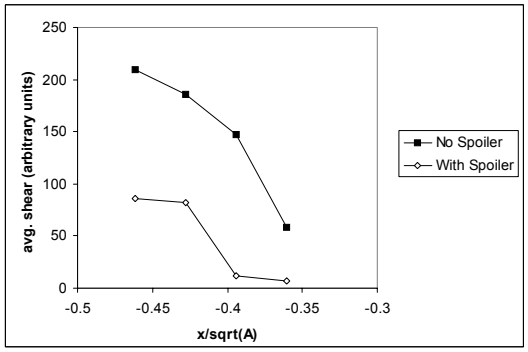

Figure 3.6.138 - Time-averaged shear stress (arbitrary units) around the c-pillar of the Rover 200 model (15%)

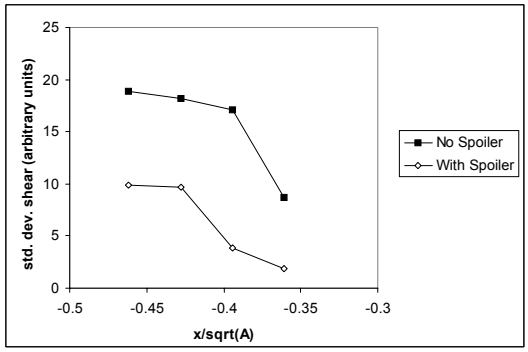

Figure 3.6.139 - Fluctuating shear stress (standard deviation) around the c-pillar of the Rover 200 model (15% scale)

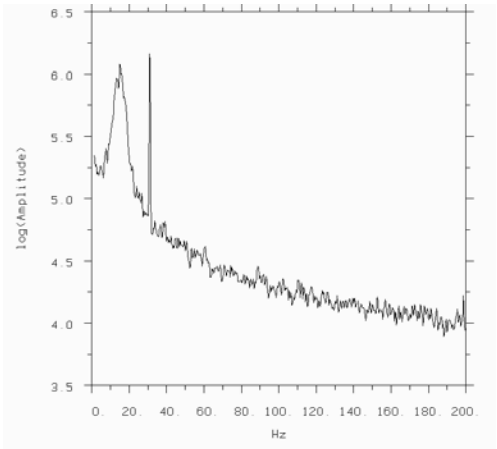

Figure 3.6.140 - Autospectral density of shear stress at z/L = 0.86 on the centreline of the Rover 200 model without spoiler (15% scale)

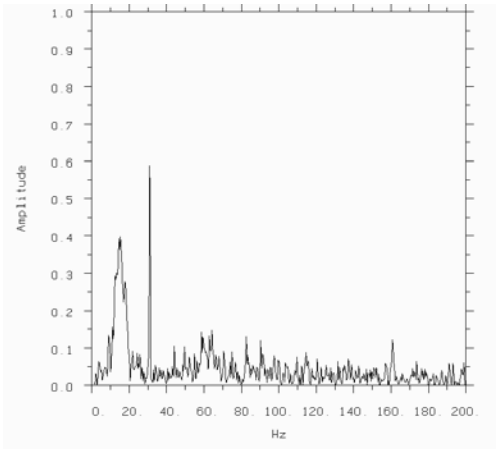

Figure 3.6.141 - Coherence between shear stress at z/L = 0.86 on the centreline and reference hot-wire at x/sqrt(A)=-0.24, y/sqrt(A)=0.24, z/sqrt(A)=0.75 for the Rover 200 model without spoiler (15%)

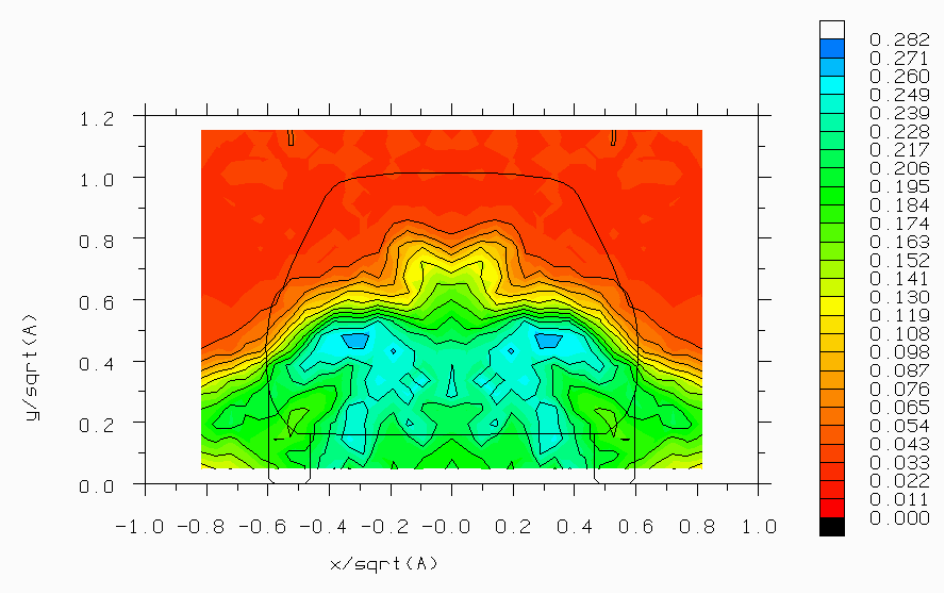

Figure 3.6.142 - Fluctuating total pressure coefficient (standard deviation) one base dimension behind the Rover 200 model without spoiler (40% scale) (data mirrored)

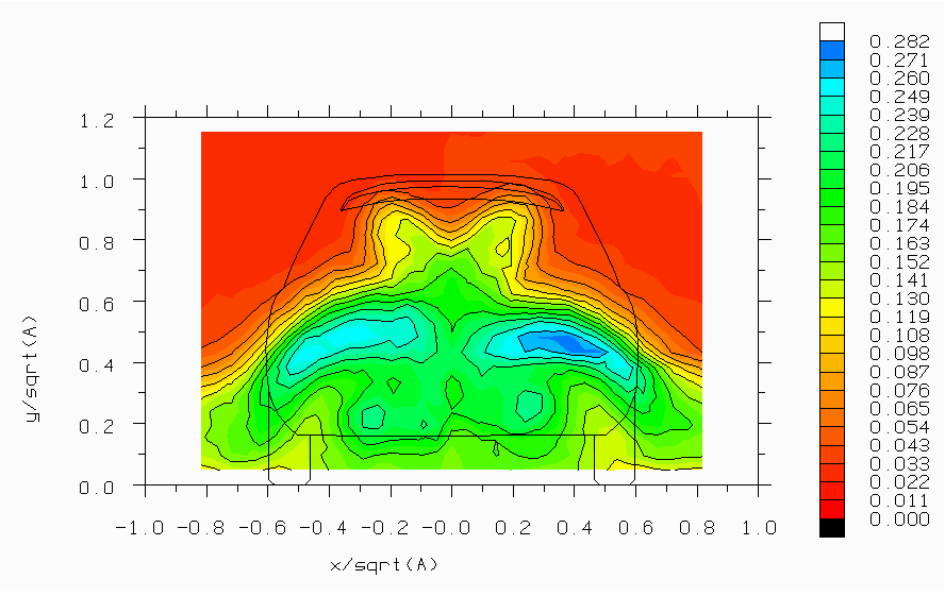

Figure 3.6.143 - Fluctuating total pressure coefficient (standard deviation) one base dimension behind the Rover 200 model with spoiler (40% scale)

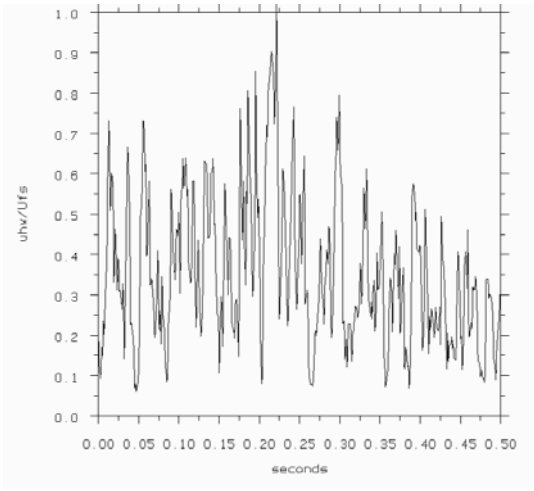

Figure 3.6.144 - Time-trace of hot-wire effective velocity at x/sqrt(A)=0.14, y/sqrt(A)=0.24, z/sqrt(A)=0.75 in the wake of the Rover 200 model with spoiler (40% scale)

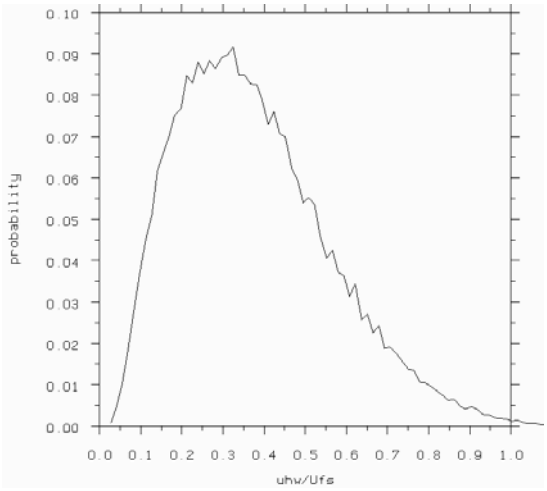

Figure 3.6.145 - Probability density of hot-wire effective velocity at x/sqrt(A)=0.14, y/sqrt(A)=0.24, z/sqrt(A)=0.75 in the wake of the Rover 200 model with spoiler (40% scale)

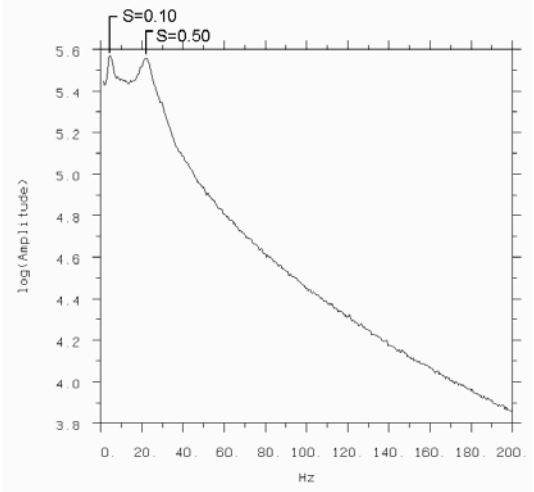

Figure 3.6.146 - Autospectral density of hot-wire effective velocity at x/sqrt(A)=0.14, y/sqrt(A)=0.24, z/sqrt(A)=0.75 in the wake of the Rover 200 model with spoiler (40% scale) (Re=9.3×10^5)

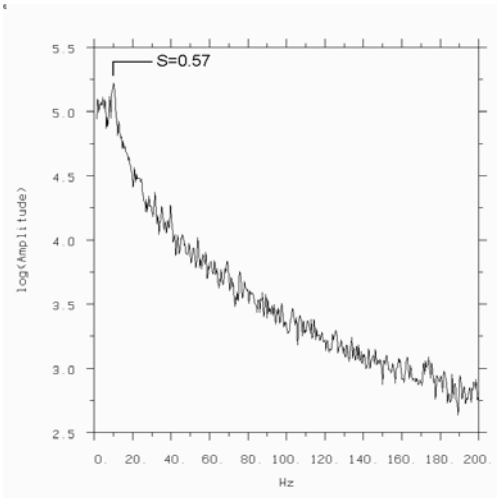

Figure 3.6.147 - Autospectral density of hot-wire effective velocity at x/sqrt(A)=0.14, y/sqrt(A)=0.24, z/sqrt(A)=0.75 in the wake of the Rover 200 model with spoiler (40% scale) Reduced velocity: Re=3.8×10^5

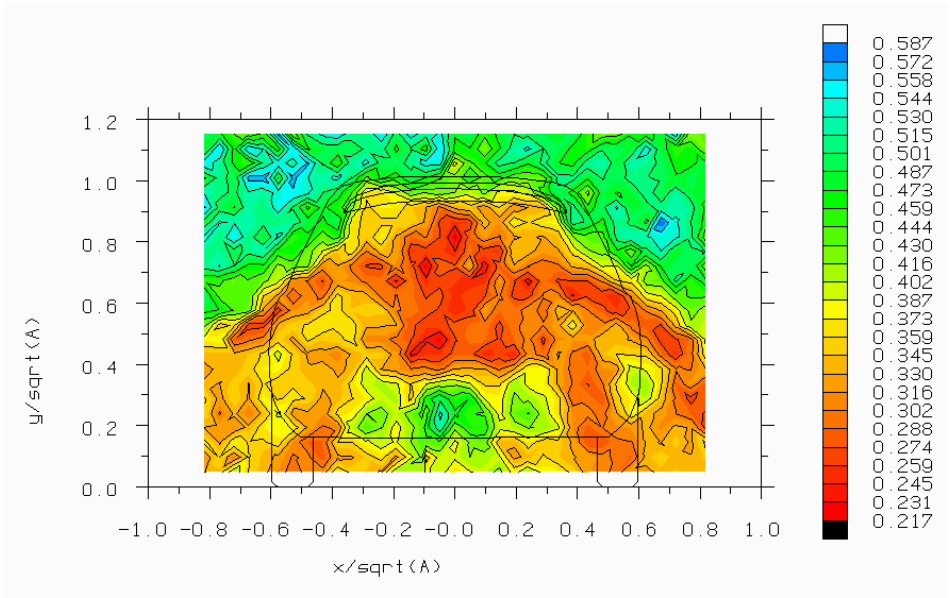

Figure 3.6.148 - Fraction of total pressure coefficient fluctuation due to unsteadiness near S=0.10 (S=0.04-0.15, f=1.8-6.8hz) one base dimension behind the Rover 200 model with spoiler (40% scale)

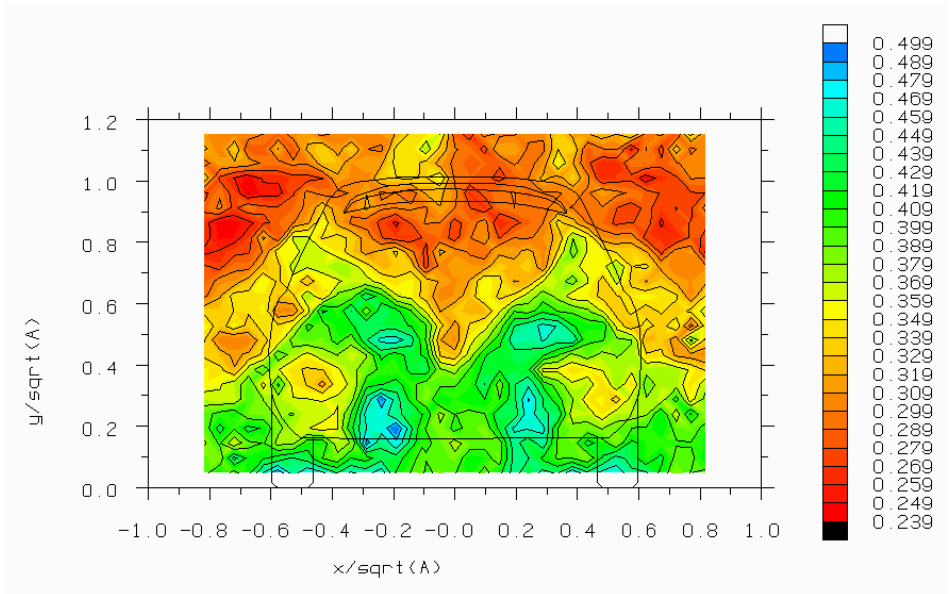

Figure 3.6.149 - Fraction of total pressure coefficient fluctuation due to unsteadiness near S=0.50 (S=0.39-0.61, f=17-27hz) one base dimension behind the Rover 200 model with spoiler (40% scale)

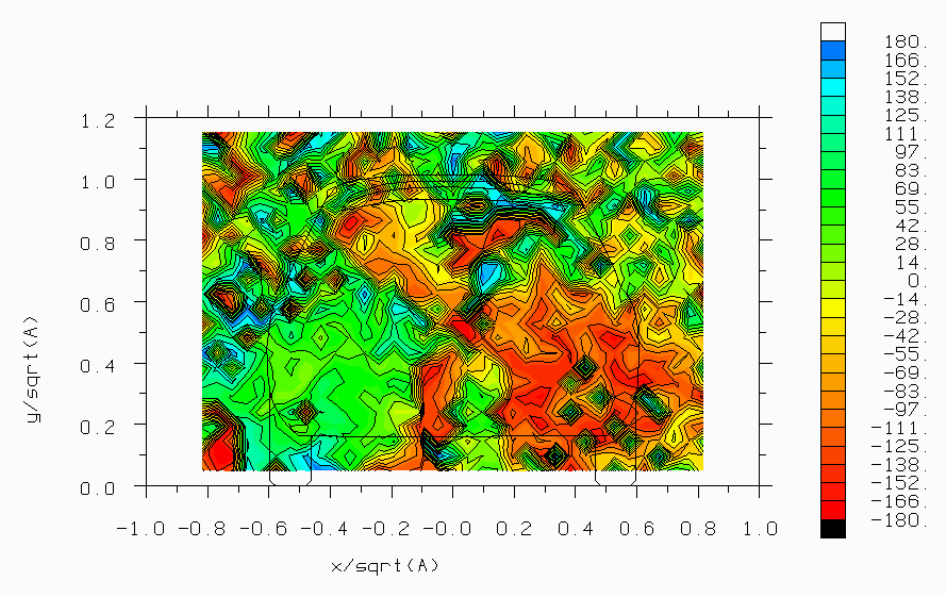

Figure 3.6.150 - Total pressure cross-spectral phase near S=0.10 one base dimension behind the Rover 200 model with spoiler (40% scale)

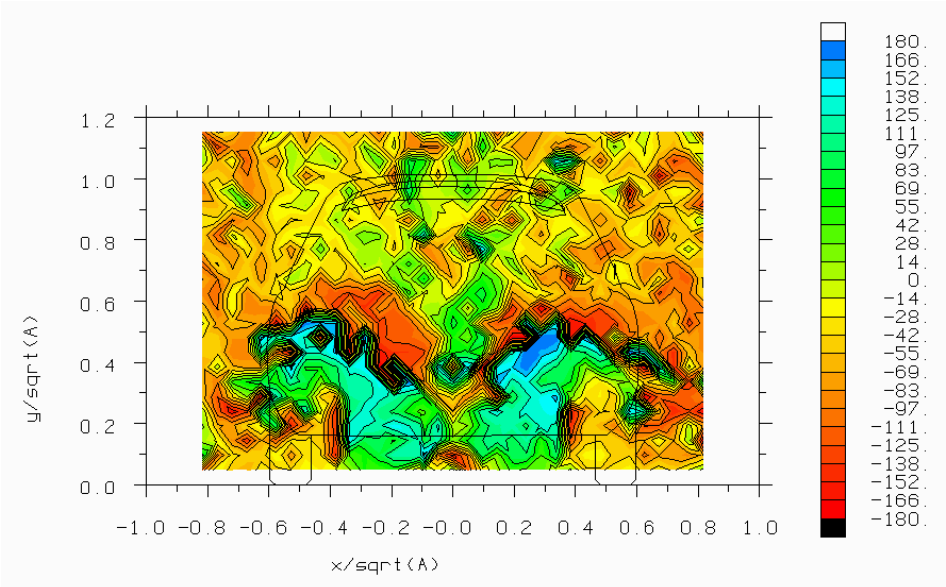

Figure 3.6.151 - Total pressure cross-spectral phase near S=0.50 one base dimension behind the Rover 200 model with spoiler (40% scale)

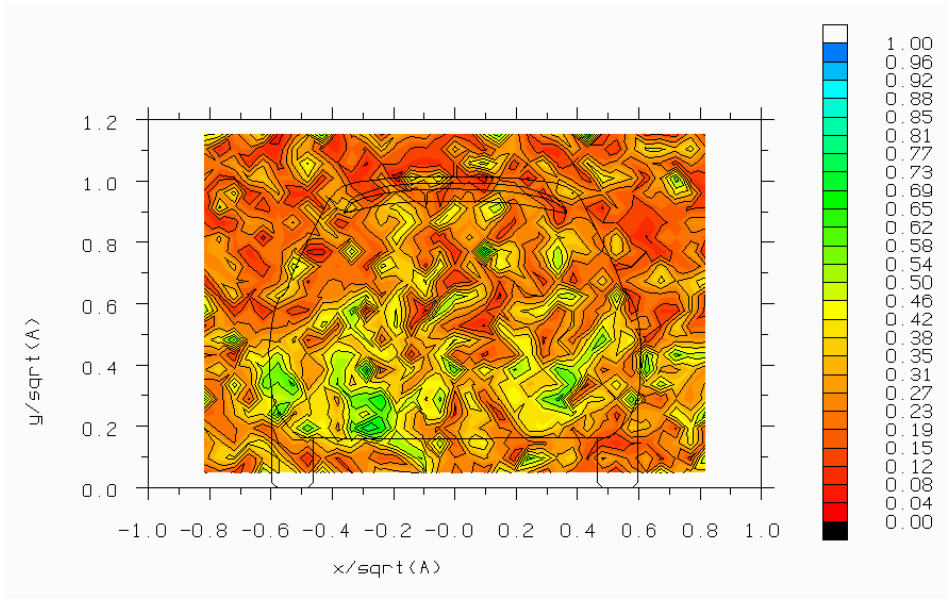

Figure 3.6.152 - Coherence between total pressure and reference hot-wire (at x/sqrt(A)=0.14, y/sqrt(A)=0.24, z/sqrt(A)=0.75) near S=0. 10 one base dimension behind the Rover 200 model with spoiler (40% scale)

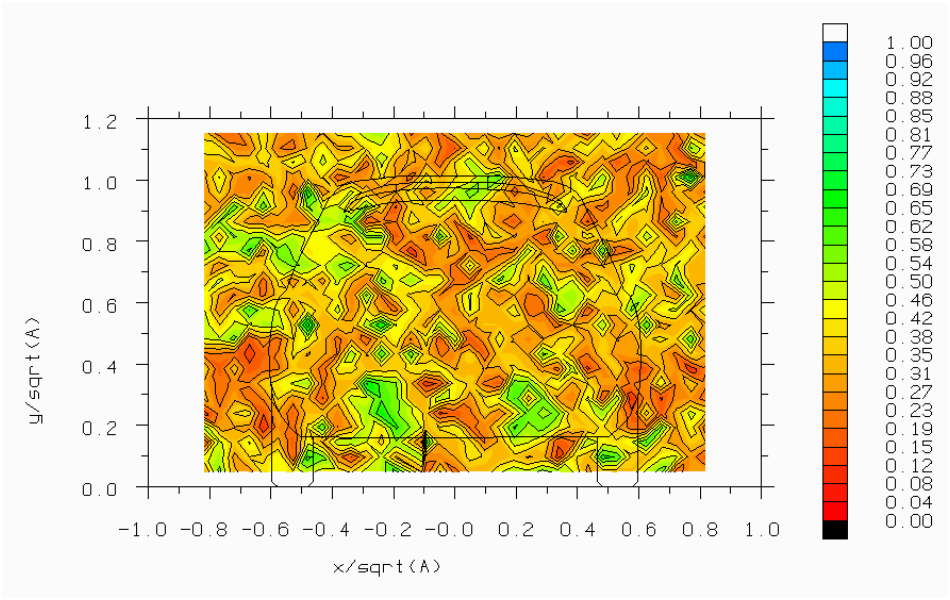

Figure 3.6.153 - Coherence between total pressure and reference hot-wire (at x/sqrt(A)=0.14, y/sqrt(A)=0.24, z/sqrt(A)=0.75) near S=0.50 one base dimension behind the Rover 200 model with spoiler (40% scale)

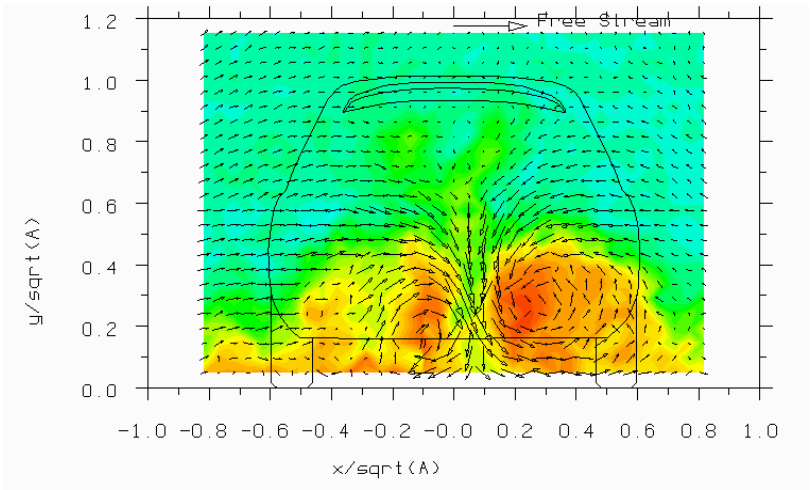

Figure 3.6.154a) t=0.0s, t/T=0

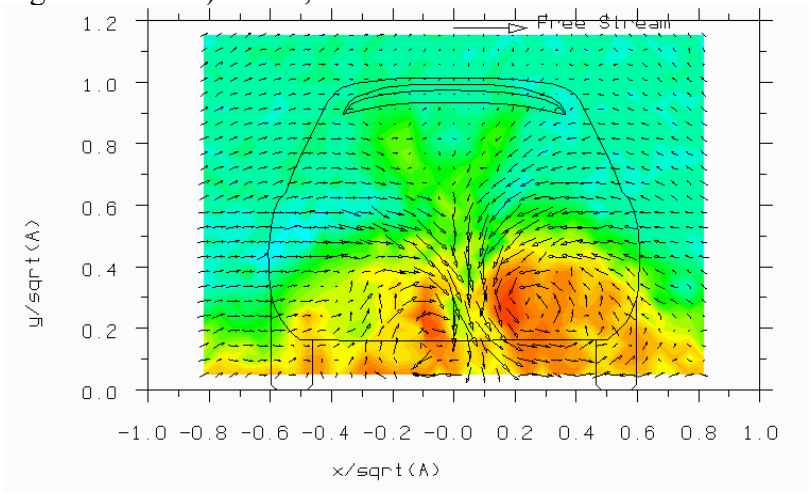

Figure 3.6.154b) t=0.041s, t/T=0.177

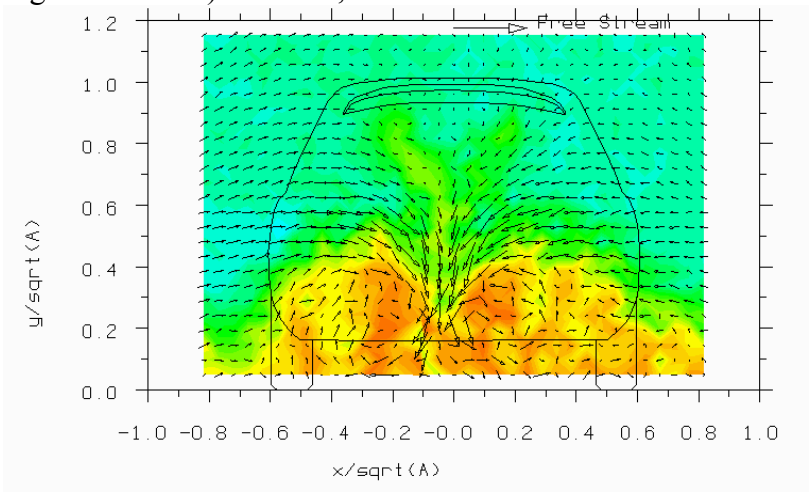

Figure 3.6.154c) t=0.083s, t/T=0.354

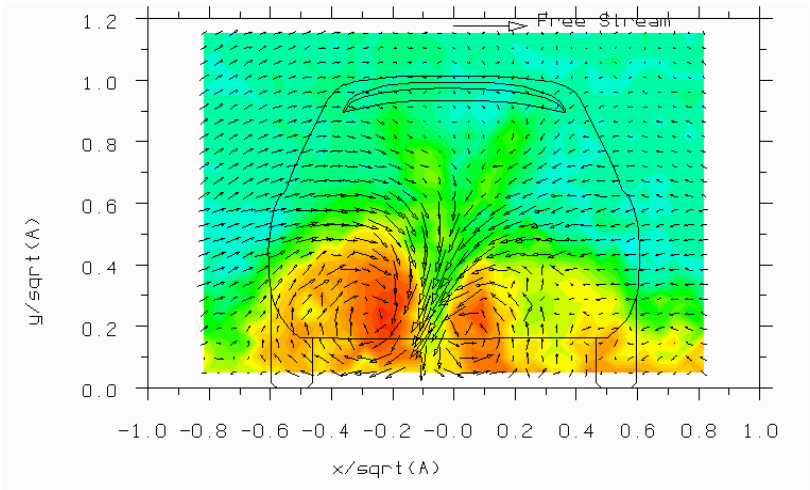

Figure 3.6.154d) t=0.124s, t/T=0.531

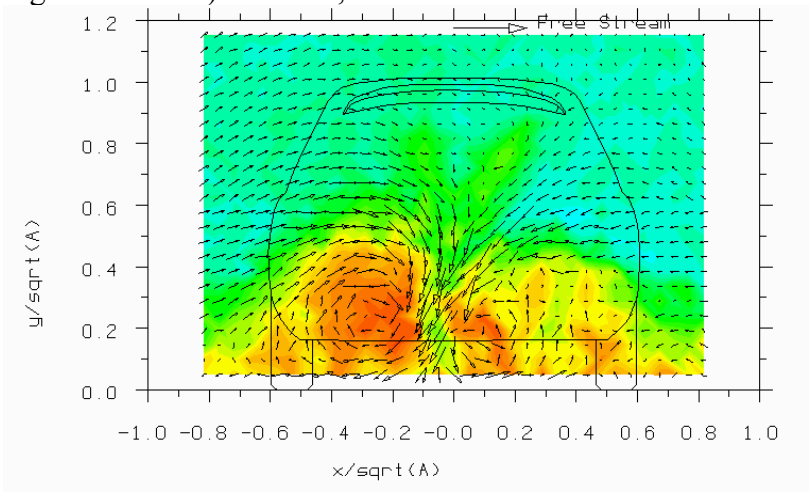

Figure 3.6.154e) t=0.165s, t/T=0.708

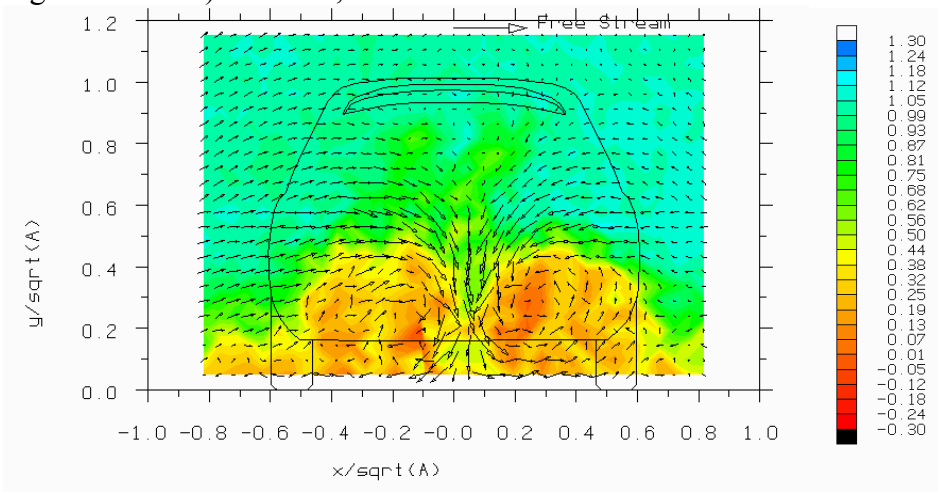

Figure 3.6.154f) t=0.207s, t/T=0.885

Figure 3.6.154 - Sequence showing total pressure coefficient and velocity vectors reconstructed from S=0.10 one base dimension behind the Rover 200 model with spoiler (40% scale)

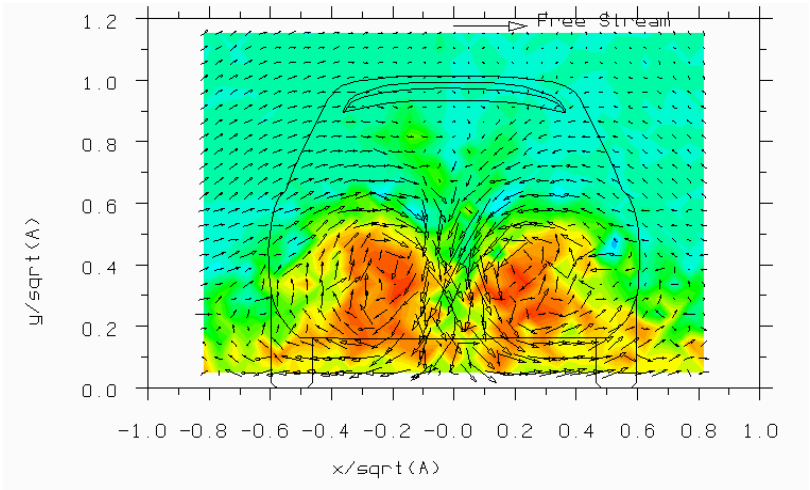

Figure 3.6.155a) t=0.0s, t/T=0

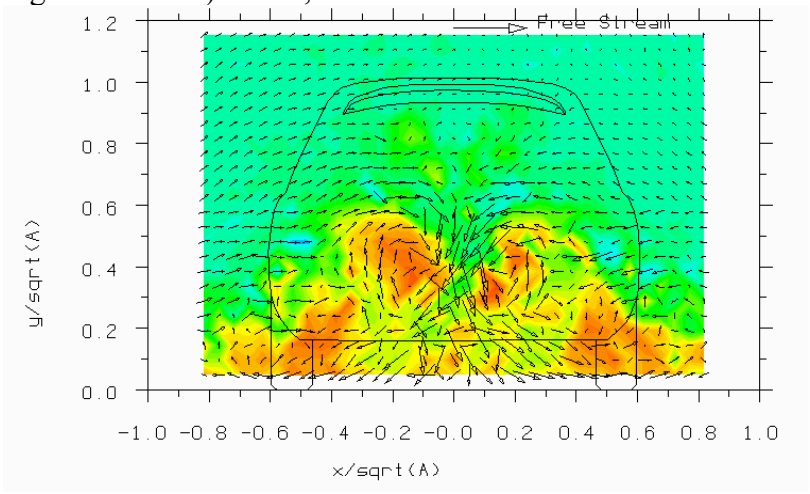

Figure 3.6.155b) t=0.0076s, t/T=0.169

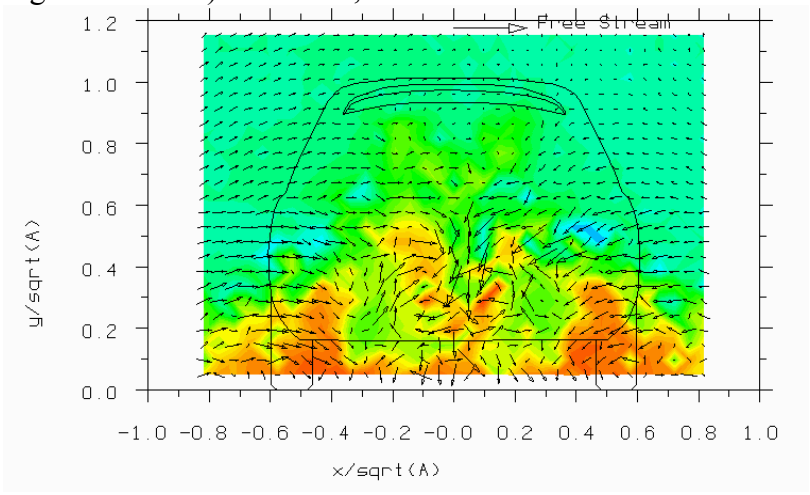

Figure 3.6.155c) t=0.0152s, t/T=0.338

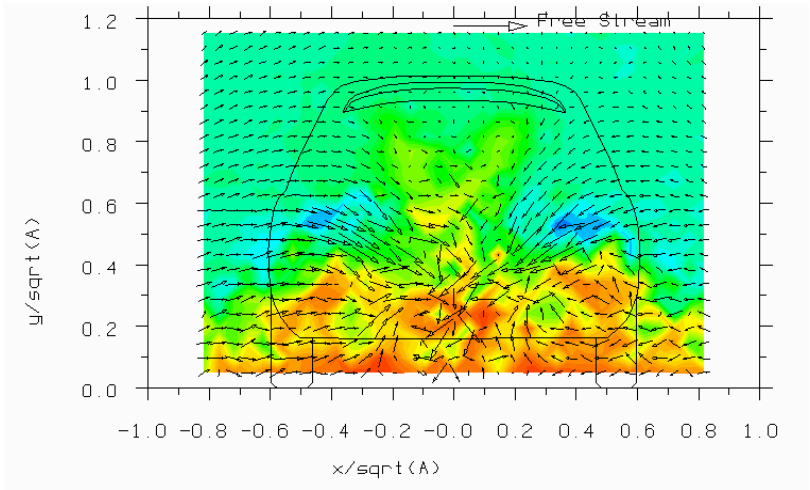

Figure 3.6.155d) t=0.0227s, t/T=0.504

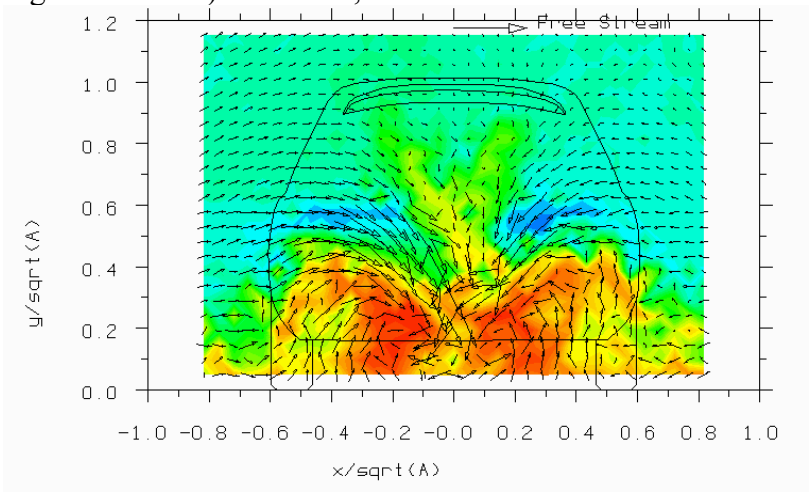

Figure 3.6.155e) t=0.0303s, t/T=0.673

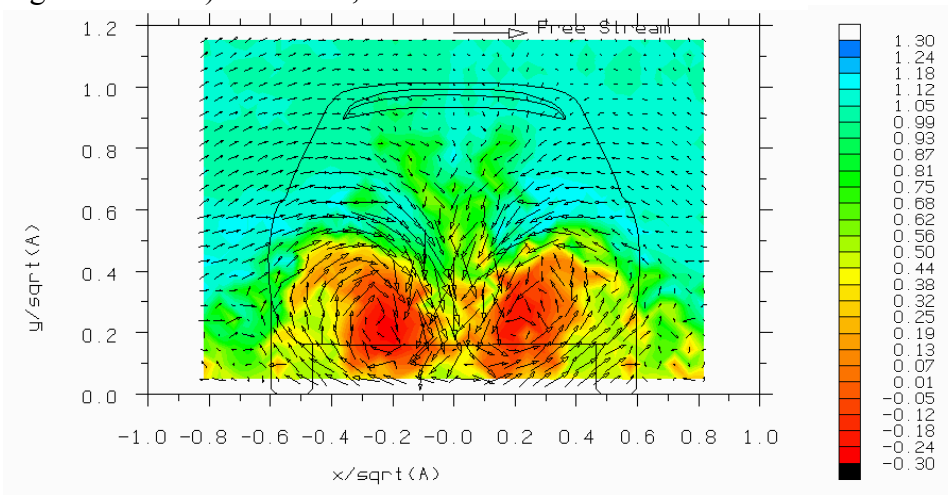

Figure 3.6.155f) t=0.0379s, t/T=0.842

Figure 3.6.155 - Sequence showing total pressure coefficient and velocity vectors reconstructed from S=0.50 one base dimension behind the Rover 200 model with spoiler (40% scale)

FIGURES FOR CHAPTER 4 – CFD SIMULATIONS

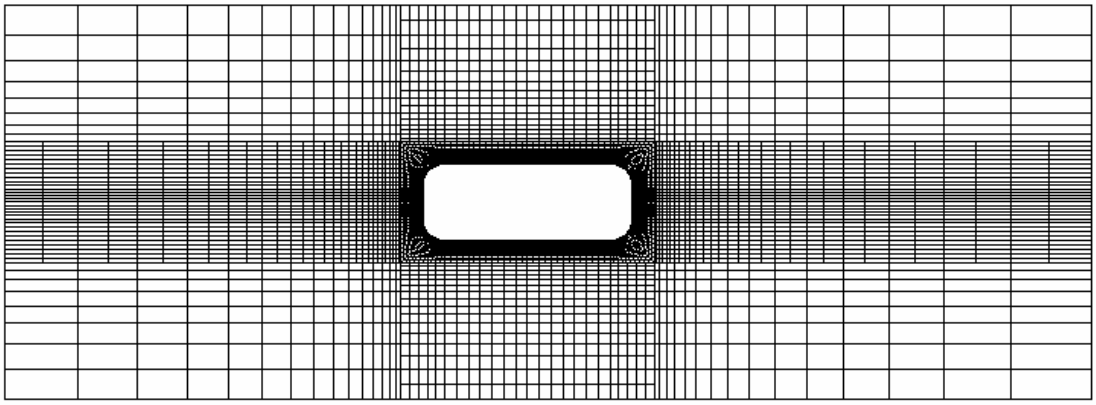

Figure 4.2.1a) Cartesian/o-type hexahedral grid with extensive grid embedding

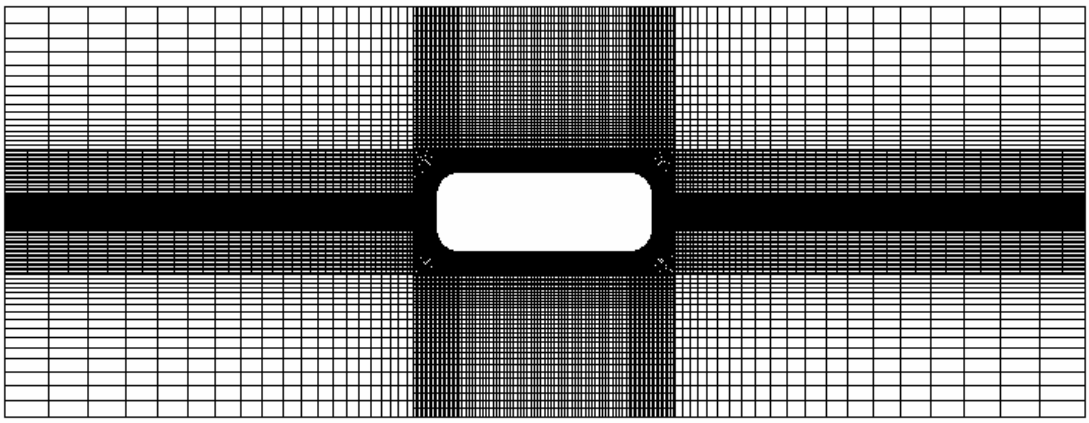

Figure 4.2.1b) Finer Cartesian/o-type hexahedral grid with extensive grid embedding

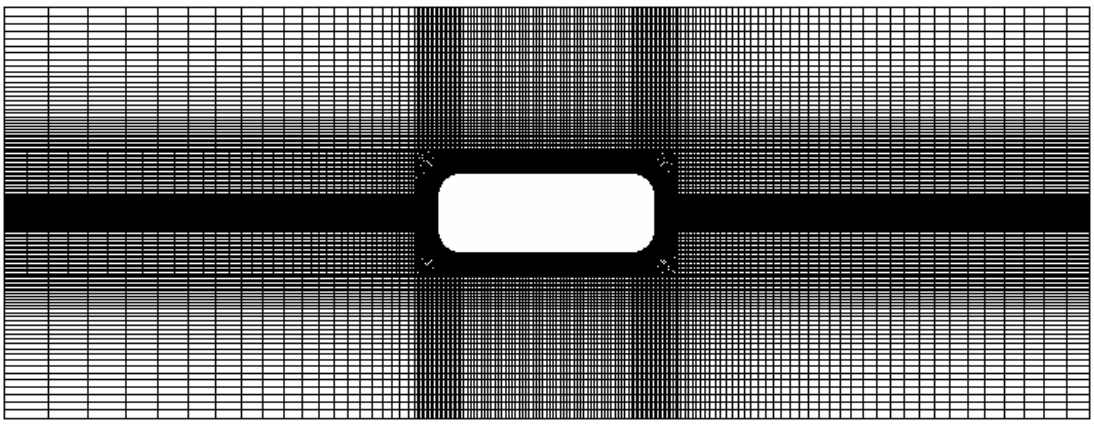

Figure 4.2.1c) Cartesian/o-type hexahedral grid with reduced grid embedding

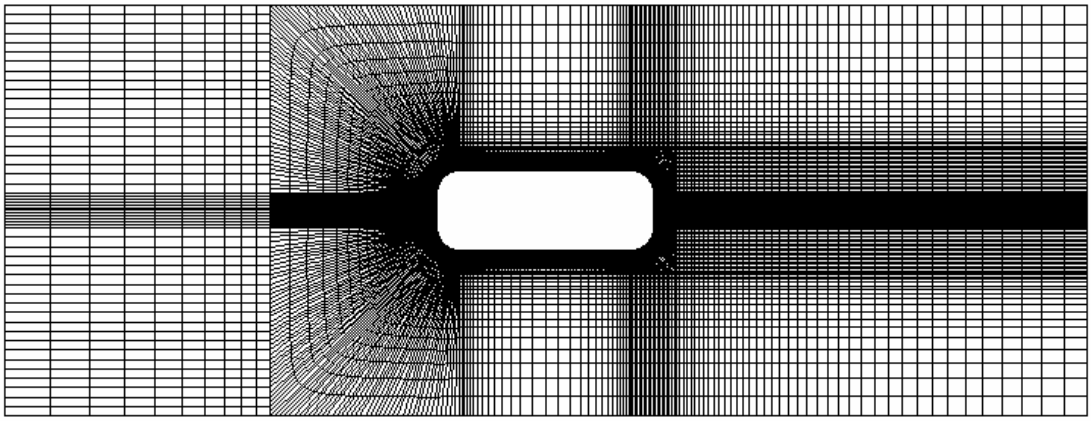

Figure 4.2.1d) Cartesian/o-type hexahedral grid with embedding (more o-type mesh)

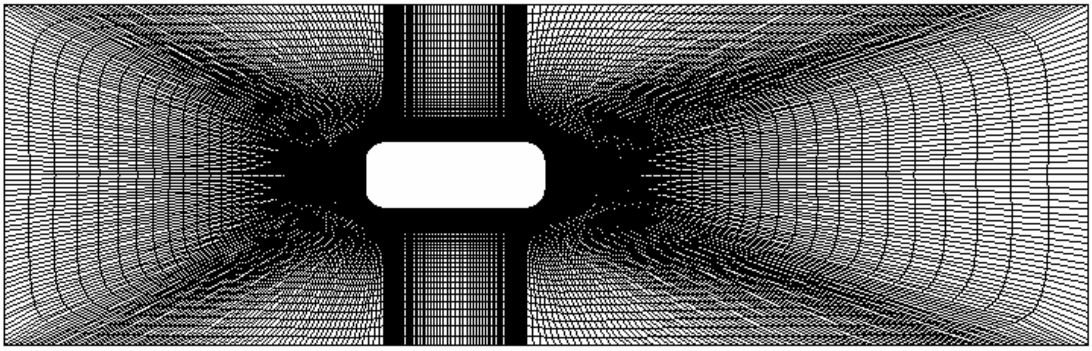

Figure 4.2.1e) O-type hexahedral grid without embedding

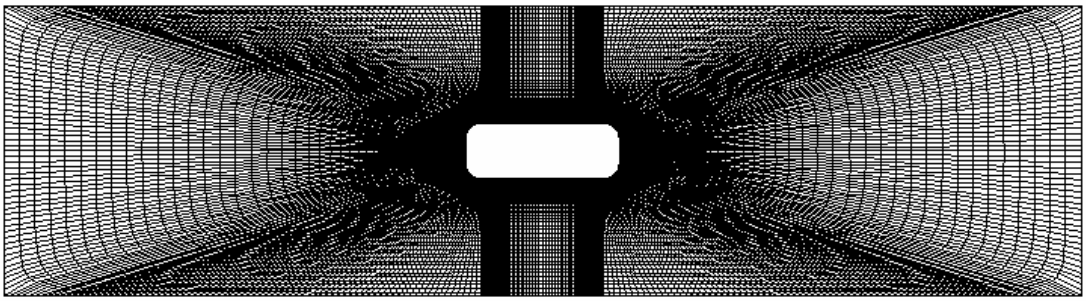

Figure 4.2.1f) O-type hexahedral grid, no embedding, extended inlet length

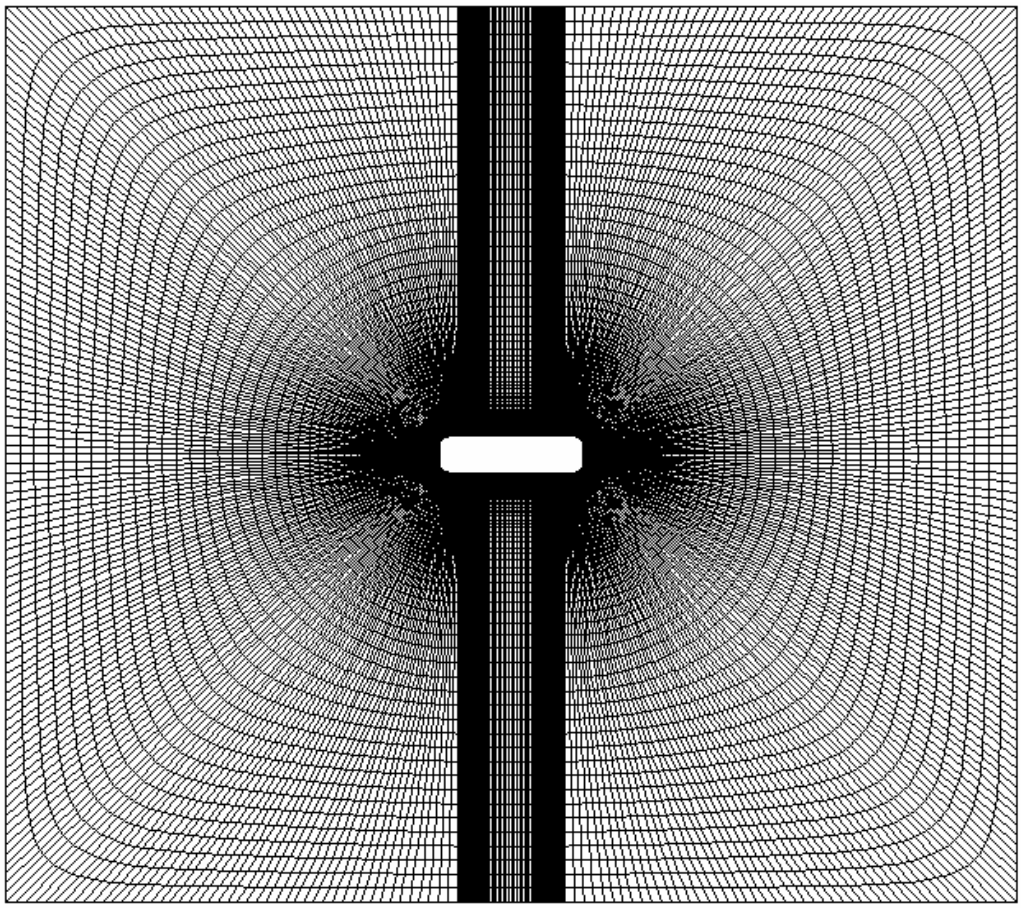

Figure 4.2.1g) O-type grid, no embedding, extended inlet length, extended width

Figure 4.2.1 – Evolution of hexahedral grid topologies for the two-dimensional symmetric models

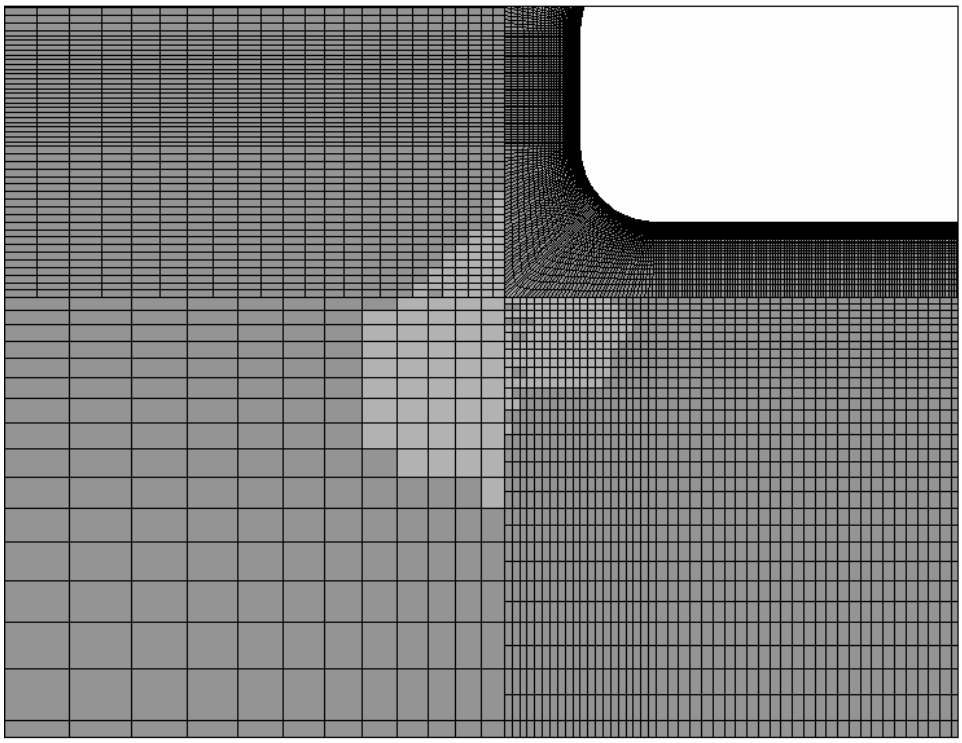

Figure 4.2.2 – Total pressure coefficient at a grid embedding boundary showing spurious increases in total pressure (lighter grey)

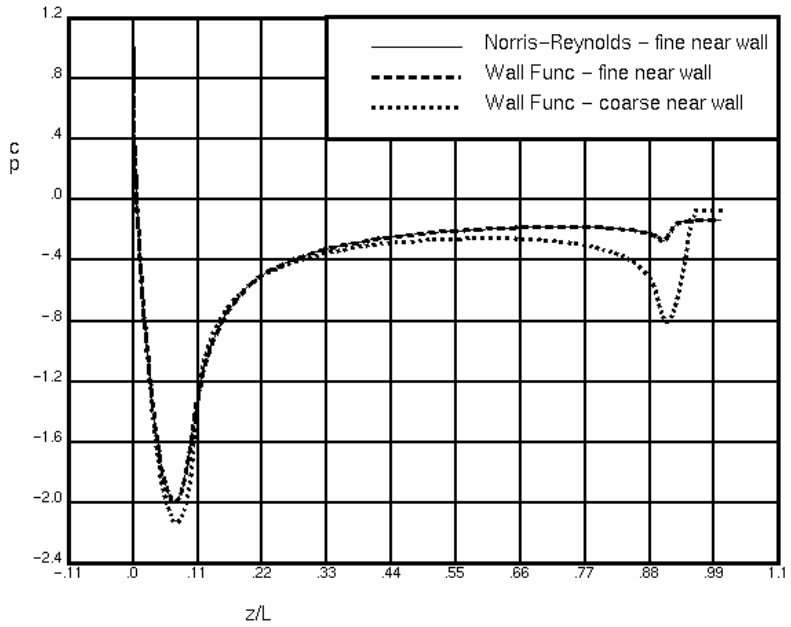

Figure 4.2.3 – Effect of near wall cell spacing and boundary layer treatment on pressure distribution for the Docton model

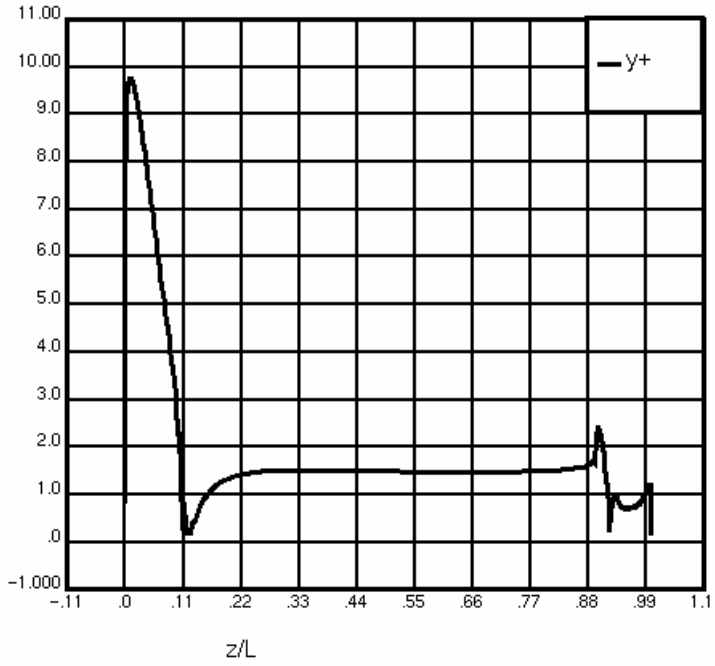

Figure 4.2.4 - Distribution of y+ for simulation of Docton model with near wall cell spacing of 0.06mm

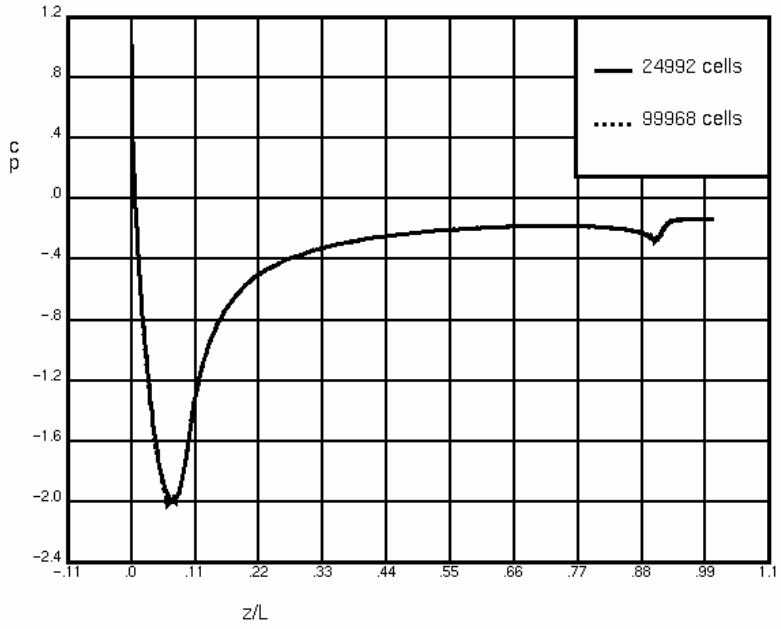

Figure 4.2.5 - Demonstration of grid independence by doubling number of cells in all directions for the Docton model

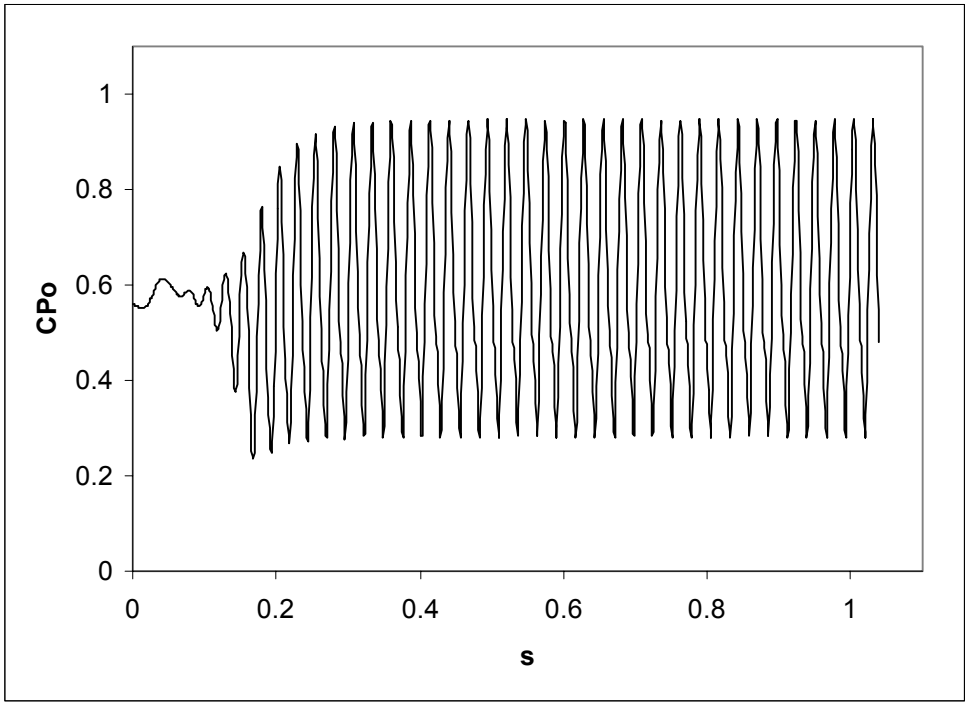

Figure 4.2.6a) Δt=0.001s

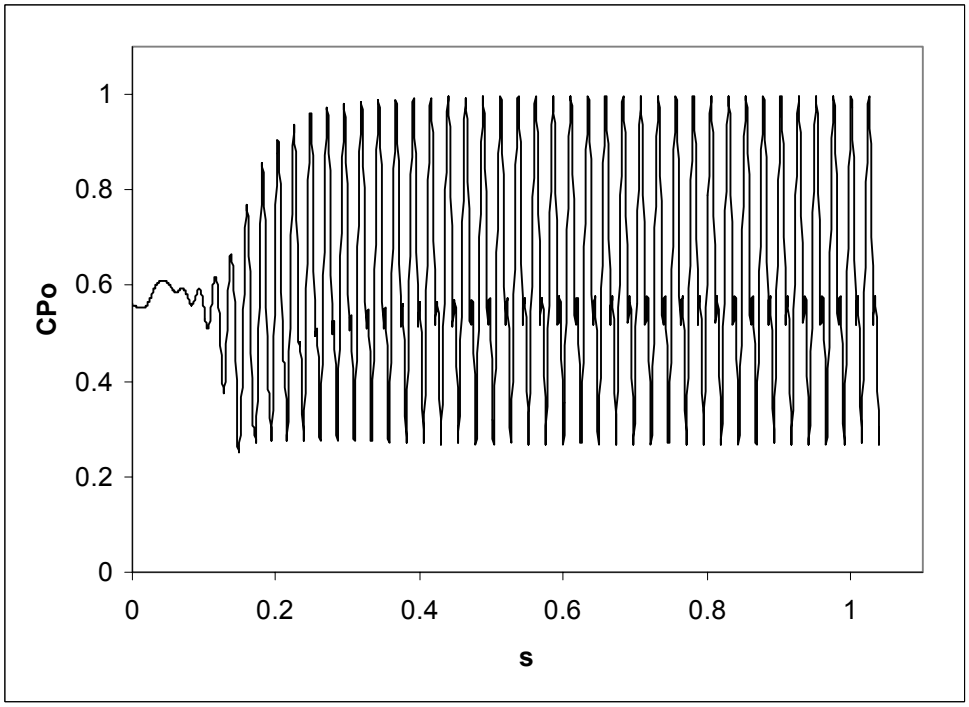

Figure 4.2.6b) Δt=0.0005s

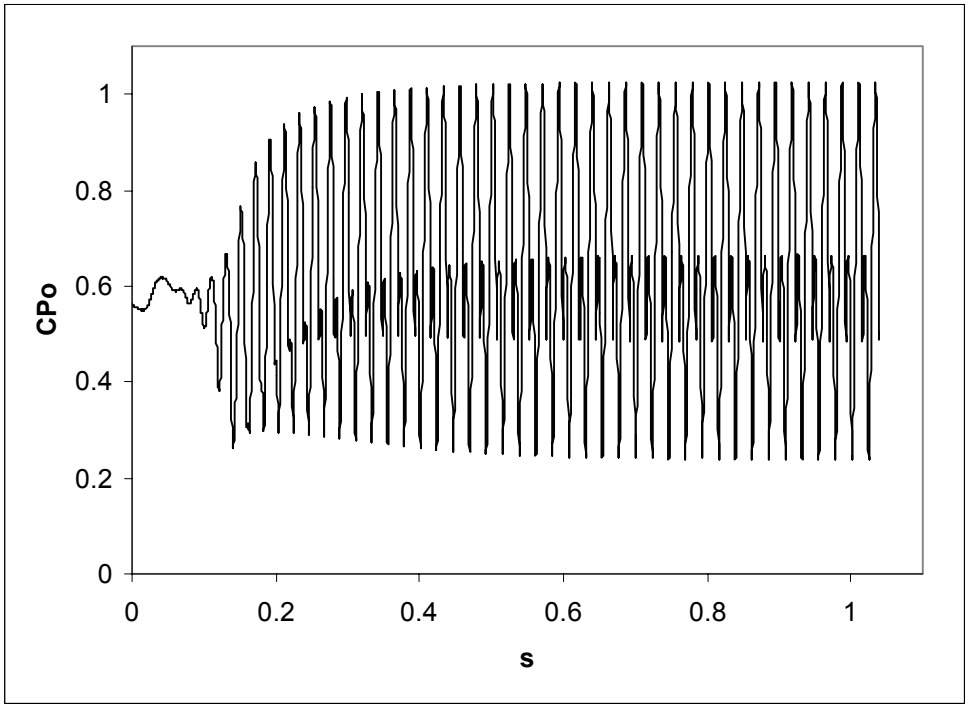

Figure 4.2.6c) Δt=0.00025s

Figure 4.2.6 - Time-history of total pressure coefficient at x/W=0.3, z/W=2.0 in the wake of the PARAD1 model with different time-steps

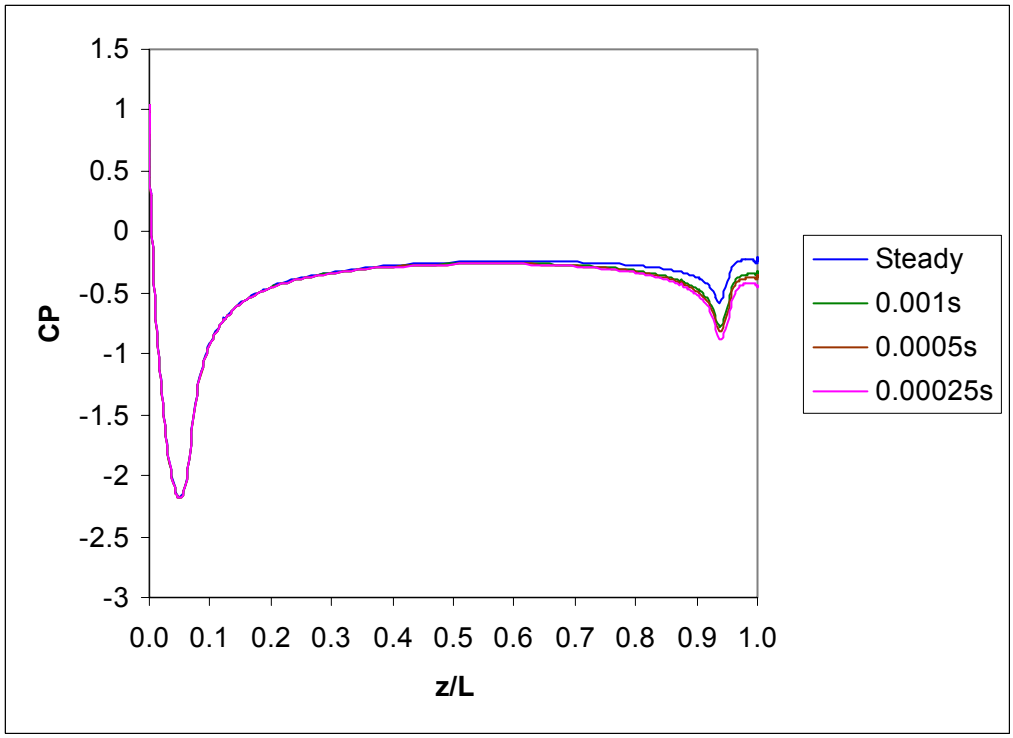

Figure 4.2.7 – Surface pressure distributions on the PARAD1 model for steady and unsteady simulations with various time-steps (k-ε turbulence model)

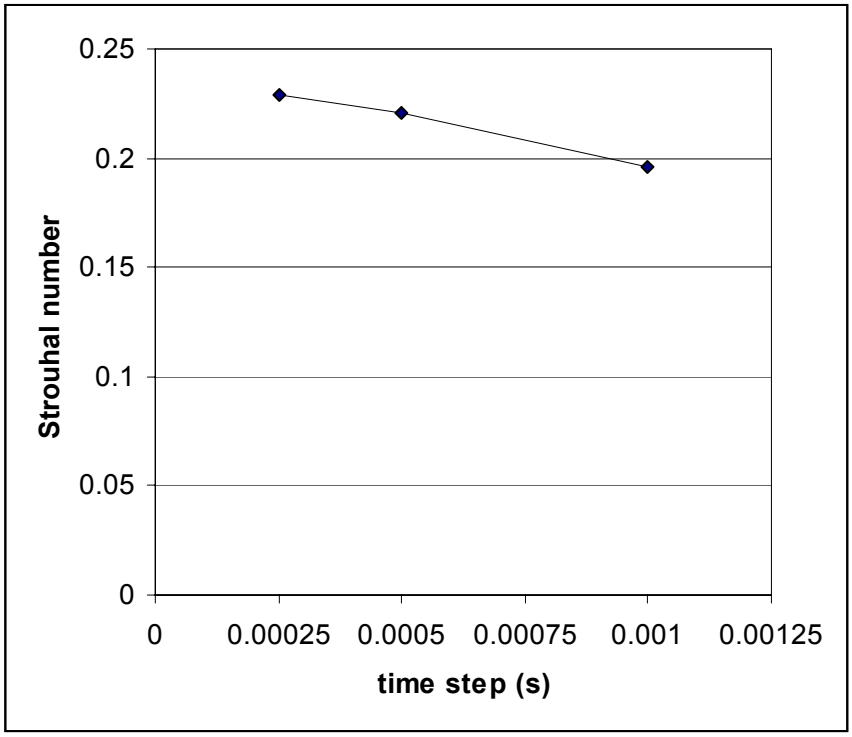

Figure 4.2.8 – Effect of time step on predicted Strouhal number for the PARAD1 model

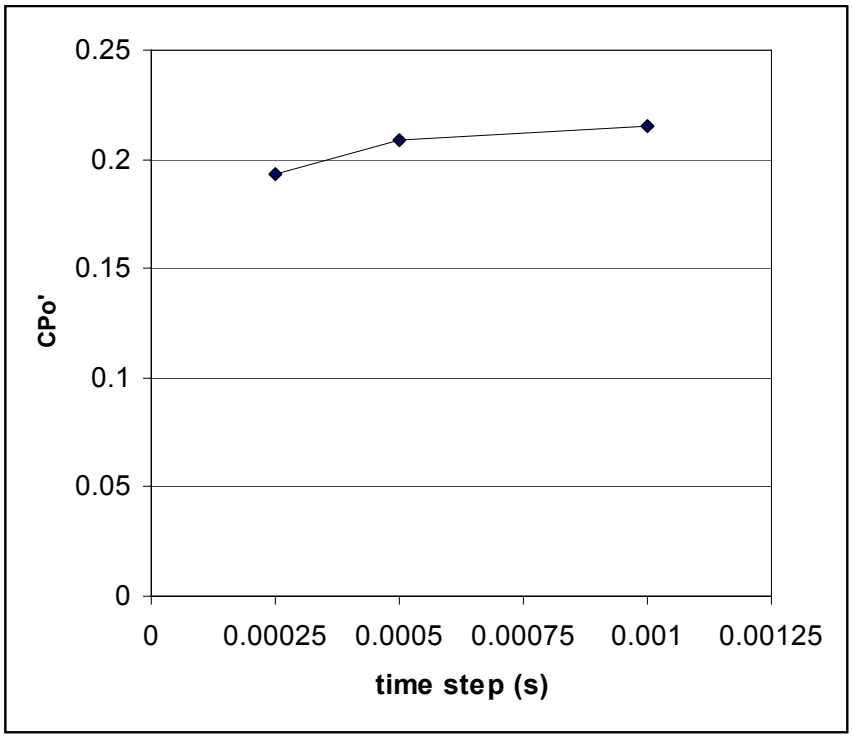

Figure 4.2.9 – Effect of time step on predicted total pressure coefficient fluctuation at x/W=0.3, z/W=2.0 in the wake of the PARAD1 model

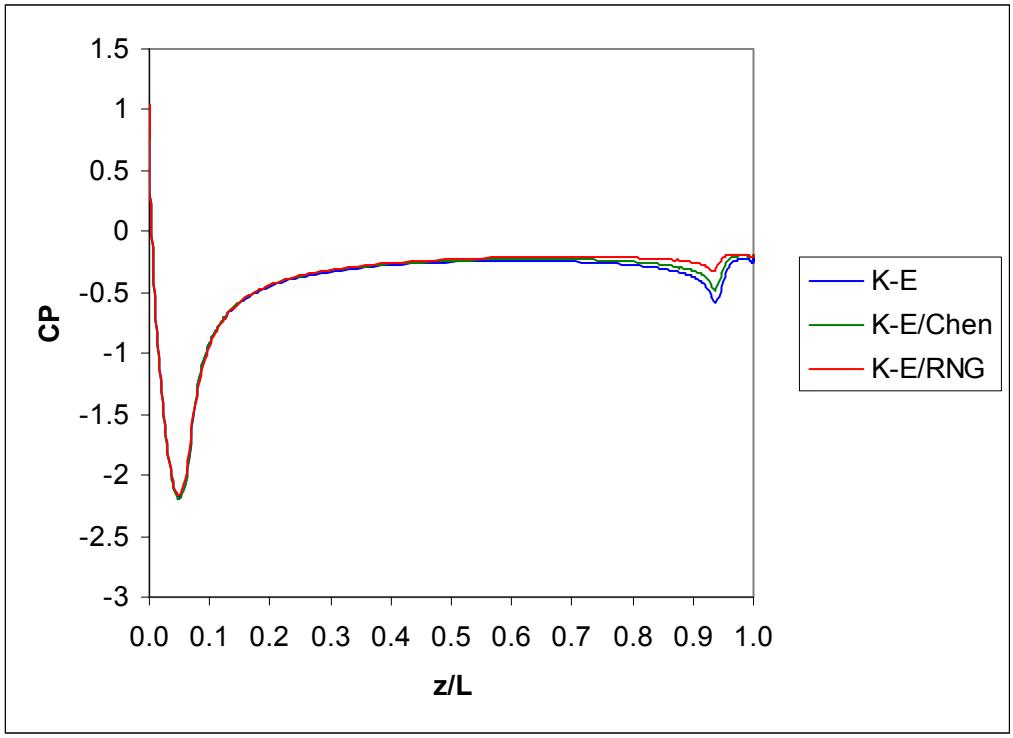

Figure 4.2.10 – Effect of turbulence model on PARAD1 surface pressure distribution for steady simulations

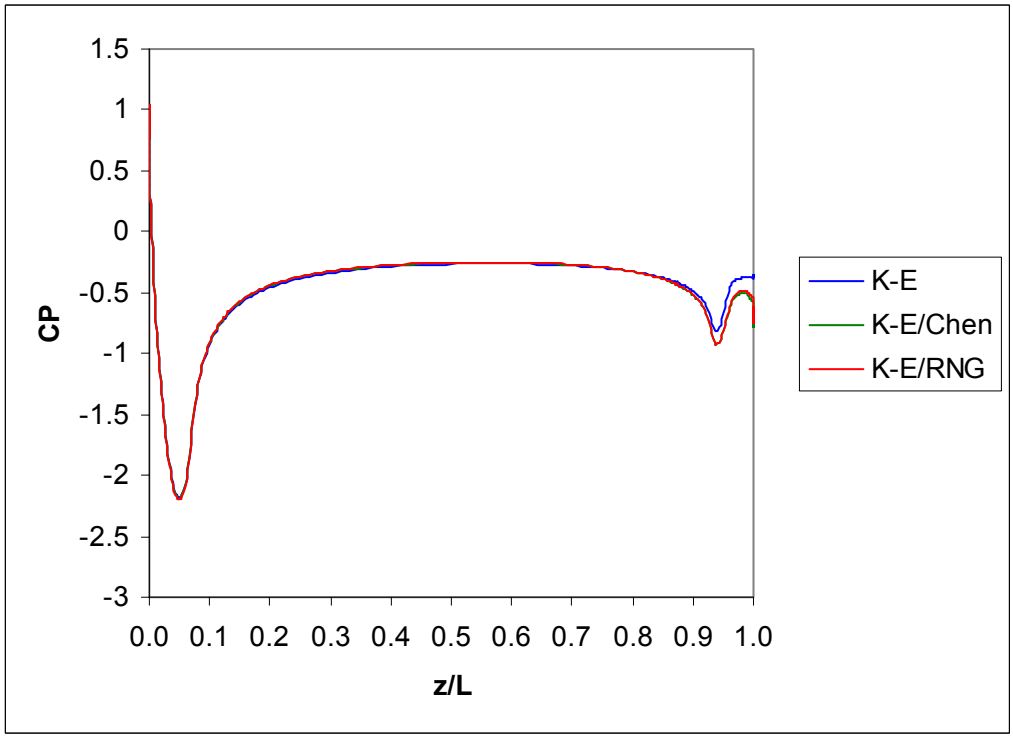

Figure 4.2.11 – Effect of turbulence model on PARAD1 time-averaged surface pressure distribution for unsteady simulations (Δt=0.0005s)

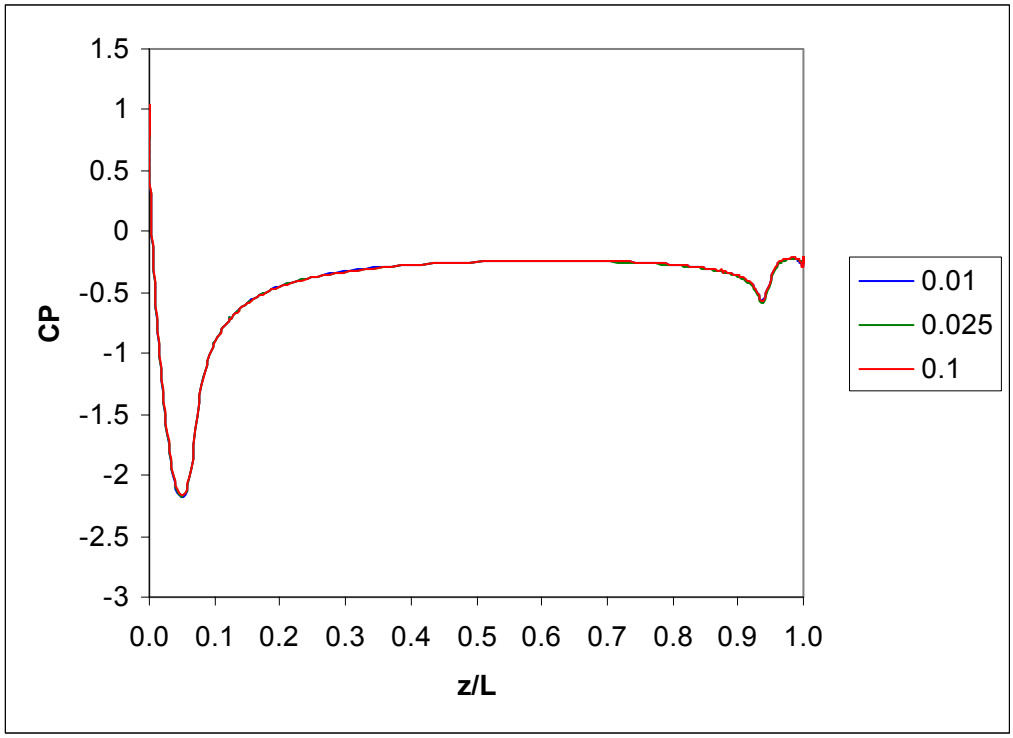

Figure 4.2.12 – Effect of inlet turbulence intensity on the predicted surface pressure distribution around the PARAD1 model (steady solution, k-ε turbulence model)

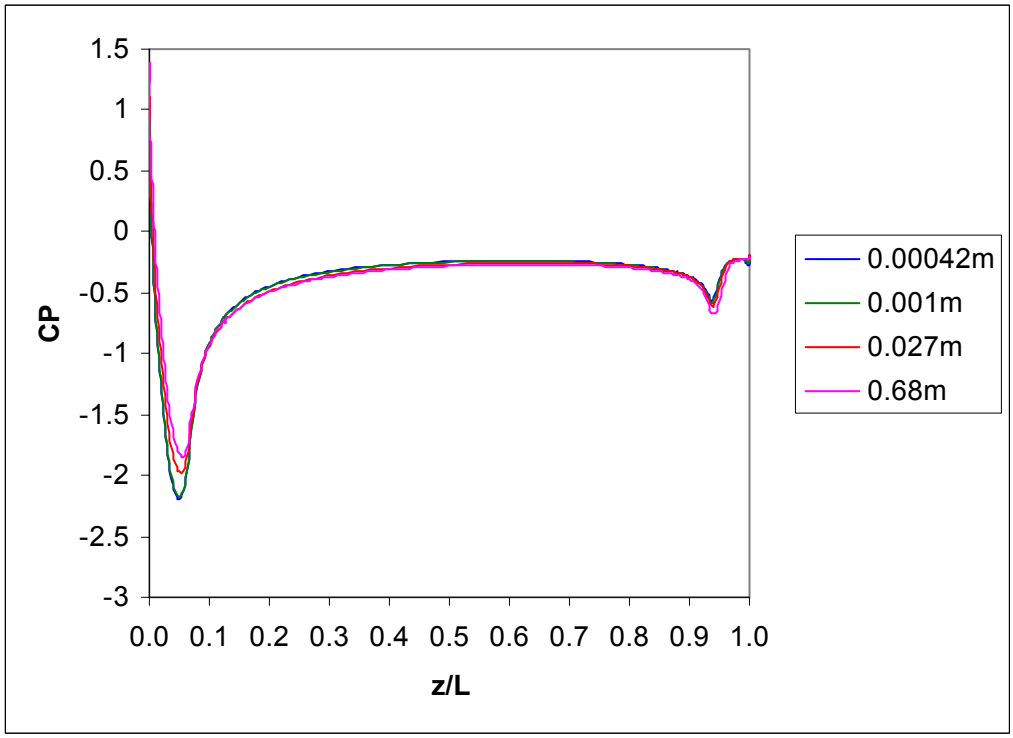

Figure 4.2.13 – Effect of inlet turbulence length scale on the predicted surface pressure distribution around the PARAD1 model (steady solution, k-ε turb. model)

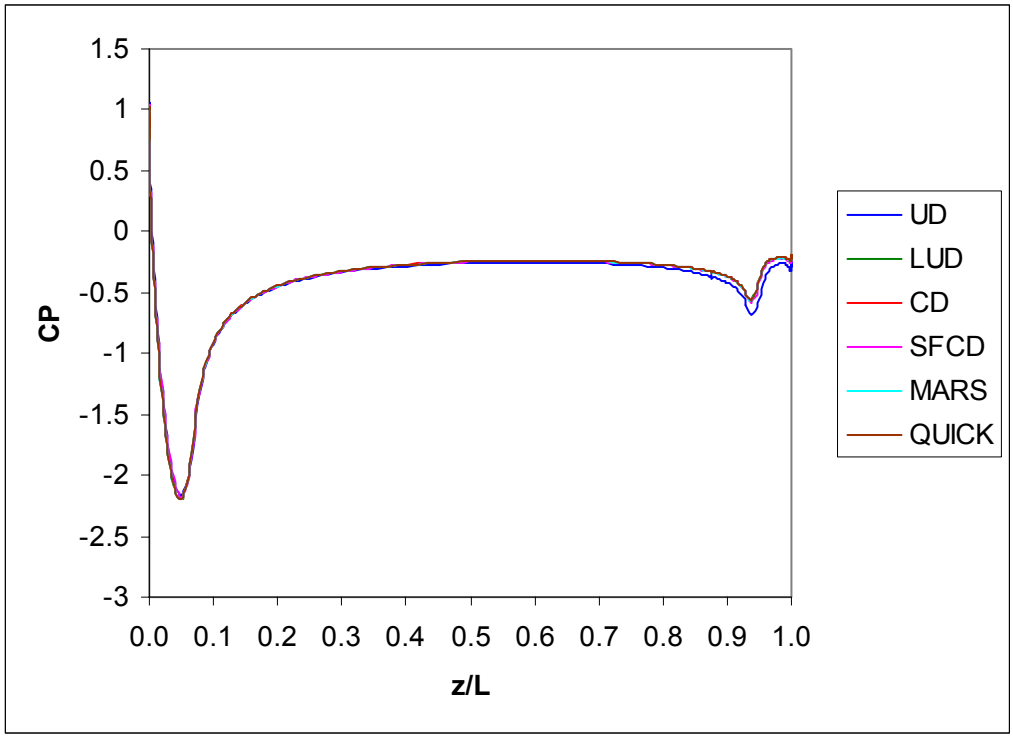

Figure 4.2.14 – Effect of spatial differencing scheme for momentum terms on surface pressure distribution around the PARAD1 model (steady, k-ε turb. model)

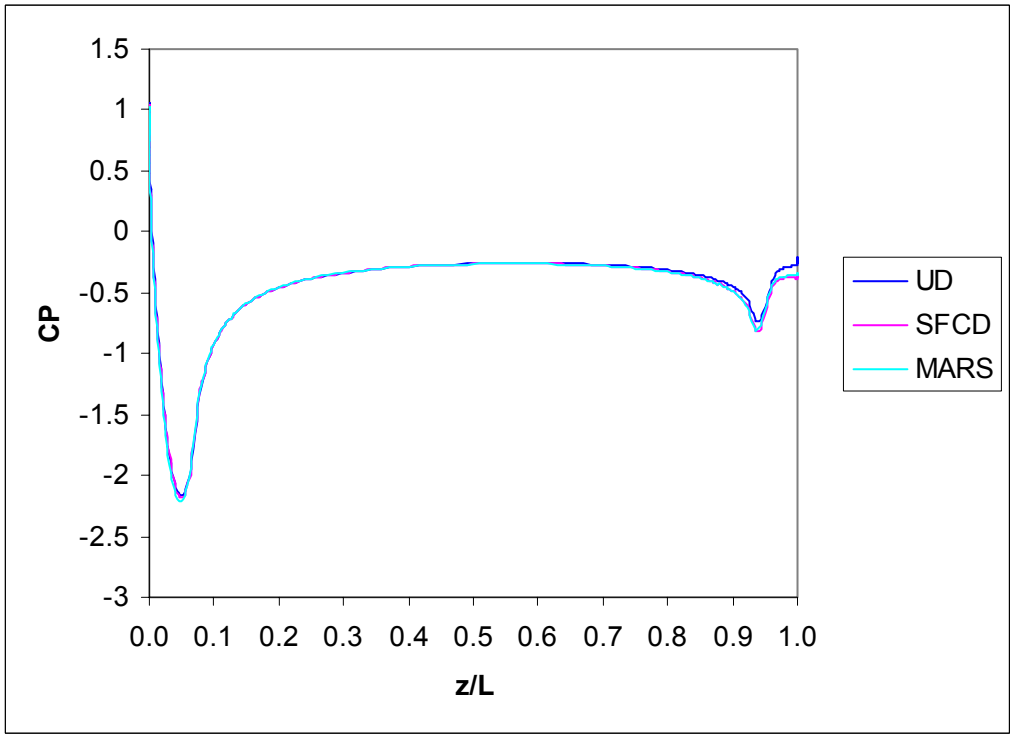

Figure 4.2.15 – Effect of spatial differencing scheme for momentum terms on pressure distribution around the PARAD1 model (time-average, k-ε turb. model)

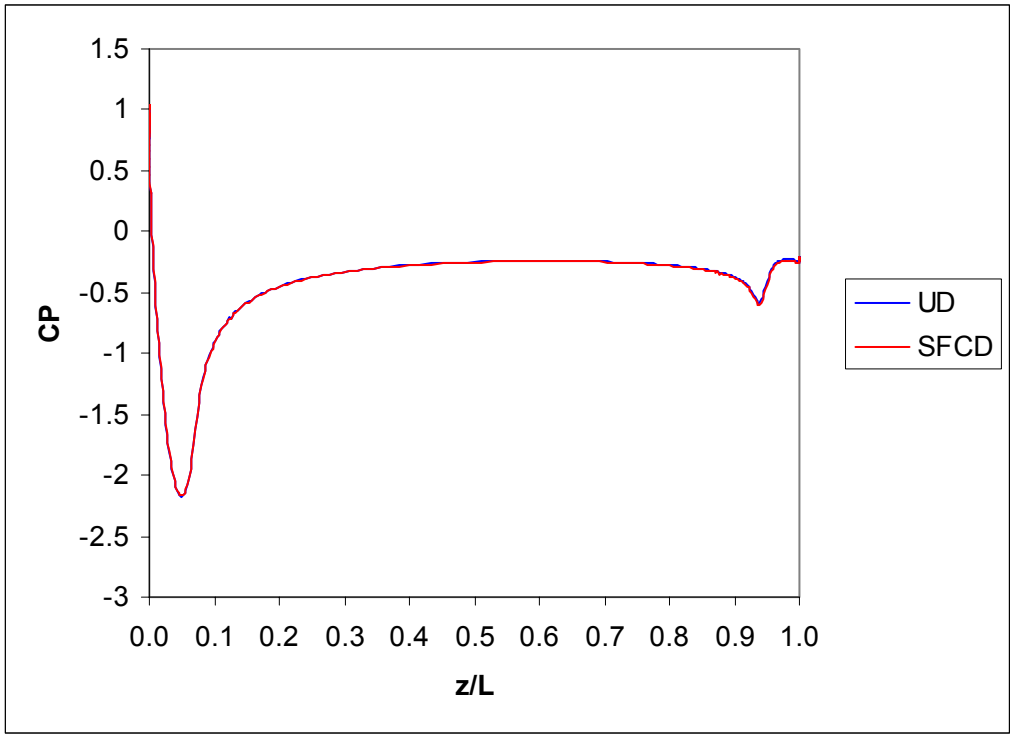

Figure 4.2.16 – Effect of spatial differencing scheme for turbulence quantities on surface pressure distribution around the PARAD1 model (steady solution, k-ε)

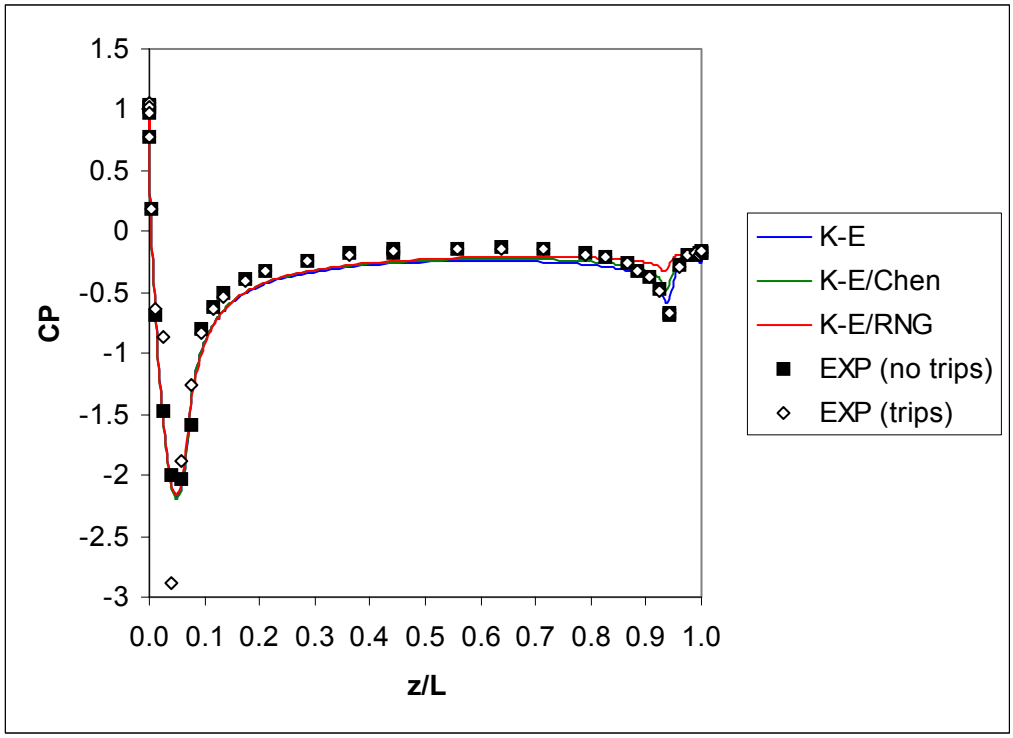

Figure 4.3.1 – PARAD1 model surface pressure distribution; comparison between steady CFD simulations and experiment

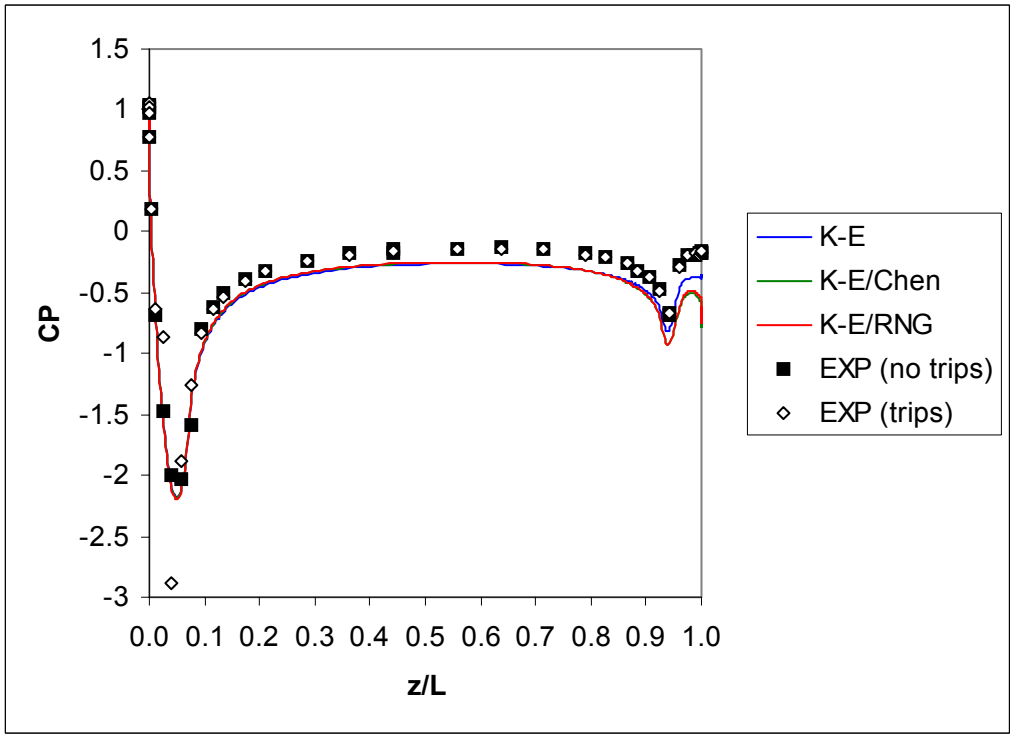

Figure 4.3.2 – PARAD1 model surface pressure distribution; comparison between time-average of unsteady CFD simulations and experiment

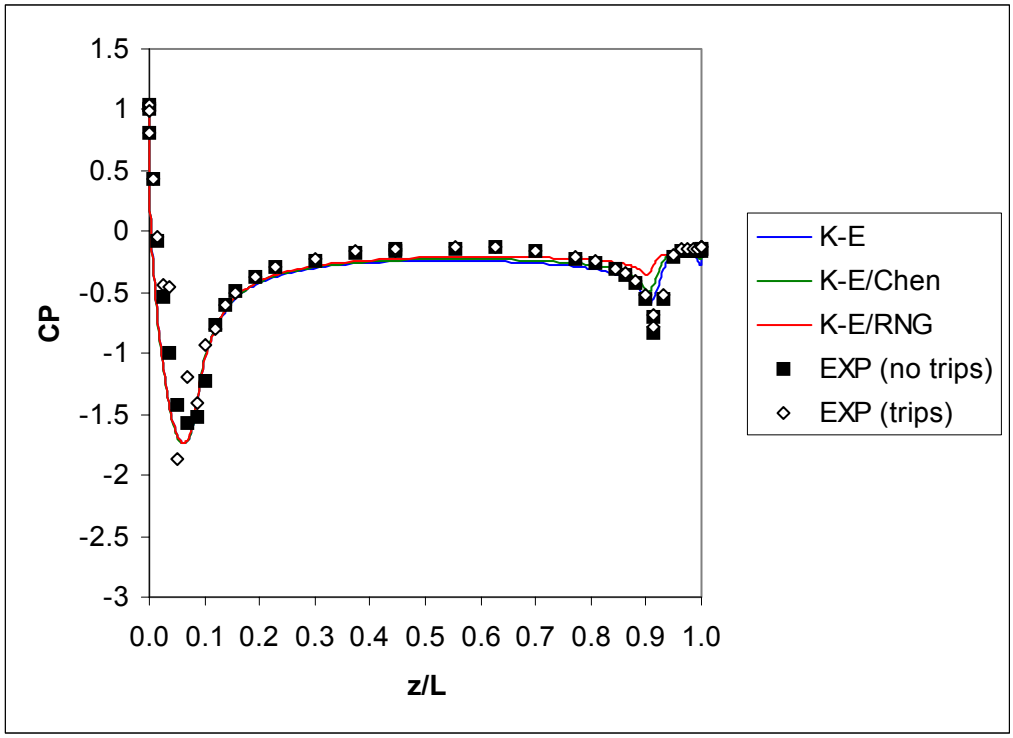

Figure 4.3.3 – PARAD2 model surface pressure distribution; comparison between steady CFD simulations and experiment

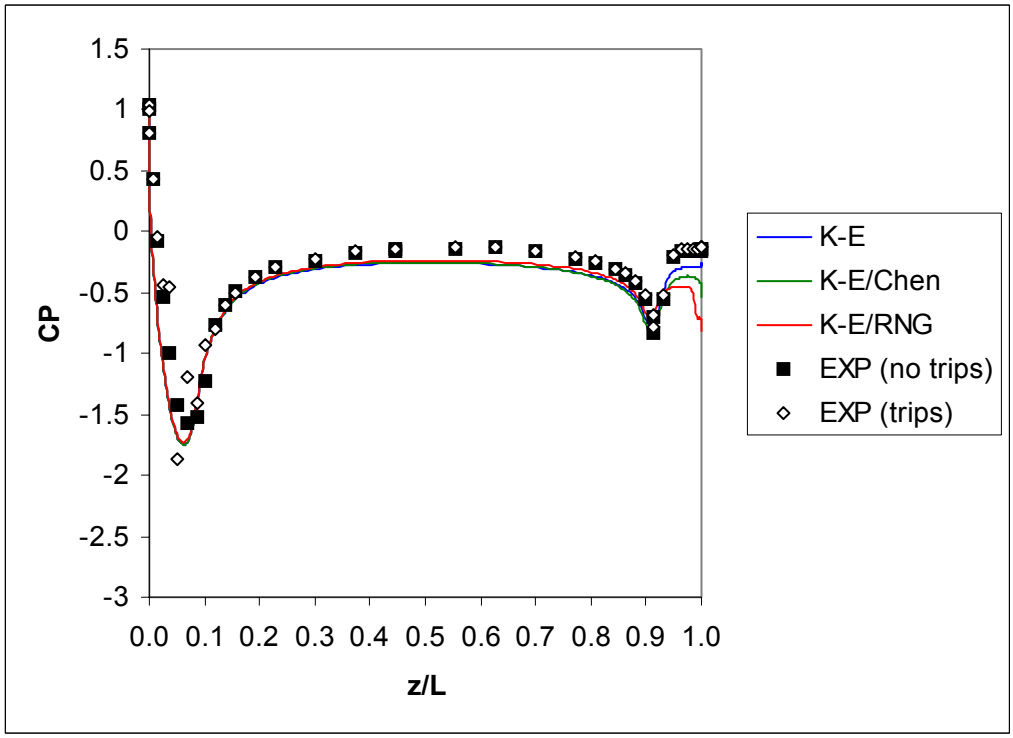

Figure 4.3.4 – PARAD2 model surface pressure distribution; comparison between time-average of unsteady CFD simulations and experiment

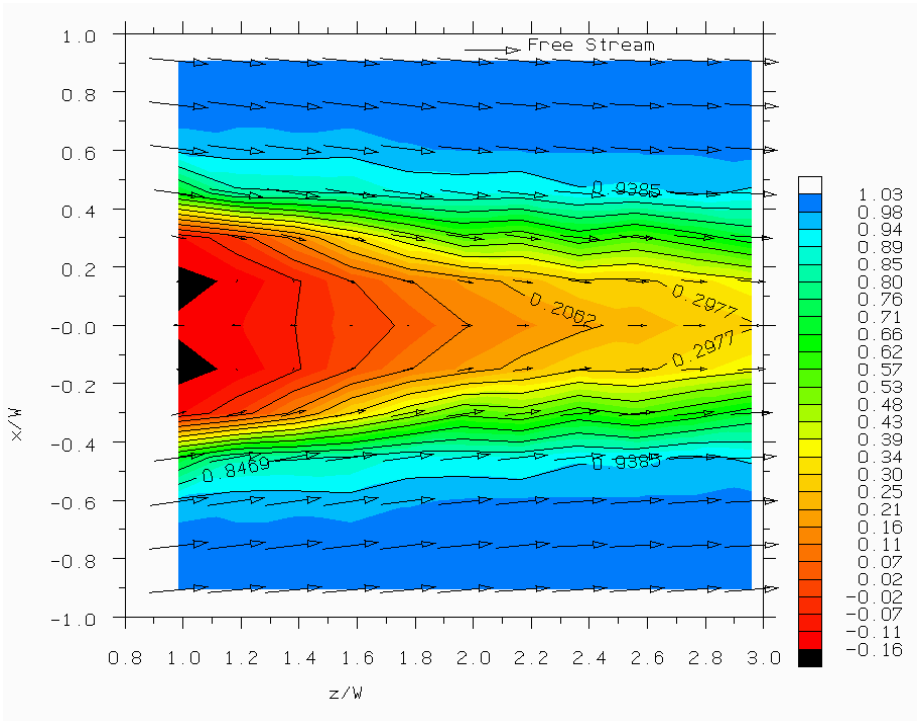

Figure 4.3.5 – PARAD1 model total pressure coefficient and velocity vectors in the wake from steady CFD simulation (k-ε turbulence model)

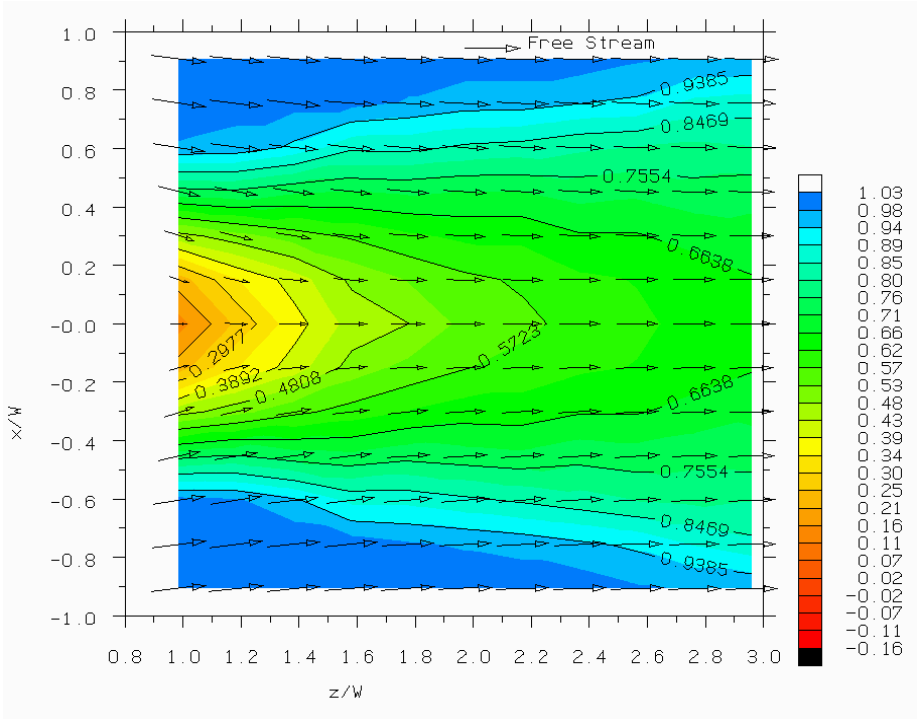

Figure 4.3.6 – PARAD1 model total pressure coefficient and velocity vectors in the wake; time-average of unsteady CFD simulation (k-ε turbulence model)

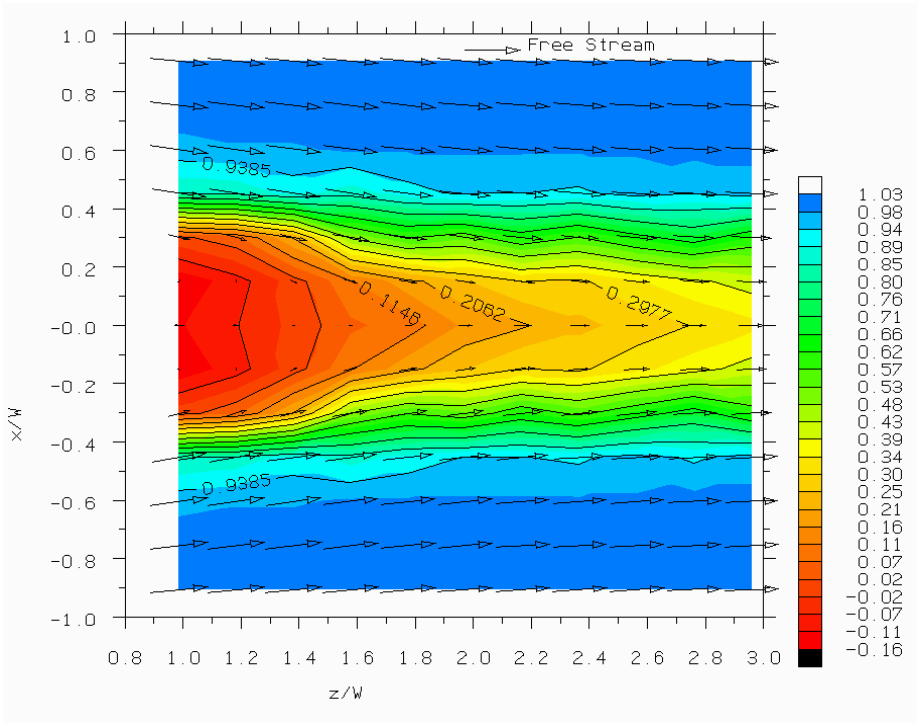

Figure 4.3.7 – PARAD2 model total pressure coefficient and velocity vectors in the wake from steady CFD simulation (k-ε turbulence model)

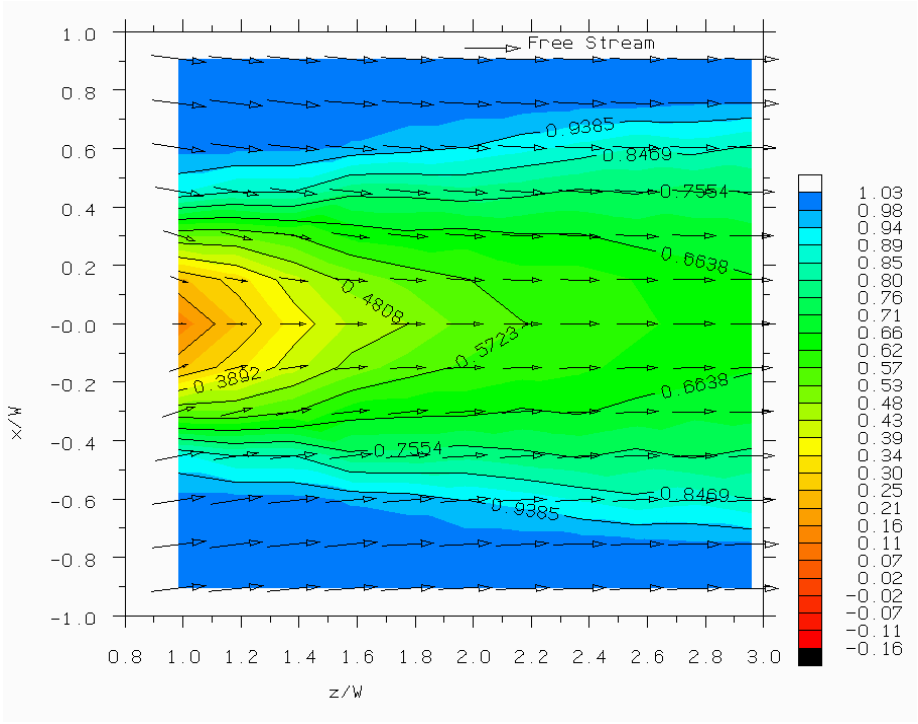

Figure 4.3.8 – PARAD2 model total pressure coefficient and velocity vectors in the wake; time-average of unsteady CFD simulation (k-ε turbulence model)

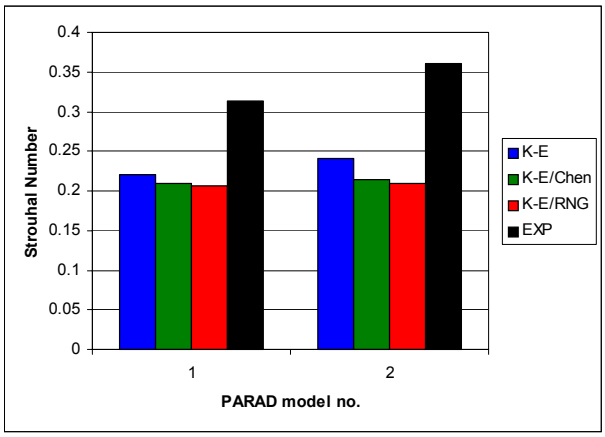

Figure 4.3.9 – Predicted and measured Strouhal number for the PARAD1 and PARAD2 models

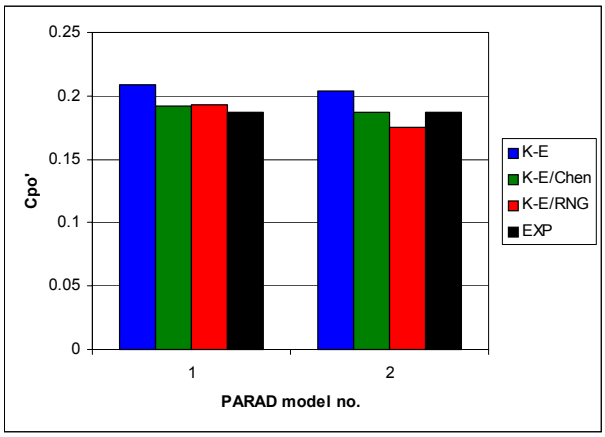

Figure 4.3.10 – Predicted and measured total pressure coefficient fluctuation near the shedding frequency at x/W=0.3, z/W=2.0 in the wake of the PARAD1 and PARAD2 models

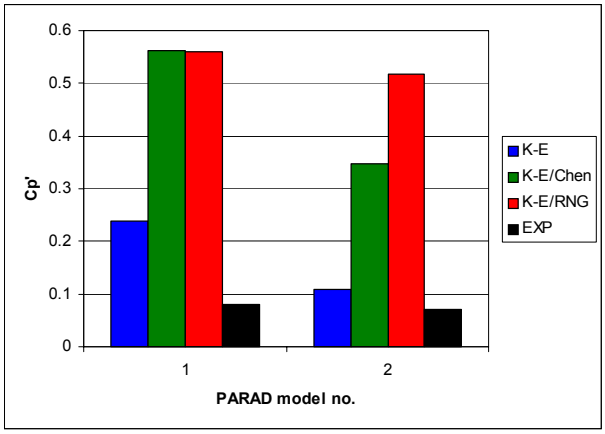

Figure 4.3.11 – Predicted and measured static pressure coefficient fluctuation near the suction spike at the rear of the PARAD1 and PARAD2 models

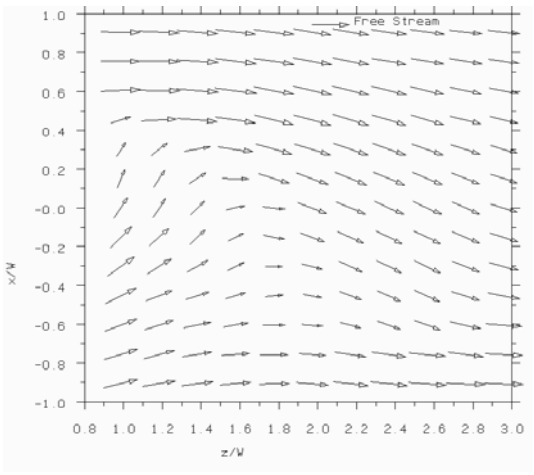

Figure 4.3.12a) t=0.0s, t/T=0.0

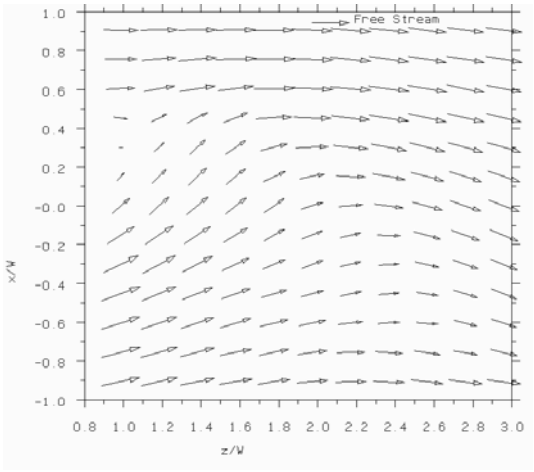

Figure 4.3.12b) t=0.004s, t/T=0.16

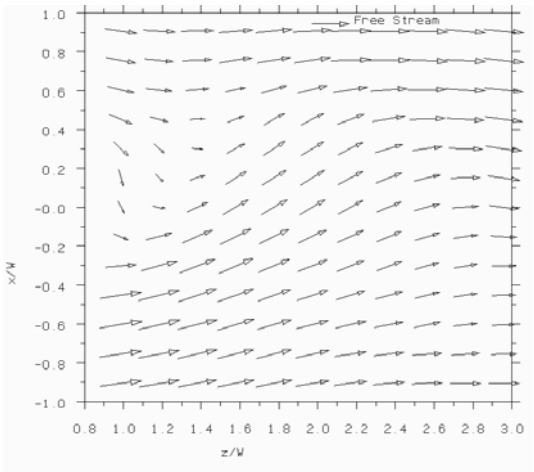

Figure 4.3.12c) t=0.008s, t/T=0.32

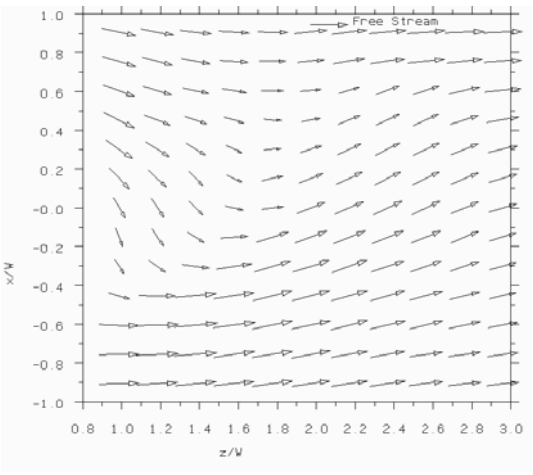

Figure 4.3.12d) t=0.012s, t/T=0.48

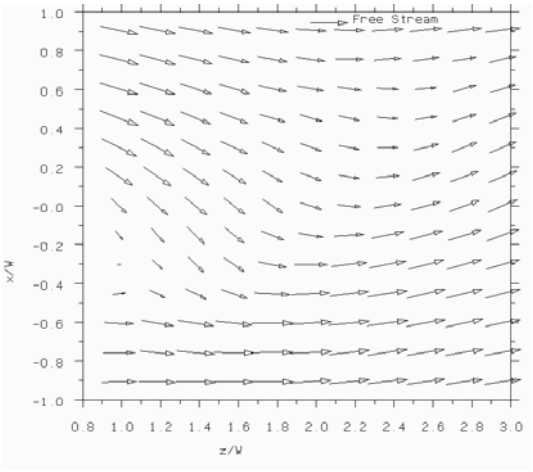

Figure 4.3.12e) t=0.016s, t/T=0.64

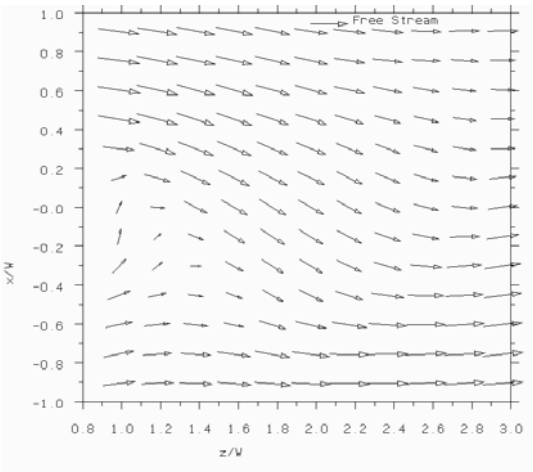

Figure 4.3.12f) t=0.020s, t/T=0.80

Figure 4.3.12 - Sequence showing velocity vectors over one shedding period in the wake of the PARAD1 model (k-ε turbulence model)

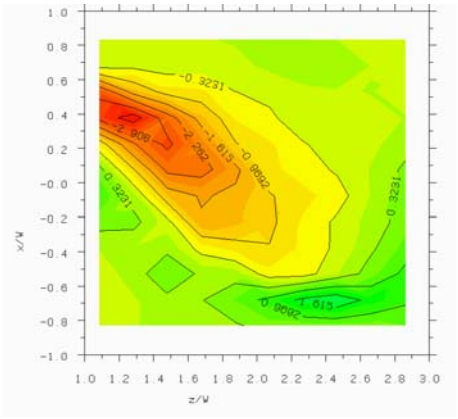

Figure 4.3.13a) t=0.0s, t/T=0.0

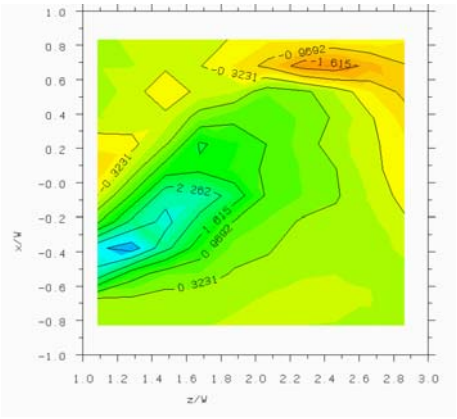

Figure 4.3.13d) t=0.012s, t/T=0.48

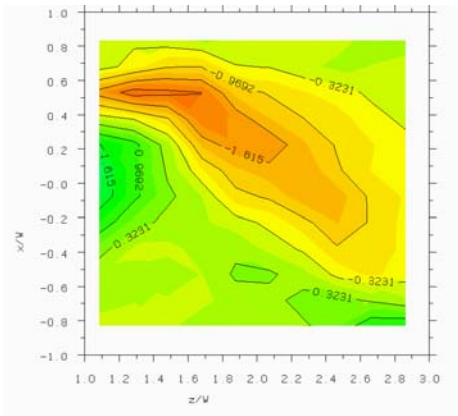

Figure 4.3.13b) t=0.004s, t/T=0.16

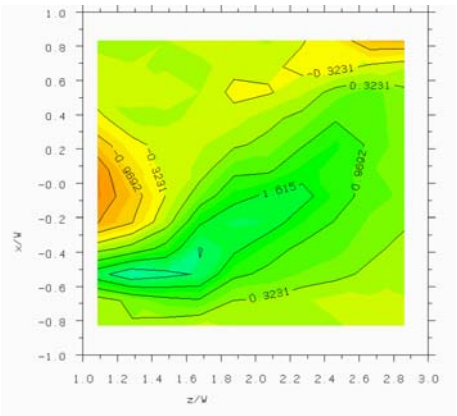

Figure 4.3.13e) t=0.016s, t/T=0.64

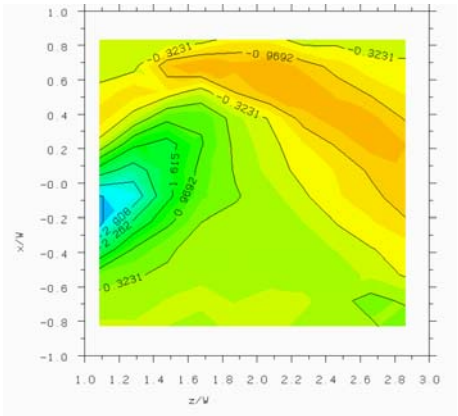

Figure 4.3.13c) t=0.008s, t/T=0.32

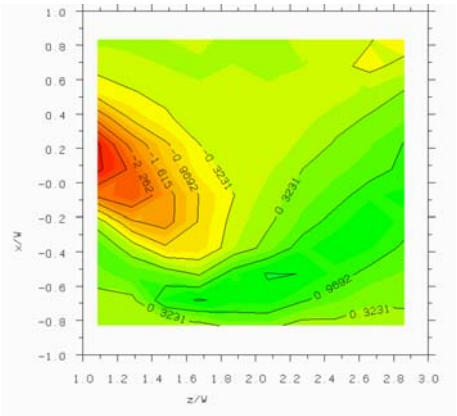

Figure 4.3.13f) t=0.020s, t/T=0.80

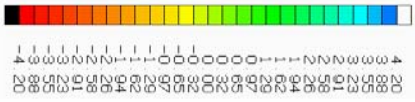

Figure 4.3.13 - Sequence showing vorticity (non-dimensionalised by free stream velocity and model width) over one shedding period in the wake of the PARAD1 model (k-ε turbulence model)

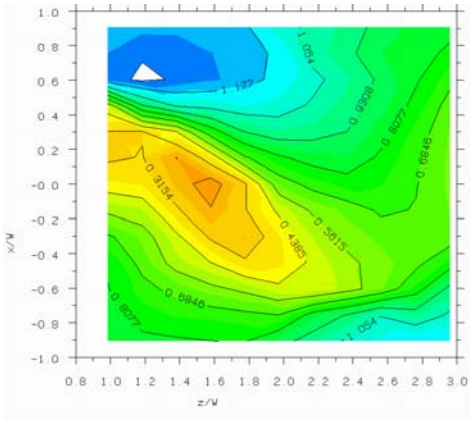

Figure 4.3.14a) t=0.0s, t/T=0.0

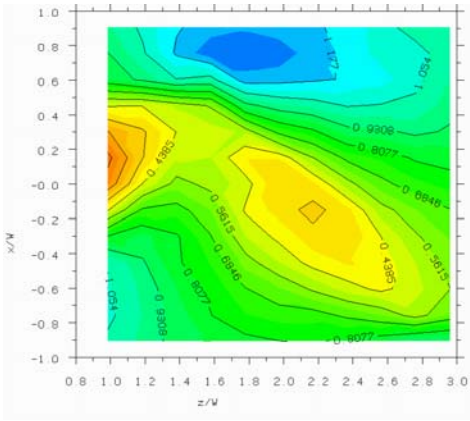

Figure 4.3.14b) t=0.004s, t/T=0.16

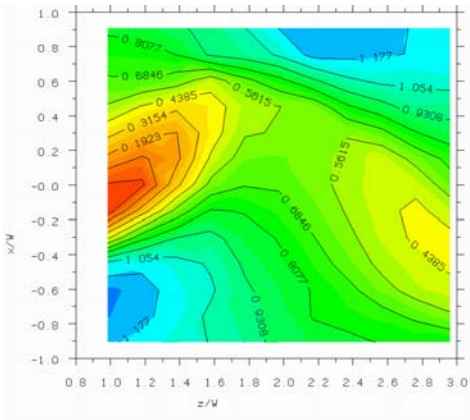

Figure 4.3.14c) t=0.008s, t/T=0.32

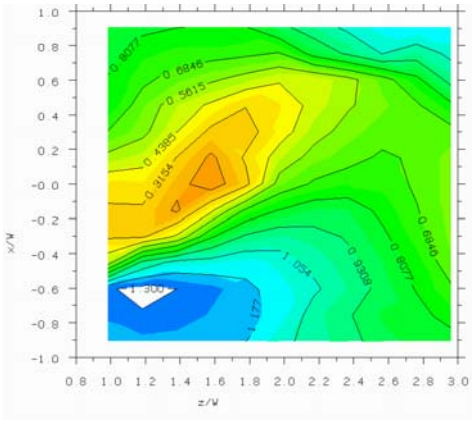

Figure 4.3.14d) t=0.012s, t/T=0.48

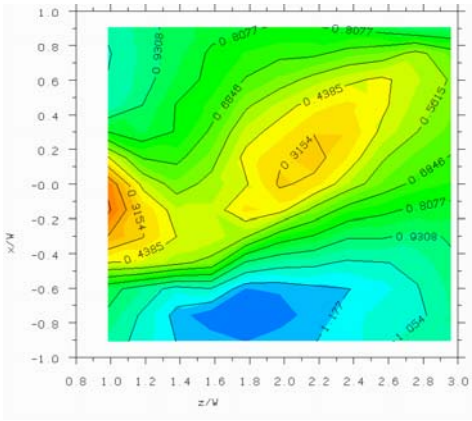

Figure 4.3.14e) t=0.016s, t/T=0.64

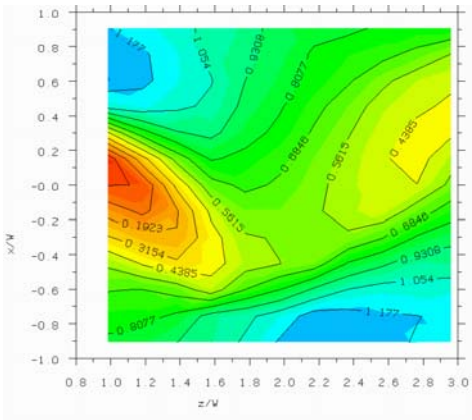

Figure 4.3.14f) t=0.020s, t/T=0.80

Figure 4.3.14 - Sequence showing total pressure coefficient over one shedding period in the wake of the PARAD1 model (k-ε turbulence model)

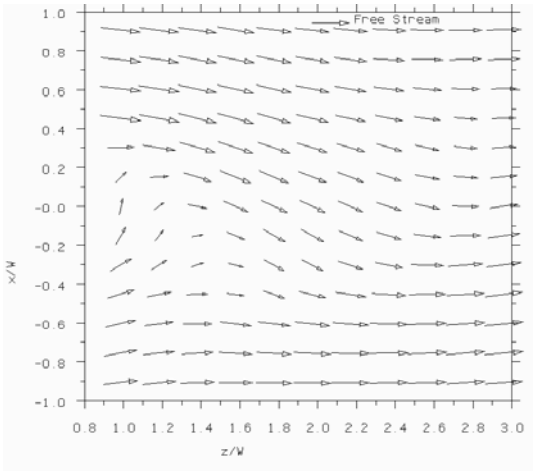

Figure 4.3.15a) t=0.0s, t/T=0.0

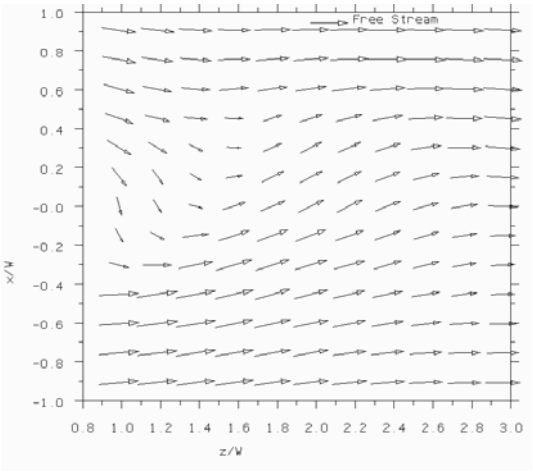

Figure 4.3.15d) t=0.012s, t/T=0.55

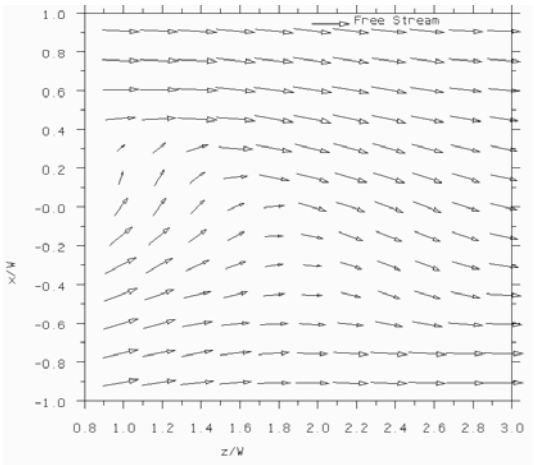

Figure 4.3.15b) t=0.004s, t/T=0.18

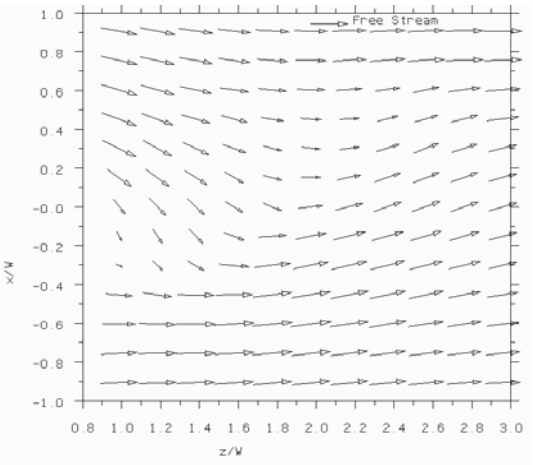

Figure 4.3.15e) t=0.016s, t/T=0.73

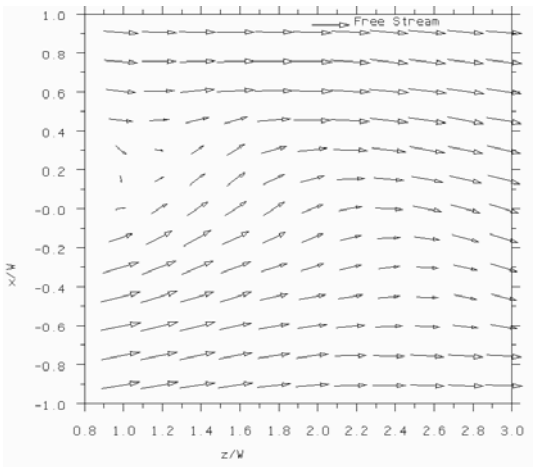

Figure 4.3.15c) t=0.008s, t/T=0.36

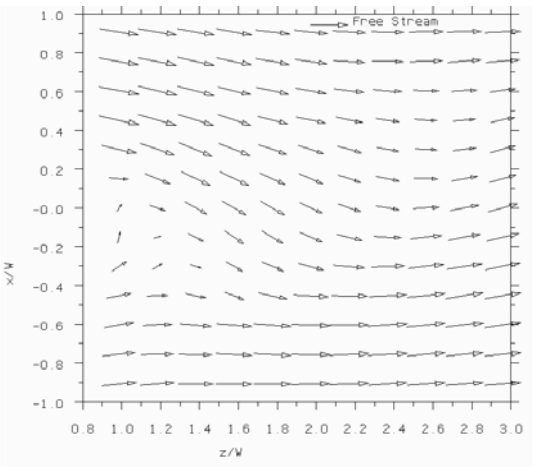

Figure 4.3.15f) t=0.020s, t/T=0.90

Figure 4.3.15 - Sequence showing velocity vectors over one shedding period in the wake of the PARAD2 model (k-ε turbulence model)

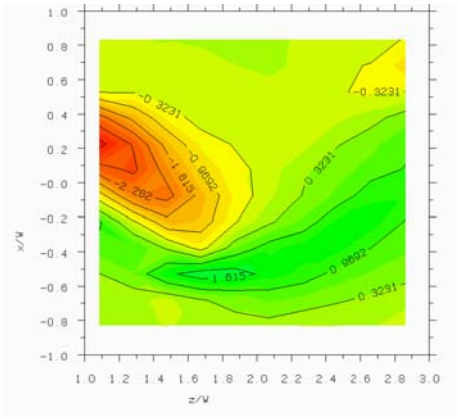

Figure 4.3.16a) t=0.0s, t/T=0.0

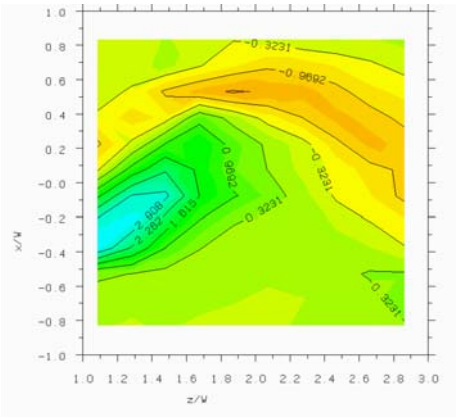

Figure 4.3.16d) t=0.012s, t/T=0.55

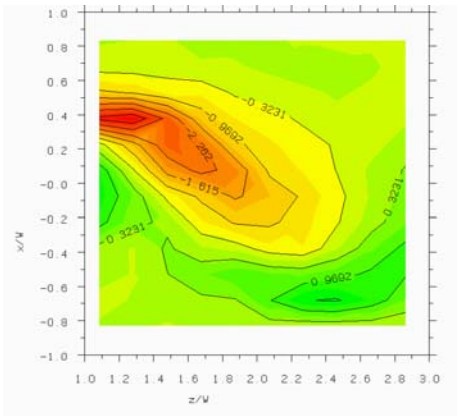

Figure 4.3.16b) t=0.004s, t/T=0.18

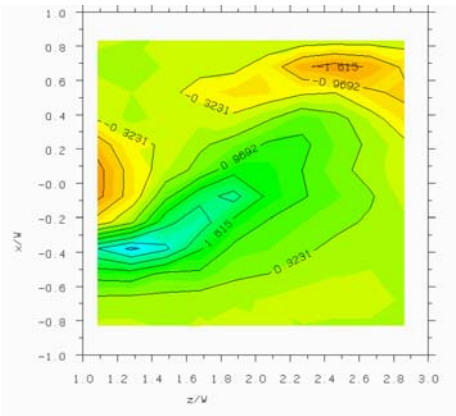

Figure 4.3.16e) t=0.016s, t/T=0.73

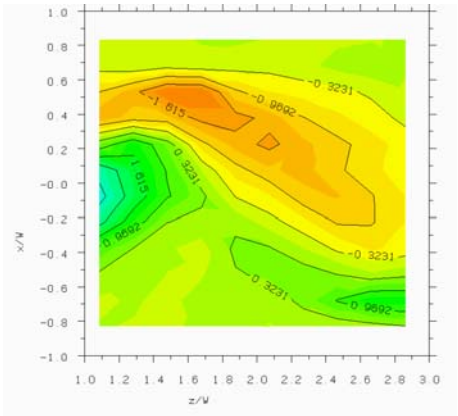

Figure 4.3.16c) t=0.008s, t/T=0.36

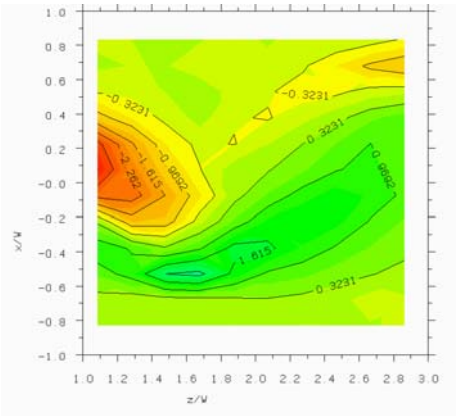

Figure 4.3.16f) t=0.020s, t/T=0.90

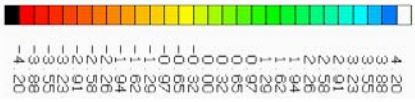

Figure 4.3.16 - Sequence showing vorticity (non-dimensionalised by free stream velocity and model width) over one shedding period in the wake of the PARAD2 model (k-ε turbulence model)

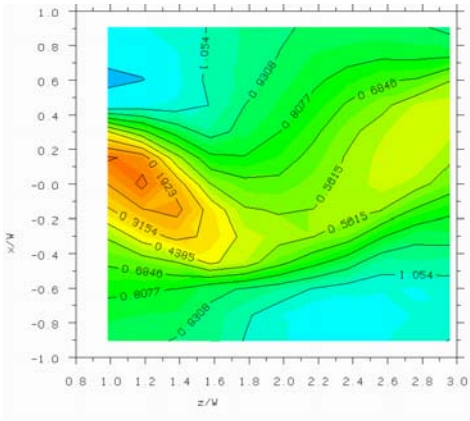

Figure 4.3.17a) t=0.0s, t/T=0.0

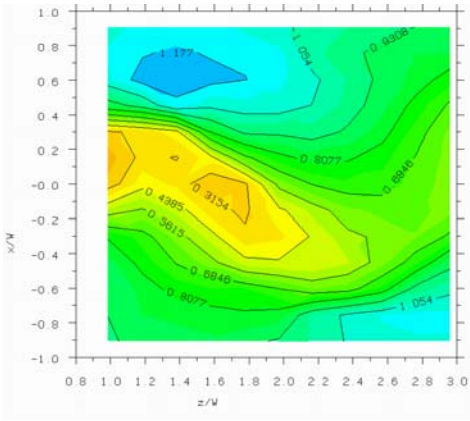

Figure 4.3.17b) t=0.004s, t/T=0.18

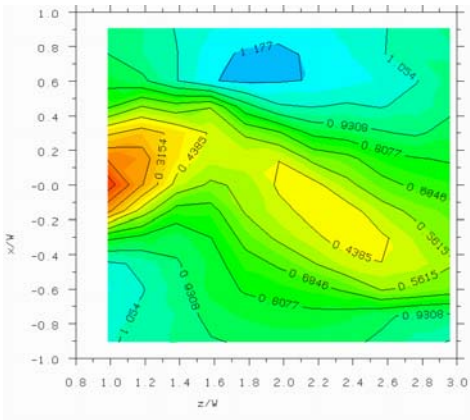

Figure 4.3.17c) t=0.008s, t/T=0.36

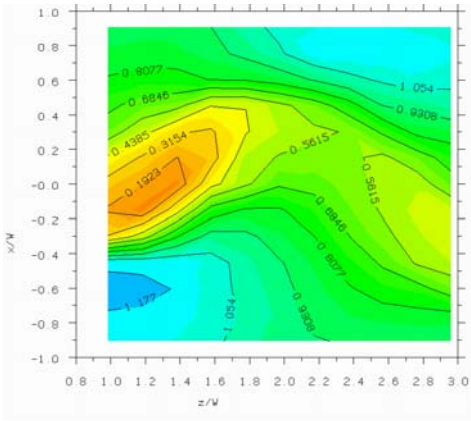

Figure 4.3.17d) t=0.012s, t/T=0.55

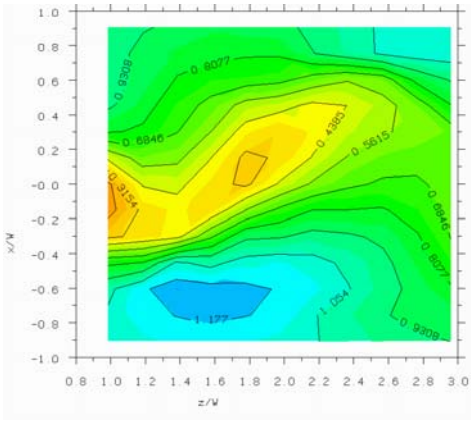

Figure 4.3.17e) t=0.016s, t/T=0.73

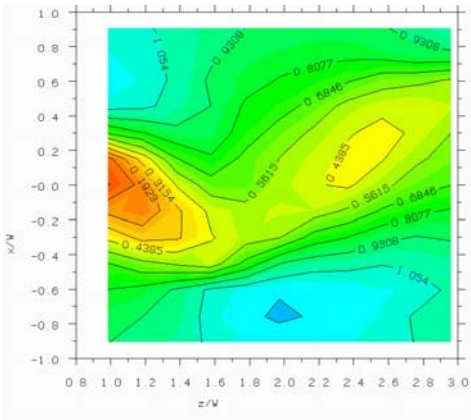

Figure 4.3.17f) t=0.020s, t/T=0.90

Figure 4.3.17 - Sequence showing total pressure coefficient over one shedding period in the wake of the PARAD2 model (k-ε turbulence model)

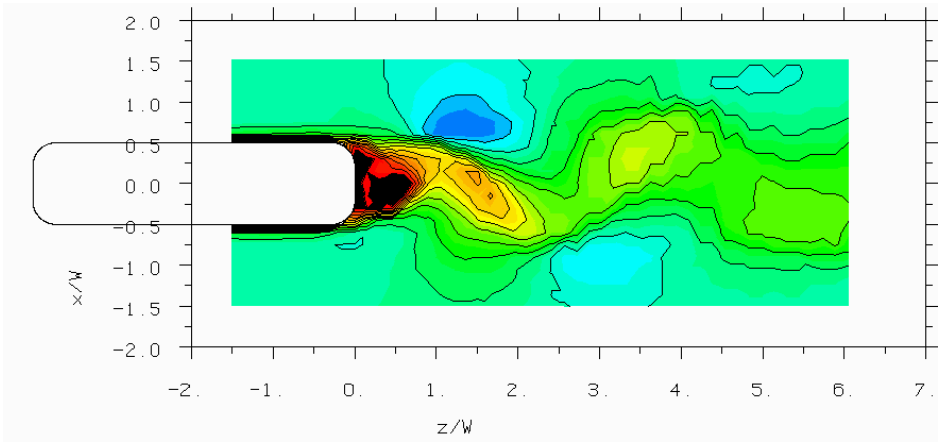

Figure 4.3.18a) t=0.0s, t/T=0.0

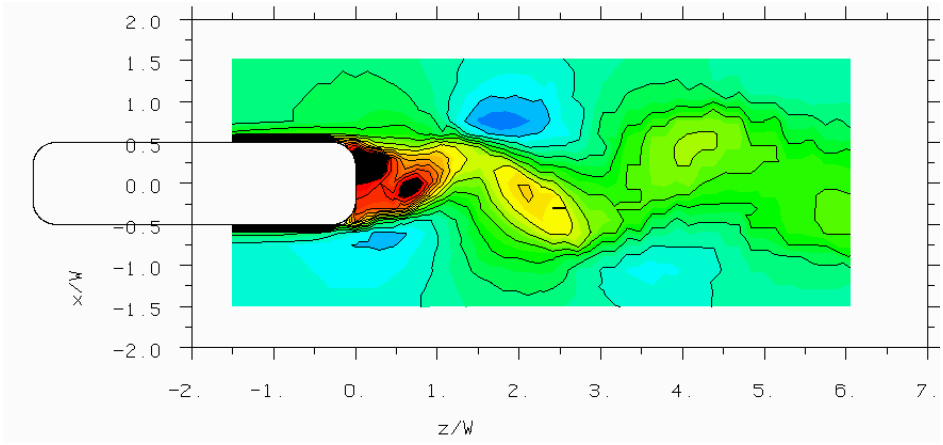

Figure 4.3.18b) t=0.004s, t/T=0.16

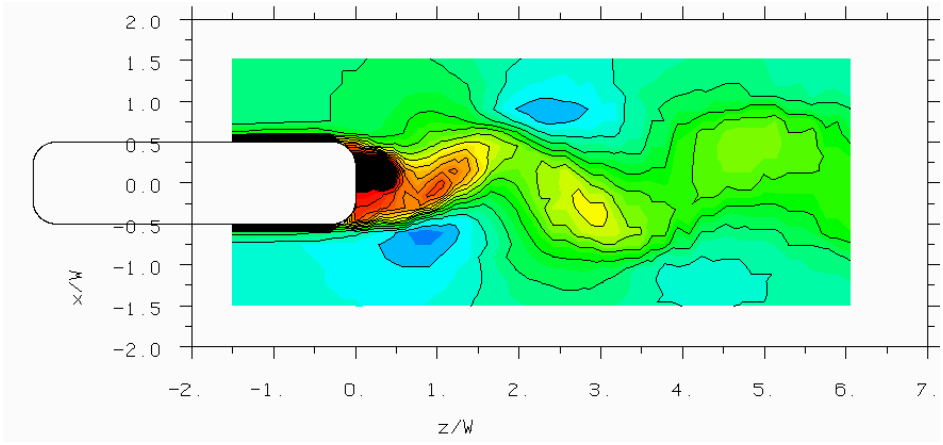

Figure 4.3.18c) t=0.008s, t/T=0.32

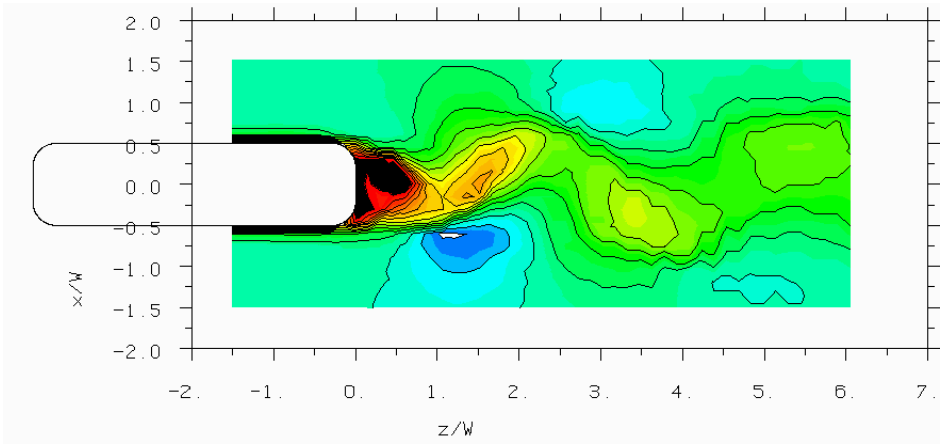

Figure 4.3.18d) t=0.012s, t/T=0.48

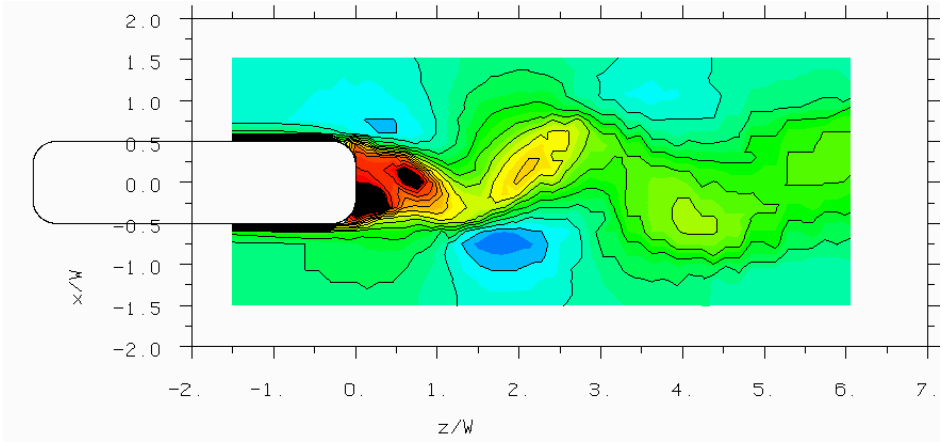

Figure 4.3.18e) t=0.016s, t/T=0.64

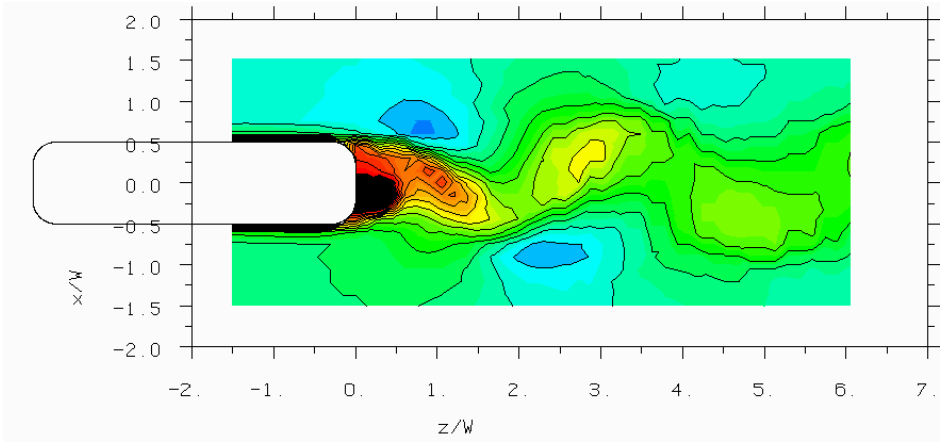

Figure 4.3.18f) t=0.020s, t/T=0.80

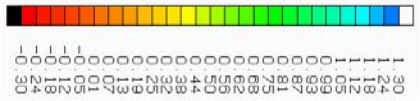

Figure 4.3.18 - Sequence showing total pressure coefficient over one shedding period in the wake of the PARAD1 model (k-ε turbulence model)

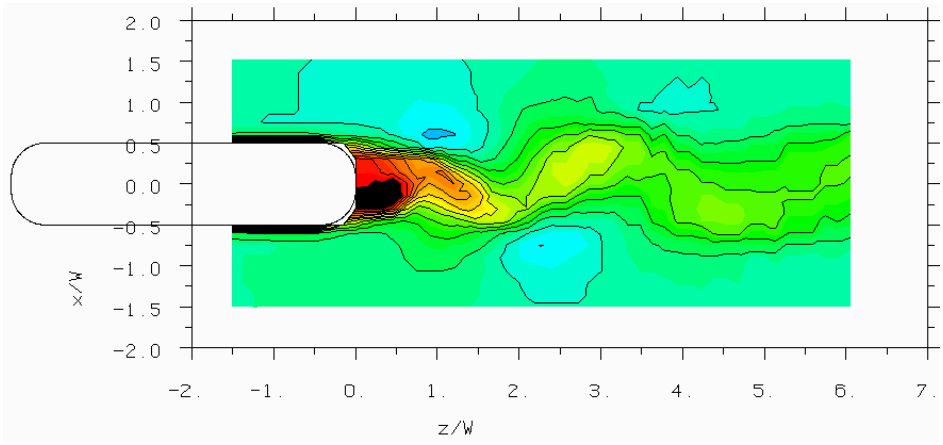

Figure 4.3.19a) t=0.0s, t/T=0.0

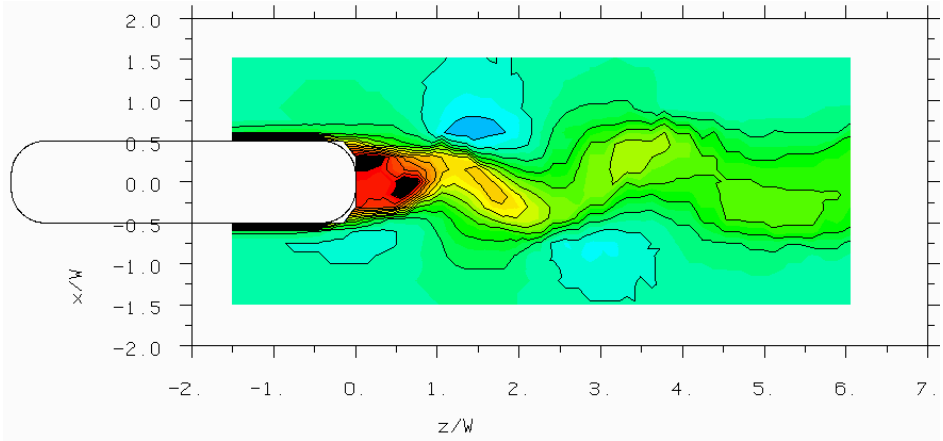

Figure 4.3.19b) t=0.004s, t/T=0.18

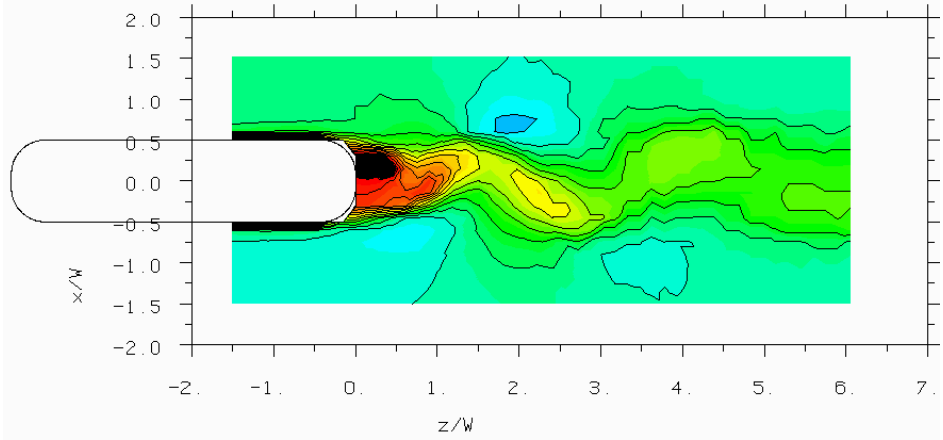

Figure 4.3.19c) t=0.008s, t/T=0.36

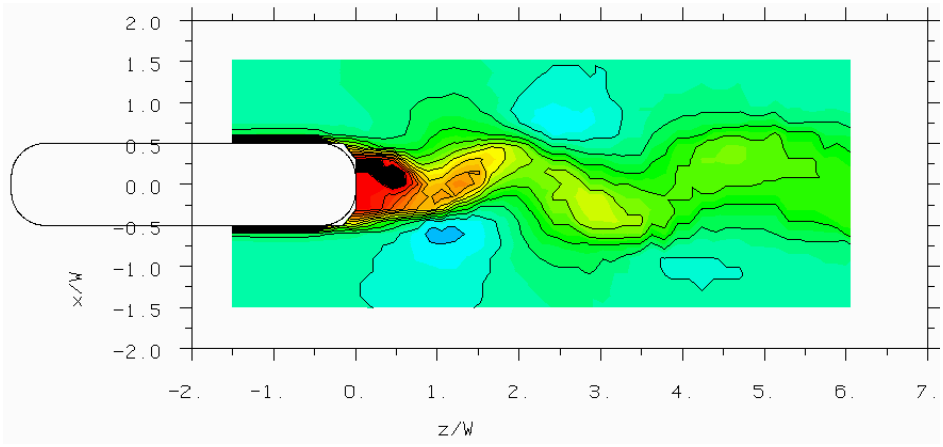

Figure 4.3.19d) t=0.012s, t/T=0.55

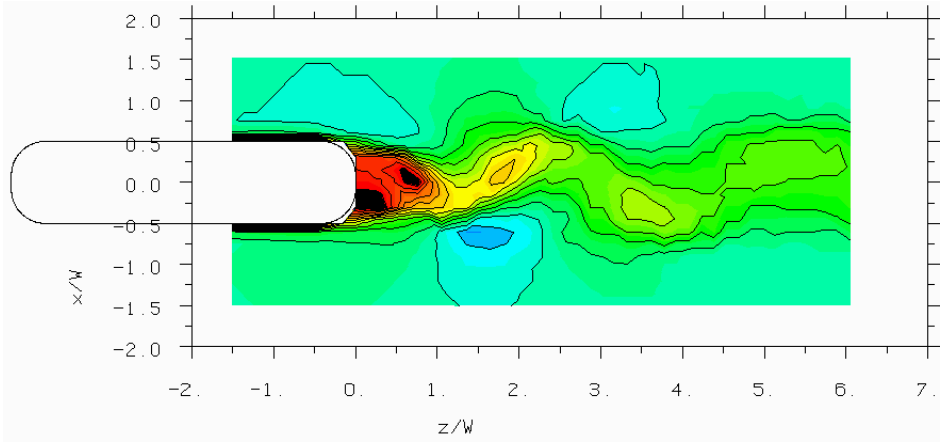

Figure 4.3.19e) t=0.016s, t/T=0.73

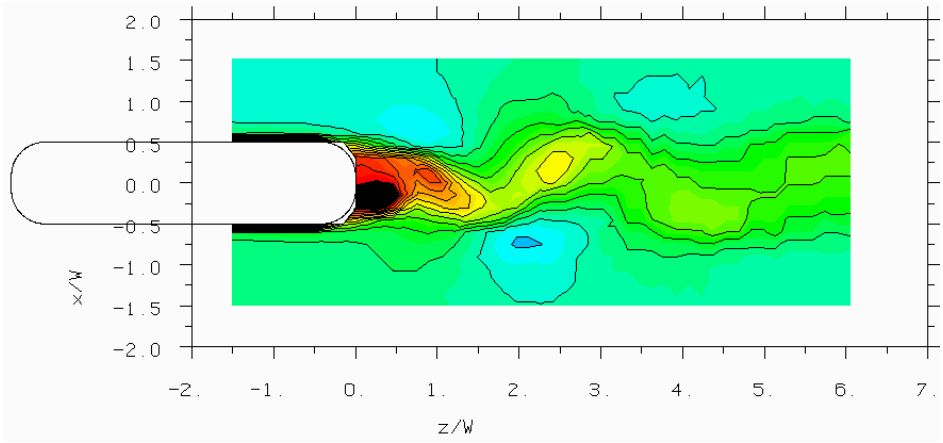

Figure 4.3.19f) t=0.020s, t/T=0.90

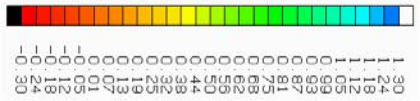

Figure 4.3.19 - Sequence showing total pressure coefficient over one shedding period in the wake of the PARAD2 model (k-ε turbulence model)

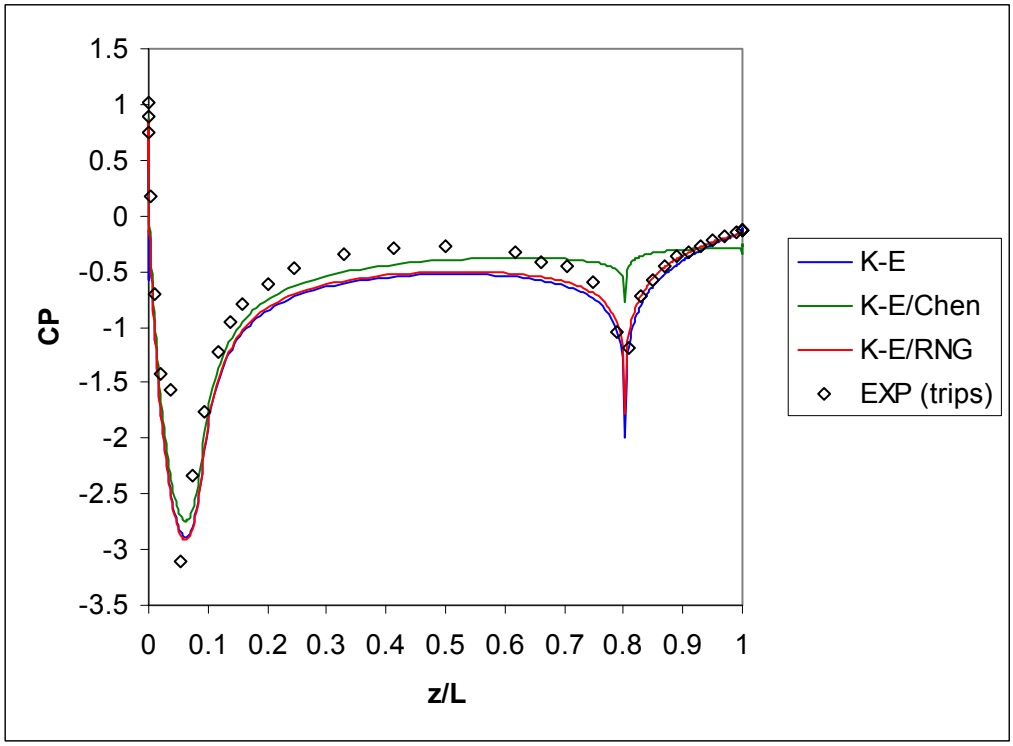

Figure 4.3.20 – 2D Ahmed model, 20° backlight, surface pressure distribution; comparison between steady CFD simulations and experiment

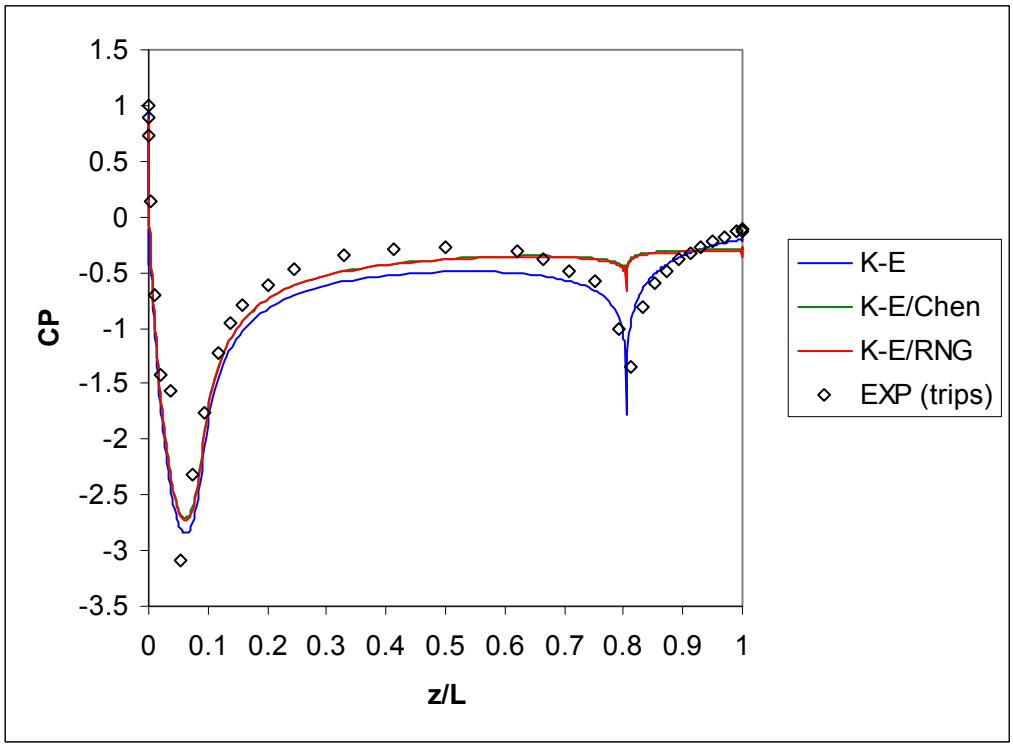

Figure 4.3.21 – 2D Ahmed model, 22.5° backlight, surface pressure distribution; comparison between steady CFD simulations and experiment

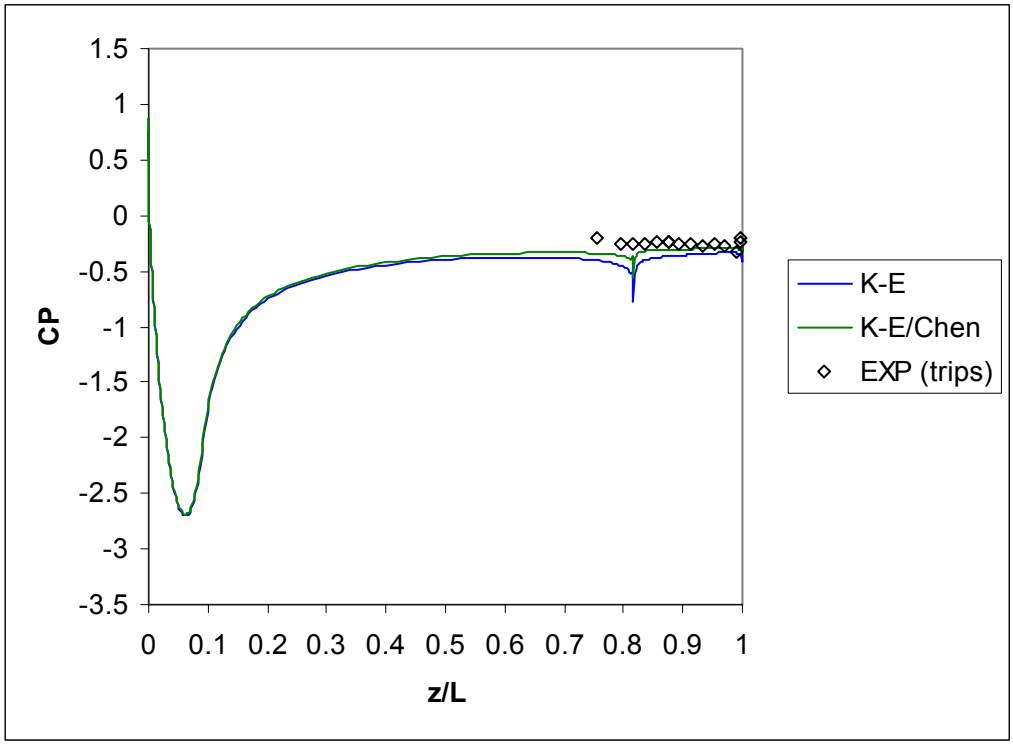

Figure 4.3.22 – 2D Ahmed model, 25° backlight, surface pressure distribution; comparison between steady CFD simulations and experiment

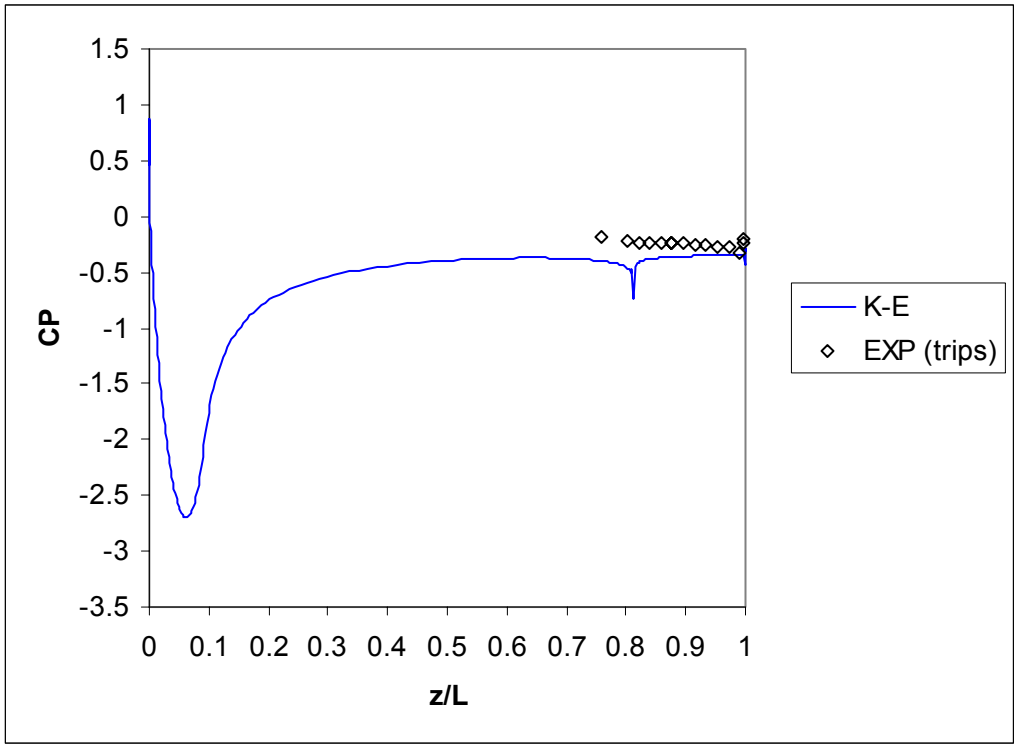

Figure 4.3.23 – 2D Ahmed model, 27.5° backlight, surface pressure distribution; comparison between steady CFD simulation and experiment

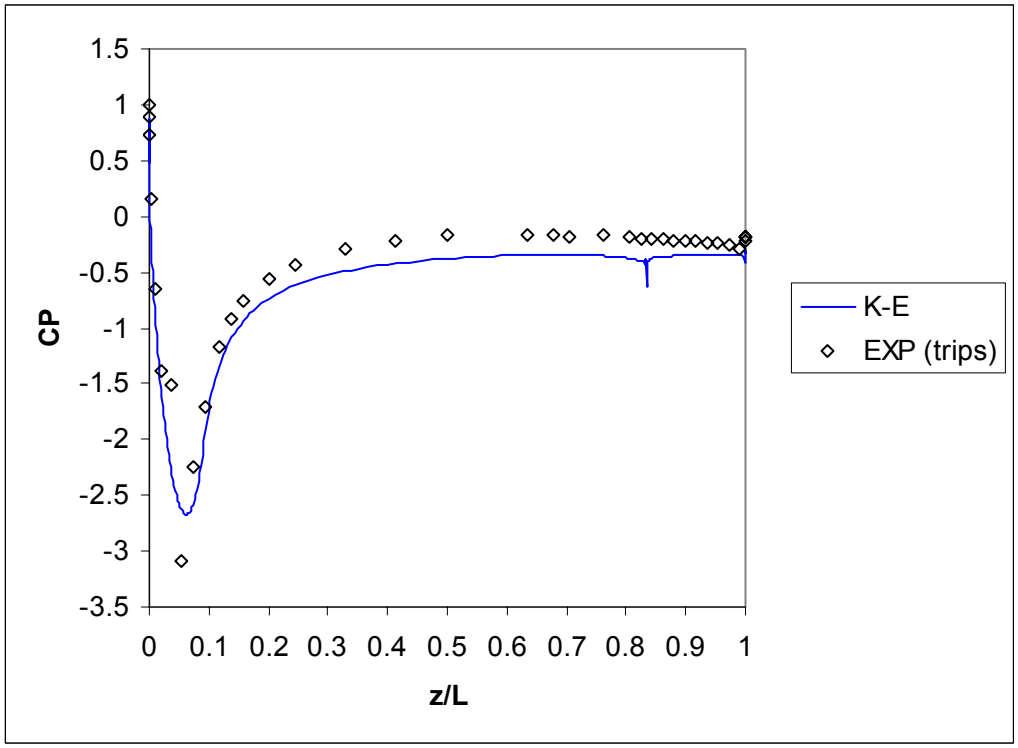

Figure 4.3.24 – 2D Ahmed model, 30° backlight, surface pressure distribution; comparison between steady CFD simulation and experiment

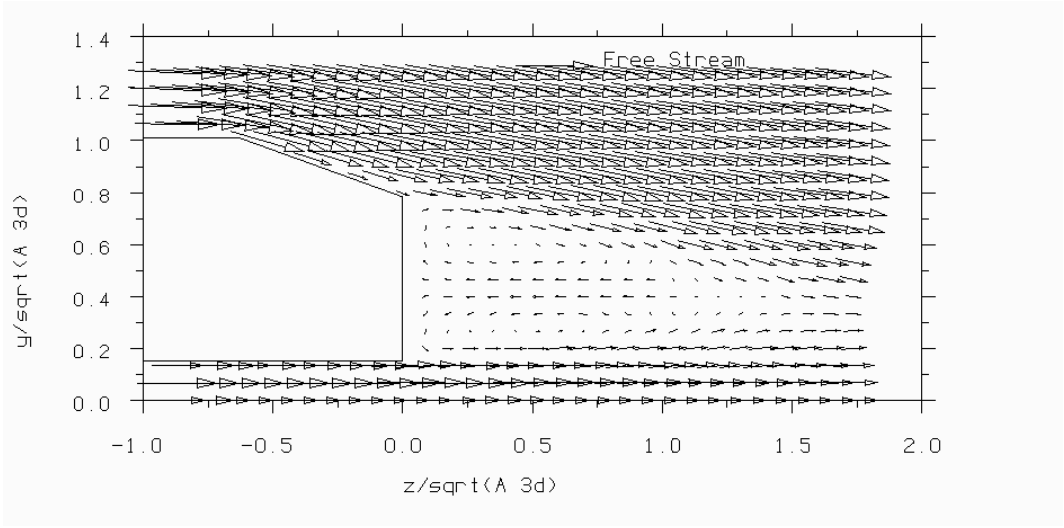

Figure 4.3.25 – Velocity vectors in the wake of the 2D Ahmed model with 20° backlight from steady CFD simulation with k-ε turbulence model

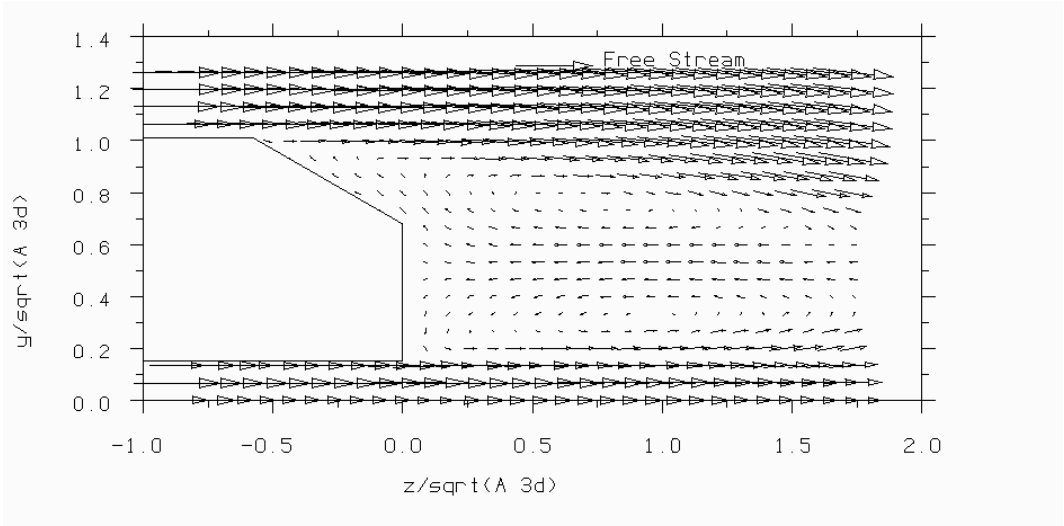

Figure 4.3.26 – Velocity vectors in the wake of the 2D Ahmed model with 30° backlight from steady CFD simulation with k-ε turbulence model

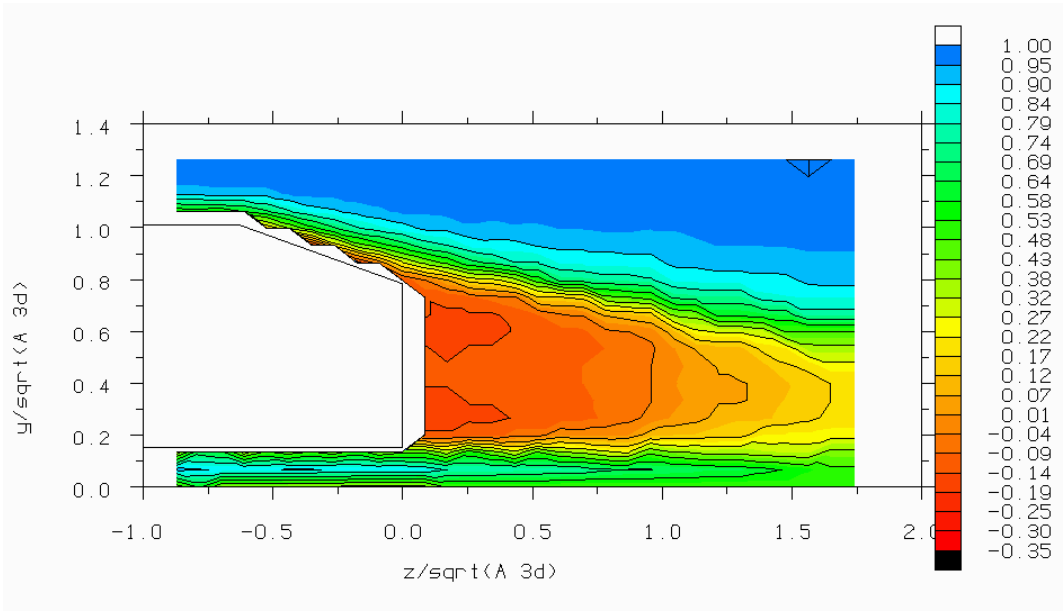

Figure 4.3.27 – Total pressure coefficient in the wake of the 2D Ahmed model with 20° backlight from steady CFD simulation with k-ε turbulence model

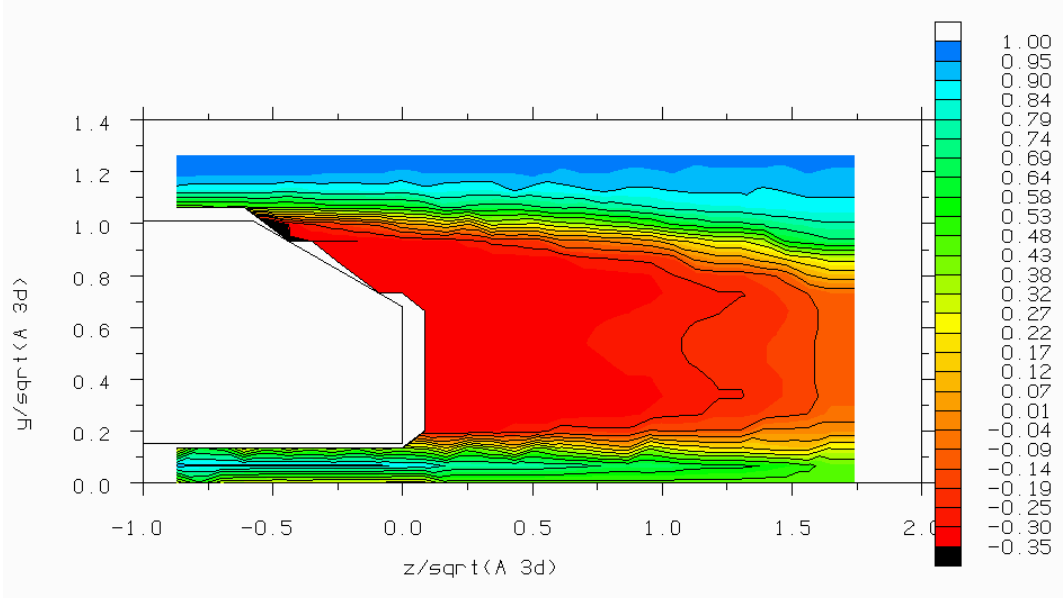

Figure 4.3.28 – Total pressure coefficient in the wake of the 2D Ahmed model with 30° backlight from steady CFD simulation with k-ε turbulence model

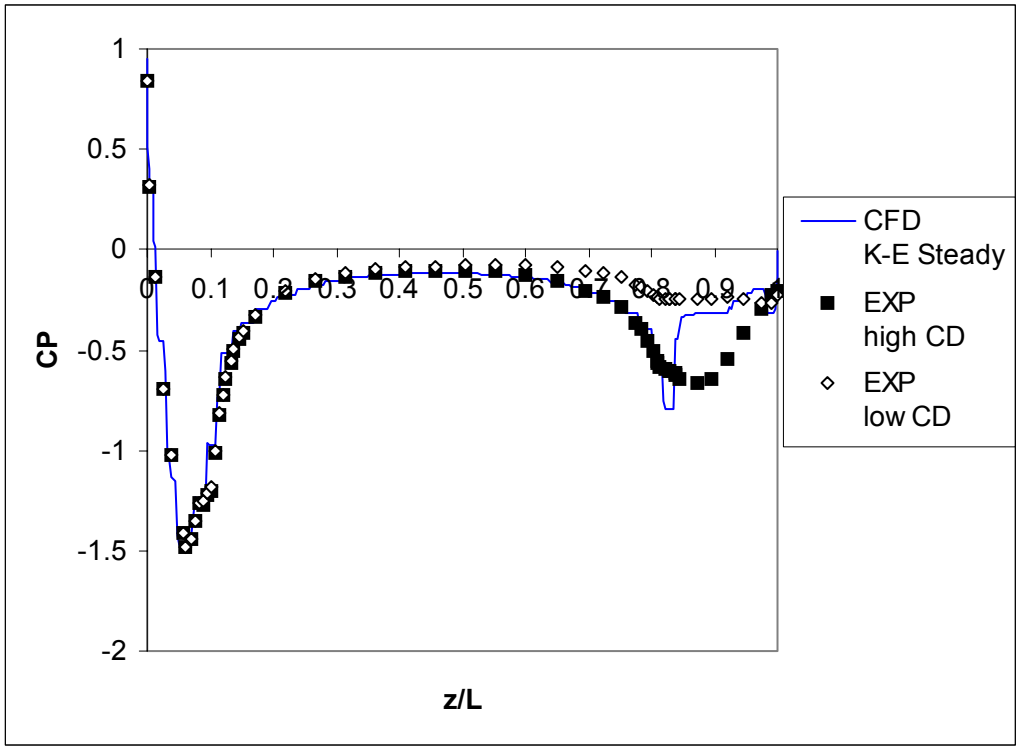

Figure 4.3.29 – 3D Ahmed model, 30° backlight, surface pressure distribution on the centreline; comparison between steady CFD simulation and experiment

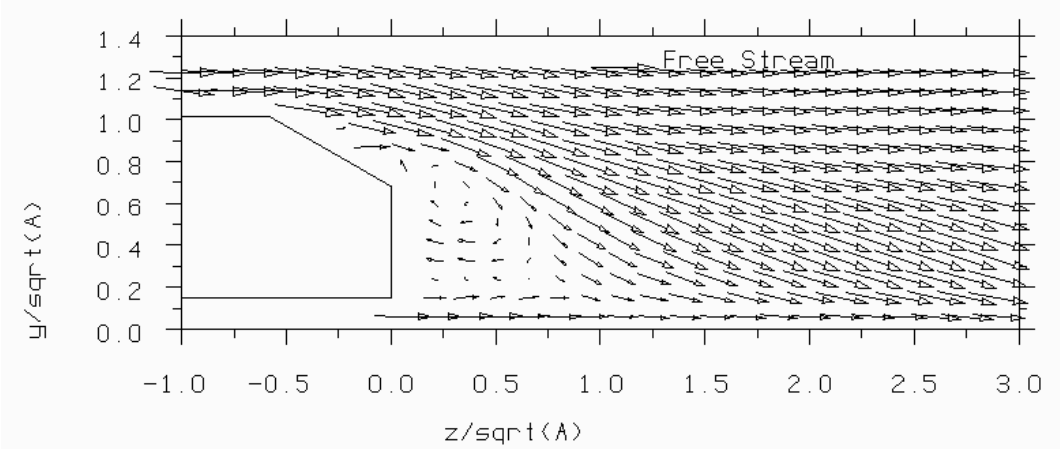

Figure 4.3.30 – Velocity vectors on the wake centreline of the 3D Ahmed model with 30° backlight from steady CFD simulation with k-ε turbulence model

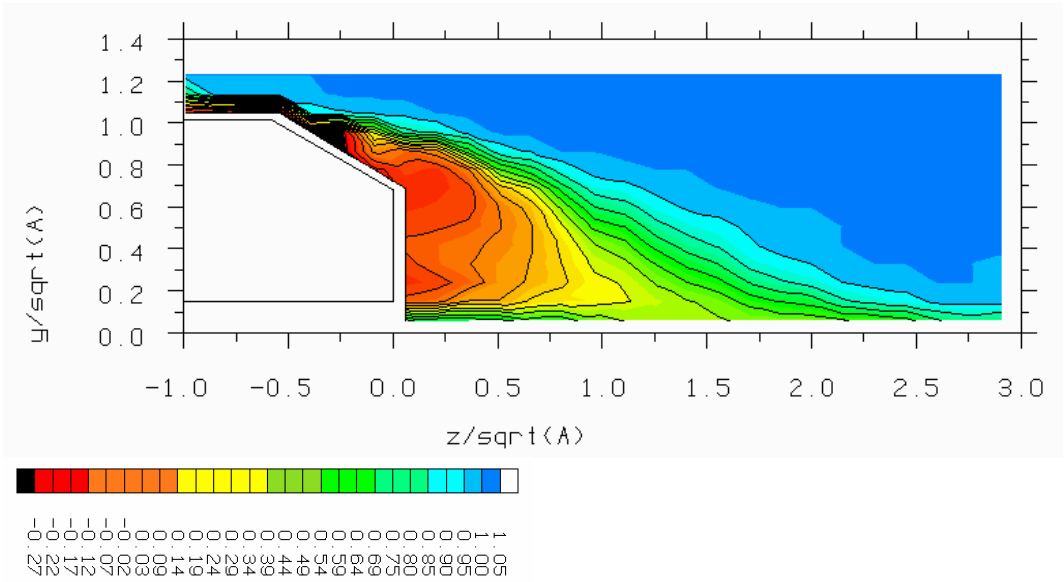

Figure 4.3.31 – Total pressure coefficient on the wake centreline of the 3D Ahmed model with 30° backlight from steady CFD simulation with k-ε turbulence model

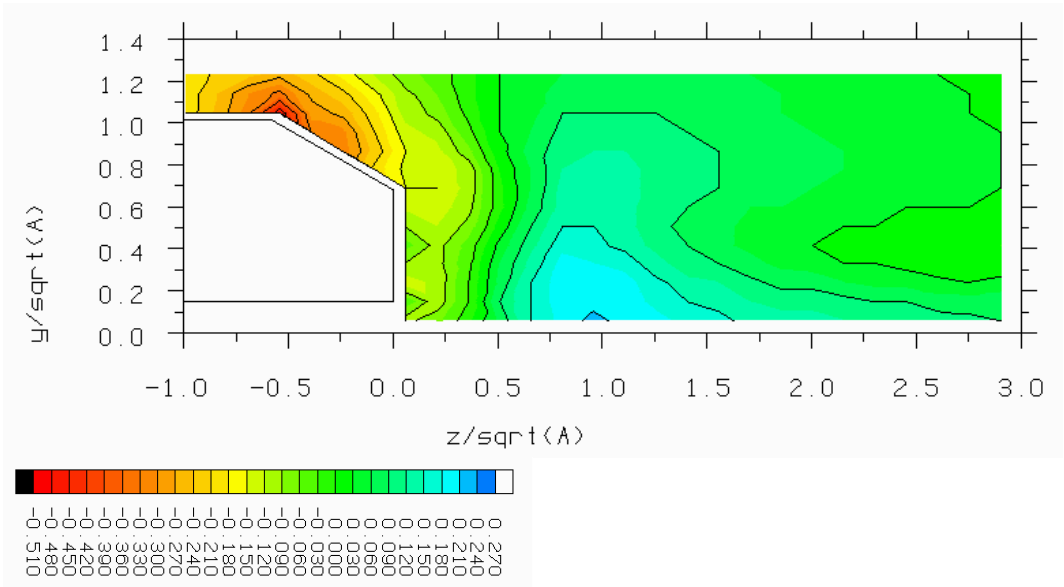

Figure 4.3.32 – Static pressure coefficient on the wake centreline of the 3D Ahmed model with 30° backlight from steady CFD simulation with k-ε turbulence model

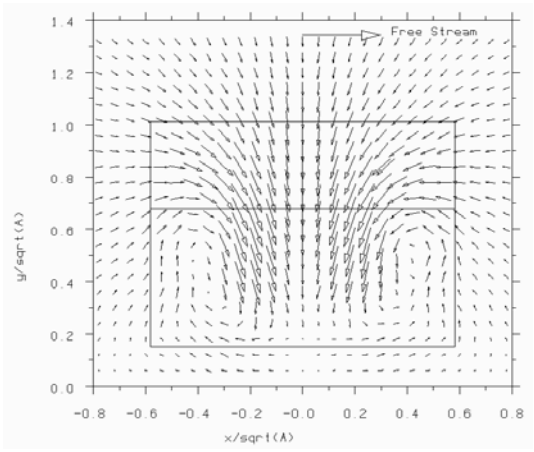

Figure 4.3.33a) z/sqrt(A) = 0.78

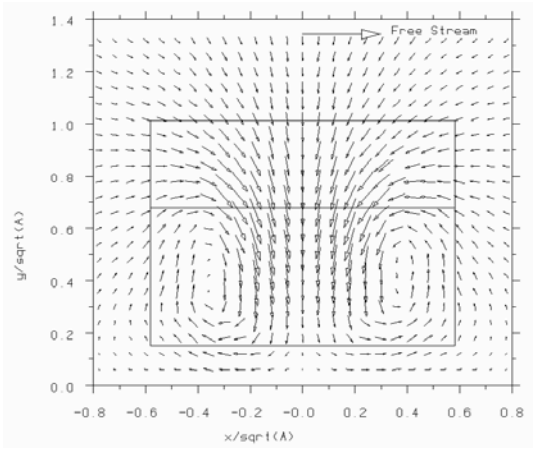

Figure 4.3.33b) z/sqrt(A) = 1.0

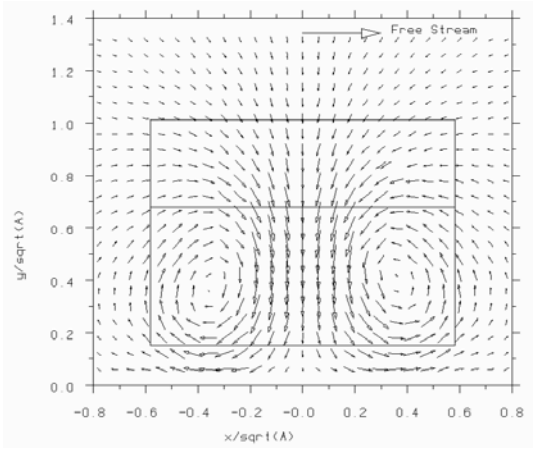

Figure 4.3.33c) z/sqrt(A) = 1.56

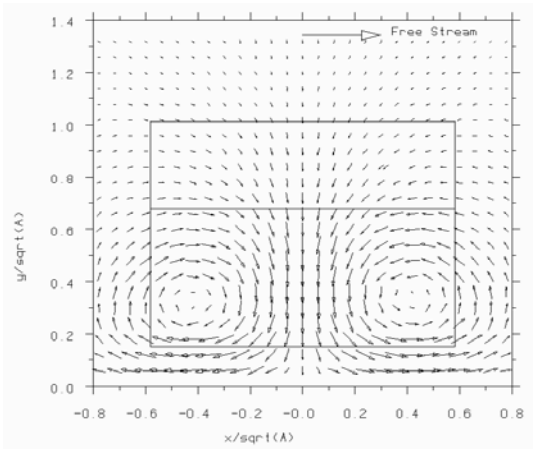

Figure 4.3.33d) z/sqrt(A) = 3.13

Figure 4.4.33 - Velocity vectors in the wake of the Ahmed model - 30° backlight – CFD simulation with k-ε turbulence model

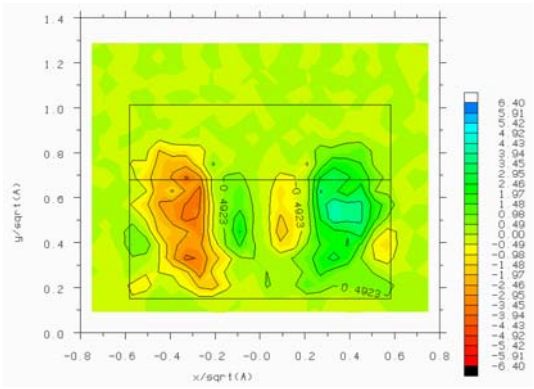

Figure 4.3.34a) z/sqrt(A) = 0.78

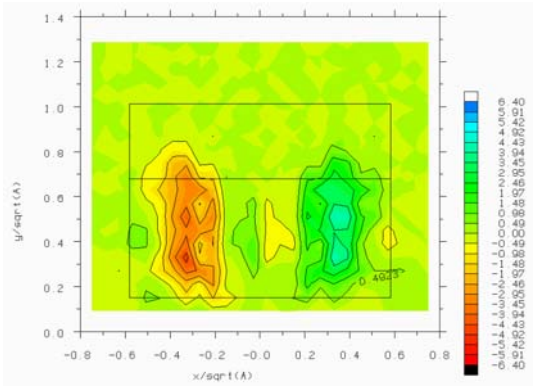

Figure 4.3.34b) z/sqrt(A) = 1.0

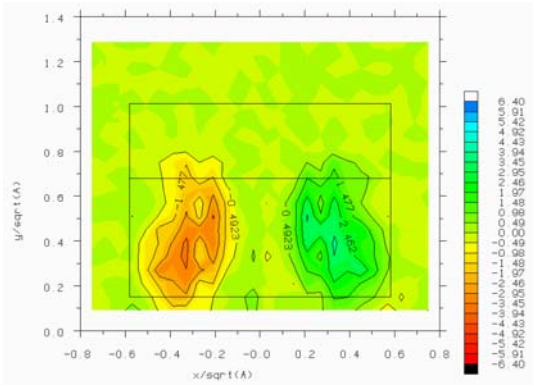

Figure 4.3.34c) z/sqrt(A) = 1.56

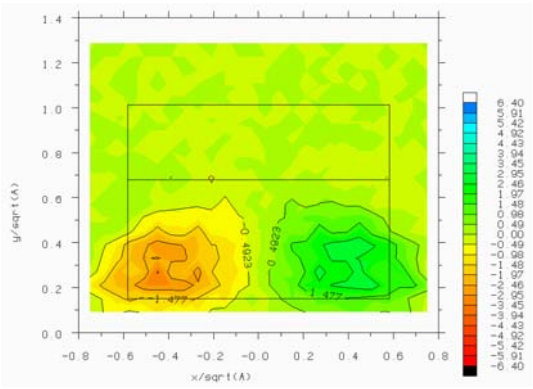

Figure 4.3.34d) z/sqrt(A) = 3.13

Figure 4.4.34 – Streamwise vorticity in the wake of the Ahmed model - 30° backlight – CFD simulation with k-ε turbulence model

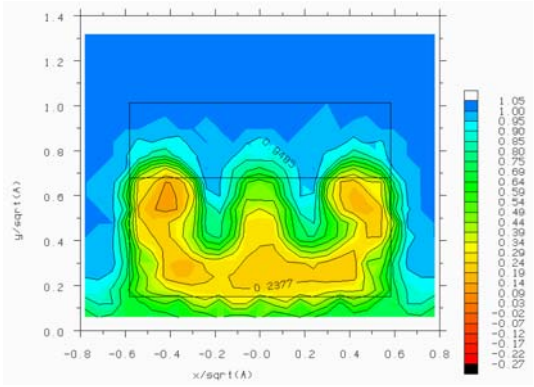

Figure 4.3.35a) z/sqrt(A) = 0.78

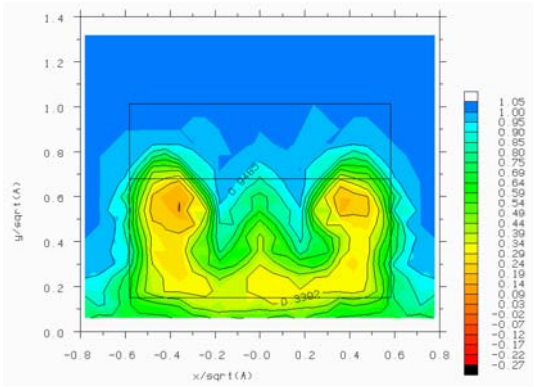

Figure 4.3.35b) z/sqrt(A) = 1.0

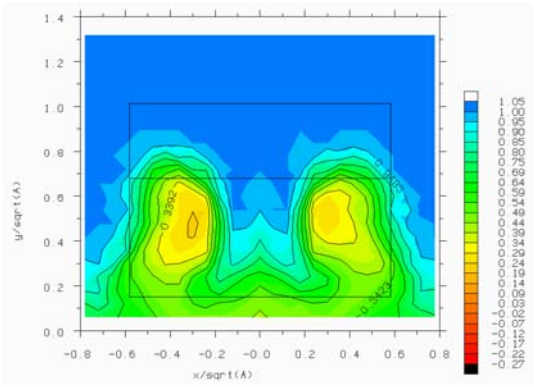

Figure 4.3.35c) z/sqrt(A) = 1.56

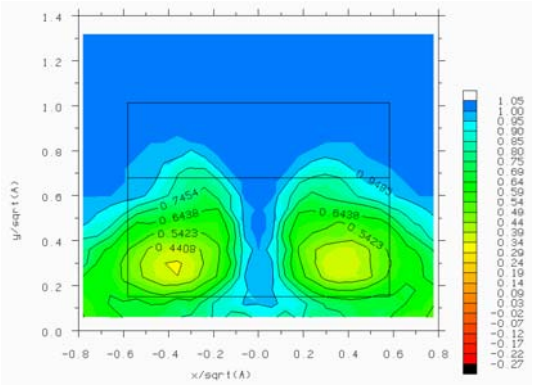

Figure 4.3.35d) z/sqrt(A) = 3.13

Figure 4.4.35 – Total pressure coefficient in the wake of the Ahmed model - 30° backlight – CFD simulation with k-ε turbulence model

FIGURES FOR CHAPTER 5 - DISCUSSION

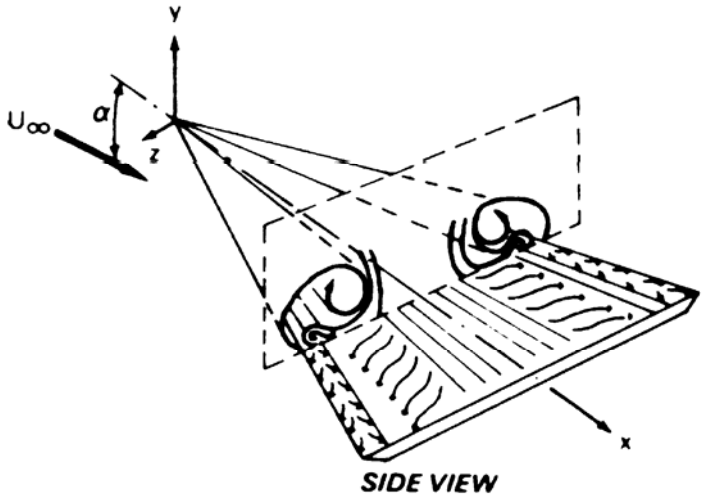

Figure 5.1.1 – Formation of trailing vortices for a delta wing showing secondary vortices outboard of main vortices (from Gad-el-Hak and Blackwelder (1985))

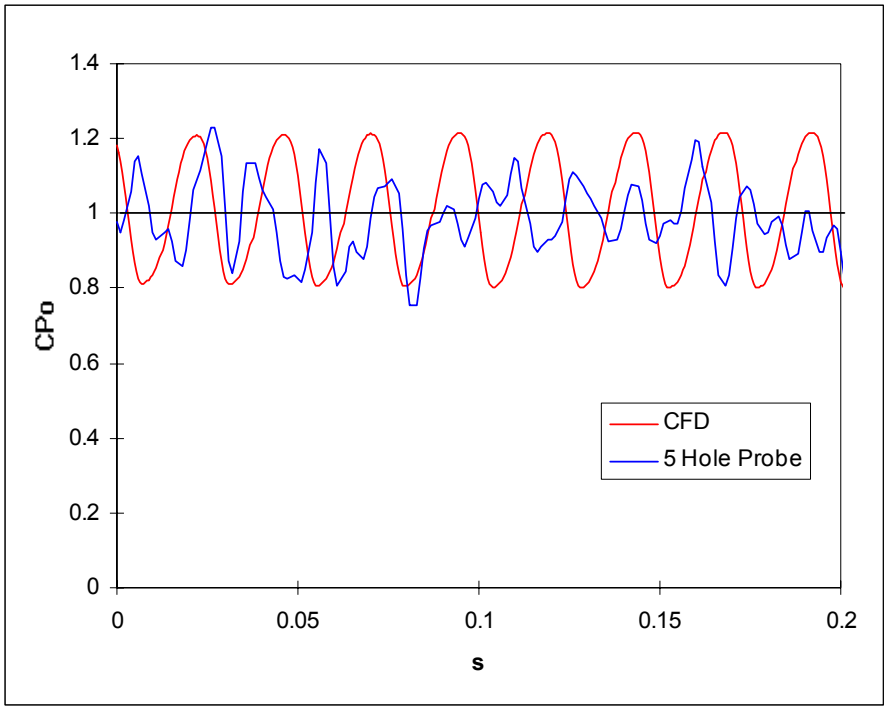

Figure 5.2.1 - Time traces of fluctuating total pressure coefficient adjacent to the wake of the PARAD1 model at x/W = 0.9, z/sqrt(A) = 2.0 from CFD and from a 5-hole probe with transfer function correction

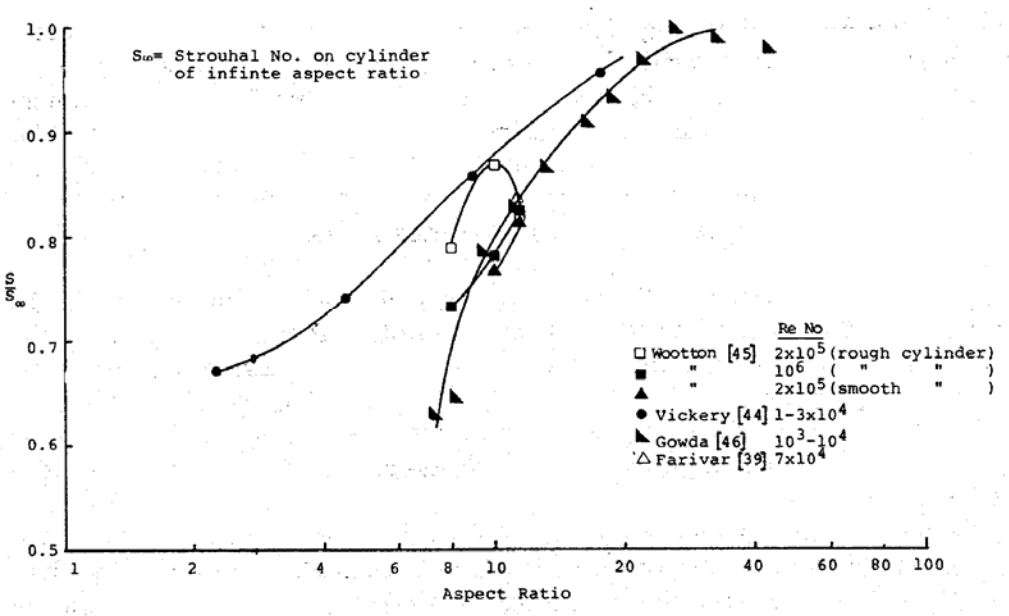

Figure 5.3.1 - Variation of Strouhal number with aspect ratio for circular cylinders (from Basu (1986))